KFA
Bilateral Seminars of the International Bureau
KERNFORSCHUNGSANLAGE JÜLICH GmbH

IXth
German-Yugoslav Meeting
on Materials Science
and Development

Emerging Materials by Advanced Processing

Edited by
Wolfgang A. Kaysser, Jutta Weber-Bock

Hirsau/Stuttgart
April 16–19, 1989

GERMAN-YUGOSLAV COOPERATION
IN SCIENTIFIC RESEARCH AND TECHNOLOGICAL DEVELOPMENT

GERMAN-YUGOSLAV COOPERATION
IN SCIENTIFIC RESEARCH AND TECHNOLOGICAL DEVELOPMENT

IXth GERMAN-YUGOSLAV MEETING ON MATERIALS SCIENCES AND DEVELOPMENT

EMERGING MATERIALS by ADVANCED PROCESSING

PRESENT AND FUTURE TRENDS
POWDERS: PRODUCTION AND PROCESSING
CONSOLIDATION
PROPERTIES
METALLIC LAYERS
PHASE DIAGRAMS

Organizer of the IXth Meeting:
Max-Planck-Institut für Metallforschung, Stuttgart

Participating Institutions:

Boris Kidrič Institute of Nuclear Sciences, Vinča/Belgrade
Institute Jožef Stefan, Ljubljana
Universities of Belgrade, Ljubljana, Skopje and Zagreb
University of Patras (GR)
Academy of Sciences and Arts of Bosnia and Herzegovina, Sarajevo
Serbian Academy of Sciences and Arts, Belgrade
Boris Kidrič Institute of Chemistry, Ljubljana
Energoinvest, Sarajevo

Kernforschungsanlage Jülich GmbH
Kernforschungszentrum Karlsruhe GmbH
Max Planck Institut für Metallforschung,
Institut für Werkstoffwissenschaften, Stuttgart
Universities of Aachen (RWTH), Hamburg (TUHH) and Karlsruhe

Herausgegeben von der Kernforschungsanlage Jülich GmbH
ZENTRALBIBLIOTHEK
Postfach 1913 · D-5170 Jülich
Telefon 02461/61-0 · Telex 833556-70 kfa d

Titelsatz: Graphische Betriebe der KFA

Druck: WEKA-Druck GmbH, Linnich

© KFA Jülich 1989

Jül-Conf-77
ISSN 0344-5798

ISBN 3-89336-026-3

OVERVIEW OF TABLE OF CONTENTS i

FOREWORD iii

WELCOME SPEECH vii

TABLE OF CONTENTS OF LECTURES xi

LECTURES

Present and Future Trends 1

Powders: Production and Processing 119

Consolidation 205

Properties 327

Metallic Layers 413

Phase Diagrams 479

LIST OF PARTICIPANTS 509

Foreword

The 9th German–Yugoslav Meeting on Materials Science and Development was held in Hirsau from April 16 to 19th, 1989 within the Governmental Agreement on Cultural and Scientific Cooperation of 1969 between the Socialist Federative Republic of Yugoslavia and the Federal Republic of Germany. In this frame several Agreements had been signed from mid to late seventies, i.e. the agreement between the Federal Administration for International Scientific, Educational, Cultural and Technical Cooperation (YUZAMS) in Belgrade and the Federal Ministry for Research and Technology (BMFT) in Bonn. Within this legal structure nine meetings on materials science and development have been held since April, 1975 to discuss scientific results of on–going bilateral cooperation projects in this area, and to pinpoint possible new areas of interest for future cooperation. The concentrated efforts in this discipline have made materials science one of the main pillars of German–Yugoslav bilateral cooperation. Organizers and participants are well aware that materials science is a key discipline for supporting developments in technologically–applied fields. These developments span the range from the design of novel materials with ascribed or defined properties for new applications (e.g. in computer engineering) on the one hand, to the fruitful impetus in traditional fields of research and development, on the other hand. The bilateral German–Yugoslav Cooperation has resulted in a considerable number of close contacts between research institutions and researchers in both countries. These contacts are also expected to serve as fruitful nuclei for multinational cooperation in programs of the European Community.

The 9th meeting in Hirsau had 43 participants in order to maintain the familiar atmosphere of a meeting in a workshop style which has proven successful for the Yugoslav–German Cooperation in the past. Two types of presentations, 15 or 30 min in length, were given. The shorter presentation was used mainly to report progress of on–going projects which were in an initial or intermediate stage of progress. In the longer type of presentations a number of review papers were given on subjects that have a direct impact on present and future projects. They were intended to provide a critical plenary introduction for the subsequent discussion, e.g. the future use of structural ceramics in the automotive industry. Longer presentations were also made on cooperation projects which have entered a final stage.

In respect to the topics and the spirit of the presentations It seems interesting to evaluate changes in the focus of materials sciences and cooperation in a time–perspective since the early days of the cooperation. For such a comparison, in particular a consideration of the differences between the 2nd and the present, 9th, meeting seems adequate. The 2nd German–Yugoslav meeting was held in Bled in 1976. Four main theme groups were represented in 23 papers. 15 papers were in German (partly delivered by Yugoslavian researchers) and 8 papers in English. The 36 papers presented at the 9th meeting in Hirsau were all given in English, an obvious step toward the internationalization of the bilateral cooperation. The presentations at the 2nd meeting in Bled had been divided into four categories: hard materials, sintering, special materials and spectroscopy. At the Hirsau meeting no reports were offered on the classical hard material. The former emphasis on sintering was replaced by a number of recently developed consolidation techniques, such as HIP, sinter–HIP and the Lanxide process. In Bled most of the functional and structural ceramics were still found under the blanket of "special materials". At that time the relation between presentations on metallic materials (including metal bonded hard materials), functional ceramics and structural ceramics (including glass) was 3 : 1 : 2. Thirteen years later, the Hirsau meeting showed a ratio of 3 : 2 : 9. What a change! Structural ceramics have become the focus of attention during the last ten years, a fact which is clearly reflected in the project topics of the German–Yugoslav Cooperation. The 9th meeting at Hirsau revealed a slightly stronger emphasis on structural ceramics on the German side, whereas functional ceramics remained a strong domain of Yugoslavian research. This fact appears to reflect the slightly different governmental and industrial funding policies in the two countries. The subjects dealt with at the Hirsau meeting were grouped as follows:

Present and Future Trends (5 review lectures)
Powders: Production and Processing (8 lectures)
Consolidation (8 lectures)
Properties (7 lectures)
Metallic Layers (5 lectures)
Phase Diagrams (3 lectures)

The grouping reflects the present trend toward processing new high–tech materials with the generic methods used in powder metallurgy or in the production of ceramics. More than 60% of the papers were concerned with processing, i.e. the route from powder or layer production to the final consolidation step.

It is expected that in future still more projects will be concerned with powder preparation and processing. Clean room and ultra clean room conditions are expected to be crucial to the production of the future class of high performance metallic, ceramic and composite materials. Materials Scientists will increasingly accept that the most required property combinations such as high thermal strength, creep resistance and satisfying toughness at low temperatures are not achievable by monolithic materials but may require taylored composite microstructures. Many of the advanced materials such as intermetallics, ceramic and metal matrix composites suffer from a low fracture toughness. New micromechanics models of composite toughening may therefore become an important subject of our future research. The multiphase composites are far from equilibrium, hence detrimental chemical reactions between the different phases, in particular between the reinforcement and the matrix, can rapidly degrade the strength of the composites. Attempts to solve those problems include research of variations of processing parameters and the coating of the reinforcing phases. Institutes of organic and anorganic chemistry will be more strongly involved in further materials science research and development than now. Annother major research effort could become the prediction of phase instabilities at the large number of nonequilibrium heterophase boundaries in composites or particulate reinforced materials. An untroubled successful development is expected for functional ceramics for electronic and optical applications. As far as we can see today, structural ceramics still encounter major problems, due to their present inadequate reliability. Improved powder production from organic precursor and revised processing (e.g. handling in clean rooms, agglomeration by freeze drying) are likely to solve part of these problems. The majority of the Materials Science Research facilities cooperating in the framework of the bilateral German–Yugoslav Agreement on Cultural and Scientific Cooperation appear to be well prepared for research on these upcoming tasks.

The next Meeting on Materials Science and Development will be held in Belgrade 1991. The mandate to initiate the organization of the 'jubilee' Xth Conference was given to Dr.Branko Djurić of Institute Boris Kidrič, Belgrade. We wish him and his coworkers the upmost success in preparing the Xth Meeting.

These proceedings contain papers on the lectures presented at the 9th German–Yugoslav meeting in Hirsau in April, 1989. They are mostly original scientific papers which were compiled by Dr. Wolfgang Kaysser and Jutta Weber–Bock from the Max–Planck–Institute for Metals Research in Stuttgart, with the purpose of making the interesting results of the cooperation available to the public. The scientific content of the submitted papers has been left unchanged, and the responsibility for it is the authors'.

The organizers, Dr. W.A. Kaysser, Dr. K.G. Nickel and J. Weber–Bock would like to thank Rainhard Laag for his assistance with the organization and Hans Ullrich, the hotelier and "chef du cuisine", for being a perfect host in the beautiful setting of "Hotel Kloster Hirsau". We are also thankful for the financial support by the International Bureau of the KFA Jülich, which made this meeting possible. Special thanks from the organizers and all participants are due to Dr. Johanna Krawczynski of KFA Jülich, who was the warm–hearted good spirit of the meeting. She provided dynamic organizational assistance and set the stage for the interdisciplinary purpose of the meeting with her introductory lecture.

Stuttgart, July 1989

Dr. W.A. Kaysser

Welcome Speech

by
Günter Petzow
Max-Planck-Institut für Metallforschung
Institut für Werkstoffwissenschaft, PML
Stuttgart

I would like to welcome you to the IX. German-Yugoslav Meeting on Materials Science and Development. It is a great pleasure for me to welcome our Yugoslavian friends - some of whom are with us from the very beginning and belong to the founders of these meetings: first and foremost Drago Kolar, Branko Djurić, Dragan Uskoković and Ivan Stamenković. I also welcome those of you who are here for the first time, and on whom we pin our hope for future success of the cooperation. It is also my pleasure to welcome all participants from Germany, some of whom I get to meet less frequently than I do meet with the Yugoslavian Colleagues. Everyone of us is glad that Dr. Johanna Krawczynski is here with us. She is our patron saint and helped us in many occasions in word and deed, with personal charm and financial infusions. A special welcome to you, Johanna. His Excellency, the Yugoslavian Ambassador, Dr. Dragovič, who wanted to give a welcome address today, unfortunately had to attend to urgent business on short notice. We appreciate his good intentions and hope he can join us next time. The same happened to Prof. Ristić and that is also really unfortunate.

For a long time, the contacts between Yugoslavian and German scientists have been direct and intense and fruitful for the scientific community of both countries. It was only in 1971 that the scientific cooperation was officially approved on a governmental level in order to give some support and assistance to these mostly private and individual initiatives. Within the scope of this bilateral cooperation, the field of materials science soon assumed a priority position. Different groups in both countries started research programs and joint projects. The results became so multiple that it was felt that all partners should meet regularly in order to report on their latest findings and on the progress of work. Under these aspects, the first meeting was held in Karlsruhe in 1975, organized by Prof. Thümmler. Since then the meetings have been held regularly either in Yugoslavia or Germany. Today we may speak already of a "tradition", which has proved its meaningfulness by its success. The meetings provide the frame for reports on research work which has been performed in institutes and by scientists of the two countries.

The last meeting took place in Brdo in beautiful Slovenia. This time it is again the the black forest as it has already been before several times. But it is the first time in this special place here in Hirsau, which appeared to be an ideal conference location to us and

hopefully will fulfill our expectations. There are some parallels between Brdo and Hirsau. Both places are beautiful, foggy and rainy. But while Brdo is a very recent and modern place - it was one of the residences of Tito - Hirsau developed from a medieval monastery. As you see from the descriptions among your meeting materials, we are here in a very traditional house, the beginning of which reaches as far back as to the 11th century. Many famous people lived here before us, including the great German poet Hermann Hesse who wrote parts of his book "The Glass Bead Game" in this house. From the point of view of a materials scientist the glass bead game might be interpreted a laudation of the encompassing philosophy of materials science; or on an even larger scale, a laudation on the complete interdisciplinary of all natural sciences, humanity and arts. This idea is expressed especially powerful by the following passage from "The Glass Bead Game" where Josef Knecht von Berolfingen, a student of the elite school of Kastalien, a land of fantasia, explains to his master teacher "Oh, if we only would be able to become knowing! If there would be a theory! Something we could believe in! Everything is contradictory, nothing fits together! Certainty is nowhere! Everything can be interpreted one way and then again the other way! The entire world history can be made to look like decay and nonsense just as well! Is there no truth? Is there no true and valid theory? The master who never had heard him talk with such vehemence answered: "There is the truth, my dear! But the theory that you want, the absolute, the perfect and only wisdom-bringing, does not exist. You should not be searching for the perfect theory my friend, but for the perfection of yourself."

Ladies and Gentlemen, I would like to leave these thoughts of Hermann Hesse completely to your own conclusions. But in some way there are some parallels to science, especially the science of sintering. Our program is truly interdisciplinary. The interaction of the disciplines on the one hand and the participating institutions from so many places on the other hand is entirely within that spirit of "The Glass Bead Game".

When we were sitting together after the last meeting in Brdo 1987, our discussion clearly showed that a reduction in size of the German-Yugoslav meeting had become a necessity. Most of you will remember the equally familiar and scientifically fruitful character of the early meetings. Cooperation in the essentially bilateral frame is based on the individual personal contacts, which naturally require this type of meeting atmosphere. Hence we tried this time in Hirsau to limit the number of participants. This automatically gave us the chance to reduce the duration of the technical program to two and a half days. We feel this an acceptable time period, since all of us are heavily involved in other time-consuming responsibilities.

The program is divided into the main topics: Present and Future Trends, Powders: Production and Processing, Consolidation, Properties, Metallic Layers and Phase Diagrams. We have strong emphasis on processing which is also a major concern of present international materials science activities. Its importance is also reflected in the subtitle of our meeting "Emerging Materials by Advanced Processing".

I would like to sincerely thank the organizers for their intricate work during the preparation of this meeting, first and foremost Wolfgang Kaysser, Klaus Nickel and Jutta Weber-Bock. They put together a promising program. The design on the title page of the program must not be misunderstood: There is no deeper meaning that only Belgrade, Stuttgart and Ljubljana appear horizontally, straight and readable. Skopje and Patras are clearly tilted and Karlsruhe, Aachen and Hamburg even appear upside down.

Despite the relaxed atmosphere of friendship and familiarity we have approximately 35 presentations ahead of us. Therefore I will stop here, wishing us all a successful meeting and a pleasant personal time in Hirsau.

TABLE OF CONTENTS OF LECTURES

Present and Future Trends 1

J. Krawczynski 3
International Cooperation in Science and Technology:
The Perfect One-Way Street to "Splendid Isolation"?

W.A. Kaysser 39
Horizons of Powder Metallurgy

D. Kolar 77
The Future of Ceramics

M.M. Ristić, P. Kostić 93
Materials Science - The Base of Progress in New Electronics

R.J. Brook 111
The Optimization of Powders for Use in Sintering

Powders: Production and Processing 119

D.P. Uskoković 121
Advances in Powder Preparation and Processing of Emerging Materials

M. Gašić, G. Ondracek, I. Stamenković 125
Densification of Highly Reactive Aluminium Titanate Powders

I. Stamenković, J. Bossert, G. Ondracek, W. Stumpfe 135
High-Tech Aluminium Titanate Ceramics

D. Spaseska 149
Influence of Precursor Prehistory on Carbon Fibre Characteristics

T. Kosmač, V. Kraševec, R. Gopalakrishnan 161
Influence of Water Removal Rate During Calcination on the Crystallization of ZrO_2 from Amorphous Hydrous Precipitates

T. Claaßen, C. Nischik, P. Greil 177
Tape Casting and Sintering of AlN

V.M. Kevorkijan, M. Komac, D. Kolar, A. Šmalc, J. Rottmann 187
Influence of Processing on the Properties of β-SiC Powders

R. Förthmann, E. Grübmeier, V.M. Kevorkijan, A. Naoumidis 197
Corrosion of SiSiC by Gases and Basic Slag at High Temperature

Consolidation 205

M. Mitkov, W.A. Kaysser 207
Influence of Sintering and Thermomechanical Treatment on Microstructure and Properties of W-Ni-Fe Alloys

A. Fetahagić, C. Gutsfeld, F. Thümmler 221
Mechanical Alloying for Development of Sintered Steels with High Hard Phase Content

M. Stubičar, D. Dužević 237
Early Stages of Mechanical Alloying in Ni-Ti and Ni-Al Powder Mixtures

M. Sindel, N. Claussen 251
Growth and Microstructural Development of Melt-Oxidation Derived Al_2O_3/Al - Base Composites

R. Janssen, N. Claussen 261
Fabrication of RBSN Composites

O. Seide, W. Krönert 283
Synthesis of High Density Cordierite Bodies

R. Oberacker, A. Kühne, F. Thümmler 297
Comparative Studies on Post-HIP and Sinter-HIP Treatments on Transformation Toughened Ceramics

T. Fetahagić, R. Oberacker, F. Thümmler 313
Process Development for Sinter-HIPing of SiC

Properties 327

W. Oroschin, M. Kulig, P. Greil 329
Precipitation Mixing of Silicon Nitride with Bimetallic Oxides

G. Angelopoulos, S. Agathopoulos, P. Nikolopoulos 349
Temperature Dependence of the Interfacial Energies in Al_2O_3-Liquid Metal Systems

M. Čeh, D. Kolar 359
Synthesis and Microstructural Examination of Synroc B

U. Jauch, G. Ondracek 369
Solid State Investigation of Ceramic-Metal Interface Bonding

B. Schulz, G. Haase 383
Thermophysical Properties of $MgAl_2O_4$

M. Miloševski, B. Bliznakovska 393
Preparation, Sintering and Thermal Expansion of $MgAl_2O_4$

S. Bratović, J. Derviškadić, B. Djuričić, M. Jamakosmanović, M. Mulalić, M. Trubelja 407
Microstructural Studies on Alumina-Zirconia and Metallized Alumina Ceramics

Metallic Layers 413

B. Popov 415
Electrodeposition of Metals and Metal Oxides from Molten Salts

B. Popov, J.B. Wagner Jr., H. Wendt, Z. Koneska 427
Electrodeposition of Titanium from Molten Salts

Z. Koneska, B. Popov, G. Jovanovski 447
Electrochemical Deposition of Titanium from Nonaqueous Media

S. Pejovnik, M. Gaberšček, J. Jamnik, D. Metelko 455
Metallic Lithium as Anode Material in Power Sources

D. Slavkov, B. Popov, Z. Koneska 467
Reduction of Chromium (VI) when Solar Selective Black Chromium is Deposited

Phase Diagrams 479

H.L. Lukas, R. Novaković 481
Thermodynamic Optimization of Phase Diagrams

R. Novaković, G. Gosh, H.L. Lukas, M.M. Ristić 491
Optimization of the Na-Tl System

S. Bošković, K.G. Nickel, G. Petzow 499
Phase Relations in the Y-Si-Al-O-N System: Controlled Manufacturing of α/β-SiAlON Composites

Participants of the IX. German–Yugoslav Meeting on Materials Sciences and Development in front of the remains of the medieval monastry of Hirsau

Some Speakers and their Auditorium

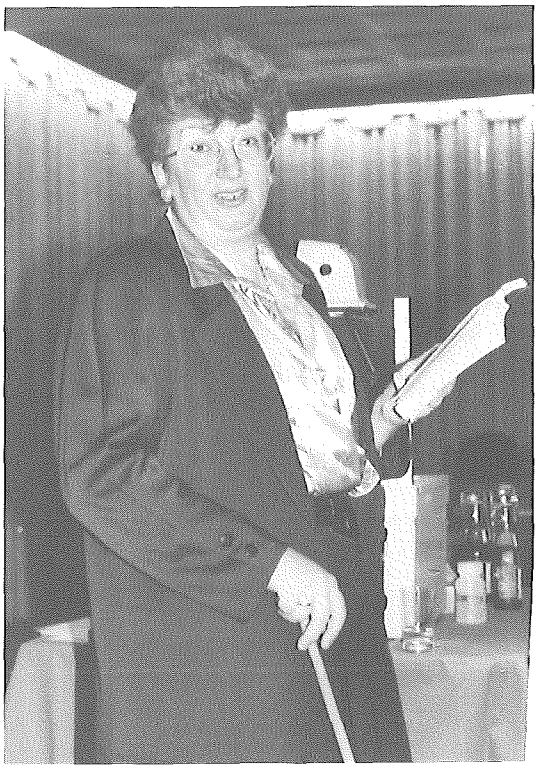

Dr. J. Krawczynski
citing Hermann Hesse
during her plenary lecture

Prof. Dr. G. Petzow at his
official welcome speech

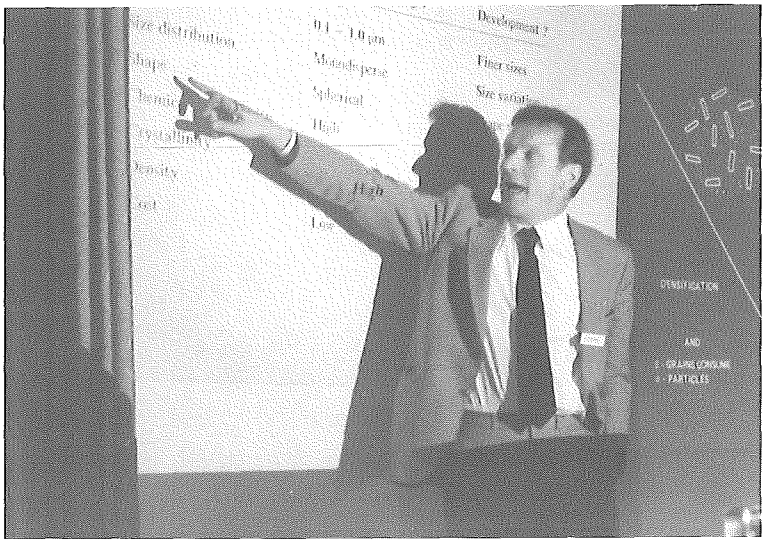

Prof. Dr. R.J. Brook giving
one of his famous perspicuous
presentations

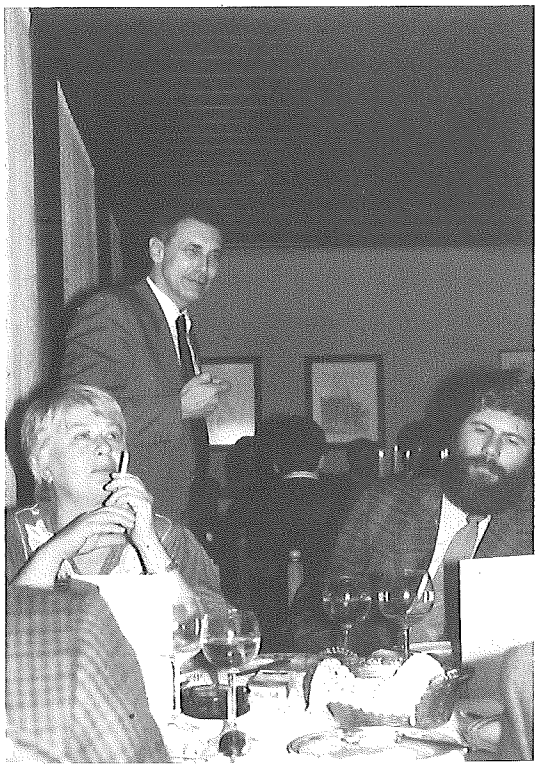

Prof. Dr. D. Kolar at his "inofficial" dinner speech, Dr. B. Schulz and J. Bossert in front

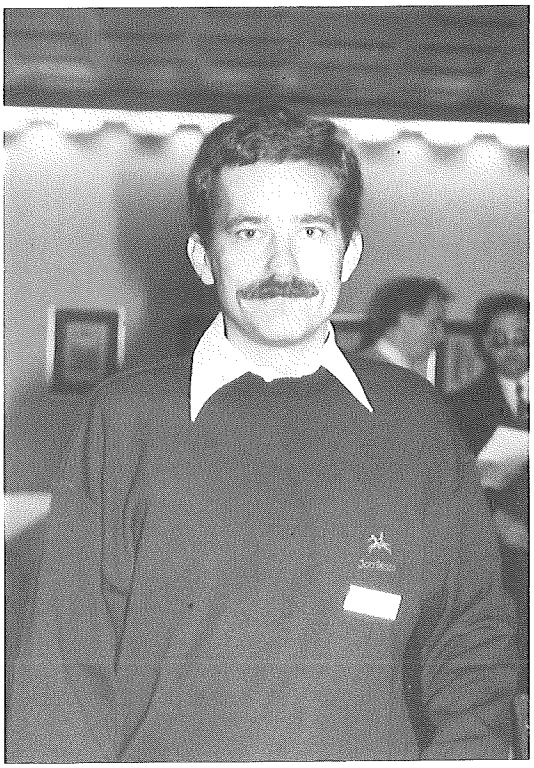

The young Prof. Dr. P. Greil surprinsing the auditorium with new methods of precipitation mixing.

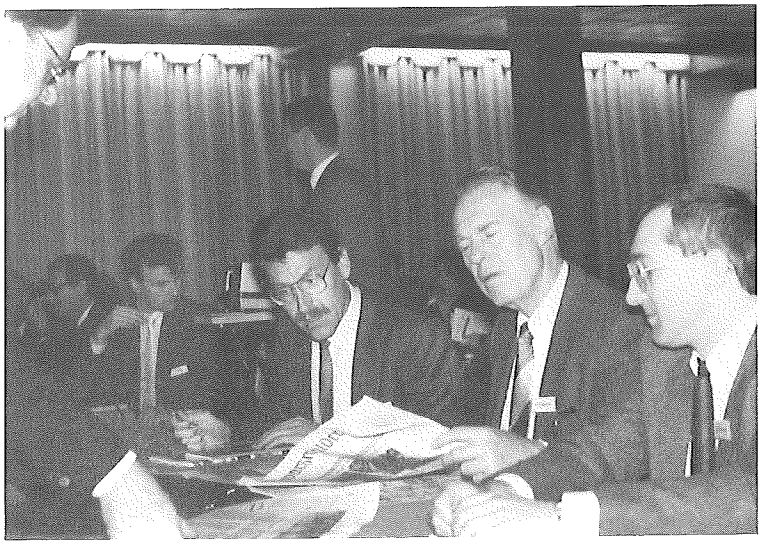

The critical auditorium during a coffee break, Dr. W.A. Kaysser, Prof. Dr. F. Thümmler and Dr. R. Oberacker

Dr. M. Mitkov explaining the details of the micro-structural development in W-Ni-Fe.

Wetting or Non-Wetting? Dr. G. Angelopoulos gives the answer.

The last presentation was given by Dr. K.G. Nickel. Materials Development on the basis of five component systems – a glimpse of the future!

Prof. Dr. S. Pejovnik, specialist on materials for power sources and on bowling.

Bilateral conversation at the reception. Dr. B. Djurić, Dr. J. Krawczynski and M.Sc. T. Fetahagić (r. to l.)

Prof. Dr. B.N. Popov during his excursion through the world of electrodeposition.

M.Sc. R. Novaković talking on her phase diagram calculations.

The future of composites – Prof. Dr. G. Ondracek gave a critical outlook.

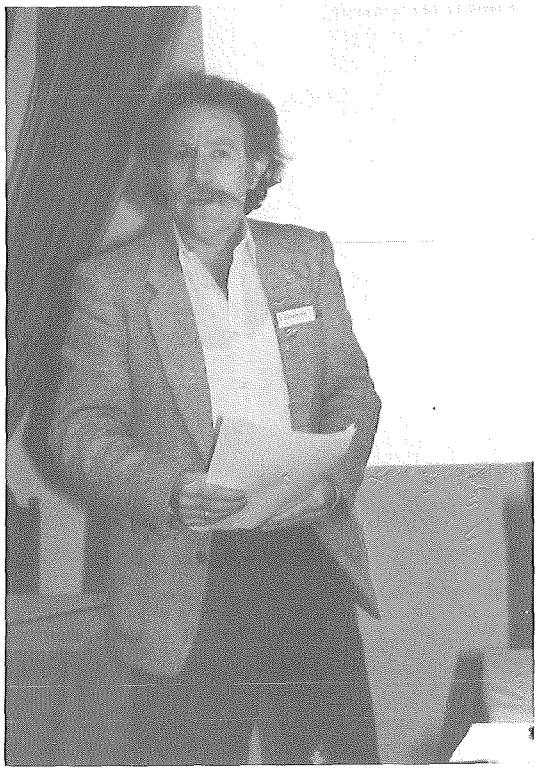

Dr. A. Naoumidis presenting a critical issue on corrosion of SiSiC.

Dr. T. Kosmač reported on ZrO_2 powder preparation.

Prof. Dr. D. Uskoković talking on powder properties and processing.

Dr. H.L. Lukas leading through the secrets of his phase diagram calculation program.

PRESENT AND FUTURE TRENDS

INTERNATIONAL COOPERATION IN SCIENCE AND TECHNOLOGY:

THE PERFECT ONE-WAY STREET TO "SPLENDID ISOLATION" ?

Johanna Krawczynski

International Bureau of KFA Jülich

1. The IXth German-Yugoslav Meeting on
   Materials Sciences and Development

2. International Environment and R & D :
   "Industrial Policy" and "Competitiveness"
   as Framework Conditions

3. Higher, Farther, Quicker - An Unfair
   Comparison between Olympic Games and World Market ?

4. International Cooperation in Science and Technology:
   The Perfect One-Way Street to "Splendid Isolation" ?

1. The IXth German-Yugoslav Meeting on Materials Sciences and Development

The IXth German-Yugoslav Meeting on Materials Sciences and Development from April 16-19, 1989 takes place in the year where will also be commemorated the 20th Anniversary of the Governmental Agreement of 1969 (1), by which scientific and technological cooperation between the Federal Republic of Germany and Yugoslavia was formally installed. This umbrella agreement and the following agreements between BMFT and YUZAMS, KFA and YUZAMS and KFA and the Research Community of Slovenia (2) have since then sheltered a great number of initiatives from their initial stages of negotiating concrete issues of mutual interest until pragmatic pinpointing of working steps and sharing of work load, and have thus provided adequate framework conditions for the ensuing project work.

Among the instruments of bilateral cooperation, the joint seminars assert their own specific importance (next to project activities proper, exchange of scientists, and on the job training), and the biannual German-Yugoslav Meetings on Materials Sciences and Development rank among the most vivid and important seminars. No doubt, the history of these Meetings will be reviewed on the occasion of the Xth Anniversary Meeting in 1991, from their early beginnings as small circles of personal and professional encounter until their present sophistication - mirroring the development of the participating institutions, their increasing number, the widening of their scope and the increasing complexity of the subject matter they are dealing with.
What has not changed, however, is that the Materials Meetings continue to be a forum of discussion and of friendship between German and Yugoslav scientists and also between generations, of women and men, for whom the "ceramic fever" is not a short-time amusement, but a life-long challenge.

Over the years the Federal Ministry for Research and Technology of the Federal Republic of Germany (BMFT) has, on the German side, funded and supported scientific and technological projects with

Yugoslavia, among which are not only such pertaining to materials sciences, but also activities in many other fields like basic and environmental research, energy research, R & D for health, biotechnology, basic research in informatics, and engineering sciences. The assistance given to our work by the Managing Board of Directors of KFA is unconditional. On the Yugoslav side YUZAMS as well as the Republican and Self Management Interest Communities for International Cooperation and for Science and Technology have contributed to the results achieved. A great number of scientific institutions both in Germany and in Yugoslavia have, with skill and perseverance, engaged in the daily endeavours of bringing to life, on a noteworthy scientific level, the intention of the agreements.

So the IXth GER-YU Materials Meeting may well be considered as the prelude of the reflections on past achievements and future plans and possibilities of our cooperation which accompany the celebration of the 20th Anniversary of the German-Yugoslav Government Agreement.

For the excellent preparation and organisation of the Meeting we are indebted to the Institut fuer Werkstoffwissenschaften, Pulvermetallurgisches Laboratorium, of the Max-Planck-Institut fuer Metallforschung in Stuttgart, to its Directors Professor Dr. Guenter Petzow and Professor Dr.R. Brook, as well as to Mrs. Jutta Weber-Bock, Dr. Wolfgang Kaysser, Dipl. Ing. Rainhard Laag, and Dr. Klaus Nickel.

Also materials sciences as one of the core key-technologies of the "IBM" (Informatics, Biotechnology, Materials) range are embedded in the socio-economic environment which determines both the behaviour of national states as actors on the international scene and which sets the margin for institutional and individual actions.
Therefore, in the following essay some features of present-day framework conditions also for our work will be discussed. The

statements are not necessarily those held by official German agencies, and, as they are of course subjective especially with regard to conclusions drawn from them, the responsibility for the present contribution is entirely with the author.

2. International Environment and R & D : "Industrial Policy" and "Competitiveness" as Framework Conditions

Established trade giants like the United States and Japan, a regional colossus like the European Community with its perspective of a single "domestic" (internal) Common Market by the end of 1992, the Eastern European countries under the new "perestroika" élan, the so-called NIC (Newly Industrialized Countries, as f.i. South Korea) and the threshold countries, all are rivalling in the aim to achieve economic growth by increasing their industrial strength and are hence promoting technological development, investing in industry build-up and engaging in the struggle for international market shares for their manufactured products. The Chairman of the US Congressional Technology Policy Task Force, Mr. Kenneth MacKay, expressed as his opinion that competition in the economic arena over the next two or three decades is going to assume the same importance that military competition did in the past three decades (Weinrib, 1988, p. 37).

The "rise of techno-nationalism" (Robert Reich, Harvard University, quoted by Johnstone, 1988, p. 58) can mirror justified fear and result in an impetus for dynamic domestic change, but it can also be exploited to the detriment of international cooperation, of joint ventures, and of global exchange of information in the scientific community. Consequently, such nationalism can lead to the withdrawal of foreign companies, to changes of funding modalities and to restrictions of possibilities of university teaching, training and conference-attending for foreign scientists, whereby political pressures and reproaches concerning threats to national security range among the more

serious implications.

Structurally, there are at least two notions by which these developments can be characterized and analyzed: that of "industrial policy" and that of "competitiveness" (3).

By government policies of support for industrial development and R & D aiming at a technological lead, the ability for a country to compete on the world market is raised. Paradoxically, although from a point of view of capitalistic free market ideology in this way a liberal exchange of goods should result, on the contrary rather protectionism is fostered, each nation for its own economy striving after comparative advantages at almost any price - be it with regard to development of innovations and advanced methods of production; with regard to sophistication and quality of manufactured goods, or to the use of processes optimized according to different parameters (raw materials, energy saving). Those countries trying to minimize manufacturing and environmental risks and refusing to take into account also global catastrophes, are likely to sooner fall behind in this competitive race than those who do not, or than those who (still) have to live by the yield of mere quantities of raw materials or of agricultural products.

Turning first to the notion of "industrial policy", governmental concern and interference of any kind over the economy in the broadest sense, including science and technology policy, have been considered, from a point of view of free market principles, as a failure of the market itself, a "failure in the allocation of resources" (Komiya, Okuno and Suzumura, 1984). Policies coping with such market failure are "industrial policies". By definition, they are governmental policies not only supplementing the market in the face of failure, but also facilitating its performance in the long run - including such far-reaching elements as "measures to deal with externalities, to combat anti-competitive structures and conduct, to promote economies of scale, to foster infant industries, to provide for basic research and development and to eliminate uncertainty in industrial development" (Matsushita, 1987, p. 542/3). In a global comparison, Japan has undertaken the most systematic approach in deliberatedly establishing such an industrial policy framework "in order to become a technology-

intensive, export-dominant powerhouse" (Cannon, 1987, p. 504).

The Japanese Ministry of International Trade and Industry (MITI) has initiated Japan's strong position on the world market by an extensively ranged industrial policy of support for new industries, promotion of R & D, adjustment assistance for declining industries, modernization of small enterprises, and protection for specific producer groups. In order to meet with structural requirements of finding new jobs, perform re-orientations for industrial workers, curb or even prevent unemployment, and planning regional adjustments, existing policies have been adapted to these more general objectives (Sekiguchi/Horiuchi, 1985, pp. 381-387).

A step by step approach was started by Japan in the 1950's and lasts until today. It consisted of the strategy first to facilitate the importation of technology, then to promote domestic R & D (including policy measures to encourage R & D in private firms like tax breaks, subsidies and research contracts). Thirdly, in the seventies, public policy became more selective and R & D on pollution control, energy, space and ocean resources was encouraged, whereas currently the policy discussion is centered around the problem of how to enhance Japan's technology base in basic technologies in order to promote a shift to high-technology production (Goto/Wakasugi, 1987, p. 269).

MITI is being advised by the Industrial Structure Council as well as by other councils, like f.i. the Telecommunications Advisory Council. "These councils (...) issue a steady stream of white papers, often termed 'visions', which form the basis for legislation for promoting or restructuring industries and encouraging R & D. MITI and other ministries also develop 'elevation plans' which specify production levels for export, as well as R & D spending for specific projects from the visions." (Prestowitz, 1988, p. 30). It seems that in Japan's group oriented hierarchy these procedures create a powerful consensus for achieving the objectives.

MITI also receives an input from the government boards of more than 300 industry associations which can contribute in defining

technological and market priorities and which set technology standards, manage joint suppliers, support joint research efforts and establish and promote development priorities for the industry (Davidson, 1987, p. 154). Within MITI, activities of specific industries are overseen by its individual bureaus and divisions. "Each division assesses world market potential, monitors foreign technology and competition, and identifies appropriate strategies and structures for its constituent industries." (ibid., p. 153). Complementing these activities of industrial policy, MITI operates through its "R & D wing" called AIST (Agency for Industrial Science and Technology) 16 government research centers which oversee and coordinate private research by industry members and play a lead role in defining and implementing joint R & D projects. Specific projects have been defined for the "IBM" topics, so the programme to promote the establishment of a Fine Ceramics Center and the "Human Frontiers" R & D project concerning artificial intelligence, intelligent robots and software. It also comprises "bionics", "the application of biological principles to the design of machines and electronic systems", including "biochips", electronic circuits based on protein molecules (Tucker, 1986, p. 28/29). Although Japan has been inviting international participation in the Human Frontiers project which has been planned for a duration of 20 years (1987-2007), in particular the American response to the proposal has been mixed. Latest MITI projects also include R & D for ceramic engines and magnetically levitated trains.

The second category, which next to "industrial policy" is particularly now often used in the context of productivity and its "key determinant: technological innovation" (Cannon, 1987, p. 507), is "competitiveness", although from a point of view of social-sciences theory it is more a catchword than a clear-cut analytical instrument. In general, the term "competitiveness" is used to describe a comparative state of a nation's economy vis-a-vis other countries. There is a great number of definitions; framework conditions for their use are not exactly determined.

In the 1985 Report of the (US) President's Commission on

Industrial Competitiveness, the term "competitiveness" has been defined as "the degree to which a nation can, under free and fair market conditions, produce goods and services that meet the test of international markets while simultaneously maintaining or expanding the real incomes of its citizens" (Weinrib, 1988, p. 34). It is an interesting point, that by referring to the "free and fair market conditions" under which (domestic) production is supposed to take place, this definition is in sofar already a "political" one, as it entirely excludes "industrial policy", that annoying instrument which apparently has enabled America's greatest competitor, Japan, to do better than the USA; indeed, today Japanese economic competitiveness is rated higher. "A combination of the yen's strength, the current restructuring of Japan's domestic economy and a consistently higher rate of growth than the United States now make possible an idea that a few years ago was absolutely unthinkable : Japan, with half America's population, could approach the United States not just in per capita outcome, but in absolute size of the gross national product." (Burstein, 1988, p. 66).

Japanese strength expressed in terms of export surplus, the ability to supply long-term capital to spark world development, industrial supremacy, and technological leadership - once elements (listed by Paul Streeten, Boston), which next to military strength permitted the United States to dominate the postwar world order, are now in American literature applied to the speculation about probabilities of a "Pax Japonica". In fact, characteristics of a "Japanese empire" are thought to already exist and at present being brought by Japan into a fitting intellectual value system in order to catch aspirations under an adequate ideological umbrella. Like the European Community (and more in particular the Federal Republic of Germany), the Japanese might, however, politically be "reluctant to fill the vacuum" and rather prefer "to preserve the blessings of their powerful economy without subjecting themselves to the costs and burdens of maintaining an empire" (Burstein, ibid., p. 65).

In the USA resentment against Japan is nourished by the fact that

"Japan only sells and never buys", whereby the US hold that Japan "should also bear more of the cost of maintaining the free world system" and "(...) support the US military presence in the Pacific, provide debt relief for the developing nations, and furnish international aid" (Prestowitz 1988, p. 35). Similarly, the European Community, in agreeing on closer bilateral cooperation with Japan, has demanded that this country would start with the necessary structural reforms for a better integration of its economy into world economy, base its economic growth more on domestic demand, raise its imports of manufactured goods and liberalize its finance markets (XXI Report on Community Activities 1987).

Inmidst of these fears and resentments the Americans have, however, not failed to critically assess their own accomplishments and are at present vividly discussing what they call "the causes of our deteriorating capabilities" (Cannon, ibid., p. 507). The US "glaring federal budget deficit" (Kennedy, 1989, p. 38), and a fast growing national debt constitute an overall heavy burden which may hamper possibilities to engage in costly R & D projects. "The relationship between finance and science has undergone a momentous shift. The scale of scientific research today makes it a capital-intensive field. Scientists working in many areas know where they want to go, they can see how to get there, but they can't raise the capital to do it" (Burstein, ibid., p. 67).

The evaluation of the reasons for their declining competitiveness has also brought to the USA an awareness for the fact that military and space expenditures in the USA are very high as compared to civil R & D. In 1987 expenditures for military R & D and space research came to some 75-80% of all US government R & D, whereas military related R & D programmes of the Departments of Defense and Energy make up some 65% of the total fiscal federal US funding for R & D in the 1990 budget as prepared by the outgoing Reagan Administration (Science Trends, January 9, 1989, p. 38). Contrary to this practice, in Japan "(...) virtually no (...) research is funded by the military" (Johnstone, ibid., p. 61).

Apparent historical evidence in the USA that large military

programmes are yielding important benefits to the civilian economy had, however, to be revised: spin-offs from military R & D far less fructify and stimulate civilian R & D than had been anticipated. The reasons for this are that R & D related to defense is often classified and too specific to be used without delay for potential commercial applications. R & D in civil industry has not been sufficiently encouraged, and government and business in the past did not pay so much attention to developing and using technical knowledge for commercial ends. Also, the assumption that government expenditures on basic research would more or less automatically redound to the benefit of commercial industries had to be questioned (Alic, 1988, p. 28-33).

Much was also discussed about Japan taking unfair advantage of the openness of the US university system and the easy access to ideas which evidently "American companies are not as good as turning (...) into products that people want to buy" (Johnstone, ibid., p. 61) as their Japanese counterparts. Moreover, at least in the US engineering community, the Japanese proclivity for "adaptation" which once was "regarded with some disdain", is now "recognized (...) as a potent form of innovation. American science continues to make world-shaking breakthroughs. But the route to commercializing them now passes through Japan, where cost-effective, quality-controlled productive processes make the difference between brilliant ideas and real-life products" (Burstein, ibid., p. 67) - the latest example being "the race to commercialize the hottest of all technological breakthroughs - the ever more temperate superconductor".

On the European level, the entering into force of the "European Single Act" (ESA) in July 1987 - in important aspects changing the 1957 Treaty of Rome by which the European Economic Community was established - gives proof, amongst others, of the development of a sophisticated instrumentation enabling the European Community to engage in the procedure of establishing an European Community for Research and Technology. The European Single Act also grants EC competence in the field of scientific and technical cooperation, which is the corner-stone of the (Second) Framework Programme for Research and Technological Development (1987-1991). This Programme is the Community's "universal instrument" in these fields (cf. The

Policy in the Fields of Research and Technological Development, December 1987, European Community Publication).

The Second Framework Programme is, indeed, the Community's endeavour to extend EC competitiveness with the help of R & D. The principle underlying the "both diversified and selective action" of the Community in R & D is a transfer of those activities in science and technology in the single member states to the Community level, the common further processing of which unequivocally offers advantages and can yield further profits. The Programme (Source : Official Gazette of the European Communities, No. L 302/5, 24 October 1987, Annex 1) has undertaken an important shifting of funds - as compared to the First Framework Programme 1984-1987 - in favour of R & D in industrial competitiveness. This area has been increased from 28.2% to 63.1 % of the total amount of 5.396 billions of ECU for the Second Framework Programme and comprises R & D in the fields 2, 3 and 4 :

- "On the way to a Large Information and Communication Market and an Informed and Communicating Society" (information technologies, telecommunications and new services of common interest, including traffic),

- "Industrial Modernization" (science and technology for manufacturing industries and for advanced materials; raw materials and recycling; technical standards, measuring methods and reference materials), and

- "Exploitation and Optimal Use of Biological Resources" (biotechnology, agro-industrial technologies, competitiveness of agriculture and farming of agricultural resources).

In a sense, of course also field 8, "Improvement of R & D Cooperation in Europe" could be subsumed under the heading of reinforcement of European competitiveness, since it deals with stimulation, valorization and use of human resources, the use of big research centers, forecasting and evaluation, statistics, and divulgation and use of R & D results.

Outside the context of the European Community, the member countries have engaged in an Europe-wide technological R & D programme, EUREKA, initiated by France and the Federal Republic of Germany. Except for the Twelve, participants to EUREKA are the EFTA-countries, Turkey and the EC Commisssion. EUREKA was founded in Paris on 17th July 1985, and after the last (6th) Ministers'Conference in Copenhagen on 15th and 16th June 1988 in this framework now about 300 projects are being worked upon. "EUREKA is open to integrated European projects in near-market research and in the areas of long-term government programmes and preventive research" (Report of the Federal Government on Research 1988, Federal Republic of Germany, p. 23). The structure of cooperation is essentially based on company initiatives. Project areas are high-tech oriented and comprise for instance :
information technologies and communications,
advanced manufacturing and automation techniques,
development of new materials, as well as laser and marine technology, biotechnology, and environmental and traffic technologies .

A prerequisite is that the proposed R & D work is aiming at a substantial technological progress and that high-tech is utilized. EUREKA, planned as the civil reply to the American Strategic Defense Initiative (SDI), hence also deliberatedly aims at reinforcing productivity and competitiveness of the European industries and economies (cf. EUREKA, Technological Cooperation in Europe, Declaration on Principles, BMFT 1988, p. 8).

Initial Community reserves with regard to scope and content of EUREKA were partly overcome by an active EC participation in this programme and by the offer of organisational assistance. The Government of the Federal Republic of Germany has stressed the need for a still higher level of participation of the European Community in EUREKA projects than has been apparent to date. The Community approach to joint R & D, in virtue of principles laid down in the European Single Act, is aiming at a balancing of interests in terms of regional, structural and social viewpoints. These principles are not expressis verbis held by EUREKA, and the ensuing "re-nationalisation" of R & D was viewed with concern by EC, even if EUREKA rules require participation of (adequately

qualified) industrial, university and research partners from more than one EUREKA country.

Moreover, by the organisation of EUREKA outside the Community framework, this program also is not subject to the - albeit still weak ! - democratic control by the European Parliament. Nevertheless, EUREKA continues to meet with approval and enthusiasm, the partners independently deciding on the contents of their projects and engaging in joint R & D on the eve of the establishment of the domestic Common Market by the end of 1992. Special importance is attached to standardization which is a key issue for a speedy realization of the common internal market for high-tech goods. In the opinion of the Federal Republic of Germany, the goal in this regard should not be the subsequent compulsory harmonization of standards. On the contrary, the idea is that the standards, if possible, accrue from joint work on technology.

In order to quantify the real impact of EUREKA (national programmes for their impact being ultimately checked by increased export rates), an evaluation procedure with specific criteria for the already agreed-upon projects has been suggested.

3. Higher, Farther, Quicker - An Unfair Comparison between Olympic Games and World Market ?

Will the USA be able to close the gap in economic competitiveness which is presently separating it from Japan? Can the European Community maintain or improve its position? Are fears of any of these rivals for being outruled by one (or two!) of the others, meaningless ? Even when an explicite reply to these questions can at present not be given, some critical remarks can be made to the effect that striving after competitiveness resembles the Olympic device for ever better performances in sporting contests. Qualifications and efficiencies are now being measured in ever smaller time sequences of a few hundredth parts of seconds, whereas on the other hand records sometimes only stand for a short time, how heavily ever they have been acquired. At the same time, competition gets harder and for those not being able to compete at the vanguard for the very first places, the satisfaction about mere participation at the Games must make up for the lack of efficiency and for the awareness of self-doubt and frustration.

Although on the one hand under the prevailing world economy conditions the achievement, maintaining or extension of competitiveness can be well considered as a necessity, it is also clear that in practice it to some extent describes a fascinating challenge particularly for such countries, which already are justified to confidently look forward to the race itself and to its outcome. Some implications of the notion of competitiveness as a tool for theorizing will be therefore discussed against this background, some traits of this term giving rise to the propositions that "competitiveness" is an unstable category for theorizing, that the comparison of military with economic

competition is inadequate and that competitiveness also can show a declining trend.

"Competitiveness" does in a situation of enduring economic rivalry not designate any "definitely" reachable quantity of this commodity. Under present world economic conditions, the tests of competitiveness are carried to ever higher levels. Hence, as a theoretic notion, competitiveness is a spiral with the inherent characteristic of indefinitely screwing up itself, in analogy not only to the Olympic Games, but also to power accumulation or to the arms race.

In the state theory of the English philosopher Thomas Hobbes (1588-1679) the idea was developed that the state can only keep itself stable in a permanent extension of power, in the process of power accumulation. Stankiewicz (1976, p. 248), however, believed that national states characterized by "sovereignty" have already reached a level of development which is not consistent any more with an hypothetical international anarchy as it was viewed by Hobbes, since the "ceaseless hunger for 'power after power'" has already been eliminated by the existence of other sovereign states. The classical political expression of an international environment of such a nature consisting of national sovereign states has been, of course, the so-called balance of power. Its economic expression comprehends a global, and more particularly, harmonized whole under the free-trade ideology, coupled with the liberal conception of the bourgeois state with its "public" (as opposed to the individual) sphere.

Alas! The conclusion that many sovereign military and economic competitors make up for global harmony, does, of course, not quite apply today, as little as it did apply some 300 years ago. Two world wars negate such an underlying ideology, like presently it is strictly negated by the mere existence of the North-South problem (not to speak of its implications). Rather, a situation seems to prevail where national states, here characterized by "competitiveness", are just following a self-interested policy of power accumulation - this time that of economic power on a highly sophisticated industrialization level.

Apart from the fact that the consequences of Hobbes' theory have never been thought to the end - namely that the mightiest state which is coming victoriously out of the power race ultimately has to destroy itself in order to escape standstill, the accumulation process so being enabled to start afresh (Hannah Arendt, 1972, p. 61) - the practice to compare military to economic competition cannot be considered to be a valid assumption either. The main reason for this is that under a military strategy like the present-day nuclear deterrence as a principle of world order together with the risk or possibility of all-out nuclear war under a conception whereby the entire population of the enemy is held hostage in an aim to prevent his striking first with nuclear arms, implications of military strategy cannot very well be termed "competition", even when the opinion prevails that this constellation has secured peace ever since the end of World War II. The equation of military and economic competition also makes it difficult to not fall victim to a conservative mode of thinking (viewing world policy mainly in terms of the East-West conflict), and it brings up endeavours to simply equate power with the quantification of national capabilities.

Today, the international system is not of a "dual" nature any more. It is "multipolar" and "polycentric". There is a great number of decision-making centres all acting according to their own legitimate interests (multipolarity), so that in international politics now a decentralized variety of decisions (polycentrism) underneath the bilateral, strategic-military level of the great powers USA and USSR has become possible. Hence the question can be asked, which capabilities could actually be "compared" and after what criteria (here, in any case, empiric findings would have to be completed by "speculative" designs, "numbers" by theorizing). National interests including the societal dimension, and national and ethnic identities must be taken into account, as well as those limits, behind which no state can retire: its "reason of state", the "law" after which it has set out and the conditions of life without which a state cannot be what it is, or even exist (Von der Gablentz, 1969, p. 47). The own security and development possibilities of a national state depend in the last instance from those of other states, and also their interests must be taken into account. Often it is forgotten in this connection, however, that

the room for options is firstly not unlimited and secondly does not have the same dimensions for all (Czempiel, 1974, p. 7).

In order to explain the structure of the international system today and consequently also differences in pace and result of the endeavours of nations to reach economic welfare for their peoples, a great number of theories has been developed in the science of international politics, ranging from historical-structural approaches (capitalism, imperialism, dependency) towards interaction theories (actors, subjects of actions and reactions, and aims and values (Czempiel, 1981)). On the other hand, without constituting proper theories of international politics, "qualitative measuring devices" have been developed, terms and notions, which as generalizations of historical evidence may also well be used as analytical tools for the sake of helping to guide investigations into the causes of the crises of nations. An example of such a notion which is at least an interesting proposal, is the term of "relative decline", which has been applied to describe and analyse Great Britain's experiences between 1895 and 1905 (which in some aspects bear a remarkable resemblance to the US experiences of today).

The argument is, that states - here Britain - in a certain period of history have failed to deal with the challenge of relative economic and industrial decline. To describe a process of decline, a point of departure has to be found. Similarly to Streeten's listing of factors by which America's leadership in the world was believed to have been composed, Friedberg (after Kennedy, ibid., p. 37) has divided the texture of Britain's power into four strands : the country's relative position in international economy (economic power), its capacity to pay for an adequate defense (financial power), its control of the seas (sea power) and its ability to defend its interests on land (military power). In all four respects, the situation around 1900 was much less comfortable than it had been in mid-century.

Very interestingly, the problem was by no means that the decline had not been registered. "Commission after commission investigated the erosion of Britain's industrial lead and market shares, the deficiencies of its scientific and technical education, its poor

health-care record, its failure to invest sufficiently in either new plants or new skills". Also, some piecemeal measures were adopted. However, a " 'national efficiency' movement (read 'competitiveness movement') agitated for much more", but "(...) all of this untimately foundered on the public's unwillingness to change old habits, to adopt foreign techniques, and to give priority to productivity. For most people, things were quite comfortable as they were (...). Ultimately, therefore, the British did not respond to the issue of 'relative decline' because of a widespread cultural and psychological - and in many ways understandable - resistance to change" (Kennedy, ibid).

Expressed in such generality, these findings no doubt also apply to crises in other countries. First attempts to solutions can, of course, only come from tackling some of the aspects of the recognized shortcomings. Concerning the future of the Soviet Union, American thinking goes into the direction of the USSR "pacifying the ethnic disputes, dealing with the huge problem of Eastern Europe, improving agriculture, and industry, and public health, satisfying the Soviet consumer(...)". The USSR being occupied with these things, suggests according to American reasoning that the US has been given a certain breathing space to do a number of things (proposed by Abshire, after Kennedy, ibid., p. 42) : "to improve the organization of American strategy (...); to improve arrangements within NATO (...); to evolve a coherent policy toward the third world and the Pacific powers; above all, to carry out a much-needed perestroika at home, which would entail closing the federal budget deficit, evolving a coherent policy on technology, pushing for radical improvements in the public school system, and changing the tax laws to encourage a higher savings rate".

In a feed-back of what the USA feel today as t h e i r relative decline in economic competitiveness when compared to the example of late-Victorian Britain, it is pointed out that the problem of having a breathing space is that one feels much less under pressure to change things. "It was not the case that the British, in their long decades of 'relative decline', constantly staggered from one crisis to the next. On the contrary, there were periods of relative tranquillity (...). When that happened, the

tendency was to go back to 'business as usual', to dismiss those pressing for structural reforms as alarmists (...)" (Kennedy, ibid.).

By definition, "competitiveness" is an internationally coloured notion since it is aiming at the production of goods and services that meet the test of the world market. As may appear from what has been discussed so far, however, reflections and actions about industrial competitiveness chiefly concern evaluations and prospects of national economies, subsequent national policies and the aim of maintaining or expanding the real incomes of (national) citizens. The Great Absentee is International Cooperation, who, although late, is now entering the stadium and insists on joining the race.

4. International Cooperation in Science and Technology : The Perfect One-Way Street To "Splendid Isolation" ?

Until now, in particular three types of ventures in Europe involving international cooperation in R & D have been successful. The first type are cooperative efforts in manufacturing industrial products, also meeting the test of international markets, which were developed against a background of foreign pressure or competition (ARIANE, AIRBUS).
The second type comprises common undertakings which have no, or only very partial, bearings to hard selling, like joint international endeavours in environmental issues. Under this heading can also be comprised long-term, risky, or future-oriented R & D which is not expected to immediately generate an industrially utilizable output.
The third type is pre-competitive R & D, involving international cooperation, which is funded by national or international agencies either generally promoting science and technology for development, or paying for specific fields or projects. Such fields or projects can be related to pure basic research (f.i. CERN) or purpose-oriented basic research, or they are considered to be technologically promising, likely to offer a potential for application, and thought apt to further experimental developments. An example of this kind is the bilateral cooperation in scientific research and technological development with threshold countries, on the German side promoted by the Federal Ministry for Research and Technology of the Federal Republic of Germany, here also with Yugoslavia.

However, with regard to R & D aiming at industrial output, there are also less favourable developments. So, the European Communities no doubt were not the first to learn that such a type

of cooperation is not as self-evident as even the existence of the Treaties would suggest, not so fruitful as even a roughly equal level of manpower-formation and availability of capital and equipment would predict and not so easy as even a more or less homogeneously developed geographical setting would allow. The failure on the set-up of an European nuclear energy potential in the early days of the European Atomic Energy Community is an example illustrating the weakness of European technology policy: joint research is often endangered when a project is nearing the stage of industrial utilization. The participating industries in that stage regularly adopt tendencies to think in competitive terms and to undertake double work, which in the case of EURATOM did not only run counter to the obligations and intentions of the Treaty establishing it, but also showed that the profit-making interest of national monopolies competing for market shares was stronger than efforts which aimed at organizing the supranational research integration of the then only six member states (Stremmel, 1988).

Likewise, the immanent challenge for EUREKA neither was the ignition spark of the underlying idea, nor the initial set-up, nor the engaging into common border-crossing R & D: the ultimate proof for its viability will be the agreement on how to jointly commercialize the results of the common R & D, including the questions of patents and licences.
In so far, it can be said that industrially applicable R & D generated on an internationally cooperative basis is often leading to national isolation, which in this context is understood as a condition resulting from selective high-technology policy choices made mainly or exclusively under a national bias.

Isolation as a "complex political orientation" (McClosky, 1967, p. 57) has never been only an inwardly directed, value-free strategy. On the contrary, its domestic root generally is of a conservative nature. The simultaneously practiced retirement from certain fields of international politics by no means indicates a lack of foreign policy interests. So the isolation deliberatedly practiced by Britain at intervals as a foreign policy strategy since the 17th century historically was both basis and outcome of the British struggle for hegemony. The balance of power configuration

enabled Great Britain to act as the holder of the balance, intervening at its choice with politics on the European mainland, whenever the balance among the Pentarchy, the "European Concert" of the five great powers (Austria-Hungary, Russia, Prussia, France and Great Britain) tended to become disequilibrated - or was believed to do so.

The "splendid isolation" practiced at the end of the 19th century was a strategy to consolidate the British Empire, dictated by economic interests and power politics, coupled with the Puritan ideology of a British mission in the world. Interestingly, this late-Victorian era in Britain, as was shown earlier, also was the period of "relative decline", the failure to meet adequately with the phenomenon of crisis in a variety of fields.

Nowadays, the old option for (splendid) isolation, in its new guise as technological isolation or techno-nationalism, accrues from the latest race - that for economic competitiveness. However, the isolationist choice is not a stable one and is permanently overturned by factual political, military and economic intertwinements and dependencies, and by the necessity of common actions for pressing global problems like droughts, earthquakes, inundations, and - also - by such ones emanating from technology-inherent risks, like huge technical accidents (Chernobyl, Bhopal, Prince William Strait) and chronical dangers linked to scientific-technological progress (climatic changes, devastation of the tropical rain woods), which ask for joint approaches and common solutions.

Next to the factual and accidental events establishing world-wide dependencies, isolation is, of course already given up when the 'de facto' fragmentation of the international system is countered by the political will for humanitarian, social, cultural, ecological - and in the last instance "defensive" military/strategic - approaches departing from a global human interest, as a conscious corrective to denials of the necessity for human solidarity. This corrective implies thinking "beyond competitiveness" and, also in the economic dimension, thinking in terms of the necessity of a solution for the North-South problem. Indeed, an awareness is growing that access to the w o r l d's

stock of knowledge must be secured, and that in the last resort "competitiveness" - like (military) "security" - is an aim which can only be reached w i t h each other and not against each other, in a division of labour which adequately pays also for such efforts and materials, which by their nature, by hitherto usage or by protectionism applied by others, are rated lower than products yielded on a high-tech basis.

Yugoslavia, which in September of this year will be the organizer of the 9th Summit Meeting of the Non-Aligned Countries, sees as a first priority of world politics the diminishing of the North-South economical gap. For the Non-Aligned Countries, international cooperation in the economic field with the western industrialized world is a continuing necessity, and it is rated as encouraging that also the Western countries slowly realize that economic development is mutually dependent, that the crisis of the developing nations must be mastered and that an equilibrated growth of world economy must be reached (International Politics, Belgrade, after Neuber, 1989, p. 12). Indeed, of course, this does not mean that then all at once in the developing nations infrastructures would have improved, sufficient experts and know-how be available, corruption and nepotism discontinued; neither does it mean that there would not be any more such things like inefficient factories, too cost- and time intensive production processes, too broad or inadequate research promotion, or bad management techniques. But framework conditions would be better and give a fresh impetus to establish prospects for the developing nations, including the challenge to cope, inside their own countries, with the same serious challenge which was so aptly referred to in the context of the Non-Aligned's expectations to the Western industrialized countries. It is the challenge also EC is facing inside its own territory, a universal problem : to engage upon a strategy towards equilibrated growth, dealing with what today is called "the social dimension".

The building of the "European House" is accompanied by asynchronic developments in East and West (Laszlo Kiss, 1988). In the political sphere there is an adverse constellation. In Western Europe there is more of a homogeneity, in particular with a view to the preparations for the internal market of 1992, although

these will not proceed fully without friction and although it is necessary to point out that the North-South cleavage inside the Community is not easy to deal with either, and that EC's actions will be eventually measured against its ESA-objective of realizing the social dimension of the internal market.

In Eastern Europe there is altogether more of a dishomogeneity. Perestroika and glasnost (if at all), occur at different velocities, and nationalities' and ethnic questions make themselves differently felt. At the same time, COMECON as an organization and EC as an organization have established formal relationships by the Joint Declaration of July 1988, and intend to cooperate on economic prognoses, on environmental issues, on statistics, and on standards and regulations.

Domestic developments in each of the Eastern European countries are thus influenced by the two great challenges posed by the EC internal market and by Gorbacev's policy, which forces those countries to think, in the political field, about democratization, political pluralism including freedom of opinion and public discussions, and civil and human rights; in the economic field about market-oriented policies and modernization strategies; in the cultural field (like it is necessary in the West !) about Europe having a common heritage : "Building the European House - with East and West Wings" (Foundation of International Understanding, FIU, Copenhagen, 1989). The answers to these diverse challenges necessitate for the Eastern European countries a complex strategy of adaptation to the outside (European) world, whereas the complementary reformation strategies should, in the ideal case, twin external adaptation to internal reformation. A regional transfrontier cooperation - like it has been shaped in the tools of the Balkan Ministerial Conference between Yugoslavia, Greece, Bulgaria, Albania and Romania, or the Alpen-Adria Working Community between Austria, Hungary, Yugoslavia and Italy - constitutes an option to, in a context of good-neighbourly relationships, develop specific strategies also for R & D. Whether we are on the way to a "Europe of Regions" (FIU, ibid.) or not, and whether this is a viable way to intensify the East-West dialogue, remains to be seen. But such system-overlapping approaches have a good chance, since they are geographically

confined and are insofar perspicuous, as they deal with "well-known", partly historically determined, partly structural problems which pose more or less the same type of challenge to all. Likewise, inside the Movement of the Non-Aligned Countries, cooperative efforts are more and more organized on lower, i.e. regional, basis, and according to distinct criteria (Neuber, ibid.), for instance after those of anti-racism between the Front States in Southern Africa, after such of participation in the CSCE-Helsinki process, or after those of being a Mediterranean country. Indeed, the Non-Aligned in this way become more heterogeneous, but they also become more flexible.

For R & D cooperation there is another very important factor which counts, which is determined by the high cost for the build-up for R & D. When research and technology are directed towards regional development, resources can be pooled and costs can be shared, although in the commercialization of the joint efforts then again the danger of the "national" card being played is not imaginary.

The phenomenon of the "intermittent baths" between international cooperation and national competition was well recognized by the German Federal Ministry for Research and Technology, which stated in its 1988 Research Report (p. 22) in the context of internationalization of production and utilization of technical knowledge : "A further feature is a hitherto unknown degree of both competition and cooperation, also at international level, in the field of research and technology, with it having become very difficult for small- and medium-sized nations, in particular, to hold their own next to the big nations and to define and assume suitable roles for themselves."

After the OECD Economic Survey for Yugoslavia (June 1988), the country's technology policy should have (much like EC's) a multi-dimensional role, aiming in the case of Yugoslavia to consolidate national unity and ease regional tensions. "The massive aid given in the past to the most disadvantaged regions has not had the expected effect : implanting large and costly new factories has created further problems, disrupting traditional social structures without bringing new skills. A wiser policy would be to exploit local resources (tourism, agriculture) in an overall plan for

constructive co-operation between the 'North' and 'South' of the country (through joint ventures) and to invest in the non-material side of development - organisation, information, technical assistance, technical and commercial training, and the like" (Aubert, 1989, p. 34).

Owing to the Report, excessive fragmentation in Yugoslavia has caused important drawbacks, like research activities and teams lacking critical mass, which derive from a combination of factors. These comprise the autonomy of units (republics and provinces) within the federation, the lack of a federal science policy until recently, and arrangements for research funding in the republics, as a consequence of which available resources are spread too thinly. The Report also mentions that "(...) smaller countries like Yugoslavia must accept that they are bound to have to import more than 90% of the new technology they use. Another approach must therefore be tried : Yugoslavia must develop its capacity to absorb foreign technology by stepping up training programmes, negotiating licences and running joint ventures. Free trade areas (two have recently been opened) can be used, too, to attract high-technology foreign firms to Yugoslav territory and to promote technology transfers" (Aubert, ibid.). Between federal units, also a harmonization in telecommunications, metrology and standards should be undertaken, whereby standardization would have both a political and an economic significance. Yugoslavia itself had, at least in its "Strategy of Technological Development of the Socialist Federative Republic of Yugoslavia" of 1987, rather opted for a quick development of own technologies under the prerequisites of intensified cooperation inside its system of self-management organisation of labour, of an adjustment of its own North-South cleavage, of a reformation of the educational system and the reinforcement of the export capability of its economy. For identified priority areas (like information technology, biotechnology, new materials, flexible production technologies and energy technologies), so-called consortia, consisting of self-management organisations of labour in industry and research organisations can apply for federal funding under a number of criteria, among them the cooperation with partners from different institutions, and optimal use of raw materials and rational use of energy, as well as social and environmental

prerequisites. Multi- and bilateral international cooperation in the economic and the scientific and technological fields for the sake of technology transfers is especially stressed.

As a conclusion, in an attempt to reply to the question, whether international cooperation in R & D is the perfect one-way street to 'splendid isolation', it can be said that partly this hypothesis has to be confirmed, partly it can be falsified.

It can be confirmed in this sense, that indeed promising beginnings, efficient research and the outlook on potential good results spoil the intentions and the practice of the cooperative efforts, particularly in industry-located or industrially-utilizable R & D, nearly into their opposite : national "industrial policy" can yield developments into the direction of singularity and protectionism, high-tech issues are being excluded from international cooperation, the rising techno-nationalism under the struggle for competitiveness is likely to undo the effects of hitherto-cooperation, hard-selling interests veil already-built up structures and pathways between partners, and commercializing the outcome of joint R & D may well break up the sophisticated but fine web of actions, reactions and interactions which has come into being by joint efforts.

In those cases, where such developments could until now be avoided, special conditions have assisted in maintaining the cooperative texture. Among these conditions are common interests of (scientific) prestige rather than profit-orientated strategies, challenges presented by the need for preservation of the environment rather than hard-selling of (manufactured) goods, joint ventures to meet outward challenges, or the availability of a market big enough and endowed with sufficient purchasing power to presumedly satisfy the commercial interests of more than one manufacturer offering goods and services (services being understood here not only as those deriving from tourism or traffic, but also as such referring to the expanding market for

intelligent software). In this respect, the EC internal market constitutes a singular and 'a-typical' tool: by its mere mass of some 320 millions of well-to-do buyers, it is potent enough to absorb a great deal of its own production. Already in the year 1986, close to 60% of imports and exports to and from EC countries took place inside the Community of the Twelve (cf. Statistik des Auslandes, EG Staaten 1988, Wiesbaden, p. 86/7), and this percentage will certainly rise.

The hypothesis of isolation can, on the other hand, be falsified insofar, as superposed interests dictate the search for joint solutions for frontiercrossing dangers, for regional necessities, for global challenges, which do simply not permit national egoisms beyond legitimate national self-interests, or which create a situation of being involved "anyhow" in extra-national commitments (perhaps even nolens volens). But, of course, also conscious choices in favour of international cooperation in R & D can be made, arising from the insight that to avoid hanging apart can some day well result in hanging all together; that international cooperation must not entail only costs, but can also yield benefits; or even that in view of the serious difficults in many countries of the world regarding their more absolute than relative decline and which cannot be ignored, responsibilities of the international community to support industrial and technological developments in other (especially developing) countries on a joint basis, exist.

The actual duality between cooperation and competition in the international arena, which has followed up the former one of cooperation and confrontation, is a relative progress, no more. The underlying problems have remained and have by no means become less pressing. This situation asks for designs for solutions which are both organisationally sound, professionally sophisticated, and scientifically and technologically efficient.
Yugoslavia's international environment is thereby changing also in the sense, that the European Communities are, beyond the existing economic cooperation, aiming to widen the scope of their contacts with Yugoslavia by introducing the dimension of science and technology into their relationships with that country, as

concretely became clear during the first seminar on materials sciences between EC and Yugoslavia at Sarajevo in September 1988.

Yet another challenge is presenting itself for Yugoslavia, that of EUREKA. Until now, partner institutions to German-Yugoslav cooperation in science and technology are in their respective countries also engaged in R & D for industry and also in advanced areas, whereas in the framework of the bilateral cooperation proper, continuous efforts have been made by both sides to on the one hand not neglect the important field of basic research, but on the other hand, there where applied and experimental research is being done, to link it as much as possible to the industrial context. The high level of Yugoslav education and training has thereby helped to reach the aim of the bilateral cooperation, which is by no means technical assistance, but which consists in working jointly and in well-defined projects on scientific-technological problems of mutual interest. Yugoslav scientists have given very valuable contributions to achieve, together with their German partners, results which partly are of high quality.

Nevertheless, in a sense, the bilateral cooperation framework has constituted until now a paradise ruled by "commercial innocence". For the first time in the history of our project work, Yugoslav research and industrial institutions are looking forward to participate, according to the rules of the EUREKA Minister Conference at Madrid in June 1987, in work for four EUREKA-projects (EUROTRAC, COSINE, EUROMAR/ELANI and BIOMATERIALS). The contributions of Yugoslav institutions for EUROTRAC, EUROMAR/ELANI and BIOMATERIALS are directly resulting from bilateral projects with the Federal Republic of Germany, whereas in the case of COSINE an humus soil of broad joint activities has contributed to achieve this participation.

Apart from the fact, that these EUREKA-activities prove the high quality of the work being done in the bilateral framework, now also here and more than before, the broader international context with its mixture of cooperation and competition will exert its influence on the Yugoslav participating institutions. This is a demand for maturing, a good possibility to withstand the temptation of technological isolation, and an appeal to stand the

challenge of the European Market, making yet another step into the direction of the long and no doubt difficult process of establishing a Yugoslav competitiveness going beyond mere quantities and dumping prices.

During the IXth German-Yugoslav Seminar on Materials Sciences and Development our meeting place is Hirsau, not far from the neighbour town of Calw, where the German author and Nobel prize winner, Herman Hesse (1877 - 1962), was born. From his book "Narziß und Goldmund" (1957, p. 47) I would like to cite some lines, which - here with respect to our Yugoslav partners - also constitute the conclusion of my lecture :

"It is not our task to come closer to each other, no more than the sun and moon can approach each other or the ocean and the land. We two, we are the sun and the moon, we are ocean and land. Our goal is not, to merge into one another, but rather to understand each other, and for each to learn to recognize and respect the other for what he is : our counterpart and complement."

F o o t n o t e s

(1) Agreement on Cultural and Scientific Cooperation between the Federal Republic of Germany and the Socialist Federative Republic of Yugoslavia, dated 28 July 1969

(2) Special Agreement between the Federal Ministry for Research and Technology of the Federal Republic of Germany and the Federative Office for International Cooperation in the Fields of Science, Education, Culture and Technique (YUZAMS) of the Socialist Federative Republic of Yugoslavia on Cooperation in the Field of Scientific Research and Technological Development of 23rd May 1975

Special Agreement between Kernforschungsanlage Juelich and YUZAMS on Cooperation in the Field of Scientific Research and Technological Development of 8th July 1977

Special Agreement between KFA and the Research Community of the Republic of Slovenia on Cooperation in the Field of Scientific Research and Technological Development of 2nd November 1978

(3) Acknowledgement :
for some aspects of the notions of "industrial policy" and "competitiveness" (USA / Japan / EC), as well as of EC's R & D policy, use has been made of :

"Research and Technology Policy of the European Community", by Jörg Stremmel and Johanna Krawczynski, EBN Yearbook 1988, forthcoming
(EBN = European Business and Innovation Center Network, Maastricht)

L i t e r a t u r e

Alic, John A., The Rise and Fall of R & D, in:
Mechanical Engineering, New York, Vol. 110, 1988, No. 4

Aubert, Jean-Eric, Yugoslavia in Crisis :
How Can Technology Help ?, in :
The OECD Observer, 155, December 1988-January 1989

Burstein, Daniel, Sun Rise, in:
Dun's Business Month, Vol. 132, 1988, No. 3

Cannon, Peter, Japanese Challenge/ American Response, in:
Vital Speeches of the Day, New York,
Vol. 53, 1987 (1st June), No. 16

Davidson, William H., Japanese Communications Policy,
New Direction and Old Dilemmas, in :
Telecommunications Policy, Guildford, Vol. 11, 1987, No. 2

Gilder, George, How The Computer Companies Lost Their
Memories, in : Forbes, New York, Vol. 141,
13 June 1988, No. 13

Goto, Akira and Wakasugi, Ryuhei, Technology Policy in Japan :
A Short Review, in : Technovation, Amsterdam,
Vol. 5, 1987, No. 4

Johnstone, Bob, Rise of Techno-Nationalism, in:
Far Eastern Economic Review, Hong Kong,
Vol. 149, 31 March 1988, No. 13

Kennedy, Paul, Can the US Remain Number One ?, in :
The New York Review of Books, Vol. XXXVI,
March 16, 1989, No. 4, p. 36 - 42.
The citations and data are taken from Mr. Kennedy's essay

and from his discussion of the books :
- The Weary Titan : Britain and the Experience of Relative Decline, 1895-1905, by Aaron L. Friedberg, Princeton University Press, and
- Preventing World War III: A Realistic Grand Strategy, by David M. Abshire, Harper and Row

Kiss, Laszlo, Vortrag ueber die Reformpolitik Ungarns anlaeßlich der Aachener Ost-West Tage im Dezember 1988, organisiert durch das Aachener Centrum fuer Europaeische Studien

Matsushita, Mitsuo, The Legal Framework of Japanese Industrial Policy, in : BYU Law Review, Vol. 30, 1987, No. 2

Neuber, Manfred, Die Blockfreien haben an Selbstbewußtsein gewonnen. Sie wollen mehr Einfluß auf Ost und West, in: Das Parlament, 24.-31. März 1989, Nr. 13-14, p. 12

Prestowitz, Clyde, Japanese vs. Western Economics, in : Technology Review, Cambridge, MA, Vol. 91, 1988, No. 4

Sekiguchi S., and Horiuchio, T., Myth and Reality of Japan's Industrial Policies, in : World Economy, Oxford, Vol. 8, 1985, No. 4

Stremmel, Jörg, Die Forschungs- und Technologiepolitik der Europaeischen Gemeinschaft, Aachen 1988

Tucker, Michael, Coming Next from Japan : The Bionic Computer ?, in : Mini-Micro Systems, Hudson, MA, Vol. 19, 1986, No. 9

Weinrib, Janet, Buddy MacKay's Battle, in : Mechanical Engineering, New York, Vol. 110, 1988, No. 4

Die Politik auf dem Gebiet der Forschung und der technologischen Entwicklung, Europaeische Dokumentation, Amt für amtliche Veroeffentlichungen der Europaeischen Gemeinschaften, Luxemburg, 1988 Manuskript von Michel Andre, Stand Dezember 1987

Dossier Forschungspolitik, Eine Analyse des Bundesberichts Forschung 1988, in : Forum Wissenschaft, Marburg, 2/88

Report of the Federal Government on Research 1988 (Abridged Version), The Federal Ministry for Research and Technology, Bonn 1988

Science Trends, Washington, Vol. LX, 9 January 1989, No. 7

Statistics EC Countries, Laenderbericht EG-Staaten 1988, Statistisches Bundesamt, Wiesbaden

Arendt, Hannah, Imperialismus : Die politische Weltanschauung der Bourgeoisie. Thomas Hobbes und der kapitalistische Markt, in : Wehler, Hans-Ulrich (Hrsg.) Imperialismus, Koeln 1972 (2)

Czempiel, Ernst-Otto, Friede und Konflikt in der Gesellschaftslehre, in : Aus Politik und Zeitgeschichte, B 20 / 1974, S. 3-29

Stankiewicz, W.J., Sovereignty as Political Theory, in : Political Studies, Oxford 1976, Vol. XXIV, p. 141-157

Von der Gablentz, Otto-Heinrich, Politische Gesittung, in : Wendland, Heinz-Dietrich (Hrsg.), in Gemeinschaft mit Strohm, Theodor, Politik und Ethik, Darmstadt 1969

The last four authors were cited after :

Krawczynski, Johanna, Das Nationalinteresse als analytische Kategorie in der Wissenschaft von der Internationalen Politik, Diss., Aachen 1984

HORIZONS OF POWDER METALLURGY

W.A. Kaysser

Max–Planck–Institut für Metallforschung
Institut für Werkstoffwissenschaft
Pulvermetallurgisches Laboratorium
Heisenbergstr. 5, 7000 Stuttgart 80

INTRODUCTION

One of the techniques which have an inherent potential to produce some of the future, taylored, high-tech materials is powder metallurgy (PM'). The efficient use of powder metallurgy depends on the combination of the scientific understanding of complex physical and chemical problems of powder production, handling, forming and consolidation with highly developed complex engineering capabilities. The interactions of materials science and engineering skills, and the inherent materials science problems which characterize the new PM' are numerous.

From the ancient powder forged pillar of Delhi to the present, powder metallurgy has shown itself to be a potent method to form special, artificial materials at times when no other techniques could handle these materials due to technological requirements such as high melting points, bad machinability, or microstructures not obtainable by other techniques. PM'high-tech materials are required to be completely free of pores and fine grained. Mechanisms of powder densification and of simultaneous microstructural changes are therefore of major technical and scientific interest.

The basic steps of conventional powder metallurgy are powder preparation, powder handling, shaping and consolidation /84 Klar/. Powders may be produced by chemical reactions from precursors or by disintegrating solid or liquid bulks. The powders are shaped in dies under uniaxial load or filled in thin walled capsules and isostatically pressed. The shaped compacts contain pores between the individual particles which amount to porosities between 60 and 10 vol.-%. It is one of the purposes of subsequent pressureless or pressure assisted consolidation, and a heat treatment below the melting temperature of the major constituents, to eliminate the pores, driven by a reduction in solid-vapour interface area. Porosity reduction requires an increasing fraction of solid material in each unit volume cell by rearrangement or by shape change of the particles (Fig.1a).

ADVANCED PM'MATERIALS BY PRESSURELESS SINTERING

Sintering of Single Phase Materials

Shape change or center to center approach during solid state sintering occurs in a quantifiable way when vacancies diffuse from pores into the grain boundaries where they are subsequently eliminated. Unfortunately, the transport of vacancies to the grain boundary sinks by bulk diffusion or by grain boundary diffusion does not provide complete densification in most metal powders of sizes between 1 and 100 μm.

During the first and second stage of solid state sintering with small amounts of additives, densification is accelerated by enhanced bulk or grain boundary diffusion /49 Kuzc/,/61 Cobl/, /69 Brook/. Surface diffusion has to be kept small enough that sufficient driving force for densification, that means a high ratio of neck area to neck volume, is maintained. The surface diffusion must, however, also be large enough to keep the dihedral area of the neck close to the equilibrium shape /80 Swin/,/88 Exne/.

Classical examples of enhanced shrinkage by the addition of a small amount of an alloying element are W or Mo doped with Ni. The bulk diffusion of W(Ni) solid solution is far below a value which would influence solid state sintering at 1400°C to a measurable degree /87 Kays1/. Two independent measurements confirm that the presence of Ni at W or Mo grain boundaries increases the grain boundary self diffusion coefficient of these materials /87 Kays1/,/70 Schi/,/85 Kays/ by a factor 500 to 5000 in the case of W, and by a factor of 25 in the case of Mo if Ni is present (Fig. 2a and b). Figure 3a and b shows the enhanced sintering of W or Mo if small amounts of Ni are present.

The third sintering stage is characterized by the transition of pore channels into isolated pores which lie along three or four-grain junctions or in the interior of the grains /82 Hsue/. During the final stage of sintering both densification (pore shrinkage) and coarsening (pore coarsening and grain coarsening) occur simultaneously. Shrinkage occurs by migration of vacancies from the pores along the grain boundaries to vacancy sinks (grain boundaries and free surfaces). In the final stage there are two phenomena by which pores coarsen: by mass transfer between isolated pores and by pore coalescence during grain growth. Figure 4 shows a scheme initially proposed by Brook /82 Broo/ for pores which is extended for second phase inclusions. It shows fourteen mechanisms which may control the migration of a boundary. In all cases a decreasing pore size at a constant total porosity results in shorter efficient pathways and an increased mobility of the pores. Mechanisms 6 and 7 show two pathways which lead to coarsening of the pores by grain boundary or lattice diffusion. It is obvious that small amounts of additives can influence all of these mechanisms, including the intrinsic boundary movement (1) and the impurity drag (2). A second set of coarsening mechanisms is based on coalescence of pores by collision when the boundaries

move /88 Kays3/. Similar arguments are valid if instead of pores second phase inclusions are present at the grain boundaries.

During grain growth, pores either remain at the boundaries or become separated and "trapped" inside the grains. Pores that are trapped usually shrink at much lower rates than pores which are at grain boundaries, since bulk diffusivity is much smaller than grain boundary diffusivity. Pore drag and pore grain boundary separation in W-0.15wt.%Ni after annealing at 1400°C for 3 h are shown in Fig.5a. There are two regimes where pores can remain attached to the grain boundaries (Fig.6a). Pores which are large enough are immobile but retard the motion of the boundary (pore control in Fig.6a) /82 Hsue/,/82 Broo/,/78 Uema/. Pores which are small enough move along with the grain boundaries without stopping their motion (boundary control in Fig.6a). The mechanisms of pore migration are shown in Fig.4. The intersection of the two regimes of pore-boundary interaction leads to a pore-boundary separation region with G^* as the smallest grain size where grain boundary/pore separation occurs (Fig.6a).

From Fig.6a the problem of manipulating final stage sintering by additives becomes obvious. Fast shrinkage at small grain sizes (yielding trajectories which pass below the separation field) requires a low surface diffusivity, D_{sv}, and a high grain boundary diffusivity, D_{gb} ($D_{gb\perp}$ perpendicular to the boundary plane can be shown to be related to the grain boundary self diffusion coefficient D_{gb}). To avoid grain boundary pore separation at medium grain size and smaller pore size the separation field has to be shifted to larger grain sizes which requires the opposite, high surface diffusion and low grain boundary diffusivity. Final stage sintering of W with Ni shows extensive grain boundary pore separation (Fig.5a) since both grain boundary and surface diffusion are increased by the presence of Ni at the grain boundaries (Fig.1a and /87 Kays1/). Figure 5b shows the microstructure of Al_2O_3 which was doped with MgO /87 Kays2/. In contrast to Ni doped W, the addition of MgO reduces the grain boundary mobility. Complete densification by pressureless sintering is possible /85 Benn/,/82 Broo/.

The bulk diffusivity of metals, which controls one major transport path for vacancies from the pore to the grain boundary via diffusion through the bulk, can only be moderately increased by doping with small amounts of an alloying metal additive. The enhancement of the grain boundary self diffusion, which controls the second major transport path for vacancies, as in W doped with Ni /85 Kays/, however, also increases the grain growth rate, leading to extended pore/grain boundary separation.

Solid State Sintering with a Second Phase

Densification, dimensional control and homogenization can also be influenced by additives which are present as second solid phase. The additive may act as a fast diffusion path for the host atoms. The additive may also form inclusions on obstacles which retard densification and grain growth. The broad variety of possible chemical interactions between the solid phases yields a complicated influence on densification and dimensional control.

An example of a simple interaction is found in W-Cu /85 Lee/. At temperatures below 1100°C, W powder does not sinter and the mutual solubility of W and Cu is negligible. Despite the insolubility, W-Cu compacts densify by solid state sintering during heating up to temperature in the solid state (Fig.7). The densification rate increases with increasing volume content of Cu. In the vicinity of the Cu particles Cu is spreading on W particles. The comparison of shrinkage and microstructural development supports a two stage model where rapidly enlarging zones of low Cu content yield initial rearrangement and shrinkage (Fig.8a,α) whereas a second massive spreading of Cu from initial Cu particles leads to a local formation of denser Cu-W particle aggregates and to a continuous macroscopic shrinkage after prolonged sintering when most aggregates form an interconnected network (Fig. 8a, β and Γ).

During final stage sintering the migration of grain boundaries may be retarded by second phase inclusions. If the bulk diffusion of the host material in the second phase inclusions is rapid, the second phase inclusions will migrate with the grain boundaries and coalesce similar to pores (compare Fig.4). Figure 9a shows W-1wt.%Ni after sintering at 1400°C for 122 h. The "bell shape" of the inclusions indicates the drag of the moving boundaries on the second phase. As a consequence of the drag forces of the inclusions on the migrating boundary the grain growth rate is reduced if the Ni concentration exceeds the solubility limit of Ni in W at 1400°C (Fig.9b) /86 Kays2/.

Sintering with a Liquid Phase

The metallic materials produced by pressureless sintering, such as hard metals, heavy metal alloys, and permanent magnets are all sintered in the presence of a liquid phase, which reflects the problems of sintering to a pore free material in solid state, but also indicates the ability to obtain dense materials by liquid phase sintering. A more detailed description of the liquid phase sintering phenomena is given elsewhere /85 Kays/. In this paper the basic shrinkage phenomena and the mechanisms of melt penetration and liquid film migration will be described.

The microstructural development and the shrinkage during sintering in the presence of a liquid phase are governed by a number of basic principles, which apply to liquid phase sintering of almost all materials /85 Kays/. In each of these materials one or more phases are solid and at least one phase is liquid at the sintering temperature. After processing, the microstructure consists often of two solid (sometimes interpenetrating) networks. Densification during liquid phase sintering is also based on rearrangement and shape change of the solid constituent particles (Fig.1b). The driving force for both phenomena results from a decrease in energy connected with the changes in the areas of the liquid/vapour, liquid/solid and solid/vapour interfaces during rearrangement and/or shape change. Melt may originate from low melting point particles or areas which have built low melting point compositions by diffusion during heating. With the condition of good wetting, the liquid phase is pulled by capillary

forces into particle necks and small pores. As a reaction to the capillary forces, particles are rearranged if their mobility allows it. This rearrangement of the solid particles is a necessary prerequisite for effective densification throughout the sintering process even during later sintering stages, when, for example, the rates of particle shape change limit the rearrangement rate. Shrinkage due to the shape change of the solid constituents always involves solution-reprecipitation processes. An example is coarsening by diffusion controlled Ostwald ripening, when the grains accomodate their shape to a changing vicinity /5/ as shown for liquid phase sintering of Mo-Ni by the etched patterns in Fig.10. A major part of the shrinkage of this system results from rearrangement when small particles are dissolved giving way for the movement of larger particles (Figs.1b and 11).

One of the main dissolution-reprecipitation processes leading to secondary rearrangement is the grain boundary penetration by the liquid phase. The penetration leads to skeleton disintegration, but also to contact dilation, particle dilation and subsequently to particle disintegration. Important consequences of grain boundary penetration are boundary alloying and liquid film migration.

Early grain boundary attack does not necessarily lead to densification. But if grain boundary attack is completed along all grain boundaries of a polycrystalline particle, particle disintegration and densification by secondary rearrangement may occur. This is illustrated in Fig.12a to c. In Al_2O_3-glass mixtures the shrinkage after particle disintegration due to secondary rearrangement could be separated from shrinkage due to primary rearrangement /82 Pejo/. Up to 1400°C, the shape and size of the polycrystalline Al_2O_3 spheres was maintained and only primary rearrangement occurred (Fig.12b). Above this temperature grain boundary attack and particle disintegration occurred (Fig.12c) and secondary rearrangement led to considerable additional shrinkage (Fig.12a) /80 Petz/,/82 Pejo/.

The penetration of the melt along grain boundaries may also initiate liquid film migration. Liquid film migration is a general phenomenon which occurs under various conditions. In recent years boundary migration in metals and ceramics, which is associated with a noticeable concentration change in the wake of the moving boundaries, has been investigated intensively. It is kown as diffusion induced grain boundary migration (DIGM) /78 Hill/ and liquid film migration (LFM) /85 Yoon/,/85 Hand/. If the solid in front of a migrating liquid film is not in equilibrium with the solute concentration of the boundary then solute will either be depleted from or diffuse into this solid. When the boundary migrates at a constant velocity a steady state concentration profile will develop. The concentration gradients in the solid close to the liquid/solid interface will be very steep. If the lattice parameter changes with the concentration of the solute and coherency of the peripheral layers of the solid is maintained, coherency strains will arise. These coherency strains raise the free enthalpy of the stressed solid which is in contact with the boundary, resulting in differences of the local concentration equilibria at either side of the liquid films. These differences cause a constant traverse of host atoms through the

liquid film, which results in the migration of the boundary.

The penetration of melt into contact areas and grain boundaries yields perfect conditions for LFM /85 Kays/. Figure 13 shows an area in an Fe particle after liquid phase sintering in the presence of Cu for 2 min. The thin liquid films have formed the bulges characteristic of LFM. Solid solutions of Fe-Cu have formed in the wake of the migrating boundaries /88 Kays3/.

Due to the operative shrinkage mechanisms liquid phase sintering yields dense PM materials. As shown above, densification requires grain growth and rearrangement. Complete elimination of pores is thus limited to systems where either fine initial powders or large amounts of suitable liquid phase are available. Typical examples of liquid phase sintered high permanent materials are hard metals (e.g. WC-Co cutting tools) or hard magnets (e.g., Fe-Nd-B shown in Fig.14 /87 Schn/).

ADVANCED PM MATERIALS BY PRESSURE ASSISTED CONSOLIDATION

For most of the complex alloy systems fine powders and suitable melt phases are not available and due to the limited capability of solid state sintering, PM'production by sintering is impossible. The powder metallurgical production of those advanced materials of great comercial interest became possible, however, when, mainly in the early eighties, modern engineering provided production facilities for powder consolidation, where simultaneously temperature and pressure could be applied to the consolidating compacts. The simultaneous application of pressure and temperature allows the complete densification of comparatively coarse, prealloyed powders with complex microstructures and high yield strength. Densification is readily attained without solid state sintering aids and without the presence of a liquid phase. Most frequently used are hot isostatic pressing and hot extrusion.

During hot isostatic pressing (HIPing) plastic flow and a number of creep mechanisms contribute to densification (Fig.15) /83 Arzt1/,/88 Kays4/. Which of these mechanisms dominates shrinkage and neck growth rate depends on a number of parameters related to the powder (size, grain size, pore size and distribution, current geometry, bulk material properties,interface properties) and parameters related to processing (pressure, temperature, time, pore size and pore size distribution).

Initial and Second Stage HIPing of Coarse Particles in Solid State

The initial neck growth and center approach rates are described by analytical equations /83 Arzt1/ and therefore theoretical predictions on the densification during HIPing have been made. HIP diagrams were developed some years ago to simplify the engineer's choice of HIP parameters which are required for densification of a particular material /83 Swin/. Due to the limited

amount of known material data, HIP diagrams were constructed with the help of best estimates from a reduced number of available basic data of a material /87 Ashb/. They still suffer from insufficient experimental verification due to to the tedious and time consuming HIP experiments required. A simple experimental method was recently presented , however, which allows the prediction of the HIP behaviour at lower densities and also provides some of the material data required for the complex calculation of the HIP diagrams /88 Kays4/. Single powder spheres were uniaxially deformed under a well controlled load f as shown schematically in Fig.16. For the calculation it was assumed that the material of the deformation zones (dark areas) is distributed homogeneously on the free surface of the particles, that means that the radius R of the particles is increasing during deformation. The particle radius R and the radius x of the contact area are connected to the reduction h of the distance between the particle center and the contact area by

$$R = \left(\frac{[2*R_o^3/3 + (R_o - h)^3/3)]}{(R_0 - h)} \right)^{-1/2} \qquad [1]$$

and

$$x = (2R*[h + (R - R_o)] - [h + (R - R_o)]^2)^{1/2} \qquad [2]$$

The deformation of the single sphere between two parallel plates was transformed into equivalent densities during HIPing. Taking into account the increasing number Z of contacts per particle during densification /83 Arzt2/, an analytical relation was obtained /88Kays4/. The relation between the external HIP pressure P and the average force f^* on a single particle during HIPing is given by /83 Arzt2/,/75 Mole/

$$f^* = \frac{4\pi R_o^2 * P}{Z*D} \qquad [3]$$

This relation was used to transform the force f on the single particle into an equivalent external HIP pressure P by setting $f = f^*$. The single spheres were deformed in a precision dilatometer under a load between 0.1 and 1 N. For comparison powders with superior sphericity and a narrow size distribution (range < 25μm) were filled in glass containers of a suitable softening range. After evacuating to 10^{-7} N/m^2 the containers were sealed and HIPed in a mini-hipper.

Figure 17 reveals the HIP density of steel C1018 samples after HIPing at 1000°C for 1 and 20 min at different external pressures. For comparison numerous HIP densities which were calculated from the results of the single sphere dilatometer experiments are included. The agreement between the predictions on the basis of the single sphere experiments and the results from the HIPed samples is excellent.

The values of $n \approx 4.44$ and $(\epsilon_0/\sigma_0^n)_{Ig} = 5.35*10^{-36}$ $s^{-1}*(m^2*N^{-1})^n$ were obtained from the log((dh/dt)/x) vs log (p/3) plot for C1018 at 900°C shown in Fig.18. Values of $n \approx 4.14$ and

$((d\epsilon_0/dt)/\sigma_0^n)_{Tg} = 6.47*10^{-34}\ s^{-1}*(m^2*N^{-1})^n$ were obtained from experients at 1000°C. These values agree well with literature data and indicate power law creep as the rate determining deformation mechanism. Figure 19a shows the deformation of a commercial high speed steel at forces f of 0.18, 0.35 and 0.74 N which are equivalent to HIP pressures of 10, 21 and 50 MPa. Figure 19b shows the predicted HIP density vs. time curves. At an equivalent HIP pressure of 10 MPa the HIP density after heating to 1150°C is predicted to be 0.70. It increases during an isothermal subsequent HIPing for 60 min to 0.78. At an equivalent HIP pressure of 20 MPA the relative densities are 0.78 and 0.93, respectively. At an equivalent HIP pressure of 50 MPa the deformation of the single sphere predicts HIP densities close to complete density or at least far above 0.93. In Fig.20 the logs of h/x vs p/3 indicate by straight lines with a slope n = 3 that power law creep is the dominating deformation mechanism. The prefactor is obtained to $((d\epsilon_0/dt)/\sigma_0^n) = 2.65*10^{-23} \pm 1.62*10^{-23}\ s^{-1}(m^2N^{-1})^n$ /88Kays5/.

The dilatometer experimenents emphasize the extent of the densification during heating for example from the deformation of AP1 spheres at loads between 0.07 and 0.26 N, which is equivalent to HIP pressures between 8 and 40 MPa. The predicted HIP densities agree well with a HIP density value of AP1 measured by Mitkov at low pressures and short isothermal HIP time /86 Mitk/. The small initial contact areas of the particles in the dilatometer experiments result in a high initial pressure which leads to rapid deformation (densification) above 800°C. The measurements predict densities of HIPed AP1 far above 0.9 after heating up to 1180°C if HIP pressures above 20 MPa are applied. The deformation rate of AP1 in the as received state has been found to be extremely stress sensitive indicating a power law creep exponent close to 10.

The deformation of single spheres does result in data of equivalent HIP densities which can be used directly to improve the precision of HIP diagrams of a certain material. For most metallic materials the creep parameters for power law creep are the most important parameters to characterize of the densification during HIPing under usual HIP conditions. The deformation rate during power law creep is related to the length change rate by

$$\dot{\epsilon} = \frac{\dot{h}}{C_2 x} = \left(\frac{\dot{\epsilon}_o}{\sigma_0^n}\right)_{Tg} * \frac{1}{27} * \sigma^n \quad , \quad [4]$$

where c_2 is a constant and h is the power law creep exponent. From plots of log (h/x) vs log p or log σ, the slope n and the value of $((d\epsilon_0/dt)/\sigma_0^n)_{Tg}$ at log(p) = 0 are obtained. For the HIP diagrams the general relation

$$\dot{\epsilon} = A * \sigma^n * \exp(-Q/RT_g) \qquad [5]$$

is used, where Q is the activation energy for power law creep and A is a constant. Combining equations [4] and [5] results in

$$A(T_g) = \left(\frac{\dot{\epsilon}_o}{\sigma_0^n}\right)_{T_g} * \frac{1}{27} * \exp(Q/RT_g) \qquad [6]$$

HIP diagrams were calculated with a standard HIP487 package /87 Ashb/. We used values for the creep constants obtained from our dilatometer experiments and for the other parameter the values for gamma-iron given by Frost and Ashby /82 Fros/. The HIP diagrams were compared to densities of C1018 samples HIPed at 1000°C at different pressures for 1 and 20 min. Figure 21 shows a HIP-diagram for 900°C calculated with the parameters given by /82 Fros/ for gamma-Fe. The isochrones are for 1 and 20 min. The agreement between the HIP diagram and the measured densities is quite good. Certain deviations would be expected, since gamma-iron will deviate from the properties of steel C1018 which contains a certain amount of carbon.

Sinter-HIP and Final Stage HIPing of Single Phase W-Ni

During usual HIPing the powders must be encapsulated in closed thin walled preforms, which is tedious and costly. Starting 1985, a new method, sinter-HIP came to the fore /87 Baue/, /87 Kola/. The development became possible by the construction of advanced HIP equipment with pressure vessels that allow dewaxing of binders, which are often added to the initial powder mixtures for superior handling, vacuum sintering and subsequent hot isostatic pressing in one cycle. The vacuum sintering is performed to closed porosity (porosity below 6%), that means, to a state, where all pores are separated from each other and completely enclosed in a dense material matrix.

Materials that can hardly be sintered to densities above 96%TD due to grain boundary pore separation, can be HIPed to complete density if power law creep yields pore elimination independent of the grain boundary sinks. If power law creep is negligible due to low applied pressures or low bulk diffusivities, an increased flow rate of vacancies from pores at the grain boundaries to the sinks may still lead to fast elimination of those pores which are situated at the grain boundaries if an external pressure is applied. When samples are subject to a high hydrostatic pressure as during HIP, the surface and grain boundary diffusion constants remain essentially constant, but the applied pressure gives much steeper gradients of the chemical potential of the vacancies and results in a faster vacancy flux towards the grain boundary sinks. The driving force for diffusional pore coarsening on the other hand remains unchanged.

Figure 22 clearly shows the grain boundary pore separation in a W-0.15wt.%Ni compact during prolonged sintering /88 Kays2/. The large pores are too immobile to remain attached to the grain boundaries. As shown in Fig.22b the application of 200 MPa at 1400°C changes the microstructure dramatically. In the wake of migrating grain boundaries all pores were eliminated. It can be shown that densification by other mechanisms, e.g. power law creep, which is most frequently observed in other systems and which depends on the bulk diffusivity, is small compared to the pore shrinkage by vacancy elimination at the grain boundaries /84

Kays/. The pore grain boundary breakaway diagram can be used for the HIP conditions after some additional kinetic considerations. If pores come into contact with a grain boundary they were subject to separation after a time interval t_c when the grain boundary has migrated into a position where the drag force of the pore is smaller than the pulling force of the grain boundary after a short time. During HIPing, pores which come into contact with a grain boundary may shrink during the time interval t_c to a size at which the attachment due to boundary control becomes dominating (Fig.6). As a result the pore subsequently migrates together with the moving boundary until it is completely eliminated (Fig.6b).

Elimination of Large Residual Pores in Composite Materials with a Softer Intergranular Phase

A number of sources can lead to residual closed pores which are still present at total porosities which are often only a part of a percent. Besides the usual porosity remaining from the starting porosity in randomly dense packed powder arrangements, undestroyed initial powder agglomerates, inhomogeneus flow of powder particles during mould filling or inhomogeneous drying rates in slip cast greens may lead to residual pores. Those pores may also originate in the thermal decomposition of inclusions at elevated temperatures.

The consolidation process and the elimination of large pores are often enhanced by adding intentionally a liquid phase. The efficiency of HIPing in the presence of a liquid phase has been shown for metallic high-tech materials, such as heavy metal alloys or hard metals and also for high tech ceramics, such as reaction sintered SIALONS or Si_3N_4 where the presence of a liquid phase is sometimes unintentionally caused by impurities or sintering aids /84 Past/,/79 Bosk/,/86 Stut/,/88 Kim/,/79 Mona/.

In these polyphase materials consisting of a comparatively mobile intergranular phase and comparatively immobile grains, large residual pores can be eliminated during sintering or final stage HIPing by liquid flow or by a mixed liquid-grain flow /84 Kang/,/87 Kays3/,/87 Kwon/. A transition from liquid flow to mixed liquid/grain flow can occur by changes in the "viscosity", the volume fraction of intergranular liquid phase and the grain size of the solid constituents /82 Kays/,/87 Kays3/. In encapsulated material, surface stresses due to an applied external hydrostatic pressure are transmitted into the interior of the bulk by the solid particles, with stress concentrations at the particle contacts. Shape change and rearrangement of solid particles "squeeze" melt out from fine capillaries providing the excess liquid for filling the larger pores.

Unencapsulated HIPing of systems with an interconnected liquid of high viscosity and with isolated pores yields the same deformation stresses at the necks of the solid particles as in encapsulated material, but reduced by the local isostatic pressure of the viscous phase. The filling of pores by the mobile phase alone results in soft spots and an inhomogeneous microstructure. To avoid this unfavourable microstructural develop-

ment, it is necessary to fix the conditions under which filling of the larger pores occurs by mixed flow of grains and viscous phase.

The elimination of large artificial pores with a diamter of 80μm during HIPing was investigated in presintered W-Ni and in presintered Al_2O_3 with additions of anorthite ($CaO \cdot Al_2O_3 \cdot 2 SiO_2$). Figure 23 shows microstructures of presintered W-Ni-samples with different Ni-content after HIPing at 50 MPa for 10 min. In the sample with a small Ni-addition of 0.35 vol.% (Fig.23a) the large artificial pores were filled with a a mixture of mobile Ni-rich phase and W grains after HIPing at 1450°C. In samples with a higher Ni-content (3.5 vol.%) a mixture of particles and Ni-rich phase is only found at the edges of the large pores, whereas the main central parts of the pores are filled with the Ni-rich phase alone.

During HIPing of presintered Al_2O_3-anorthite the large pores collapsed non-isotropically by a shearing flow of Al_2O_3 grains and anorthite (Fig.24a to d). Lower volume contents of anorthite required increased HIP pressures to initiate the pore elimination. With increasing grain size the artifical pores were filled by a mixed flow with increasing anorthite fractions in the prior pores, forming glass pockets in the case of an average grain size of more than 10μm.

Models which describe the filling of large residual pores in a material consisting of grains with a viscous intergranular phase should address two questions. Firstly, on the necessary conditions and the time dependence of pore elimination and secondly, on the extent of an increase of the ratio of the viscous phase to the grains in the prior pore space after pore elimination. The answers to both questions are expected to depend on a set of parameters such as the effective grain size G and grain shape F, volume fraction Φ and distribution S of the liquid phase, size r_p and volume fraction V_p of the pores and the applied external pressure P.

Pore elimination as such has been treated by Evans and Hsueh /86 Evan/. They developed a viscoelastic model that describes the shrinkage rate of large pores within a fine-grained body. The concept for hot isostatic pressing is based on the shrinkage potential derived from the sinter potential of the pores, the applied external pressure P and the viscous response determined by the creep characteristics of the polycrystal. In our treatment their initial assumption of a constant grain size is replaced by the assumption of simultaneous grain coarsening during the HIPing procedure. Furthermore, the shape change of the grains during creep is assumed to occur by dissolution-reprecipitation of material in the intergranular glassy layers with the diffusional transport in the glassy layers as the rate controlling step, in contrast to the earlier treatment by Evans, where Coble creep was assumed to determine the creep of the material.

During hot isostatic pressing in the presence of the liquid phase considerable grain growth may occur, which is usually well described by

$$G = (G_0^n + k_n t)^{1/n} \qquad [7]$$

where G_0 and G are the initial and the actual average, effective grain size. The growth constant is k_n; n is a factor between 2 and 3. Combining equations 6 with the viscosity dependence used by Evans, we obtain the critical time for complete pore closure

$$t_c = (G_0^3/k_3) * \{[P*r_{p0}/(2\Gamma+1)]^{(4*K1*k3/P)} - 1\} \qquad [8]$$

where Γ is the specific interface energy solid/vapour and r_{p0} is the initial pore radius. Equation [8] relates the pore removal time to the grain size, the pore size, the external pressure and to the transport properties of the intergranular liquid films. Figure 25 shows the dependence of t_c on the initial grain size and the grain growth rate k_3. The foregoing treatment indicates conditions under which pore removal is possible in a certain time interval. If the pore shrinkage rate is low, grain growth will reduce the "viscosity" rapidly and limit the possibility of eliminating the pores in practical annealing time.

The second question to be answered by a model is, whether removal of pores occurs by mixed flow of liquid and grains or by liquid flow alone. The situation at the surface of the large pore is simplified as shown in Fig.26. On the right hand side of the block in Fig.26b the pore surface is composed of grains and intergranular thin liquid films. At all other sides of the block, the bulk continues. Due to the pressure difference the viscous phase flows through the horizontal layers with an average velocity v_2 and produces a shear stress transmitted to the grains. The separation of grain G_r from the other grains is restricted by the flow of viscous phase into the flat rear area between grain G_r and its horizontal neighbour. We can obtain a relation between the time interval t_c and the force F_{sep} required for the increase of the initial layer of thickness δ_{vp} to a final thickness /88 Kays6/. The amount of liquid flown as intergranular liquid films around one grain during t_c gives a ratio to the amount of grain volume flowed into the pore which is

$$\Phi_p = 0.065 + \Phi_{10} \quad , \qquad [9]$$

where Φ_{10} is the initial liquid phase content of the material resulting from the intergranular viscous layers of thickness δ_{vp}. The result indicates that no variation in the ratio of liquid to solid grains is possible beyond this value if liquid flow occurs only in planar intergranular liquid films and if the mobility of the grains obeys such a simple dependency as discussed above. In pores filled during final stage HIPing an additional glass content of appr. 6 vol.-% is thus predicted.

From microstructural observations it is obvious, however, that much higher melt contents of up to one can be found in pores eliminated during final stage HIPing. This additional amount of viscous phase may flow through melt channels which can be present at triple junctions of grains (Fig.26c). The flow through the channel is approximated with the Hagen-Poiseuille equation to

$$dV_2/dt = \frac{\pi * P * r^4}{8 * n * (GK_2)} \qquad [10]$$

where r is the effective channel radius and n is the viscosity of the viscous phase. The factor K_2 relates a measured grain size to the grain size that is effective for this model.

The volume fraction of melt has flowed through the channels into a pore (other contributions are flow through flat films and the grain movement itself) in the time intervall t_c into eliminated pores in a matrix material with an initial glass content of Φ_{20}, is given by

$$\Phi_c = \frac{\Phi_{20}^2}{\Phi_{20}^2 + (6.31\delta_{vp}/GK_2)^3} \qquad [11]$$

Figure 27 shows Φ_c for initial melt fractions in channels of $\Phi_{20} = 0.01$, 0.025 and 0.05 and δ_{vp}/GK_2 ratios between $5*10^{-4}$ and $5*10^{-2}$.

The results are in qualitative agreement with the experimental observations. A lower δ_{vp} to GK_2 ratio, that means in our case a larger grain size, increased the amount of glass in the eliminated pores considerably. The amount of glass in the filled pores also increased with increasing initial melt content.

EXAMPLES OF ADVANCED PM'MATERIALS

As mentioned above, the use of HIPing or hot extrusion provides dense materials also from unsinterable particulate combinations, such as short fibre reinforced composites and oxide dispersion strengthened high temperature alloys. Mixtures of fibers of high strength and high stiffness with fine powders are consolidated at temperatures low enough to avoid fiber decomposition by chemical reactions with the matrix but to allow sufficient bonding to cause the fibers to adhere with the matrix. Whereas reinforcement of metals and ceramics with long fibers was not found economically viable, short fibre reinforcement, particularly with SiC whiskers, is seen to be more advantageous in respect to the cost/property improvement ratio /86 Sing/. At present the most frequently investigated systems are SiC-whisker reinforced Al_2O_3, Si_3N_4, and Al alloys /86 Sing/. A number of technical and economical problems are still unsolved. The SiC whiskers are too expensive at present. The distribution of the whiskers in the fine matrix powders and sintering to closed porosity, as well as chemical reactions between the whiskers and the matrix, still require extensive research.

Oxide dispersion hardened Al alloys or superalloys are produced by reaction milling in attritors or large ball mills. During milling, surface oxides on the powder are destroyed and finely distributed in the interior of the powders together with other intentionally added fine oxide powders due to a continuing

fracture and rejoining sequence /77 Benj/. A modification of this method is the reaction milling of a mixture of Al and graphite powder which provides an extremely homogeneous distribution of fine graphite inclusions in the Al matrix /77 Jang/. During tempering of the hot extruded milled blends, fine Al_4C_3 dispersoids form at the sites of the fine graphite inclusions. The tensile strength of this material at 400°C is 50 % of the RT tensile strength.

HIPing and other new consolidation methods such as hot extrusion also allow fast densification and defect healing of coarse, unsinterable powders with highly nonequilibrium and unusual microstructures. Such powders with unique microstructures are produced by rapid solidification due to high cooling rates and high undercooling, resulting in refinement of microstructures, decreased segregation, formation of metastable and new phases as well as in increased solid-solubility ranges. Gas or water atomization are valuable methods for producing rapidly solidified powders for high performance materials in large quantities. In these methods a thin falling stream of the molten alloy is disintegrated into fine droplets by the impact of high pressure gas or water jets /84 Klar/.

An important aspect of the microstructural refinement is the cooling rate of the droplets which determines in the absence of undercooling, the velocity of the solidification front. The cooling rate is governed by the convective heat transfer from the droplet to the surrounding flowing gas. The cooling rates range from 10^4 to 10^7 Ks^{-1} for droplets of 50 μm (argon) to 5 μm (helium) in diameter, respectively. For a group of advanced PM'materials the use of particles with fine microstructures is not sufficient, but segregation-free microstructures are required. They allow the formation of highly supersaturated solid solutions yielding for example an amount of extremely fine precipitates during aging often far in excess of what could be obtained by solid solution homogenization and subsequent precipitation annealing at temperatures of lower solid solubility. These precipitates are often stable against further coarsening due to a low equilibrium solid solubility of the alloying elements in the solvent at application temperatures. Segregation-free solidification is possible only if the growth velocity of the solidification front is larger than the diffusional speed of the solute atoms /86 Boet/.

In Cu-7wt.%Sn a solidification front velocity of approximately 4 ms^{-1} is then required for segregation-free solidification, which is high compared to the velocities of 0.02 ms^{-1} obtained during cooling of an atomized 5μm droplet /see also 88 Gree/. To obtain a sufficiently fast solidification front movement in fine melt droplets, considerable undercooling of the liquid is necessary before solidification. Undercooling is possible if potent heterogeneous nuclei are absent. The probability of a potent heterogenous nucleus to be present in a droplet decreases with decreasing droplet volume, if heterogeneous nucleation at surface nucleation sites which form during atomization are neglegted. The number of powder particles which have solidified after considerable undercooling, that means in which highly potent nuclei had been absent, therefore increases rapidly with decreasing particle

size. Due to extensive engineering efforts, facilities are available today, where the required fine powders can be produced in large quantities at increasing cost efficiency.

From the abundance of recent developments of materials from rapidly solidified powders, three examples are subsequently presented. The first example, the aluminides, illustrate the beneficial use of high cooling rates to obtain finer microstructures. The other two examples a dispersion strenghtened Cu-Sn alloy and a Cu-Ti-B alloy are indicative of the advantages of high undercooling on the microstructure and the properties of atomized powders.

Aluminides (intermetallics) have recently become the object of considerable interest as a potential structural material for high temperature applications. The cubic $L1_2$ (Ni_3Al) and B2 (FeAl, NiAl) structures yield special properties such as a low specific weight (compared to the superalloys), high strength and high elastic moduli which make them interesting for mass-critical applications in aircraft and space industry. Excellent corrosion-resistance up to 800°C combined with high yield strength at elevated temperatures, open a wide field in coatings, especially in oxygen-rich hot gases, with an optimum relation of price to performance. A major problem for high temperature structural applications of coarse-grained intermetallics is their extreme brittleness, whereas single crystals and polycrystals with grain sizes smaller 20μm display considerable ductility at room temperature /87 Schu/. The failure of coarse grained materials results from an insufficient number of easily to activated glide systems, and weak grain boundary structures with a sensitivity to segregation of impurity atoms. Several remedies exist to improve the unfavoured properties, the most promising one being the use of rapid solidification to obtain fine grained materials. Figure 29 shows Ni-Al, Fe-Al and Ni_3Al powders which were obtained by Ar-atomization /88 Laag/. These microstructures indicate that PM techniques, including atomization, may at least improve the forming process of intermetallic parts.

A homogeneous distribution of fine oxides, that means dispersion strengthened material, can be obtained directly from rapidly solidified melts. The argon atomized Cu-7Sn particle in Fig.30a shows an area where segregation-free solidification occured. Undercooling was increased by minimizing the number of potent nuclei. With the addition of Al, the metal oxides which were the initial potent nuclei of the melt were transformed into fine, dispersed Al_2O_3 particles of low potency. A homogeneous distribution of Al_2O_3 particles was obtained in areas that solidified segregation-free /88 Rzes/ (small, bright spots in Fig.30b). If further undercooling or more rapid heat extraction during recalescence can be achieved, those "in situ" dispersion strengthened materials may be of commercial interest in the future.

Alloys of Cu-Ti are mainly used as electric conductors and contact materials with increased microhardness on only slightly decreased electrical conductivity compared to unalloyed Cu /85 Schr/. The mechanical and electrical properties of Cu-Ti can still be improved by the addition of boron resulting in disper-

sion hardened copper-alloys for welding-machines. If suitable amounts of B and Ti are added to Cu, extremely stable TiB_2 precipitates are thought to form during ageing, with a negligible amount of Ti and B remaining in the solid solution, providing an increased hardness at high electrical conductivity. During cooling of ternary Cu-Ti-B melts at rates below 10^4 Ks^{-1} the primary solidification of TiB_2, however, yields precipitates, which are too coarse for effective precipitation hardening. In atomized powders the primary precipitation of TiB_2 during solidification is suppressed due to undercooling and a high cooling rate. Ti and B are kept in a supersaturated Cu solid solution, which provides a hardness of more than 500 $HV_{0,1}$ after ageing the powders at moderate temperatures /88 Bosi/.

THE FUTURE OF PM MATERIALS

PM materials have been recognized by most of the governments of the technologically leading countries as one of the keys for the development of advanced technologies. German PM research and development, for example, was supported in 1987 by the BMFT (Bundesministerium für Forschung und Technologie) with 60 million DM. The faith in the potential of powder metallurgy is based on two points

- PM can give individual answers to specific material requirements. The inherent flexibility of PM materials, compared to cast materials, results from an almost unlimited number of workable phase combinations, which include ceramics, polymers and metals. PM is one of the most promising ways to produce complex composites.

- PM allows the production of refined, more homogeneous and highly supersaturated materials. New classes of materials can be used, which require small grain sizes, such as the intermetallic phases.

Powders will increasingly be used to form thin layers or layered structures. Plasma spraying of powders has already become an important method to obtain high quality surface coatings. Spray deposition of atomized liquid droplets on substrates is increasingly serving the same purposes. Fine droplets feed a rapidly solidifying thin liquid layer on a substrate, a method which smoothly bridges the gap between PM and casting technology.

Acknowledgement

The continued support of the Internationales Büro of KFA Jülich and the Deutsche Froschungsgemeinschaft is thankfully acknowledged.

REFERENCES

/49 Kucz/ G.C.Kuczynski, Trans AIME, 185(1949)169.
/61 Cobl/ R.L.Coble, J.Appl.Phys., 32(1961)787.
/69 Broo/ R.J.Brook, J.Am.Cer.Soc., 52(1969),56.

/70 Schi/ V.W.Schintelmeister and K.Richter, Planseeberichte für Pulvermetallurgie, 13(1970),3.
/75 Mole/ O.Molerus, Powder Tech., 12 (1975), 259.
/77 Benj/ J.S.Benjamin, M.J.Bonaford, Met.Trans., 8A(1977)1301.
/77 Jang/ G.Jangg, F.Kutner and G.Korb, Powder Met.Int., 9(1977) 24-26).
/78 Hill/ M.Hillert and G.Purdy, Acta Metall. 26(1978)333-340.
/78 Uema/ K.Uematsu,R.M.Cannon,R.D.Bagley,M.F.Yan,U.Chowdry, and H.K.Bowen, in Int. Symposium of Factors in Densification of Oxide Non-Oxide Ceramics, eds. H.Saito and S.Somiya, Hakone, Japan (1978),190.
/79 Bosk/ S.Boskovic,L.J.Gauckler,G.Petzow, and T.Y.Tien, Powder Met.Int.,11 (1979)169-170.
/79 Mona/ R.D.Monahan and J.W.Halloran, J.Am.Ceram.Soc.,62(1979) 564-567.
/80 Petz/ G.Petzow and W.A.Kaysser, in Science of Ceramics 10, ed. H.Hausner, (Weiden, FRG, Deutsche Keramische Gesellschaft, (1980),269-280.
/80 Swin/ F.B.Swinkels and M.F.Ashby, Powder Metallurgy, 23(1980)1-7.
/82 Broo/ R.Brook,S.P. Howlett and Su Xing Wu, in "Sintering-Theory and Practice, eds. D.Kolar, S.Pejovnik and M.M.Ristic,"Material Science Monographs", Elsevier Scientific Publishing Company, Amsterdam, (1982),135-144.
/82 Hsue/ C.H.Hsueh, A.G.Evans and R.L.Coble, Acta Metall., 30(1982),1269.
/82 Kays/ W.A.Kaysser,D.J.Kwon and G.Petzow, Proc. PM'82 Europe, Florence (1982)23-30.
/82 Pejo/ S.Pejovnik, D.Kolar, W.J.Huppmann and G.Petzow, in Sintering - Theory and Practice, eds. D.Kolar, S.Pejovnik and M.M. Ristic, Elsevier Scientific Publishers, Amsterdam (1982)361-365.
/83 Arzt/ E. Arzt, M.F. Ashby, K.E. Easterling, Met. Trans.,14A (1983)211.
/83 Arzt2/E.Arzt, Acta Met., 30(1982)1883.
/83 Swin/ F.B.Swinkels, D.S.Wilkinson, E.Arzt, M.F. Ashby, Acta Met., 31(1983)1829.
/84 Kang/ S.-J.L.Kang, W.A.Kaysser, G.Petzow, and D.N.Yoon, Powder Met., 27(1984)97-100.
/84 Kays/ W.A.Kaysser, M.Mitkov and G.Petzow, Proceedings "Colloquium on Unconventional Forming Processes in Powder Metallurgy", 19.-20. Sept., Paris (1984).
/84 Klar/ Metals Handbook, Ninth Edition, Volume 7, Powder Metallurgy, coordinator E.Klar, American Society for Metals, Metals Park,Ohio (1984).
/84 Past/ A.E.Pasto,J.T.Neil,C.L.Quackenbush, Ultrastructural Processing of Ceramics, Glasses and Composites, eds. L.L.Hench and D.R.Ulrich, Wiley and Sons,New York (1984).
/84 Petz2/G.Petzow and W.A.Kaysser, in Sintered Metal-Ceramic Composites, ed. G.S.Upadhyaya, Elsevier Science Publishers, Amsterdam (1984),51-70.
/85 Benn/ S.J.Bennison and M.P.Harmer, J.Am.Ceram.Soc. 68(1985)C22-24.
/85 Kang/ S.-J.L.Kang, W.A.Kaysser, G.Petzow and D.N.Yoon, Acta Metall., 33(1985)1919-1926.
/85 Kays/ W.A.Kaysser, M.Hofmann-Amtenbrink and G.Petzow, Powder

Metallurgy, 28(1985),199-206.
/85 Kays/ W.A.Kaysser and G.Petzow, Powder Metallurgy, 28(1985)145-150.
/85 Lee/ J.S.Lee,W.A.Kaysser and G.Petzow, in "Modern Developments in Powder Metallurgy", eds. E.N.Aqua and C.M.Whitman, MPFIF-APMI, Princeton,N.J., 17(1985)99-112.
/85 Hand/ C.A.Handwerker, J.W.Cahn, D.N.Yoon and J.E.Blendell, in Atomic Transport in Alloys: Recent Developments, eds. G.E.Murch M.A.Dayananda, (Dayton, OH, TMS/AIME Publications,1985).
/85 Schr/ H.Schreiner, in Mitteilungen aus dem Ausschuß für Pulvermetallurgie, eds. W.J.Huppmann, H.Hassel; Powder Met.Int., 17(1985)195-198.
/85 Yoon/ D.N.Yoon, J.W.Cahn, C.A.Handwerker, J.E.Blendell and Y.J.Baik, in Interface Migration and Control of Microstructure, (Washington, NBS, 1985).
/86 Boet/ W.J.Boettinger, S.R.Coriell, in Science and Technology of the Undercooled Melt, Eds. P.R.Sahm, H.Jones, C.M.Adam. NATO ASI Series E; no.114. 81-110,1986.
/86 Evan/ A.G.Evans and C.H.Hsueh, J.Am. Ceram.Soc., 69(1986)444-448.
/86 Hsue/ C.H.Hsueh,A.E.Evans,R.M.Cannon and R.J.Brook, Acta Metall., 34(1986)927-936.
/86 Mitk/ M.Mitkov, W.A.Kaysser, G.Petzow, in "Sintering '85", eds. G.C. Kuczynski et al., Plenum Press, NY and London, (1986)
/86 Sing/ R.F.Singer and M.J.Couper, in Powder Metallurgy 1986 - State of the Art, Powder Metallurgy in Science and Practical Technology, Vol.2, eds. W.J.Huppmann, W.A.Kaysser and G.Petzow, Verlag Schmid, Freiburg (1986)177-204).
/86 Stut/ D.Stutz,P.Greil,and G.Petzow, J.Mat.Science Letters, 5(1986)335-336.
/87 Baue/ R.Bauer, Powder Met.Int.,19(1987)13-17.
/87 Schu/ E.M.Schulson, J.Powder Metallurgy, 23(1987)1.
/87 Kays1/W.A.Kaysser, M.Hofmann-Amtenbrink and G.Petzow, in Sintering'85, eds. G.C.Kuczynski, D.P.Uskokovic, H.Palmour III and M.M.Ristic, Plenum Press, New York (1987), 121-132.
/87 Kays2/W.A.Kaysser, M.Sprissler, C.A.Handwerker and J.E.Blendell, J.Am. Ceram.Soc., 70(1987)339-343.
/87 Kays3/W.A.Kaysser, Proc.First International Conference on Ceramic Powder Processing Science,Orlando, 1-4 Nov.1987, eds. G.Messing and H.Hausner.
/87 Kays4/W.A.Kaysser, M.Aslan und G.Petzow, in Sinter/HIP-Technologie, Hrsg. H.Kolaska, Pulvermetallurgie in Wissenschaft und Praxis, Band 3, Schmid-Verlag, Freiburg, 67-86(1987).
/87 Kola/ Sinter/HIP-Technologie, Hrsg.H.Kolaska, Pulvermetallurgie in Wissenschaft und Praxis, Band 3, Verlag Schmid, Freiburg (1987).
/87 Kwon/ O.H.Kwon and G.L.Messing, in Sintering 85', eds. G.C.Kuczynski, D.P.Uskokovic, H.PalmourIII, and M.M.Ristic, Plenum Press, New York (1987) 165 - 171.
/87 Schn/ G.Schneider, E.-Th.Henig, H.H.Stadelmaier, G.Petzow, Proceedings of the 5th Int. Symp. on Magn. Alloys, Bad Soden, FRG (1987) 347-362

/88 Bosi/ D.Bosic, R.Laag, W.A.Kaysser, M.Mitkov and G.Petzow, Proceedings: of the VIII Yugoslav-German Meeting on Materials Science and Development, Brdo pri Kranju, Yugoslavia, eds. D.Kolar, M.Kosec and J.Krawczynski, KFA-Jülich, ISBN 3-89336-001-8, (1988)379-383.

/88 Exne/ H.E.Exner, Acta metall., in print.

/88 Kays1/W.A.Kaysser, Y.S.Kwon, I.H.Moon and G.Petzow, unpublished.

/88 Kays2/W.A.Kaysser and I.S.Ahn, submitted to Modern Developments in Powder Metallurgy, Vols.17 to 19.

/88 Kays3/W.A.Kaysser, to be published in Z.Metallkde.

/88 Kays4/W.A.Kaysser, M.Aslan, E.Arzt, M.Mitkov and G.Petzow, Powder Metallurgy, (1988)63-69.

/88 Kays5/W.A.Kaysser, M.Aslan, and G.Petzow, Proceedings of International Conference on Hot Isostatic Pressing of Materials: Applications and Developments, Antwerpen, 25.-27.April 1988, Royal Flemish Society of Engineers, 1.11-1.16.(1988).

/88 Kays6/W.A.Kaysser, A.Frisch, M.Aslan, and G.Petzow, Proceedings of International Conference on Hot Isostatic Pressing of Materials: Applications and Developments, Antwerpen, 25.-27.April 1988, Royal Flemish Society of Engineers, 2.1-2.10 (1988).

/88 Kays7/W.A.Kaysser and G.Petzow, J.Appl.Anorg.Chem., 100,1021-1025(1988).

/88 Kim/ D.J.Kim,P.Greil,and G.Petzow, J.Am. Ceram.Soc., in print.

/88 Laag/ R.Laag, W.A.Kaysser and G.Petzow, Proceedings: of the VIII Yugoslav-German Meeting on Materials Science and Development, Brdo pri Kranju, Yugoslavia, eds. D.Kolar, M.Kosec and J.Krawczynski, KFA-Jülich, ISBN 3-89336-001-8, (1988)395-402.

/88 Rzes/ K.Rzesnitzek, W.A.Kaysser, and G.Petzow, in Ceramics and Metals; Proceedings: of the VIII Yugoslav-German Meeting on Materials Science and Development, Brdo pri Kranju, Yugoslavia, eds. D.Kolar, M.Kosec and J.Krawczynski, KFA-Jülich, ISBN 3-89336-001-8, (1988)371-378.

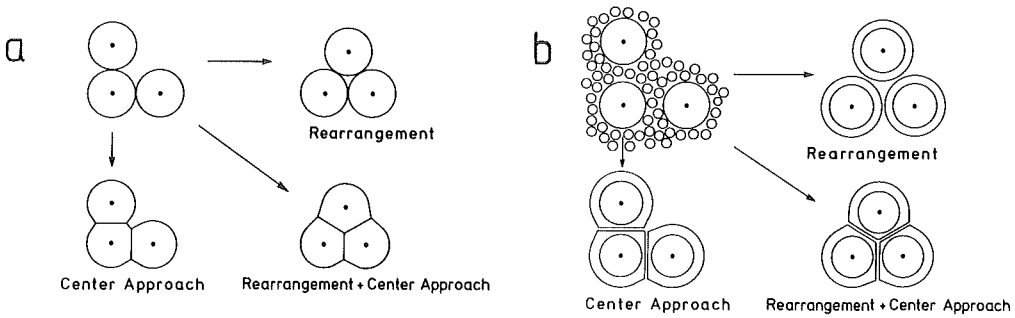

Fig.1 Shrinkage by rearrangement and center approach (shape change) during sintering. a) Monosized grains without coarsening. b) Grains with broad size distribution and coarsening.

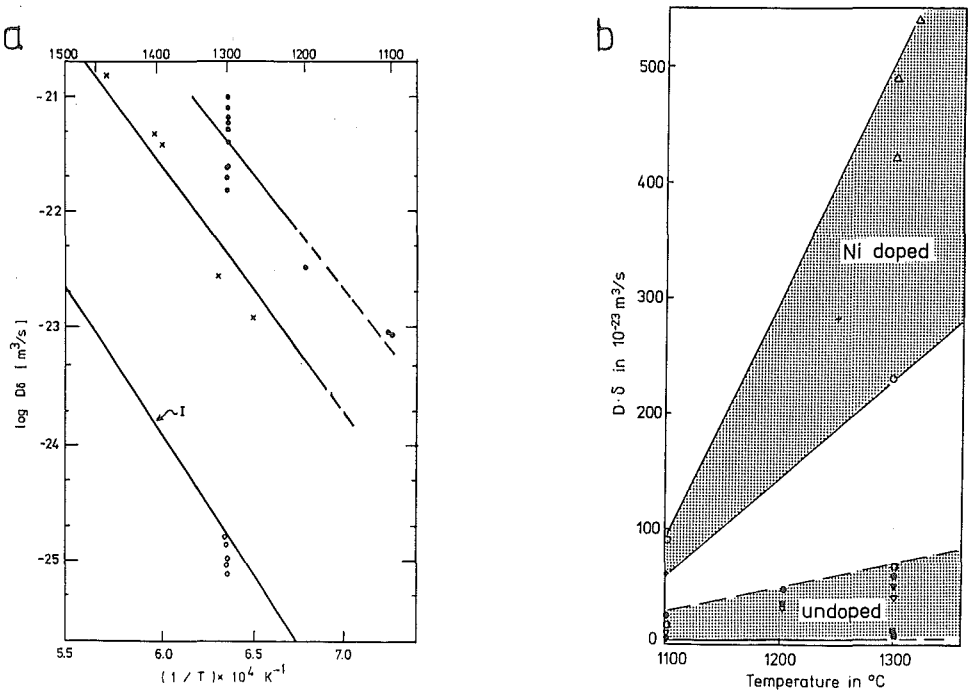

Fig.2a W; undoped I /70 Schi/, o /85 Kays/; Ni-doped x /70 Schi/, ● /85 Kays/.
Fig.2b Mo /85 Kays/.
Fig.2 Grain boundary self diffusion coefficients of undoped and Ni-doped W and Mo .

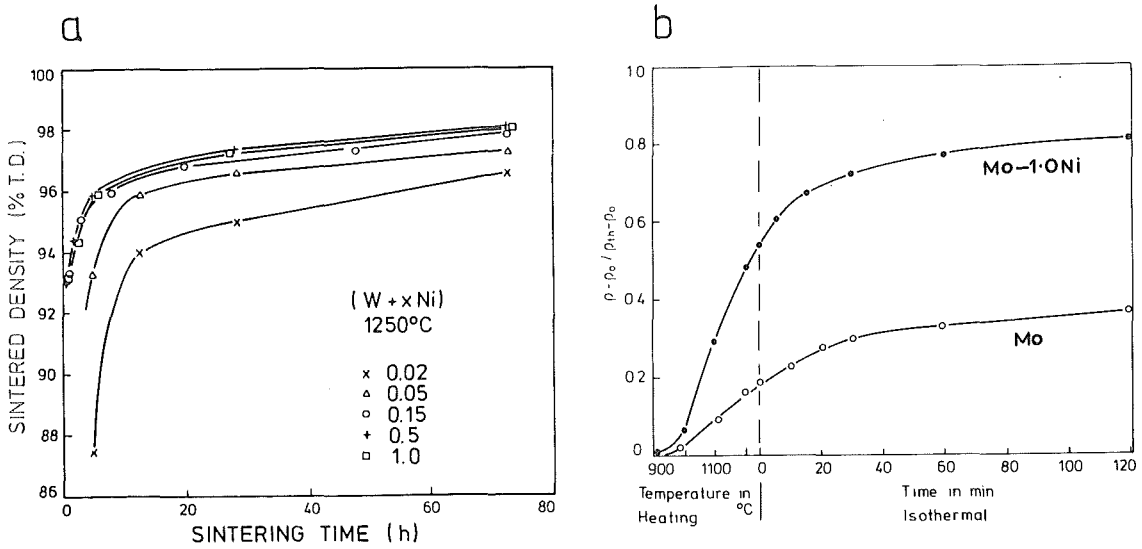

Fig.3a W-Ni compacts (200 MPa) during isothermal sintering at 1250°C (in wt.%)/88 Kays2/.
Fig.3b Mo-Ni compacts (200MPa) during heating to 1240°C and subsequent isosthermal annealing (ρ actual density, ρ_0 initial density, ρ_{th} theoretical density).
Fig.3 Shrinkage of Mo and W in the presence of Ni.

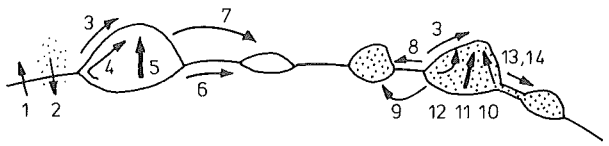

Fig.4 Mechanisms of grain boundary migration control. ○ pores, ⊛ second phase inclusions.

1 Intrinsic boundary movement, 2 impurity drag, 3 pore movement by lattice diffusion in the host material, 4 pore movement by surface diffusion, 5 pore movement by vapour transport, 6 pore coarsening by grain boundary diffusion, 7 pore coarsening by lattice diffusion, 8 inclusion coarsening by grain boundary diffusion, 9 pore coarsening by lattice diffusion, 10 inclusion movement by interface diffusion, 11 inclusion movement by grain boundary diffusion in the inclusion, 12 inclusion coarsening by lattice diffusion, 13 inclusion coarsening by interface diffusion, 14 inclusion coarsening by bulk diffusion in the second phase.

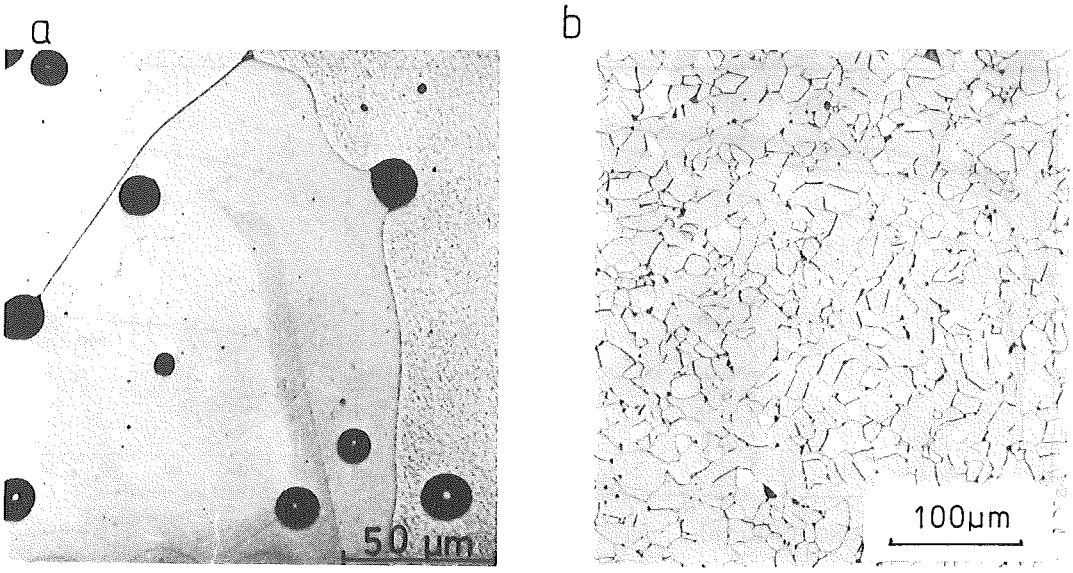

Fig.5a Microstructure showing pore drag and pore/grain boundary separation during final stage sintering of W-0.15Ni at 1400°C for 3h /88 Kays2/.
Fig.5b Al_2O_3 doped with 0.1wt.% MgO after hot pressing at 1800°C for 5 min /87 Kays2/.
Fig.5 Influence of Ni and MgO on complete densification of W and Al_2O_3.

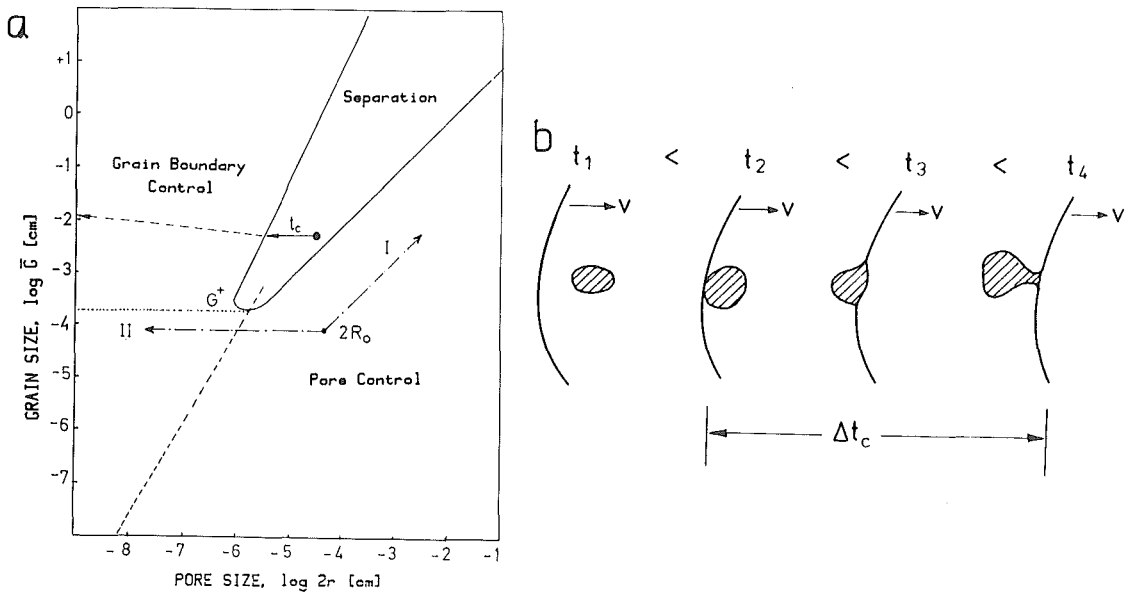

Fig.6 Pore/grain boundary separation during final stage sintering.
Fig.6a Pore/grain boundary separation diagram. $2R_o$ is the initial grain size.
Fig.6b Critical time t_c. A pore is passed by a grain boundary.

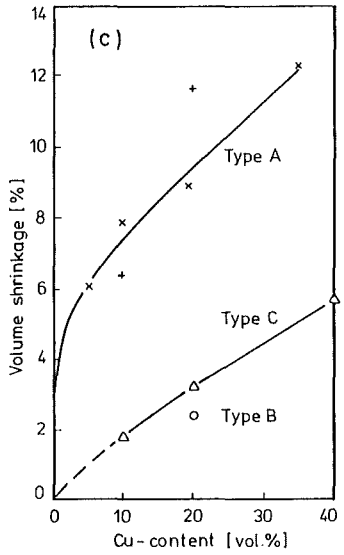

Fig.7 Volume shrinkage of W-Cu compacts after sintering at 1050°C for 1h /85 Lee/. A, B and C are W powders with an average particle size of 0.8, 5.0 and 2.4 μm.

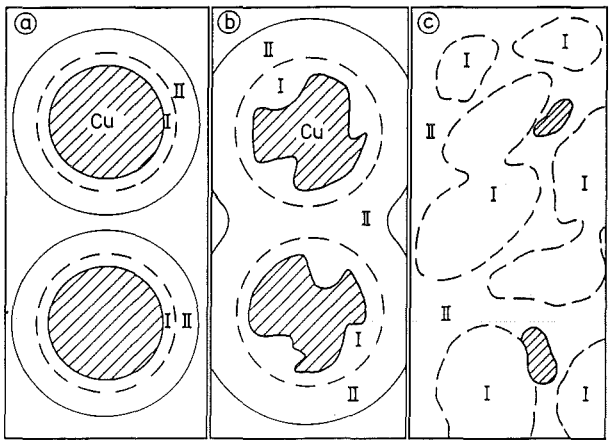

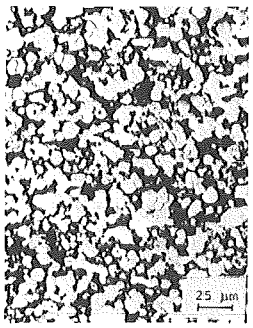

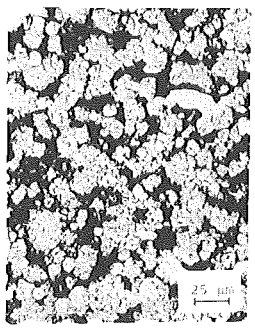

Fig.8a Shrinkage by aggregate formation starting from isolated individually shrinking aggregates (α). A zone (II) of rapidly spreading Cu is connecting the initial Cu particles (β). As a subsequent step dense Cu rich aggregates (I) form (Γ) /85 Lee/.

Fig.8b Enlargement of aggregates during sintering of W-10Cu at 1050°C for (α) 5 min and (β) 16 h.

Fig.8 Spreading of Cu and aggregate formation in W-Cu compacts during solid state sintering (85 Lee).

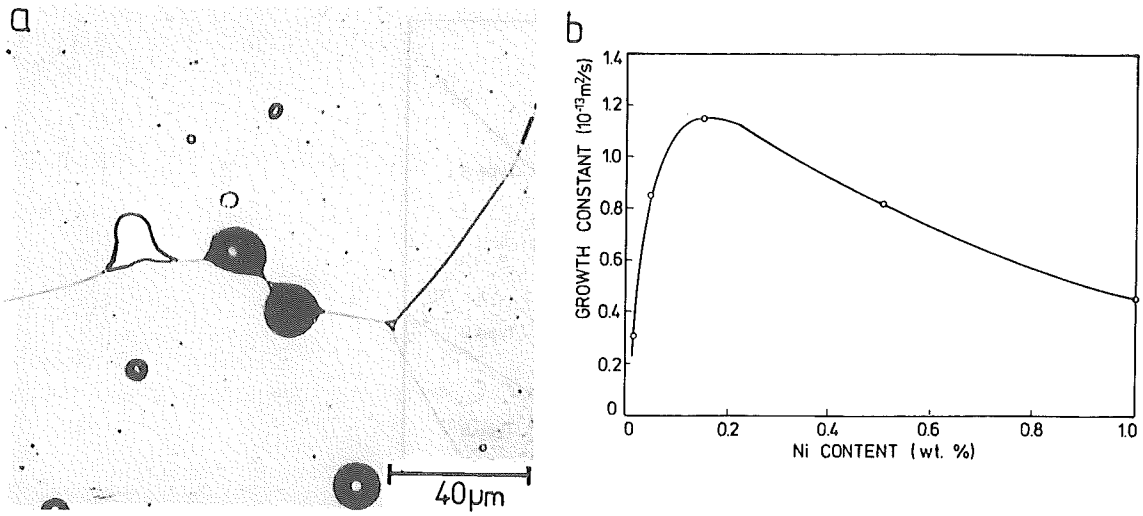

Fig.9a Second phase drag and separation of second phase inclusions from the boundary in W-1wt.%Ni after sintering at 1400°C for 122 h /88 Kays2/.
Fig.9b Grain growth constants of W-Ni compacts during sintering at 1250°C.
Fig.9 Influence of a small amount of second phase with mutual solubility of the components on boundary drag and grain growth /88 Kays2/.

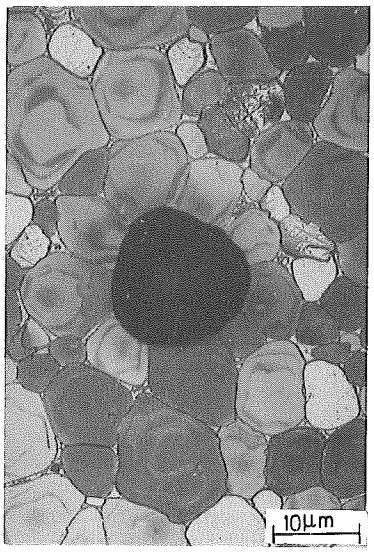

Fig.10 Microstructure of Mo-4wt.%Ni after cyclic liquid phase sintering between 1300 and 1460 °C (Held at 1460 °C for 30 min in each cycle). Etched with Murakami's solution /85 Kang/. The bulk material is densely packed, the center is a pore.

$$\frac{dh}{dt} = \frac{const}{h^2} - \frac{h}{2R} \times \frac{dR}{dt}$$

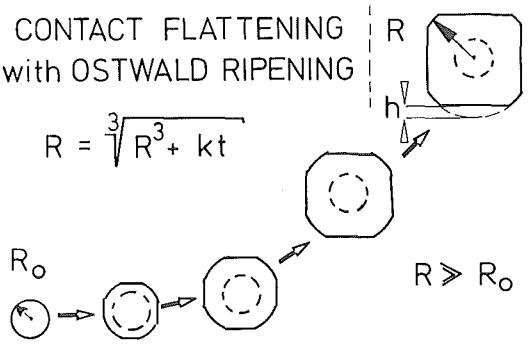

Fig.11 Shape accomodation during Ostwald ripening.

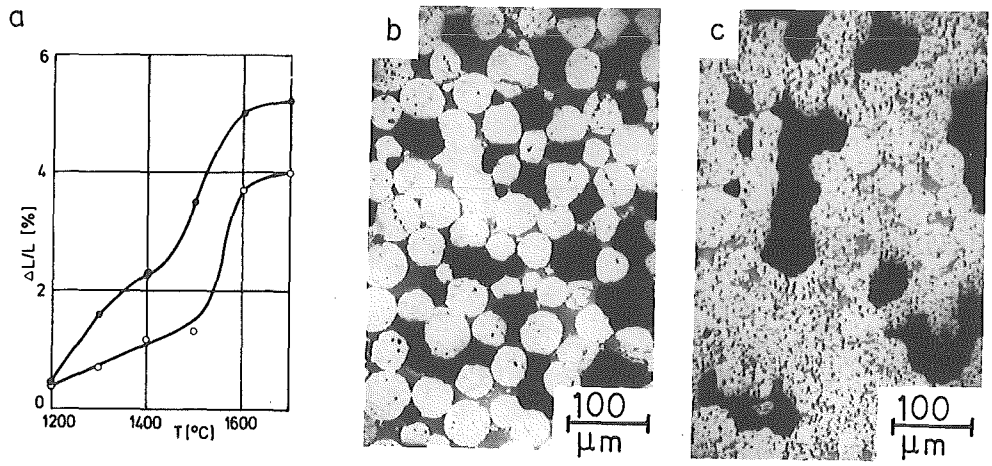

Fig.12 Microstructure and shrinkage during liquid phase sintering of Al_2O_3-alkali borate glass /80 Petz/, /82 Pejo/. a) - Shrinkage ° after 1 min, • after 120 min. b) - Microstructure after 1h at 1400°C. c) - Microstructure after 1h at 1700°C.

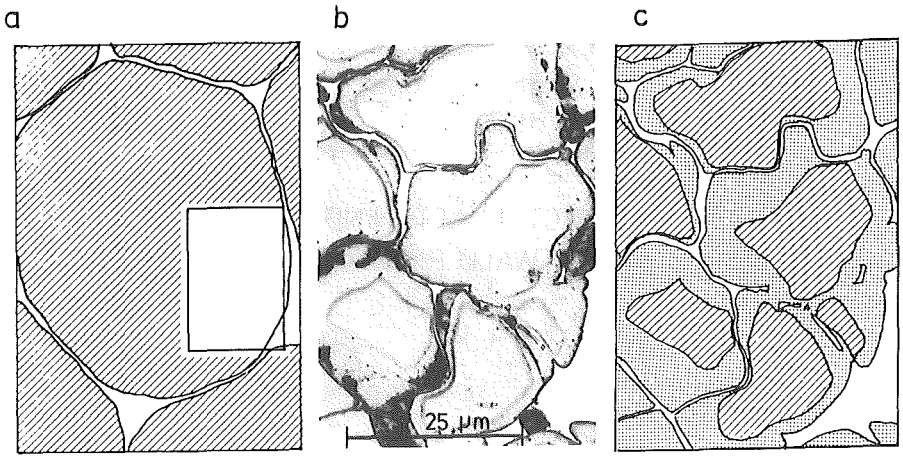

Fig.13a Overview, schematic
Fig.13b Microstructure
Fig.13c Formation of solid solution, schematic; white: melt, dotted: solid solution Fe(Cu), lined: unalloyed Fe
Fig.13 Liquid film migration in Fe-10Cu during liquid phase sintering at 1120°C /85 Kays2/.

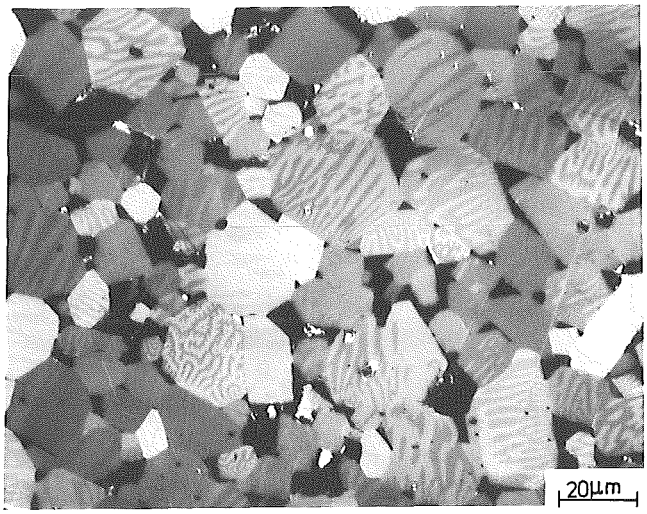

Fig.14 Pore free microstructure of liquid phase sintered Fe-18.5Nd-6.5B. The magnetic grains are indicated by the Kerr effect. The dark areas are solidified eutectic melt.

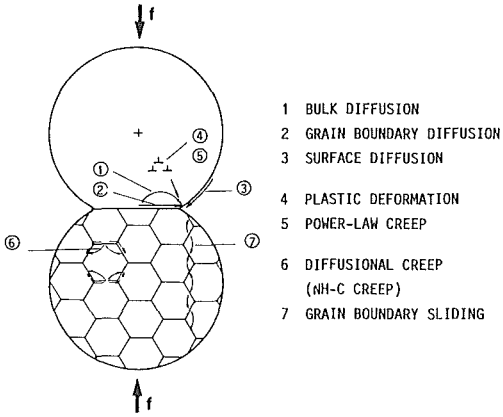

Fig.15 Transport mechanisms operating during HIPing.

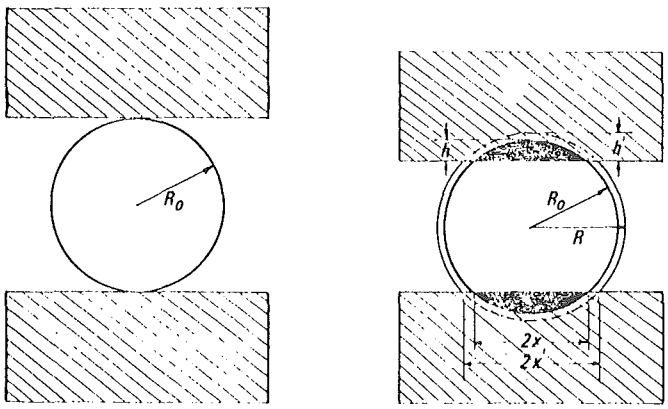

Fig.16 Schematic diagram of sphere between two parallel plates.

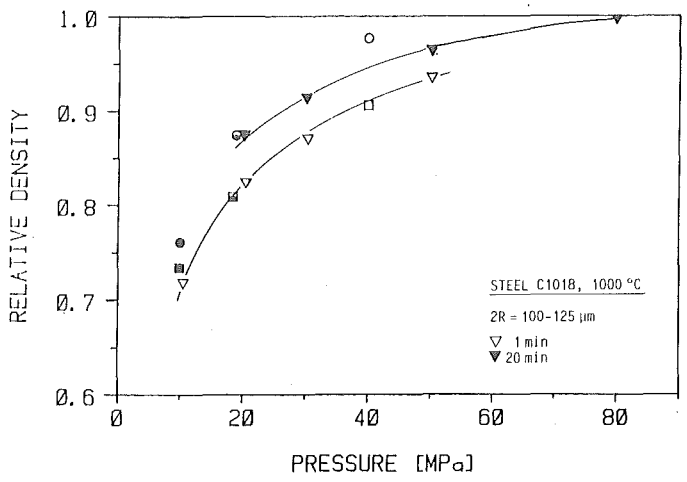

Fig.17 Comparison of HIP densities calculated from single sphere dilatometer measurements and obtained after HIPing of C1018 and Cu. HIP describes HIPed specimens. f and $p_{HIPäq}$ describe the force on single spheres in the dilatometer and the equivalent HIP pressure. HIP densities from C1018 (Particle size 100-125 µm) after 1 and 20 min. Calculated densities from single sphere deformation (Particle size 180 µm):
f=0,45 N, $p_{HIPäq}$=40 MPa, □ 1 min, ○ 20 min;
f=0,25 N, $p_{HIPäq}$=18 MPa, ◪ 1 min, ◒ 20 min;
f=0,16 N, $p_{HIPäq}$= 8 MPa, ■ 1 min, ● 20 min

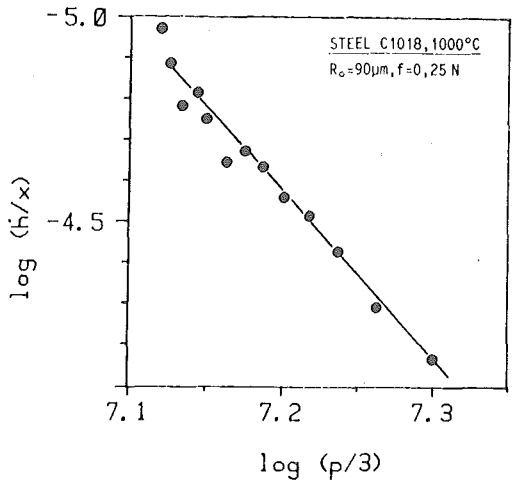

Fig.18 Stress dependency of the deformation rate of C1018 at 1000°C.

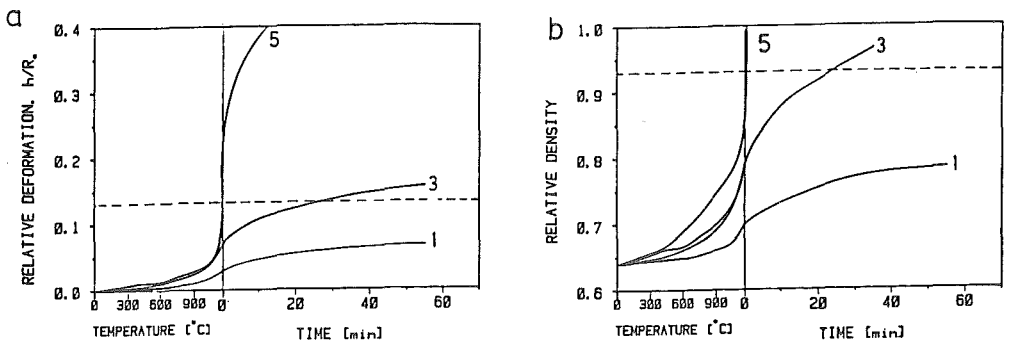

Fig.19a Relative deformation.
Fig.19b Relative density
Fig.19 Deformation of high speed steel spheres (diameter 150 µm) in a dilatometer during heating up an subsequent isothermal annealing at 1150 °C (Loads: 1 = 0.18N, 3 = 0.35N, 5 = 0.74N).

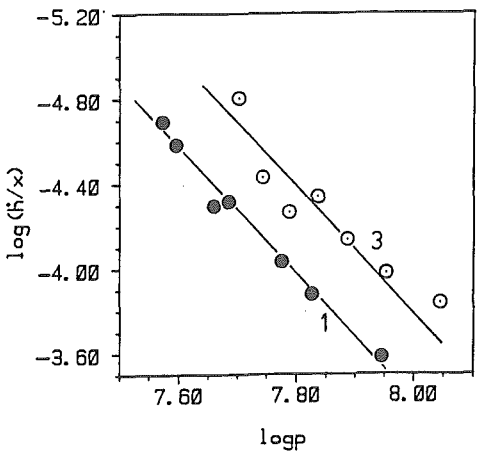

Fig.20 Deformation rate vs pressure of high speed steel spheres.

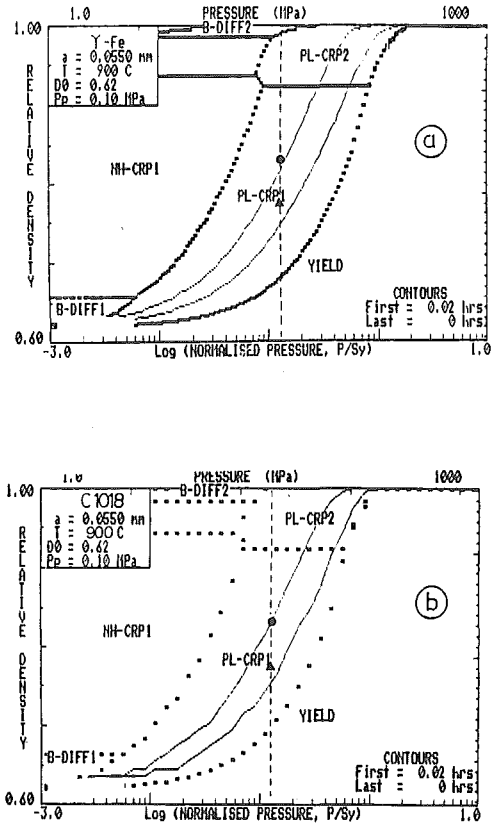

Fig.21 HIP diagramm of gamma-Fe (C1018) at 900 °C. a) Parameters from Frost and Ashby /82 Fros/. b) Modified parameters from dilatometer experiments.

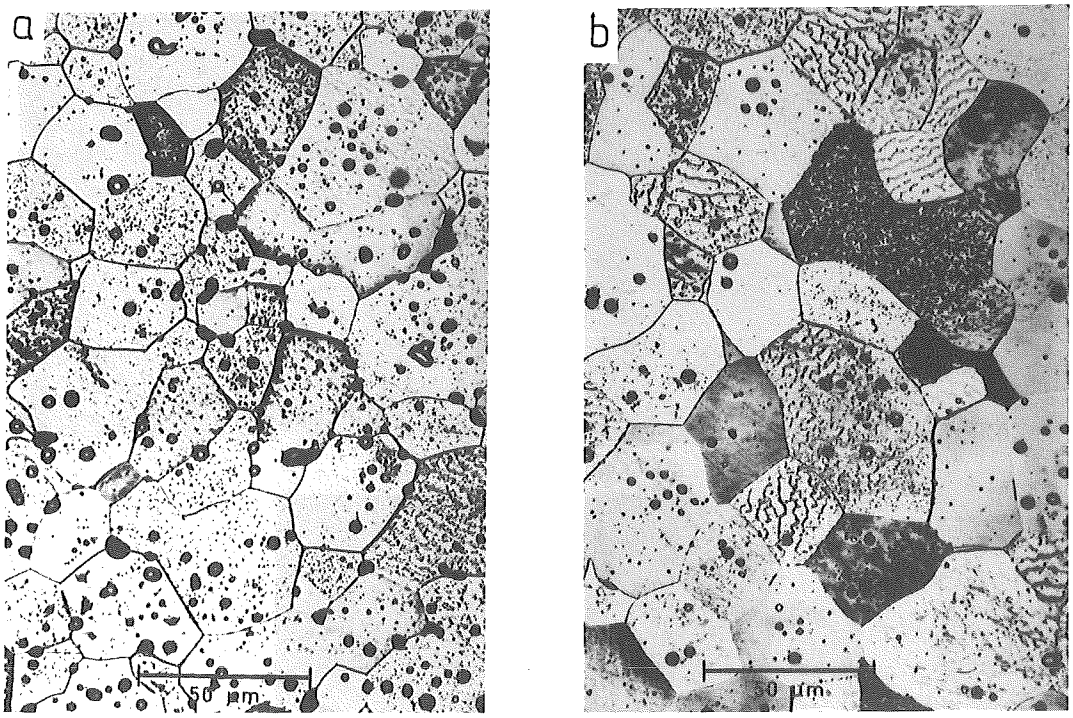

Fig.22a After sintering for 1h.
Fig.22b After sintering for 1h and subsequent HIPing at the same temperature for 1h at 200 MPa /88 Kays2/.
Fig.22 Microstructure of W-0.15Ni after annealing at 1400°C.

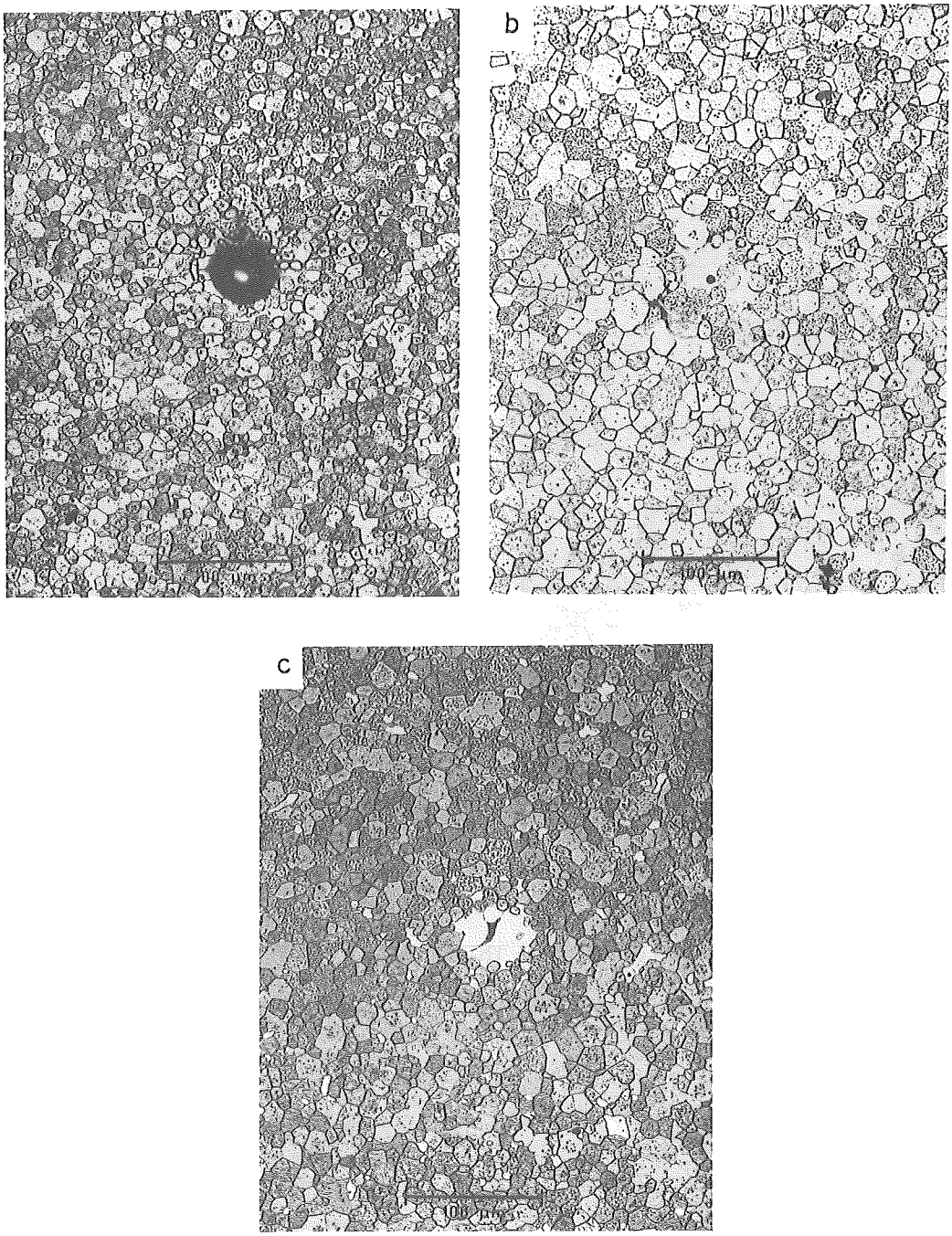

Fig.23 Closed large artificial pores in presintered W-Ni after HIPing for 10 min at 50 MPa. a) W-0.35 vol.-% Ni, 1350°C. b) W-0.35 vol.-% Ni, 1450 °C. c) W-3.5vol.-% Ni, 1450 °C.

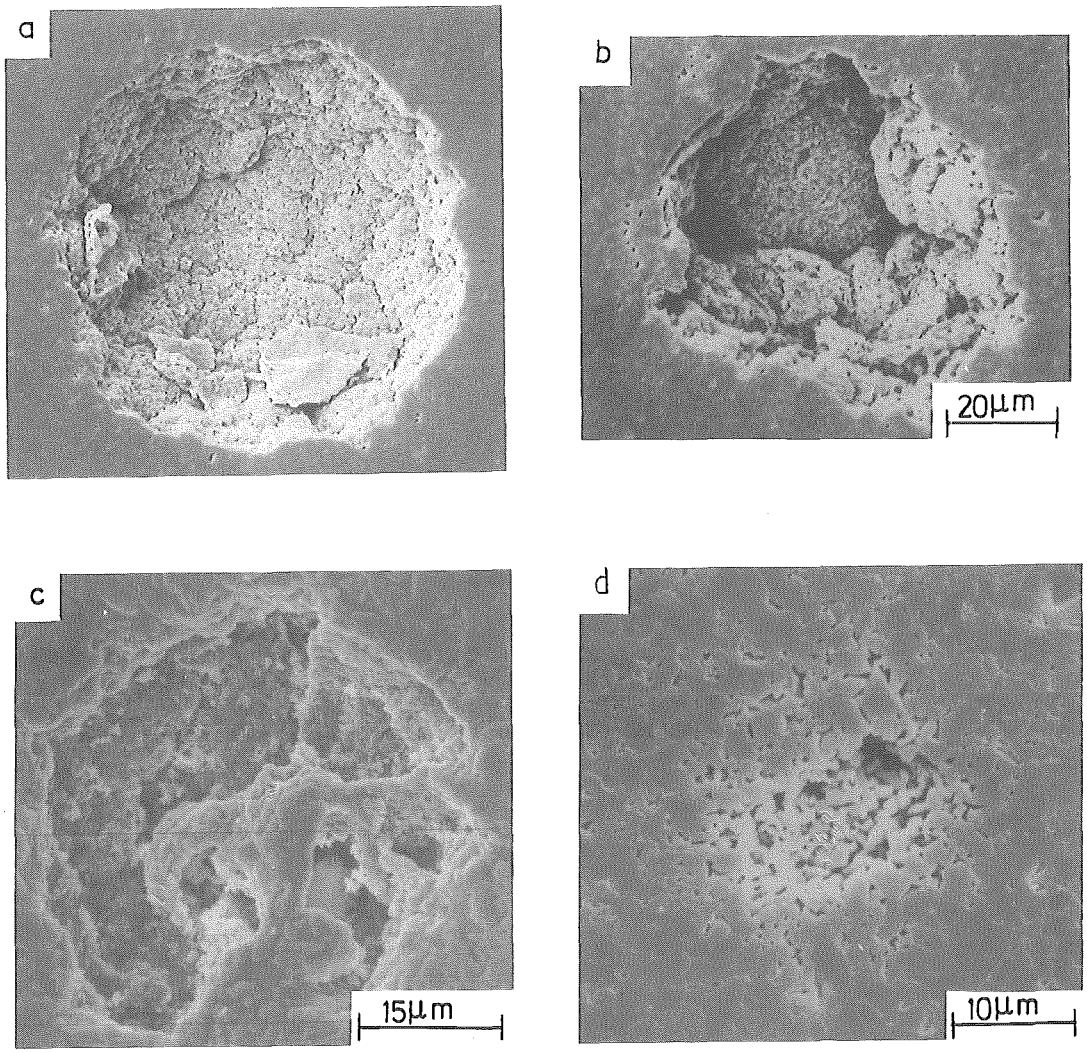

Fig.24 Closing of artificial pores in presintered Al_2O_3-anorthite after HIPing for 30 min. Al_2O_3-1.5vol.% anorthite HIPed at a) 10 MPa b) 20 MPa c) 50 MPa. d) Al_2O_3-10 vol.-% anorthite after HIPing at 10 MPa for 30 min.

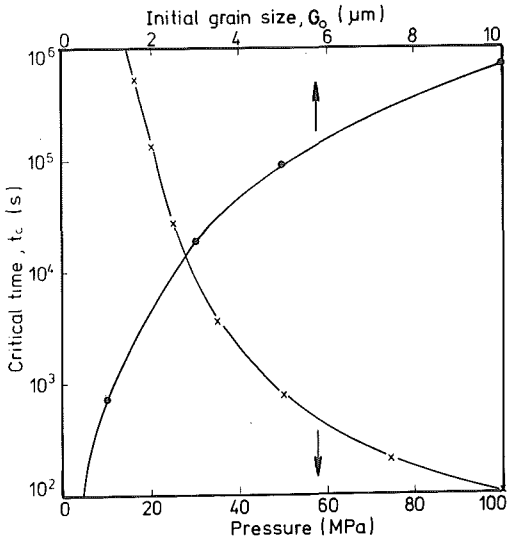

Fig.25 Critical time, t_c, for pore elimination depending on the initial grain size (K_1 = 7.5*10^{25} Pasm^{-3}, r_{po} = 4*10^{-5}m, Γ = 0.7Jm^{-2}, P = 50MPa, k_3 = 10^{-19}m^{3}s^{-1}) and on the isostatic pressure (G_o = 10^{-6}m, other data as shown before).

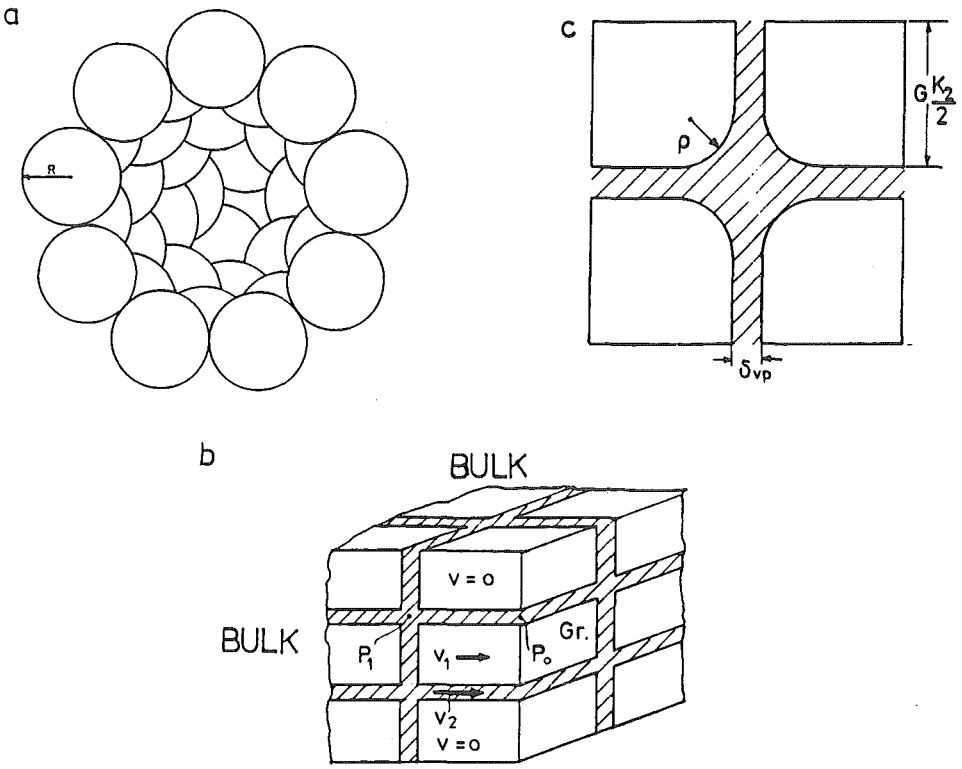

Fig.26a Overview.
Fig.26c Channel at pore surface.
Fig.26b Section through the bulk at the bulk/pore interface.

Fig.26a to c Geometries used for calculation of the pore filling.

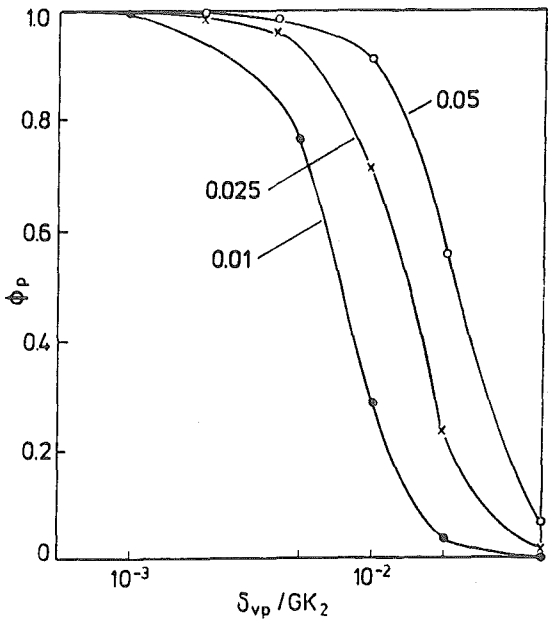

Fig.27 Additional volume fraction of melt in eliminated initial pores as a function of the ratio between thickness of planar intergranular melt layers and the effective grain size. The numbers give the initial volume ratio of melt to grains.

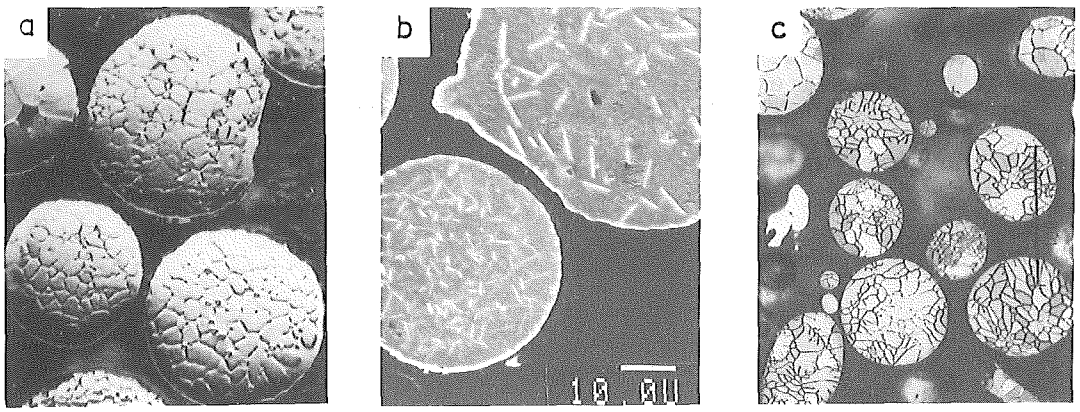

Fig.28 Microstructure of Ar atomized a)NiAl, b) FeAl, c)Ni_3Al.

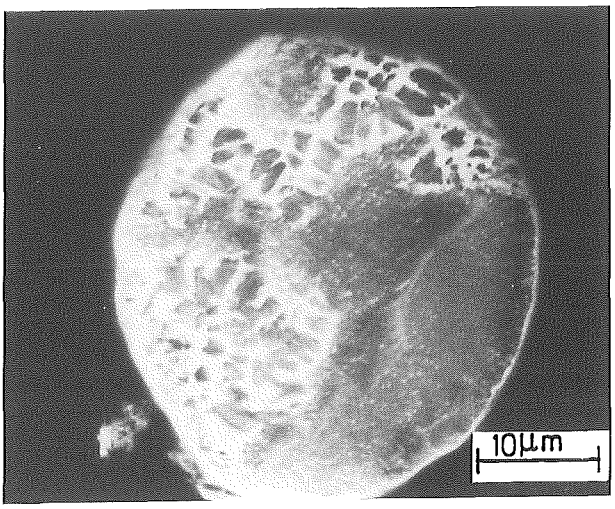

Fig.29 Microstructure of Ar atomized Cu-7wt.%Sn, purified with Al addition. The bright spots show the fine Al_2O_3 particles.

THE FUTURE OF CERAMICS

Drago Kolar

"J. Stefan" Institute, University of Ljubljana,
Ljubljana, Yugoslavia

Ceramics and powder metallurgy are the central topics of joint research within the bilateral German - Yugoslav cooperation project in the field of materials science and development. This was among the first projects started within the agreement on cooperation and reflected the widespread scientific interest in these fields in the early seventies. It is proper on the occasion of the 9^{th} German - Yugoslav Meeting on materials science and development to review the recent status of ceramic science and technology and to critically review the prospects in the near future.

Advanced ceramics are considered to be in the emerging phase of their life cycle. During the past 10 - 15 years, ceramics has undergone a dramatic revolution. Novel approaches to preparing and processing ceramic solids have been developed, ingenious ways of avoiding the most serious disadvantage of ceramics, brittleness, have been introduced, and new mass aplications have begun to open up in such areas as sensors, orthopedics, photonics and heat engines.

The main applications of advanced ceramics are in electronics, telecomunications and electroengenering industries. Ceramics for these applications, so called "electronic" or "functional" ceramics represent today around 70 % of market volume of advanced ceramics. The other important group is "engineering" or "structural" ceramics for applications which demand resistance to high mechanical, thermal or chemical stress. Data on market volume of advanced ceramic vary. Recent critical assessment of various sources is summarised in table I (1). The main segments of electronic ceramic market are shown in table II and various types of ceramics in structural ceramics group are listed in table III.

Estimations of future market growth are optimistic. At the time being, the growth rate per year of electronic ceramics in Japan is estimated to be about 10 %. Future market estimations from various sources diverge considerably from one another. They range from fantastic ("ceramic fever") to utterly pesimistic. However, even pesimistic forecasts predict much faster growth of advanced ceramics than in most other industrial sectors. The United States Advanced Ceramics Association forecasted five year growth (1987 - 1992) for electronic ceramics is > 9 % (2).

Table I: Market volume of advanced ceramics in 1987 (estimation in US $ million) (1)

	World	Japan	USA	Europe	Fed.Rep. Germ.
Total	11000	7000	1900	1400	(590)
100 %		70	17	13	(5)
Electronic Ceramics	7600	5400	1600	600	(325)
69 %		71	21	8	(4)
Structural Ceramics	3400	2300	300	800	(265)
31 %		68	9	23	(8)

Table II: Product groups in structural ceramics

Bioceramics
Chemoceramics (catalysts!)
High-temperature ceramics
Ceramic heat exchangers
Machine construction ceramics
Engine construction parts
Nuclear ceramics
Cutting ceramics
Wear-resistant ceramics

Table III: The world market for electronic ceramic components in 1987 (%)

Capacitors	32
Packages/Substrates	28
Ferrites	21
Piezoelectrics	11
Resistors	6
Sensors	2
Optoelectronics, Superconductors, etc.	1
Value	$ 7 600 million
Pieces	100 000 million

Versatility of electronic ceramics

Table IV, taken from ref. 5, lists some functions and applications of electronic ceramics.

Versatility of ceramics in electronics is based on the possiblity to vary the electrical properties in wide limits.Conduction, for example, may be electronic or ionic, with conductivity values that run from insulators through semiconductors and conductors to superconductors. Moreower, properties may be sensitive to such external conditions as temperature, pressure, moisture and surrounding gas atmosphere. The electrical properties of ceramics are not only a function of the allowable energy states of the electrons that form bonds, which is determined by atomic composition, but also a function of crystal structure and

polycrystalline nature of ceramics. Traditionally, insulation was the most important application of ceramic materials in electronics. Even today, the largest market single segment of electronic ceramics belongs to insulating ceramic packages for integrated circuits. The basic material is Al_2O_3. Several other ceramic materials shows electronic conductivity of various types. For example, the crystal structure of cobalt oxide allows

TABLE IV

FUNCTIONS AND APPLICATIONS OF ELECTRONIC CERAMIC MATERIALS

Function	Material	Main application
Insulating	Al_2O_3, BeO; SiC, BN, Si_3N_4, AlN	Substrates, semiconductor package, insulator
Dielectric	$BaTiO_3$, $SrTiO_3$	Condenser
Electro-optic	$(Pb,La)(Zr,Ti)O_3$	Electro-optic element
Semiconducting	Mn, Ni, Co, Fe oxide ZrO_2-group, SiC-group, SnO_2, α-Fe_2O_3, ZnO, $MgCr_2O$-TiO_2, $BaTiO_3$, $SrTiO_3$, ZnO, SiC	NTC thermistor, high temperature thermistor, gas sensor, humidity sensor, PTC thermistor, BL condenser, varistor
Conducting	SiC, $MoSi_2$, $LaCrO_3$, $LaCrO_3$, $LaCoO_3$	Heated parts of furnace, MN power generation, electrode for fuel cell
Superconducting	$SrTiO_3$, $LiTi_2O_4$, $Ba(Pb,Bi)O_3$, $LiTi_2S_4$, $PbxMo_6S_8$, $YBa_2Cu_3O_{7-x}$	Superconducting wire, magnetic floating, Josephson element
Ion conducting	ZrO_2-group, LaF_3, β-Al_2O_3, Li_3N, Na-βGa_2O_3	Oxygen sensor, ion sensor, Na-S battery, fuel cell
Piezoelectric	$Pb(Zr,Ti)O_3BaTiO_3$-crystal ZnO	Oscillator, supersonic element, piezoelectric buzzer, surface wave element
Pyroelectric	$Pb(Zr,Ti)O_3$, $PbTiO_3$, $LiTaO_3$	Infrared sensor, temperature sensor

semiconducting electronic mobility comparable with silicon. Vanadium dioxide behaves in a similar way at low temperatures, however due to slight modification in its crystal structure at about 60°C, the material switches to metallic type conductivity. The crystal structure of rhenium trioxide alows it to conduct electricity like in metal regardless of its temperature (3).

In addition, some ceramic materials exhibit special structure and composition related properties such as piezoelectricity, pyroelectricity, ferroelectricity and ferromagnetism.

Besides wide possibilities to influence the electrical properties by adjusting the atomic composition and crystal structure, modern electronic ceramics increasingly rely on possibilities offered by concious manipulating the polycrystalline microstructure of ceramics. The main characteristics of ceramic microstructure are various phases, pores and grain boundaries. Until recently grain boundaries and pores were considered unnecessary in the structure of ceramics. The mayor research effort was directed toward surpressing the porosity and preventing the extensive grain growth. Discovery of semiconducting phenomena in PTC and varistor ceramics triggered extensive research to control and optimize the grain boundary structures. The whole new research field was opened concerned with precipitation of impurities at grain boundaries and tayloring of grain boundary area. Another approach in contemporary electronic ceramics is the active use of pores in catalysts and sensors. The action of "chemical" sensors is based on the change of surface electrical conductivity resulting from adsorbtion or condensation of moisture or gases on pore surface.

Therefore, the microstructure control efforts in electronic ceramics may be grouped into three categories, with the aim to achieve (4):

(a) uniform ceramics that act like single crystal

(b) controlled grain boundary ceramics

(c) controlled pore ceramics.

Potential of microstructure control in electronic ceramics - examples and development trends:

1. Uniform ceramics: PLZT (Lead-lanthanium-zirconium titanate) is used in transparent form for manufacture of fast switching eye - protection goggles. To achieve transparency, fully dense structure is needed, since pores cause light scattering; large grain size is also required, since grain boundaries also cause light scattering. From the same reason, precipitation of a second phase at the grain boundaries must be avoided. Those features were achieved by the use of fine, homogenous starting materials and carefully controlled firing schedule. The easiest way is hot pressing. Fig. 1 shows microstructure of fully dense, coarse grain size PLZT ceramics.
2. Controlled grain boundary ceramics: ZnO varistors (Variable resistors) are composed of doped semiconducting ZnO grains embeded in Bi_2O_3 based matrix. Impurities in ZnO grain boundaries compensate for n-type conduction and grain boundaries act as effective isolating bariers for electrical

current at low voltages. At high voltages, however, electrons have enough energy to surmount the conduction barrier between the grains and the current flows readily through the varistor. The voltage at which the varistor switches from poor to good conductance is controlled by varying the size and doping of the ZnO grains and the thickness of the insulating layers between the grains. Fig. 2 shows heterogenous multiphase microstructure of ZnO - varistor. Since grain boundaries determine the properties, heterogeneity, second phases and some remanent porosity are not detrimental.

3. Controlled - pore ceramics: $MgCr_2O_4$ - TiO_2 humidity sensors exhibit a resistance change of nearly five orders of magnitude across a relative humidity range from 0 to 100 %. Resistance change is a consequence of the increase in surface proton conductivity caused by the physical adsorption of H_2O on pore surface. To operate properly, typical ceramic has porosity of about 35 % and controlled pore - size distribution between 0.1 and 0.3 um.

Examples quoted above may serve as a quidance for near future development of electronic ceramics. It seams likely that future applications of electronic ceramics will continue in the directions of (a) the single - crystal like, (b) the controlled grain boundary and (c) the controlled - pore ceramics. Progress will depend on our understanding of grain boundary, interface and surface phenomena in ceramics and technolgical ability to reproducibly control the grain boundaries.

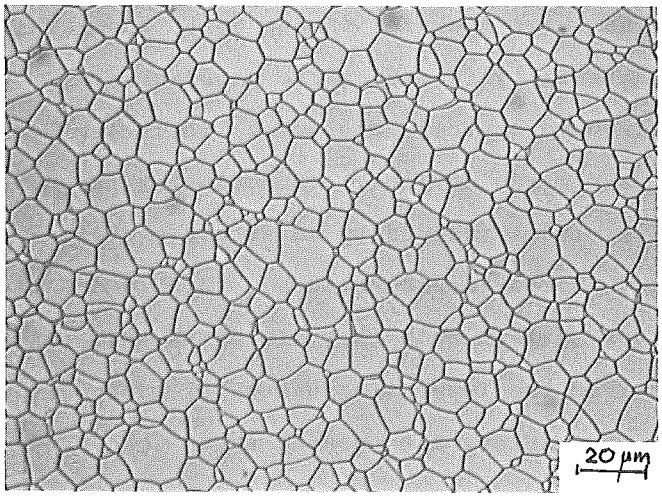

Fig. 1: Microstructure of hot pressed PLZT ceramic. For transparency, material must be fully dense, without second phase inclusions and with grain size large enough to prevent light scattering at grain boundaries.

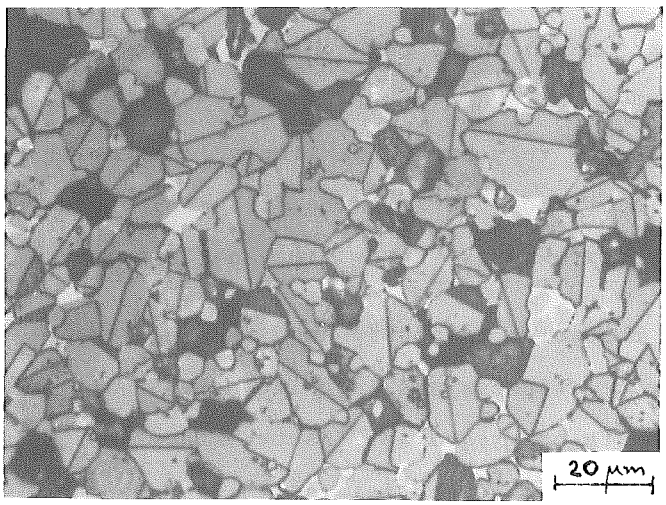

Fig. 2: Microstructure of doped ZnO varistor. The voltage at which a varistor switches from poor to good conductance is controlled by grain boundary phenomena. Minor inclusions of second phase and some porosity are not critical for device operation.

Applications of advanced ceramics in electronics will continue to expand in the near future. Among most promising areas are sensors, particularly for automatic manufacturing, robotics and vehicles, microwave devices, photonics, including low loss fibres and various wave guide devices, (functioning through the change in refractive index induced by an electric field), multilayer packages for VLSI electronic devices, thin layers technology and superconductors. Research in this fields is well under way, as may be concluded from the increasing number of papers in journals and proceedings, and markets are opening up.

Potential of engineering ceramics

In last decades, considerable progress in the structural applications of high performance, high temperature ceramics was achieved. Examples are tough cutting tools, extrusion dies, tread guides, wear resistant spray nozzles, gaskets and linings for chemical apparatus and numerous others. Potential for new applications is very high, particularly in motor and process industries (heat exchangers). The status of engineering ceramics was recently reviewed by Petzow (10) and Thummler (11).

The major obstacles in widespread structural applications of ceramics are brittleness and incosistency. Great success has been achieved in recent years and fracture toughness K_{IC} values in excess of 20 MPa $m^{1/2}$ seem realistic (6). Progress is based on major advances in ceramic processing, component fabrication technology, various toughening approaches and brittle materials design procedures.

The basic approach to improve the toughness of ceramics is reduction of the size and concentration of preexisting crack initiators, such as microcracks and pores, by decreasing grain size and increasing density. Grain sizes in the micron range and densities around 99 % of theoretical value are achievable. However, this is not enough. To be accepted in constructions, ceramic must be reproducible and reliable. Inconsistency of ceramic result largerly from shortcomings in the maunufacturing process and not from deficiencies in the ceramics intrinsic properties.

On the basis of extensive experimental and theoretical work, general guidelines for making high quality structural ceramics has been formulated:

- Use of an unagglomerated powder with narrow size distribution and one micron or less in size
- Manufacture of green microstructure which has a uniform distribution of pores and as many interparticle contacts as possible, approaching that of close packing
- Choosing sintering variables such that densification rather than grain coarsening occurs and that pores remain pinned to grain boundaries.

The first prerequisite for the preparation of high quality, reliable ceramics is availability of raw materials of sufficient purity and size consistency. To meet the demand, novel chemical routes for the synthesis of unagglomerated, micron size inorganic powders were developed.

Chemical preparation of powders is traditional, well established technology, however not for ceramic industry. Conventional chemical approaches for making fine particulate solids involve coloidal suspensions followed by the removal of the solvent. Bayer alumina process and titania pigment production are the familiar examples. However, if the suspension is simply dried by heating and evaporation, coarse crystals and agglomerates usually result. For preparation of dense, fine grained ceramics such powders must be subjected to intensive milling. In spite of the development of new types of milling machines with improved efficiency, the degree of milling is limited and resulting powder has broad grain size distribution. The milling operation introduces impurities, particularly harmful for electronic ceramics. Novel chemical processes designed with the principal aim to avoid agglomeration include various sol-gel processes starting from metallic salt solutions or metal alkoxides (7), thermal degradion of polymers and vapor phase reactions.

Although many new chemical processes were successfully demonstrated on laboratory or even semi-industrial scale, cost effectivness remains the problem. This remains the challenging area for chemical engineering and technology.

The next important step in ceramic processing is shaping. High green density and homogeniety is required.

Since agglomerates are inherent to the conventional dry-powder pressing technology, other consolidation routes with the potential of avoiding agglomeration or destroying the agglomerates are sought. Isostatic pressing at room and high

temperature and injection molding are already well established technologies. Merits of direct consolidation of colloidal systems by filtration, gravitation or centrifugal settling and electrophoresis have been demonstrated by several authors. The basic approach is to avoid spontaneous agglomeration in colloidal systems by producing repulsive forces between particles either electrostatically or sterically. To illustrate the advantages of not yet widely used colloidal methods of consolidation, results reported by Lange (8) may be quoted. Authors compared the flexural strength of Al_2O_3-ZrO_2 composite ceramics shaped by filtering and conventional dry pressing and obtained the average strengths 896 MPa and 550 MPa, respectively.

Dramatic improvement in toughness of engineering ceramics has been achieved by introducing into ceramics crack-closing particles and crack-retarding fibres and whiskers. Well known examples is PSZ, where strenghts of 500 - 1500 MPa and fracture toughnesses of about 12 - 16 MPa $m^{1/2}$ at room temperature were reported (9).

Among the most important goals to promote the use of engineering ceramics is development of proper design practice, which should fully apply multiaxial stress criteria. Moreover, long term behavior under cycling load is to be taken into account. A comprehensive review of the requirements of design practice has been recently prepared by Thummler (11).

Advanced structural ceramics with increased reliability and accetable cost already hold some firm market positions, such as cutting tools and spray nozzles. But potentially most important

future application for tough, reliable ceramics is, of course, auto engine components. Glow plugs and turbocharger rotors have been introduced already. Development is continuing on valves, piston caps and components made of SiC and Si_3N_4, on combustion chamber components made of PSZ and on regenerator cores made of aluminum silicates. The increased use of ceramic coatings is also forseen.

Concluding remarks

Applications and markets for advanced ceramics are rapidly expanding. Today's advanced ceramics differ considerably from technical ceramics of 30 years ago. New knowledge is accumulating rapidly resulting in increased reproducibility, reliability and versatility of ceramics. Total world market of advanced ceramics more than tripled in the last 10 years and will grow even faster in the near future.

With improved properties the strategic role of advanced ceramics in industrial products is increasing. It seems proper to finish this short review recolling the statement formulated by Kingery at the recent World Congress on High Tech. Ceramics (12). In the next decade ceramics may still represent but a small part of world commerce, but it will mostly consist of critical components of devices valued at a hundred or thousand times more than the ceramics itself. Thus, advanced ceramics will play a vital role in the economies of the industrial nations in the next century. Companies or nations which are not recognizing the potential of

advanced ceramics will be seriously handicaped in their industrial capabilities.

References

1. H. Reh, Interceram No. 2, pp. 25 - 30, (1989)
2. T. J. Dwyer, R. B. McPhilips, Am. Cer. Soc. Bull., 67 (12) 1894-1896 (1989)
3. H. K. Bowen, Scientific American, October 1986, pp. 147-154
4. S. Hayakawa, Industrial Res. Development, February 1983, pp. 142-147
5. N. Ichinose, IEEE Electc. Ins. Mag., 4 (3) 24-30 (1988)
6. A. R. C. Westwood, S. R. Winzer, pp. 225 - 242 in Advancing materials research, ed. by A. Psaras and H. D. Langford, National Academy Press, Washington 1987
7. J. D. Mackenzie pp. 15 - 26 in Ultrastructure Processing of Ceramics, Glass and Composites, ed. by L. L. Hench and D. R. Ulrich, Wiley New York 1984
8. F. F. Lange, pp. 59 - 75 in Microstructure and Properties of ceramic materials, ed. by T. S. Yen and J. A. Pask, North Holland Physics Publishing, Amsterdam 1984
9. R. W. Rice, Chem. Tech. 13 230 (1983)
10. G. Petzow, pp. 62-77 in Max-Planck Ges. Jahrbuch 1986, Vandenhoeck-Ruprecht Verlag Gottingen 1987
11. F. Thummler, Engineering Ceramics, paper prepared for the 1st European Ceramic Society Conference, Maastricht, June 1989 (to be published in Proceedings)
12. W. D. Kingery, pp. 31-40 in High Tech. Ceramics (part A) ed by P. Vincenzini, Elsevier Amsterdam 1987

M.M.Ristić and P.Kostić

Serbian Academy of Sciences and Arts, Committe for Physical Chemistry of Materials, Knez Mihailova 35, Belgrade, Yugoslavia,and
Center for Multidisciplinary Study, University of Belgrade, Slobodana Penezica 35, Belgrade, Yugoslavia.

MATERIALS SCIENCE - THE BASE OF PROGRESS IN NEW ELECTRONICS

ABSTRACT

In this paper the topic of materials science beginning, to be a multidisciplinary field of science is considered. Its influence on the progress of the new electronics will be specially analised and illustrated examples of mutual conections between materials science and some natural and technical science disciplines.

INTRODUCTION

The base of modern science-technical progress is presented by energy systems, automatization and materials. Materials are special importance, becouse, their progress determines the progress of energy systems and automatization /1/. Therefore, special attention is dedicated recently to materials science, which investigates the correlation between composition, structure and characteristics of the

materials with theirs behaviour under thermal, chemical, mechanical, electrical and magnetic influence.

Materials use started from the beginning of civilization, and the names of different time periods are connected with the names of materials which were mainly used at that time. Materials science as multidisciplinary field of science did not appear until the sixth decade of this century, conecting physics, physical-chemistry and solid state with the tehnology of materials /2/. Today, materials science is currently conected with almost all natural and technical disciplines. The progress of technics and technology is directly depending on accomplishments of materials science, proven by examples of progress in astronautics, electronics, production of machinery atc.

Taking this into account, we will analyse a few characteristic examples of development leading to new electronics due to the accomplishments of materials science.

IMPORTANCE OF MATERIALS FOR PROGRESS OF THE ELECTRONICS

Qualitative improvement in electronics, as shown in the recent past, were first of all the result of discoveries in materials science. Similar to the influence of transistors on the new progress of tehnology in electronics, it is expected that the new ceramic materials hawing specific properties will influence the development of entire new technologies in this technical field. Further progress of

integrated ceramic packages is shown on Fig.1. as an example /4/. Materials science directly influences the solution of intergration and miniaturisation (Fig.2) problems.

Complex applications of ceramic materials in electronics result from their abilitiesof serving different atomic and electronic mechanisms in constructed new ceramic components. Fig.3. shows shematically properties versus structure of electronic ceramic materials. The way how materials science can influence the progress of new electronics and the new components and how complex structures were obtained becomes obvious.

Multilayer condensators, piezoelectic transducers and PTC-thermistors use the properties of ferroelectric perovskite materials with high dielectric permitivity, with a broad spectrum of piezoelectric coefficients and of anomalous electrical conductivity. The similar domain structure as in the feroelectric perovskites was discovered in the ferrimagnetic oxide ceramics (e.g. $NiFe_2O_4$). Hard and soft ferrites are analogous to hard and soft PZT-ceramics. Different mechanisms to previous are operative in termistors and other ceramic, used for sensors. Therefore, the ionic conduction is used for oxygen sensors and batteries. Humidity sensors are using surface conductivity. Adsorbed molecules of water are dissociating into hydroxyl and hydrogen ions which change electrical conductivity. Grain boundary phenomena(Fig.4.) /3/, such as the formation mechanisms of thin isolation layer between conducting zones,

are of essential meaning for the operation of multilayer capacitors, varistors and PTC-termistors /4/.

Thanks to accomplishments of materials science we possess today complex sensors for temperature, gases and humidity and are developing adaptive actuators, ceramic modules for electroluminiscence displays and voice modulators. To obtain these functions components are required which include different kinds of sensors, tranducers and initiators, together with thermistors and varistors /4/. A good indication of the enormous development in these new electronic materials is given by the annual saling throughout the world and in different countries (Tables 1 and 2) /5/.

Table 1. Annual sales of new electronics in the world (in $10^6$$)

Product	1977	1986	1991 (est.)	1995 (est.)
Electronic Components	813	4808	10820	21375
Different Tools	58	433	885	1625
Thermal Engines	0	?	80	675
Others	34	167	329	825

Table 2. Sales of new ceramics in different countries (10^6\$)

Country	1977	1986	1991 (est.)	1995 (est.)
Japan	398	2587	5900	12100
USA	362	2024	4500	8650
Germany	42	254	550	1100
England	38	167	390	825
France	32	151	335	675
Canada	10	72	170	375

SUPERCONDUCTING CERAMICS - THE NEW AGE OF ELECTRONICS

Today we can say that the golden age of electronics is continuing by the discovery of high-Tc superconducting ceramics.

Heike K.Onnes, a dutch physicist, discovered superconductivity in 1911. (Fig.5.). He observed that the electrical resistivity of mercury practically disappeared at 4K (critical temperatutre T_c), and was awarded the Nobel Prize/6/. After this initial discovery only small improvements of the critical temperature were obtained. Only metals and metal alloys were considered as superconducting materials, and oxidizing these materials was obtained to

lead to a loss of the superconducting properties. The best results were obtained in 1973. on alloy Nb_3Ge with T_c=23K (J. R. Gavaler). In the meantime Bardeen, Cooper and Schrieffer in 1972. were avorded the Nobel Prize for the theory of superconductivity (BCS theory). They also suggested the necessity for the another mechanisms at hypotthetical T_c>90K.

Nevertheless, two researchers at IBM Research Laboratories in Rusdlikan, Johannes Georg Bednorz and Karl Alex Mueller began in 1983. research on superconductivity of metal oxides. Finally, in december 1985. they obtained critical temperature 35K on Ba-La-Cu-O compound, and published this result in April 1986,/7/ (and took a Nobel Prize in 1987). The further progress was very fast. Two Japanese scienists, Tetsuya Oriushi and Yoshihisa Osono found critical temperature at 44K in Nb-Ge-Al-O thin films in February 1986. . After this, many scientists all over the world started investigations in this direction, discovering superconducting materials which were in the news almost daily. Paul C.W.Chu from Houston University menaged to shift the critical temperature from 35 to 50K/8/ by applying hydrostatic pressure on Ba-La-Cu-O material . Finally, in February 1987. he measured a critical temperature of 92K in a Y-Ba-Cu-O (1-2-3) compound /9/. Until now the highest stable critical temperature (over 105K) was founded on Bi-Sr-Ca-Cu-O compound/10/.

The 1-2-3 compound has a tetragonal (non--superconducting) and an orthorhombic perovskite structure with superconducting properties (Fig.6.). Oxygen content plays a great role on the development of the superconducting properties /11/. This material could also be used as a good oxygen sensor (Fig.7.) /12/. That means the 1-2-3 compound has complex properties and presents a kind of modern material. The best indication on the intensity of investigations on ceramic superconducting materials we may obtain from estimated annual sales predicted (Tab.3.)/4/.

Table 3. Predicted of new high-T_c ceramic superconductors in the world (10^6\$)

Application	1987	1992	1997	2002
Integrated Circuits	25	75	225	400
Sensors	5	25	125	200
Medicine	150	300	500	750
High energy Physics	25	150	150	200
Electroenergetic	5	10	20	40
Transport	0	1	5	10
Magnetic Separations	5	25	60	175
Total	215	586	1085	1775

SOME COMMENTS ON THE FUTURE OF MATERIALS SCIENCE

For further development in materials science, obtaning materials with predesired properties is very important. This is one of the reasons why methods to predict equilibrium phase diagrams have been developed /13/. This evolution is directly conected with the abilities to obtain new materials. Taking all point into account, materials science will serve as a base of future technology progress (Fig.8.). Analysing the whole world wide technological progress in the field of electronics, biotechnology, new materials and new energy systems S.Saito /14/ showed, that the progress of materials already today is the prime condition which ensures the highest level of progress in electronics (Fig.9.).

REFERENCES

/1/ M.M.Ristić, The base of materials science, Science Dumka, Kiev, 1984.

/2/ Materials and Man's Needs, NSF, Washington, 1980.

/3/ P.Kostić, O.Milošević, D.Uskoković, M.M.Ristić, J.Physics B, 150(1988)175.

/4/ R.E.Newnhman, Adv.Cer.Mat.,3(1988)12.

/5/ M.Schober, Am.Cer.Soc.Bull.,66(1987)1698.

/6/ G.Fisher, M.Schober, Cer,Belletin, 7(1987)1087.

/7/ J.G.Bednorz, K.A.Muller, K.Takahashi, Science, april(1987)73.

/8/ C.W.Chu, P.H.Hor, R.L.Meng, L.Gao, Z.J.Huang, Y.Q.Wang, Phys.Rev.Lett., 58(1987)405.

/9/ M.K.Wu, J.R.Asburn, C.J.Torng, P.H.Hor, R.L.Meng, L.Gao, Z.J.Huang, Y.Q.Wang, C.W.Chu, Phys.Rev.Lett. 58(1987)908.

/10/ H.Meada, T.Tanaka, M.Fukutoni, T.Asano, A New High T_c Oxide Superconductor Without Rere Earth Elements, patent.

/11/ P.Kostić, Philosophies and Prognosis in High T_c Superconductor Ceramics, Silicate Industriels (in press).

/12/ J-He Park, P.Kostić, Mat.Lett.,6(1988)393.

/13/ Thermodynamic Optimisation of Phase Diagrams, Max PlancK Institute for Metal Research, Stuttgart, 1988.

/14/ S.Saito, Present and Future World Market for High Technology Materials, preprint.

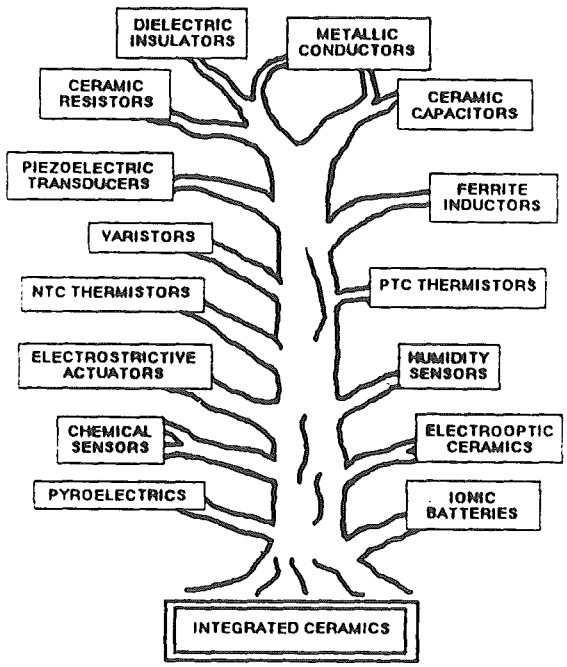

Fig.1.

Integrated ceramic packages of the future can incorporate many different components.

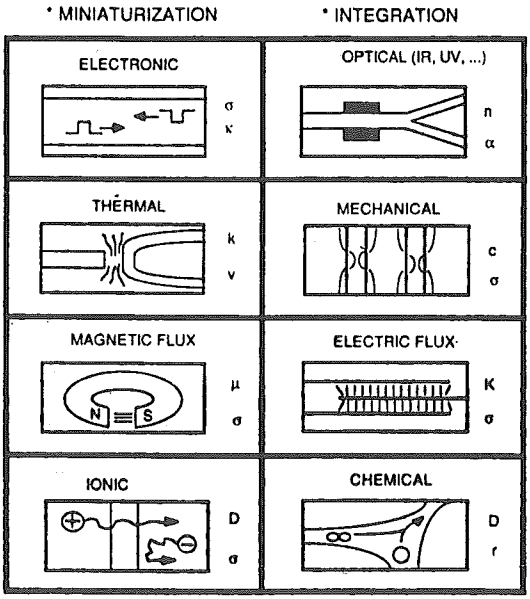

Fig.2.

Circuitry in ceramic materials for use in electronic packages, intergrated optics, cooling systems, electromecanical transducers, magnetic recording, multilayered actuators, ionic batteries, and chemical sensors.

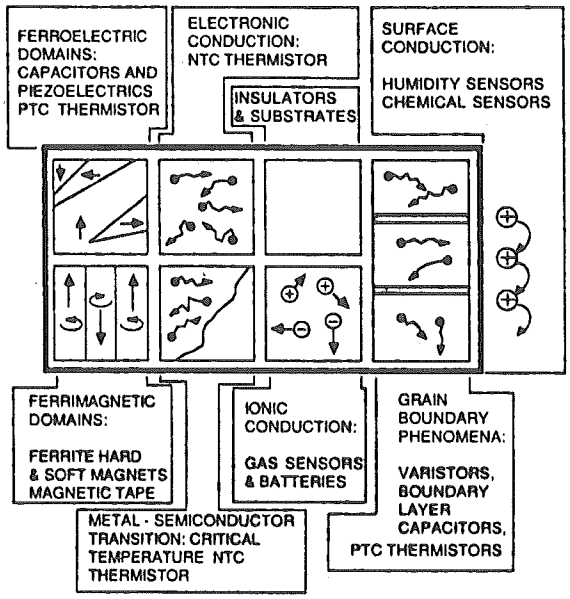

Fig.3.

Ionic and electronic mechanisms involved in electro-ceramic components.

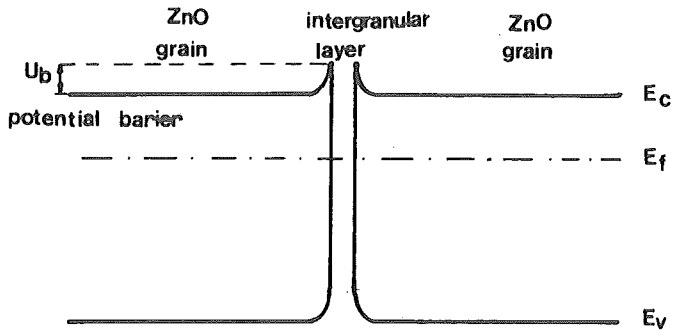

Fig.4.

Potential barrier formed between two grains in ZnO-varistors

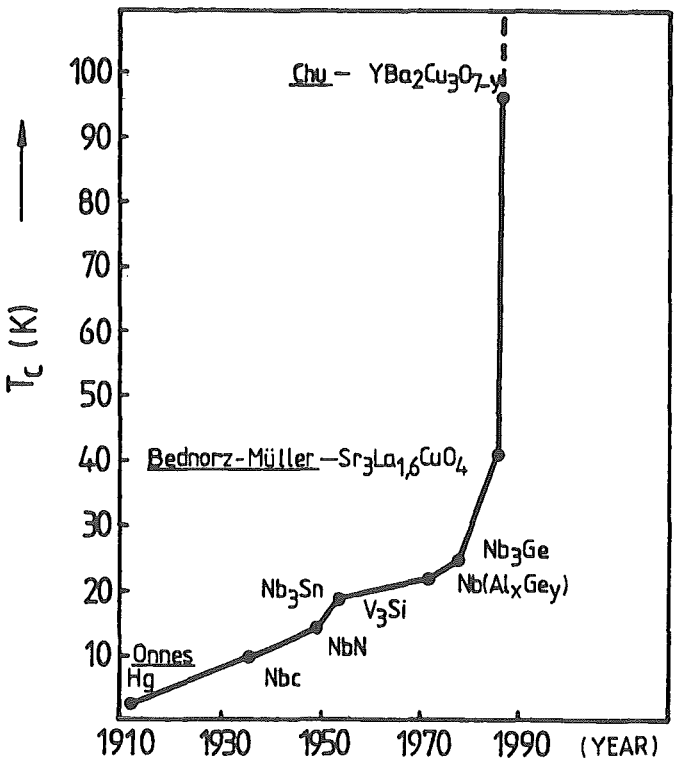

Fig.5.

Evolution of the critical temperature subsequent to the discovery of the superconducting phenomenam.

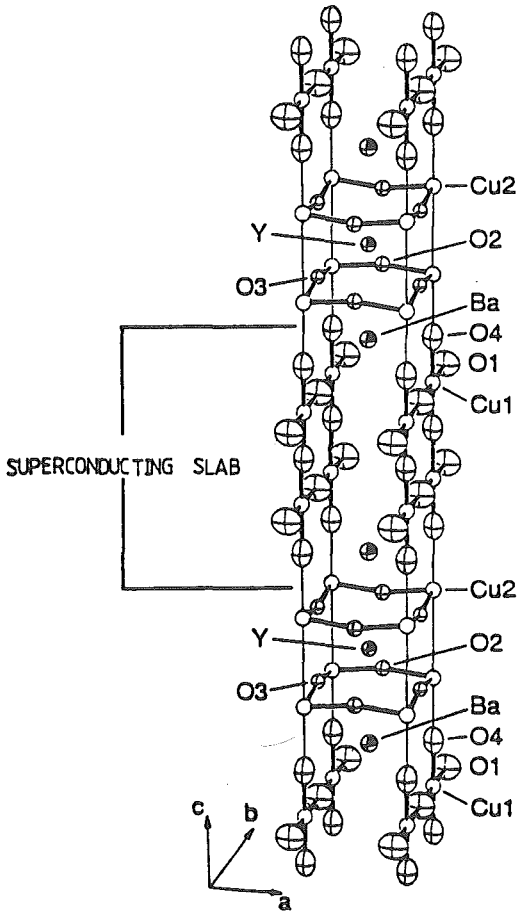

Fig.6.

Crystal lattice of $YBa_2Cu_3O_y$ with superconducting slab.

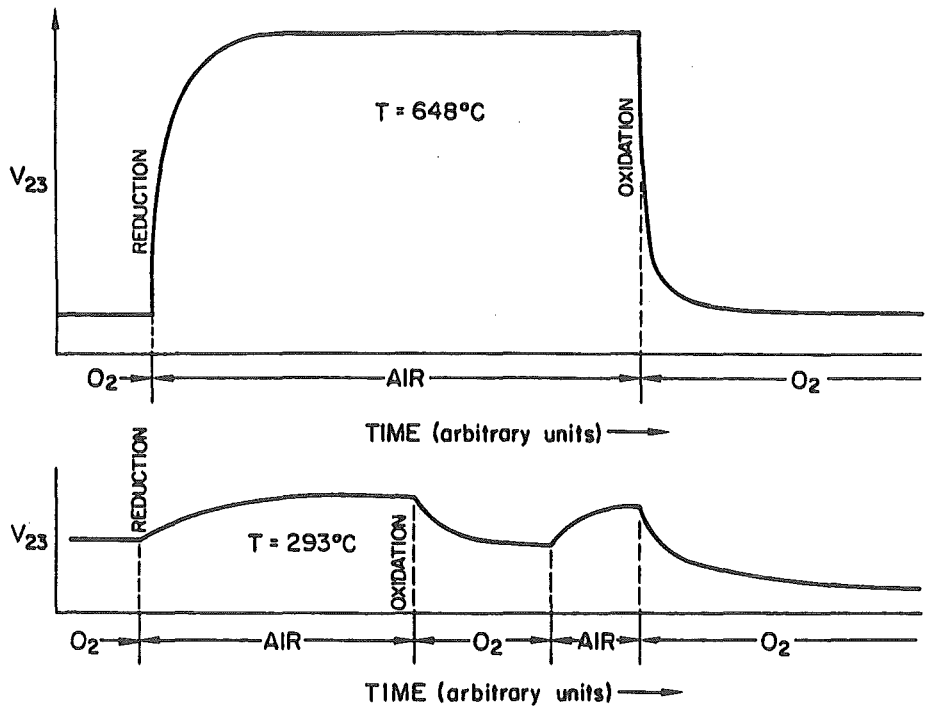

Fig.7.

Oxygen diffusion in a 1-2-3 compound for oxidation and reduction.

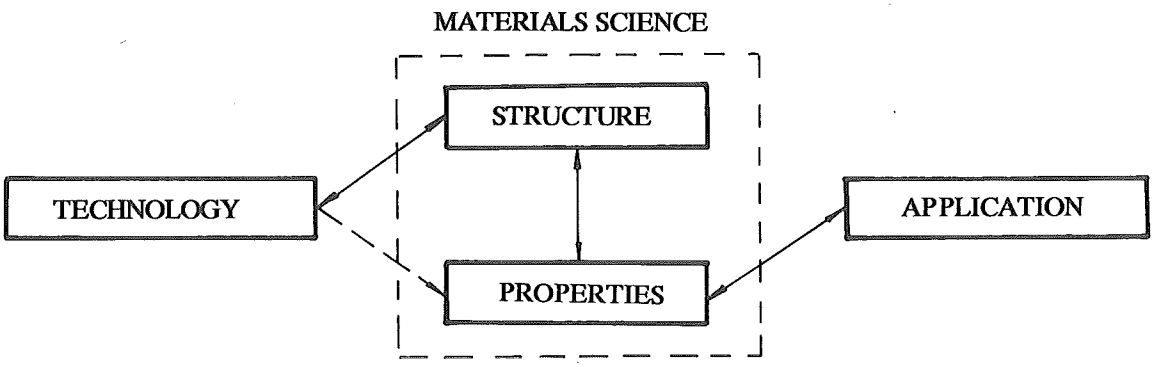

Fig.8.

Mutual interaction between technology and applications.

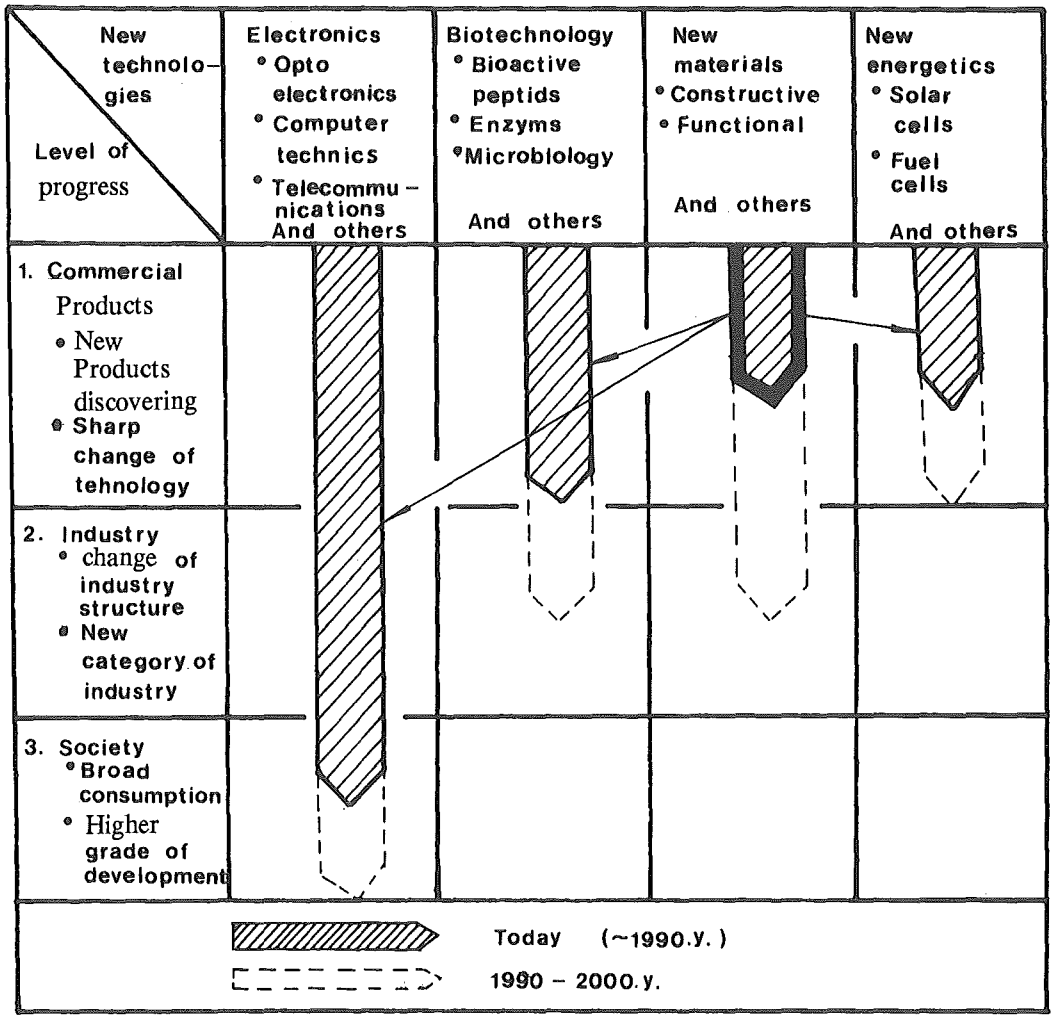

Fig.9.

Prognosis of technology progress until the year 2000. and situation of electronics.

THE OPTIMIZATION OF POWDERS FOR USE IN SINTERING

R.J. Brook
Max-Planck-Institut für Metallforschung
Institut für Werkstoffwissenschaft
Pulvermetallurgisches Laboratorium
Heisenbergstr. 5, D - 7000 Stuttgart 80
West-Germany

Abstract

In recent years the introduction of chemical preparation methods has greatly improved the quality of control which can be exercised over the properties of powders intended for use in sintering. It is therefore now important to identify the desired powder characteristics so that powders of optimal quality can be prepared. A number of the properties of powders which need to be considered in such a design process are reviewed.

Introduction

A general trend can be recognized in ceramic microstructures whereby the complexity of the structure is reduced as a greater degree of control over uniformity and reliability is achieved. Subsequently a degree of deliberate complexity can be reintroduced as microstructures are sought which can provide improved properties as, for example, in respect to toughness. A similar trend can be identified with powders: the first requirement has been to remove accidental variations from the powders and to ensure that control is achieved over powder character; it then becomes possible to design powders more deliberately in the task of reaching sintered components that are free from faults. The great success of recent work in preparing powders which have a simple and uniform structure is to be recognized; it is now important to define the deliberate modifications to the basic simple powder structure which are now required in order to offer further improvements in component performance.

There are many parameters describing the quality of a powder which have been found significant in determining the suitability of the powder for sintering. These include size, size distribution, shape, chemical homogeneity, degree of crystallinity, density, cost; general targets for these parameters which would be suitable for all applications are unlikely to exist. Nonetheless proposals can be made, as in Table 1, which will apply for many circumstances.

Table 1

Character	Conventional Target	Development
Size	0.1 - 1.0 μm	Finer sizes
Size distribution	Mono disperse	Size variation
Shape	Spherical	Shape variation
Chemical homogeneity	High	Coatings
Crystallinity		Mono crystal
Density	High	
Cost	Low	

Powder Size

The connection between the size of a powder and its sinter activity has long been established[1]. For fine powders the atom diffusion distance from grain boundary to neck is shorter, the driving force for densification is greater (free energy of the solid/gas interface), and the quantity of material which must be moved for a given degree of shrinkage is much reduced; with consideration that the cross sectional area through which the atoms can diffuse is also reduced for finer powders, relationships can be developed which link the rate of densification to an inverse power of the powder particle size (typically -3 or -4 depending on detailed atomistic diffusion mechanisms). This strong dependence - a halving of the powder particle size

typically results in a tenfold increase in the densification rate - has been recognized in terms of the much increased sinter activity of fine powders.

The attractions of selecting small powder sizes as design targets are therefore considerable. One may, for example, process a given ceramic composition in furnaces with lower maximum operating temperatures; this can be a considerable convenience particularly if temperatures can be reduced to the 1450°C provided by silicon carbide furnaces. More dramatically, if one wishes to prepare composites based on the co-sintering of ceramics and of polymers or if one wishes in general to avoid reactions between different phases during sinter processing then this ability of very fine powders to densify under low temperature heat treatments becomes significant. A number of factors, however, would suggest the avoidance of excessively fine sizes; among these it is important to recognize that sinter temperatures greater than the eventual application temperature should be used in order to avoid microstructural changes during component use; anyone who has worked with powders will also be familiar with the growing handling difficulties encountered in such processes as pressing when fine powders are involved.

For these reasons, target sizes between 0.1 and 1 μm are conventionally adopted. The preponderance of this range is unlikely to change; it is perhaps worth noting, however, that any future changes to this span of sizes will probably occur in the direction of finer powder. The current interest in nano-size powders is a case in point[2]; the extreme handling difficulties of such powders, however, and indeed the need to process them in the same chamber in which they have been prepared indicate the problems that are likely to arise with very fine systems. Application are likely to be limited to examples where particularly stringent control of interface reactivity is required; other examples may arise where, as in the case of superplasticity, the properties of the sintered piece rely upon ultra fine grain sizes.

Size distribution

In early ceramics work, deliberately selected size distributions of powders were commonly used in order to reach high green densities. Thus in the refractories industry, the mixing of up to seven different size grades of powder has not been uncommon. A disadvantage with such distributions is that the presence of grains of

widely different size can encourage the development of grain growth and can even nucleate the development of abnormally large sized grains. For those ceramics where the desired properties require small flaw sizes (for high mechanical strength), it is important to avoid large grains since these themselves act as flaws. Similarly the ability of large grains to limit the density which can be reached during sintering is to be seen as a disadvantage. As a consequence, the conventional target for high performance ceramics is to use powders which have a relatively narrow size distribution.

This trend has been taken to its extreme in the advocacy of mono disperse powders for the fabrication of ceramics[3]. These powders were seen as exceptionally attractive in that they offered the opportunity to prepare green microstructures which were free from packing faults. It was, however, later discovered that the tendency of such powders to form ordered regions of limited size led to a total structure in which these ordered regions were themselves separated by disordered boundaries. During sintering these boundaries became sources of flaws in the structure as the ordered regions preferentially densified. It is now therefore recognized that the best green microstructure consists of a uniform homogeneous packing of the particles which avoids high degrees of ordering; this can best be achieved by using a powder in which a slight distribution of sizes around the mean is present[4]. The target is to achieve a sufficiently narrow distribution that any tendency to excessive grain growth is avoided but to have sufficient diversity that the formation of ordered regions is also avoided. Fortunately this distribution is closely approximated by the products of many chemical preparation methods.

In terms of future development a degree of optimization of the size distribution can be expected as the compromise between high green density and the avoidance of grain growth is resolved. The changes are, however, likely to be evolutionary rather than spectacular.

Shape

Spherical particles have long been seen as a target in part because of the improved packing performance which can be expected and in part because of the better adherence to theoretical models developed on the basis of spherical grains. A potential

future development, however, is the more deliberate tuning of shape in order to reach microstructures in which the grains are themselves acicular or platelet shaped. Such extended grain shapes have been found valuable in enhancing the toughness of the resulting ceramic; it is therefore important to find ways in which such grain shapes can be developed. Although, as in the case of silicon nitride[5], this is often achieved during sintering with the assistance of suitable additives, it can be seen that a further possibility is to develop powder particles which are themselves shaped and which can act as precursors for the later grain structure. Examples would include the preheating of the green compact to develop the powder shape as in the heat treatment of sol-gel mullite precursors[6] in halogen containing atmospheres to produce grains of needle like form. With the extreme significance of enhanced toughness for the future application of ceramics in engineering applications, this exploitation of powder shape is to be seen as a promising line of development.

Chemical Homogeneity

The key target in current sintering practice is the attainment and retention of structural homogeneity during processing. It is critical to avoid any departures from uniformity which can later emerge in the fired component as structural faults or flaws. It is therefore important to avoid variations in grain density, in grain size or in chemical composition as one moves from place to place within the green structure. The benefits that arise in the sintering of oxide or non-oxide ceramics by using chemical precursors which are themselves highly homogeneous have been evidenced in terms of the lower firing temperatures and more reproducible properties which emerge.

In looking for developments in respect to chemical distribution it is important that homogeneity at the multi-grain level be retained. Possibilities for change include therefore the use of chemical coatings; these can be attractive where one seek to introduce the sinter additive as a coating on the particle, a result being that the additive is present in the structure at precisely those locations where it is required for the densification process[7]. As the design of sintered microstructures becomes more sophisticated and the use of grain boundary phenomena plays a larger part in the properties of finished components so can we expect that this deliberate planting of chemicals in the grain boundary regions by way of coatings will become a more

regular part of powder preparation.

Of the various characteristics of ceramic powders this is one where considerable changes in future powder design can be expected.

Crystallinity

In addition to the outer appearance of the powder grain and its ability to take part in a packed green structure, the internal microstructure of the powder particle is crucial for optimum behavior during sintering. A clear example is the problem caused by powder particles which are themselves less than fully dense; the subsequent sintering of the particles themselves leads to an enhanced shrinkage[8] during the sintering of the component; since the reduction of firing shrinkage and the exact definition of the resulting component shape are critical for reliable and economic component production such poor or low density phase particles are to be avoided.

Difficulties have also been recognized in the sintering of powder particles which are themselves polycrystalline. The risk is that if grain growth within the particle takes place at the same time as sintering between the particles, single crystal structures which extend over many particle units can occur[8]. The resulting single crystal region is of large and irregular shape and can act as an impediment to subsequent component densification. This problem can be avoided if the grain particles are themselves mono crystalline as in the case of the powders prepared by the milling of fusion cast zirconias[9].

Cost

A feature of chemically prepared powders is a relatively high cost. If we recognize the sums which are available for the fabrication of one gram of material for use in different applications (Table 2) then we can see that a number of the chemically prepared powders are excluded for important ranges of application (motor vehicles). The two factors which currently restrict the widespread application of ceramics in mechanical engineering are the uncertain reliability and the relatively high cost. Many of the characteristics which have been considered in earlier paragraphs address

the question of reliability; the issue of cost, however, itself remains critical. It is of the upmost importance in designing powder processing routes to take all opportunities which are offered for cost reduction. A number of savings will only arise at later stages when full advantage of the economies of scale can be taken. A number of processes such as those based on alkoxides are, however, unlikely to allow cost effective powder preparation for any but the most exotic applications. Consideration of such issues from the earliest stages of any development is to be recommended.

Table 2

Approximate costs of 1 gram of material used in different applications

Motor Vehicles	DM	0.01
Aircraft	DM	1.00
Spacecraft	DM	100.00

Conclusions

Dramatic progress has been made in enhancing of the properties of ceramics for ever more exacting applications. The improvements in strength, in toughness and in the sheer variety of properties which can now be provided is indeed remarkable. In a similar way, the introduction of chemical processing methods has greatly refined the quality of powders which can be prepared and the degree of control which can be exercised over powder character. In general, the stage has been reached where reliability and reproducibility in a powder can now be attained and where accidental variations in grain form, grain shape, grain chemistry or crystallinity can now to a large extent be avoided. A critical task in the immediate future is therefore to optimize powder design by seeking the correct compromise positions in such matters as powder size distribution and powder shape. If systematic and careful exploitation of the several variables can be routinely incorporated into ceramic fabrication

procedures then the benefits could be striking; in view of the cost considerations which arise when we try to compensate for fabrication errors (use of composites or of hot isostatic pressing or of procedures for non-destructive evaluation) the development of optimized powders still offers one of the surest ways towards reliable and cost effective component manufacture.

References

(1) C. Herring, J. Appl. Phys., 21, 301 (1950)

(2) H. Hahn, J.A. Eastman and R.W. Siegel, Ceram. Trans. 1, 1115-1122 (1988)

(3) E.A. Barringer and H.K. Bowen, J. Am. Ceram. Soc. 65, C: 199-201 (1982)

(4) E. Liniger and R. Raj, J. Am. Ceram. Soc. 70, 843-849 (1987)

(5) G. Wötting and G. Ziegler, Interceram 35, 32-35 (1986)

(6) K. Okada, N. Otsuda, R.J.Brook and A.J. Moulson, to be published

(7) N. Kimura, S. Abe, Y. Hayoshi, J. Morita and H. Okamura, 2nd Int. Conf. Ceram. Powder Processing Science, Berchtesgaden, FRG (1988)

(8) L.H. Edelsen and A.M. Glaeser, J. Am. Ceram. Soc. 71, 225-235 (1988)

(9) Y.L. Chen and R.J. Brook, Br. Ceram. Trans. J. 88, 7-12 (1989)

POWDERS:
PRODUCTION AND PROCESSING

ADVANCES IN POWDER PREPARATION AND PROCESSING OF EMERGING MATERIALS

D.P. Uskoković

Institute of Technical Sciences of the Serbian Academy of Sciences and Arts, Belgrade, Yugoslavia

Synthesis of emerging metallic and ceramic materials by advanced powder processing includes direction of elementary procedures from the powder preparation, the control of sintering process and its microstructural constituents which has dominant influence on the final properties of materials. In the field of preparation of metal powders for emerging materials a great interest for rapidly solidified crystalline and amorphous powder[1] has appeared in recent time. There are different methods enabling fast cooling powders preparation with rates higher than 10^3 K/sec and offering great advantages. The circumvention of segregation and workability problems, obtaining finer microstructure, extention of solubility and the formation of metastable phases, including amorphous phases, are some of advantages which could be obtained by rapid solidification. Different rapid solidification methods in both metal and ceramic systems, their advantages and limitations will be considered in this paper. In recent time there is a large interest for mechanical alloying as well. This method is offering a series of advantages in the synthesis of amorphous systems.

The increase of interest for chemical methods for the synthesis of multiphase ceramic materials with well defined characteristics is the consequence of the possibility to obtain materials with better final characteristics and greater reliability[2]. A variety of methods are presently being used to generate these starting powders. Precipitation from homogeneous solutions, phase transformation, aerosols routes for synthesis, thermal decomposition and hydrolysis, hydrothermal reaction at high pressure and different mechanical technique (spray drying, freeze drying etc.) will be analysed. Different emerging materials and their characteristics will be considered from the standpoint of applied methods of synthesis. The method of self-propagation

combustion synthesis will be specially considered. Although this method is well known for a quite a long time, larger interest for it appeared recently[3]. One of the advantages is that it can be used simultaneously with pressing offering new prosperous possibilities. The production of different borides, carbides, nitrides, hydrides, silicides, intermetallics and composite compounds will be analysed in details.

The consolidation of rapidly solidified crystalline and amorphous powders is very important[1,4]. Namely, in many cases the development of emerging materials with predicted composition and properties using rapidly solidified crystalline of amorphous powders is limited because sintering temperature or other consolidation temperatures are too high to maintain metastable constituents and to prevent their dissolution or decomposition. The dynamic consolidation, the cold extrusion, high static pressure consolidation, hot pressing, hot isostatic pressing and strain powder rolling methods of rapidly solidified crystalline and amorphous powders are used for obtaining materials with theoretical density. Although some of the mentioned methods are still in development, specially in the case of amorphous systems we will not wait too long for their commercial application.

Consolidation of the ceramic powders obtained by different chemical methods is usually performed by conventional sintering process. The advantages obtained by improved or advanced consolidation methods, like rate controlled sintering[5] or hot isostatic pressing[6] are well known and widely used presently. They will be also the matter of our consideration.

References:

1. M. Zdujić, D. Uskoković, "Rapidly Solidified Crystalline and Armorphous Powder-Problems and Perspective" in SINTERING '87, ED. S. SOMIYA et al., Elsevier, 1988, 1504.
2. E. Matijević, "Production of Menodispersed Collodial Particles", Annu.Rev.Materials Sci., 15 (1985), 483.
3. Z.A. Munir, "Synthesis of High Temperature Materials by Self-Propagation Combustion Methods", Ceram.Bull., 67, (1988), 342.
4. P.H. Shingu, "Metastability of Armorphous Phase and its Application to the Consolidation of Rapidly Quenched Powders", Mater. Sci. & Eng., 89 (1988), Accepted for publ.
5. H. Palmour III, T.H. Hare, "Rate Controlled Sintering Revisted" in SINTERING '85, Eds. G.C. Kuczynski et al., Plenum, 1987, 17.
6. "Emergent Process Methods for High-Technology Ceramics", Eds. R.F. Davis et al., Plenum, Mat.Sci.Res., 17, (1984), 842.

DENSIFICATION OF HIGHLY REACTIVE ALUMINIUM TITANATE POWDERS

M.Gašić*, G.Ondracek**, I.Stamenković*

*Institute of Nuclear Sciences "Boris Kidrič"-Vinča,Beograd Yugoslavia

**Institut für Gesteinshüttenkunde (Glas, Keramik, Binde- und Verbundwerkstoffe), Rheinisch-Westfälische Technische Hochschule Aachen (RWTH), Germany

1. INTRODUCTION

There is an increasing interest in aluminium titanate ceramics due to their potentials as high-tech ceramics and biomaterial /1,2/.

The problem of aluminium titanate eutectoid-like decomposition between 1300 and 700°C has been widely investigated; it was demonstrated that the substitution of Al by Mg ions to build $Al_{1.8}MgO_{0.1}Ti_{1.1}O_5$ is most effective in reducing the thermal decomposition rate /3/.

Besides the common preparation methods of aluminium titanate powders by conventional solid state reaction of starting Al_2O_3 and TiO_2 /4/, there are some efforts of obtaining Al-titanates by non-conventional methods /5-9/. However, these papers revealed the problem of preparing ceramics starting with very active powders. Among these problems the adsorption of gases and vapors and agglomeration of particles are dominant. Having these problems on mind the authors applied different consolidation methods like pressing, slip-casting, ultracentrifugal casting, gravitational sedimentation of electrostatically stabilized aqueous suspensions, long dwell time pressing etc.

In the present work a comparative investigation of densification process of aluminium titanate powders obtained via hydrolysis of Ti-alkoxide in presence of corundum or by hydrolysis of two alkoxide components (cohydrolysis) was performed. The experimental work was realized with isostatic pressing followed by sintering as well as with hot pressing technique.

2. ALUMINIUM TITANATE POWDERS

The synthesis of powders having the stoichiometry of aluminium titanate was realized using the procedures of controlled hydrolysis of one alkoxide /6/ (powder SH), or cohydrolysis of two alkoxides /7,8/ (powder CH), being performed even at room temperature /9/.

The results of thermal analysis of the investigated powders are shown in figure 1.

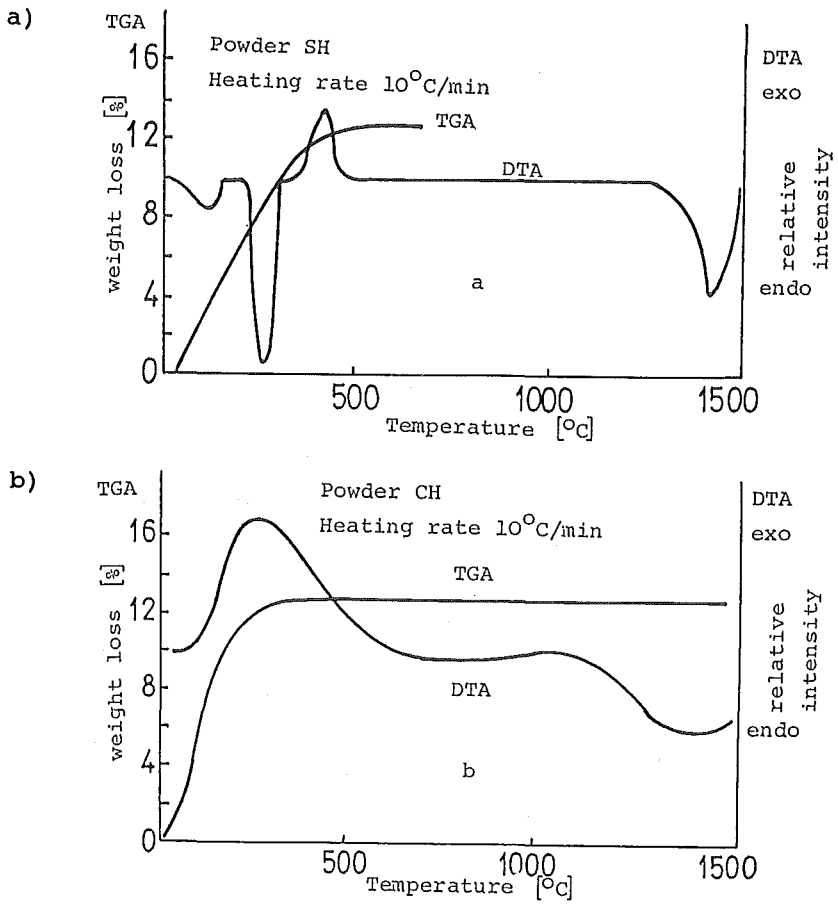

Figure 1. TGA and DTA curves of "as synthesized" powders a) powder SH and b) powder CH

According to the curves in figure 1a the adsorbed and crystalline water from the SH-powder was removed up to 300°C. At about 350°C the burn out of organic matters started and is completed at approximately 450°C. The precipitated titanium oxide corresponds to the calculated formula $TiO_2.0.5\ H_2O$. According to the DTA curve, the formation of aluminium titanate occured at 1280°C; the highest rate of its synthesis was between 1370°C and 1400°C.

For the CH-powder the differential thermal analysis curve (DTA) in figure 1b shows an exothermic peak between 100 and 400°C, representing the "burn out" of organic components, being overlapped by dewatering processes. The occurence of aluminium titanate is obvious already at 1060°C and passes its maximum between 1220°C and 1320°C. It could be ascribed to the very fine particles of both oxides and their intimate contacts being realized during cohydrolization of the alkoxide solutions.

After powder preparation the produced SH- and CH-powders were dispersed in an ethyl alcohol solution of $Mg(NO_3).6H_2O$ and after drying annealed at 650°C for one hour, resulting in two powders containing 2.2 wt% MgO.

For further experiments these two powders were used, as well as the CH powders as synthesized.

The powder characteristics of the obtained calcined powders are summarized in table 1, supplemented by corresponding scanning electron micrographs shown in figure 2.

Table 1. Characteristics of calcined powders

	Powder SH	Powder CH
MgO, wt%	2.2	2.2
Surface area, m^2/g	21 - 27	245 - 265
Particle mean diameter (calculated), µm	0.06	0.006
Particle clusters size range, µm*)	0.1 - 0.3	0.1 - 0.2

*)According to scanning microscope micrographs

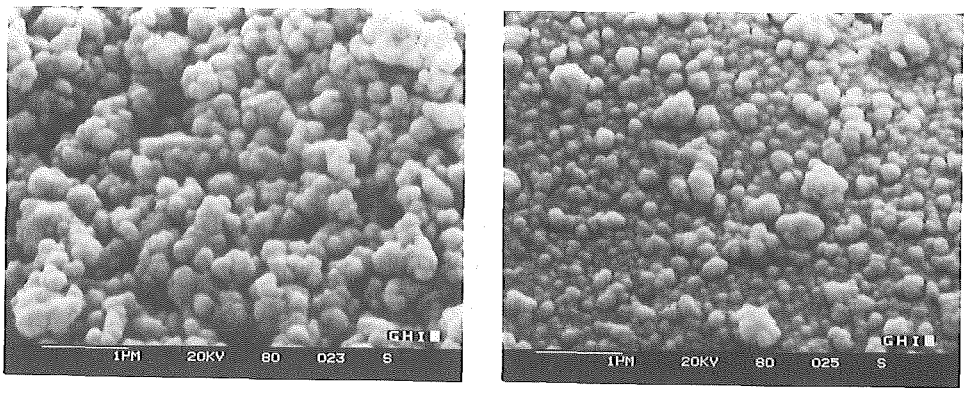

a) b)

Figure 2. Scanning electron micrographs of calcined powders: a) SH powder and b) CH powder

3. ISOSTATIC PRESSING AND SINTERING

Since uniaxial pressing of submicron powders is usually dissatisfying, the isostatic wet bag pressing was performed under pressures of 98 MPa and 157 MPa.

As can be seen in table 2 the obtained densities after isostatic pressing were rather low.

Table 2. Densities of samples after isostatic pressing

Sample	Pressure 98 MPa density (g/cm^3)	% TD	Pressure 157 MPa density (g/cm^3)	% TD
a) SH + 2.2% MgO	1.83	50	1.98	54
b) CH + 2.2% MgO	1.12	30	1.29	35
c) CH as synth.	1.22	33	1.37	37

Shrinkage curves achieved by hot stage microscopy are shown in figure 3. The investigated pellets were obtained by isostatic pressing at 157 MPa. The shrinkage of both samples started at about 700°C, the maximum shrinkage rate occurs at about 1200-1400°C. As to expect for very fine powders the total shrinkage for SH powder lies in the interval of 15-20%, whilst the shrinkage for CH powder is considerably higher. Bearing this on mind difficulties during sintering as sample distortion, cracking, low density etc. have been to be expected.

Isostatically pressed samples were sintered at 1400°C for 1h. The heating rate up to 500°C was 4°C/min, and was changed in the interval from 500°C to 1400°C to 10°C/min. The heating rates were chosen according to the DTA-TGA investigations.

The densities of isostatically pressed samples sintered at 1400°C-1h are given in table 3.

It can be seen that the sample SH has the highest density in the pressed as well as in the sintered condition, which leads to smallest shrinkage. The CH samples, with and without MgO, behave themselves very similar, whilst the sample CH without MgO shows the highest shrinkage. On the basis of these results it can be concluded that by using the procedure of isostatic pressing followed by sintering a broad interval of densities may be obtained (75-95% TD).

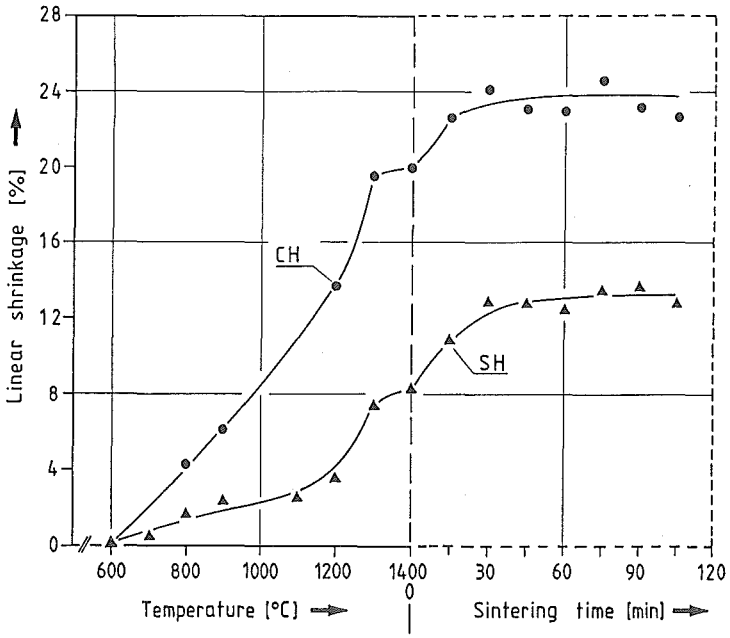

Figure 3. Shrinkage curves of samples isostatically pressed at 157 MPa; heating rate: 15 K/min.; atmosphere: air

Table 3. Densities of isostatically pressed and sintered samples

Sample	Pressure 98 MPa		Pressure 157 MPa	
	density (g/cm^3)	% TD	density (g/cm^3)	% TD
a) SH + 2.2%MgO	3.33	90	3.47	94
b) CH + 2.2%MgO	2.76	75	3.14	85
c) CH as synth.	2.96	80	3.16	85

The presence of crystal phases in the sintered aluminium titanate samples investigated at different densification steps is pointed out in table 4. Both starting powder mixtures, for SH- and for CH-samples, contained TiO_2 in anatase phase but its crystallinity level was rather low and not well defined peaks have been obtained. An increase of crystallinity however was noticed with powders heated at 650°C, and TiO_2-rutile, as a minor phase, has been

detected in SH-powder. After heating at 1400°C-1h in both samples the beta Al_2TiO_5 was present.

Table 4. Results of X-ray analysis of aluminium titanate samples

Sample	Powder SH	Powder CH
As synthesized	Corundum + Anatase	Anatase + (amorphous phase)
Powder with 2.2wt% MgO calcined at 650°C	Corundum + Anatase + Rutile (minor phase)	Anatase + (amorphous phase)
Pellets isostatically pressed and sintered at 1400°C/ 1h	β- Al_2TiO_5	β-Al_2TiO_5

In figure 4 the micrographs obtained by SEM investigation of isostatically pressed and sintered samples are presented.

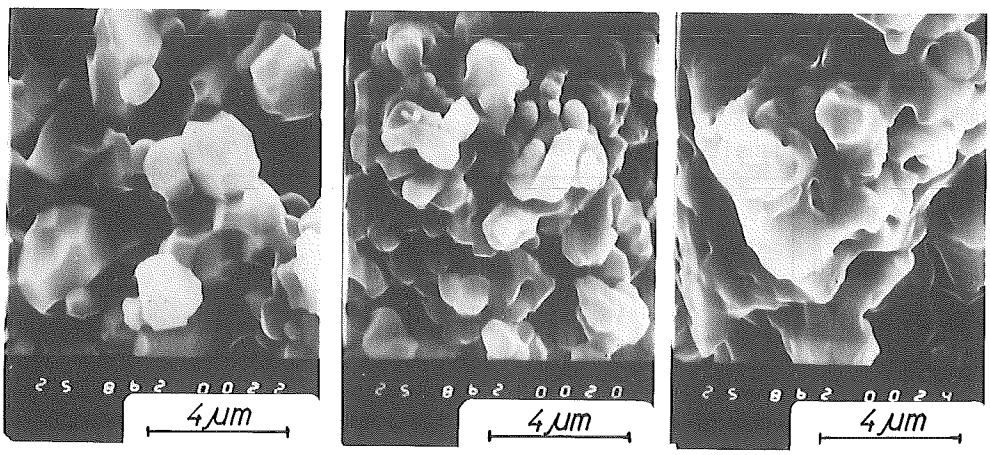

SH + MgO CH + MgO CH as synth.

Figure 4. Scanning electron micrographs of fracture surfaces of samples isostatically pressed at 157 MPa and sintered at 1400°C-1h

As can be seen there the grains of isostatically pressed and sintered samples have more regular shape in comparison with the grains of cold pressed and sintered samples /9/. The grain sizes of sample SH + MgO ranged from 0.5 to 3.8 μm and the cracks between grains are less pronounced. The grain sizes of samples CH + MgO ranged from 0.3 to 2.4μm. In sample CH as synth. strongest grain growth occured, but the origin of small grains is still visible. The size of the largest grains is about 5.5-6.0μm.

As a consequence of this comparison it may be concluded that MgO additions play an important role in preventing grain growth.

4. HOT PRESSING

Hot pressing of samples was performed in vacuum using "Astro" facility. Pellets having a diameter of approximately 10 mm and a height of 5 mm were produced in a graphite die with pyrolytic carbon paper spacers. The heating rate was 40°C/min. Starting from 600°C and up to maximum temperature the pressure of 30 MPa was applied. The applied pressure was released after soaking time at maximum temperature and the samples were furnace cooled down. The obtained samples were black. Some of them were investigated directly after hot pressing, and some of them were heated in an oxygen atmosphere at 1000°C - 1h.

The densities of hot pressed samples, after treatment in O_2 at 1000°C-1h, are presented in table 5.

Table 5. The densities of hot pressed samples after oxidation in O_2 at 1000°C-1h

Sample	density (g/cm^3) 1200°C/0,5h	1300°C/0,5h	1350°C/2h
a) SH + 2.2% MgO	-	3,45	3,65
b) CH + 2.2% MgO	3,10	3,40	3,55
c) CH as synthesized	-	3,30	3,50

X-ray analysis of hot pressed samples, after oxidation in O_2 at 1000°C-1h, revealed the presence of corundum, rutile and beta Al_2O_3 in different proportions, as given in table 6.

Table 6. X-ray analysis of hot pressed samples after oxidation in O_2 at 1000^oC-1h

Conditions	Sample		
	SH + 2.2wt% MgO	CH + 2.2wt% MgO	CH as synthesized
1200^oC/0.5h	Corundum + Rutile + β-Al_2TiO_5 (minor phase)	Corundum + Rutile + β-Al_2TiO_5 (minor phase)	Corundum + Rutile + β-Al_2TiO_5 (minor phase)
1300^oC/0.5h	Corundum + Rutile + β-Al_2TiO_5 (minor phase)	Corundum + Rutile + β-Al_2TiO_5	Corundum + Rutile + β-Al_2TiO_5
1350^oC/2h	Corundum + Rutile + β-Al_2TiO_5	Corundum + Rutile + β-Al_2TiO_5	Corundum + Rutile + β-Al_2TiO_5

According to these results the densities presented in table 5, are in fact the densities of mixture of diferent phases and the formation of aluminium titanate ceramics was far from completion. This is why the calculation of percentage of theoretical density did not make sense.

X-ray analysis of hot pressed samples made directly after hot pressing revealed the presence of corundum, rutile, beta Al_2TiO_5, TiO, Ti_2O_3 and other Ti-oxides with different Ti/O ratio, smaller than 2.

These preliminary hot pressing experiments revealed many problems in obtaining high dense aluminium titanate ceramics. First of all is the experiment performance in reduction atmosphere due to the graphite die and vacuum. In such circumstances TiO_2 could be easily transformed in substoichiometric forms. It is well known that the Ti_2O_3 (dark violet or black) can arise in reduction conditions already at 200^oC, and dark brown TiO_2 can arise at 990^oC. Having these facts on mind we tried to work with very high heating rates and short annealing times, in order to prevent reduction caused by graphite, but it was shown that under all conditions (shorter and longer annealing time) the reduction of TiO_2 proceeds. During oxidation in O_2 atmosphere it was possible to oxidize the different Ti-oxides to TiO_2, but no "reinforcement" of Al_2TiO_5 formation occured.

Comparing the results obtained using isostatic pressing followed by sintering with those achieved by hot pressing clearly favourizes isostatic pressing followed by sintering in order to get single phased aluminium titanate ceramics.

ACKNOWLEDGEMENTS

The authors gratefully acknowledge the experimental assistance of Mrs. W. Stumpfe, Mr. O.Seide, Mr. Č.Pović and Mr. M.Memedović.

5. REFERENCES

1. P.J.Gualtieri: "Ceramic materials in Vehicles - Why and Where?", Interceram, No.2 (1987), p.32-35.
2. G.Ondracek, I.Stamenković: "Composites and Biomaterials", FR Germany-Yugoslavia Cooperation in Materials Sciences Intern. Bureau Kernforschungsanlage Jülich (1988).
3. M.Ishitsuka, T.Sato, T.Endo, M.Shinada: "Synthesis and Thermal Stability of Aluminium Titanate Solid Solutions",J.Am.Ceram.Soc., 70 (1987) 2, p.69-71.
4. I.Stamenković, W.Stumpfe, J.Bossert: "Synthesis of aluminium titanate by starting oxides interaction" (in German), Report Institute für Gesteinshüttenkunde, Glas, Bio- und Verbundwerkstoffe der RWTH Aachen (1988).
5. S.Hori, R.Kurita: "Sintering of CVD Aluminium Oxide Titanium Oxide Powder", Int. J.High Technology Ceramics, 1 (1985) p.59-67.
6. H.Okamura, E.A.Barringer, H.K.Bowen: "Preparation and sintering of monosized Al_2O_3-TiO_2 composite powder", J.Am.Ceram.Soc., 69 (1986) 2, C22-24.
7. P.A.Brugger, A.Mocellin: "Preparation of composite Al_2O_3-TiO_2 particles from organometallic precursors and transformations during heating", J.Mat. Sci., 21 (1986) p.4431-4435.
8. M.K.Morrow, C.E.Holocombe, C.A.Cromer: "Preparation of aluminium titanate crucibles by slip casting for high-temperature applications" Union Carbide - Oak Ridge Y-12 Plant, Y-1831 (1972).
9. I.Stamenković, J.Bossert, G.Ondracek, W.Stumpfe: "High-tech aluminium titanate ceramics", IX. German-Yugoslav Meeting on Materials Science and Development "Emerging Materials by Advanced Processing", 16-19. April 1989, Hirsau (FR Germany).

HIGH-TECH ALUMINIUM TITANATE CERAMICS

I. Stamenkovic*, J. Bossert, G. Ondracek, W. Stumpfe

Rheinisch-Westfälische Technische Hochschule
Institut für Gesteinshüttenkunde
- Glas, Keramik, Binde- und Verbundwerkstoffe -
Mauerstr. 5, D-5100 Aachen

SUMMARY

To prepare pure ("high tech") aluminium titanate powders two preparation routes have been performed:

- the solid state reaction of oxidic components
- the sol-gel route.

The surface areas of aluminium titanate powders prepared by solid state reaction of alumina and titania at 1500°C and subsequent different milling procedures ranged between 3.2 and 5.5 m^2/g. According to sintering experiments performed at 1500°C the sinterability of these powders was restricted. Sintered samples contained grains of about 4 micrometers in diameter and microcracking was revealed. Due to the milling procedure impurities were present in all sintered materials.

Sol-gel routes led to fine aluminium titanate powders the surface areas of which ranged between 25 m^2/g in the case of hydrolysis route and 255 m^2/g if the cohydrolysis route was used. This serie of aluminium titante (AT) powders was characterized by very poor cold compactibility (< 58% TD) but provides extremely high sinterabilities; high dense samples (≥ 95% TD) have been obtained at sintering temperatures of about 1400°C. The material was pure and fine grained and in those cases, where the grain size ranged below one micrometer, no microcracking was noticed in the bulk ceramic.

1. INTRODUCTION

Aluminium titanate ceramics, already introduced as a thermal insulator ("portlining material") in the field of advanced engine production, offer a number of further potentials as a high-tech ceramics [1] as - for example - in medicine. Since its structural components AL_2O_3 and TiO_2 behave themselves biocompatible aluminium titanate ceramics could be considered also as a biomaterial candidate [2].

* presently on leave from Boris Kidric Institute Beograd-Vinca

In order to further improve its purity, microstructural stability and therefore its technological reproducibility and properties like its mechanical strength research and development work has been directed towards the synthesis of fine grained, stabilizers containing ceramics. The starting aluminium titanate powders were produced by using different preparation techniques like solid-state reaction, melting, chemical vapor deposition and alkoxide hydrolysis [3,4].

Starting with the oxidic components aluminium titanate may be prepared within an extremely wide temperature range between 1000 and 1600°C [5], but 1500°C has been specified best to produce the stoichiometric compound, where the use of anatase is considered to be advantageous [6]. The produced aluminium titanate mainly contained minor phases of Al_2O_3 or TiO_2 or different solid solutions.

Amongst the group of aluminium titanate stabilizers evidently MgO, SiO_2, Fe_2O_3, ZrO_2 and alkalies provide highest effectiveness. To produce appropriate powders prereacted aluminium titanate (AT) has been crushed in different mills like ball mill [7], attritor mill [8] or vibro mills [9]. The published results, however, are dissatisfying with respect to reproducible and definite powder charcteristics. - This is why Japanese authors [10] used non-conventional chemical vapor deposition (CVD) to produce highly active Al_2O_3-TiO_2 powders. Conventional sintering of these powders led to 89% of theoretical density of the pellets at 1300°C and 95.5% of theoretical density at 1400°C. The material, however, was not single phase containing ß-Al_2TiO_5, nonreacted Al_2O_3 and TiO_2, where the excess of Al_2O_3 was distributed along the grain boundaries of small AT-grains (≈ 3µm in diameter). Also present in the microstructure were large grains (20-50 µm), pores and microcracks.

Using metal alkoxides as starting components (cohydrolization) [11, 14] resulted in narrow particle sized nonagglomerated and chemically controlled AT powders [11], which could be sintered at 1550°C/4h to high (nonspecified) densities. The average grain size was low (1.3 µm) and no texture was observed causing - according to the authors - high stability against crack propagation [11].

Furthermore by hydrolysis of Ti-alkoxide and narrow particle sized Al_2O_3 powder (0.4 - 0.6 µm) alumina coated particles have been prepared, which could be compacted up to extremely high green densities by intensive centrifugation and sintered in the temperature range between 1350 and 1400°C up to 99% of the theoretical density. However crystal domains and cracks between the domains were formed due to AT thermal expansion anisotropy. To avoid the crack formation alternative powder preparation methods have been proposed by the authors [12, 13].

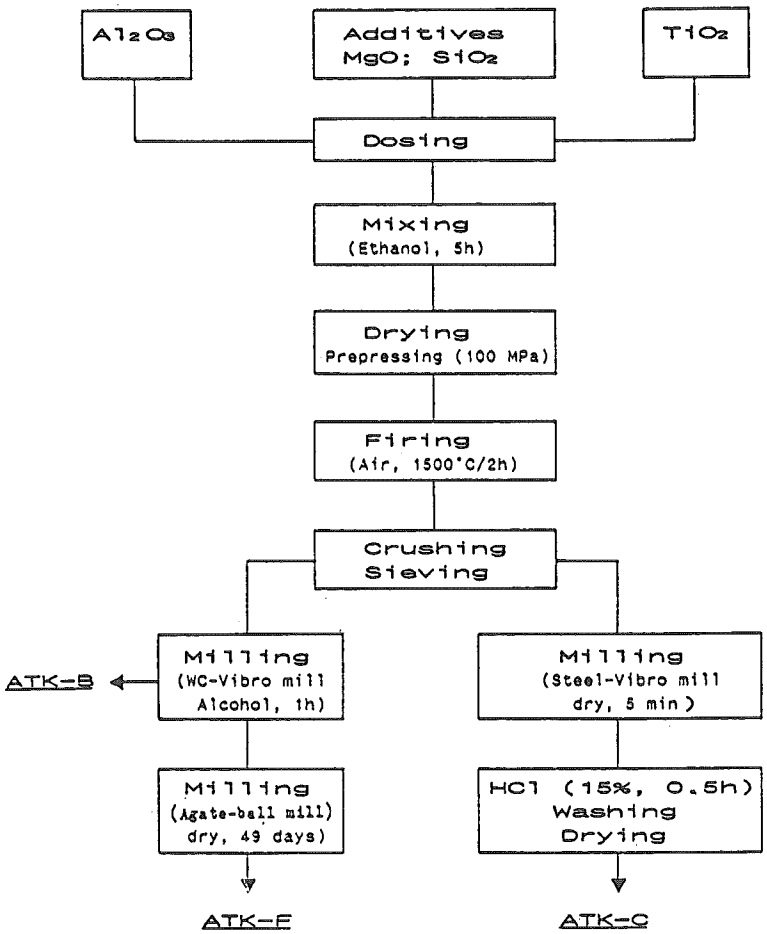

Figure 1: Schematic Flow Diagram of Aluminium Titanate Powders Preparation, starting with Oxides.

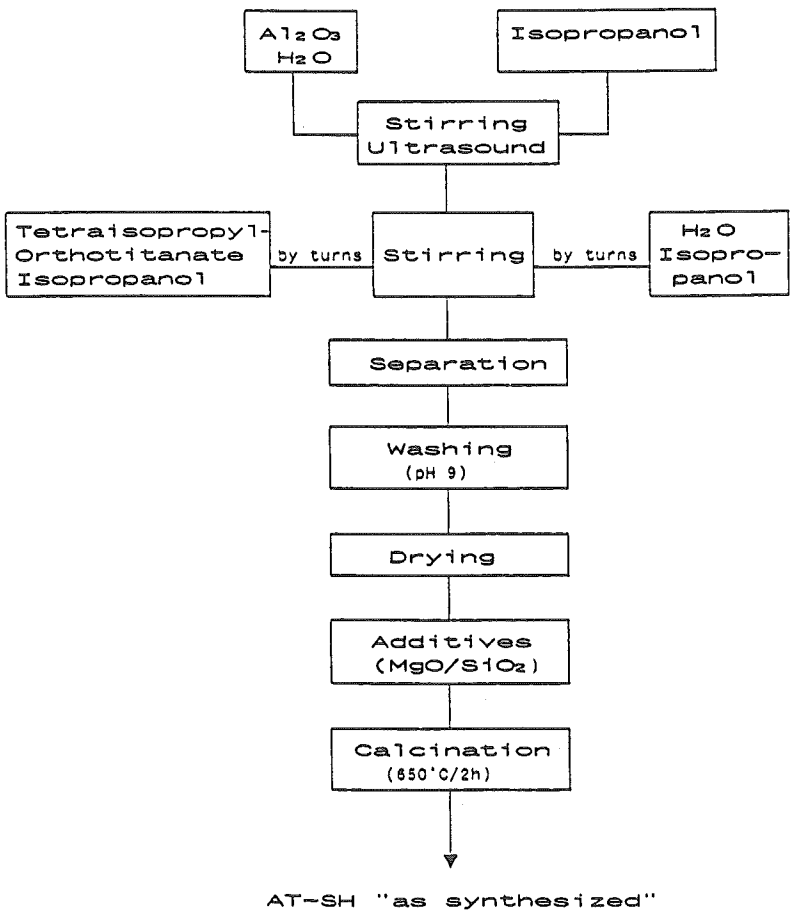

Figure 2: Schematic Flow Diagram of Aluminium Titanate Powder Preparation by Sol-Gel-Procedure. (Single Component Hydrolysis)

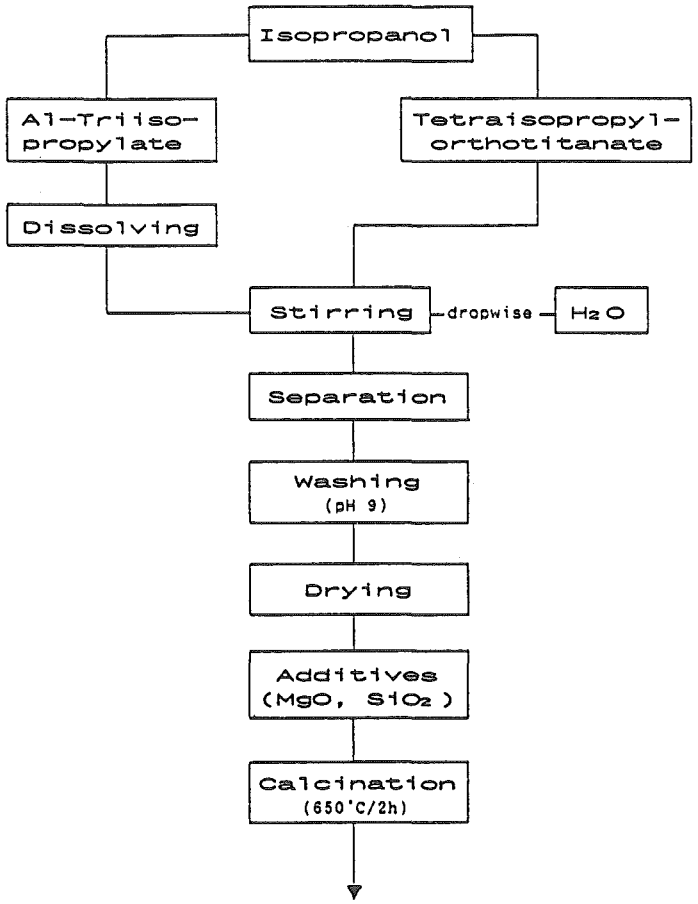

Figure 3: Schematic Flow Diagram of Aluminium Titanate Powder Preparation by Sol-Gel-Procedure. (Cohydrolysis)

Based on these results from the literature and bearing in mind the potential of AT in the field of biomaterials the present work was dedicated primarily to pure powder synthesis, powder characterization, compaction and sintering behaviour.

2. PREPARATION OF ALUMINIUM TITANATE POWDERS

The used preparation techniques - solid state interaction of Al_2O_3 and TiO_2 (fig. 1) and sol-gel processing (fig. 2, 3) - and corresponding processing parameters have been choosen and/or optimized according to literature recommendations and own experiences gained in the available experimental facilities. Intending to produce aluminium titanate powders for bioceramics commercial starting powders and chemicals of high purity have been choosen (fig. 4).

Chemicals	Characteristics	Producer
TiO_2	purity: > 99 wt% surface area: 7.3 m^2/g crystal phase: Anatase	Merck
Al_2O_3	purity: 99.7 wt% surface area: 8.2 m^2/g crystal phase: Corundum SEM-particle size: 0.08-0.22 µm	Alcoa
Tetraisopropyl-orthotitanate	Ti content > 98% density: 0.965g/cm^3	Merck
Al-Triiso-propylate	Al content > 98% melting point 135°C	Merck

Figure 4: Starting components characterization

Powder	Phase	Minor phase
B	Aluminium Titanate	Corundum + Rutile
C	Aluminium Titanate	Corundum
F	Aluminium Titanate	Corundum + Rutile
SH (as synthesized)	Corundum Anatase	–
CH (as synthesized)	Anatase	–

Figure 5: X-ray analysis of aluminium titanate powders

It is obvious from fig. 5 that aluminium titanate powders obtained by solid state reaction contained minor quantities of the starting oxides due to the specific volume changes of reactants during the transformation. Experiments to produce single phased AT by repeated comminution, pressing and sintering increased the reaction ratios but also the impurities "jeopardizing" this approach.

The powders obtained via hydrolysis of metal organics behaved, in fact, like mixtures of single oxides, where in "SH-powder"- according to DTA-results - the phase formation occured in the temperature range between 1370 and 1400°C, whilst the respective phase formation in "CH-powder" took place at 1270 ± 50°C due to its very fine particle size and the intimate contacts between those particles [15].

Considering the powder characteristics of B, C and F, fig. 6 clearly points out, that no substantial influence of mill type nor jar material on the surface area exists, but also that differences in the impurity contents occur.

Powder	Surface area, m^2/g	Particle size range, µm	Bulk density g/m^3 loose	Bulk density g/m^3 tap	Impurity content,%
B	5.5	< 23*	1.2	1.8	1.51 (WO_3, CaO, NiO, Fe_2O_3)
C	3.2	< 23*	0.9	1.7	1.96 (Fe_2O_3)
F	5.1	< 17*	1.1	1.5	
SH	24	0.13-0.3**	0.4	0.6	-
CH	255	0.06-0.2**	0.2	0.3	-

Figure 6: Characterization of different AT powders
*Laser particle size analysis, **scanning electron micrograph

3. DENSIFICATION OF ALUMINIUM TITANATE POWDERS

Double acting cold pressing as well as isostatic cold pressing was applied to shape and densify the AT powders considerable here. The influence of compacting pressure on the green densities is shown in Fig. 7.

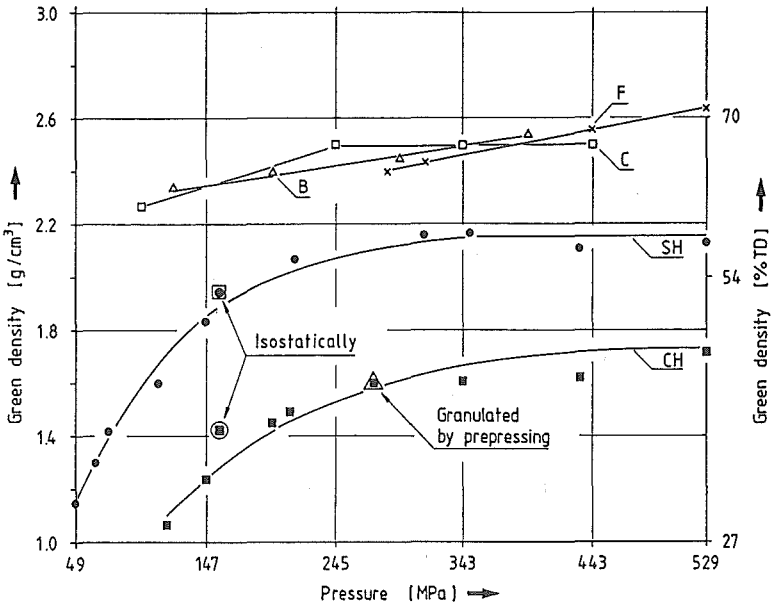

Figure 7: The influence of compaction pressure on green densities

In the case of AT powders obtained by solid state reaction the relatively high green densities (65 - 71% TD) could be correlated with a homogeneous "two fraction particle size distribution" created during milling, whilst the far lower densities of the CH-powder (< 47% TD) may be ascribed to agglomerations in the very fine powder mixture. Since the other sol-gel powder type SH does not result in much better densification the general conclusion for sol-gel powders is to mix them in colloidal liquids to get a more homogeneous overall particle size distribution after drying the mixture. Cold compacting densities below 60% TD are considered to be insufficient with respect to nonuniform, high shrinkage and crack suppression during sintering [16] (comp. Fig. 8).

From the sintering results, graphically shown in Figure 9, it may be concluded

- that a slight influence of pressing pressure on sintering densities exists for all powders compacted above at least 100 MPa which, however, is not practically relevant in most cases
- that the samples isostatically cold pressed do not differ in sintered densities in comparison with those made by double acting cold pressing
- that the lower green densities of sol-gel type powders (Fig. 7) are compensated by sintering compared with powders from solid state oxide interaction or - in other words - that the sinterability of sol-gel powders is higher.

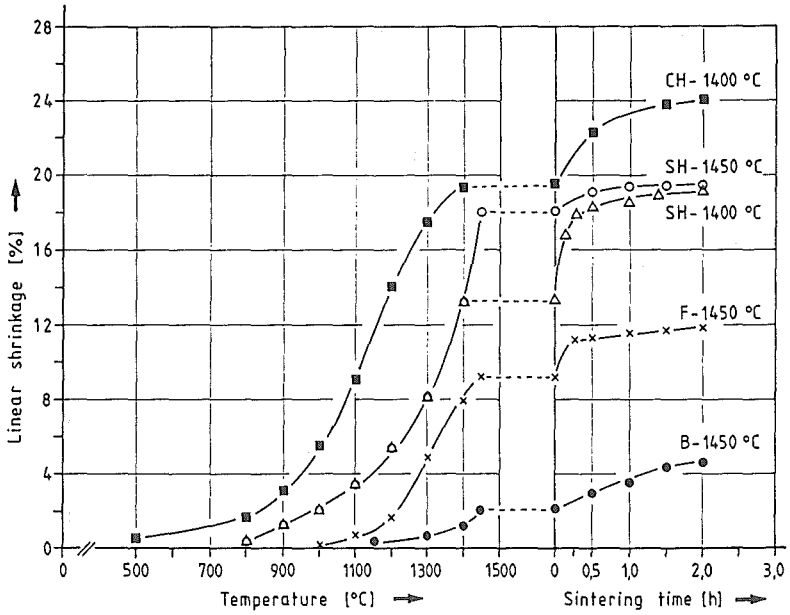

Figure 8: Shrinkage curves of differently prepared aluminium titanate powders (hot state measurements)
heating rate: 15°C/min; atmosphere: air

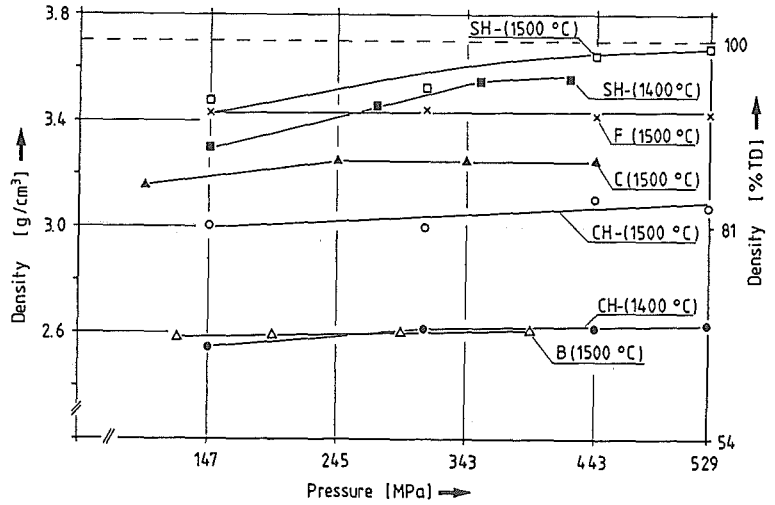

Figure 9: Densities of aluminium titanate sintered at 1400°C/2h and 1500°C/2h

4. STRUCTURAL CHARACTERIZATION OF SINTERED ALUMINIUM TITANATE

The qualitative chemical analysis of SH- and CH-type sintered aluminium titante did not show any presence of impurities, except magnesium added as a stabilizing component. This, however, does not hold true for the samples produced by solid state reactions as demonstrated in Fig. 10. In this case, the presence of contaminations is due to the milling procedures, which were similar for both samples. In order to test how to reduce the impurities, the iron containing C-type powder has been treated by hot HCl, washed and centrifugated. The starting Fe_2O_3 content of 1.96 wt% was decreased to an order of 100 ppm.

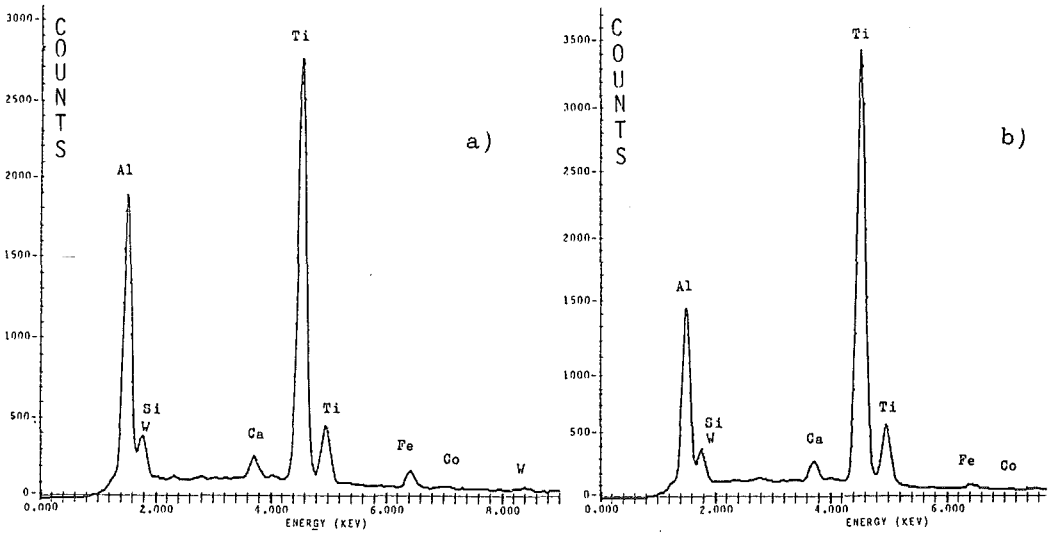

Figure 10: Surface analysis of AT sintered samples at 1500°C a) B; b) F

Qualitative X-ray and quantitative grain size analysis of sintered AT-samples (Fig. 11) points out the predominance of the beta-aluminium titanate phase.

The traces of corundum phase present in some sintered samples being the consequence of TiO_2 losses during powder preparation [17] are considered to be technologically advantageous by some authors [18], but may be suppressed by increasing the Ti-alkoxide content in the starting mixture.

An additional investigation of sintered AT-samples was made by electron scanning microscopy. Some of the obtained micrographs are shown in Fig. 12, reflecting clearly the differences in grain size as given in Fig. 11. Referring to literature cracks are suspected above critical grain sizes of about 1-2 µm diameter [7]. Quantitatively, indeed, the presence of such microcracks was noticed in all samples except those of CH-type aluminium titanate.

Powder type	Sintering temperature [°C]	Phase			Grain size [µm]	
		major	minor	traces	range	average
B	1500	ß-Al_2TiO_5	Corundum	Rutile	≤18.3	4.5
C	1500	ß-Al_2TiO_5				
F	1500	ß-Al_2TiO_5		Rutile	≤9.9	4.0
SH	1400	ß-Al_2TiO_5		Corundum	0.69-5.0	2.1
CH	1400	ß-Al_2TiO_5		Corundum		
CH	1500				0.32-2.9 (clustering)	1.09

Figure 11: X-ray and grain size analysis of sintered aluminium titanates.

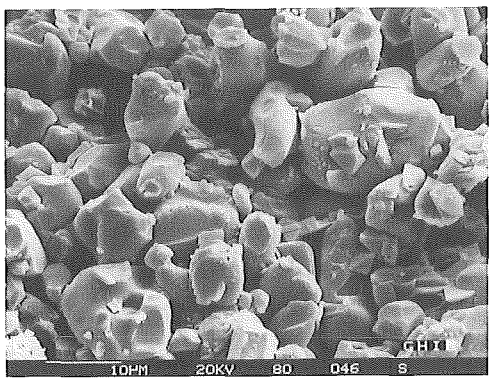

a

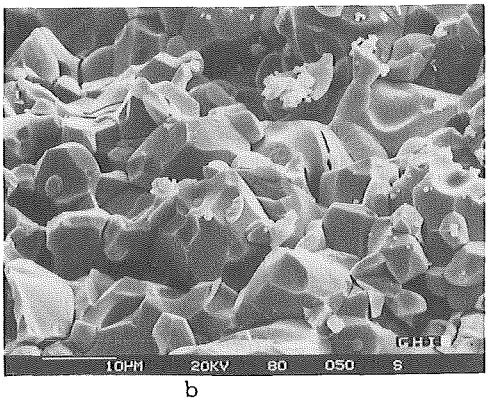

b

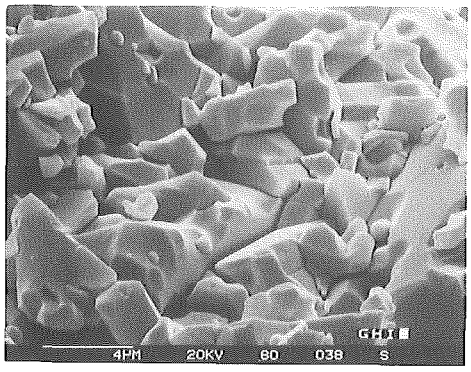

c

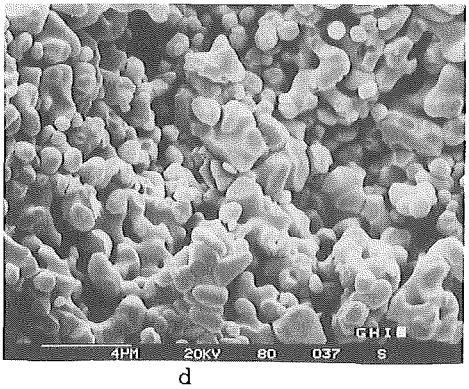

d

Figure 12: Scanning electron micrographs of fracture surfaces:
a: B sintered at 1500°C; b: F sintered at 1500°C
c: SH sintered at 1500°C; d: CH sintered at 1500°C

5. REFERENCES

1. Byrne, W.P., Morell, R., Lanson, J., "Thermal Expansion Characterization and Thermal Stability of Aluminium Titanate", Science of Ceramics, Vol. 14, ed. D. Taylor, The Institute of Ceramics, Shelton, Stoke-on-Trent, 1988.

2. Ondracek, G., Stamenkovic, I., "Composites in Biomaterials", Publ. Internationales Büro Kernforschungsanlage Jülich, 1988.

3. Day, J.P., Locker, R.J., "Decomposition behaviour of Aluminium Titanate Solid Solutions, ENVICERAM 88, Köln, Dezember 1988.

4. Freudenberg, B., Mocellin , A., "Aluminium Titanate Formation by Solid State Reaction of Coarse Al_2O_3 and TiO_2 Powders", J. Am. Ceram. Soc., 71, 1, 1988, 22-28.

5. Walter, H., "Aluminiumtitanat als Basis für temperaturwechselbeständige Werkstoffe", Silikattechnik 27, 9, 1970, 304-306.

6. Hennicke, H.W., Lingenberg, W., "The Formation and Decomposition of Aluminium Titanate-I. The Reaction of Formation of Al_2TiO_5", Ber. DKG, 1985, 62, 9/10, 1985, 439.

7. Cleveland, J.J., Bradt, R.C., "Grain Size/Microcracking Relations for Pseudobrookite Oxides", J. Am. Ceram. Soc. 61 11/12, 1978, 478.

8. Pena, P., DeAza, S., Noya, J.S., "Thermal Stability of Al_2TiO_5-$Al_6Si_2O_{13}$-ZrO_2 Composites Obtained by Reaction Sintering" (see Reference 1).

9. Margulis, O.M., Kamenetzkij, A.B., "Characteristic Properties of Aluminium Titanate Products", Ogneupory 1-2, 1965, 23-27.

10. Hori, S., Kurita, R., "Sintering of CVD Aluminium Oxide-Titanium Doixide Powders", Int. J. High Technology Ceramics 1, 1985, 59-67.

11. Kawasaki, S., Hamano, K., Nakagawa, Z., Ohya, Y., "Microstructure and Mechanical Strength of Aluminium Titanate Ceramics" The XXII Symp. on Basic Ceramics, Kyoto (1984). (Abstract)

12. Okamura, H., Barringer, E.A., Bowen, H.K., "Preparation and Sintering of Monosized Al_2O_3-TiO_2 Composite Powders" J. Am. Ceram. Soc. 69, 2 (1986) C22.

13. Kamya, S., Bowen, H.K., "Microstructural Refinement of Al_2O_3-TiO_2 Composite by Cyclic Annealing" 1. Int. Conf. on Ceramic Powders Processing Science, Orlando-Florida (1987).

14. Priger, P.A., Mocellin, A., "Preparation of Composite Al_2O_3-TiO_2 Particles from Organometallic Precursors and Transformations during Heating" J. Mat. Sci., 21 (1986) 4431-4435.

15. Stamenkovic, I., Ondracek, G. and Gasic, M., "Aluminium Titanate Ceramics obtained by Sol-gel Procedure" 7th Int. Symp. on Ceramics Bologna (1988).

16. Colomban, Ph., "Gel Technology in Ceramics, Glass-Ceramics and Ceramics-Ceramics Composites" Ceramic Int. 15 (1989) 23-50.

17. Bradley, D.C., Mehrapotra, R.C., Gaur, D.P., "Metal Alkoxides", Academic Press, New York (1978).

18. Hamano, K., Ohya, Y., Nakagawa, Z., "Microstructure and Mechanical Strength of Aluminium Titanate Ceramics-II" (see reference 11).

ACKNOWLEDGEMENTS

The authors gratefully acknowledge the experimental assistance of Mr. O. Seide and Mr. Z. Feng as well as the assistance of Mrs. Schmitz and Mr. Trechas in preparing the manuscript.

INFLUENCE OF PRECURSOR PREHISTORY ON CARBON FIBRE CHARACTERISTICS

D. Spaseska
Faculty of Technology and Metallurgy
University "Kiril and Metodij", Skopje, Yugoslavia

Abstract

In this work the influence of precursor (polyacrylonitrile-PAN fibres) characteristics on the obtained carbon characteristics is described. Three types of precursors were used having different characteristics reflecting the prehistory of their production.

The first stage of carbon fibres production ist mainly responsible for the characteristics of the final product, hence special attention was payed to the investigation of the oxidation and cyclization of PAN fibres. To derive a mathematical relationship which correlates the most important parameters of the thermal treatment process, the experimental planning method has been used.

The characteristics of the obtained carbon fibres indicate that a good choice of the precursors as well as of parameters of thermal treatment process was finally made.

Introduction

The process for producing high-quality carbon fibres from poyacrylonitrile (PAN) precursors is closely related to several factors as well as to the "prehistory" of precursors and to the conditions of the thermal treatment schedule at some different stages.

"Prehistory" of fibre as a factor of this process includes the composition and structure of precursors. The conditions of the process include temperature, time of treatment, flow rate of gas atmosphere, the rate of leading the evolved gases away, the presence of a catalyst, the reaction rate and so on.

Of significant importance for carrying out the thermal treatment of PAN fibres as well as for the characteristics of the final product, is the "prehistory" of PAN precursor which was subject of investigation of several authors: Dr. Fitzer, Müller, Watt, Johnson and so on /1,2,3,4/. The works of Fitzer and Müller point out that with polyacrylonitrile copolymers, the cyclization and oxidation on reactions take place in the same time, but with homopolymers, oxidation takes place after cyclization (Fig.1).

Watt and Johnson /3/ have investigated the influence of the acid group present on the mechanisms of this process. They point out that the acidic constitutents of precursor act as initiator for the ladder polymer by a mechanism shown by Grassie, which occurs rapidly at 230° C and is shown in the following (Fig.2).

The presence of acrylate comonomers influences the mechanism of the degradation process differently from acidic monomer. For example, the ester degradation can relate to the reaction of chain breaking of the comonomer unite /5/.

As a result of chain breaking, two redicals are obtained which will react as follows:

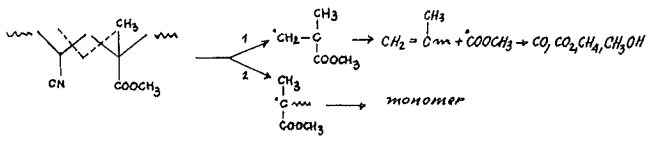

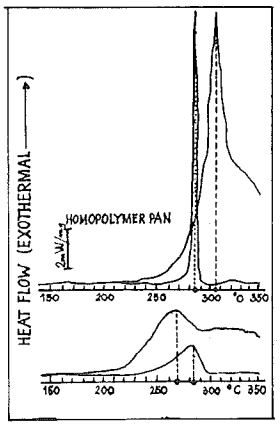

Fig. 1 DSC during stabilization treatment in nitrogen and air

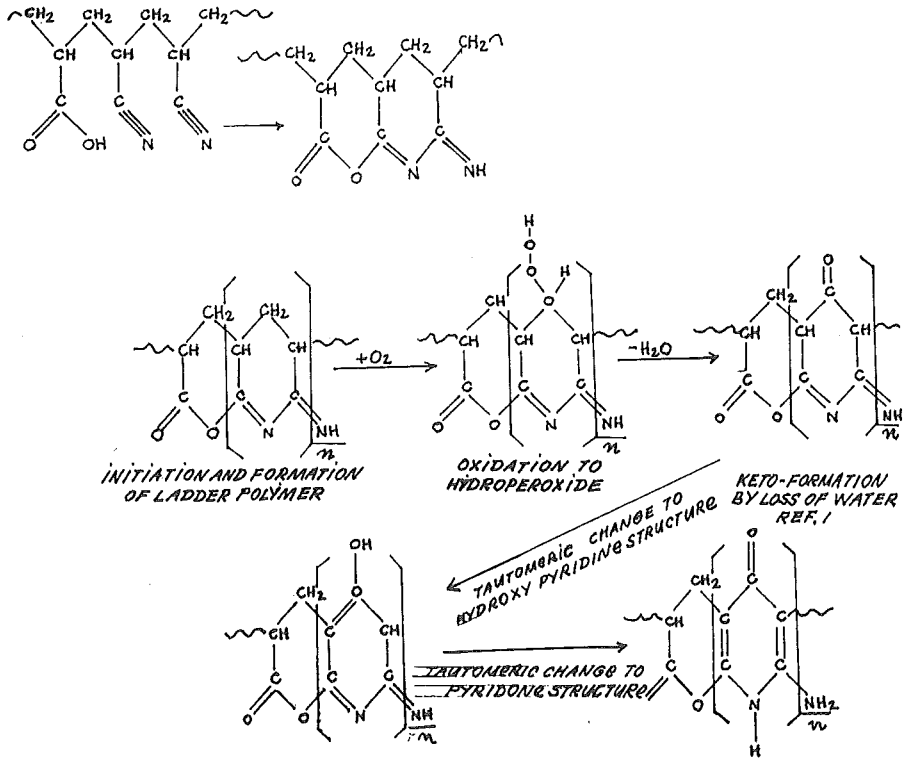

Fig. 2 Mechanism of thermal treatment of PAN fibres with an acidic constituent

This is the general mechanism for the acrylate comonomers but variations of it are known, depending on the comonomers.

The process of obtaining the cyclic structure, starting from PAN fibre as a precursor, is significantly influenced by the regular molecular structure, as well as by the polymer molecular weight.

The conditions for the thermal treatment process are well studied. Layden /6/ has correlated the factors of time, temperature and the fineness (diameter) of the precursors. In addition the pronounced influence of atmosphere, heating rate and others on the process are known.

To obtain carbon fibres with good characteristics all mentioned factors are of importance, as well as it is their interaction. The factors are important for the first stage of cyclization and oxidation, as well as for the carbonization.

Experimental Procedure and Results

Two types of precursors with different composition have been investigated. The precursor A has a higher quantity of acidic monomer than the precursor B. In addition two precursors (A and C) with the same composition but different degree of orientation were compared. The conditions of the thermal treatment process in both cases were considered. The obtained characteristics of oxidized fibres were related to the characteristics of the final carbonized product. The precursors A and B had the following characteristics:

Physical and mechanical characteristics:

a) precursor A

fineness	4,38 dtex
tensile strength	35,02 CN/tex
elongation	32,29 %

b) precursor B

fineness	4,09 dtex
tensile strength	35,09 CN/tex
elongation	32,32 %

The composition content was almost the same for both samples A and B:

A:		B:	
C	63,50 %	C	64,35 %
H_2	3,30 %	H_2	3,22 %
N_2	22,69 %	N_2	22,98 %
O_2	10,51 %	O_2	9,45 %

The third sample (C) had the same composition as the fibres A, but the degree of orientation was much higher as indicated by the given characteristics:

fineness	1,17 dtex
tensile strength	42,7 CN/tex
elongation	16,3 %

The characteristics of precursor C are the reflection of the modified thermomechanical history by which the fibre was obtained.

The thermal oxidation of the obtained raw materials, was carried out at 250° C in the discontinuous working conditions. The investigations of the thermally treated fibres were made after the working temperature of 250° C was reached. Four variables (x_1 = 0.055 to 0.067 g/f/dtex), heating rate (x_2 = 2 to K/min), air flow (x_3 = 6.4 to 20 l/h) and heating time, after the achievement of the working temperature (x_4 = 2 to 6 h). To carry out the experiments in this way, was indispensable because of the need of determination the optimal conditions of the first stage of the process for obtaining carbon fibre, that means the stage of oxidation and cyclization. For this purpose, several techniques have been used as well as DTA, TGA, DSC, elemental analysis, IR spectrophotometry etc. They were used because of their possibility to study the kinetics and mechanisms of the thermo-mechanical degradation process of these fibres.

DSC investigations gave curves, presented in Fig. 3. From these curves we conclude that the oxidation process at the fibre with higher content of acidic group (fibre A) starts in a lower temperature region compared with the system B. This agrees with literature data describing the inhibitor action of acid monomers present. It is clear that after the process starts in system B, the oxidation is carried out at a higher rate in system B than with A, that is represented in Fig. 4. The oxygen contents in the two fibres, during isothermal treatment period, are shown in Fig. 4 (systems A and B).

According to these data, the system B shows a higher inertion in comparison with A, but the adsorption rate of oxygen is increased rapidly up to the maximum value after which the rate decreases (Fig. 5).

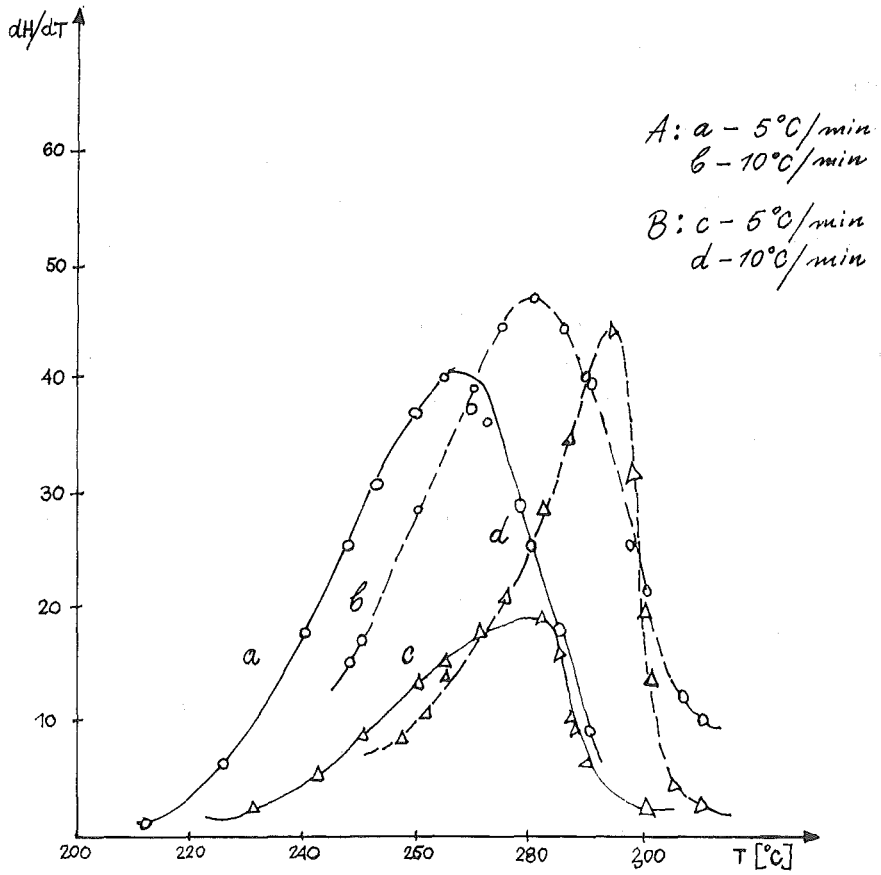

Fig. 3 - DSC curves for two types of fibres
A and B at heating rates of 5 and 10 K/min

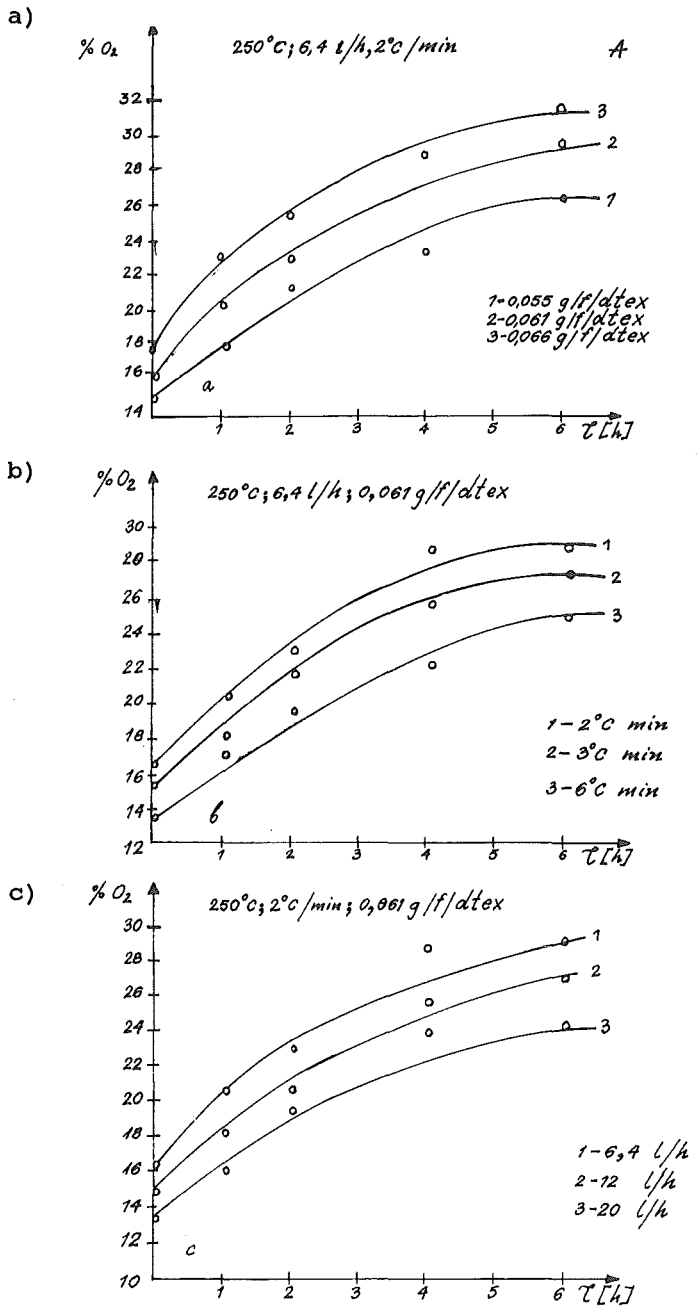

Fig.4.1 Dependence of the oxygen content in relation with a) fibre tenacity b) heating rate c) air flow (system A)

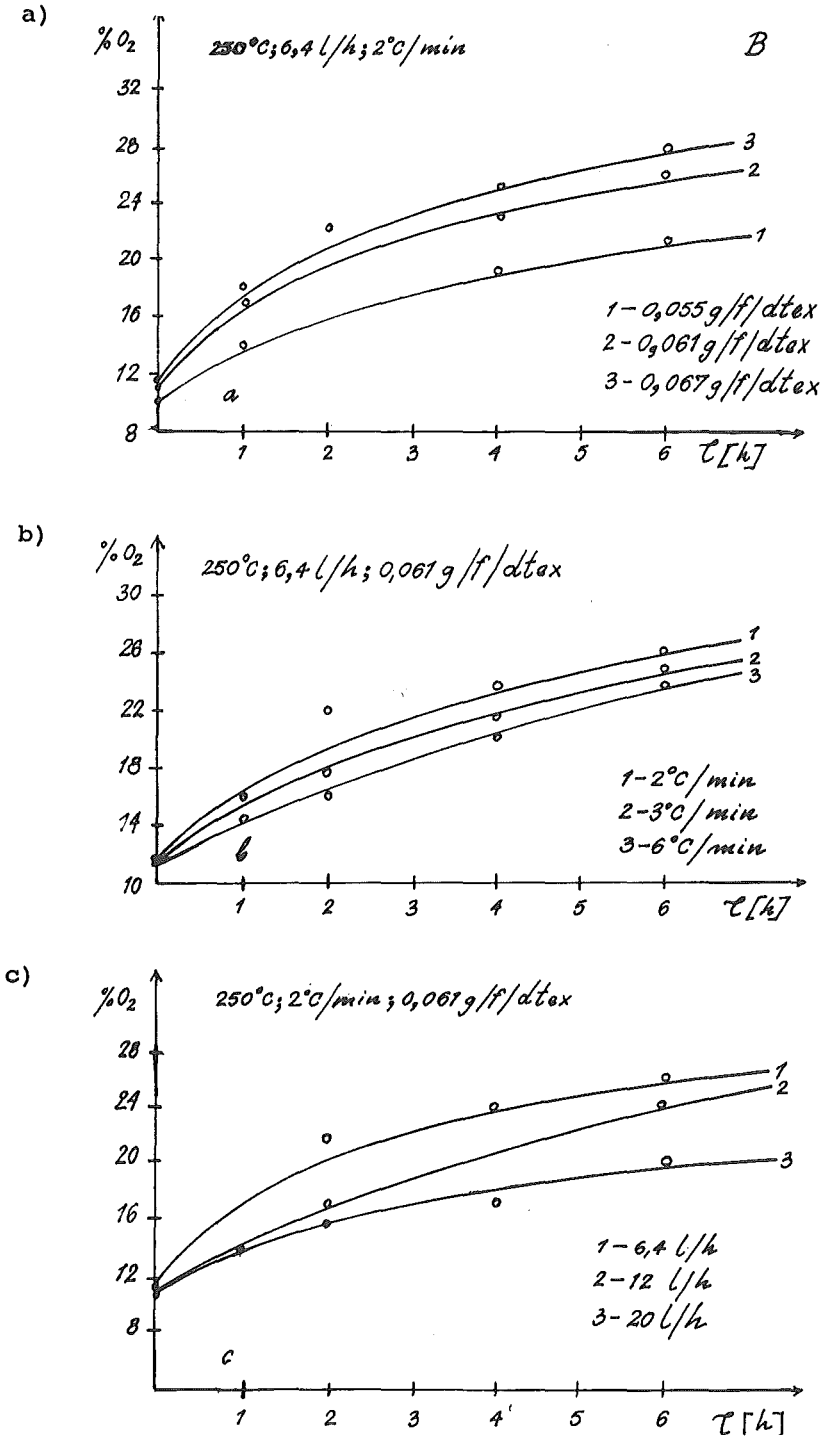

Fig.4.2 Dependence of the oxygen content on a) fibre tenacity, b) heating rate, c) air flow for the system B

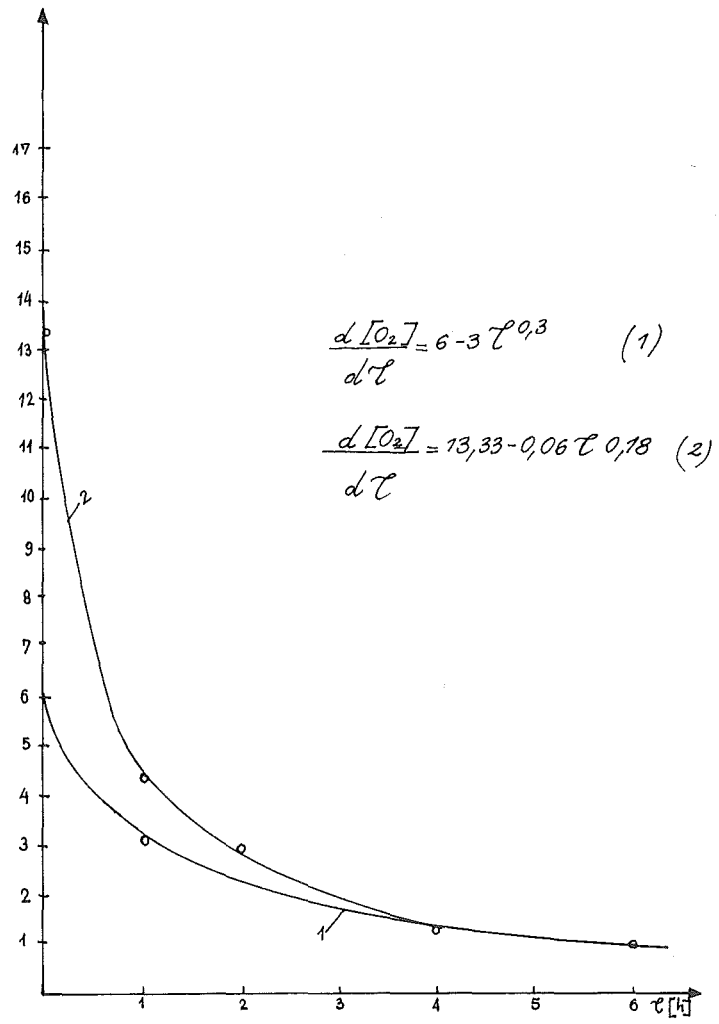

Fig. 5 Dependence of oxidation rate on the treatment time

As a result of a required rapid reaction, it is necessary to do the thermal treatment at modified working conditions. The inertion of the system B needs an increase of the rate of the degradation process in polythermal region or its initiation. This can be achieved by increasing the heating rate up to the working temperature of 250° C. Also after the cyclization and oxidation process starts, the temperature must be decreased to a lower value, because it is necessary to slow down the rate of degradation during isothermal annealing.

Another way to initiate the thermal oxidation process of system B is, of course, the application of pure oxygen during the starting stage, that means during polythermal region. But this is not useful, however, for the isothermal region.

To determine the optimal processing conditions for the first stage of carbon fibre production the method of experiment planning was used. As a reflection function, the oxygen content is taken. As natural variables tension (x_1), heating rate (x_2), air flow rate (x_3) and heating time (x_4) after reaching the working temperature have been used.

By the method of experimental planning a model relationship was derived between characteristics of the obtained products and the parameters of the thermal treatment of starting fibres. The model equations for treatment of fibres A and B for the thermo-oxidative treatment are given by

$$A: y = -1.775 + 312.34\, x_1 - 0.812\, x_2 - 0{,}13\, x_3 + 2.54\, x_4$$

$$B: y = -1.42 + 230\, x_1 - 0.15\, x_2 - 0.16\, x_3 + 2.28\, x_4$$

where x_1, x_2, x_4 are the natural variables mentioned above.

From these model equations we conclude that fibre B needs a longer time for the thermal oxidation treatment, in comparison with system A, although a greater quantity of oxygen is adsorbed in a lower temperature region. During thermal oxidative treatment of system B, the treatment time at the first stage must be taken as a function of its higher inertion, as discussed above. It is necessary to modify this process to achieve a better final product.

The modification of the process is indispensable also for precursors with a higher degree of orientation, indicated by the final characteristics of treated fibres obtained. The main

characteristics of the obtained carbon fibres provided from the precursors A, B, C are as following:

Tensile strength	2 GPa	2,4 GPa	3 GPa
Young's modulus	194 GPa	195 GPa	277 GPa

Conclusion

The study of the influence of precursors with different composition and degrees of orientation on the requirements of the thermal treatment process showed that this process must be modified depending on the nature of the precursors. Improved results for the carbon fibres from the precursors B and C are a reflection of the correct direction of the used modification of the process.

References

1. E. Fitzer, W. Hrohs and H. Heine, Carbon Vol. 24, No. 4, pp 387-395 (1986).

2. E. Fitzer, D.I. Müller, Polym. prep. Am. Chem. Soc. Div. Polym. Chem. No. 1, 396 (1973).

3. W. Watt, W. Johnson, Nature Vo. 257, September 18, 210-212 (1975).

4. N. Grassie and R. Mc Guchan, Europ. Polym. J., Vol. 8, pp. 257 (1972).

5. N. Grassie and R. Mc Guchan, Europ. Polym. J., Vol. 8, pp. 865 (1972).

6. G.K. Layden, Carbon, Vol. 10, p. 59 (1972).

INFLUENCE OF WATER REMOVAL RATE DURING CALCINATION ON THE CRYSTALLIZATION OF ZrO_2 FROM AMORPHOUS HYDROUS PRECIPITATES

T. Kosmač, V. Kraševec and R. Gopalakrishnan

Jožef Stefan Institute, Ljubljana, Yugoslavia

Introduction

The crystallization of hydrous zirconia as well as the occurence and stability of the transitional metastable tetragonal (mt) phase were rather intensively investigated ([1-8]). Thus the existence of mt phase at low temperatures has been attributed to many factors such as anionic (mainly OH) impurities([1]), structural similarities between amorphous and mt structure([2,3]), crystallite size effect, based on the assumption that the surface energy of mt phase is lower than that of monoclinic (m) phase ([4-6]), strains at the crystallite boundaries([5,7]), nonstoichiometry([2,8]), absence of m nuclei for the transformation([6,7]) etc. Due to the simultaneous occurence of many of above mentioned effects, however, the evolution of crystalline ZrO_2 is still not completely understood. Thus some of the most important questions such as the role of water vapour pressure during calcination in the crystallization process([9-11]), the defect structure formation of crystalline mt phase([12]) and its transformability to the monoclinic structure remained unanswered. Therefore in the present work the crystallization of mt zirconia from amorphous hydrous precipitate was studied with respect to various calcination conditions. Furtheron an attempt was made to clarify the occurence and the nature of large nearly

single crystalline regions (so called domains) which were found especially in vacuum calcined powders. This, in turn may also help to elucidate the origins governing the mt → m transformation.

Experimental procedure

Amorphous hydrous zirconia was precipitated by pouring 1M zirconyl acetate solution into 2 M aqueous ammonia solution. The final pH after precipitation was 10.5. The precipitate was washed several times with distilled water and divided into two portions. One portion was subsequently washed with methanol and dried at room temperature, while the other portion was dried at 120°C in an oven overnight. The former batch is denoted as methanol washed and the later as water washed precipitate, respectively.

Precipitates were calcined under various atmospheres such as vacuum (1 mbar) and flowing H_2 and O_2. The gases were either humidified by bubbling them through water kept at 30°C or they were dried by passing through silica gel and molecular sieves kept at liquid nitrogen temperature. The calcination was performed at different temperatures for various times and with different heating regimes.

DTA and TGA experiments were performed in air and in reduced (1 mbar) air pressure atmosphere ("vacuum") using a standard Netsch aparatus, the heating rate was in both cases the same, i.e. 10°C/min.

An X-ray diffractometer with Ni-filtered Cu K_α radiation was used to

characterize the calcined powders. Phase identification was based on XRD profiles.

The microstructural features and the structure of calcined powders were studied by transmission electron microscope (TEM).

Results

The thermograms of a methanol washed and dried (120^{o}C overnight) precipitated powder in air and in vacuum are represented in fig. 1 a and b) respectively. The thermal behaviour of the powder treated in air does not differ significantly from any other thermogram of hydrous zirconia reported in the literature. The endothermic effect caused by dehydration of the amorphous powder is followed, when the dehydration is almost completed, by a strong exothermic effect - so called glow effect. According to the literature the later one arises from the "explosive" transformation of the amorphous ZrO_2 into the crystalline mt phase ([13,14]). It should be noted, however, that both TGA and especially DTA curves show slight discontinuities during dehydration on heating in various atmospheres. Similar discontinuous dehydration path was found in the literature and was ascribed to the prehistory of hydrated powders used for thermal analysis([15]). The comparison between thermograms in air and in vacuum shows, that the dehydration in vacuum starts earlier (i.e. at lower temperatures) with respect to that in air, whereas the weight loss seems to be in both cases nearly the same at the temperature of "explosive" crystallization. The later is accompanied by an abrupt release of retained water, which corresponds to appr. 0.6 - 1 % of weight loss in the case of air

calcination. In vacuum, however, during explosive crystallization a good part of the powder was blown out from the sample holder of DTA/TGA aparatus, such that the amount of released water could not be determined. This indicates that the glow effect is considerably stronger in vacuum with respect to that in air. Since the nature of the glow effect is not well understood, although it obviously plays an importante role during crystallization, its occurence and magnitude were investigated in more details. Fig. 2 shows that during continuous heating in air a sharp exothermic effect appears at 426^{o}C; if the precipitated powder is isothermally heated slightly below that temperature, the magnitude of the glow effect decreases with decreasing temperature of isothermal treatment, whereas the time needed for its appearance increases. Of course, the time dependent occurence of the glow effect is always restricted to temperatures close to 400^{o}C. Thus, for example, isothermal heating at 360^{o}C did not result in any measurable exothermic effect even after prolonged heating (up to 3 days). However, if after short (2,5 h) isothermal heating at 360^{o}C the temperature was raised a sharp glow effect of lower intensity appeared at 420^{o}C, whereas after prolonged heating at 360^{o}C no glow effect could be observed during further increase in temperature. Similarly, rapid heating of the powder up to 360^{o}C (by placing it into the furnace kept of this temperature) did not result in any glow effect during further heating.

It should be noted, that after all above described experiments the calcined powders were fully crystalline but they differed in the amount of mt and m phase respectively. The influence of

calcination conditions, i.e. temperature, time and atmosphere on the amount of transformed m phase is represented on Figs. 3 - 5, where the peak positions of mt and m phases are indicated by arrows. After calcination at 400°C only vacuum calcines were amorphous whereas calcination under dynamic atmospheres resulted in crystalline powders, the amount of m phase being increased in the order: dry H_2, wet H_2, dry O_2 and wet O_2. From these results it appeared that wet atmosphere during calcination favours the mt → m transformation. After calcination at 450°C, vacuum calcines were also crystalline but showed only mt phase profiles. Other calcination atmospheres resulted in higher m phase content with respect to the calcination at 400° C otherwise showing the same trend of ability for transformation with respect to various gases. After 20 hours calcination at 600°C in vacuum only traces of m phase could be observed while in dry hydrogen as well as in all other atmospheres (not shown on fig. 5) the mt phase has completely transformed to m structure.

Discussion

According to Whitney ([14]), hydrous zirconium dioxyde, forming by adding a base to an aqueous zirconyl salt solution, is assumed to consist of exceedingly small ZrO_2 crystallites attached by unstable covalent bonds to chemically adsorbed water molecules. No specific stoichiometric Zr hydrates are known to exist, therefore amorphous zirconia is often called as hydrous zirconia. Thus the dehydration of hydrous zirconia on heating was assumed to occur more or less continuously. However, DTA of precipitated powders often showed slight discontinuities, which were first

ascribed to the decomposition and/or burn out of organic or inorganic precursors. Rijnten([16]) was first who proposed different stages of dehydration during calcination of hydrous zirconia, depending on preparation conditions:

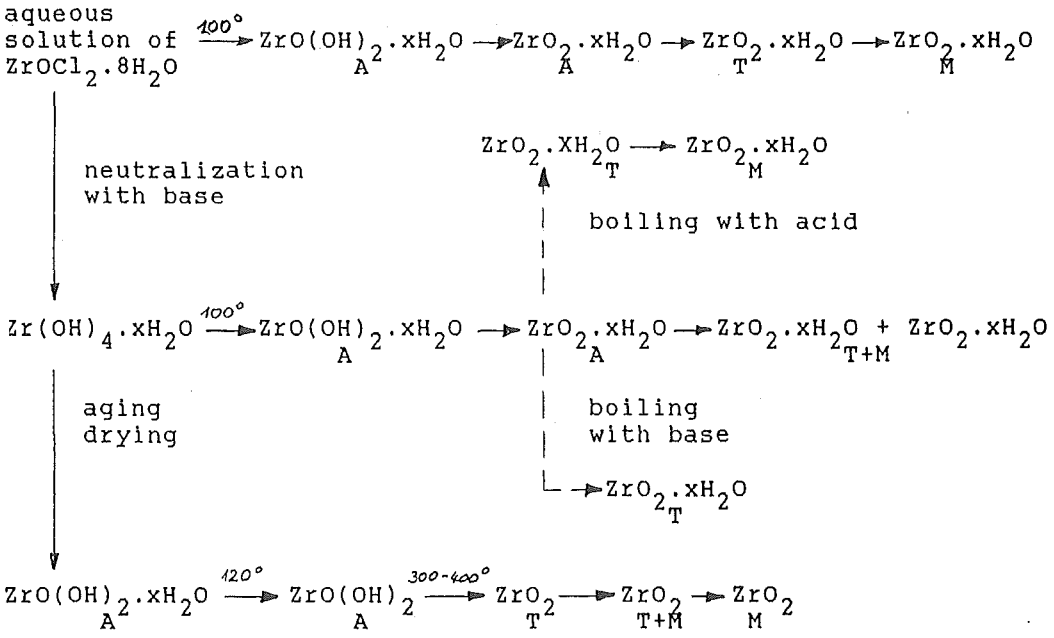

He claimed that most of the above compounds have been identified experimentally except the amorphous ZrO_2. In contrast, Whitney proposed, (based on the results of Clearfield ([17])) that the first step in dehydration follows the equation:

$$[Zr_4(OH)_8(H_2O)_{16}][OH]_8 \longrightarrow \underset{(ZrO_2.2H_2O)}{[Zr_4(OH)_8][OH]_8} + 16H_2O$$

This reaction can be induced at room temperature by passing hydrous zirconia over anhydrous H_2SO_4 or P_2O_5. Further dehydration requires heating and is accompanied by disruption of

Zr - OH - Zr bonds following the equation:

$$[Zr_4(OH)_8][OH]_8 \rightarrow [Zr_4(OH)_2O_6][OH]_2 + 6H_2O$$
$$(ZrO_2.0,5H_2O)$$

It is assumed that Zr atoms in $[Zr_4(OH)_2O_6]^{2+}$ cation are linked by 6 oxygen atoms and two OH groups. Whitney also stated that further loss of H_2O from $[Zr_4(OH)_2O_6]^{2+}$ cation is not possible without the nucleation of crystalline ZrO_2. Henceforth the strong exothermic peak, i.e. glow effect, should be associated with the transformation of $[Zr_4(OH)_2O_6][OH]_2$ into the crystalline ZrO_2 lattice. According to the same author, pronounced crystallization starts above 350°C, in aggreement with other literature data ([2]).

The discontinuities in our thermograms (up to appr. 300°C) can be explained by different dehydration stages as proposed by Rijnten ([16]). Although an additional effect of amonia salt decomposition and/or burn out should not be excluded. Nevertheless , it is worth noting that all discontinuities seem to arise at approximately the same weight loss i.e. they are shifted toward lower temperatures in the case of vacuum with respect to air. More significant difference in DTA path between both calcination atmospheres arises at temperatures above 350°C: in air a weak endothermic effect at 350°C is overlapped by a stronger exothermic one which ends up with pronounced glow effect at 435°C; in vacuum, on the other hand, the last endothermic peak is well pronounced and no exothermic reaction could be observed until explosive crystallization at 440°C starts. In this case the magnitude of the glow effect is considerably larger. According to

Whitney ([14]) the exothermic effect at 350°C in air should arise from the onset of crystallization while the subsequent glow effect would represent the spontaneous crystallization of the rest of the amorphous material. In this view the time dependence of the glow effect as well as the complete crystallinity after prolonged isothermal heating at 360°C could be easily understood. Contrary to this in vacuum the exothermic peak at 350°C is absent and no time dependent glow effect was ever detected. This indicates that in vacuum there is no crystallization at temperatures until the glow effect appears. This is in aggreement with our obervations of in situ TEM crystallization ([12]), which revealed that the crystallization started from one single nucleation center and spread over the whole aggregate, forming one single crystalline region (domain) as shown in Fig. 6 . The absence of the crystallization process below the glow effects in vacuum can be tentatively explained by too fast removal of water at lower temperatures which does not allow required ordering of zirconium and oxygen atoms to form Zr-O-Zr bonds up to the temperatures at which the glow effect appears. This is in aggreement with our calcination experiments in reducing and oxidizing atmospheres using dry and wet gasses, respectively. The magnitude of the glow effect seems to reflect not only the amount of untransformed amorphous powder but also (and especially) the degree of disorder in anhydrous amorphous structure before spontaneous crystallisation. The later one resulted in highly distorted mt lattice as well as in the formation of colour centers (black powder!), which can be considered as an evidence of substoichiometric ZrO_2. It is therefore not surprising that a

recovery of such a structure at extraordinary high temperatures (up to 1200°C) is needed before mt → m transformation can take place. Thereby increased ability for mt → m transformation with increasing water vapour pressure during calcination could be explained.

Conclusions

- During air calcination the crystallization of hydrous zirconia starts below the temperature of spontaneous crystallization (characterised by the glow effect).
- Glow effect in air is time dependent and is sensitive to the heating rate as well as to the time of isothermal treatment.
- In vacuum always an explosive crystallization takes place. Crystallization starts from one nucleation center and spreads over the whole aggregate transforming it into one crystalline, but highly distorted domain.
- The magnitude of the glow effect seems to reflect not only the amount of amorphous phase but also the degree of disorder in the anhydrous amorphous structure before spontaneous crystallization.
- The rate of water removal during calcination influences the nucleation of crystalline mt phase: if the atomic rearrangement which is required, when Zr-OH-Zr bonds are replace by Zr-O-Zr bonds, can not follow the dehydration rate, the nucleation of crystalline phase can not take place until spontaneous crystallization occurs.

- Highly distorted mt structure, formed during spontaneous crystallization in vacuum, is also substoichiometric such that extremely high temperatures are required for its recovery and mt ⟶ m transformation.

Literature

1. R. Cypres, R. Wollast and J. Raucq, "Polymorphic Conversion of Pure Zirconia", Ber. DKG, 40, 527-532 (1963)
2. J. Livage, K. Doi and C. Mazieres, "Nature and Thermal Evolution of Amorphous Hydrated Zirconium Oxide", J. Amer. Ceram. Soc.,51, 349-353 (1968)
3. V. G. Keramidas and W. B. White, "Raman Scattering Study of the Crystallization and Phase Transformations of ZrO_2", J. Amer. Ceram. Soc. 57, 22-24 (1974)
4. R. C. Garvie, "The Occurance of Metastable Tetragonal Zirconia as a Crystallite Size Effect", J. Phys. Chem., 69, 1238-1243 (1965)
5. R. C. Garvie, "Stabilization of the Tetragonal Structure in Zirconia Microcrystals", J. Phys. Chem. 82, 218-224 (1978)
6. R. C. Garvie and M. F. Goss, "Intrinsic Size Dependence of the Phase Transformation Temperature in Zirconia Microcrystals", J. Mater. Sci., 21, 1253-1257 (1986)
7. T. Mitsuhashi, M. Tenihara and U. Tatsuke, "Characterization and Stabilization of Metastable Tetragonal ZrO_2", J. Amer. Ceram. Soc. 57, 97-101 (1974)
8. M. J. Torralvo, M. A. Alario, "Crystallization Behaviour of Zirconium Oxide Gels", J. Catal., 86, 473-476 (1984)

9. Y. Murase and E. Kato, "Influence of Water Vapor on the Crystallization of ZrO_2 from $Zr(OH)_4$", Yogyo Kyokai shi, 88, 225-229 (1978)

10. Y. Murase and E. Kato, "Effects of H_2O on Crystallization of ZrO_2", Ber. DKG, 57, 86-87 (1980)

11. Y. Murase and E. Kato, "Role of Water Vapor in Crystallite Growth and Tetragonal Monoclinic Phase Transition of ZrO_2", J. Amer. Ceram. Soc. 66, 196-200 (1983)

12. T. Kosmač, V. Kraševec, R. Gopalakrishnan and M. Komac, "Crystallization of ZrO_2 from Amorphous Precipitates and its Influence on the Microstructure of Sintered Ceramics", accepted for publication in Advances in Ceramics 13

13. S. Gimblett, A. A. Rahman, K. S. W. Sing, Thermal and Related Studies of Some Zirconia Gels, J. Chem. Tech. Biotechnol. 30, 51-64 (1980)

14. E. D. Whitney, "Kinetics and Mechanism of the Transition of Metastable Tetragonal to Monoclinic Zirconia", Trans. Faraday Soc., 61, 1991-2000 (1965)

15. C. Bettinali, G. Ferraresso, "Relations Between Crystalline Phases, Crystall Size, Water Loss and Thermoluminiscence in the System ZrO_2-H_2O", J. Am. Ceram. Soc. 53, 495-497 (1970)

16. H. Th. Rijnten, "Formation, Preparation and Properties of Hydrous Zirconia", p.p. 315-372 in Physical and Chemical Aspects of Adsorbents and Catalysts, Ed. B. G. Linsen, Academic Press, NY 1970

17. A. Clearfield, "Structural Aspects of Zirconium Chemistry", Rev. Pure and Appl. Chem. 14, 91-108 (1984)

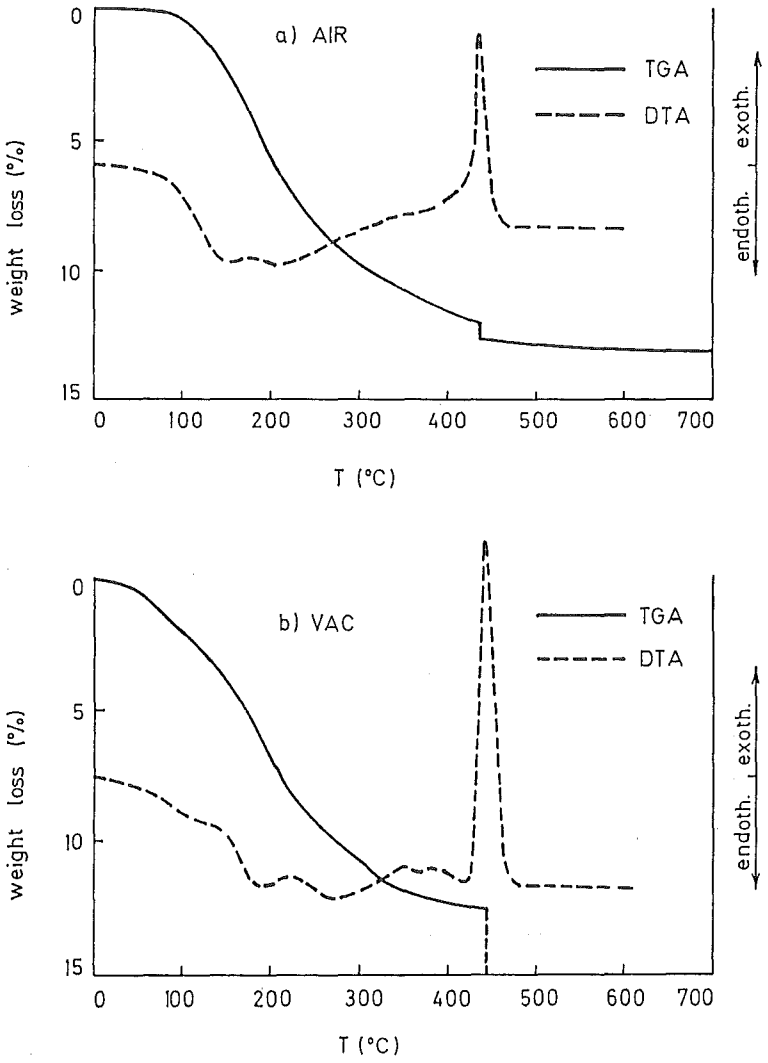

Fig. 1. Thermal characteristics of hydrous zirconia precipitate (a) in air and (b) in vacuum

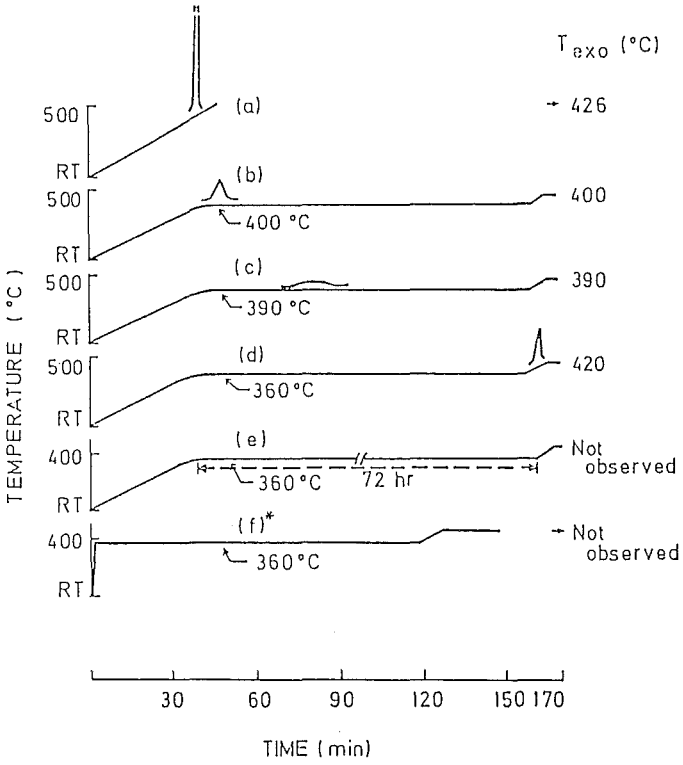

Fig. 2. Influence of heating schedule on the exothermic peak (glow effect) during crystallization

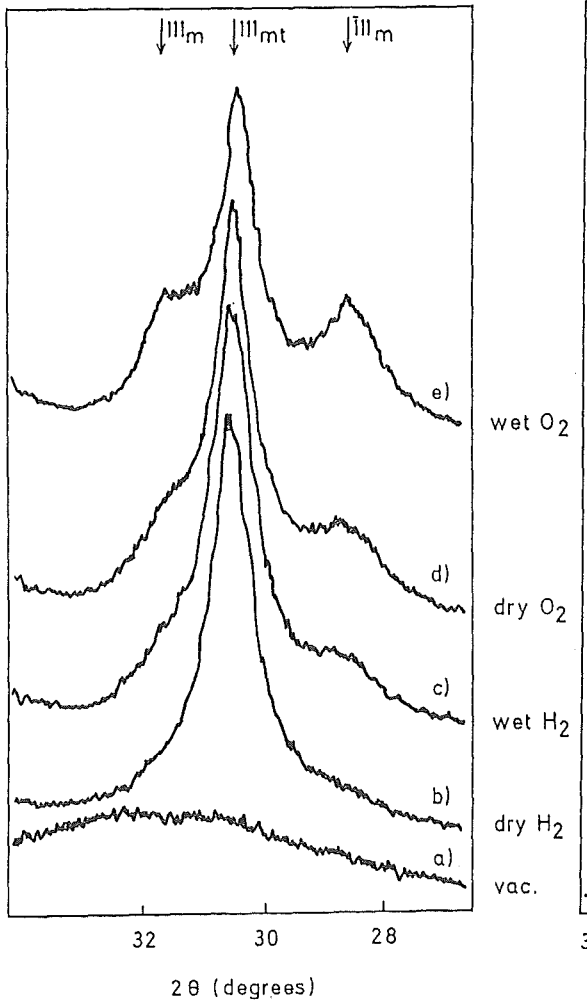

Fig. 3

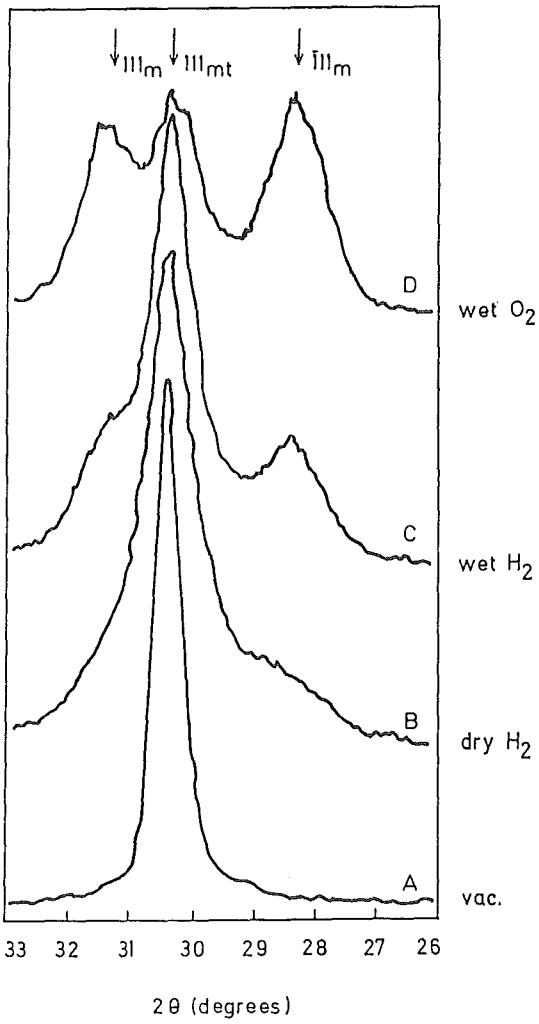

Fig. 4

Fig. 3. XRD profiles of methanol washed precipitates calcined at 400°C for 1 hour in (a) vacuum, (b) dry H_2, (c) air, (d) wet H_2, (e) dry O_2 and (f) wet O_2

Fig. 4. XRD profiles of methanol washed precipitates calcined at 450°C for 1 hour in (a) vacuum, (b) dry H_2, (c) wet H_2 and (d) wet O_2

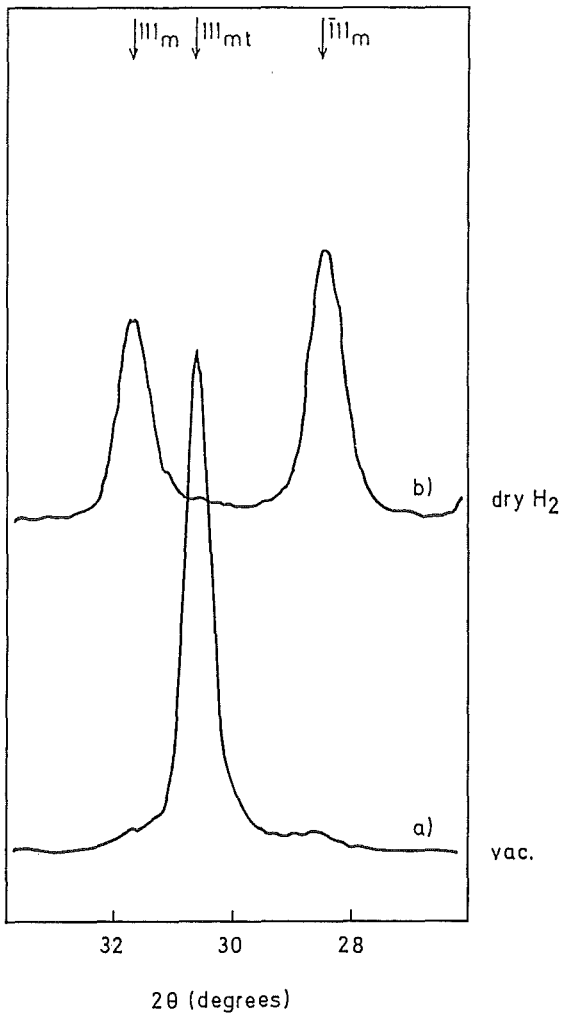

Fig. 5. XRD profiles of methanol washed precipitates calcined at 600°C in (a) dry H_2 and (b) vacuum

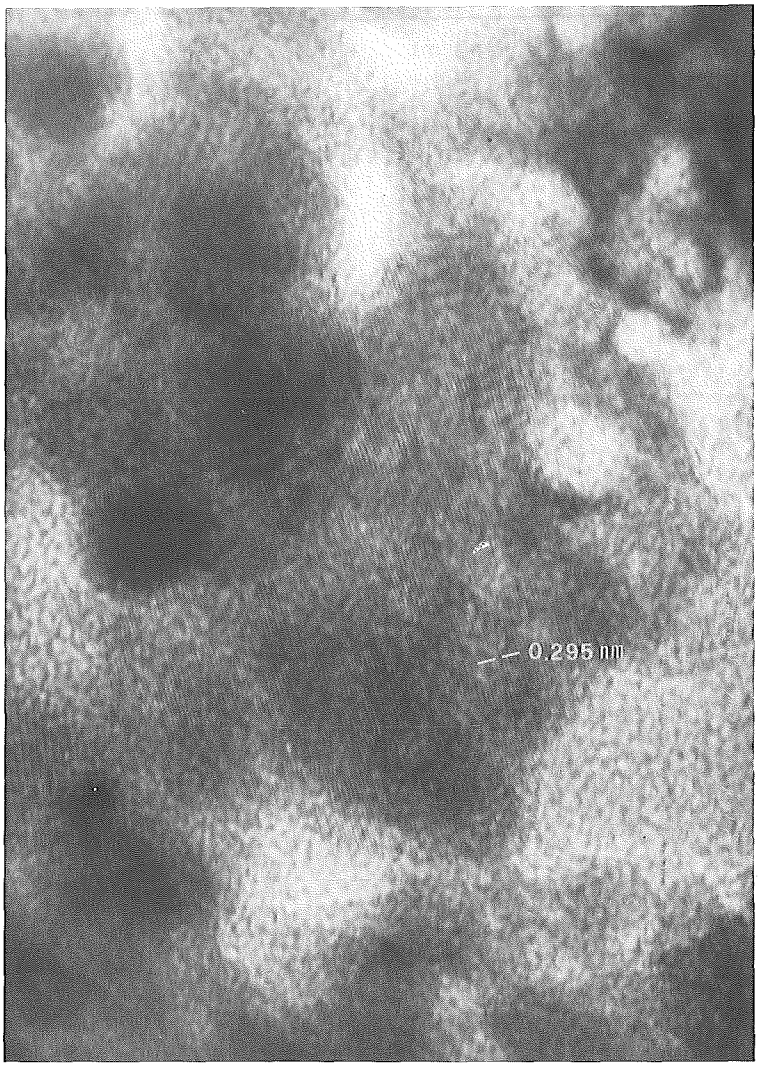

Fig. 6. 111 lattice fringes in an aggregate of methanol washed precipitate calcined at 450^{o}C for 1 hour in vacuum

Tape Casting and Sintering of AlN

Thomas Claaßen, Carmen Nischik and Peter Greil
Technische Universität Hamburg - Harburg
Arbeitsbereich Technische Keramik
P.O.Box 90 14 03
D-2100 Hamburg 90

Introduction

During the last decade investigations on aluminium nitride (AlN) ceramics have been concentrated on its application as a substrate and packaging material for high performance electronic devices. AlN is distinguished by a high thermal conductivity combined with a low electrical conductivity and a coefficient of thermal expansion, which is compatible to that of silicon ($\alpha_{RT-200^oC} \sim 2.7\ 10^{-6}/K$), table 1.

electrical conductivity	:	$10^{-11} - 10^{-13}$ $(\Omega\,cm)$
thermal conductivity	:	100 - 200 W/mK
coefficient of thermal expansion	:	$3.3 - 3.9$ $10^{-6}/K$ $(RT - 200^oC)$
theoretical density	;	$3.26\ g/cm^3$
bending strength	:	≤ 370 MPa
toughness	:	≤ 3.4 $MPa\sqrt{m}$
thermal stability	:	$\leq 1000^oC$ (O_2)
		$\leq 2000^oC$ (N_2)

Table 1 *Some properties of AlN collected from data sheets of the AlN producers ANCeram, Tokuyama, Toyo Aluminium and /1/,/2/ and /3/.*

Due to the excellent thermal stability up to 1000 ^oC in oxidizing and 2000 ^oC in inert atmosphere /1/ as well as good mechanical properties /2/,/4/ AlN was considered as a potential engineering material to be used under severe high temperature and thermal gradient conditions. AlN powders may only be sintered to full density in the presence of sintering aids, which form a liquid phase upon heating /5/. The formation of solid solutions or precipitation of secondary phases, however, has to be depressed

in order to retain a high thermal conductivity in the sintered compact /6/. Thus the amount and distribution of oxygen in the starting AlN powder mixtures has to be controlled by improved powder processing techniques in a water and oxygen free environment. Oxygen contamination originating from surface hydrolysis and oxidation reactions of AlN powder particles

$$AlN + 3\ H_2O \longrightarrow Al(OH)_3 + NH_3 \qquad [1]$$

$$4\ AlN + 3\ O_2 \longrightarrow 2\ Al_2O_3 + 2\ N_2 \qquad [2]$$

may be reduced by the addition of carbon, which forms AlN in a nitrogen atmosphere

$$Al_2O_3 + 3\ C + N_2 \longrightarrow 2\ AlN + 3\ CO \qquad [3]$$

Using the pyrolytic carbon, which is in situ formed during the dewaxing process of the organic additives, the oxygen content of the final product may be minimized by improved processing control. The aim of the present work is to examine the influence of the powder processing conditions and the slurry composition on the oxygen content of tape cast AlN. The chemical composition of the non-aqueous AlN slurry will be optimized with respect to slurry rheology and residual oxygen content in the sintered products.

Experimental Procedures

A high purity AlN was used with 3 vol.% of Y_2O_3 as sintering aid. Table 2 shows the characteristics of the starting powders.

Material	AlN	Y_2O_3
Producer	H.C. Starck	H.C. Starck
Quality	Grade C	feinst
Grain size [µm]	1.0	0.3
Sp. surface area [m^2/g]	5.0	14.05
Oxygen content [wt. %]	2.1 (1.7*)	---
Carbon content [wt. %]	0.06	0.13

Table 2 *Powder characteristics after : "Werkszeugnisse" Herrmann C. Starck, Berlin GmbH & Co. KG.*

**value from own oxygen determination*

The powders were mixed in a planetary ball mill for 24 hours with an azeotropic mixture of methylethylketon (MEK, 66 vol.%) and ethanol (34 vol.%) as the suspension

medium. A solid-liquid ratio of 63.1 to 29,2 wt.% was chosen with 7.7 wt.% of organic dispersants, binders and plastizisers. Table 3 shows a typical composition of the AlN slurry for tape casting.

AlN		97 vol.%	63.1 wt.%
Y_2O_3		3 vol.%	
Solvant	MEK[1] + Ethanol[1]		29.2 wt.%
Dispersant	Alkylphosphat[2]		
Binder 1	Polyvinylbutyral[3]		
Binder 2	Polyvinylbutyral[3]		7.7 wt.%
Plasticizer 1	Dibutylphtalat[1]		
Plasticizer 2	Polyethylenglycol[1]		

***Table 3** Composition of an AlN-tape casting slurry.*

The rheological behaviour of the slurries was characterized with a rotary viscosimeter (RV20, HAAKE, D-7500 Karlsruhe 41, FRG). Shear stresses were continoustly measured between shear rates of 0 and 100 s^{-1} , from which the viscosities at shear rates of 2 and 60 s^{-1} were calculated. Relative viscosities were determined by calculating the ratio of slurry to fluid viscosities. A discontinously working tape casting bench was used to produce AlN tapes with a mean thickness of 150 - 200 µm, a width of 100 mm and a length of 1200 mm. The laboratory scale bench was equipped with a double blade casting head, shown in fig. 1.

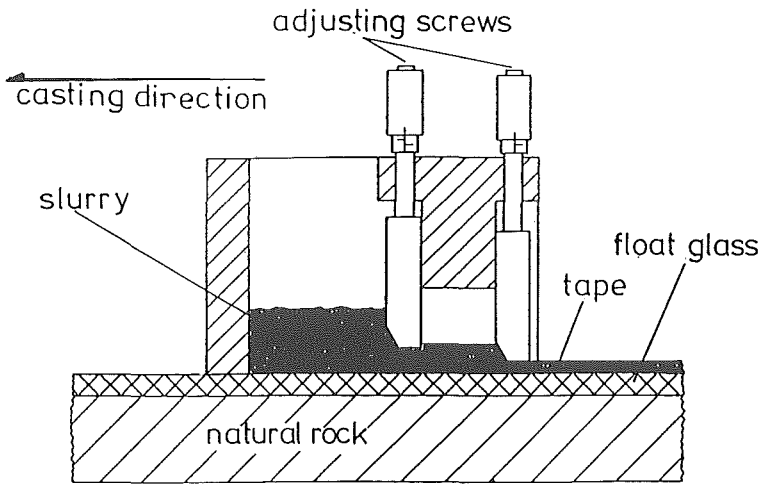

***Figure 1** Laboratory tape castng bench.*

1: E. Merck, Darmstadt, FRG 2: Hoechst AG, Frankfurt a. M., FRG
3: Monsanto, St. Louis, USA

The surface of float glass sheets was used as casting substrate. After evaporation of the solvant from the cast, a green tape consisting of 88 - 89 wt.% ceramic powder and 11 - 12 wt.% organic compounds was obtained. The tapes were cut to either a quadratic shape (45x45 mm) or a round shape (40 mm diam.) and stacked to laminates of 30 - 40 sheets. The laminates were thermopressed at 110°C and 50 MPa for 30 minutes. The dewaxing process was carried out in an tube furnace under vacuum or flowing nitrogen atmosphere. The applied dewaxing cycles are listed in table 4.

10 K/min	---›	350 °C	N_2
20 h	----	350 °C	
10 K/min	---›	450 °C	N_2
20 h	----	450 °C	
10 K/min	---›	300 °C	vacuum
25 h	----	300 °C	

Table 4 Dewaxing cycles.

All samples were sintered in a graphite heated resistance furnace in boron nitride coated graphite crucibles in nitrogen atmosphere (0.2 MPa). The samples were heated up to the peak temperature of 1800 °C with a linear heating rate of 20 K/min. After 30 min of isothermal sintering the specimens were cooled down with 10 K/min. The oxygen content was measured after slurry preparation, tape casting, lamination dewaxing and sintering. A gas analyzer with nitrogen-oxygen determinator (TC-436, LECO Instrumente GmbH, Kirchheim, FRG) was used. The powdered samples were filled in a nickel capsule, copper was added and then heated up to 2600 °C in a LECO EF-400 furnace with graphite crucible. A calibration measurement with pure AlN and pure SiO_2 was carried out before. The measurement technique provides an accuracy of ± 0.1 wt.%.

Results and discussion

Fig. 2 shows the influence of the slurry composition on the viscosity at a constant shear rate of 60 s^{-1}. The addition of binder 1 results in the most pronounced reduction of the viscosity as compared to the other slurry components. Thus the slurry viscosity can easily be controlled by variation of binder 1 concentration within a small range.

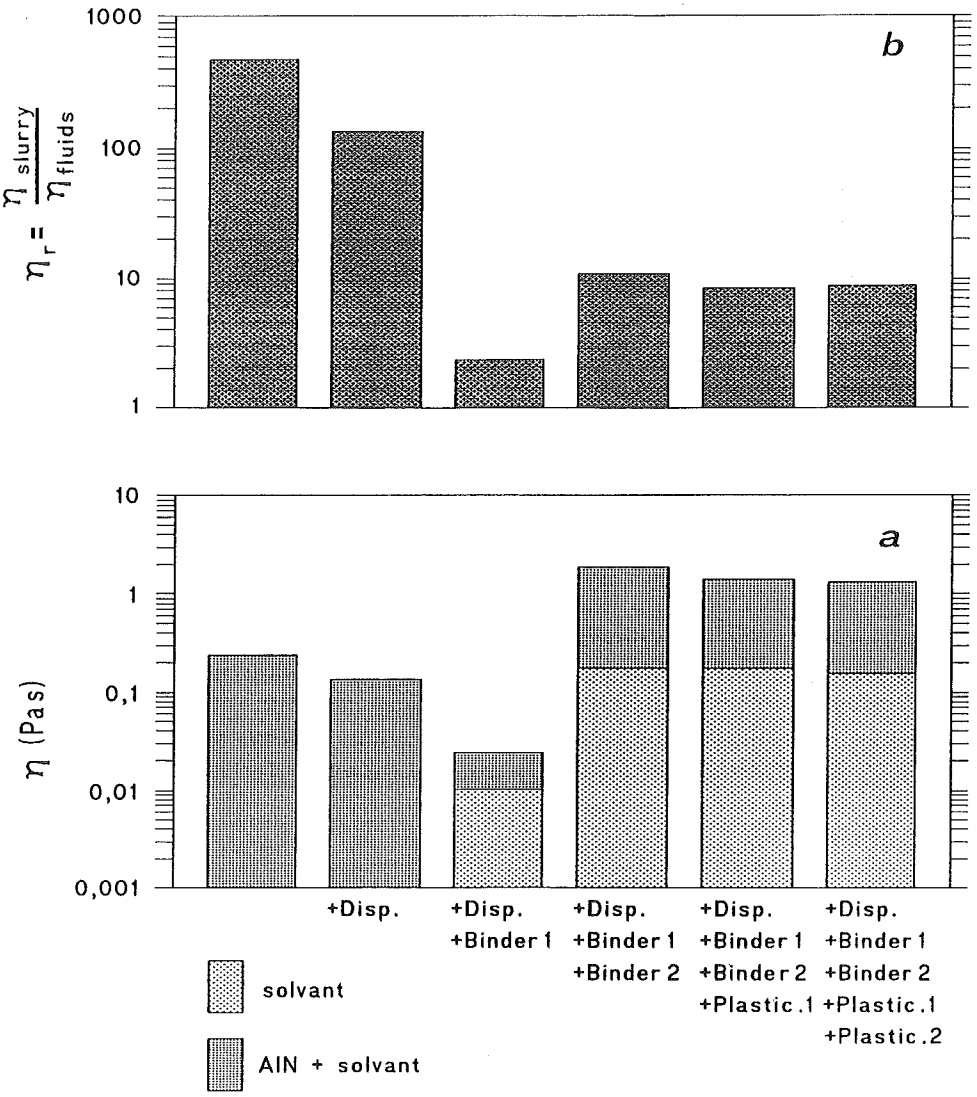

Figure 2 *Influence of the organic components on the slurry viscosity η (a) and relative viscosity η_r (b).*

Fig. 3 shows the effect of the volume content of the alkylphosphate dispersant /7/,/8/ on the slurry viscosity at two different shear rates. While the high rate viscositiy at 60 s^{-1} remains nearly uneffected, the low rate viscosity at 2 s^{-1} slowly increases with dispersant concentrations higher than 0.1 wt.%. A remarkable increase is observed at concentrations above 0.4 wt.%. Thus the fabrication of thick tapes may be possible, because the higher low shear rate viscosity stabilizes the tape on the substrate after high shear rate casting.

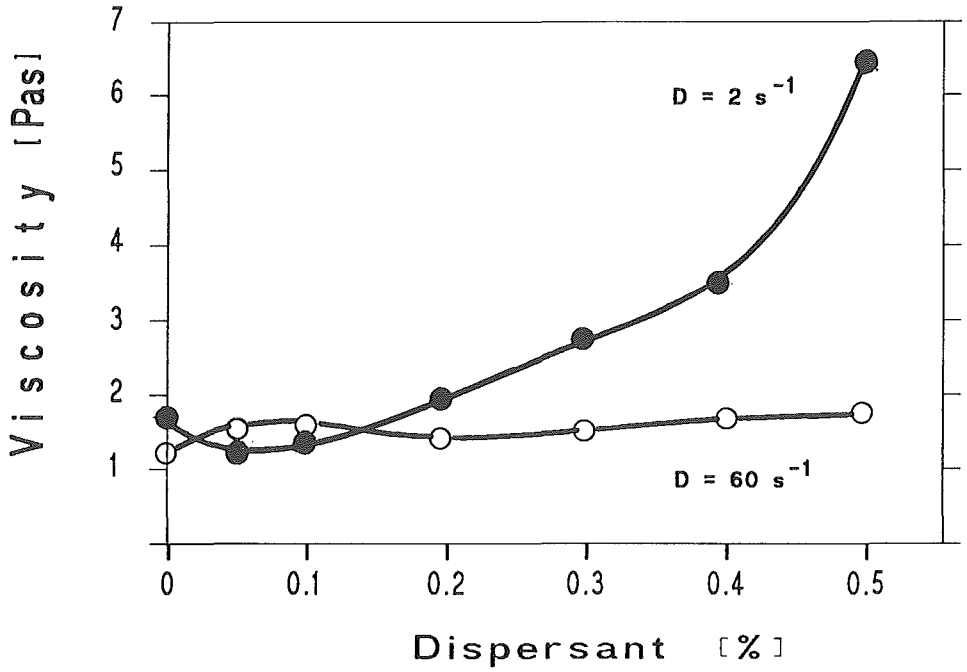

***Figure 3** Influence of the Dispersant on the low shear viscosity and on the viscosity at the casting shear rate of the AlN tape casting slurry with constant amount of binder (7.5 wt.%) and plasticizer (6.0 wt.%).*

The variation of the oxygen content during each separate step of the powder processing was examined. Fig. 4 summarizes the results of the oxygen measurements. The processing related oxygen contamination was calculated from the total oxygen content, C_{tot}, the oxygen contents of the starting powders AlN and yttria, C_{AlN} and C_Y , and the oxygen content of the 5 organic compounds, $C_{org,i}$, i = 1..5, as

$$\Delta C = C_{tot} - x_{AlN} C_{AlN} - x_Y C_Y - \sum_{i=1}^{5} x_i C_{org,i}$$

where x denotes the weight fraction of the slurry components. The oxygen content of the starting AlN powder was measured as 1.7 wt.%. Due to the exposition to ambient atmosphere the oxygen content increases with ΔC = 0.9 wt.% to an amount of 2.6 wt.% after slurry preparation, whereas only minor oxygen pickup takes place during drying of the green tapes and pressing of the laminates. A maximum oxygen content of approximately 3 wt% was achieved, i.e. an oxygen increase of 80% as compared to the starting powder. Depending on the specific dewaxing process a slightly reduced oxygen content was found after dewaxing, which may pimarily be attributed to the

oxygen content in the organic components. After sintering a considerable decrease of the oxygen content to values below that of the starting powder occured. The lowest value of 1.3 wt.% was obtained from samples, which were dewaxed at the highest temperature of 450 °C. The reduction of the oxygen content during sintering may be explained by the carbothermal reduction and nitridation of the oxide according to equation [3]. Due to the extremely uniform distribution of the C from the decomposition of the organic compounds the pyrolytic C is highly effective in reducing the surface oxygen, which may further be promoted by a high nitrogen pressure.

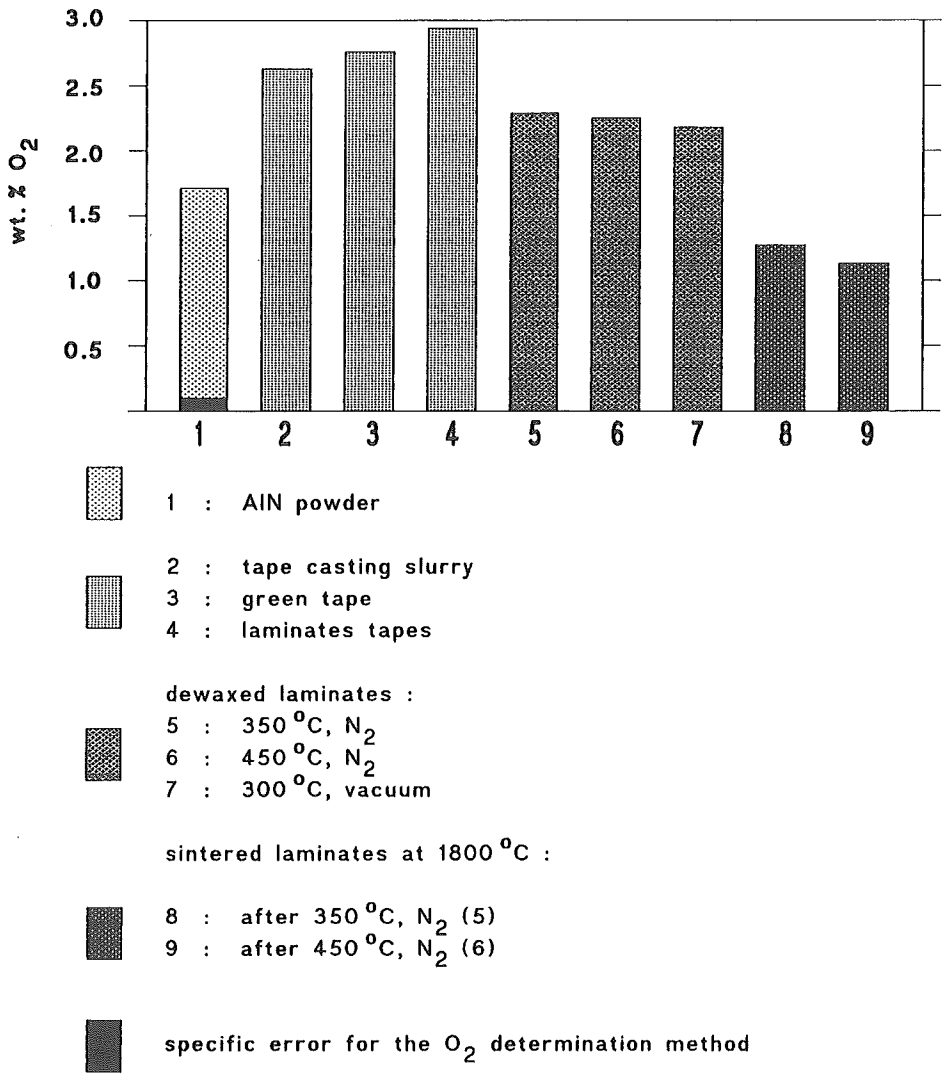

Figure 4 *Variation of the oxygen content during the processing of AlN laminates*

Conclusions

Low oxygen containing AlN laminate ceramics can be prepared by controlling the oxygen content via optimized processing conditions. Using the in situ formed carbon from the decomposition of the organic slurry components, surface oxygen on the AlN powder particles may be removed and an oxygen content in the sintered product lower than that of the starting powder can be achieved. Thus, AlN powders with a higher surface oxygen content may also be used to form low oxygen containing AlN ceramics, which may be used as substrate as well as structural components.

5. Acknowledgement

The authors whish to thank G. Kaiser, Max-Planck-Institut für Metallforschung / Pulvermetallurgisches Laboratorium, Stuttgart, for the oxygen analyses and helpful discussions.

6. References

/1/ Abid, A.; Bensalem, B.; Sealy, B.J. : The thermal stability of AlN.- Journ. Mat. Sci. 21, pp. 1301 - 1304, 1986.

/2/ Billy, M.; Mexmain, J. : Processing and Properties of Aluminium Nitride, a New Candidate for High Temperature Applications.- Sprechsaal 118 (3), pp. 245 - 249, 1985.

/3/ Brunner, D.G. : Foliengießen, Sintern und Anwendung von Aluminiumnitrid.- Sprechsaal 121 (3), pp. 181 - 186, 1988.

/4/ Sakai, T.; Iwata, M. : Effect of Oxygen on Sintering of AlN.- Journ. Mat. Sci. 12, pp. 1659 - 1665, 1977.

/5/ Schwetz, K.A.; Knoch, H.; Lipp, A. : Sintering of Aluminium Nitride with low Oxide Addition.- in Riley. F.L. (ed,) : Progress in Nitrogen Ceramics.- pp. 245 - 252, Martinus Nijhoff Publishers, Boston 1983.

/6/ Kranzmann, A.: Wärmeleitfähigkeit von drucklos gesinterten AlN-Substratkeramiken.- PhD thesis, Universität Stuttgart, 1988.

/7/ Mikeska, K.; Cannon, W.R. : Dispersants for Tape Casing Pure Barium Titanate.- Adv. Ceram. 9, pp. 164 - 183, 1985.

/8/ Chartier, T.; Streicher, E.; Boch, P.: Phosphate Esters as Dispersants for Tape Casting of Alumina.- Cer. Bull. 66 (11), pp. 1653 - 1655. 1987.

/9/ Fister, D.: AlN and BN Powders for Advanced Applications.- Cer. Eng. Sci. Proc. 6, pp. 1305 - 1312, 1985.

/10/ McCauley, J.W.; Corbin, N.D. : High Temperatur Reactions and Microstructures in the Al_2O_3-AlN System.- in Riley, F.L. (ed.) : Progress in Nitrogen Ceramics.- pp. 111 - 118, Martinus Nijhoff Publishers. Boston 1983.

/11/ Mistler, R.E.; Shanefield, D.J.; Runk, R.B. : Tape Casting of Ceramics.- in Onoda, G.Y.; Hench, L.L. (ed.) : Ceramic Processing before Firing.- pp. 411 - 448, John Wiley & Sons, New York 1978.

/12/ Morris, J.R.; Cannon, W.R. : Rheology and Component Interactions in Tape Casting Slurries.- Mat. Res. Soc. Symp. Proc. 60, pp. 135 - 142, 1986.

/13/ Shanefield, D.J.; Mistler, R.E. : Fine Grained Alumina Substrates: I, the Manufacturing Process.- Cer. Bull. 53 (5), pp. 416 - 420, 1974.

/14/ Trontelj, M.; Kolar, D. : Pressureless Sintering of Aluminium Nitride to High Density.- Journ. Mat. Sci. Lett. 8, pp. 136 - 137, 1973.

INFLUENCE OF PROCESSING ON THE PROPERTIES OF β-SiC POWDERS

V.Kevorkijan, M.Komac, D.Kolar, A.Šmalc, J.Rottmann*
"J. Stefan" Institute, Ljubljana, and *IRW, KFA Jülich

1. INTRODUCTION

The pressureless sintering of SiC to high final densities requires extremely fine and chemically pure starting powders, which - in general - can not be prepared directly by chemical synthesis. Prior to batch preparation and shaping adequate processing of powders is therefore necessary, which commonly involves comminution, classification and chemical purification. In general, the average grain size must be about 0.5 μm, while particles coarser than 3 - 5 μm are harmful. Oxygen content up to 1 wt. % and 0.5 % nitrogen and metallic impurities can be tolerated.

Comminution is a very important step in the case of the processing of the α-SiC powder which normally starts from rather coarse grained Acheson silicon carbide. In contrast, low reaction temperature of the carbothermic synthesis of β-SiC enables, in principle, the preparation of fine powders containing high fraction of sub-micrometre particles [1]. Milling becomes thus less important or can even be avoided. Instead, classification methods can be effectively employed in order to obtain the desired cut sizes.

In the present paper the results of the processing of commercial and β-SiC powders prepared in laboratory are described. In order to reveal the efficiency of processing procedures, as well as the importance of different powder characteristics, sintering experiments were also performed.

2. EXPERIMENTAL WORK

β-SiC powders which were used in the present investigation were either prepared by the authors via carbothermic reduction of SiO_2 (in further text denoted as IJS) or supplied by H.C. Starck (B- 10), Ibiden (UF-0090), Mitsui Toatsu (MSC 20) and Superior Graphite (HSC 100 GL).

The chemical purification of IJS powders involved the removal of excess carbon by heating the powders in air at 750°C for 24 hours, while two procedures were

used in order to remove SiO_2: washing of powders with hydrofluoric acid at 60 - 90°C or exposing the powders to the flow of dry gaseous HF at 600°C. The concentration of residual free carbon and oxygen was determined according to the methods described in [2,3]. Metallic impurities which were introduced into powders during milling were removed by washing with HCl.

Milling of powders was performed in steel or agate planetary mills, using ethanol as a milling liquid. Milling variables were fixed as follows:

$mass_{sample}$: $mass_{balls}$ = 1:3
$mass_{sample}$ (g): $V_{ethanol}$ (ml) = 1:1

Slurries for sedimentation studies were prepared by dispersing β-SiC powders in water at pH 11 adding Lomar-D (Diamond- Shamrock) as a wetting agent.

Powders for sintering studies were doped with constant additions of 0.6 wt. % B and 4 wt. % C. Boron was added in the elemental form while phenolformaldehide resin was used as a carbon precursor. Samples were mixed in planetary ball mill using polyethylene jar and balls, isostatically pressed and heated in flowing argon for 4 hours at 450°C to permit carbonization and vaporization of organics. Sintering was performed at 2000 - 2200°C for 15 to 60 minutes in static argon atmosphere.

3. RESULTS AND DISCUSSION

3.1 Chemical treatment of powders synthesized by carbothermic reduction

An appreciable amount of unreacted carbon and silica (up to 35 % C and 30 % equivalent oxygen) was present in the reaction product after carbothermic reduction, especially if the synthesis was performed at low temperatures, e.g. 1150 - 1200°C. After heating in air for 24 hours at 750°C the residual free carbon content was 0.08 $\pm$ 0.01 wt. % irrespective of the starting free carbon concentration.

The oxygen concentration and specific surface area of the SiC powders after treatment with gaseous HF as a function of the temperature of carbothermic reduction are shown in Fig. 1. Obviously, a correlation exists between the oxygen content and the specific surface area of β-SiC powder. The purification method turned out to be very efficient especially in comparison with other methods [4]. This is demonstrated by the low oxygen content ($\ll$ 0.1 wt. %) of the coarser SiC powders synthesized at temperatures above 1250°C. Higher oxygen content of finer powders, prepared at lower reaction temperatures is explained by the reoxidation of these powders, which could take place rather easily due to their fineness. As reported recently, physisorption of water, followed by chemisorption and formally

by the formation of SiO_2 was observed on the surface of submicrometre SiC powders during the storage at room temperature [5]. The repeated HF treatment of SiC powders just prior to sintering could thus enhance densification (see section 3.3.).

The temperature of the reaction with gaseous HF must not exceed 700°C because the decomposition of SiC by HF becomes favourable in that temperature range.

3.2 Milling and sedimentation

The effect of milling on the particle size distribution was studied on Starck B-10 powder. As expected, particle size reduction as a function of milling time is rather pronounced in the first hours of milling and then levels off (Fig. 2.). As evident from distribution curves, the fraction of particles above 5 μm remains unchanged, suggesting that weak aggregates were crushed preferentially, while hard coarse particles remained. This was additionally confirmed by SEM inspection of milled powder. The fraction of submicrometre particles was increased by approximately 10 %. During milling, heavy contamination with metallic debris occurs due to the wear of mill jar and balls. Leaching with diluted HCl shifts the metallic impurity content to the acceptable level (Table I). However, fine fractions of powders were partially lost during decanting and water washing steps, thus decreasing the yield of milling.

Table I: Concentration of metallic impurities in β-SiC powder after milling and HCl leaching.

Fe	Ni	Cr	Mn(ppm)	Milling time (h)
	Before leaching			
12.700	27	530	57	1
47.300	80	2280	215	6
87.300	136	4300	430	12
149.000	220	7500	710	24
	After leaching			
1.960	29	820	67	

In order to avoid the problems arising from contamination with metals agate jar and balls were used. While the efficiency of milling is comparable to steel mill, excessive wear of agate balls makes this procedure uneconomic.

The suitability of employing the planetary milling in the production of fine SiC powders with high yield in the submicrometre range appears thus disputable, in particular with regard to coarse hard particles (> 3 μm) resisting the comminution which strongly affect densification. Other milling techniques - turbomilling, attrition milling - were reported as being rather successful [6,7]. Nevertheless, the problems arising from residual coarse particles and contamination with elements other than oxygen still exist.

Sedimentation in the liquid medium represents a generally recognized method of classification of solid particles. In our studies, a 10 % water slurry of β-SiC was used. As evident from Fig. 3., the effect of sedimentation can be increased by adjusting the pH of the slurry to 11 where the minimum in zeta-potential was established. Further enhancement of sedimentation can be obtained by improving the wettability of hydrophobic SiC particles by the addition of surfactant [8]. Lomar - D (naphtalene sulphonic acid condensate) was used in the present investigation.

An attempt was made to evaluate quantitatively the sedimentation process for the case of cut off size 1 μm, the time of sedimentation being 120 hours. It was calculated that the efficiency of separating the particles with d < 1 μm was about 60 %. This figure confirms that the classification by sedimentation in liquid media is not very effective in the submicrometre range. Coarse particles with d > 1 μm were also present in the classified powder fraction, indicating that the applied sedimentation technique needed optimization. By changing the way of introducing the SiC slurry into the column, the fraction of coarse particles was reduced.

The influence of residual Lomar D which remains occluded on the surface of particles, on the sinterability was also examined. A significant drop in the final density, of the order of 5 - 7 %, was noted if the washing of sedimented powders was insufficient. Thus the washing of powders by flocculation - ultracentrifuging - redispersion sequence was necessary in order to obtain the adequate purity of the powder.

3.3 Sintering studies

Sintering experiments were performed in order to assess the relative importance of particle size and size distribution, and chemical purity, particularly oxygen concentration, in densification of β-SiC. Four different commercial β-SiC powders were used. They can be roughly divided into two groups with regard to particle size distribution (Fig. 4.). Broad distribution with approximately 40 % of particles having diameter in the range 1-10 μm is characteristic for B-10 and HSC 100 GL powder. In contrast, MSC 20 and UF-0090 powders exhibit a rather narrow size distribution, predominantly in the sub-micrometre range. Figs. 5 and 6 show the effect of temperature on the sintered density. As expected, higher densities were

obtained in the case of finer powders. More or less expressed density maxima are also evident. By increasing the sintering temperature, the abnormal grain growth is also promoted which in turn inhibitis the densification. This is especially pronounced in case of powders with broad particle size distribution.

The influence of oxygen contamination on the densification, especially in view of a possible oxygen pick-up during the storage of powders was also evaluated. Thus, β-SiC powders were purified with HF, immediately mixed with additives and sintered. The results are also shown in Figs. 5 and 6. Compared to powders which were stored for 100 hours or more before sintering, density is increased, while density maximum moves towards a lower temperature in case of the coarser B-10 and HSC 100 GL powders. These rather pronounced effects are somewhat surprising, especially with regard to the role which free carbon plays in the sintering of SiC. It seems that at very low oxygen concentrations, what we believe was achieved with a repeated HF treatment, other factors that are also known to control the densification of β-SiC, become less critical resulting in improved sinterability (provided of course that the general requirements for sinterable SiC powders are fulfilled).

In contrast to expectations, UF-0090 powder does not exhibit the best densification behaviour. It is possible that a rather rapid oxygen pick-up occurs after cleaning with HF due to high fineness of the powder, which in turn is reflected in reduced sinterability. This assumption, however, still needs verification.

4. CONCLUSIONS

As exemplified by sintering experiments β-SiC powders can be sintered to high final densities, provided that very strict requirements regarding powder morphology and chemistry are fulfilled. Hence, in order to convert crude SiC powders into sinterable quality, an extensive processing subsequent to chemical synthesis is necessary. In order to test the efficiency of processing methods discussed in the present paper, the IJS β-SiC powder was processed by sedimentation and chemical purification. Samples densify to 98.5 % T.G. during pressureless sintering at 2060°C in argon.

References

[1] V. Kevorkijan, M. Komac, D. Kolar, The Influence of Preparation Conditions on the Properties of beta-SiC Powders Synthesized by Carbothermic Reduction, Proc. Int. Conf. "Ceramic Powder Processing Science", Berchtesgaden, 1988 (in press).

[2] K. A. Schwetz, J. Hassler, A Wet Chemical Method for the Determination of Free Carbon in Boron Carbide, Silicon Carbide and Mixtures Thereof, J. Less-Common Metals, 117, 7-15 (1986).

[3] J. Rottmann, F. Schleifer, Gase in Metallen, Ed. H. M. Ortner, DGM, 1982, pp. 343-355.

[4] J. Brynestad, C. E. Bamberger, D. E. Heatherly, J. F. Land, Comm. Amer. Ceram. Soc., 67, C184-C185 (1984).

[5] P. Matje, K. A. Schwetz, Surface Oxygen Pick-up in Submicron SiC and B_4C Sintering Powders at Room Temperature, Proc. Int. Conf. "Ceramic Powder Processing Science", Berchtesgaden, 1988 (in press).

[6] J. L. Hoyer, Ultrafine Ceramic Powders Produced by Turbomilling, Amer. Ceram. Soc. Bull., 67, 1663-1668 (1988).

[7] P. Matje, K. A. Schwetz, Alpha Silicon Carbide Sintering Powder by Milling Process and Wet-Chemical Purification, in Ceramic Powder Science, Ed. G. L. Messing, ACS, 1988, pp. 460- 468.

[8] E. Carlstrom, M. Persson, E. Bostedt, Slip Casting and Sintering of SiC, Paper presented at 87^{th} Ann. Meet. ACS, Pittsburgh, 1987.

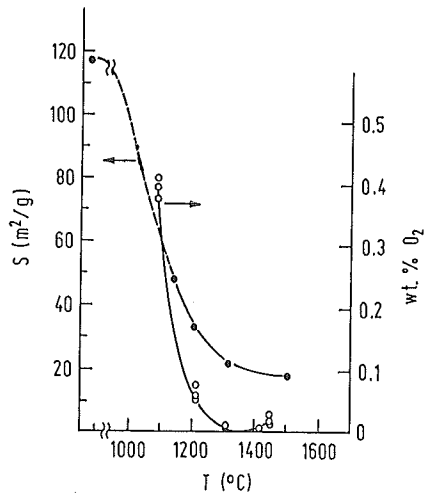

Fig.1: Specific surface area and oxygen content of β-SiC powders vs. temperature of carbothermic reduction.

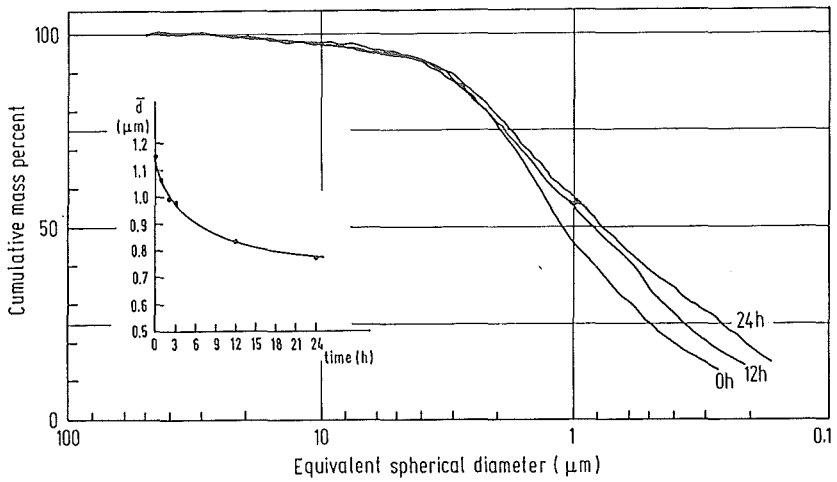

Fig.2: The influence of milling time on the particle size distribution and the mean partcile size of the B-10 SiC powder.

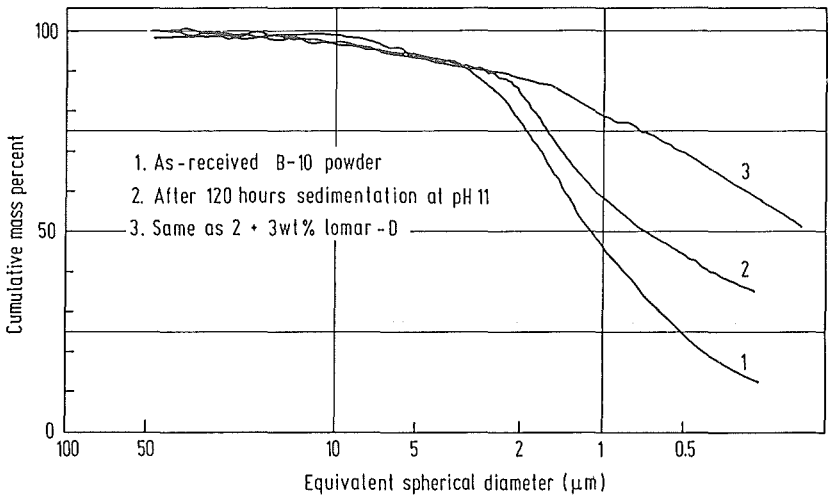

Fig.3 The influence of sedimentation conditions on the particle size distribution of B-10 SiC powder; fraction taken from the upper part of the column.

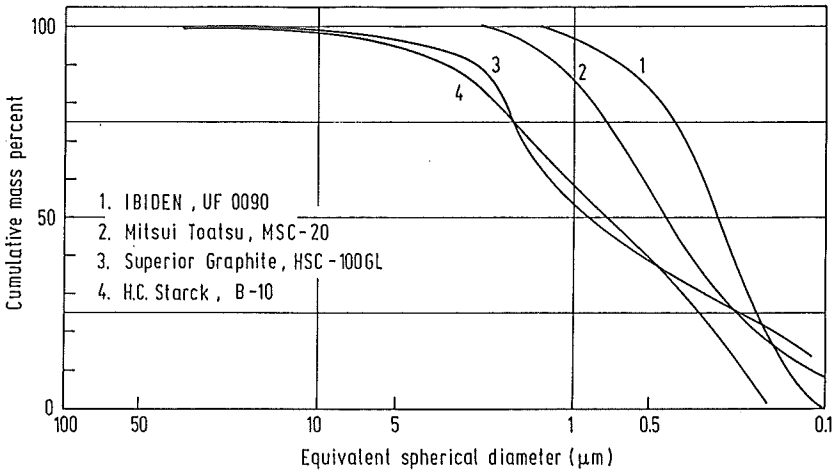

Fig.4: Particle size distribution of as - received β-SiC powders.

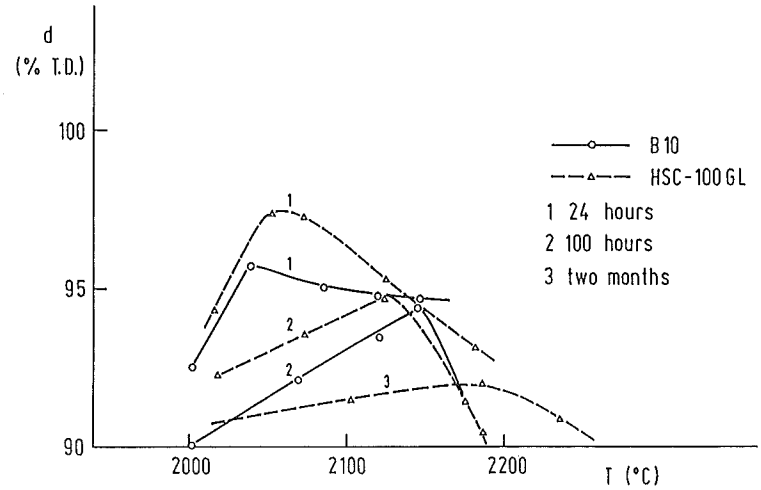

Fig.5: Effect of temperature and time of storage after HF treatment on the sintered density of B-10 and HSC 100 GL β-SiC.

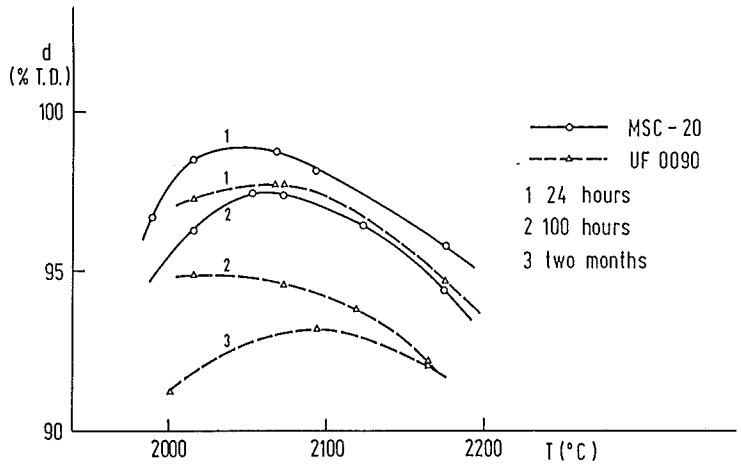

Fig.6: Effect of temperature and time of storage after HF treatment on the sintered density of MSC 20 and UF - 0090 β-SiC.

Corrosion of SiSiC by Gases and Basic Slag at High Temperature

R. Förthmann[1], E. Grübmeier[1], V.M. Kevorkijan[2], A. Naoumidis[1]
[1]Kernforschungsanlage Jülich, FRG
[2]Institut "Jozef Stefan", Ljubljana, YU

The corrosion behaviour of silicon-infiltrated silicon carbide (SiSiC) and the corrosion-induced changes of mechanical properties were investigated at temperatures between 1200 and 1400 °C without an with contact to a basic coal slag.

1. SAMPLE PREPARATION

The SiSiC specimens were cut from tubes obtained from SIGRI, Meitingen, FRG. The specimens were grinded to dimensions of 60 x 3,5 x 4,5 mm and polished reaching a surface roughness below 0,15 µm. One set of 15 samples was used for measuring the average bending strength before corrosion.

2. EXPERIMENTAL

Isothermal gas corrosion tests were made by using tube furnaces capable of temperatures up to 1400 °C[1)]. The furnace was supplied with different gases (air, nitrogen, argon, hydrogen, sulfur dioxide, hydrogen sulfide) or mixtures of these gases which can be saturated additionally by water vapour at any temperature up to 100 °C. The slag corrosion tests were done at Ljubljana by covering the samples with slag powder and heating in air at 1250 °C[2)]. The slag composition is given in table 1.

Oxide	Amount/at.%
SiO_2	35.4
CaO	25.9
Al_2O_3	19.9
MgO	11.5
Fe_2O_3	3.9
K_2O	1.4
Na_2O	1.1
TiO_2	0.8
MnO	0.1

Table 1: Composition of the basic coal slag

After corrosion the silicon carbide samples were investigated by using the following methods:

- Four-point bending strength measurement,
- X-ray diffraction analysis,
- Scanning electron microscopy,
- Electron microprobe analysis.

3. RESULTS

3.1 Corrosion of SiSiC in water /hydrogen mixtures and air at 1370 °C and 1240 °C

Isothermal corrosion tests in water vapour/hydrogen at 1370 ± 10 °C resulted in the formation of dense silicon oxide layers on the surface of the SiSiC samples which were indentified by X-ray diffraction to be α-cristobalite. The parabolic growth kinetics of these layers indicates that oxygen diffusion in the dense oxide layer controls the oxidation rate.

The measured bending strength data were evaluated by means of the Weibull statistics which describes the probability (W) of having strength values below a given strength (σ) by the equation

$$W = 1 - \exp\left\{-\left(\frac{\sigma}{\sigma_M}\right)^m \ln 2\right\} .$$

The "median strength" (σ_M) is the strength at W = 0.5, the Weibull parameter (m) discribes the scatter of the measured strength data. If log $\{-\ln(1-W)\}$ is plotted as a function of log σ, straight lines are obtained with the slope m and the median strength at log $\{-\ln(1-W)\} = -0.159$. Fig. 1 shows such "Weibull plots" of SiSiC bending strength data before and after corrosion in a water vapour/hydrogen/nitrogen atmosphere at 1370 °C. In this case an increase of strength was observed which was found to be correlated to the presence of nitrogen in the gas phase. By electron microprobe analysis nitride-containing inclusions were detected in the interface of Si phase and SiC phase which may

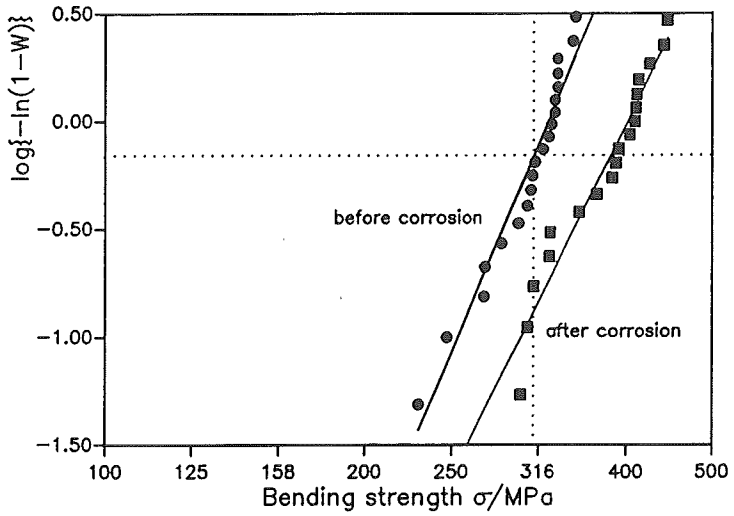

Fig. 1: The bending strength of SiSiC increased after 30 days corrosion in a $H_2O/H_2/N_2$ atmosphere at 1370 °C (Weibull plot)

explain the strength increase. This effect was not observed at very low oxygen partial pressures. If SiSiC is heated for 30 days at 1370 °C in dry H_2/N_2 atmosphere (with 1-10 vpm H_2O), no silicon oxide layer is formed, but a pore zone reaching 50-100 µm depth from the sample surface. In this case a significant decrease of the bending strength was observed after corrosion (Fig. 2). Under these conditions active corrosion occurs which is characterized by

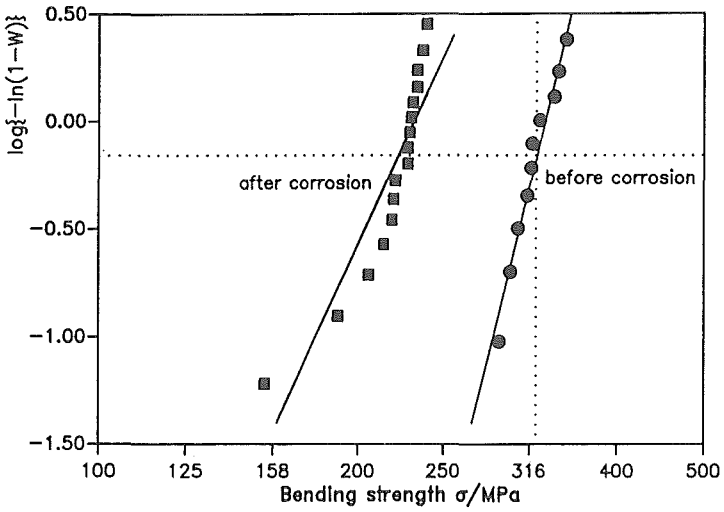

Fig. 2: The bending strength of SiSiC decreased after 30 days corrosion in a H_2/N_2 atmosphere with 8 vpm H_2O at 1370 °C (Weibull plot)

SiO evaporation leaving the observed pore zone. SEM photographs of the fracture surface show that these pores give rize to crack initiation during the bending test (Fig. 3).

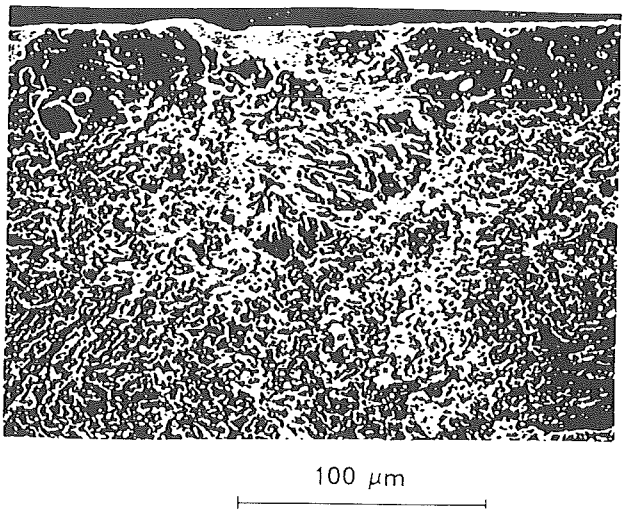

Fig. 3: After corrosion of SiSiC in dry H_2/N_2 atmosphere (30 days 1370 °C), crack initiation during bending test is observed in the corrosion-induced pore zone (SEM photograph of the fracture surface)

At lower temperatures as e.g. 1240 ± 10 °C the strength increase of SiSiC after exposure to N_2-containing atmospheres is more pronounced, even at very low oxygen partial pressures. As can be seen from Fig. 4, the median bending strength was increased by 10-30 % over the whole range of oxygen partial pressures.

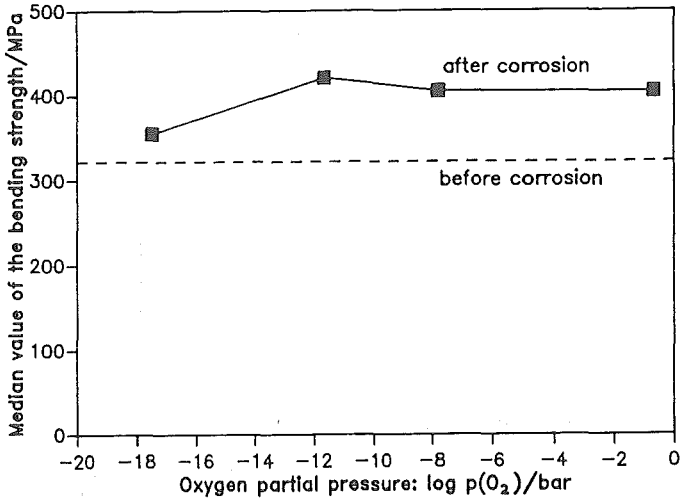

Fig. 4: The median bending strength of SiSiC increased by 10-30 % after corrosion at 1240 ± 10 °C in N_2-containing atmospheres nearly independently of the O_2 partial pressures.

3.2 Corrosion of SiSiC by basic slag at 1250 °C

Contrary to the very good corrosion resistance of SiSiC in N_2-containing oxidizing atmospheres severe attack of the SiSiC specimens by basic coal slag was observed. After 175 hours exposure at 1250 °C in air the surface showed an irregular distribution of glassy slag phase, crystalline slag phase, corrosion products, and pores.

This slag corrosion of SiSiC led to a significant decrease of the median bending strength from 322 MPa (before corrosion) to 170 MPa after 175 hours corrosion (Fig. 5).

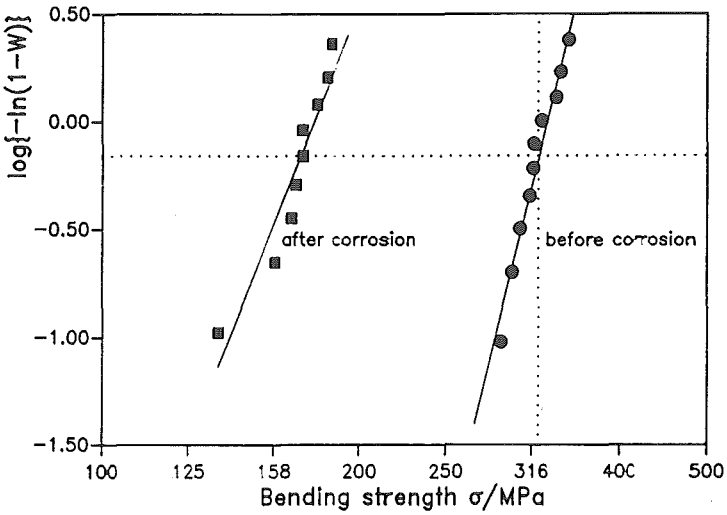

Fig. 5: The bending strength of SiSiC decreased significantly after 175 hours exposure to basic slag at 1250 °C (Weibull plots)

A detailed investigation of the corrosion zone by means of electron microprobe analysis resulted in the formation of an iron/nickel silicide phase together with several pores in the interface between SiSiC and glassy slag layer (Fig. 6). The average composition of this silicide phase measured by point analyses is given in table 2. From these data the silicon to metal

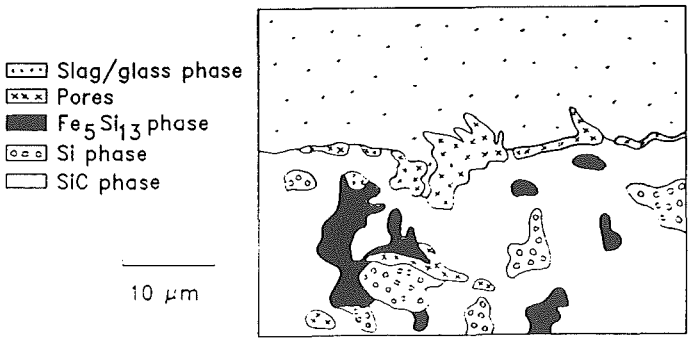

Fig. 6: The corrosion of SiSiC by basic slag at 1250 °C led to the formation of iron silicides and pores in the interface SiSiC/glassy slag phase (EMP results)

Inclusion	Si(wt.%)	Fe(wt.%)	Ni(wt.%)
I	56.9±0.9	43.5±1.7	0.24
II	57.9±1.4	45.3±1.0	0.30

Table 2: Composition of the silicide phase (EMP results)

atomic ratio was calculated to be Si/Fe+Ni = 2,56 ± 0.19 corresponding to the formula $(Fe_{4.97}\ Ni_{0.03})\ Si_{12.8\ \pm\ 0.9}$. This composition is in good agreement with the Fe_5Si_{13} phase described by M.K. FERBER et al. at Oak Ridge in 1985. The formation of this very brittle silicide phase together with many pores may be the reason for the observed decrease of bending strength. It would be important to investigate the corrosion behaviour of SiSiC materials in presence of basic slags with lower iron content.

REFERENCES

1. R. Förthmann, E. Gyarmati, A. Naoumidis: "Corrosion of Silicon Carbide Ceramics at High Temperatures in Water Vapor-containing Atmospheres", Proceed. VIIIth German-Yugoslav Meeting on Materials Science and Development, Brdo pri Kranju, May 18-21, 1987 (Jül-Spez-446, 1988) p. 231-240

2. V. Kevorkijan, M. Komac, T. Fetahagic, V. Strumberger: "Investigation of Alpha-SiC Hot Corrosion in the Presence of Basic Slag", Proceed. VIIIth German-Yugoslav Meeting on Materials Science and Development, Brdo pri Kranju, May 18-21, 1987 (Jül-Spez-446, 1988) p. 241-248

3. M.K. Ferber, I. Ogle, V.J. Tennery, T. Henson: "Characterization of Corrosion Mechanisms Occurring in a Sintered SiC Exposed to Basic Coal Slags", J. Am. Ceram. Soc. 68 (1985) 191-197

CONSOLIDATION

INFLUENCE OF SINTERING AND THERMOMECHANICAL TREATMENT ON MICROSTRUCTURE AND PROPERTIES OF W–Ni–Fe ALLOYS

M. Mitkov and W. A. Kaysser*

Institute Boris Kidric, Belgrade, Yugoslavia , POB 522
* Max-Planck-Institute fur Metallforschung Pulvermetallurgisches Laboratorium
Heisenbergstr. 5, 7000 Stuttgart 80

ABSTRACT

Densification and microstructural development during sintering of W–Ni and W–Fe–Ni alloys between 1100 and 1470°C were investigated. In solid state sintering densification and grain growth ceased at Ni or Ni/Fe contents above 0.15 wt.%. During liquid phase sintering densification was enhanced by increasing amounts of the lower melting additives. Dense liquid phase sintered samples where cold or warm worked to different degrees by rolling and rotating forging. The deformation of individual grains was measured. The distrubution of the dislocation densities in individual grains was calculated from shape and size of grains which formed during annealing of the worked samples in solid or partially liquid state. Dislocation densities of up to 10^{15} m^{-2} were deduced right in the vicinity of contact areas of adjacent W grains even after only a slight macroscopic deformation of the material by 5%. At higher degrees of deformation recrystallization of deformed initial W grains and their subsequent disintegration by the penetration of liquid phase lead to considerable grain refinement. The mechanisms of recrystallization, stress induced boundary migration and melt penetration into the recrystallized fine grained materials are discussed.

INTRODUCTION

In spite of the improved understanding of the major mechanisms leading to microstructural changes during liquid phase sintering of heavy metal alloys [1–7], only minor attention has been paid to the influence of material deofmation which generaly results in an increased dislocation density. Since the liquid phase sintering in heavy metal alloys occurs before recrystallization starts, the increased dislocation density in some regions of the material may modify the grain growth behaviour as indirectly suggested by previous work [8–14]. Clear explanations on the mechanisms were impossible because a broad variety of driving and retarding forces might have been effective during the experiments reported in the literature. A major cause for the broad variety of forces was the presence of pores and the presence of chemical non-equilibria. Pores hinder or retard the migration of grain boundaries or other interfaces which might be induced for example by the presence of high dislocation densities [15, 16]. Chemical non-equilibria, in particular the non-equilibrium concentration of the W solid solution have been shown to induce liquid film migration [6, 13, 17–20].

In the present work liquid phase sintered 90W–7Ni–3Fe alloys were cold rolled and rotation forged to various reductions to introduce strain in the W particles. The deformed material was subsequently resintered. Chemical driving forces due to concentration changes of the liquid and solid phase during resintering were exluded by performing the initial sintering and the resintering treatment at the same temperature. The microstructural development during resintering was essentially reduced to changes which were caused by the presence of an increased dislocation density, because of no pore presence during resintering of the prestrained alloys.

EXPERIMENTAL PROCEDURE

The W–Ni–Fe alloys were prepared from fine metal powders by liquid phase sintering at 1470°C in flowing dry hydrogen. The powders had mean particle sizes of 1,5 μm [W], 5 μm [Ni] and 3 μm [Fe]. The final density of the sintered material reached the theoretical value. The sintered samples were cold rolled to give height reductions of 5, 15 and 50% and rotation forged with the volume reduction of 25% [without intermediate anneals]. Subsequently the samples were liquid phase sintered at 1470°C. Another set of samples were sintered after deformation in the solid state region at 1420°C. The samples were polished and etched by the usual metallographic procedure.

RESULTS

After initial liquid phase sintering [prior to deformation] the alloy consisted of single crystal W/Fe, Ni/ grains [subsequently called original W grains] embedded in a Fe-and Ni-rich matrix. The W grains were connected at the contact regions by boundaries. Figure 1 shows the microstructure of samples which were annealed in solid state at 1420°C for 3 min after cold rolling. In the sample reduced by 15%, new grains with diameters of approximately 6 μm recrystallized at a few contact areas between the original W grains [arrows in Fig. 1a]. In samples reduced 50%, several new grains formed at most contact areas between the original W grains [Fig. 1b]. The microstructures of the forged sample [25% reduction] after solid state sintering at 1420°C for 3 and 40 min are shown in Fig. 2.

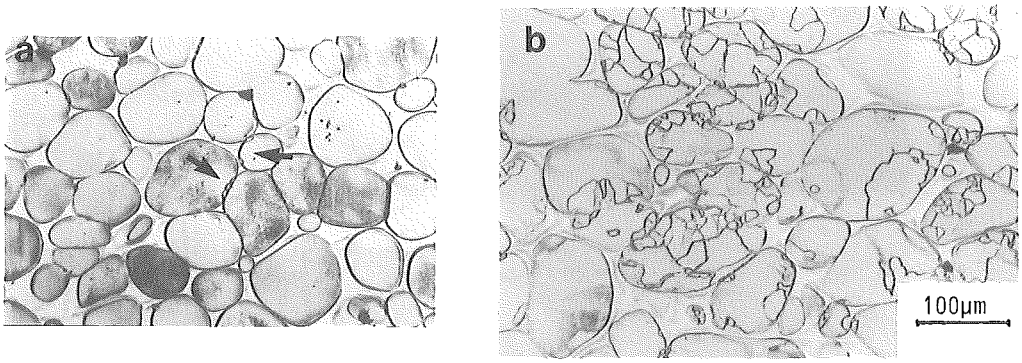

Figure 1 – Microstructures of a prestrained W–7Ni–3Fe heavy metal alloy solid state sintered at 1420°C for 3 min. a) – 15% reduction b) – 50% reduction.

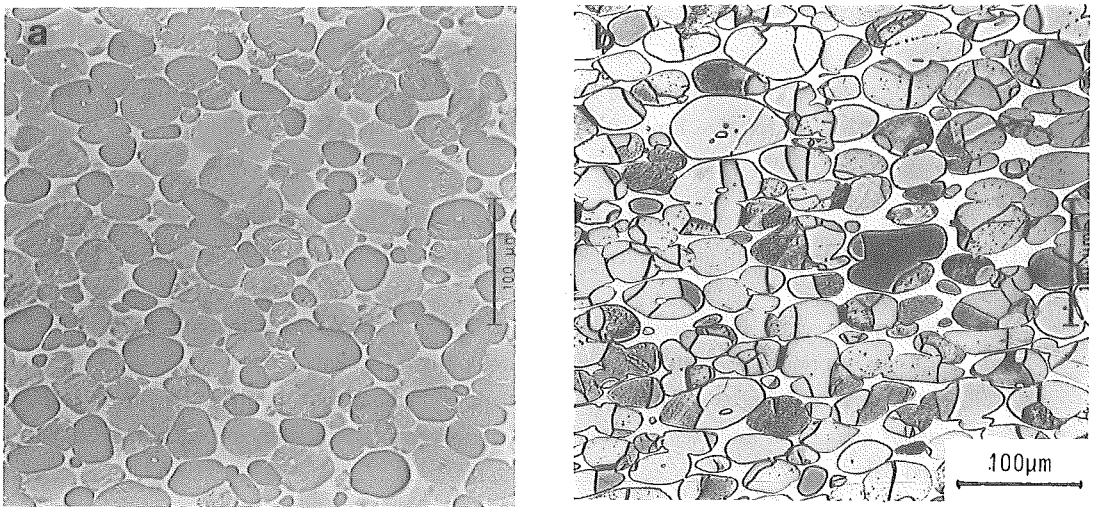

Figure 2 – Microstructures of a prestrained alloy solid state sintered at 1420°C for a) 3 min and b) 40 min (forged, 25% reduction)

In the sample reduced by 25% and solid state sintered for 3 min [Fig. 2a] some new grains with diameters of a few µm recrystallized also at contact areas. During prolonged sintering up to 40 min [Fig. 2b] recrystallized grains growth into the interior of the original W particles forming new grain boundaries, some of them being wavy.

The microstructures of prestrained samples after liquid phase sintering at 1470°C are shown in Figs. 3 to 6.

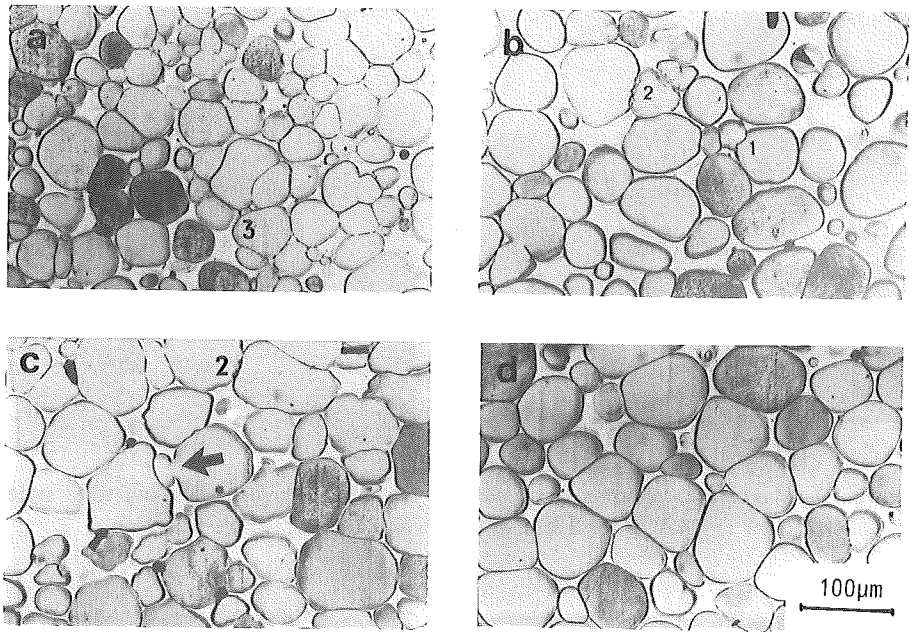

Figure 3 – Microstructures after liquid phase sintering of a 5% prestrained W–7Ni–3Fe heavy metal alloy at 1470°C for a) – 1 min, b) – 10 min, c) – 40 min and d) – 720 min.

After short liquid phase sintering of the samples, six distinct microstructural features were found, which had not been present in the microstructures of the material after final liquid phase sintering.

/i/ New grains with diameters between 5 and 35 μm showed up at the necks and in the interior of original W grains (Fig. 5a, indicated by 3 in Fig. 3a).

/ii/ Original W grains grew at the expense of their immediate neighbour despite the simultaneous increase in interface area caused by this process (indicated by arrows in Fig. 3b, 3c and 6a).

/iii/ Thin liquid films penetrated along the grain boundaries and triple junctions of the newly formed grains, leading to detachment ant to disintegration of the original W grains (Fig. 5b and 6c).

/iv/ Thin liquid films were present in many contact areas replacing the initial boundaries (Fig. 4a and 6b).

/v/ Some thin liquid layers between the original W grains developed a wavy shape (indicated by 2 in Fig. 3b, 3c and 6b).

/vi/ Grain boundaries in the necks between original W grains developed a wavy shape (indicated by 1 in Fig. 3b and 6b).

After a short liquid phase sintering (up to 10 min) of samples which were reduced by 5%, the formation of new grains was restricted to the imediate contact region. The diameters of the new grains were between 5 and 7 μm. In addition the features /iv/, /v/ and /vi/ were found to a large extent.

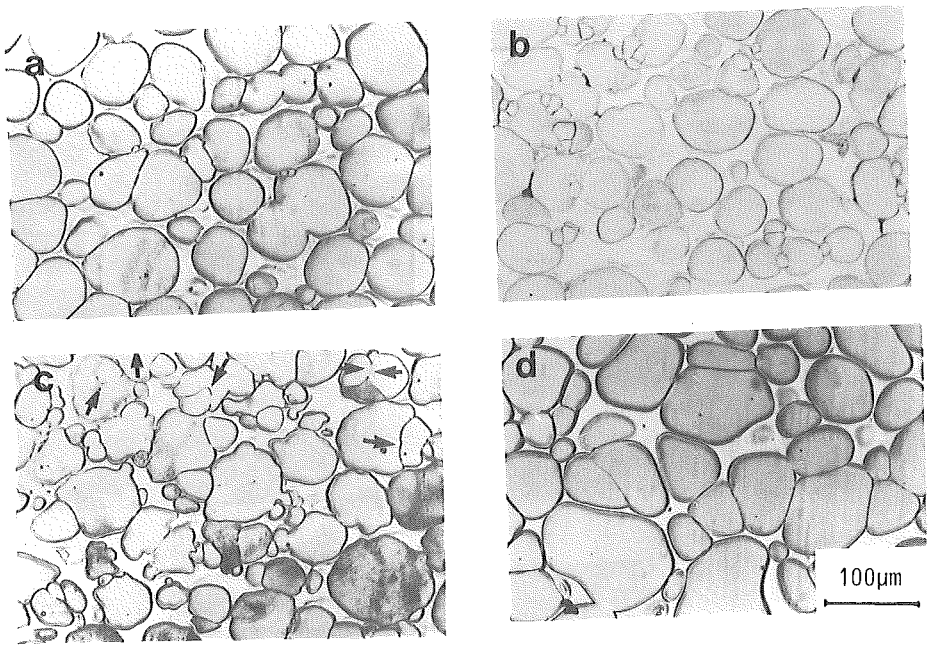

Figure 4 — Microstructures after liquid phase sintering of a 15% prestrained W—7Ni—3Fe heavy metal alloy at 1470°C for a) — 1 min, b) — 10 min, c) — 40 min, d) — 720 min.

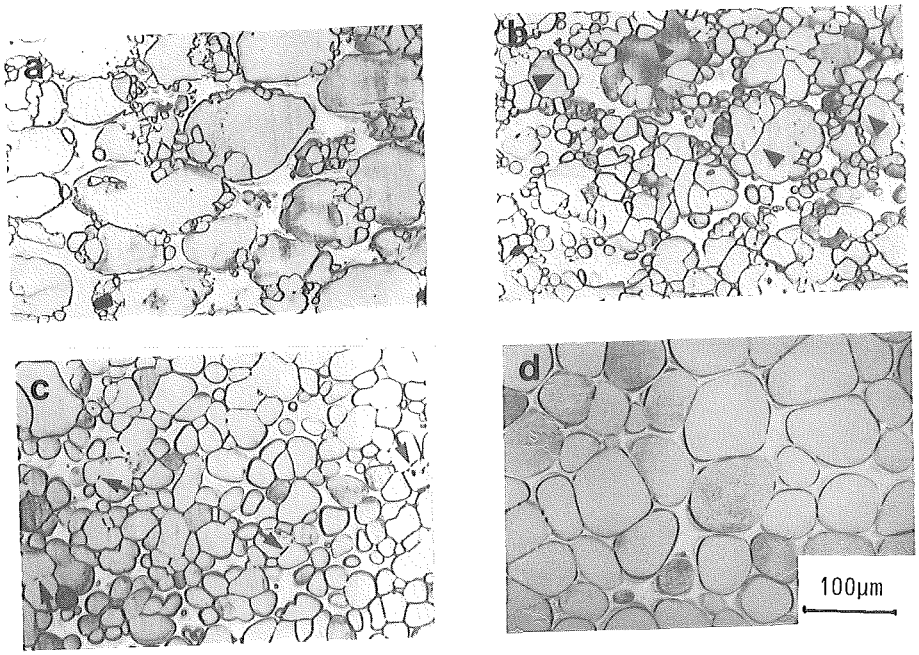

Figure 5 — Microstructures after liquid phase sintering of a 50% prestrained W—7Ni—3Fe heavy metal alloy at 1470°C for a) — 1 min, b) — 10 min, c) — 40 min, d) — 720 min.

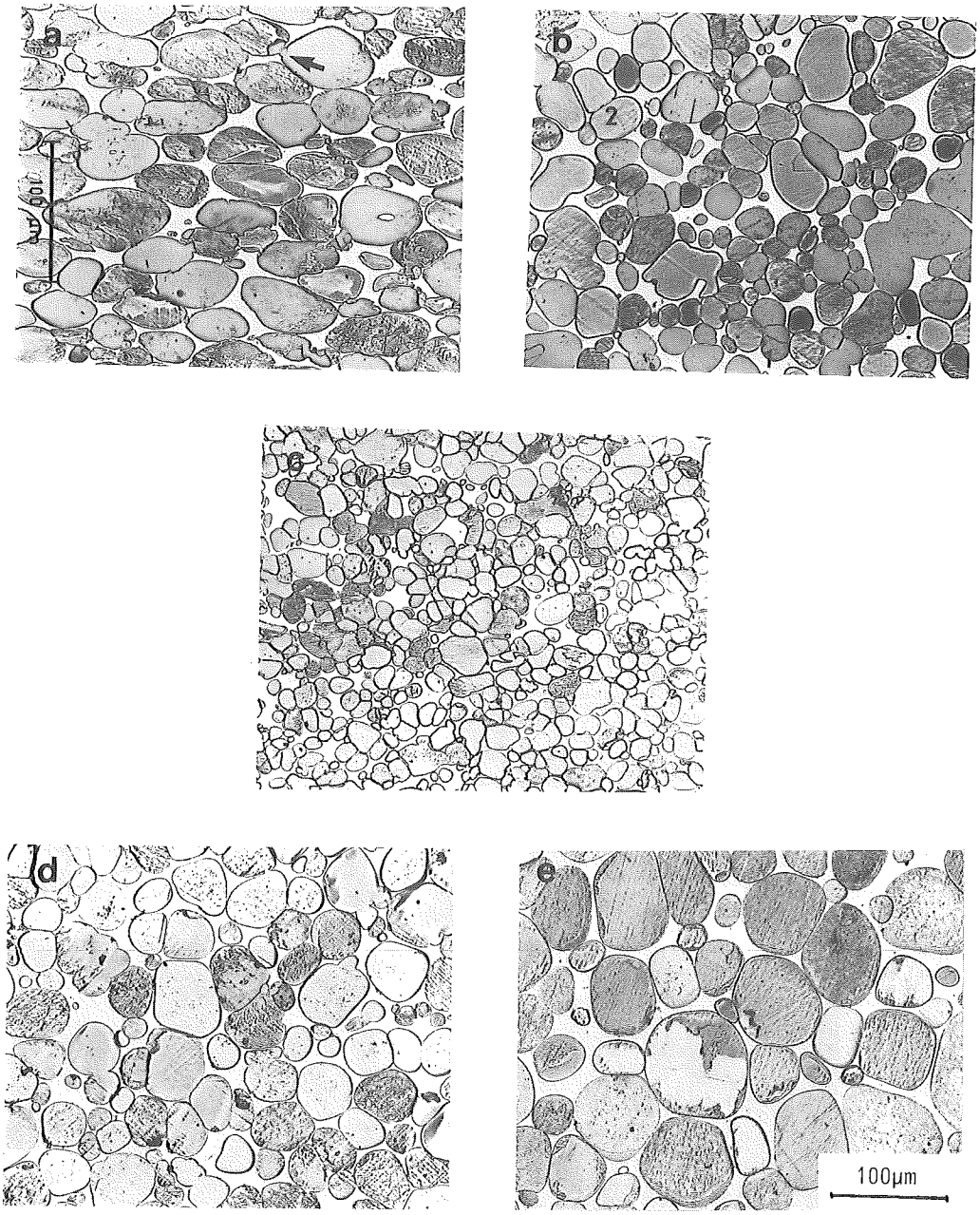

Figure 6 — Microstructures asfter liquid phase sintering of forged (25% reduction) alloy at 1470°C for a) 1 min, b) 10 min, c) 40 min, d) 120 min, e) 480 min.

During prolonged sintering (40 min and more) the features /ii/ became more characteristic (Fig. 3c). In 15% reduced samples liquid phase sintering at 1470°C for 1 and 10 min led to the formation of new grains in the contact areas between the particles with average diameters of 5 and 10 μm (Fig. 4a and b). Some of the newly formed grains still appear to grow into the interior of the single crystal grains after prolonged liquid phase sintering (arrows in Fig. 4c). After liquid phase sintering for 720 min the boundaries between the particles were mostly straight again (Fig. 4d). In 25% reduced forged samples some new grains appear in the neck regions, some of them already grown, followed by wavy shape formed boundaries (Fig. 6a). The deformed starting grain shape is still present in the structure. Wavy shape boundaries are also obvious in the neck regions between the original W grains. During prolonged sintering, liquid film penetration become more pronounced (Fig. 6b), leading furtheron to particle disintegration (Fig. 6c). The microstructure analysis (Fig. 6c) yields evidences for the miscellaneous grain growth.

As mentioned above the majority of initial boundaries in the neck areas are replaced by thin liquid layers during liquid phase sintering of the prestrained samples. The particle contact area ratio, R_1, is defined as the ratio of contact area where two particles are separated by a thin liquid films to the particle contact area where the particles are separated by a boundary of the type present after initial liquid phase sintering. The changes in R_1 with sintering time at 1470°C following 5 and 15% deformation are shown in Fig. 7. The replacement of grain boundaries by liquid films is more pronounced in alloys reduced by 5% than in the alloys which are reduced by 15% during cold rolling.

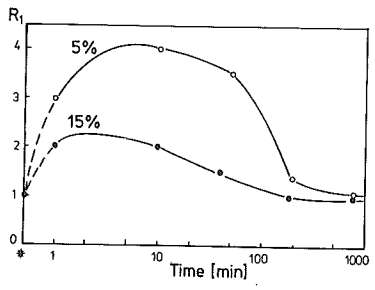

Fig. 7 – Particle contact area ratio, R_1, in cold rolled W–7Ni–3Fe after liquid phase sintering at 1470°C (* after solid state sintering at 1420°C for 3 min). R_1 is defined as the ratio of contact area where two particles are separated by a thin liquid film to the area where the particles are separated by a boundary of the type present after initial liquid phase sintering.

Figure 5 shows the microstructures of the cold rolled (reduction 50%) W–Ni–Fe heavy metal alloy after liquid phase sintering at 1470°C. After annealing 1 min many new grains with diameters smaller 5μm have formed at most contacts (Fig. 5a). Larger grains formed in the interior of the original W grains (Fig. 5b). After liquid phase sintering for 10 min only a few areas in the particles were left, where no new grains formes (triangles in Fig. 5b). The formation of new grains is followed by the penetration of melt along the newly formed grain boundaries. At the periphery of the original W grains the new grains are detached and appear to move toward the melt-rich pools. After 40 min of annealing

disintegration of the original W grains is pronounced (Fig. 5c). Small newly formed and detached grains visible in the microstructure after sintering 10 min partly disappeared or spheroidized in the annealing interval between 10 and 40 min (compare Fig. 5b and c). After prolonged liquid phase sintering (720 min, Fig. 5d) the microstructure shows the usual coarsened grains, very similar to the initial microstructure of the liquid phase sintered undeformed samples.

Figure 8 shows the average chord length L_3 of the W(Ni, Fe) particles and the detached grains after sintering samples which had been reduced 50% by cold rolling. The state after solid state sintering at 1420°C for 3 min is indicated by the asterisk. During liquid phase sintering the formation of new grains and particle disintegration result in a drastic grain refinement which is still present after annealing for 40 min. During prolonged liquid phase sintering the grains coarsen again. The average intercept length, L_3, measured at times over 40 min fits the relation $L_3(t)^n = L_3(2400)^n + k \cdot t_s$, with $n = 1/3$, $k = 3.41 \cdot 10^{-18}$ $m^3 s^{-1}$ and $t_s = t - 2400$ s, where t is the isothermal annealing time.

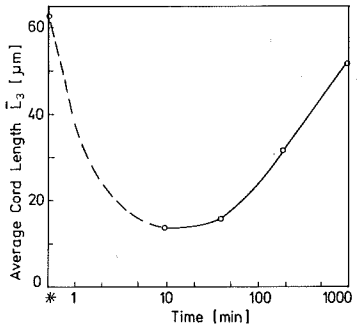

Figure 8 — Average chord length of grains of a W—7Ni—3Fe heavy metal alloy, reduced 50% by cold rolling, after liquid phase sintering at 1470° (* indicates the state after solid state sintering of the prestrained sample at 1420°C for 20 min).

Figure 9 shows a schematic summary of the microstructural development observed during solid state and liquid phase sintering of the prestrained W—Ni—Fe alloy.

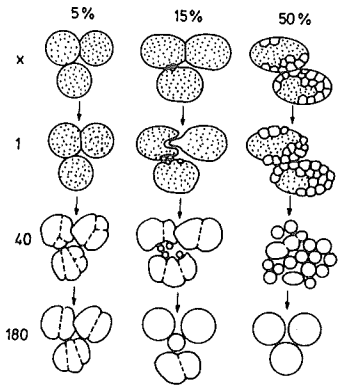

Figure 9 — Schematic description of the microstructural development during solid state and liquid phase sintering of a prestrained W—7Ni—3Fe alloy. x after solid state sintering at 1420°C for 3 min; 1, 40, 180 after liquid phase sintering at 1470°C for 1, 40 and 180 min.

After sintering samples which were reduced 15% at 1420°C for 3 min the diameters of the newly formed grains (Fig. 1a) are less than 6 μm, hence the formation of the grains required a minimum dislocation density greater than 10^{15} m^{-2}. The deformation of contact areas yields dislocation densities on this order of magnitude and higher, within 3 μm from the contact planes. During liquid phase sintering the decrease of the dislocation density in the wake of moving boundaries caused thin liquid films to migrate from the contact areas against their center of curvature into one of the adjacent grains indicating a dislocation density of $5 \cdot 10^{14}$ and $1.4 \cdot 10^{14}$ m^{-2} at distances of 15 and 25 μm from the contact areas, respectively.

After liquid phase sintering of 50% reduced samples, grains smaller than 5 and 9 μm in size were present in the contact areas and in other peripheral areas of the original W grains, corresponding to equivalent dislocation densities above $2 \cdot 10^{15}$ and $6 \cdot 10^{14}$ m^{-2}, respectively. In the interior of the original W grains dislocation densities of $1.3 \cdot 10^{14}$ m^{-2} were indicated. The microstructures in Fig. 5a and 5b indicate that the recrystallization starts at the periphery of the particles and proceeds toward the interior of the particles. The delayed start of recrystallization and the larger size of the newly formed grains in the inner parts of the particles are likely to be due to the lower dislocation densities in the interior of the particles.

Figure 10 shows schematically the typical minimum dislocation densities in various areas of the prestrained original W grains obtained from the size of grains newly formed during solid state and liquid phase sintering of the prestrained material.

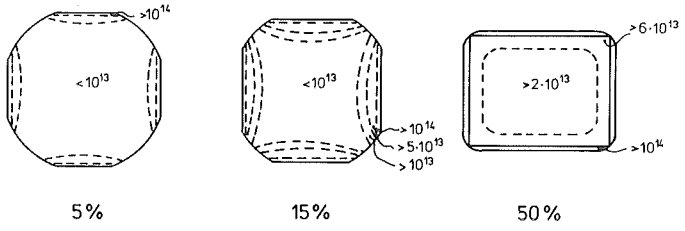

Figure 10 – Dislocation density (in m^{-2}) in W grains of prestrained W–Ni–Fe. Reduction by cold rolling in %.

Liquid Film Penetration during Liquid Phase Sintering

The penetration mechanism of thin liquid films along the boundaries between original W grains and along the grain boundaries of newly formed grains is not yet clear, despite the important changes of the microstructure caused by the penetration, e.g. a reduction of the grain size instead of the usual grain coarsening.

After liquid phase sintering of the slightly deformed alloy (5% reduction) thin liquid films (thickness < 1 μm) became visible in many contact areas. This means the initial boundaries were replaced by liquid phase layers (Figs. 3a, 3b and 5). It requires that the specific boundary energy γ_{gb} is smaller than twice the surface energy γ_{sl} before deformation and that γ_{gb} is larger than $2\gamma_{sl}$ after deformation. It is suggested that the excess free energy of the boundary in the presence of high dislocation densities near to the boundaries, (that means after deformation) composes of the increased energy of the atoms at the interface itself and of the increased energy of thin adjacent bulk layers.

DISCUSSION

Recrystallization, Grain Growth and Dislocation Density

During solid state and liquid phase annealing of cold deformed W heavy metal alloy new grains form in cintact areas and in the interior of the original single crystal W(Ni, Fe) grains. The formation and growth of the new grains depends on the energy reduction through the elimination or rearrangement of dislocations. The reduction in strain energy must overcome the energy increase which results from the formation of additional interface area when the new grains form and grow. The present observations will be discussed at first with respect to the magnitude of both energies, as well as the resulting driving forces.

The maximum potential difference at a grain boundary due to the dislocation density difference at either side is obtained when the coherency of the adjacent grains is completely lost and the energy of the dislocations transforms directly without relaxation into an average increase of the chemical potential , $\Delta\mu_1$. For this case the increase in the chemical potencial is estimated by [21, 22]

$$\Delta\mu_1 = \Omega E_v \Delta\rho \tag{1}$$

where E_v is the average specific line energy of the dislocations and Ω is the molar volume of the host material and $\Delta\rho$ is the change in the dislocation density. The isolated approximately spherical grains in the originally single crystal W grains tend to shrink due to their curved interfaces. The unrelaxed potential difference at either side of the grain boundary due to the curvature is [22]

$$\Delta\mu_2 = -4\gamma_{gb}\,\Omega/G \tag{2}$$

where 4/G is the sum of the two principial curvatures. In approximation G is the grain size, and γ_{gb} is the grain boundary energy. Calculations with $\Delta\mu_1 = \Delta\mu_2$ indicate that the reduction of dislocation density by the newly formed grains has to be considerable to overcome the surface tension of the curved interface.

After liquid phase sintering of 5% reduced samples new grains were observed in the contact areas with sizes between 5 and 7 μm, which is equivalent to a reduction in dislocation densities in the order of 10^{15} m^{-2}. The dislocation density in as-deformed metal sufficient to initiate recrystallization in about 10^{12} cm^{-2} [26]. Recrystallization nuclei are in general not ideally perfect and can already contain dislocations. For that reason, the difference in dislocation densities which provides the driving force for primary recrystallization is always less than 10^{12} cm^{-2}.

Larger grains were not observed, which indicates that the deformation outside the direct contact areas is small and that the dislocation density decreases steeply to much lower values within 3μm from the contact plane.

Figure 11 shows a model where a liquid film of approximately 1 μm thickness penetrates along prior grain boundaries [23]. At the top of the penetrating liquid film, material with high dislocation density dissolves in the melt, diffuses along the melt layer and precipitates at solid/liquid interfaces which are not part of the contact areas [24]. With an initial thickness of the „liquid film" of $1.24 \cdot 10^{-10}$ m (roughly a monolayer of Ni being segregated at the boundary) the model yields 1016, 164 and 32 s for the complete penetration into a boundary at the contact area with the dislocation densities of 10^{13}, 10^{14} and 10^{15} m^{-2}. These values fit well to the experimentally observed times (compare Figs. 3, 4 and 5). In addition some evidence of the penetration as described is given from the microstructures (x in Fig. 4).

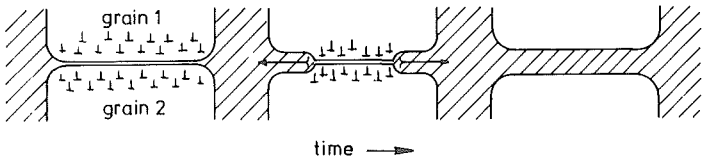

Figure 11 — Schematic representation of the penetration of a melt layer along a deformed boundary between original W grains.

Disintegration of Original W Grains

During prolonged liquid phase sintering grains newly formed in original W grains are detached from the original grains and move toward adjacent liquid pools (Fig. 5b). The detachment of grains from the polycrystalline areas requires the penetration of melt along the grain boundaries. The detachment also requires sufficient cross sectional area for the melt flow during the grain movement and a certain spheroidization of the grains at triple junctions and at the nodes of four adjacent grains. The spheroidization is equivalent to the opening of triangular melt chanels along the triple junctions of grain boundaries. The melt channels at triple junctions of grain boundaries tend to increase their size if γ_{gb} is larger than $3\gamma_{sl}$. The penetration of melt into grian boundaries between two grains requires γ_{gb} to be larger than $2\gamma_{sl}$. Calculations on various models suggest that a fast opening of the melt channels along triple junctions depends on a prior melt penetration along the planar boundary areas [25].

CONCLUSIONS

In samples which are 5% reduced the deformation is essentially restricted to the immediate contact areas. Due to thin dislocation-rich layers at the boundaries, most of the initial boundaries between the particles were replaced by thin liquid films of up to 1 μm. The penetration occurs by a mechanism where material of increased dislocation density dissolves at the front of the penetrating liquid film and precipitates with lower dislocation density at other grains.

After 15% reduction the resintered samples show liquid film migration driven by the difference in dislocation density of the dissolving and the reprecipitating material. The dislocation densities are 10^{16} m^{-2} in the contact areas with a depth of up to 10 μm and between $1 \cdot 10^{14}$ and $8 \cdot 10^{14}$ m^{-2} in the interior of the original W grains.

50% reduction of the original W grains yields an excess dislocation density of $5 \cdot 10^{15}$ m^{-2} at the periphery of the grains which decreases continuously to $5 \cdot 10^{13}$ m^{-2} toward the interior of the original grains. The boundaries of grains forming throught the original W grains during liquid phase sintering are subsequently penetrated by thin liquid films. Melt channels at triple junctions widen until detachment of the grains occurs, resulting in a complete disintegration of the recrystalizzed original grains. This mechanism reduces the average grain size by a factor of four.

ACKNOWLEDGEMENT

We thank the International Büro of the KFA-Jülich for the continuous support of this work.

References

1. W.J. Huppmann et al., „The Elementary Mechanisms of Liquid Phase Sintering – I. Rearrangement," Z. Metallkde., 70(1979) 707–713.
2. W.J. Huppmann, „The Elementary Mechanisms of Liquid Phase Sintering – II. Solution-Reprecipitation," Z. Metallkde., 70(1979) 792–797.
3. G. Petzow and W.A. Kaysser, „Basic Mechanisms of Liquid Phase Sintering," Sintered Metal-Ceramic Composites, ed. G.S. Upadhyaya (Amsterdam, Elsevier Science Publishers, 1984), 51–70.
4. W.A. Kaysser and G. Petzow, „Present State of Liquid Phase Sintering," Powder Metallurgy, 28(1985) 145–150.
5. D.N. Yoon and W.J. Huppmann, „Grain Growth and Densification during Liquid Phase Sintering of W–Ni," Acta Metall. 27(1979) 693–698.
6. D.N. Yoon and W.J. Huppmann, „Chemically Driven Growth of Tungsten Grains during Sintering with Liquid Nickel," Acta Metall., 27(1979) 973–977.
7. S.S. Kim and D.N. Yoon, „Coarsening Behaviour of Mo Grains Dispersed in Liquid Matrix," Acta Metall., 31(1983) 1151–1157.
8. E.G. Zukas and D.T. Easch, „Possible Reinforcement of the W–Ni–Fe–Composite with W Fibers," J. Less-common Met., 32(1973) 345–353.
9. E.G. Zukas, P.S.Z. Rogers and R.S. Rogers, „Unusual Spheroid Behaviour During Liquid Phase Sintering," Int.J. of Powd.Met. and Powd. Tech., 13(1977) 27–33.
10. G. Petzow and W.J. Huppmann, „Fluessigphasensintern," Z. Metallkde., 67(1976) 576–582.
11. M. Hofmann-Amtenbrink et al., „Kosseluntersuchungen zur Korngrenzenwanderung in verformtem Wolfram in Anwesenheit von Nickel, „Z. Metallkde., 77(1986) 368–376.
12. W.A. Kaysser, F. Puckert and G. Petzow, „Recrystallization and Grain Boundary Migration During Sintering," Powder Metallurgy International, 12(1980) 188–191.
13. W.A. Kaysser and S. Pejovnik, „Grain Boundary Migration During Sintering of Mo with Ni Additions," Z. Metallkde., 71(1980) 649–653.
14. W. Schatt et al., „Influence of Dislocations on Solid State and Liquid Phase Sintering," Powder Metallurgy Int., 19(1987) 14–19, and 19(1987) 37–39.
15. R. Brook, „Pore-grain Boundary Interactions and Grain Growth," J. Am. Ceram. Soc., 52(1969) 56–57.
16. C.H. Hsueh, A.G. Evans and R.L. Coble, „Microstructure Development during Final/Intermediate Stage Sintering – I. Pore/Grain Boundary Separation," Acta Metall., 30(1982) 1269–1279
17. C.A. Handwerker, J.W. Cahn, D.N. Yoon and J.E. Blendell, „The effect of Coherency Strains on Alloy Formation: Migration of Liquid Films," Atomic Transport in Alloys: Recent Developments", G.E. Murch ed. M.A. Dayananda (Dayto, OH, TMS/AIME Publications, 1985).

18. D.N. Yoon, J.W. Cahn, C.A. Handwerker, J.E. Blendell and Y.J. Baik, „Cohernсy Strain Induced Migration of Liquid Films through Solids", Interface Migration and Control of Microstructure (Washington D.C., NBS, 1985).

19. W.-H. Rhee, Y.-D. Song and D.N. Yoon, „A Critical Test for the Coherency Strain Effect on Liquid Film and Grain Boundary Migration in Mo–Ni–(Co–Sn) Alloy," Acta Metall., 35(1987) 57–60.

20. M. Hofmann-Amtenbrink, W.A. Kaysser and G. Petzow, „Grain Boundary Migration in Recrystallized Mo Foils in the Presence of Ni," J. Physique, C4(1985) 545–552.

21. P.A. Beck, P.R. Sperry and H.Hu., „The Orientation Dependence of the Rate of Grain Boundary Migration," J. Appl. Phys., 5(1950) 420–425.

22. H.P. Stuewe, „Driving and Dragging Forces in Recrystallization", Recrystallization of Metallic Materials, ed. F. Haessner (Stuttgart, Riederer Verlag, 1978), 11–21.

23. W.A. Kaysser, W.J. Huppmann and G. Petzow, „Analysis of Dimensional Changes During Sintering of Fe–Cu", Powder Metallurgy, 23(1980) 86–91.

24. S.-J.L. Kang et al., „Growth of Mo Grains around Al_2O_3 Particles During Liquid Phase Sintering" Acta Metall., 33(1985) 1919–1926.

25. W.A. Kaysser, „Influence of Dislocations on the Basic Mechanisms of Liquid Phase Sintering in W–Ni–Fe", to be submitted to Int. J. Refractory and Hardmetals.

26. S.S. Gorelik, „Recrystallization in Metals and Alloys", Mir Publishers, Moscow, 1981.

Mechanical Alloying for Development of Sintered Steels with High Hard Phase Content

A.Fetahagic, C.Gutsfeld, F.Thümmler

Universität und Kernforschungszentrum Karlsruhe

Abstract

Sintered steels with 10-30vol% of disperse transition metal carbides have been developed using mechanical alloying, pressing and liquid phase sintering. The importance of mechanical alloying itself and of several process parameters was evaluated for these new group of sintered steels. The best results for mechanical properties and microstructure have been achieved by mechanical alloying for short attrition times. In order to press and sinter these materials heat treatment under hydrogen atmosphere before consolidation is necessary to reduce oxygen content and the cold hardening of the mechanical alloyed powders. The large improvement of the material properties through mechanical alloying can be explained by the better carbide distribution, higher sintered densities, smaller grain sizes and better mechanical clasping of these carbides in the steel matrix.

1. Introduction

High speed steels belong to the most important wear resistant materials. Their manufacturing by the PM route requires a strictly controlled sintering temperature-time schedule because the formation and distribution of the precipitated hard carbides depend on these parameters. Another way to achieve wear resistance of sintered steels is to disperse insoluble hard carbide phases within the steel matrix. A recently developed sintered steel with a transition metal carbide content of 10-30 vol% uses this concept and shows interesting mechanical properties without the afore metioned problems during manufacture./1/

To achieve a homogeneous microstructure, strong mechanical adhesion of the hard particles and optimized mechanical and wear properties it was found that mechanical alloying is a very important step for producing these materials.

The purpose of this work was to evaluate the importance of the

processing-step itself and of several process parameters.

2. Principle of mechanical alloying

Mechanical alloying, today a widely known PM-process, was developed by J.S. Benjamin for oxid-dispersion-strengthened nickel-base alloys /2/. The process is defined as a high energy ball milling technique for producing composite metal powders with controlled microstructures by repeated cold welding and fracture of powder particles.
Fig. 1 shows the microstructures of ASC100.29 iron powder processed with 10 vol% NbC and 0.6% P added as Fe_2P into various stages of mechanical alloying. After two and half hours of processing an internal lamellar structure was established (starting stage). After five hours repeated fracturing and cold welding leads to a decrease of the thickness of the individual lamellae in the composite particles- a typical intermediate stage of the MA process. At steady state (10h) the thickness of the individual lamellae cannot be resolved by optical microscopy. The lamellae have become very fine and carbide particles are clasped between them.

3. Experimental procedure

The experimental work consisted of two stages: firstly the mechanically alloyed powders were observed using several methods to obtain information about the process itself. Secondly mechanically alloyed powders were consolidated by liquid phase sintering to discover the best relationship between properties and processing expenditure for these materials.

3.1. Mechanical alloying and powder characterization methods

The starting materials used in this work were carbonyl iron powder 99.5% pure (BASF) with particle size range of 4-5 μm, water atomized ASC 100.29 (Höganäs) 99.8% pure, 20-175 μm, niobium-carbide (H. C. Starck), with D_{50}=2.2μm. Phosphorus was added as Fe_2P, (GfE), D_{50}=14.5μm, process charges consisted of 200, 100 and 50 g of the Fe-10vol%NbC-0.6%P mixture. Processing was performed in a laboratory high energy attritor in n-heptane to avoid oxidation. The water cooled container was filled with 1 kg of steel balls (3.0 mm diameter). The mill speed was 1500 rpm. The attritor speed and weight of the balls were kept constant, whereas the milling time as well as the proportions of the various constituents of the charge were varied. After milling, the powder was dryed in a vacuum furnace at 180°C.

The particle size distribution was measured using Cilas Particle size analyser model HR 715 (a laser method). X-ray diffraction investigations were performed in a Siemens 500 diffractometer using CuK_{α} radiation.
Microstructures and morphologies of MA powders were observed by optical and scanning electron microscopy.
To remove the effects of oxidation and cold hardening the mechanically alloyed powders were annealed in argon as well as in hydrogen atmospheres at different temperatures. The oxygen content of the powders and the compressibility was measured.

3.2. Sintering and characterization of the samples

After annealing 0.6%C and 0.5% lubricant (Kenolube) was added and mixed for 1 hour in a Turbula mixer. Powder compaction was performed coaxially under a pressure of 550 MPa, then the added lubricant was burned out and the samples were sintered at 1280°C, dwell time = 48 min in flowing hydrogen atmosphere. The density measurement, tensile tests and Vickers hardness measurement were conducted and microstructure was examined by optical and transmission electron microscopy.

4. Results and discussion

4.1. Characterisation of mechanical alloyed powders

4.1.1 Influence of processing time and ball to powder ratio

The attriting process itself is subjected to several variables. Therefore the milling time was varied as well as the proportion of balls to powder in the mill to investigate its effect on this processing step. The mechanically alloyed powders (Fe-10vol%NbC-0.6%P added as 2.4% Fe_2P) were taken after varied processing times to investigate powder particle size distribution. Fig. 2a shows the distribution of powder particle size as a function of attriting time. After 30 min the powders attrited with a ball to powder ratio of 10:1 have become more than two times larger than the original ones and the range of powder particle distribution is wider. (Early stage of processing). As the MA process continues the particles are plastically deformed, become harder and cannot withstand further deformation without fracturing. As a result there is a sharp decrease in the amount of very coarse particles and the range of powder sizes is narrower (intermediate stage).After 5 hours processing mean diameter becomes less than 10 microns, similar to the starting powders and the particle size distribution decrease further to a narrow range (final stage).

Fig. 3 shows scanning electron micrographs of these powders.
Using coarser starting powders like ASC100.29 (D_{50}=75μm) under the same milling conditions, the principle dependence of processing stages and milling times are nearly the same (see Fig. 2b). The final stage is also reached after 5 hours, but the particle sizes of the completly processed powders are much smaller then those of the starting powders. Consequently fracturing of the strongly deformed and embrittled powders leads to rather similar particle sizes.
Changing the ball to powder ratio there has found to be a very strong influence on the necessary milling time for reaching the individual process stages. Looking ahead to a possible use of this process in industry one can establish the ratio of processing time/ charge size (h/gr), which can be interpreted as the specific efficiency of the attritor for this process. Fig.4 shows the dependence of mean particle size on this specific ratio for three different ball to powder ratios.
By comparison of 100g charge (10:1) against a 200g Charge (5:1), it can be seen that these powders pass through the welding predominance region similarly and the maximal particle sizes are also similar, although this stage is reached in half the time by using a 10:1 ratio than by using a 5:1 ratio. After the maximum in particle size a decrease has been reached for both charges, but this decrease is sharper for charges, processed at a 10:1 ratio. The processing is finished after 5 hours for 100 gr charge (10:1), but for 5:1 ratios not earlier than 20 hours.

4.1.2. X-ray-diffraction measurement for determing crystal sizes of mechanically alloyed powders

X-ray diffraction measurements of powder samples can also be used to follow the mechanical alloying process. The decrease of crystal sizes can be calculated from Scherrer formula /3/ by comparing the intensities of the iron (110) and the niobium carbide (111) diffraction peaks with those in a blended mixture. Fig.5 shows respectively the X-ray diffraction profiles of the elemental b.c.c. Fe and the f.c.c. NbC reflections of non attritated and mechanically alloyed powders (10:1 ratio) after different milling times. The calculated crystal sizes for both elements are presented in Fig. 6. During the first 2.5 hours of mechanical alloying there is a large decrease in crystal size for both elements. It can also be seen that the crystal size of the brittler niobium carbide decrease quicker than its of the ductiler iron.
In the period between 2.5 h and 7.5 h both curves continues to decrease, although not so rapidly as in the first stage. After 7.5 hours the crystallite sizes stay approximately constant at

about 25 nm for both elements. The process ranges are rather similar to that found by particle size distribution measurement.
A second question to be answered by X-ray diffraction was, whether the powders can be consolidated with powder metallurgy methods without or with only small recrystallisation. The same powders were annealed at 800°C under argon atmosphere. Below this temperature no economical PM consolidation like powder forging or hipping is possible for steel powders. The X-ray diffraction peaks in Fig 7. of these heat treated powders demonstrate, that recrystallisation has taken place in the mechanically alloyed powders.

4.1.3. Optimization of the annealing process for the mechanically alloyed powders

Annealing of these powders before conventional consolidation has two aims: firstly to remove strain hardening introduced during the milling process and to improve cold pressing behaviour, and secondly to reduce the oxygen content, brought into the powders during the process. Fig. 8 shows the green and sintered densities of 5h mechanically alloyed and heat treated powders as a function of the annealing temperature . Heat treatment was carried out in an argon atmosphere. Green density decrease throughout the mechanical alloying from nearly 76%TD to 63.5%TD without any heat treatment. To improve this an annealing temperature of 600°C is necessary to reach green densities around 70%TD. A higher annealing temperature of 800°C does not appreciatively improve the green densities. The densities measured after sintering the samples at 1280°C also increase marginally with higher powder annealing temperatures.
The oxygen adsorption of the powders through mechanical alloying was also of great interest for the sinterablility of the materials. Because of the very fine starting powders and the many new fresh powder surfaces created by the milling there is a large, nearly linear adsorption of oxygen with time into the powders as shown in Fig. 9. If one changes the ball to powder ratio the oxygen content of the powders over the whole process remains constant for each stage, although the milling time is shortened from 20 h to 2.5 h. Therefore oxygen adsorption is not a factor of the milling time but of the process stage powders are in.
Heat treatment under argon atmosphere does not change the oxygen content drastically. Only a heat treatment under hydrogen at 600°C can reduce the powder oxygen content to approximately twice of that of the initial powders (Fig. 9). Higher annealing temperatures under hydrogen atmospheres leads to a small increase in oxygen content. They are therefore not suitable for reducing the oxygen content.

4.2. Influence of mechanical alloying on the properties of sintered materials

As discussed in 4.1.2. there is no industrial useable consolidation method found for the mechanically alloyed steel powders without a completely recrystallisation. Therefore it was decided to carry out sintering under flowing hydrogen atmosphere at sintering temperatures of 1280°C, whereby liquid phase was formed by the ternary iron-phosphorus-carbon-eutektikum of the steel matrix at temperatures over 900°C. Fig. 10 shows the relative densities as a function of attrition time of a 10:1 charge. In comparsion to the non attritated powders the densities increase strongly through short attrition times. The decrease of sintering densities of the longer attritated powders is caused by the lower attainable green densities and pressing defects. Looking at the pore morphology shown in Fig. 11, large rounded pores can be seen in the non attritated samples caused by liquid phase forming of larger Fe_2P-particles. After mechanical alloying Fe_2P-particles are dispersed very finely in the matrix and the activity of these powders is higher, so that less small pores remain in the material. After longer attrition times the pores become elongated. The lamellar structure of the powders and the remaining cold hardening leads to pressing defects in the pressed samples which cannot be removed totally through liquid phase sintering. The carbide distribution in the non mechanically alloyed materials can be also seen from these micrographs. Large agglomerates of niobium carbides are left, beside areas without any carbides. The steels which are only short time mechanically alloyed have a very homogeneous carbide distribution, agglomerates can no longer be found. Longer attrition times do not improve the homogenenity of this carbide distribution.
The microstructure of the etched samples (Fig.12) shows a greatly reduced grain size of the mechanically alloyed qualities in comparison to that without attrition. This effect is not propotional to the milling time, after reducing the grain size, caused by short processing times, longer attrition does not lead to further decrease in grain size. Because recrystallisation of the powders has taken place, this effect can only be explained by the impeding of grain growth through the fine dispersed niobium carbides as known also from oxide dispersion strengthened superalloys. Transmission electron micrographs show that grain boundaries are restrained on such carbides.(Fig.13) To determine the influence of these effects on the mechanical properties, tensile testing was carried out on as sintered samples without any heat treatment. Fig. 14 shows the results of mechanical testing. The tensile strength is increased about 30% only by mechanical

alloying of 1/2 hour. Also the plastic strain is increased by a factor of 4 by short processing times. Longer attrition times leads to a small decrease in the strength and a small increase of elongation. Therefore tensile testing confirms the great efficiency of the mechanical alloying process and also that short processing times are optimal for the mechanical properties. The increase of Vickers hardness through mechanical alloying is obtained firstly through the increase of the sintered densities through the processing.
These effects of great improvement of the material properties can be explained by the better carbide distribution, higher sintered densities, smaller grain sizes and better mechanical clasping of these carbides in the matrix. Fig. 15 shows a transmission electron micrograph of such a grain boundary between a niobium carbide particle and the steel matrix. No diffusion area can be seen even at such high magnification.

5. Conclusions

Mechanical alloying of sintered steels with hard insoluble carbide phase content exhibit some very interesting effects:
-The processing time can be strongly influenced by changing the ball to powder ratio. For good efficiency of the process the ball to powder ratio should be greater than 10:1.
-Heat treatment of the powders under hydrogen is necessary for consolidting these alloys by coaxial pressing and liquid phase sintering, otherwise the bad compactibility and the high oxygen content hinder the sintering.
-The reduced crystal size through mechanical alloying cannot be exploited since recrystallisation takes place at temperatures below 800°C
-Mechanical alloying for short times leads to a great increase in sintered densities, tensile strength and also in fracture strain of this material.
-Longer attrition times lead to reduced sintered densities and strengths, only the fracture strain increases.
-No diffusion areas could be found between the carbides and the steel matrix, bonding of the carbides has be to considered as a mechanical clasping of the carbides in the matrix.
Therefore mechanical alloying is necessary in producing wear resistant sintered steels with high carbide content homogeneous microstructure and good mechanical properties. The efficiency of the processing step is high, short time mechanical alloying leads to an optimal increase of properties. In combination with the liquid phase sintering under reducing atmospheres at temperatures of 1280°C a larger scale manifacturing of these alloy systems

seems to be possible.

Literature

/1/ Thümmler F., Oberacker R., Klausmann R.: Sintered Steels with High Carbide Content. Modern developments in Powder Metallurgy, Volumes 18-21, 1988

/2/ Benjamin J.S., Voilin T.E.: The Mechanism of Mechanical Alloying. Metallurgical Transactions,5(1974),1929-1934

/3/ Kest A.R.: Solid State Chemistry and its Applications, John Kiley & Sons, 1984, Chichester, New York, Brisbane, Toronto, Singapore

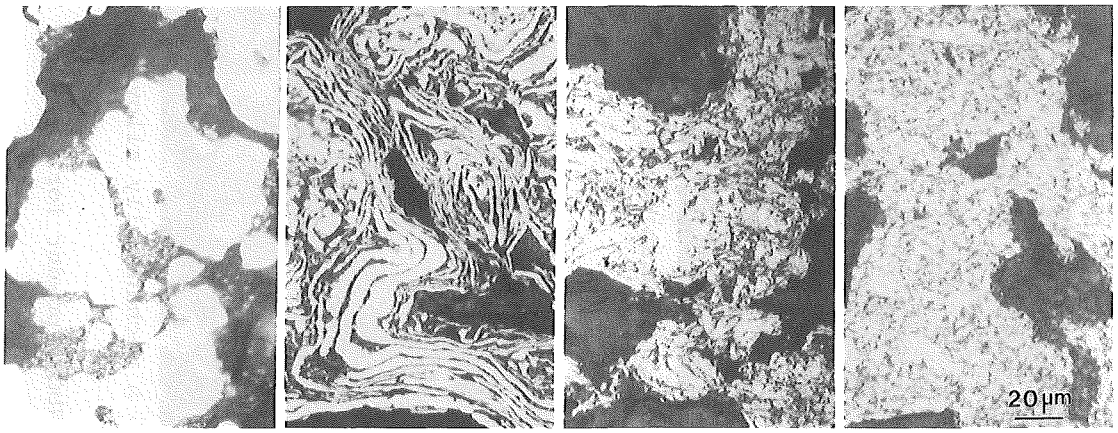

Fig. 1: Microstructures of Fe-10vol%NbC-0.6%P-powders after mechanical alloying for various times

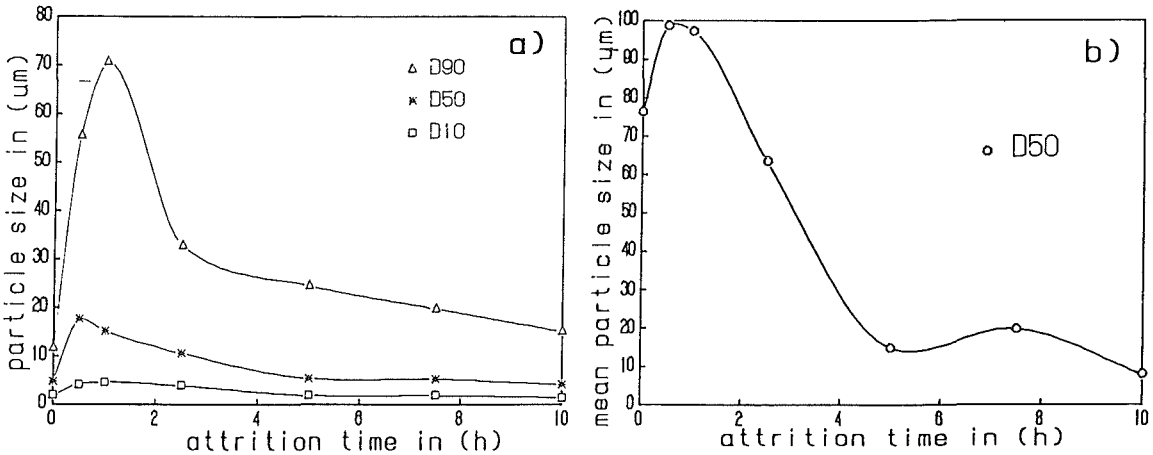

Fig. 2: Particle size distribution after mechanical alloying as a function of attriting time for a) Carbonyl-iron powder and b) ASC100.29 iron powder

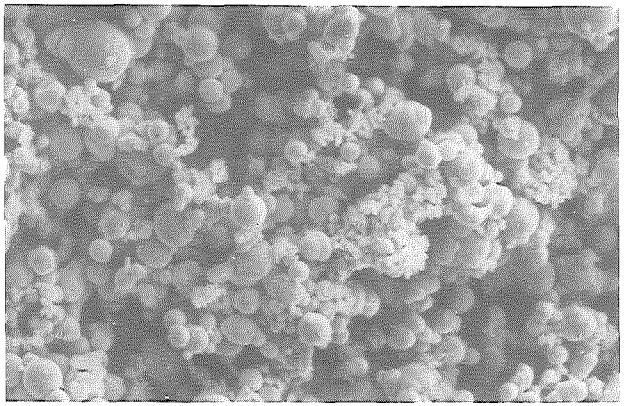

0 h mechanically alloyed

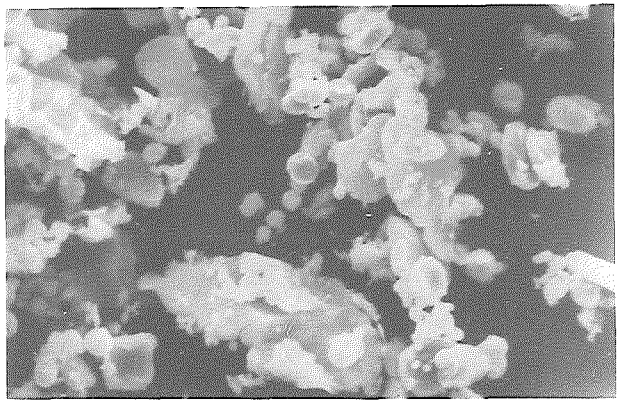

30 min mechanically alloyed

10 µm

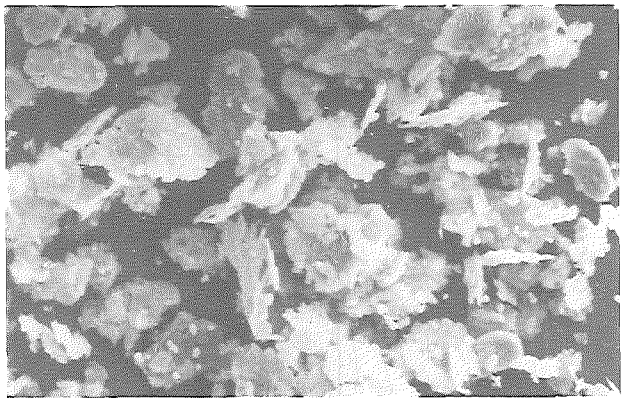

2.5 h mechanically alloyed

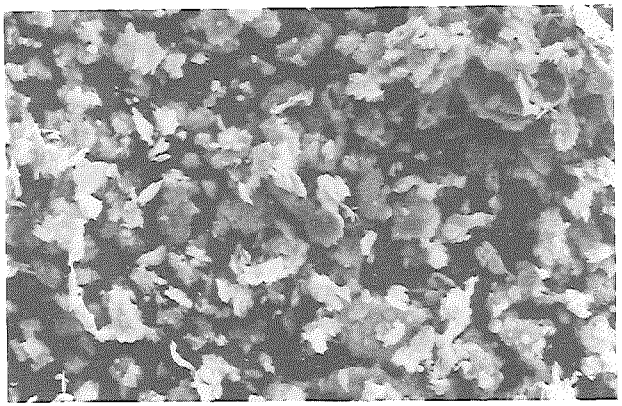

5 h mechanically alloyed

Fig. 3: SEM microgaphs of mechanically alloyed Fe-NbC-P-powder for various times

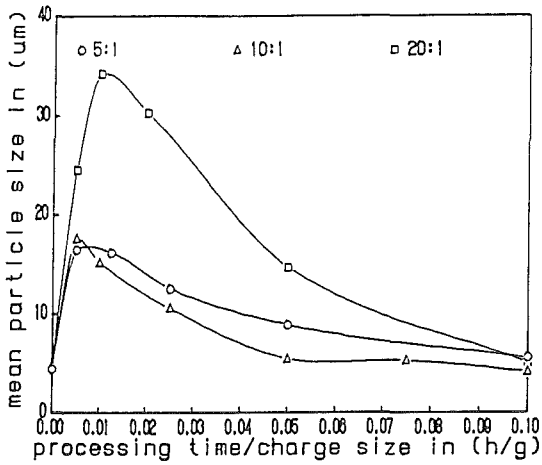

Fig. 4: Dependence of the mean particle size on the ratio processing time / powder charge size for three different ball to powder ratios.

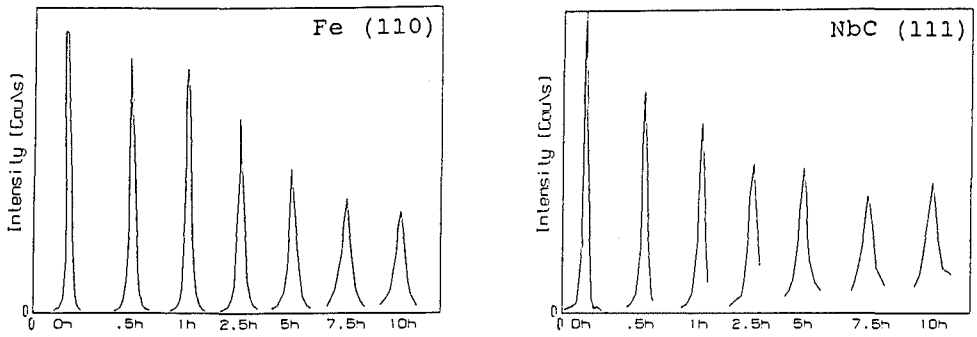

Fig. 5: Change of X-ray diffraction profiles for the Fe-NbC-P system during mechanical alloying for Fe (110) and NbC (111)

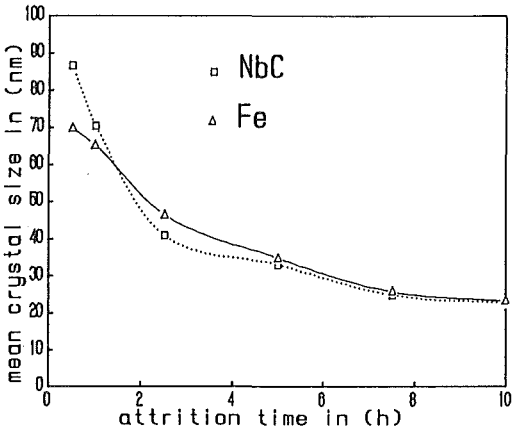

Fig.6: Calculated crystallite size of iron and niobium carbide powders as a function of MA time

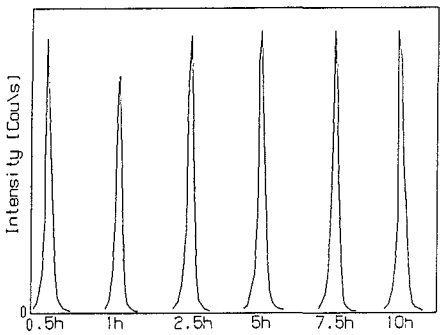

Fig.7: X-ray diifraction peaks of iron after mechanical alloying and annealing at 800°C under Ar-atmosphere

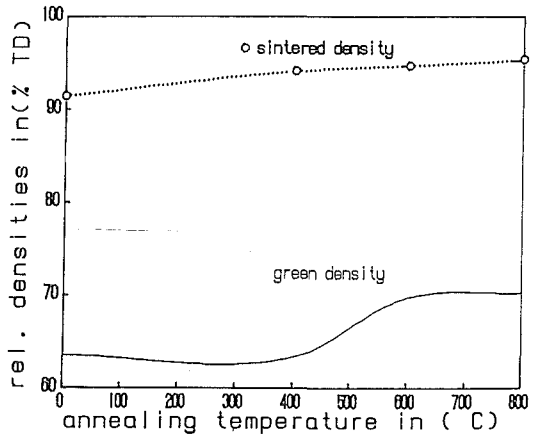

Fig.8: The influence of annealing temperature on the relative densities of Fe-NbC-P

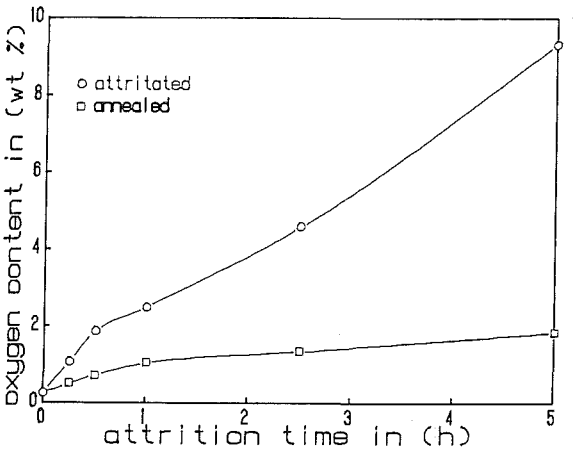

Fig.9: Oxygen content of mechanically alloyed powders (20:1 charge ratio) as a function of attrition time

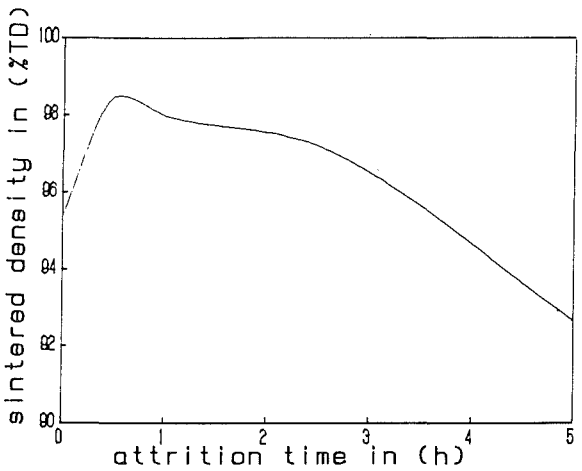

Fig.10: Sintered density as a function af attrition time of Fe-10vol%NbC-0.6P-0.6%C (10:1 charge ratio)

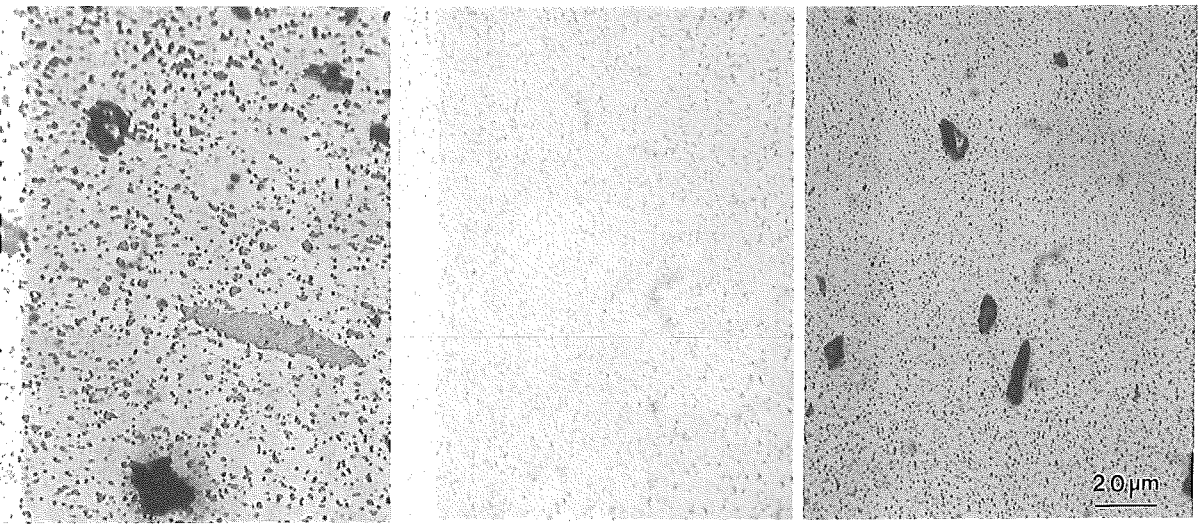

Fig.11: Pore morphology and carbide distribution of sintered Fe-10vol%NbC-0.6%P-0.6%C in dependence on the attrition time

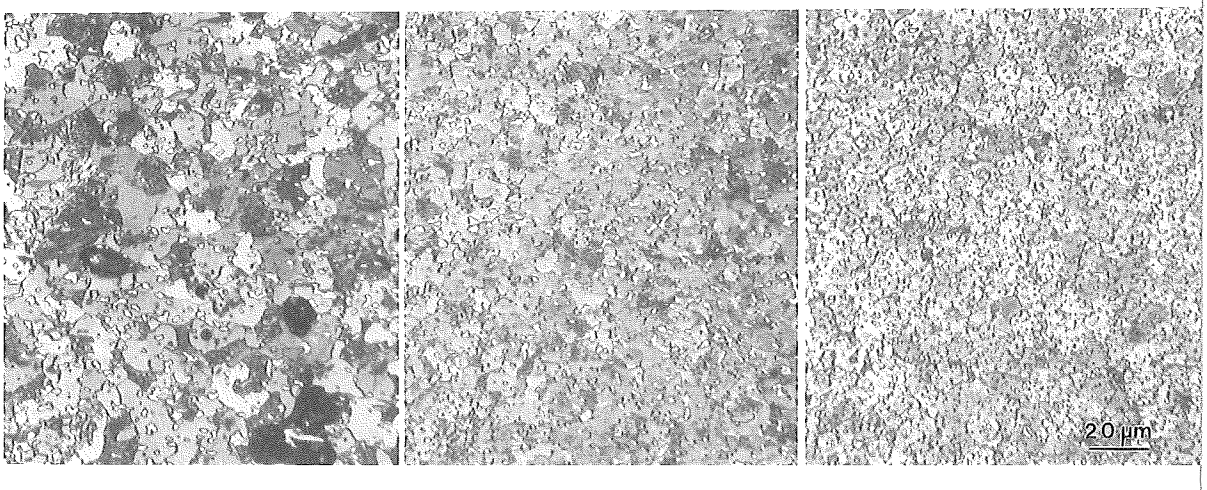

Fig.12: Microstructure of the Fe-NbC-P-C materials after various milling times

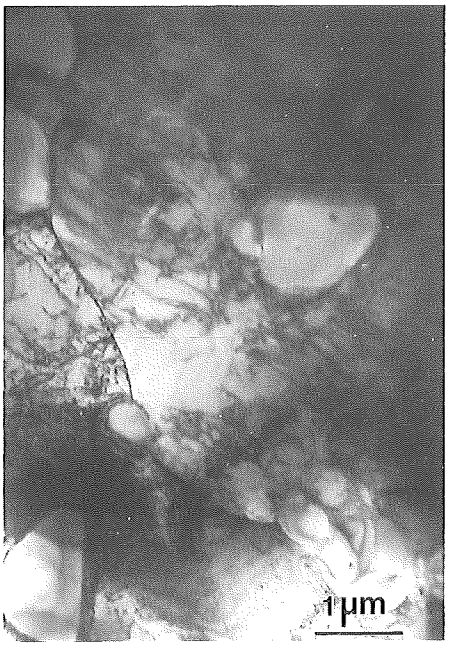

Fig.13: Transmission electron micrograph of a sintered sample showing restraining of grain boundary on niobium carbides

Attrition time (h)	0	0.5	1	2.5	5
Sintered density (%TD)	95.3	98.5	98.0	97.2	92.7
Hardness (HV40)	214	264	258	236	203
Tensile strength (MPa)	584	894	870	807	536
Elongation (%)	1.2	7.7	8.7	10.6	3.4

Fig.14: Mechanical properties of sintered Fe-10vol% NbC-0.6%P-0.6%C-materials

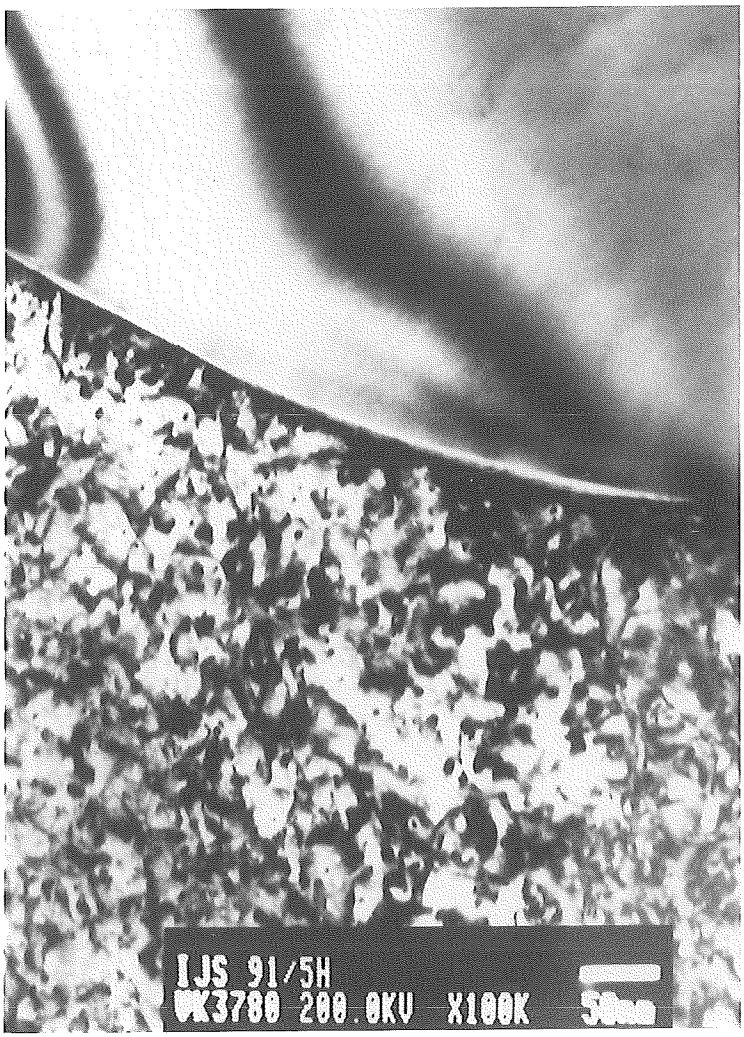

Fig.15: Transmission electron micrograph of the grain boundary between niobium carbide and the steel matrix

EARLY STAGES OF MECHANICAL ALLOYING IN Ni-Ti AND Ni-Al POWDER MIXTURES

M.Stubičar and D.Duževi[c]*

Department of Physics, Faculty of Science and Institute of Physics of the University, Marulićev trg 19, 41001 Zagreb, POB 162, Croatia, Yugoslavia

*"Rade Končar" Electrotechnical Institute, Baštijanova bb, 41000 Zagreb, Croatia, Yugoslavia

ABSTRACT

The high energy ball milling technique has been found recently to yield a wide variety of amorphous alloy powders, many of which could not be obtained before by the rapid solidification technique. As such mechanical alloying provides a simple and inexpensive competitive means to rapid quenching for producing amorphous powders of technical use.
Different researchers apply different ball milles and different milling conditions. It is important to know how amorphization by mechanical alloying, or vice versa, is influenced by the milling regimes. In our experiments we use a rotating ball mill with centrifugal acceleration reaching to near 10 g value and the normal air atmosphere. As a precursor a powder mixture of the stochiometry Ni_2Ti of the well explored system Ni-Ti was chosen. The main interest is concentrated on the system Ni-Al with the stochiometry of Ni_3Al_2.
As far as we know this system is yet untackled by the mechanical alloying technique. In the range of 100 h milling time complete amorphization apparently did not occur, either in Ni-Ti or in the Ni-Al system. Nevertheless, a considerable degree of amorphization was accompanied by marked phase changes in both systems as observed by x-ray powder diffraction. Further investigations on the milling conditions, as well as various analyzes of the samples extracted after different milling times are in progress.

INTRODUCTION

In the creation of materials with predetermined properties the powder metallurgy route offers considerable advantages in comparison to other techniqus. Besides the conventional ways of modeling material characteristics by means of cold- and hot-working of ingots (bulk tayloring) and by various subsequent surface treatments (surface tayloring), it is also possible to extend the engineering influence on the very origin of consolidated products by exploiting the powder state (powder tayloring).

Ball milling was developed a long time ago and at the time it was recognized as an uniquely efficient method for optimizing powder properties by comminution and high-degree homogenization. However, the high-energy ball milling,developed recently, has been found to yield even amorphous or crystalline alloyed powders or their mixtures, most of which could not be obtained before by other preparation procedures, including even such powerful technique as rapid solidification. Thus, mechanical alloying offers a simple and economically competitive means in comparison with other available methods for producing intentionally taylored powders suitable for technical applications.

Despite the great number of experimental reports dealing with the subject, the very notion of high-energy ball milling still remains rather obscure as regards to the influencing power of several crucial processing parameters, even on laboratory scale. The data appearing in papers are rather incomplete, and cannot easily be compared to each other. Thus a way out of this problem is to establish the pertinent values of processing variables for the experiments in order to be able to test the efficiency of one's own equipment by carrying out preliminary investigations on a well established precursor system, which is most similar to the system under investigation.

The actual objective of this study was the investigation of amorphization and mechanical alloying phenomena appearing in the Ni-Al system, since this system might synthezise the cementing phases for refractory carbides and similar substances. The four stable intermetallic phases of this system (ε-Al_3Ni, δ-Al_3Ni, β-AlNi and γ-$AlNi_3$) are themselves very hard /1/, and have proven technically interesting in several other respects. The metastable, high-temperature Ni_3Al_2 phase has also been detected after quenching from 1600 K to room temperature /2/. By splat cooling /3/ and rapid quenching from vapour /4/ the metastable solid solubility of the nickel in aluminium has been extended to 7 and 11 at.%, respectively. In addition, new metastable phases were found, and even a pure amorphous phase in a concentration range from 49.3 to 75.4 at.% Ni /5/. This last finding served as an incentive to choose a composition from the interval just given for the ball milling in our own experiment. As a fiducial

system the Ni-Ti binary appears to be the most appropriate, so a precursor mixture of the stoichiometry Ni_2Ti from the middle of the respective easily amorphizable composition range established by high-energy ball milling has been chosen.

EXPERIMENTAL

In our experiments the milling was done using a laboratory centrifugal ball mill (Heidelberger Colloidmühle, Vetter K.G., Heidelberg, F.R.G.) and an agate container of a rather complicated inside geometry (Fig.1), originally designed for a single ball of 25 mm in diameter. The rotational speed could be continuously adjusted in a range of 0 to 380 rpm, the latter speed being used throughout the experiments. This value is actually the rotational speed of the container axis round the axis of the apparatus (motor), and is achieved by means of an appropriate counterpoised excenter, whereas the container itself retains a practically fixed azimuthal position (apart from some slight oscillations). This forces the ball(s) to rotate with the same angular speed as is that of the container and at the same time this raises centrifugal pressure on the container wall. By using Fig.1 it is easy to express the centrifugal acceleration in terms of the ball radius, r, i.e.

$$w^2 r = \left(\frac{380}{60}\right)^2 (0.07 - r),$$

which in the case of a single 25 mm diameter ball gives a value of 91.05 m s^{-2} (thus about 9 g), or in the case of a single 5.25 mm diameter ball a value of 106.48 m s^{-2} (about 11 g), i.e. an average value of 10 g. We used various balls and ball combinations, as shown in Table I.

In the course of experiments we observed a dramatic difference between milling with one and with a few balls: in the latter case, besides the smooth rolling action along the wall, there also occured terrible shocks among the balls and between the balls and the container wall or the cover of the container. However, with the use of only one ball or many balls the milling action is a smooth rolling process inside the ball mass.

In our case the milling atmosphere was air, and no other liquids or lubricants were used. High purity aluminium (99.999 %, Koch Light 5N) and nickel (>99%, Fluka A.G., puriss.) powders with 19.8 and 4.9 μm average grain size (as measured by Fisher SSS) were used; titanium of analytical purity (titanium sponge, British Drug House) was used in granulated form with granules of about 1 mm in diameter. These granules were separately hammered and preliminary milled with a single agate ball for 4 hours to obtain a resonably fine fraction.

Seven grams of Ni-Ti powder mixture of Ni_2Ti stoichiometry and about 10 grams of Ni-Al powder mixture of approximate Ni_3Al_2 stoichiometry (actually $Ni_{28}Al_{20}$) were weighed and milled cumulatively with various ball combinations. The processing dynamics in terms of the designations given in Table I is shown in Table II. After different milling times small quantities of samples were extracted from the container for the purpose of X-ray diffraction analysis using film technique. A Siemens 114.6 mm Debye-Scherrer camera and nickel-filtered copper radiation were used. The samples were filled into glass capilaries of 0.3 mm in diameter and exposure time was about 20 hours. For scanning electron microscopy the samples were placed on the sample holder, and were covered with carbon layer.

RESULTS AND DISCUSSION

The sequences of the X-ray powder diffraction patterns of the samples milled for different total times are reproduced in Figs.2 and 3. Corresponding d-values are calculated and listed in Tables III and IV. In addition, the scanning electron micrographs of significant samples are given in Figs.4-7. From the results presented in this report the general conclusion can be drawn that milling with a single ball, be it agate or hard metal (regimes A and D), for reasonable times, leads only to lattice distorsions, causing neither real amorphization nor alloying processes. This conclusion might be extended to milling with many steel balls (regime E). In contrast, the shocking action of several balls (regimes B and, particularly, C) strongly pushes the process in either direction, i.e. the alloying and amorphization processes occur simultaneously. We would like to note here that the X-ray powder diffraction patterns taken from samples at the end of the milling for both systems under investigation

do not conform with any intermetallide, oxide or nitride registered in the ASTM Data File available to us. Thus, the new phases seem to be obtained in both the Ni-Ti and the Ni-Al system. It is also evident that these phases have a highly amorphyzed structure.

On the basis of the results described above one may conclude that in our case amorphization and alloying in both systems take place simultaneously. The obtained degree of amorphization cannot be simply attributed to the particle size effect, because the smallest diameter observed does not drop much below 100 nm (Fig.4-7), and with the given upward scattering it is still too large to provoke such a drastic halloing of diffraction lines. The amorphization may be the effect of mechanical stresses existing within the particles. What is more surprising is the fact that amorphization was not complete as has been observed in other similar experiments reported /6/. The possible answer might be sketched along the lines expressed in the paper of Schultz /7/, who investigated the high-energy ball milling effect in powder mixtures of the Ni-Zr system, using Fritsch's laboratory equipment (Pulverisette model 5) with a centrifugal acceleration of 12 g value, which is comparable with the characteristical 10 g value for our apparatus. He assumes that the partial crystallization which occurs at high intensity milling is due to the development of heat. This may relate particularly to the Ni-Al system which forms intermetallics via a strong exotermic reaction /1/. Another possible explanation might be the lack of a protective atmosphere in our experiments which might favor atoms of oxygen or nitrogen to penetrate into the crystal lattice in order to form some complex compounds, and this reaction might prevent amorphization. Therefore, the use of a controlled atmosphere in our experiments could help to resolve this problem. However, the decision on whether the non-appearance of a total amorphization is due to nonmetal atoms present in the lattice or should not be delayed until the results of chemical and other relevant analyses of prepared powders become known.

ACKNOWLEDGEMENT

The authors are wholeheartly grateful to Dr J.Krawzynski and Dr W.A.Kaysser for the invitation and for the financial support for one of the authors(D.D.) to attend the 9th German-Yugoslav scientific meeting held in Hirsau (F.R.G.) and to present this contribution; and

also to Professors B.Leontić and E.Babić and to Mr D.Mandjurov and Mr M.Goger for their interest in this work, to Mrs. J.Čorko for typing the manuscript. Financial support from the Self-Managed Council for Scientific Research of Croatia (Yugoslavia) and the N.B.S.T. (U.S.A.) is gratefully acknowledged.

REFERENCES:

/1/ D.Dužević, Poroškovaja metalurgija, 155 (1975) 98.
/2/ L.N.Guseva, G.S.Makarov, Dokladi AN SSSR, 77 (1951) 615.
/3/ A.Tonejc, D.Ročak, A.Bonefačić, Acta Metallurgica, 19 (1971) 311.
/4/ D.Dužević, A.Bonefačić, D.Kunstelj, Scripta Metallurgica, 7 (1973) 883.
/5/ D.Dužević, Ibid, 9 (1975) 543.
/6/ R.B.Schwartz, Materials Science and Engineering, 97 (1988) 71.
/7/ L.Schulz, Ibid, 97 (1988) 15.

Table I. Designations of Milling Ball Combinations

Designation	Material	Number of Balls Ø25mm	Ø16mm	Ø12mm	Ø10mm	Ø5,52mm	Total mass (g)
A	agate	1	-	-	-	-	22
B	hardmetal	-	2	-	-	-	55
C	"	-	4	1	7	-	160
D	"	1	-	-	-	-	105
E	steel	-	-	-	-	500	350

Table II. Distribution of Total Milling Time among Ball Combinations

System	Total time (hours)	Hours per Combination in Order of Appearance (cf. Table I) A	B	C	D	E
Ni-Ti	0	-	-	-	-	-
"	72	72	-	-	-	-
"	102	72	30	-	-	-
"	109	72	30	7	-	-
"	122	72	30	20	-	-
"	130	72	30	20	8	-
Al-Ni	0	-	-	-	-	-
"	8	8	-	-	-	-
"	15	8	-	7	-	-
"	20	8	-	12	-	-
"	40	8	-	32	-	-
"	44	8	-	32	-	4

Table III. d-values of X-ray diffraction patterns in the system Ni-Ti taken after different total milling times (cf. Table II).

ASTM-values (in Å) with indices (hkl) in brackets		Total milling time (hours)					
Ni(fcc)	Ti(hex.)	0	72	102	109	122	130
-	2,557(010)	2,552	-	2,56	-	-	-
-	-	-	-	-	2,50	2,50	2,50
-	-	-	-	2,45	-	2,45	2,45
-	2,342(002)	2,334	-	2,32	-	-	-
-	2,244(011)	2,245	-	2,23	-	-	-
-	-	-	-	-	2,20	-	-
-	-	-	-	-	-	2,18	2,18
-	-	-	-	2,07	-	2,08	2,08
2,034(111)	-	2,029	2,03	2,03	2,03	-	-
1,762(200)	-	1,759	1,76	1,76	1,77	-	-
-	-	-	-	-	1,68	1,69	1,69
-	1,726(012)	-	-	-	-	-	-
-	1,475(110)	1,478	1,48	1,48	1,48	1,48	1,48
-	1.332(103)	1,333	1,33	1,33	-	-	-
-	1,276(200)	-	-	-	-	-	-
1,246(220)	1,247(112)	1,247	1,25	1,24	1,25	1,26	1,26
-	1,233(201)	-	-	-	-	-	-
-	-	-	-	-	-	1,20	1,20
-	1,171(004)	-	-	-	-	-	-
-	1,122(202)	-	-	-	-	-	-
-	1,065(014)	1,065	1,06	1,06	1,07	-	-
1,062(311)	-	-	-	-	-	1,03	1,03
1,017(222)	-	1,017	1,017	1,02	1,02	-	-
-	0,990(203)	0,990	-	0,99	-	-	-
-	0,946(211)	0,946	-	0,94	-	0,95	0,95
-	-	-	-	-	-	0,93	0,93
-	0,918(114)	0,915	-	0,917	-	-	-
-	0,893(212)	-	-	0,89	-	-	-
0,881(400)	0,880(015)	0,883	0,88	-	-	-	-
-	0,863(204)	-	-	-	-	-	-
-	0,851(300)	-	-	0,85	-	0,85	0,85
-	0,821(213)	0,823	-	-	-	-	-
0,808(331)	-	0,81	0,81	0,81	-	-	-
0,788(420)	-	0,788	0,79	-	-	-	-

Table IV. d-values of X-ray diffraction patterns in the system Ni-Al taken after different total milling times (cf. Table II)

ASTM-values (in Å) with indices (hkl) in brackets		Total milling time (hours)					
Ni(fcc)	Al(fcc)	0	8	15	20	40	44
-	-	-	-	2,86	2,86	2,86	2,86
-	-	-	-	-	-	2,44	2,44
-	2,338(111)	2,338	2,338	-	-	-	-
2,034(111)	2,024(200)	2,034	2,04	2,04	2,04	2,04	2,04
1,762(200)	-	1,762	1,76	1,78	1,78	1,78	1,78
-	-	-	-	1,66	1,66	-	-
-	-	-	-	1,57	1,57	-	-
-	1,431(220)	1,432	1,43	1,44	1,44	1,44	1,44
1,246(220)	-	1,244	1,25	1,25	1,25	1,25	1,25
-	1,221(311)	1,221	1,22	-	-	-	-
-	1,169(220)	1,169	1,17	1,17	1,17	1,17	1,17
-	-	-	-	1,08	1,08	-	-
1,062(311)	-	1,056	1,06	1,07	1,07	1,07	1,07
1,017(222)	-	1,015	1,02	1,02	1,02	1,02	1,02
-	1,012(400)	-	-	-	-	-	-
-	0,929(331)	0,928	0,93	-	-	-	-
-	0,906(420)	0,906	0,91	-	-	-	-
0,881(400)	-	0,880	0,88	-	-	-	-
-	0,827(422)	0,826	0,83	-	-	-	-
0,808(331)	-	0,808	0,81	-	-	-	-
0,788(420)	-	0,788	0,79	-	-	-	-
-	0,779(333)	0,779	0,78	-	-	-	-

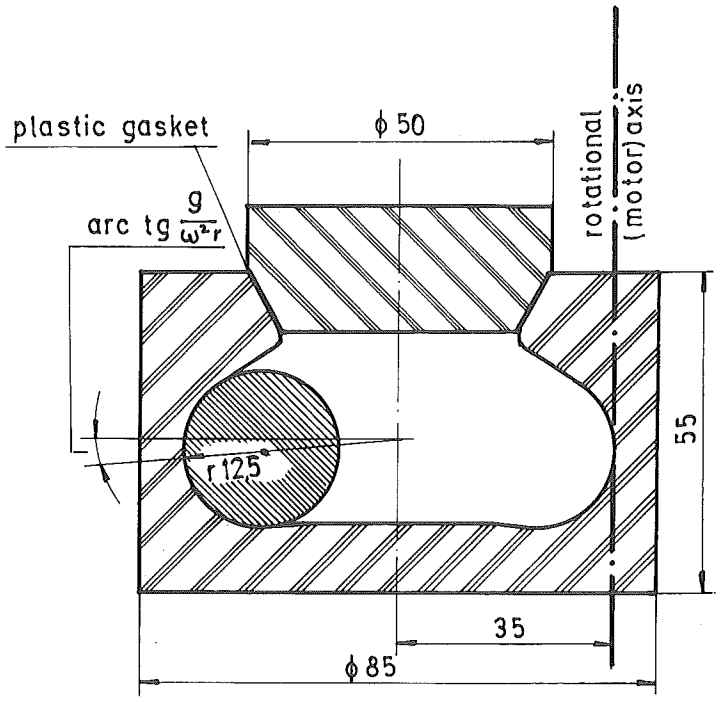

Fig.1 Sketch of the container design.

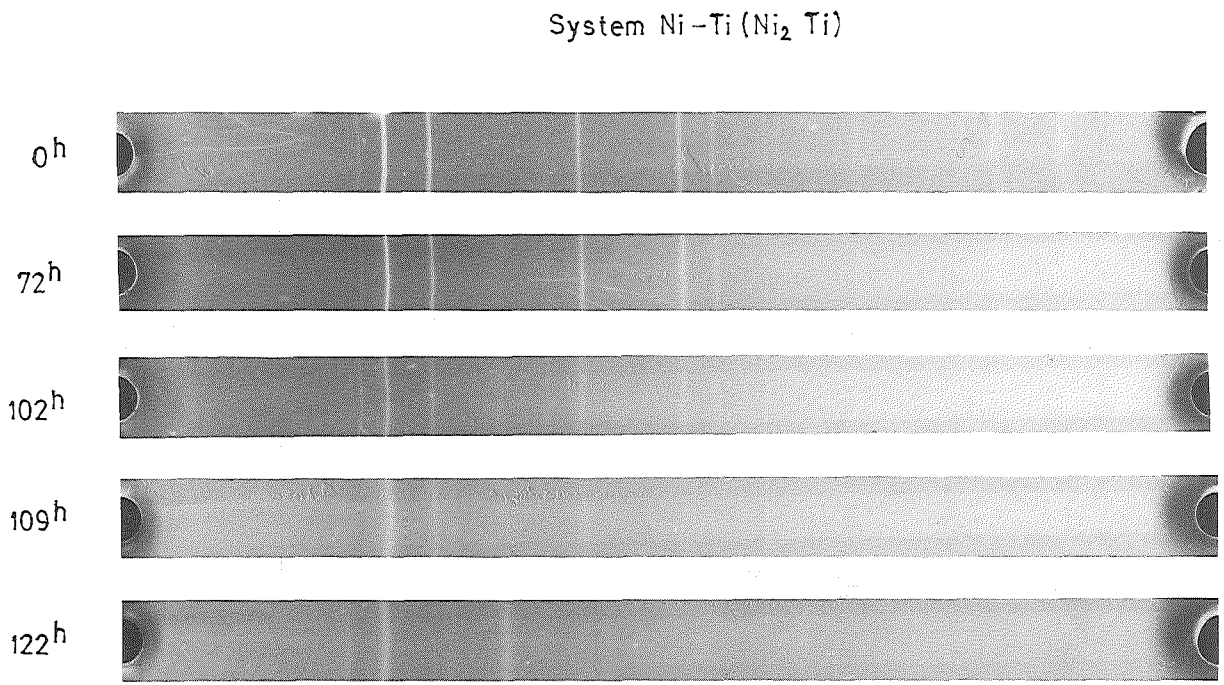

Fig.2 X-ray diffraction powder patterns of samples of Ni-Ti powder mixture extracted after different total milling times (cf. Table II).

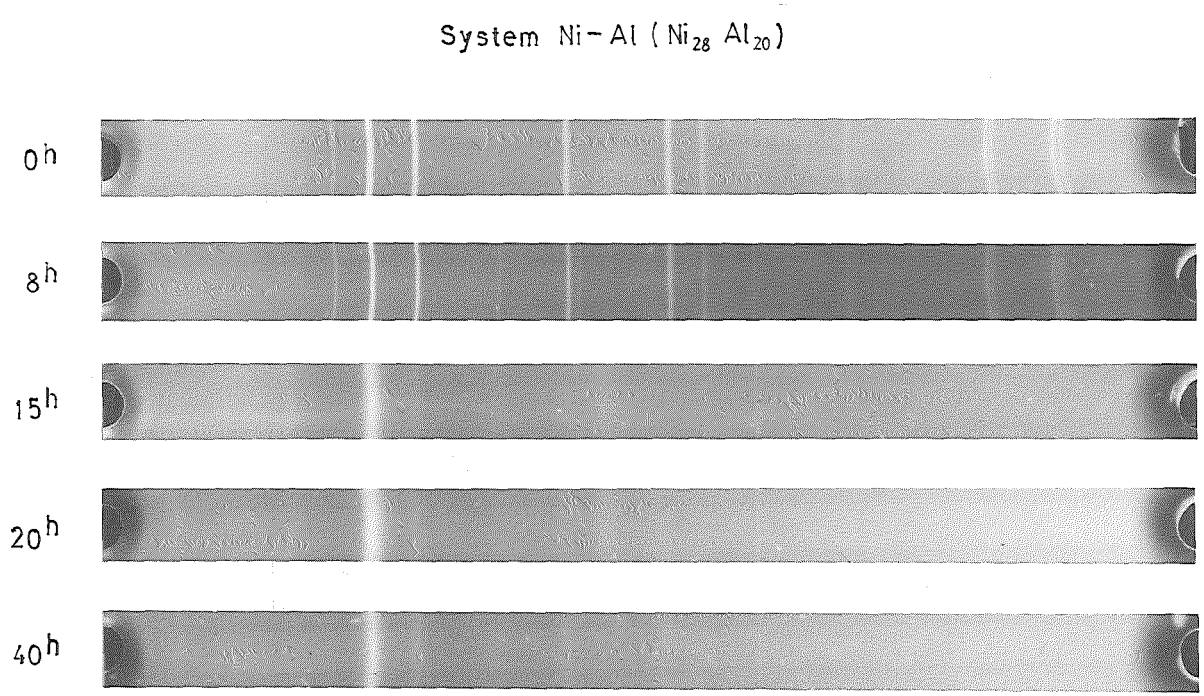

Fig.3 X-ray diffraction powder patterns of samples of Ni-Al powder mixture extracted after different total milling times (cf. Table II).

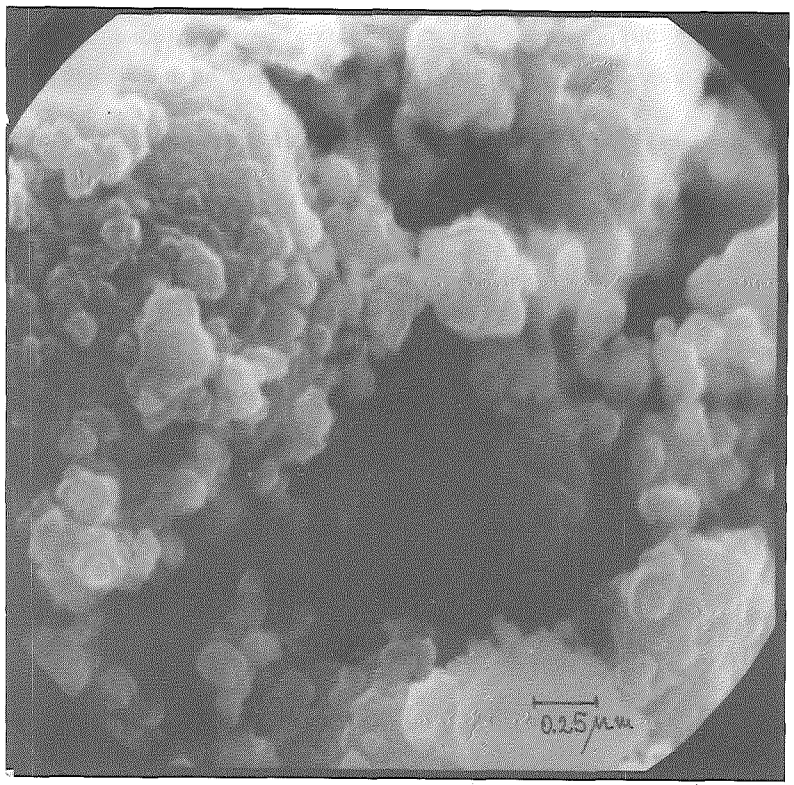

Fig.4 Scanning electron micrograph of Ni-Ti powder sample extracted after 122 hours of milling (cf. Table II).

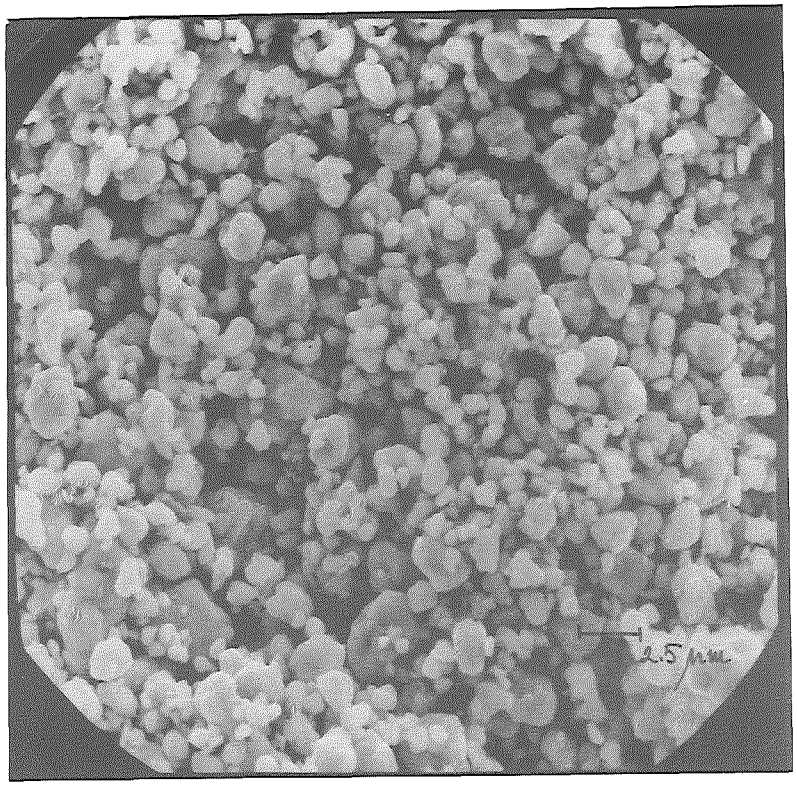

Fig.5 Scanning electron micrograph on Ni-Al powder sample extracted after 15 hours of milling (cf. Table II).

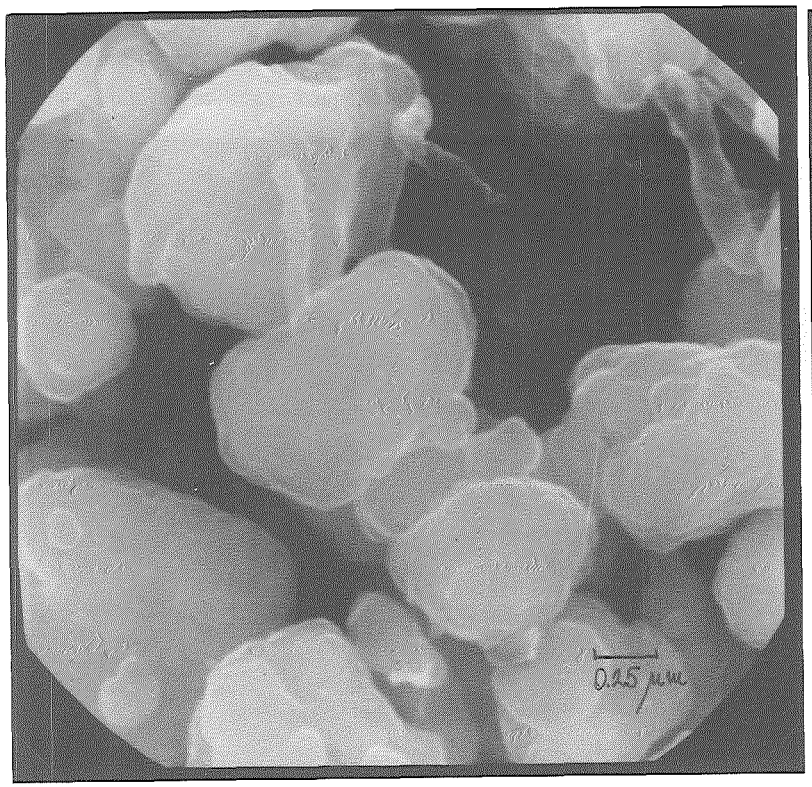

Fig.6 Scanning electron micrograph of Ni-Al powder sample extracted after 15 hours of milling (cf. Table II).

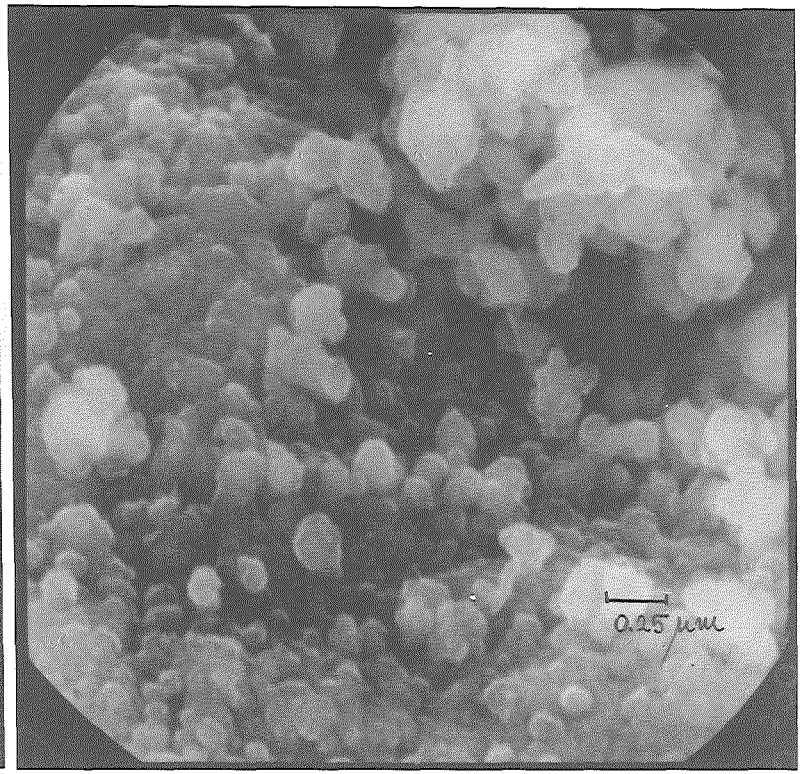

Fig.7 Scanning electron micrograph of Ni-Al powder sample extracted after 40 hours of milling (cf. Table II).

Growth and Microstructural Development of Melt-Oxidation Derived Al_2O_3/Al - Base Composites

M. Sindel and N. Claussen
Technische Universität Hamburg-Harburg, F. R.G.
Advanced Ceramics Group

Abstract

The microstructural evolution of an Al_2O_3/Al composite grown from the molten metal surface either into free space or into a filler material is discussed. The filler materials to be "infiltrated" were different α-Al_2O_3 powders, Al_2O_3 fibers, SiC particles and SiC whiskers. The matrix formation mechanism and the reaction kinetics are discussed with respect to reaction temperature and filler type. The microstructure of matrix and matrix-filler composites is presented and K_{Ic} and fracture strength, are given.

1. Introduction

The oxidation of molten metals is a widely investigated subject, mostly done to prevent this undesired reaction. Recently this type of reaction was applied in a controlled way to manufacture ceramic-metal composites. This new melt-oxidation process, also known as Lanxide process /1/, is based on the reaction of molten metals with a vapor phase oxidant. A solid ceramic body is formed by a directed growth process of the oxide either into free space or a preformed filler body. The porous filler body, usually formed by conventional P/M techniques, can be coated with a growth barrier so that nearly the initial shape of the body is maintained after reaction.

Most processing techniques for fabricating ceramic materials are based on sintering which always involves dimensional changes usually associated with several draw-backs. Also, techniques involving little or no shrinkage, such as CVI, slurry or sol-gel infiltration of porous preforms exhibit disadvantages, e.g., high residual porosity, long exposure times and high costs etc..

The directed oxidation of molten metals represents an alternative technology overcoming some of these limitations.

2. Experimental

The specimens were prepared in a commercial box furnace using heating rates of 10 K/min up to mostly 1325 K and dwell times of 12 to 48 h. A scheme of the reaction process is given in Fig.1. The received composites were characterised by optical microscopy, SEM and TEM as well as by X-ray diffraction and energy-dispersive analysis in SEM and TEM. Fracture strength and KIc were measured by ISB in four or three point bending. The reaction kinetics were examined using a commercial microbalance. For the metal melt oxidation process to take place the aluminum has to contain certain elements, e.g. Mg (about 0.5-5 w/o) and Si (about 1-10 w/o) /1/. The filler materials used were two different sized α-aluminas (3 μm and 13 μm, H.C.Starck), alumina-zirconia fibers (PRD-166, DuPont) ,SiC grains (53 μm, LONZA), and SiC whiskers (SCW1-SH, Tateho).

3. Results and Discussion

3.1 Microstructure

At the beginning of the oxidation process a Mg/Al-spinel layer is formed containing the microchannels responsible for the time-linear weight gain of the process. This channel structure is maintained in the α-Al_2O_3 product which grows on top of the primary spinel layer. A typical example of the channel structure is shown in Fig.2. Through the three-dimensionally interconnected channels visible as bright areas liquid metal is supplied to the reaction front by capilarity forces. Numerous low-angle boundaries are found between the alumina grains formed by the oxidation process (see Fig.3). Furthermore dislocations at the grain boundary indicate a glass- phase free interface. The channels are only stable at high-angle boundaries /2/. When the matrix grows into an inert filler material, the same growth principle applies. A system of channels is formed and the matrix surrounds the filler perfectly, as shown for example in Fig.4. The TEM micrograph in Fig.5 shows the reaction formed alumina matrix grains to be in the size of ~1-2 μm. When a small grain size alumina filler, e.g. 3 μm or smaller, is used, the formation of the matrix is hindered, and infiltration is imperfect, i.e., inhomogeneous and porous. TEM study of the product reveals a much smaller grain size of the matrix alumina formed by oxidation (Fig.6). The reason for this behavior is not yet understood. Like coarse particles, continuous fibers can be embedded by the matrix. The ZrO_2- containing alumina fibers used in the present study are completely enclosed in the dense matrix. (The micrograph shows the unidirectional fiber arrangement in Fig.7). In

the same way non oxide fillers can be used. In the case of a SiC filler, the particle size must not be too small (i.e. < 1 μm) because SiC will be consumed by the reaction with the aluminum as demonstrated with small SiC whiskers in Fig.8. When coarse SiC particles are used, the matrix grows around the particles (see Fig.9) and the metal "cleans" the particle surface from SiO_2 according to the follwing reaction

$$4Al + 3SiO_2 \rightarrow 2Al_2O_3 + 3Si.$$

3.2 Kinetics

The matrix growth is different to many other oxidation reactions, linear in time. The weight-gain as a function of time is shown in Fig.10. Two temperature plateaus at 1425 and 1325 K were used . During the first plateau a long incubation period is exhibited before linear growth is attained. This is probably due to the formation of the initial spinel layer. A drop in temperature of 100 K done after 5 h causes a sharp change in the slope of the curve. This behavior suggests a thermally-activated process of the form $\Delta m \sim \exp(-Q/kT)$ as the rate-controlling process for this reaction. However, this is a preliminary result and further work needs to be done on the kinetics of this process. The macroscopic growth velocity is in the range of ~2cm/24h, it is mainly affected by the content and type of alloying elements.

3.3 Mechanical Properties

Due to the residual metal in the ceramic composite the physical behavior is modified with respect to the oxide alone. The content of metal phase can be manipulated by several parameters like reaction time, alloy composition, type of filler material etc.. Usualy it is in the range of 3-30 w/o. A high metal content e.g., 30 w/o, results in enhanced toughness of the material. Some mechanical properties are given in table 1. The fibers used in these experiments enhance the strength to 400 MPa, whereas the coarse SiC particles (53 μm) reduce the strength to 200 MPa but an enhanced fracture toughness of 6 $MPa\sqrt{m}$ remaines. The properties of the SiC and the Al_2O_3 fiber composite are however not optimized yet. The main reason for the toughening is the plastic deformation of the metal phase. During crack propagation the plastically deformed metal particles bridge the crack. Complete necking of the aluminum can be observed on the fracture surfaces (Fig.11). In this case the good bonding between fiber and matrix is obvious since no pull-out occured. This can be improved by suitable coatings of the fibers /3/.

4. Conclusions

The process of directed oxidation of molten metals is suitable to produce dense, tough and strong ceramic composites. One of the main advantages is the shrinkage-free processing. Characteristic of the process are the formation of an initial spinel layer and the time linear growth.

Literature

/1/ M.S. Newkirk et al., Formation of Lanxide Ceramic Composite Materials, J.Mat.Res., 1 (1986), 81-89;
/2/ M.K. Aghajanian et al., Properties and Microstructures of Lanxide Al_2O_3-Al Ceramic Composite Materials, J.Mat.Sc., 24, 658;
/3/ P. Barron-Antolin et al., Properties of Fiber-Reinforced Alumina Matrix Composites, Ceram.Eng.Sci.Proc., 9 (1988), 759-766;

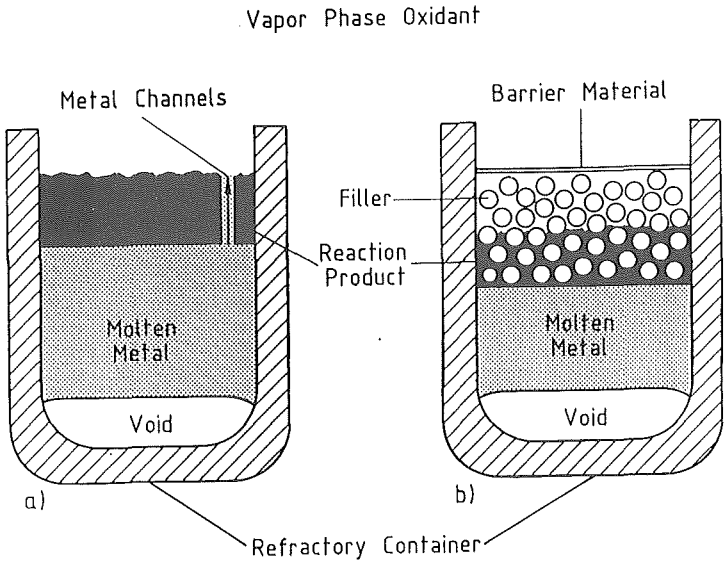

Fig.1: Schematic diagram of the melt-oxidation process, growth of metal/oxide composite, a) into free space and b) into filler.

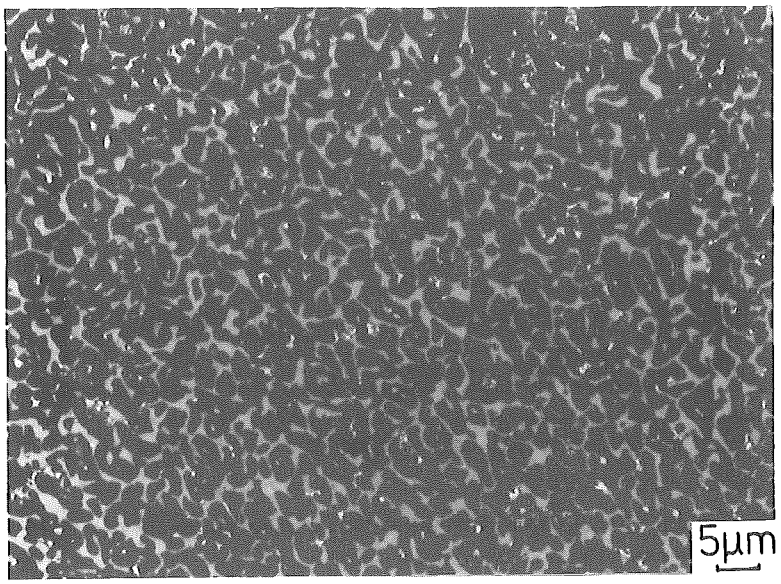

Fig.2: Optical micrograph of an Al_2O_3/Al product grown at 1325 K in air. Dark phase is α- Al_2O_3, bright phase aluminum alloy.

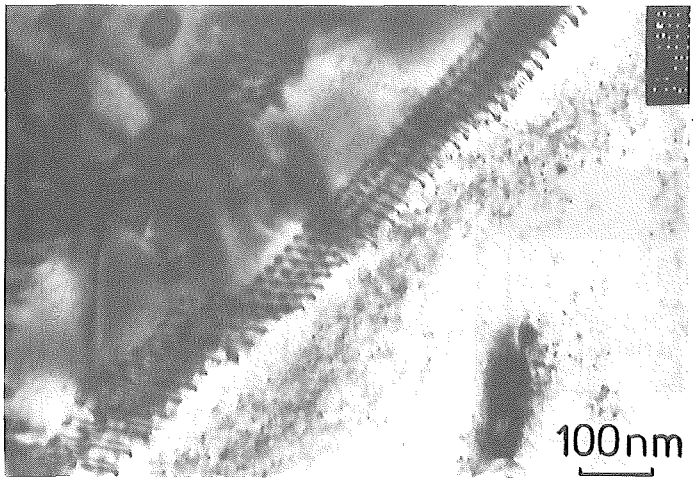

Fig.3: TEM micrograph of Al-alloy/Al_2O_3 matrix.

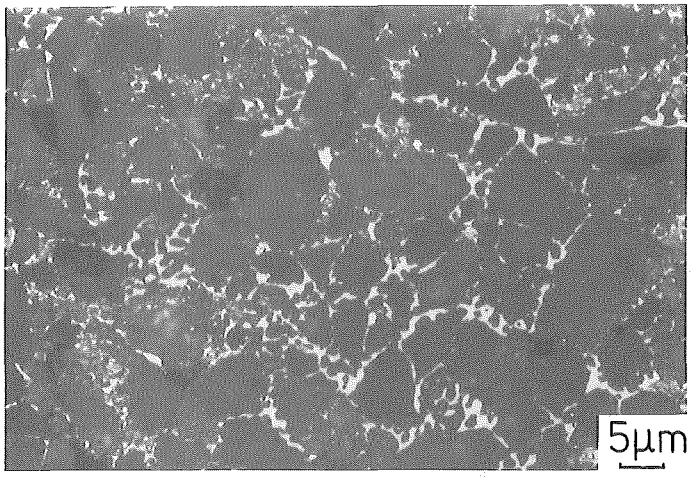

Fig.4: Optical micrograph of Al-alloy/Al_2O_3 matrix grown at 1325 K into a coarse (13 µm) α- Al_2O_3 filler.

Fig.5: TEM micrograph of Al-alloy/Al_2O_3 matrix grown into a coarse (13 µm) α- Al_2O_3 filler.

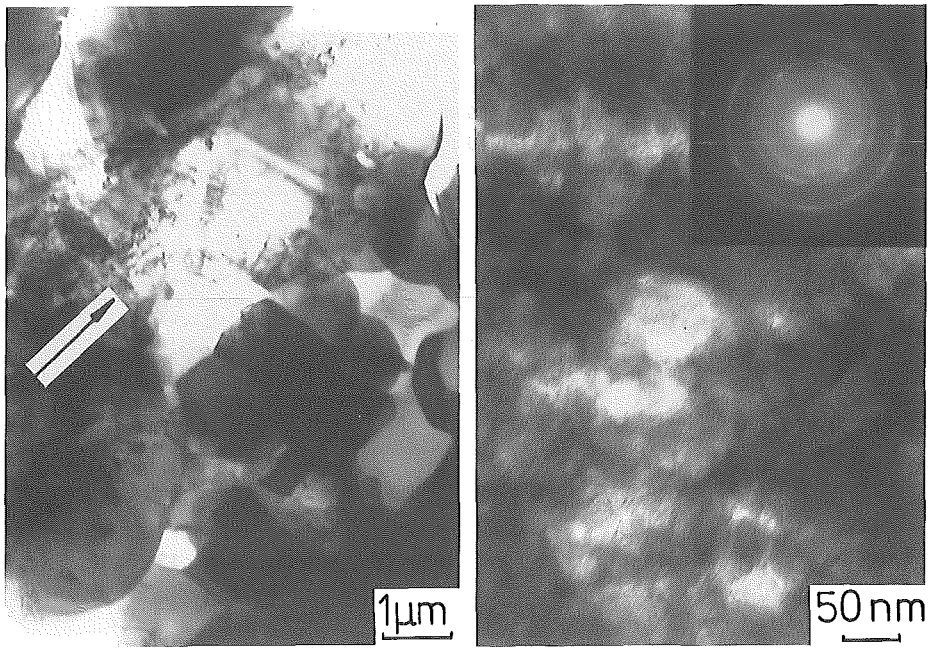

Fig.6: TEM micrograph of Al-alloy/Al_2O_3 matrix grown into a fine (3µm) α- Al_2O_3 filler, a) general microstructure, b) magnification and electron diffraction pattern of area marked with arrow.

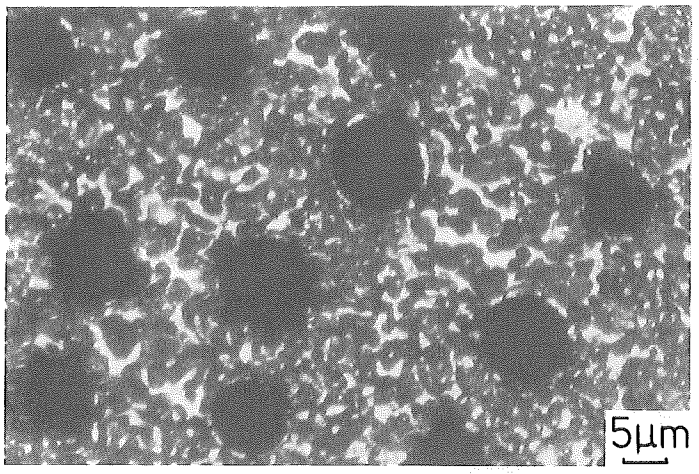

Fig.7: Optical micrograph of Al-alloy/Al_2O_3 matrix grown into ZrO_2-containing Al_2O_3 fibers.

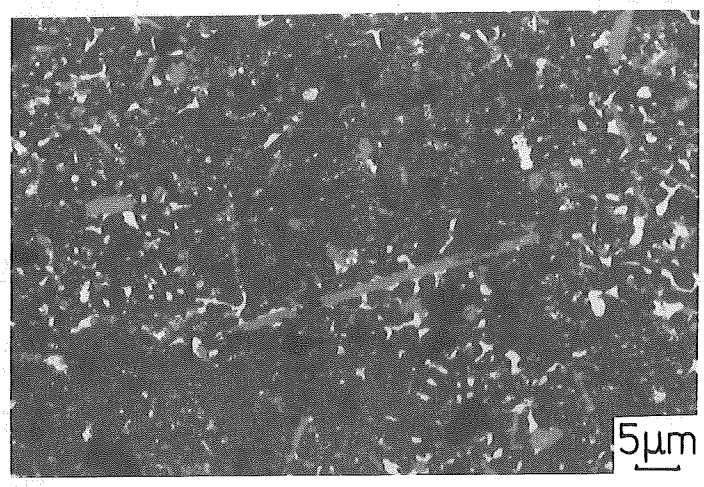

Fig.8: Al-alloy/Al_2O_3 matrix grown into SiC whiskers at 1325 K. The small whiskers has been severely attacked by the reaction with molten aluminum.

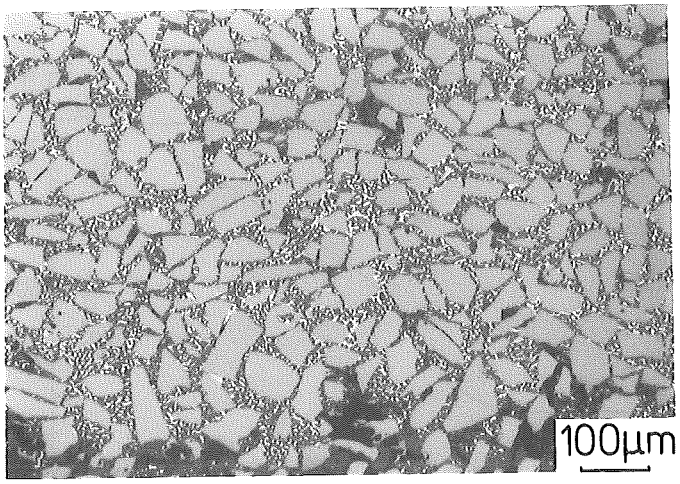

Fig.9: Al-alloy/Al_2O_3 matrix grown into a (53µm) SiC filler at 1325 K.

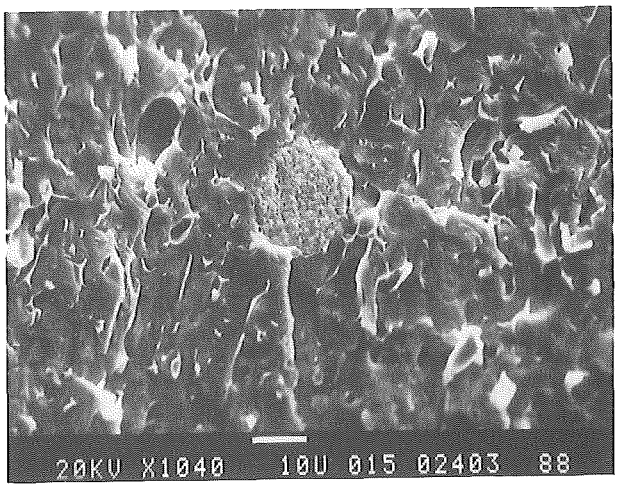

Fig.10: Thermogravimetry diagram of Al-alloy/Al_2O_3 matrix growth into free space.

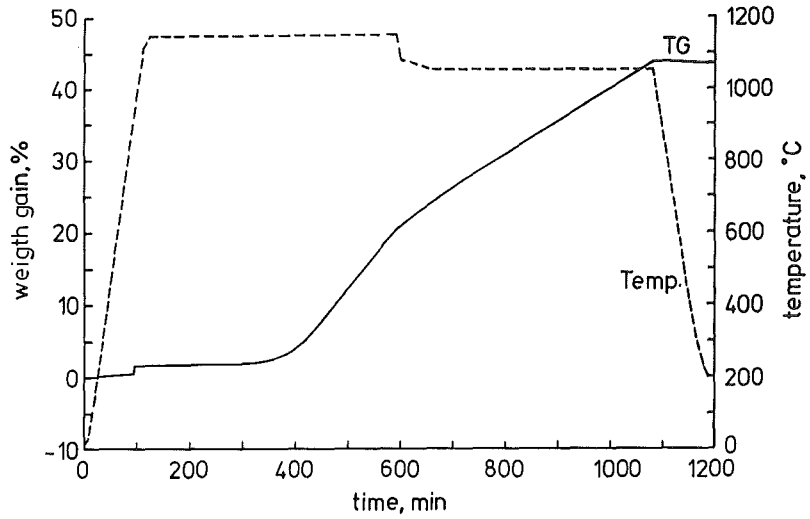

Fig.11: Fracture surface of a composite with Al-alloy/Al_2O_3 matrix and Al_2O_3 fibers.

	bending strength, MPa	fracture toughness, MPa$\sqrt{m}$	
matrix	350	9.5	Ref.2
matrix + SiC particles (53μm)	201	6	this work
matrix + ZrO_2-containing Al_2O_3 fibers	402	n.d.	this work

Table 1: Mechanical properties of Molten-Metal derived Ceramic Composites

Fabrication of RBSN Composites

Rolf Janssen and Nils Claussen

Technische Universität Hamburg-Harburg
Advanced Ceramics Group
D 2100 Hamburg 90, F.R.G.

Introduction

Composites based on reaction bonded silicon nitride (RBSN) offer essential advantages compared to hot-pressed (HPSN) and sintered (SSN) silicon nitride based materials, e.g. simple P/M processing, easy green state machining and low shrinkage. Due to the volume expansion during silicon nitridation, the shrinkage of RBSN composites is negligible and the shrinkage of post densified RBSN is < 8%. This offers a high loading capacity of reinforcing components compared to conventional ceramics with shrinkages of 15 - 20 % .

High strength second- phase particles of various shapes, located in the field of a propagating crack, can improve the fracture toughness of ceramics by a reduction of the stress intensity/1/. Incorporation of rod-shaped (fibers or whiskers) or disk-shaped (platelets) particles can increase K_{IC} by deflection and bridging of the crack. The reinforcing component must be stable during manufacturing of the composites and should not degradate or react with the matrix material and the atmosphere. Degradation of the reinforcing component is well-known in the case of polycrystalline fibers (e.g. Nicalon) where grain growth, cristallization of amorphous parts and phase reactions lead to a decrease of fiber strength during high- temperature processing. In the case of monocrystalline reinforcements such as whiskers or platelets degradation can occur due to phase reactions and changes of morphology .

Silicon carbide reinforced silicon nitride composites offer a high potential for advanced mechanical applications. Degradation of the silicon carbide component during processing of the composites in nitrogen occurs according to the reaction

$$3\ SiC(s) + 2\ N_2(g) \rightarrow Si_3N_4(s) + 3\ C(s) \qquad [1]$$

Annealing in oxygen- containing atmosphere results in silica formation on the surface:

$$SiC(s) + 2\ O_2(g) \rightarrow SiO_2(s) + CO_2(g) \qquad [2]$$

The open porosity of the RBSN samples enhances the silica formation. In the case of SiC-fiber reinforced RBSN composites, fiber degradation during reaction bonding was reported such as pitting and production of α-silicon nitride whiskers on the fiber surface /2/ leading to strength degradation of fibers. However, other authors did not observe this type of degradation /4-6/. Degradation of SiC whiskers during reaction bonding of silicon has not yet been observed/7-11/.

The aim of this work was to investigate the degradation mechanism of the most promising components for reinforcing RBSN (SiC, B_4C, TiB_2) under reaction bonding conditions.

Experimental

Materials

The following powders were used in the experiments.

Components	Shape	Size [µm]	Supplyer
SiC	equiaxed	0.1 - 2 diameter	Starck
SiC	whisker	0.1 - 1 "	Tateho
SiC	platelet	40 - 200 "	American Matrix
B_4C	whisker +	1 - 10 "	American
	platelet	5 - 150 length	Matrix
TiB_2	equiaxed +	0.5 -20 diameter	Starck
	platelet	5 - 15 length	
Si	equiaxed	0.8 - 6 diameter	Starck

Annealing and Reaction Bonding

A small quantity (0,2 g) of the reinforcing component was annealed in an alumina crucible in a tungsten heated furnace with a 'quasistatic' atmosphere together with reacting silicon samples. The set-up is based on a cold-wall vacuum furnace. The total nitrogen pressure was set up in the range of 960-980 mbar. A molybdenum protective hood was placed over the crucibles and silicon samples to improve the equilibrium conditions with respect to an experiment in flowing nitrogen, where traces of formed Si and SiO vapor will be quickly removed.

The influence of reaction atmosphere was investigated using pure nitrogen and a mixture of nitrogen, hydrogen and helium. Hydrogen additions are assumed to assist the removal of the SiO_2 layer from the Si surface /12/, where as hydrogen and helium additions enhance the molecular diffusivity and thermal conductivity /13/. The total annealing time was 70 h in both cases.

Composites were prepared by attrition milling in MEK and ethanol (2:1). After rotovap drying, test bars were uniaxially prepressed at 50 MPa in a metal die and isostatically pressed at 500 MPa. Nitridation was carried out in a vacuum furnace as described earlier at temperatures between 1100 and 1450°C with a cycle time of 70 h.

Determination of Reaction Kinetics

Silicon carbide powder was used to determine the kinetics of the SiC nitridation reaction [1] in a thermal balance (Netzsch STA 409) in flowing nitrogen at 1420°C.

Mechanical Testing

The flexural strength of the reaction bonded samples was measured in four point bending with 20/40 mm span. Fracture toughness was measured by an indentation method (ISB) using a load of 200 N.

Microstructure Analysis

The phase composition was analyzed by XRD using copper K_α-radiation (Philips PW 1820) before and after annealing. Morphology and chemical composition were examined by analytical SEM (Jeol JSM840A with Link EDS using a ultra-thin window).

Results and Discussion

Stability of Reinforcing Component

Silicon Carbide

Si_3N_4 - SiC composites can only be fabricated when a certain ratio of nitrogen-partial pressure to temperature is kept according to the possible decomposition reactions [1] and [3].

$$Si_3N_4(s) \rightarrow 3\ Si(l) + 2N_2(g) \qquad [3]$$

Thermodynamic calculations based on data given in Table 1 indicate a decomposition of SiC during reaction bonding of Si according to reaction [1].

nitridation of Si is normally carried out at atmospheric N_2 pressure in the temperature range between 1100 and 1450°C. SiC is thermodynamically not stable at temperatures < 1440°C and 0.1 MPa N_2 (Fig.1)/14/ .

Annealing of β-SiC powder (polytype 3C) shows no influence of heat treatment on phase composition - analyzed by XRD - during annealing in N_2 or N_2-He-H_2 (Fig. 2). The same result is found using SiC whiskers (polytypes 3C,6H,4H)(Fig.3). SEM investigations also indicate no influence of heat and nitrogen treatment on morphology and chemical composition; only Si and C is detected using EDS (Fig. 4).

The reason for the thermodynamically unexpected stability of SiC in N_2 is assumed to be the protective effect of the SiO_2 layer on the surface of SiC. TEM investigations shows , that this layer is dense and can be estimated to be 2 nm thick /15/. This agrees with BET and oxygen measurements, from which the SiO_2 layer thickness on SiC whiskers is calculated to be 2 nm whereas the SiO_2 layer on SiC powder is limited to 0.2 nm.

At the beginning of the nitridation reaction, no contact areas can be formed between the SiO_2 on the surface of SiC and the Si in the pressed compact due to the separating effect of SiO_2 on the Si surface. With increased Si_3N_4 formation during reaction bonding, the contact components change to SiO_2 on the SiC surface and Si_3N_4 which forms on the Si surface. As consequence, a reaction between the SiO_2 on the SiC surface and the Si can be disregarded. Under nitriding conditions, SiO_2 on the SiC surfaces will decompose according to the reaction

$$SiO_2\ (s) \Rightarrow SiO\ (g) + 1/2\ O_2\ (g) \qquad [4]$$

The equilibrium partial pressure of SiO is calculated by Gibbs energy change

$$\Delta G^{O} = -R*T*\ln\left[P_{SiO}*P_{O_2}^{1/2} \right] \qquad [5]$$

for pure N_2 atmosphere.

During the nitridation process, the reaction chamber must be refilled stepwise with N_2 due to the consumption of N_2 by the Si nitridation reaction . N_2, however, contains traces of O_2 (< 3 vpm) and - due to the replenishment of the chamber - the O_2 content can increase up to 20 vpm, resulting in a decrease of SiO partial pressure.

The SiO_2 layer on Si particles decomposes during silicon reaction bonding according to the reaction

$$Si\ (s) + SiO_2\ (s) \Rightarrow 2\ SiO\ (g) \qquad [6]$$

with a SiO partial pressure in the range of $4*10^{-6}$ to $8*10^{-3}$ bar at a temperature of 1000 - 1400°C (Fig.5). The SiO partial pressure according to reaction [6] is more than 10^5 times higher than the partial pressure of the decomposition reaction [4] of surface SiO_2 on SiC and the equilibrium of reaction [4] is shifted to the right side and the 'protective' SiO_2 on SiC surfaces becomes stable.

The thermodynamic calculations are based on equilibrium conditions which can not be achieved in the real reaction- bonding process. In this case, the SiO partial pressure is reduced by an active catalytic reaction of SiO during beginning α-Si_3N_4 formation and precipitation on the cold parts of the furnace.

According to the 'static' atmosphere in the experimental design, the decrease of P_{SiO} is rather low compared to experiments under flowing nitrogen. Therefore, the decomposition reaction of SiO_2 on SiC surfaces is suppressed by reaction [6] at the beginning of the nitridation. When all SiO_2 is removed from the Si surface by reaction [6], decomposition of SiO_2 from SiC surfaces occur. According to the oxygen contamination of the nitrogen and small remaining traces of gaseous SiO, the decomposition of SiO_2 on SiC surface (reaction [4]) is supposed to be suppressed for a certain period of time.

Products of the SiO_2 decomposition reaction are gaseous substances which must be transported from the SiO_2 surface to the gas atmosphere. The evaporation rate of a gaseous substance in vacuum can be estimated by the equation/16/:

$$\frac{m}{t*A} = P * \left(\frac{2\pi RT}{M} \right)^{-1/2} \qquad [7]$$

m = mass of vapor
t = time
A = area
M = molecular weight
P = partial pressure
T = temperature

The evaporation time for a 1 nm layer of SiO_2 evidently depends on the partial pressure of SiO etablished during the decomposition. At $P_{SiO}=10^{-5}$, the layer is removed in a few seconds, whereas at $P_{SiO}=10^{-10}$ several days are necessary. At $P_{SiO}=10^{-12}$ the

decomposition time is in the range of years and the layer is stable during nitridation (Fig. 6).

The decomposition reaction of SiC in N_2 can be divided into chemical reaction and diffusion to the reaction surface. Due to the lack of data a theoretical realistic approximation of the total reaction kinetics of SiC nitridation is not possible.
The thermal balance experiment with SiC powder annealed in flowing N_2 indicates a very fast SiO_2 decomposition during the heating period with a weight loss of 1.18%. This value is in good correlation which the oyxgen content of the starting SiC powder (Fig.7). During annealing at 1420°C, a weight gain of 9.22% was observed which may be explained by the nitridation reaction of SiC (reaction [1])(Fig.7). Stoichiometric nitridation of SiC would involve a theoretical weight change of 46,7% per mole SiC.

From experience it is known that SiC-heating elements exhibit a rather low reaction rate at temperatures up to 1350°C; at higher temperatures the reaction kinetics depend on the gas atmosphere (amount of oxygen and water vapor)and the active surface.

As a summary, it is evident that SiC components are stable during silicon nitridation under certain conditions. Decomposition of SiC can be assumed to occur in combination of the following conditions :

- no contamination of the gas atmosphere with oxygen and water vapor
- flowing gas atmosphere
- low oxygen contamination of the silicon used
- very long temperature/time cycle (sometimes necessary for large components)
- long time at temperatures in the range 1350 - 1440°C

Stabilization of SiC during nitridation of silicon can thus be achieved by keeping these parameters in the respective way.

Boron Carbide

B_4C is a suitable material for reinforcement of Si_3N_4 according to its high thermal expansion coefficent and Young's modulus compared to Si_3N_4 . Assuming strong bonding at the interface of matrix and reinforcing component, the thermal mismatch results in residual matrix compressive stresses.
Phase analysis (X-ray-diffraction) shows pure B_4C in the starting mixture of platelets and whisker, whereas in the annealed

material an additional peak at $d_{(hkl)}$ = 2.51 Å is observed. This lattice spacing corresponds with $d_{(111)}$= 2.51 Å indicating the formation of β-SiC (Fig. 8). No morphological change is observed by SEM investigations.
At high temperature B_4C, SiC and SiB_6 are found in the ternary system B-C-Si/17/. During nitridation a reaction between B_4C and the gaseous species takes place as indicated by the phase change, hence, a degradation of the reinforcing components is possible.

Titanium Boride

TiB_2 also exhibits a high expansion coefficent and Young's modulus. The most attractive advantage of TiB_2 as a reinforcement is the low electric resistance of $\sim 10^{-5}$ Ωcm which makes electrical discharge machining possible.
X-ray diffraction analysis indicates the formation of a new unknown phase during annealing in N_2 or N_2-He-H_2 at temperatures between 1100°C and 1450°C (Fig. 8). SEM characterization shows no influence of the heat treatment on the morphology . Because of rapid decomposition and the low aspect ratio of the platelets, TiB_2 does not seem to be attractive for reinforcement of RBSN .

RBSN - SiC composites

SiC can be used as reinforcing component for RBSN due to the protective influence of the silica layer on SiC. Thermodynamic calculation of the decomposition of this SiO_2 layer shows that a remarkable amount of SiO can be produced at high temperatures. This SiO formed during decomposition of SiO_2 from SiC surfaces reacts with nitrogen according to

$$3\ SiO(g) + 2N_2(g) \rightarrow Si_3N_4(s) + 1.5\ O_2(g) \qquad [8]$$

and increases the nitridation rate of remaining Si (Fig.9). The amount of remaining unreacted Si at high nitriding temperatures depends on the purity and morphology of the used Si powder. The powder used in this investigation shows a high reaction above the melting of Si. Due to the exothermic nature of the Si nitridation, macropores are formed around the SiC component with a decreasing effect on the mechanical properties of RBSN - SiC composites. Addition of 20 vol.-% SiC platelets reduces the strength from 200 MPa to 70 MPa, whereas the fracture toughness is within the same range. The toughening effect of SiC whiskers or platelets is suppressed by the negative efect of macropore formation and, therefore, K_{IC} of RBSN with 20 vol.% SiC powder, whiskers and platelets is slightly reduced (Fig.10).

Addition of nitriding additives increases the nitridation at low temperatures and decreases the amount of remaining Si at high temperatures and, as a consequence, decreases the macropore formation around the SiC component. This effect is found when 5 wt.-% Y_2O_3 and 2 wt.-% Al_2O_3 are added. RBSN - SiC platelet composites containing Y_2O_3 and Al_2O_3 shows the expected reinforcing effect of SiC platelets by a thoughness increase of about 40 % , whereas the strength is limited by the size of the large platelets used (Fig.10). Crack deflection is observed as the main toughening mechanism (Fig.11).

Conclusions

SiC can be used as reinforcing component for RBSN without critical decomposition of SiC due to the protective effect of surface SiO_2 , however, certain conditions must be fulfilled. Decomposition mainly depends on the thickness of SiO_2 on Si and SiC surfaces, on the O_2 amount of nitriding atmosphere and on nitridation conditions.
The use of B_4C and TiB_2 as reinforcing material is limited due to a reaction with the gas phase during nitridation.
The mechanical properties of RBSN - SiC composites are controlled by the occurrence of a macropores at high nitridation temperatures. Composites containing sintering additives shows a toughness increase when large platelets are added.

1. K.T.Faber, A.G.Evans
Crack deflection process
Acta Metall. 31 (1983) pp.565-576
2. T.L. Starr, J.N.Harris, D.L. Mohr
Reaction-sintered silicon nitride composites with short fiber reinforcement
Ceram.Eng.Sci.Proc. 8 (1987) pp.985-991
3. R.T. Bhatt
Mechanical properties of SiC-fiber reinforced reaction bonded Si_3N_4-composites
Techn. Rep. NASA TM-87085 (1985)
4. N.D. Corbin, G.A. Rosetti, S.D. Hartline
Microstructure/ property relationships for SiC-filament reinforced RBSN
Ceram.Eng.Sci.Proc. 7 (1986) pp.958-986
5. M.W. Lindley, D.J. Godfrey
Silicon nitride ceramic composites with high toughness
Nature 229 (1971) pp.192-193
6. D.B. Fischbach, D.B. McLaren
Exploratory research on silicon nitride composites
Techn. Rep. DOE/ET 13389-T1 (1982)
7. R. Carlsson, R . Lundberg
Fiber and whisker reinforcement of ceramic matrix components
Proc. of the Int. Symp. on Fine Ceramics Arita 1987 pp.47-61
8. R. Lundberg, L. Kahlmann, R. Warren, R. Pompe, R. Carlsson
Silicon carbide whisker reinforced silicon nitride composites
Am. Ceram. Soc. Bull. 66 (1987) pp.330-333
9. T.L. Starr, J.N. Harris
Fabrication of slip cast reaction sintered silicon nitride composites
II. Int. Symp.on Ceramic Materials & Components for Engines, Lübeck/F.R.G. 1986 ed. by W. Bunk, H. Hausner DKG-Verlag
10. F. Takao, W.R. Cannon, S.C. Danforth
Colloidal processing of SiC-whisker reaction bonded Si_3N_4-composites
to be published
11. J.W. Huang
SiC-whisker reinforced sintered reaction bonded silicon nitride
Annual Meeting of Am. Ceram. Soc. 1988 Cincinatti
12 N.J. Shaw
The combined effect of Fe and H_2 on the nitridation of silicon
J. Mat. Sci. Let. 1 (1982) pp.337-340
13. H. Kim, C.H. Kim
The influence of the various transport properties of the nitriding atmosphere on the formation of reaction bonded silicon nitride
J. Mat. Sci. 20 (1985) pp.141-156

14. K.G. Nickel, M.J. Hoffmann, P. Greil, G. Petzow
Thermodynamic calculations for the formation of SiC-whisker reinforced Si_3N_4-ceramics
Advanced Ceramic Materials 3 (1988) pp.557-562
15. M. Rühle
private communication
16. O. Kubaschewski, G.B. Alcook
Metallurgical thermochemistry
Pergamon Press Oxford (1979)
17. R. Telle
Aufbau und Sinterverhalten von mehrphasigen Keramiken im Hartstoffsystem B_4C-SiC
Dissertation Universität Stuttgart (1985)
18. G.Effenberg, L.Lukas
Phase diagram and thermodynamic information on the system(s) Si-N-C-Mg-O-S-Y
Study Contract between European Atomic Energy Community and Max Planck Institut für Metallforschung No.320087

$$G = m_1 - m_2*T + m_3*T*(1-\ln T) - m_4*\frac{T^2}{2} - m_5*\frac{1}{2T} - m_6*\frac{T^3}{6}$$

compound	m_1	m_2	m_3	m_4	m_5	m_6
SiO_2(s)	-928927.94	-225.83121	43.926626	0.0380070	-968941	------
SiC(s)	-91168.69	-229.52467	41.138666	0.01012731	-156482	-1.7465E-6
SiO(g)	-118798.22	-21.29347	39.375719	-0.001087	-2951825	2.1061E-7
Si(l)	-8162.47	-114.35272	22.822297	0.0038582	-353760	-------
O_2(g)	-10717.43	20.96957	31.70734	0.0036300	-------	-2.9322E-7
CO_2(g)	-428886.24	-155.54717	60.838957	0.00071552	-7572639	-------
CO(g)	-129619.91	-20.85442	36.618715	0.0003245	-3995892	-------
Si_3N_4(s)	-773234.3	-342.57457	73.734669	0.11354838	-508878	-2.8902E-5
N_2(g)	-18261.21	-20.33974	35.578409	0.00076749	-3775612	-5.0419E-9
C(s)	-16025.56	-146.34235	24.438744	0.00043514	-3162686	-------
Si(l)	40363.05	-110.49313	27.196000	------	-------	--------

Table 1 : enthalpies of elements and compounds considered in this work /18/

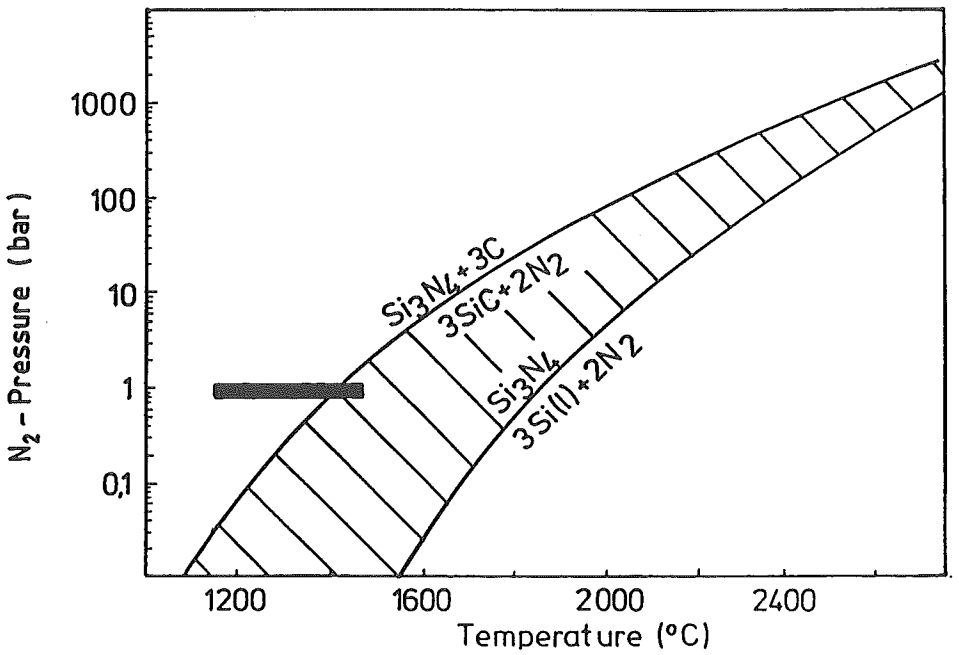

Fig.1 : influence of nitrogen partial pressure and temperature on phase composition of Si_3N_4-SiC composites /13/

nitrogen pressure and temperature during reaction bonding of Si_3N_4

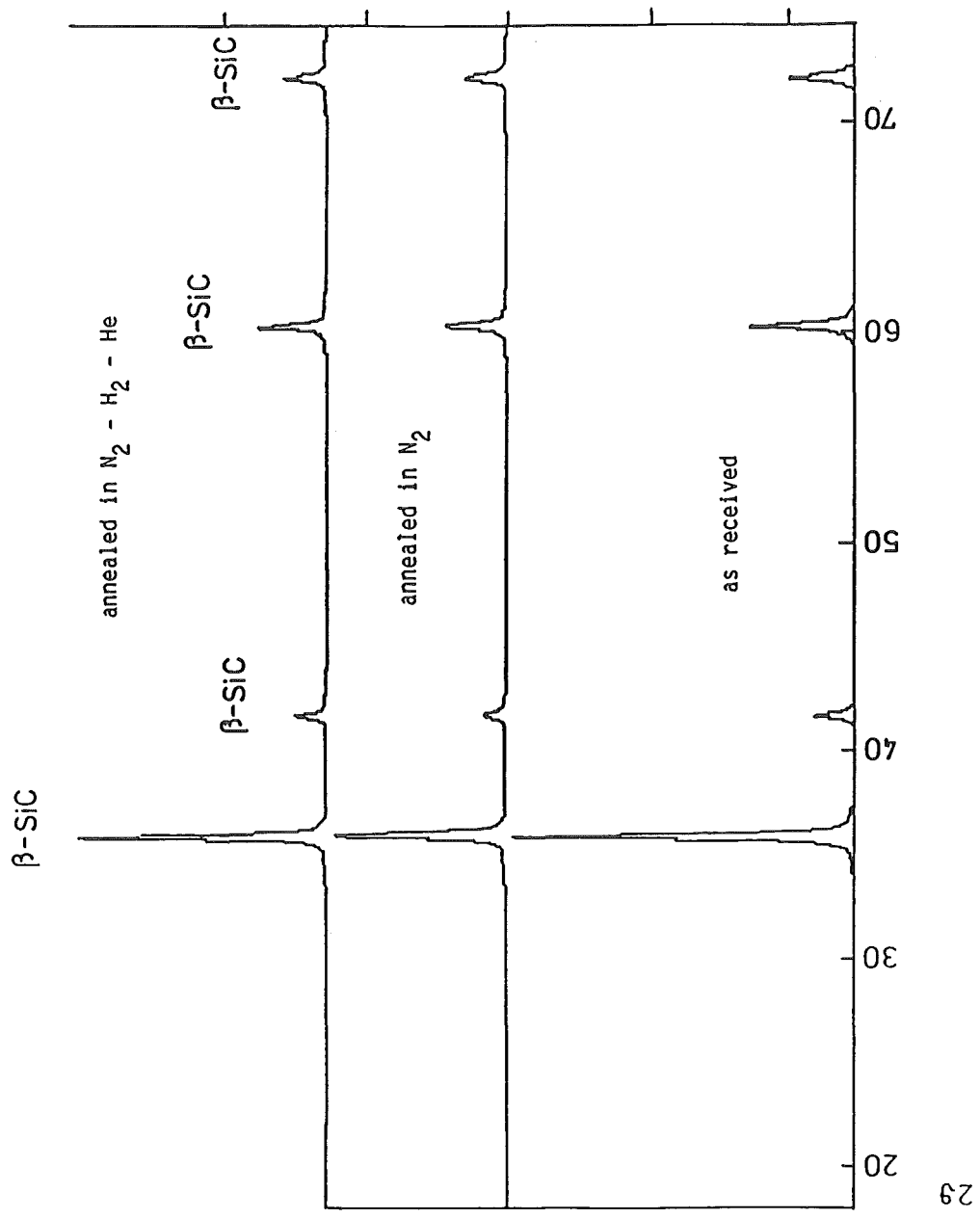

Fig.2 : influence of heat treatment at 1100 - 1450°C in different atmospheres on β-SiC powder

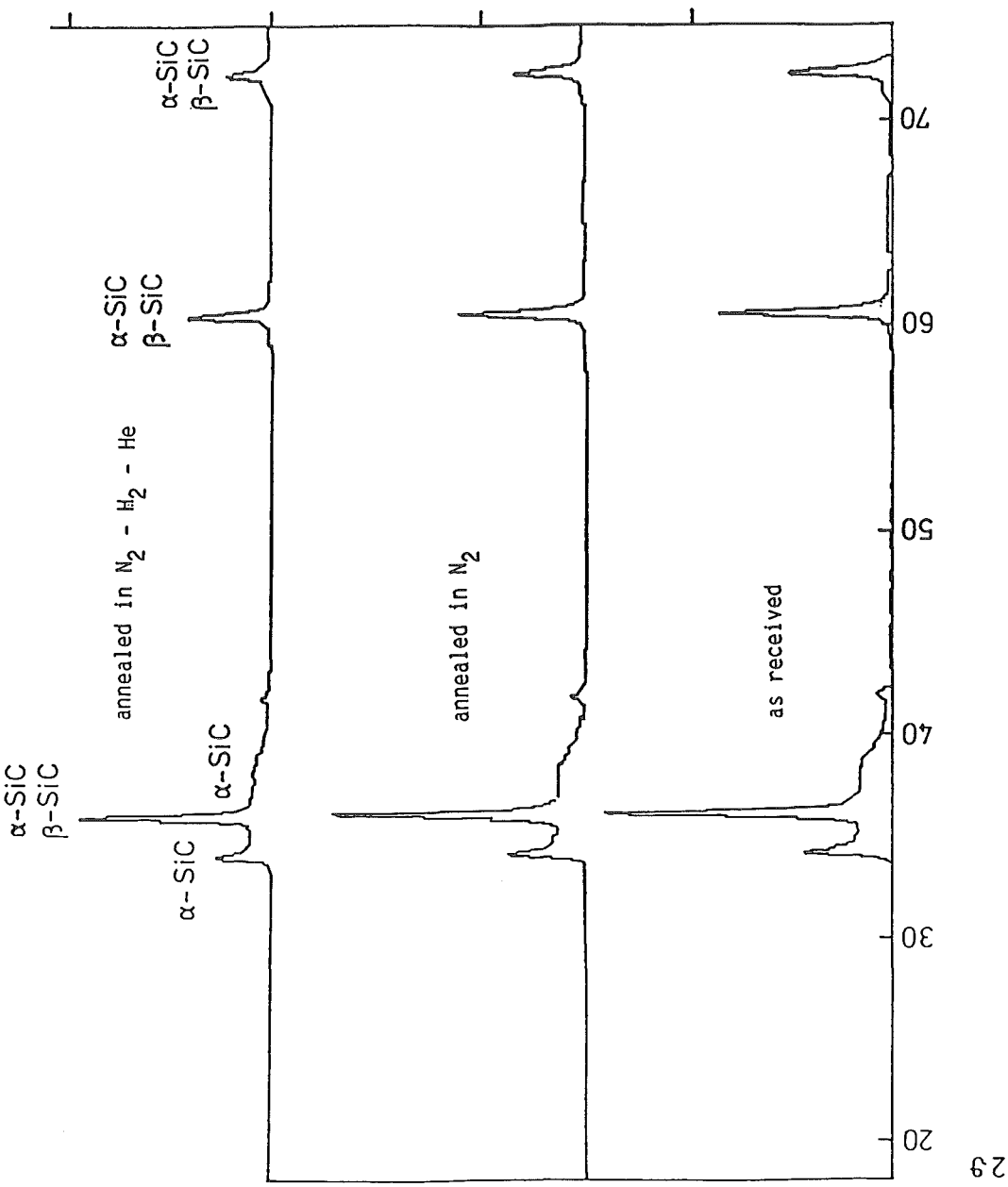

Fig.3 : influence of heat treatment at 1100 - 1450°C in different atmospheres on SiC whiskers

as received

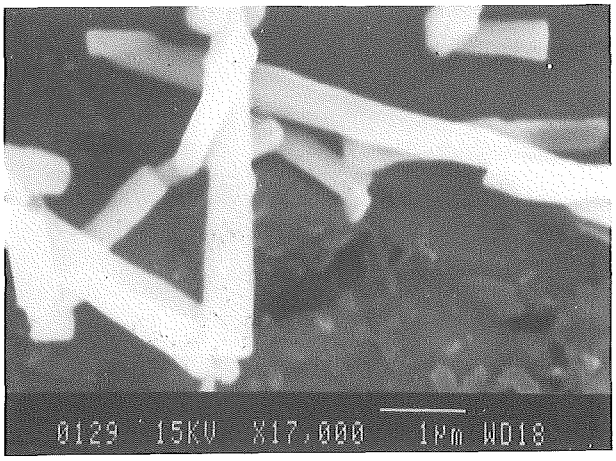

annealed in N_2

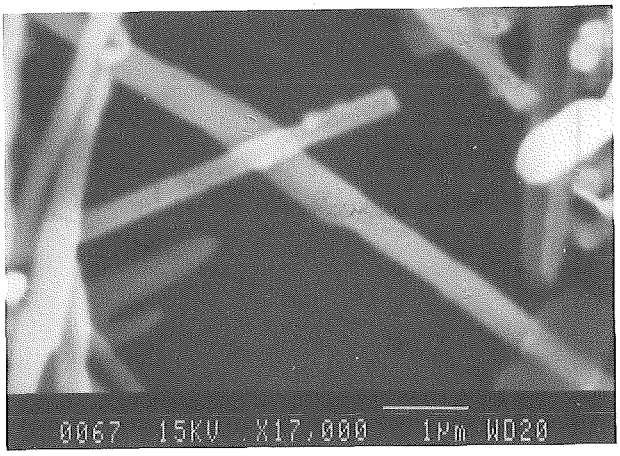

annealed in
N_2 - H_2 - He

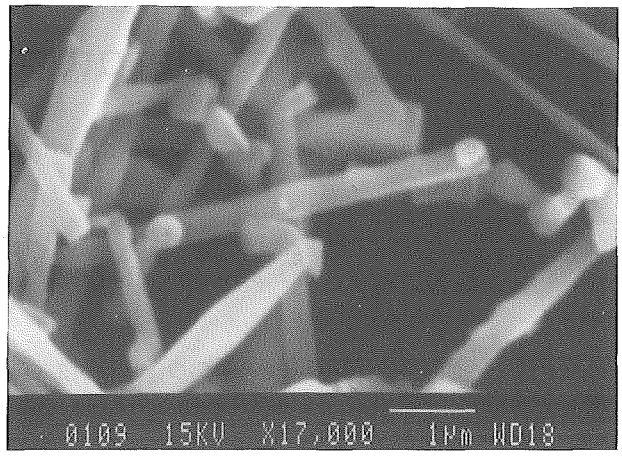

Fig.4 : influence of the heat treatment on the morphology of SiC whiskers

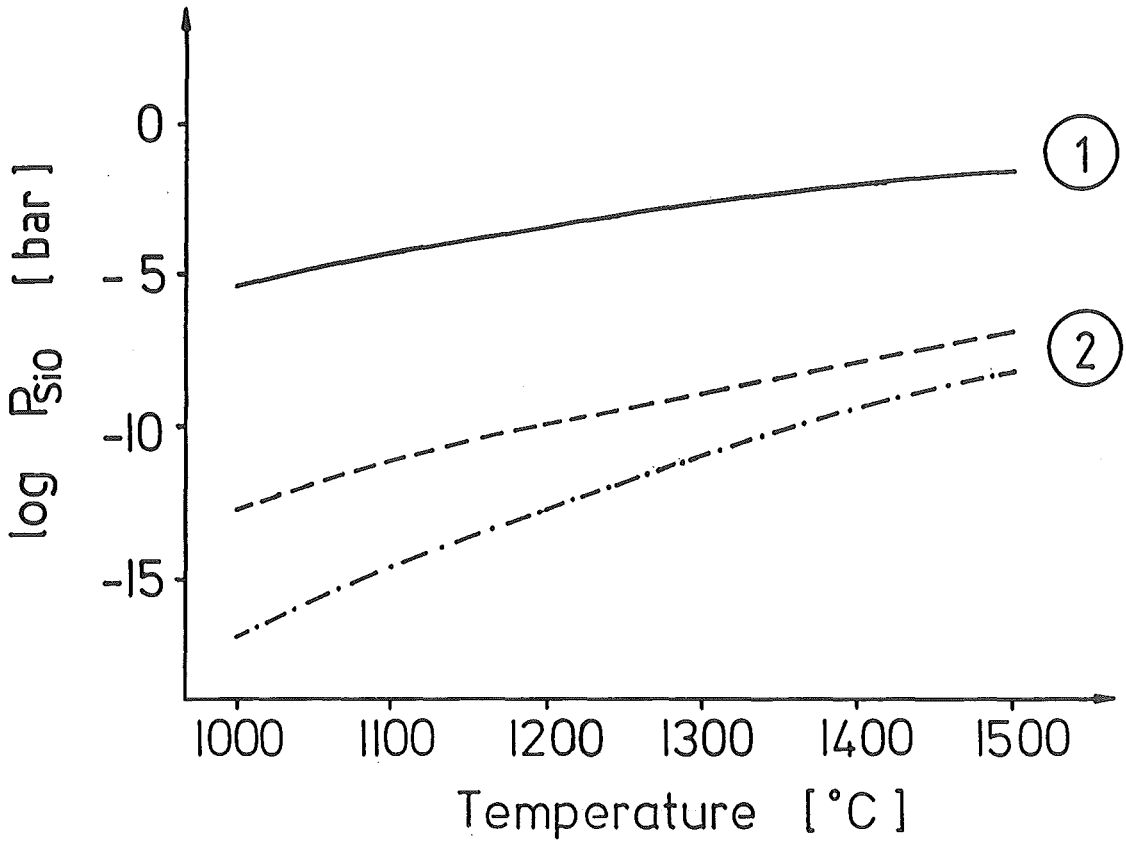

Fig.5: decomposition of SiO_2 on Si and SiC substrates

$SiO_2(s) + Si(s) \rightarrow 2\ SiO(g)$

1 ——— on a silicon substrate in pure nitrogen

$SiO_2(s) \rightarrow SiO(g) + 0.5\ O_2(g)$

2 ----- on a silicon carbide substrate in pure nitrogen

-·-·-· on a silicon carbide substrate in nitrogen containing 20 ppm oyxgen

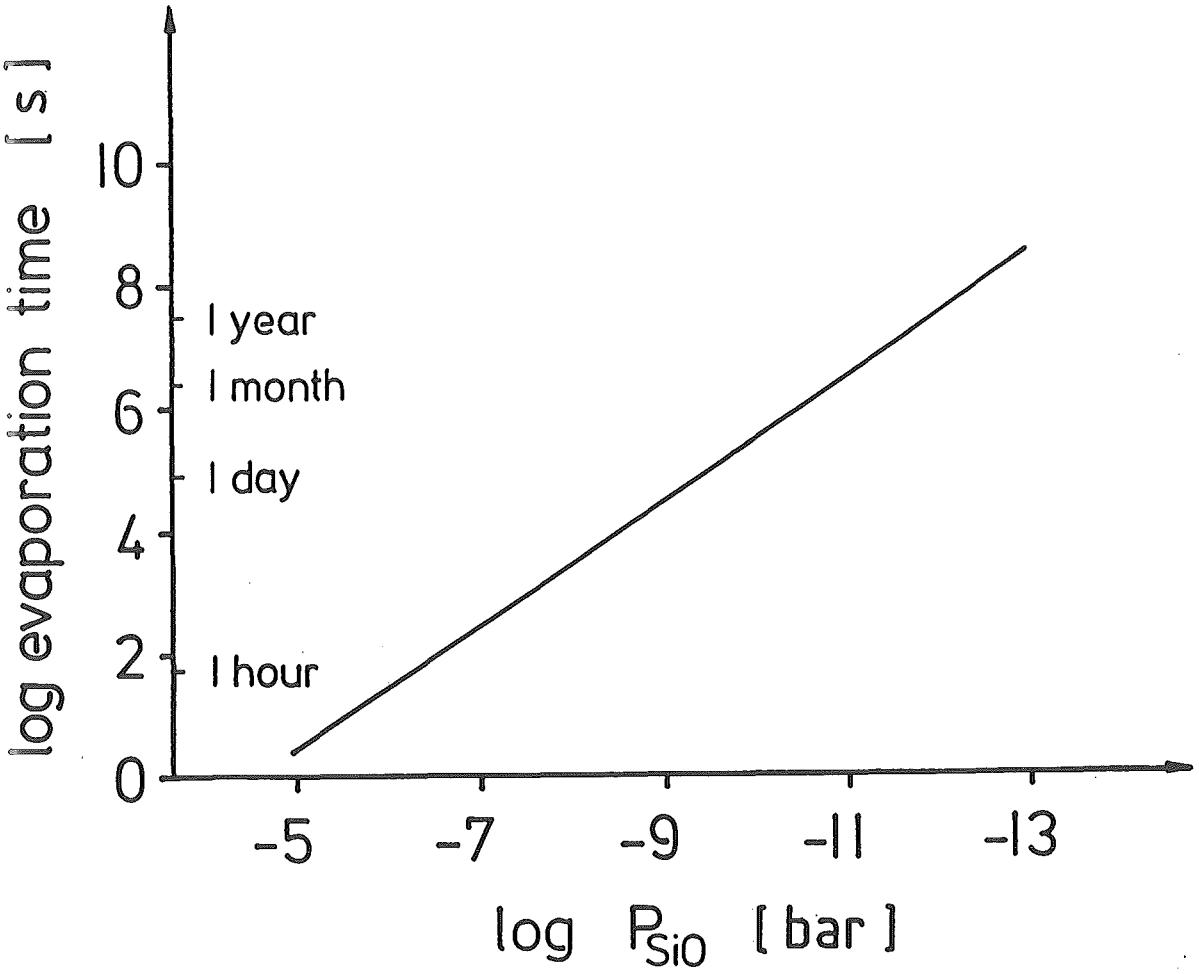

Fig.6 : evaporation time for a 1 nm SiO_2 on SiC in vacuum at T= 1400°C

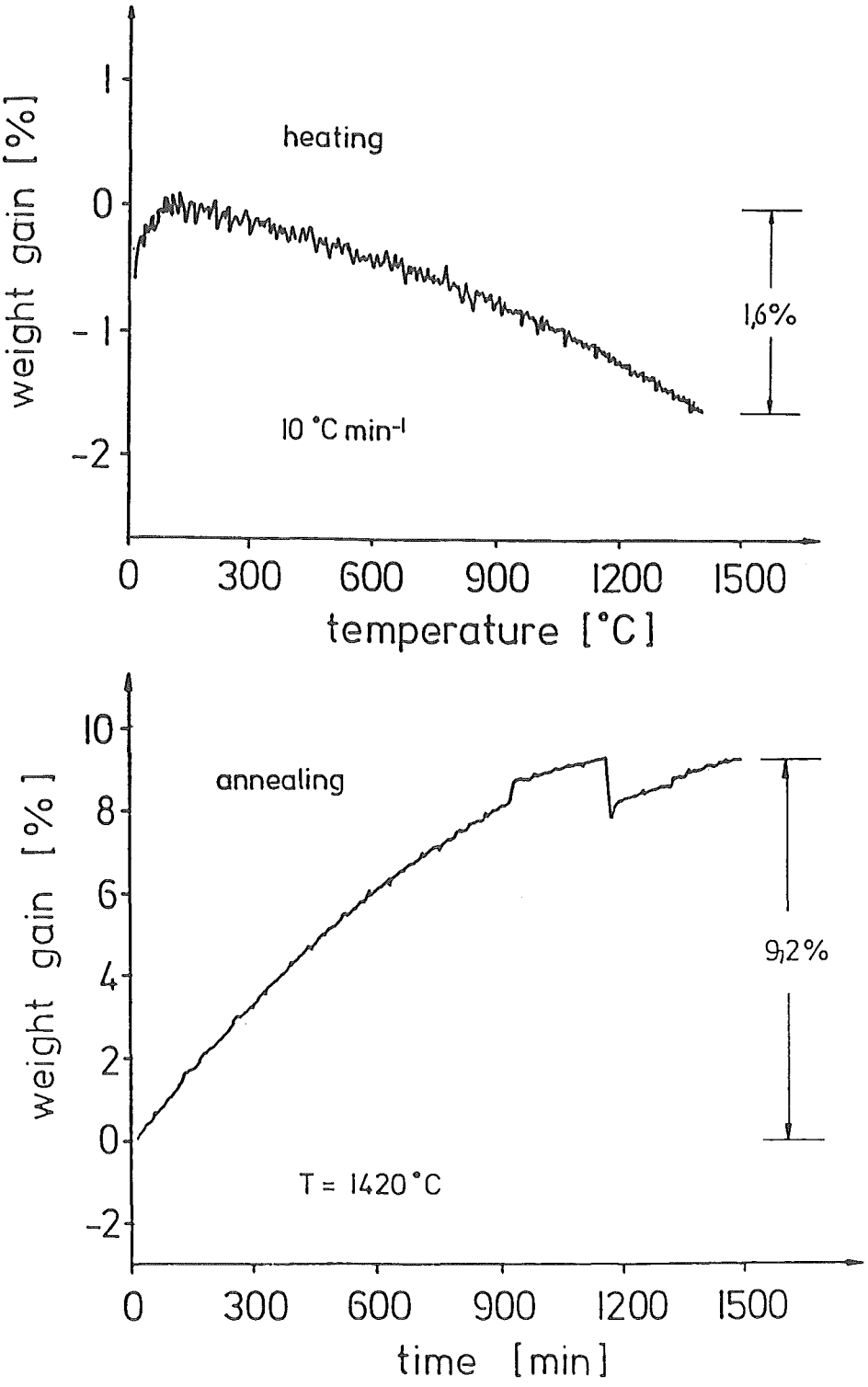

Fig.7 : thermal balance analysis of SiC powder in flowing N_2

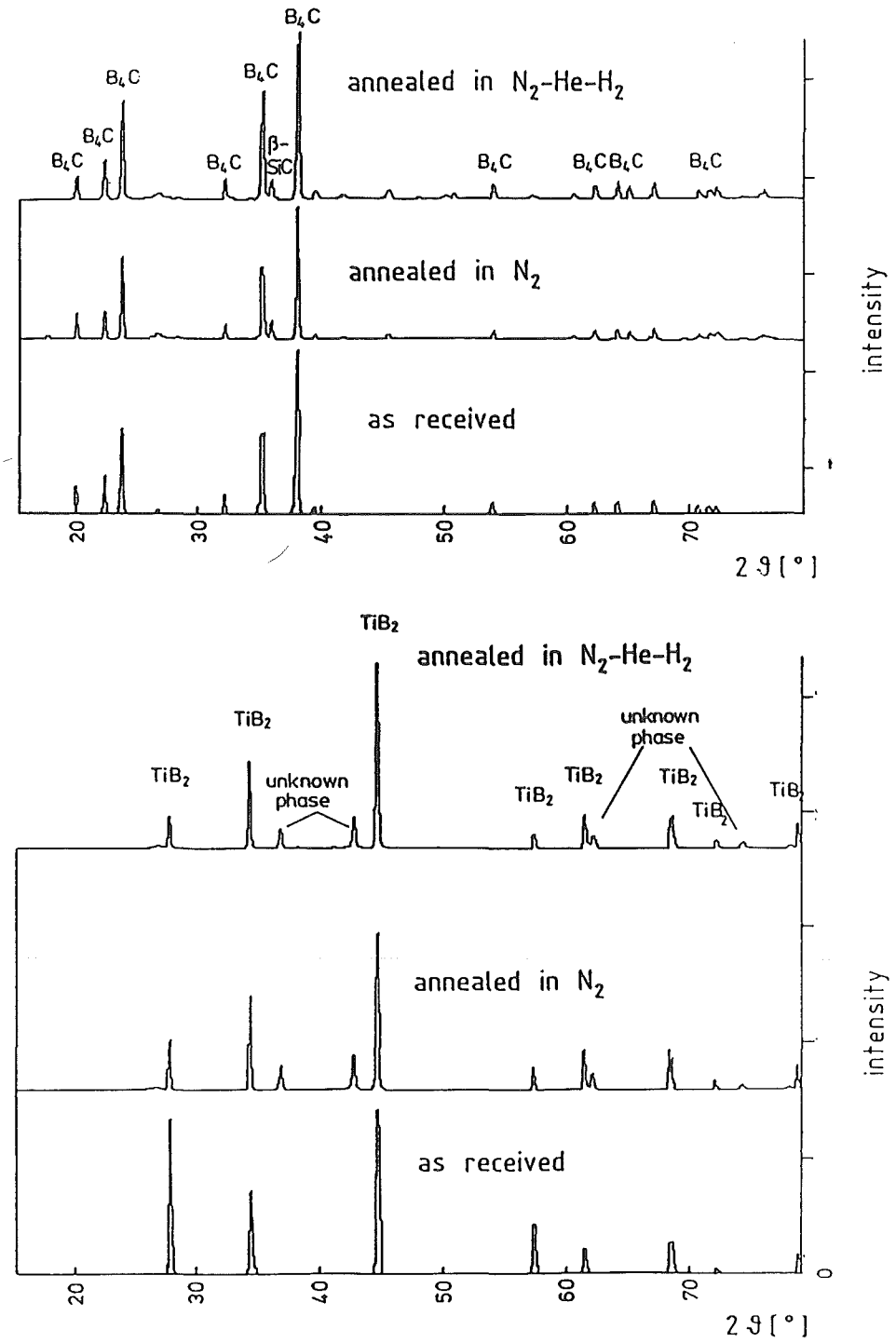

Fig.8 : influence of heat treatment at 1100 - 1450°C in different atmospheres on B_4C and TiB_2

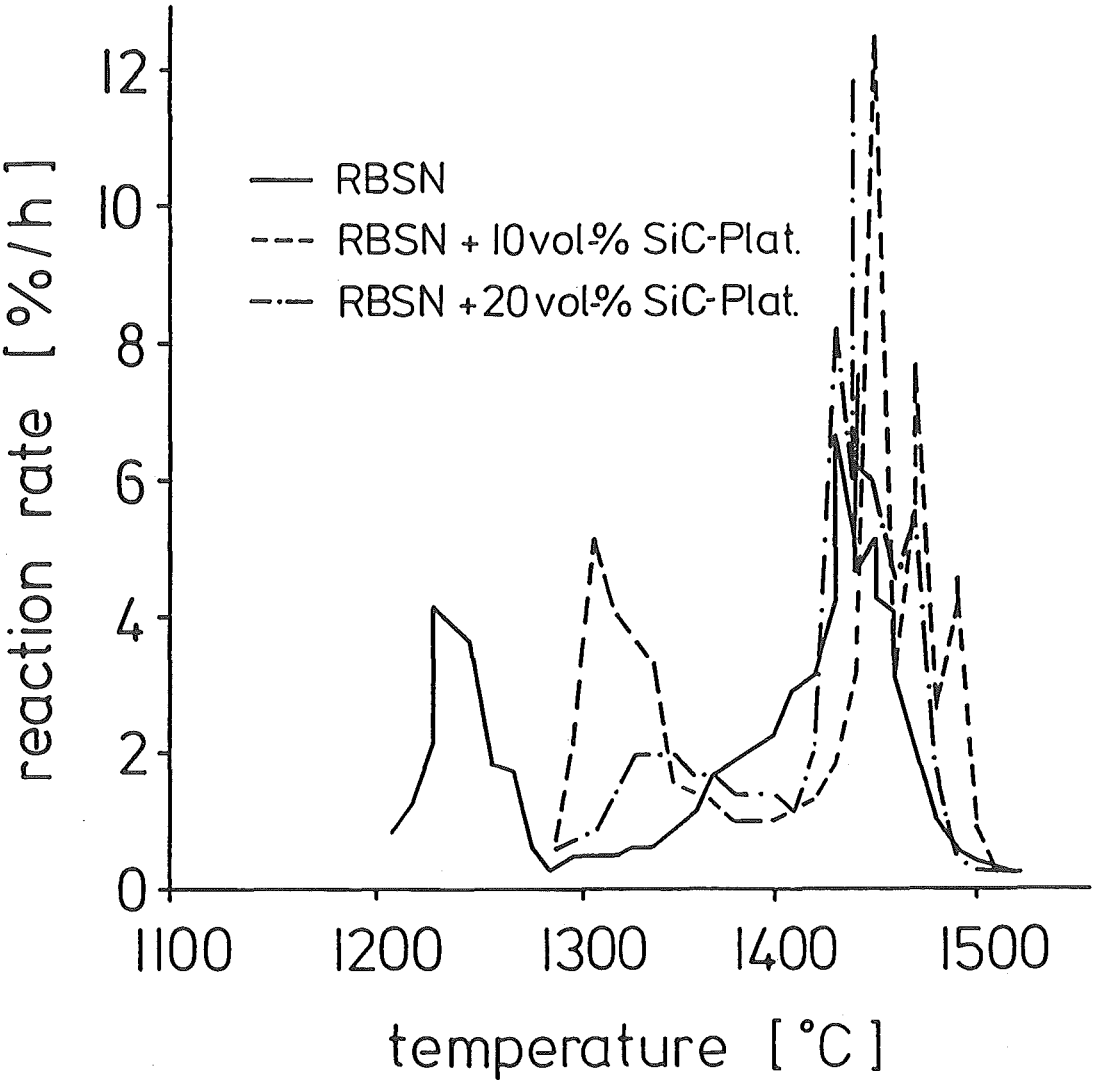

Fig.9 : reaction rate of RBSN and RBSN - SiC composites calculated by nitrogen consumption during nitridation

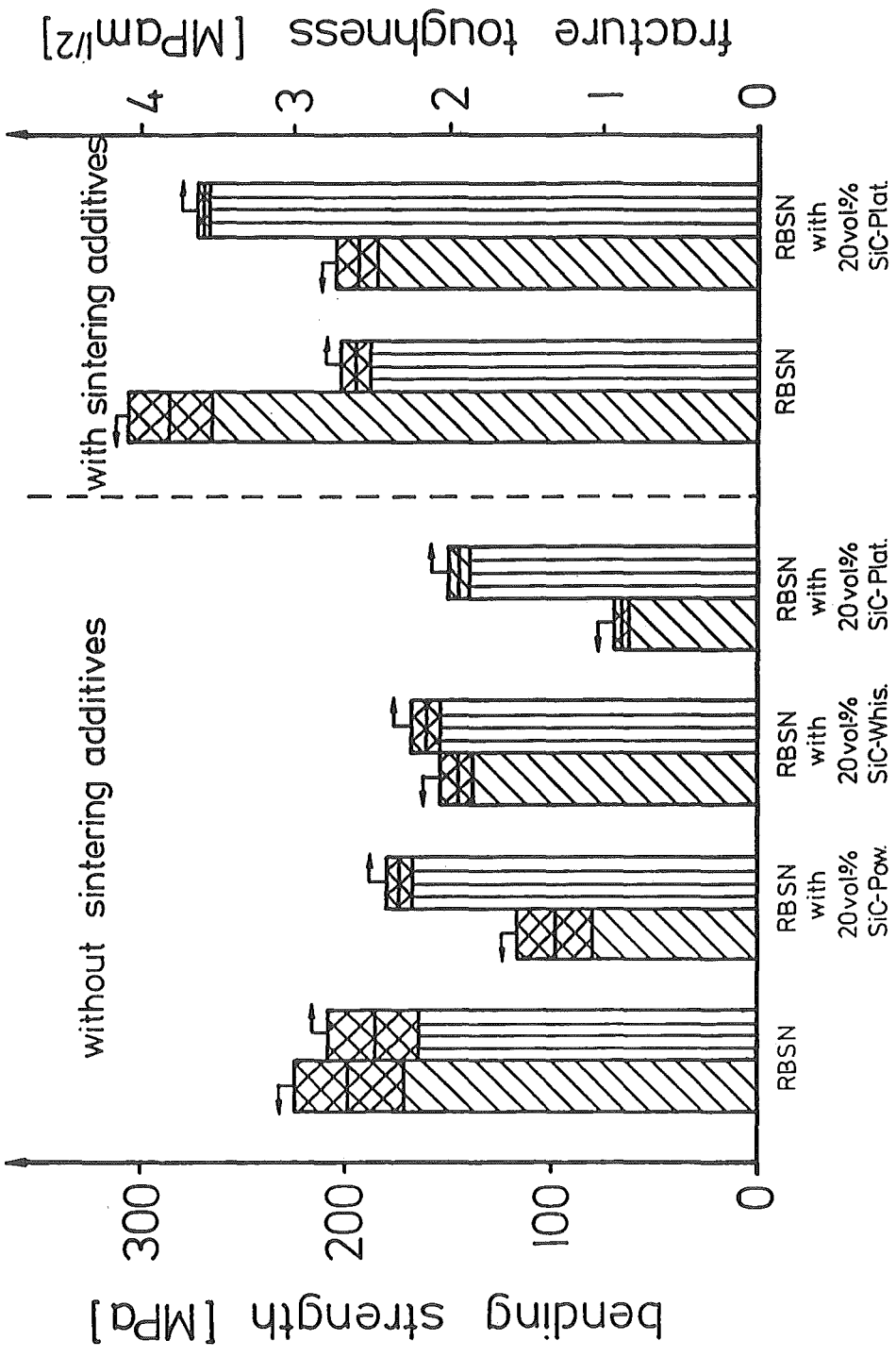

Fig.10 : strength and toughness of RBSN and RBSN - SiC composites

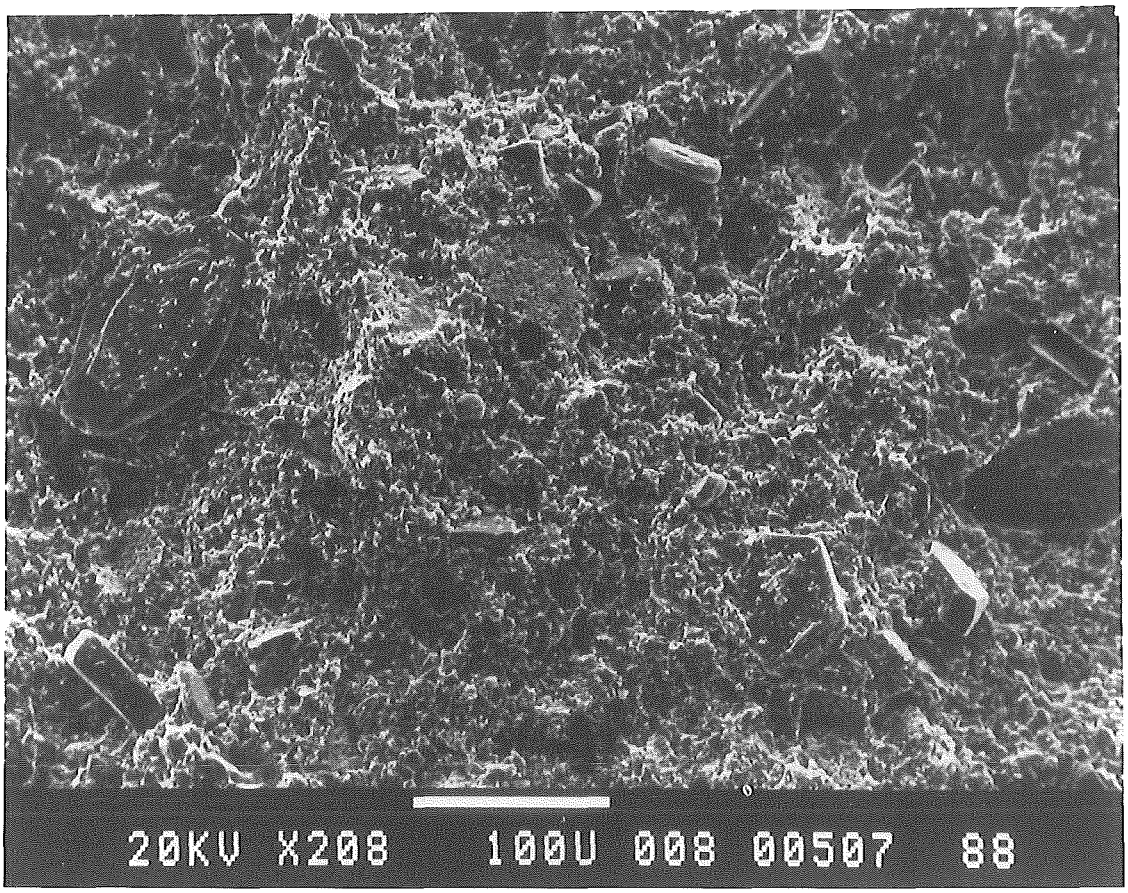

Fig.11 : RBSN with 20 vol.-% SiC platelets, fracture surface SEM

Synthesis of High Density Cordierite Bodies

O. Seide, W.Krönert
Institut für Gesteinshüttenkunde der RWTH Aachen
Mauerstr. 5, D-5100 Aachen

1. Introduction

Cordierite ($2MgO\ 2Al_2O_3\ 5SiO_2$) is still today an attractive ceramic material due to its unusually low coefficient of thermal expansion and excellent thermal shock resistance. Progresses in industrial processing engineering and new or improved technologies require materials withstanding periodical or rapid temperature changes without damaging. Therefore, the cordierite attracted great interest in research and development during the last decade (Fig. 1).

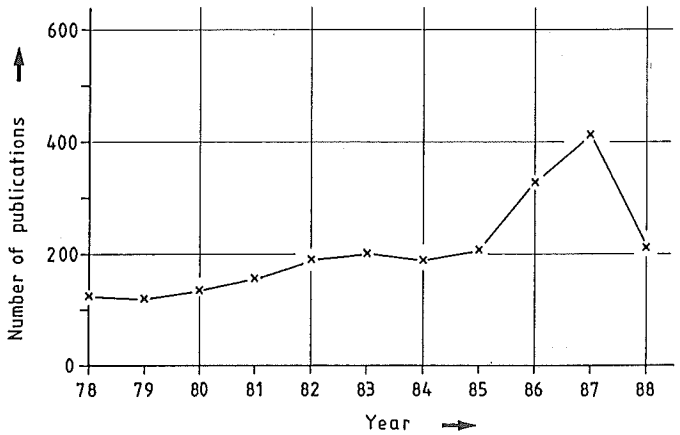

Fig. 1: Number of publications dealing with cordierite materials during the last decade (ref. to Chemical Abstracts Data Base)

2. Synthesis

Synthetic cordierite L. BURGEOIS firstly synthesized in 1883 by fusing a batch of cordierite composition /1/. Ceramic bodies containing cordierite came into practical

use since 1917. But only 1932 cordierite was identified to be responsible for the low thermal expansion of magnesium-alumina-silicate bodies /2/.

The main problem of dense cordierite body production is caused by its extremely narrow sintering interval comprising only about one Seger cone /3/. This could be illustrated by the reproduction of the ternary system $MgO-Al_2O_3-SiO_2$ revised by OSBORN AND MUAN (Fig. 2) /4/. RANKIN AND MERWIN conducted in 1918 the first systematic exploration of the system $MgO-Al_2O_3-SiO_2$ and found cordierite as one of the two ternary compounds /5/. The other is Sapphirine.

The primary crystallization field of cordierite occupies a central position in the system. The first melt is formed at 1355°C. With respect to Fig. 2, which is not an isothermal section by the projection, the composition of Cordierite melting incongruently into mullite and glass phase seems to be placed in the mullite field. In fact cordierite is invariable in comparison due to the solid state formation between cordierite and mullite (cross-hatched line in Fig. 2).

Cordierite is usually synthesized via three main routes:

1. The "classic" route is to sinter oxides. A vast variety of raw materials has been used during the years depending on their composition and impurities in consideration of the desired properties, as well as on fabrication methods and processing conditions (e.g. extruded honeycomb supports) /6, 7, 8/.
2. The glass-ceramic approach represents melting of a glass with subsequently crystallization of cordierite /9, 10/. Cordierite has a lower density than glass of cordierite composition made by devitrification.
3. The sol-gel route uses metal alkoxides as starting materials forming a sol via hydrolysis. Crosslinking reactions lead to a gel and its structure can be controlled by several parameters like alkoxide concentration and type, pH, water to alkoxide ratio, solvent, catalyst, reaction time and temperature. The gel microstructure determines the morphology and properties of the final particles. The amorphous sol-gel powders were used to sinter cordierite with high densities (> 90 % of theoretical density) at temperatures less than 1000°C /11, 12, 13/.

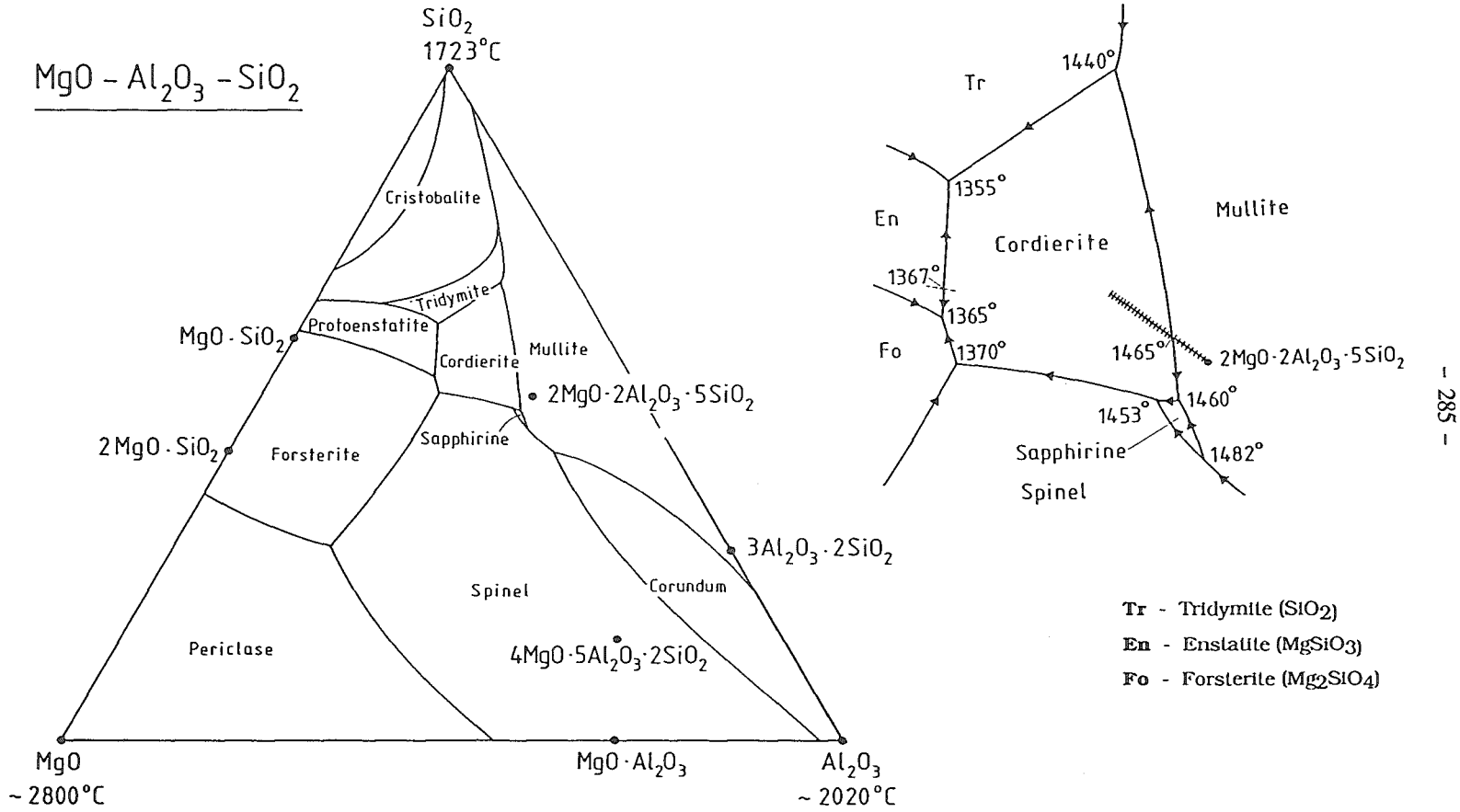

Fig. 2: Ternary sytem MgO-Al_2O_3-SiO_2 (ref. OSBORN AND MUAN)

3. Structure

Cordierite exists in two modifications, i.e.an orthorhombic low temperature form and a hexagonal high temperature form called indialite /14/. The transformation between the two polymorphic forms proceeds continuously in an order-disorder distribution of Al- and Si-atoms, where the complete ordered atoms correspond to the low temperature cordierite /15/.

The initial crystalline form occurring by solid state reactions or devitrification of glasses is the high-temperature modification studied in this paper. High temperature cordierite is isostructural with the mineral beryl ($Al_2Be_3Si_6O_{18}$) and shows a similar thermal expansion behaviour /16/. Both are cyclosilicates forming hexagonal rings of SiO_4^{4-} tetrahedras. A skeletal model of the structure of cordierite is presented in Fig. 3 /17/. The crystal structure of cordierite consists hexagonal rings formed by five Si and one Al tetrahedra sharing the corners. The six-membered rings are connected with additional Al tetrahedra and Mg octahedra network in such a way, that cavities are formed parallel to the c-axis. The dimensions of the cavities between two succeeding rings alternate periodically and hence its morphology looks like a pearl chain /18/.

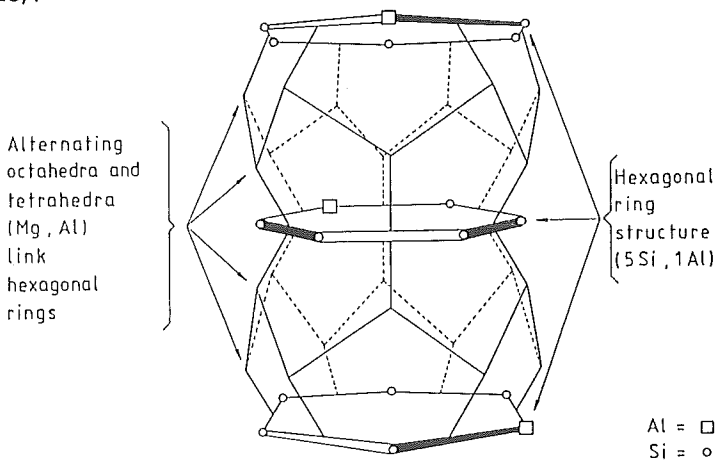

Fig. 3: Skeletal model of cordierite

The low average thermal expansion of cordierite is related to its relatively "rigid" tetrahedral framework and the anisotropic expansion of Mg octahedra isolated from each other. This anisotropy leads to a slight rotation of the hexagonal rings, which effects a contraction of the structure along c-axis and an expansion along the a- and b-axis /19, 20/.

4. Application

The application of cordierite containing materials corresponds to a wide range like high porosity kiln furnitures, catalytic exhaust supports and special products as substrates for multilayer ceramics. Some examples of cordierite application are listed in Table 1 /21, 22/.

Tab. 1: Applications of cordierite containing materials

APPLICATION	PROPERTIES
KILN FURNITURES	
	resistance against rapid and frequent temperature shocks; low strength
DENSE AND POROUS PRODUCTS FOR ELECTRICAL HEATING	
ceramic insulators	high thermal stability; low thermal expansion; high temperature shock resistance
GLASS-CERAMICS	
components for space telescopes with ultra-low expansion; radomes	low thermal expansion; high modulus of rupture; radar transparency
ELECTRONICS AND PACKAGING INDUSTRY	
ceramic substrates for multilayer ceramics; high frequency capacitors	low dielectric constant; low thermal conductivity; low thermal expansion
CATALYTIC SUPPORTS	
heat exchangers; catalytic converters for automotive emission control; woodstove combustors; molten metal filters for refractory industry; catalytic combustors; catalyst in the chemical processing; ozone abatement in jet aircraft passenger cabins; reduction of NO_x emissions	low thermal expansion; refractoriness and inertness; coating with high surface materials or noble metals; controlling of porosity and pore size
BIOTECHNOLOGY	
substrates for mass cell propagation in bio-reactors	

Many articles were published concerning investigations to improve properties of cordierite, especially fracture toughness and modulus of elasticity, by combining with other substances, e.g. mullite, ZrO_2, Si_3N_4, SiC, Al_2O_3, MgO, $ZrSiO_4$, B_4C in form of powders or whiskers /23, 24, 25/. Cordierite honeycombs e.g. coated with metal oxides as TiO_2, WO_3, MoO_3, V_2O_5 were tested to increase the catalytic activity for reduction of NO_x in power plants /26/. Some properties of cordierite referred to MUSSLER AND SHAFER are presented in Table 2 /27/.

Density (ASTM ref. 13/0293)	2.51 g/cm^3
Thermal Expansion Coefficient (25-800°C)	$1.5 \cdot 10^{-6}$ K^{-1}
Dielectric constant (25°C / 1MHz)	5.0
Bending strength	245 MPa
Fracture toughness (K_{IC})	2.3 MPa·m$^{1/2}$
Vickers hardness	8.2 GPa
Young's modulus	139 GPa
Shear modulus	45 GPa
Poisson's ratio	0.31

Tab. 2: Properties of cordierite

5. Experimental

Different cordierite materials were used for preparation specimen. Powder A is a milled cordierite monolith, sample B a crystalline powder prepared by devitrification of a glass of cordierite composition. Preliminary sintering experiments yielded to densities ranging between 60 % and 70 % of theoretical density. Therefore, the milling process was optimized using an attritor *NETZSCH PE 075*. The best results were obtained by micronizing in isopropyl alcohol during one hour.

The specific surface area was determined by BET method to 6.4 m^2/g for powder A and 4.8 m^2/g for powder B. The particle size distribution curves obtained by the *Silas*

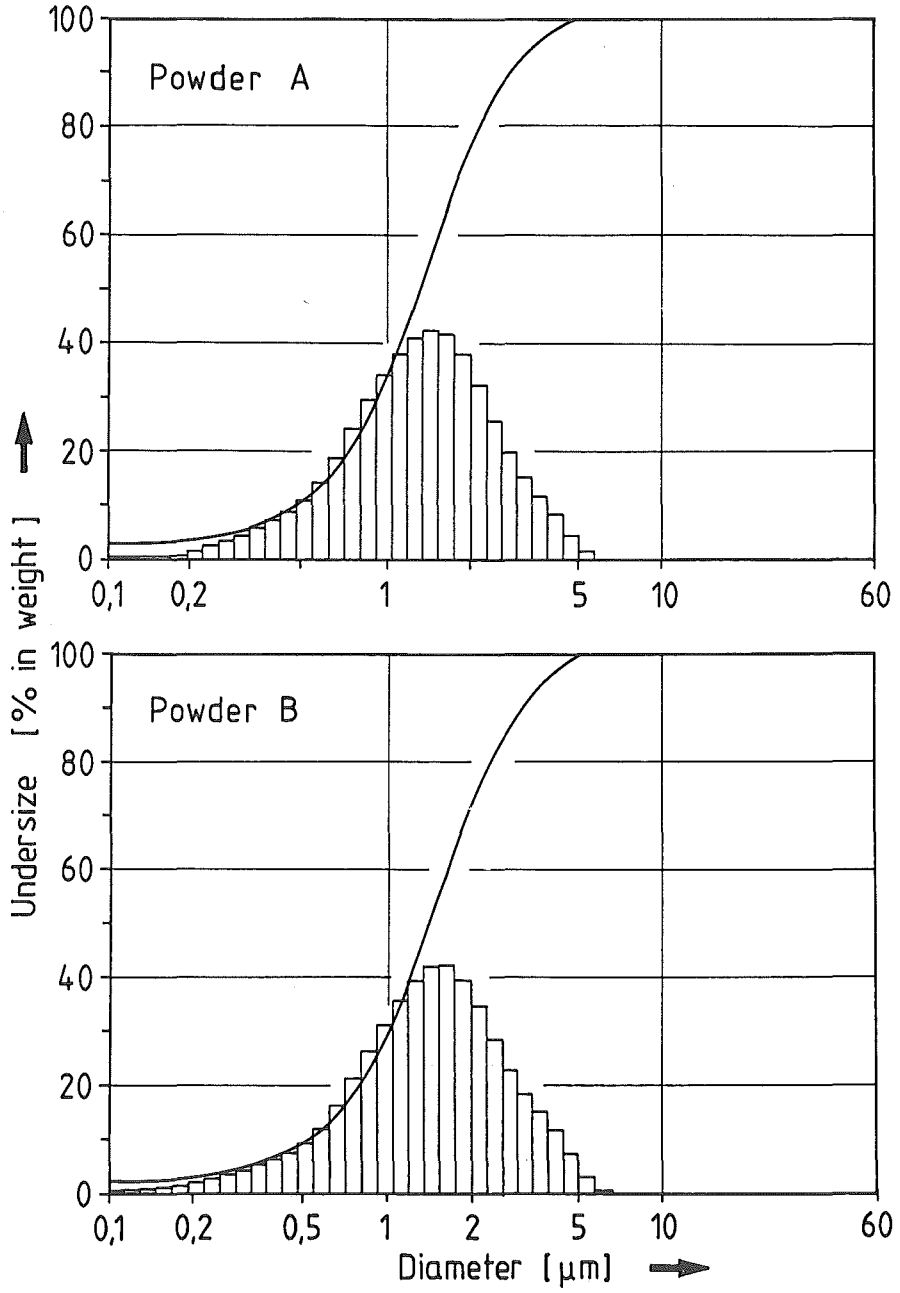

Fig. 4: Particle size distribution (SILAS) of attritor milled cordierite powders

Granulometer HR 850 shows Fig. 4. The mean particle size amounts 1.3 µm for powder A and 1.4 µm for B. These results are confirmed by scanning electron micrographs shown in Fig. 5.

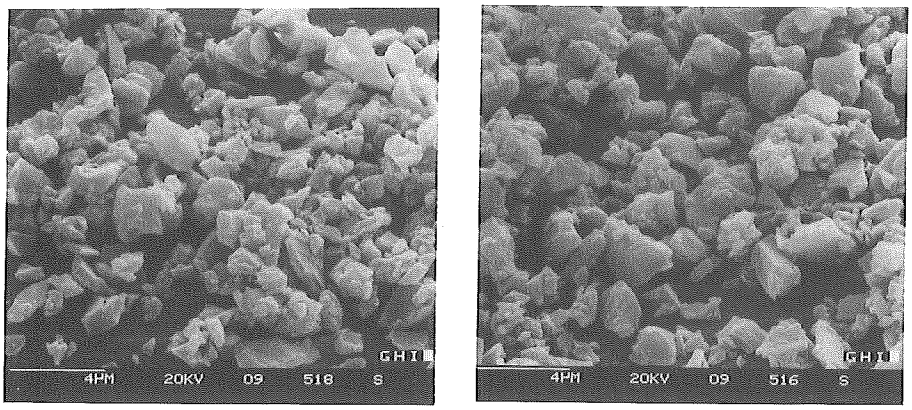

Fig. 5: Scanning electron micrographs of attritor milled cordierite powders A (left) and B (right)

Samples were prepared without binder by uniaxial pressing with double effect. The diameter of pressed tablets was 10 mm. Pressing load was applied in a range from 50 to 550 MPa. The influence of pressure on green density is illustrated in Fig. 6. Achieved green density was ~66 % of theoretical density. Extended sintering experiments were carried out with green bodies pressed between 100 and 350 MPa.

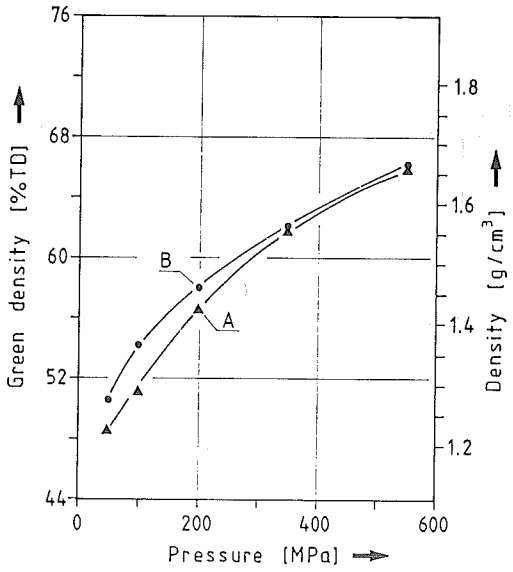

Fig. 6:
Influence of pressure on green density of cordierite powders A and B

The sintering behaviour was measured by high temperature dilatometer type *NETZSCH 402 E*. Specimen were shaped to rectangular bars of 25 x 5 x 5 mm. The heating rate was 10 K/min. The maximum temperature was limited to 1360°C avoiding the temperature of the lowest eutecticum. Considerable shrinkage was revealed about 1200°C as shown in Fig. 7. Shrinkage rates increase to maximum values between 1280 and 1360°C. The coefficients of thermal expansion were measured during cooling obtaining 2.3 $10^{-6}K^{-1}$ for sample A and 2.1 $10^{-6}K^{-1}$ for B (20 to 1350°C) corresponding to the values cited in literature /9, 22/. There exists no obvious influence of firing time on the shrinkage at 1360°C.

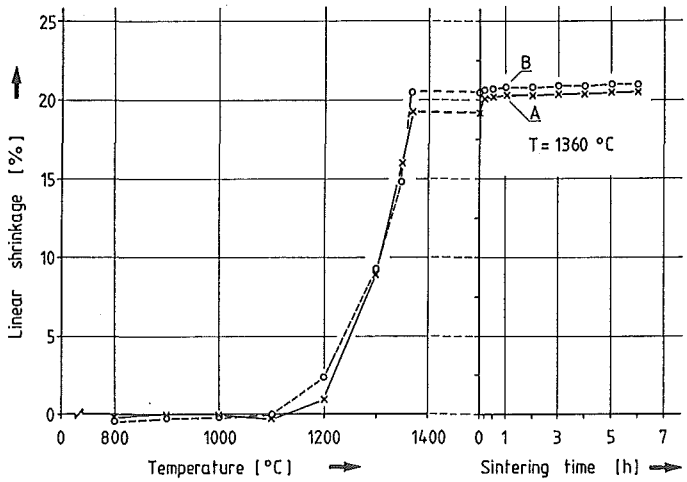

Fig. 7: Linear shrinkage curves of cordierite powders A and B

According to the results of dilatometric measurements the pressed green samples were sintered in a programmable laboratory furnace at temperatures of 1200, 1280 and 1350°C for three hours with a heating rate of 10 K/min. The results are plotted in Fig. 8. The influence of pressure on density is more pronounced for sample A than for B, especially for sintering temperatures lower than 1300°C although both show quite similar green densities. This behaviour can be explained by their resembling physical powder characteristics as particle size distribution, specific surface area or morphology. The difference in sintering densities of sample A and B is caused by higher impurity content of sample A. Chemical analysis is presented in Tab. 3. The values fit well with those calculated from cordierite composition (2 : 2 : 5).

The micrographs of fracture surfaces obtained by scanning electron microscope investigations of samples A and B are shown in Fig. 9. The higher porosity of sample B is obvious in comparison with sample A. Phase analysis was determined by X-ray powder

diffraction method. The X-ray diffractograms are plotted in Fig. 10 with the reflex angles and intensities of high cordierite representing the dominant phase (ICPDS ref. card 13/0293).

	Powder A (wt%)	Powder B (wt%)	Cordierite* (wt%)
SiO_2	49.88	51.27	51.36
Al_2O_3	35.08	34.10	34.86
MgO	13.66	14.46	13.78
TiO_2	0.73	0.14	---
Fe_2O_3	0.60	0.02	---
K_2O	0.04	0.01	---
Na_2O	0.01	---	---
Loss on Ignition (1050°C)	0.16	0.06	---

Tab. 3:
Chemical analysis of cordierite powders A and B
(* theoretical values)

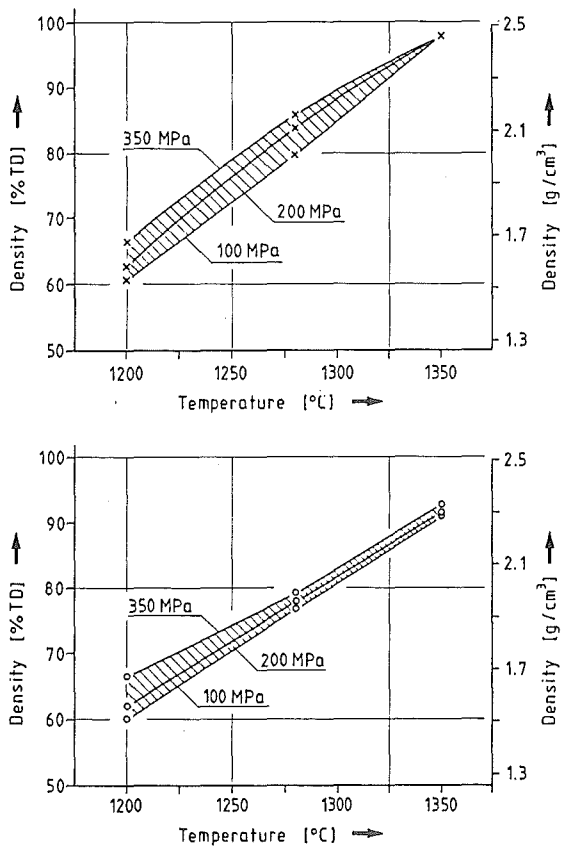

Fig. 8:
Influence of sintering temperature and pressure on density of sample A and B

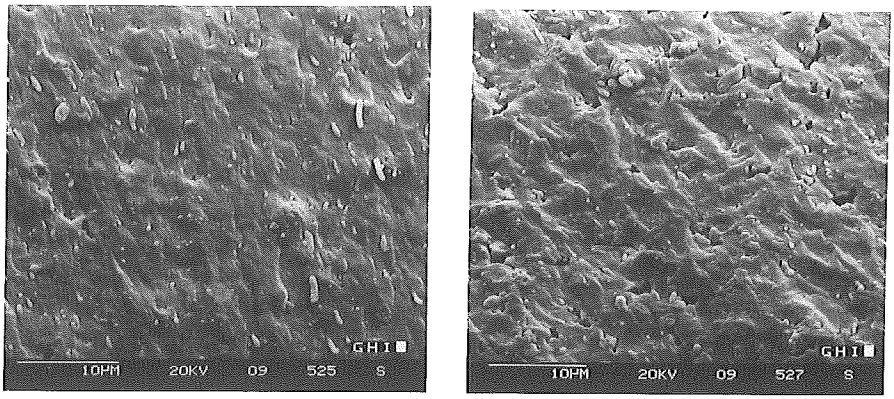

Fig. 9: Morphology of fracture surfaces: sample A (left) and B (right)

5. Conclusion

The experimental work was realized with two different prereacted cordierite samples:

A - synthesized by solid state reaction of raw materials.

B - obtained by devitrification of glass having cordierite composition.

The starting powders were prepared by intensive attritor milling achieving similar physical properties. The green body densities ranged between 60 % and 70 % of theoretical density pressed between 100 and 350 MPa. Sintering experiments realized in the temperature range from 1200 to 1350°C revealed the following:

a) The influence of pressure on sintered bodies were evident up to 1300°C for powder A and 1250°C for B.

b) Higher sintering densities of sample A were ascribed to its higher impurity content.

c) Sample A sintered at 1350°C reached ~95 % of theoretical density showing uniform microstructure. Sample B treated under the same conditions sintered to density of ~90 % of theoretical density and developed similar microstructure.

It is intended to acquire extended microstructural analysis of prepared cordierite bodies. The mastered sample preparation procedure is included into investigations of thermomechanical properties of compound ceramics containing homogeneous dense cordierite as matrix phase.

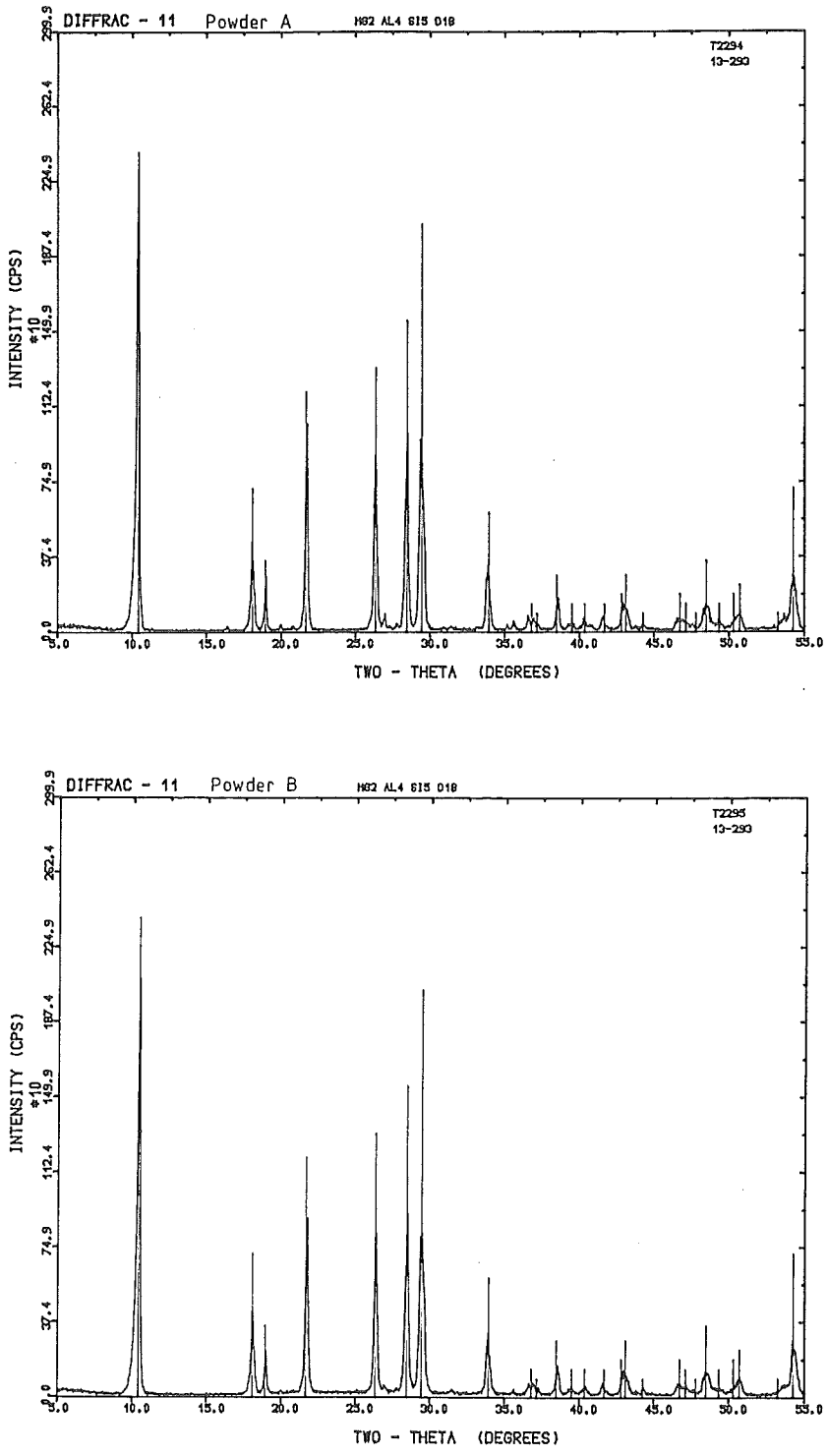

Fig. 10: X-ray diffractograms of cordierite powders A and B sintered at 1350°C/6h

6. Acknowledgments

The authors thank Dr. I. Stamenkovic for valuable comments on the manuscript and W. Stumpfe for technical assistance.

7. References

1. Burgeois, L.: Ann. chim. phys. **29** (1883), 433
2. Geller, R.F., Insley, H.: Thermal Expansion of some Silicates of Elements in Group II of the Periodic System. J. Res.Nat. Bur. **9** (1932), 35-46
3. Reh, H.H.: Wege zur Entwicklung einer dichten Cordieritmasse. Sprechsaal **97** (1964), 145-149
4. Levin, E.M., Robbins, C.R., McMurdie, H.F.: Phase Diagrams for Ceramists. Amer. Ceram. Soc., Columbus/Ohio, 2nd ed. (1969), Fig. 712
5. Rankin, G.A., Merwin, H.E.: The Ternary System $MgO-Al_2O_3-SiO_2$. Amer. Journ. Sci. **45** (1918), 301-325
6. Krönert, W., Schwiete, H.E., Suckow, A.: Die Bildung von Cordierit aus Talk,Kaolin und den Oxiden im Dreistoffsystem $MgO-Al_2O_3-SiO_2$. Ziegelind. **17** (1964), 729-733
7. Lachmann, I.M., Bagley, R.D., Lewis, R.M.: Thermal Expansion of Extruded Cordierite Ceramics. Am. Ceram. Soc. Bull. **60** (1981), 202-205
8. Rasch, H., Yilmaz, V.: Cordierit in keramischen Werkstoffen und sein Verhalten gegenüber anderen Phasen des Systems $MgO-Al_2O_3-SiO_2$. Keram. Z. **40** (1988), 20-24
9. Tyrrell, M.E., Gibbs, G.V., Shell, H.R.: Synthetic Cordierite. U.S. Bureau of Mines Bulletin 594, Washington (1961)
10. Schaeffer, A.: Glas - Traditional Product and Material with Innovative Potential. Radex-Rdsch. (1988) No.4, 657-668
11. Zelinski, B.J.J., Galiano, M.L., Uhlmann, D.R.: Sintering Behaviour of Sol-Gel-Derived Anorthite and Cordierite Glass Powders. in: Ultrastructure Processing of Advanced Ceramics, ed. J.D. Mackenzie, D.R. Ulrich. John Wiley & Sons (1988), 855-864
12. Bernier, J.C., Vilminot, S., Rehspringer, J.L., El Hadigui, S., Poix, P.: Sol-Gel Processes and Synthesis of Dielectric Powders for Multilayer Ceramics. in: High-Tech Ceramics, ed. P. Vincenzini. Elsevier Science Publishers , Amsterdam (1987), 1443-1450.
13. Sporn, D., Naß, R., Schmidt, H.: Development of Microstructure in Sol-Gel-Derived Mullite and Cordierite Ceramics. Kurzreferate der Jahrestagung der DKG, München (1988), 75-77
14. Miyashiro, A., Iiyama, T.: A Preliminary Note on a New Mineral, Indialite, Polymorphic with Cordierite. Proc. Jpn. Acad. **30** (1954), 746-751
15. Meagher, E.P., Gibbs, G.V.: The Polymorphism of Cordierite: II. The crystal structure of Indialite. Can. Mineral. **15** (1977), 43-49
16. Ikawa, H., Otagiri, T., Imai, O., Suzuki, M., Urabe, K., Udagawa, S.: Crystal Structures and Mechanism of Thermal Expansion of High Cordierite and Its Solid Solutions. J. Am. Ceram. Soc. **69** (1986), 492-498
17. Evans, D.L., Fischer, G.R., Geiger, J.E., Martin, F.W.: Thermal Expansions and Chemical Modifications of Cordierite. J. Am. Ceram. Soc. **63** (1980), 629-634
18. Schreyer, W.: Synthetische und natürliche Cordierite I. Mischkristallbildung synthetischer Cordierite und ihre Gleichgewichtsbeziehungen. N. Jb. Miner. Abh. **102** (1964), 39-67
19. Agrawal, D.K., Stubican, V.S., Mehrotra, Y.: Germanium-Modified Cordierite Ceramics with Low Thermal Expansion. J. Am. Ceram. Soc. **69** (1986), 847-851
20. Hochella, M.F. Jr., Brown, G.E., Ross, F.K., Gibbs, G.V.: High-Temperature Crystal Chemistry of Hydrous Mg- and Fe-Cordierites. Am. Mineral. **64** (1979), 337-351

21. Hummel, F.A.: A Review of Thermal Expansion Data of Ceramic Materials, Especially Ultra-Low Expansion Compositions. Interceram **33** (1984) No.6, 27-30
22. Lachmann, I.M.: Ceramic Honeycombs for Catalysis and Industrial Applications. Sprechsaal **119** (1986), 1116-1119
23. Lachmann, I.M., McNally, R.N.: Monolithic Honeycomb Supports for Catalysis. Chemical Engineering Progress **81** (1985) No.1, 29-31
24. McCoy, M.A., Heuer, A.H.: Microstructural Characterization and Fracture Toughness of Cordierite-ZrO_2 Glass-Ceramics. J. Am Ceram. Soc. **71** (1988), 673-677
25. Claussen, N., Petzow, G., Nieszery, K., Panhorst, W., Weißkopf, K.L.: Keramischer Formkörper. Offenlegungsschrift DE 3445765 A1, Deutsches Patentamt (14.12.84)
26. Hutter, F., Schmidt, H., Koschlig, H.J., Danowski, F.: Entwicklung eines Trägerkatalysators für die Rauchgasentstickung im SCR-Verfahren. in: ENVICERAM 88, Abstracts, Köln (7.-9. Dezember 1988)
27. Mussler, B.H., Shafer, M.W.: Preparation and Properties of Mullite-Cordierite Composites. Am. Ceram. Soc. Bull. **63** (1984), 705-710

Comparative Studies on Post-HIP-and Sinter-HIP Treatments on Transformation Toughened Ceramics

R. Oberacker, A. Kühne, F. Thümmler
Institut für Keramik im Maschinenbau, Institut für Werkstoffkunde II
Universität Karlsruhe

1. Introduction and Definition of Terms

Hot isostatic pressing (HIP) is a well established method used for consolidation of many metal or ceramic powder materials. Depending on the specific behaviour and requirements of a given system, different variants of the HIP process are used. Although a large number of sub-variants are known at the present, the different HIP methods can be subdivided into the three groups schematically represented in Fig. 1.

The difference between the encapsulated and the containerless HIP methods represented in Fig. 1 is obvious. The former demand for a sophisticated and -in many cases- costly encapsulation technique, while the latter require the ability of the material to be densified to the state of closed porosity by pressureless sintering. The containerless methods in principle differ only from each other by the intermediate cooling and reheating step during the Post-HIP treatment, which is avoided in the Sinter-HIP process. In most cases, clear criteria exist for a prediction, whether encapsulated or containerless HIPing will be the better choice for a given system. On the other hand, a selection between the Post- and Sinter-HIP process has often to be made without such criteria, due to the lack of a comparable data base for many materials of interest.

The Sinter-HIP process today is mainly used in the production of hardmetals, where moderate processing parameters, especially moderate pressure conditions, are sufficient for densification of the material. Due to the relatively small differences in the pressureless and the pressure assisted part of the sintering cycle, a new generation of Sinter-HIP furnaces could be developed, resulting in economical advantages of Sinter-HIPing compared to a separate sintering and Post-densification procedure. The application of Sinter-HIP to ceramic materials is still at its beginning. Economic advantages can be expected for example in the case of Sinter-HIPed Si_3N_4, where the processing parameters for sintering and pressure assisted densification are not so far from each other. The situation for oxide ceramics sintered without liquid phases seems to be quite different. They usually can be sintered under normal air atmosphere in relatively cheap furnaces at low costs compared to sintering in the high pressure HIP vessel presumably needed for the final pressure assisted part of the HIP cycle. Therefore the materials properties will be a main criterion. Differences in properties can arise either from irreversible effects resulting from the cooling-reheating procedure, or from differences in sintering atmosphere or temperature regimes used in the two HIP variants regarded.

All these effects can be expected to play a role in ZrO_2 transformation thoughened oxide ceramics, which therefore have the character of a model material in the following experimental comparison on Post-HIP and Sinter-HIP processing.

2. Experimental Procedure

Two groups of fine grained ceramic materials were included into the experimental programme:

- A high strength tetragonal zirconia with 2 (TZP-2Y), resp. 3 mole % (TZP-3Y) of Y_2O_3 as stabiliser.
- ZrO_2-thoughened Al_2O_3 containing 10 to 21 volume % of unstabilised ZrO_2 (ZTA-10 ...ZTA-21).

In such materials processing defects are very likely to remain or develop during pressureless sintering. Therefore, HIP methods have to be applied for making use of their high strength potential [1,2]. On the other hand, pressureless sintering to the state of closed porosity is usually possible at relatively low temperatures without intolerable grain growth. In addition, they cover the whole range of thoughening mechanisms reaching from purely stress induced transformation to pure microcrack thoughening [3,4]. Therefore these materials are ideal representatives for a comparison of the two containerless HIP-methods mentioned above.

2.1 Starting Materials and Preparation of Green Compacts

The raw powders used for the production of these materials are given in Table 1. The TZP powders were supplied in the as spray dried condition and could be press compacted without further treatment. The ZTA powder mixtures were prepared by attrition mixing of the raw powders for 1.5 hours using isopropanol as dispergent and Al_2O_3-balls (95% Al_2O_3) as milling media. Drying was performed at 40°C in a rotary evaporation dryer, followed by granulation through a 150µm sieve. The powders and mixtures were then uniaxially compacted in a floating die at 50 MPa to plates of 65x45x8 mm. The plates were sealed in polyurethane and recompacted at 300 MPa in a cold isostatic press.

2.2 Dilatometer Measurements

Specimens for the dilatometric measurements were cut from the green plates. Densification was studied using a commercially available dilatometer equipment in the case of pressureless sintering in air atmosphere. The size of the specimens was 8x8x15 mm in this case.

For the HIP- and Sinter-HIP experiments, a newly developed dilatometer was used. This dilatometer can be plugged in the commercial HIP-vessel used for the experiments. Its temperature capability is RT .... 2000°C and it can be used under inert gas atmospheres

from 0.1 mbar to 2000 bar. In contrast to the commercial systems meanwhile available, the measuring range is much larger. A total change in length of 6 mm can be recorded with a resolution of better than 0.1 µm. This allows for the use of specimens with dimensions of 10x10x25 mm. This size is big enough to be relevant for most practical situations, regarding the surface- to volume relation. The specimen holder of the dilatometer is shown in Fig. 2. The length changes are mechanically transduced to a sensor system situated in the thermally not affected part of the furnace.

Like in every dilatometer, the measured signal has to be calibrated, taking into consideration the thermal expansion of the graphite specimen holder, temperature differences over the length of the specimen holder and the transducer rod, and here also somewhat different sensor characteristics under low and very high pressures. Due to the proper design, this effects are very small compared to the total length changes of the specimens during Post- and Sinter-HIP treatments. They are reproducible, and a calibration in dependance of the momentary temperature - pressure conditions is easily possible, leading to a very close approximation of the real change in length of the specimen. Only for a higher accuracy, as it is needed e.g. for estimation of a thermal expansion coefficient, a calibration curve has to be measured under identical temperature - pressure - time conditions as the experiment regarded.

2.3 Mechanical and Microstructural Characterisation

Besides the dilatometer specimens, complete plates were consolidated by sintering plus Post-HIP or Sinter-HIPed under different conditions. For characterisation the plates were cut into bending test specimens of 3.5x4.5x45 mm. Strength was measured in 4-point bending with 20 and 40 mm inner and outer span, at a loading rate of 2 N/s. K_{IC} was measured either by microindentation (MI) [5], using a Vickers-diamond loaded with 98N, or by 3-point bending (NB) of specimens with a sharp natural pre-crack, introduced by a bridge method [6]. Microstructure was characterised by SEM of ground, polished and thermally etched surfaces and by quantitative X-ray diffraction regarding the ZrO_2-modifications [7].

3. Experimental Results

3.1 Tetragonal Zirconia Polycrystals

3.1.1 Densification Behaviour of TZP

In sintering of the TZP problems arise from the graphite parts of the HIP furnaces usually used at the process temperatures regarded. Graphite combines with oxygen impurities forming CO, which partly reduces the ZrO_2, resulting in black colored surfaces of Post-HIPed specimens, and black bulk specimens after Sinter-HIP. The sintering behaviour is negatively influenced by the CO contaminated inert gas atmosphere compared to sintering in air. As the densification curves (Fig. 3) are identical up to about 1250°C, this may be

due to the stabilising effect of the cubic ZrO_2-modification by C or an oxygen deficiency. The density reached at this temperature is about 84% TD. Regarding the character of the porosity at this state (Fig. 4), it becomes clear, that mainly pores which are interconnected and open to the surface are present. Therefore, higher sintering temperatures have to be applied to reach pore closure under Sinter-HIP conditions compared to sintering in air atmosphere.

A complete Sinter-HIP-cycle is shown in Fig. 5 for the TZP-2Y-material. Pressurisation after reaching the state of closed porosity leads to a spontaneous increase in shrinkage, clearly visible from the shrinkage rate signal dL/dt. Densification, as it can be distinguished from the shrinkage curve is complete far before the maximum applied pressure of 150 MPa is reached.

3.1.2 Comparison of Post-Densified and Sinter-HIPed TZP

In a couple of preliminary experiments the influence of sintering and HIP conditions was studied. Specimens were sintered in the HIP furnace under Ar atmosphere to different amounts of closed porosity, marked with A, B and C in Fig. 4. Subsequently they were directly pressurised or cooled down and Post-HIPed. The pressure assisted part of these procedures took part at 150 MPa in the temperature range between 1300 and 1500 °C. Full density was reached in all experiments. No significant influence of the intermediate cooling-reheating step on hardness, fracture thoughness, grain size and phase composition of the Post-densified specimens was observed. The main parameters responsible for grain growth and amount of cubic phase were the maximum processing temperature and the total processing time at this temperature.

As a small grain size and the absence of cubic phase are desired, sintering was carried out only to the highest amount of closed porosity (point "C" in Fig. 5), and the temperature for the pressure assisted part of the process cycle was chosen to 1300 °C in the main experiments. Three process variants result from this parameters, schematically compared in Fig. 6. One Sinter-HIP cycle, where the temperature is decreased and the pressurisation takes part directly after reaching pore closure at the density level D_1, and two Post-HIP cycles. One of them differs only by the cooling and reheating step from the Sinter-HIP treatment (index "b"). The other combines sintering in air atmosphere (requiring a lower sintering temperature) with a more typical Post-HIP treatment, where pressurisation takes place by charging the required amount of process gas into the cold containment and allowing for thermal expansion of the gas during heating (index "w"). This process variant exhibits the shortest soak times or the shortest time interval at temperatures above a critical temperature T_{krit} for grain coarsening effects.

The properties reached are represented in Fig. 7 and Table 2. All HIP variants result in densification up to the theoretical density of the materials. Except for the grain size, no significant difference in the properties of the 3 mole % Y_2O_3-stabilised materials becomes visible. The grain size of both, TZP-3Y and TZP-2Y is on the same level and can be qualitatively correlated to the soak time at processing temperature. The properties of the

less stabilised TZP are much more sensitive to the processing conditions used. The highest strength level combined with the lowest standard deviation of strength values results from the Sinter-HIP cycle. The materials consolidated by the two Post-HIP variants exhibit a significantly lower strength and a wider strength distribution. Hardness and K_{IC} (MI) are not influenced by the intermediate cooling-reheating step. On the other hand, there is a strong increase in hardness and K_{IC}, if the Post-HIP cycle is carried out under optimum conditions, that means sintering in air and pressurisation of the cold HIP containment. The process temperatures are low enough to avoid the occurence of cubic phase, and all materials are nearly complete in the tetragonal state, measured on the as sintered surface. During grinding and crack propagation at fracture, the tetragonal phase transforms partly to the monoclinic, depending on the stabiliser content. In the TZP-3Y transformation thoughening seems to play a minor role, in contrast to the TZP-2Y, where about 50 % of the microstructure undergo the transformation.

3.2 ZrO_2-Thoughened Al_2O_3

3.2.1 Densification Behaviour of ZTA

Densification behaviour of Al_2O_3 containing 21 vol-% ZrO_2 (ZTA-21) is compared in Fig. 8 for the pressureless and the pressurised part of a Post- and a Sinter-HIP cycle. In contrast to the TZP materials, densification is not essentially influenced by the sintering atmosphere. Pore closure can be reached at least at the same temperature under Ar in the HIP furnace as in air atmosphere. In both process variants densification is completed before the processing parameters reach the stationary state. Therefore it can be concluded, that neither the maximum pressure of 150 MPa, nor the HIP-temperature of 1450 °C are required for complete densification.

Even the transformation tetragonal → monoclin becomes visible from the HIP-dilatometer measurements. The gas pressure of about 50 to 70 MPa present at this state of cooling seems not to have an influence on the transformation temperatures, which are the same, when the pressure is released before cooling. The transformation in the Sinter-HIP ZTA21 takes place at 650 to 575 °C. The Post-HIP material shows a transformation interval of 440 to 390 °C.

3.2.2 Comparison of ZTA Materials Consolidated by Post- and Sinter-HIP Treatments

Depending on the grain size relation, optimum volume fraction of unstabilised ZrO_2 in ZTA is in the range from about 10 to 15 vol.% [2, 3, 8]. At higher ZrO_2 contents, microcrack formation increases heavily, combined with a drastic loss in strength and a decreasing fracture thoughness. Therefore emphasis was put mainly on the compositions ZTA-12 and ZTA-18, which should confine the optimum and the critical ZrO_2 volume fraction. Additionally, a ZTA-10 and a ZTA-21 material were prepared to get further information on the ZrO_2 transformation behaviour.

Although the preparation of Post-HIP dilatometer specimens containing 21 vol-% ZrO_2 particles was feasible (cf. Fig. 8), cracks were visible at the corners of the presintered specimens. The larger plates failed by critical crack propagation during cooling after sintering. The Sinter-HIP TZP-21 plates remained uncracked on the other hand, although they were cooled at the same rate.

Fig. 9 shows the effect of the pressure assisted densification treatment on the microstructure. In the as sintered state, micropores are present at triple points, and processing defects with a size similar to that of the alumina grains are visible. The Post- or Sinter-HIP treatment leads to the elimination of such defects and microporosity. The mean diameter of the Al_2O_3- grains is between 0.6 and 0.8 µm depending on the ZrO_2-content and the processing route. Post-HIPing results in a somewhat smaller grain as Sinter-HIPing, due to the longer process time required for pressurisation at high temperatures in the Sinter-HIP cycle. The ZrO_2 mean grain size is about 0.25 µm in all specimens.

The mechanical properties and ZrO_2-phase composition are given in Table 3. Bending strength and fracture thoughness decrease by increasing the amount of ZrO_2 particles from 12 to 18 vol-%. At 12 vol-% ZrO_2, a similar bending strength results from Post- and Sinter-HIP treatment. At 18 vol-% ZrO_2, the strength of the Sinter-HIP material is significantly lower. The fracture thoughness is always lower in the case of Sinter-HIP, compared to the Post-HIP-specimens.

The fraction of ZrO_2 which has been transformed to the monoclinic symmetry depends strongly on the ZrO_2 content. In the as fired state, the monoclinic fraction of ZTA-10 is on a similar level as in ZTA-12. In the as sintered ZTA-21 it reaches about 80 %, compared to 67 % of the Sinter-HIPed ZTA-21. This difference is in accordance with the fact, that the sintered ZTA-21 plates had failed during cooling, while the Sinter-HIPed plates did survive. A "critical" ZrO_2 content is already reached at 12 vol-%, as can be seen by the strong increase in monoclinic fraction in the as fired and the ground state of the ZTA-12.

4. Discussion of Results

From the results it becomes rather clear, that for a comparative treatment of the Post- and Sinter-HIP method for transformation thoughened oxides, many factors have to be regarded besides the transformation effect itself as a potential source of irreversible microstructural damages.

For the TZP materials regarded, the sintering atmosphere is one of these factors. Although there seems to be no direct influence of HIP atmosphere on the room temperature strength of Post-HIPed TZP [8], the dilatometer experiments clearly indicate, that densification is impeded in a partly reducing Ar + CO atmosphere, as it is present in the usual graphite heated HIP furnaces presently used. Therefore, Sinter-HIP requires enhanced processing temperatures and results in slightly coarser microstructures as they develop during Post-HIPing of materials presintered in air atmosphere. As the tendency for transformation of these materials strongly depends on their grain size, sintering atmosphere indirectly influences the mechanical properties. Regarding the TZP-2Y and the TZP-3Y chosen as the

usual representatives of these group of materials, the latter can be stated to be "overstabilised" for the processing conditions used in our investigation. The grain size is small enough in every case to prevent a spontaneous transformation during cooling. Even in the fracture surface only a very small amount of tetragonal ZrO_2 is transformed to the monoclinic symmetry. Therefore no difference in properties of Post- or Sinter-HIPed TZP-3Y can be expected.

Even in the TZP-2Y only a very small amount of spontaneous transformation is detectable in the as sintered or HIPed surface. On the other hand, about half of the material has been transformed in the fracture surface during crack propagation in the bending test. Therefore, transformation toughening is a mechanism clearly active in this material. Whether microcrack formation caused by t → m transformation in the cooling-reheating step can explain the difference in strength characteristics of the Post- and Sinter-HIPed TZP-2Y qualities seems to be doubtful on the other hand. From the fractographic analysis, a special type of processing flaws was found to be present in many Post-densified specimens (Fig. 10), in contrast to the Sinter-HIP specimens. The reason, why these type of flaws are healing out during Sinter-HIP and not in the Post-HIP treatment is not yet clear. Possibly, they are stabilised during the cooling step in the Post-densification process.

The spontaneous t → m transformation during cooling more distinctly occurs in the ZTA materials investigated. A great difference is observed in the behaviour of the ZTA 12 and the ZTA 18, where the amount of ZrO_2 spontaneously transformed increases from about 5 to 60 % in the sintered as well as in the Post- oder Sinter-HIPed condition. Obviously neither strength, nor thoughness properties show an advantage for the Sinter-HIP material. Therefore it seems justified to conclude, that the intermediate cooling during Post-HIP treatment does not change the microcrack configuration reached in the final microstructure. Only in a very narrow interval at the upper end of the here investigated ZrO_2 contents advantages for the Sinter-HIP process become visible. Here, transformation during the intermediate cooling step leads already to critical crack propagation causing really irreversible damaging of the material. Due to the enhanced density, this does not occur in the Sinter-HIP material. Unfortunately, this effect seems only to be of academic interest, as the optimum strength-thoughness combinations in ZTA are reached at much lower ZrO_2 volume fractions.

Although the few experiments carried out on this subject are far away from providing a basis for a final assessment, they reveal, that the role of the ZrO_2 transformation as a potential source of an irreversible microstructural damage during the cooling-reheating step of Post-HIPed transformation thoughened ceramics is of minor importance. More attention has to been paid to other factors, like the microstructure present at the beginning of the pressure assisted part of the densification cycle and its role on further densification.

Acknowledgement

The authors thank T. Jüngling and D. Meyer for their contribution to the experiments. The help of Mrs. M. Ganz and R. Müller with the preparation of the manuscript is gratefully acknowledged.

5. Literature

[1] Lange F.F.: Processing-Related Fracture Origins:I. Observations in Sintered and Isostatically Hot-Pressed Al_2O_3/ZrO_2 Composites. J. Amer. Ceram. Soc. 66 (1983) 396

[2] Hori S.,Yoshimura M., Somiya S.: Strength-Toughness Relations in Sintered and Isostaically Hot-Pressed ZrO_2-Toughened Al_2O_3. J. Amer. Ceram. Soc. 69 (1986) 169

[3] Claussen N.: Microstructural Design of Zirconia-Toughened Ceramics (ZTC). In: Science and Technology of Zirconia II (Claussen N., Rühle M., Heuer A.; Eds). J. Amer. Ceram. Soc. Columbus, Ohio (1984) p. 325

[4] Evans A.G., Cannon R.M.: Toughening of Brittle Solids by Martensitic Transformations. Acta metall. 34 (1986) 761

[5] Niihara K., Morena R., Hasselman D.: Evaluation of K_{IC} of Brittle Solids by the Indentation Method with Low Crack-to-Indent Ratios. J. Mater. Sci. Letters 1 (1982), 13

[6] Liu T., Grathwohl G.: Crack Resistance curve of ZrO_2/Al_2O_3 with Long Natural Sharp Cracks. Zirconia 88, Dec. 17, 1988, Bologna, Italy

[7] Müller R.A., Smialek J.L., Garlick A.G.: Phase Stability in Plasma-Sprayed Partially Stabilized Zirconia-Yttria. In: Science and Technology of Zirconia I (Heuer A.H., Hobbs L.W., Eds.). Amer. Ceram. Soc., Columbus, Ohio (1981), p. 241

[8] Green D.J.: Critical Microstructures for Microcracking in Al_2O_3-ZrO_2 Composites. J. Amer. Ceram. Soc. 65 (1982), 610

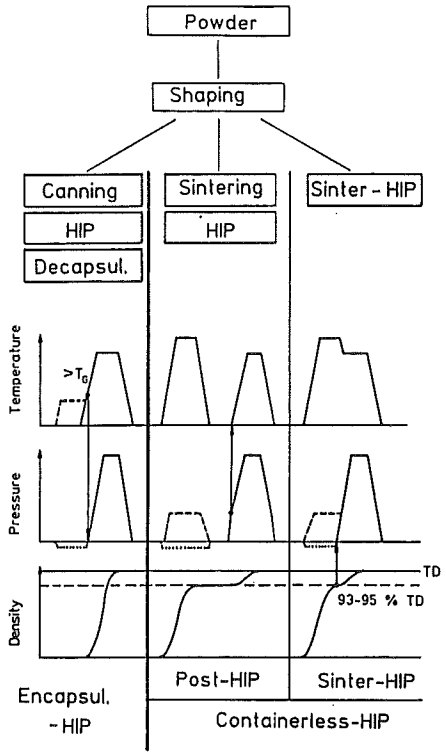

Fig. 1: HIP - processing variants (schematic)

	TZP-2Y	TZP-3Y	ZrO_2	Al_2O_3
ZrO_2	n.d.	n.d.	n.d.	0.0001
Al_2O_3	<0.005	0.092	0.017	>99.9
Y_2O_3	3.56	5.24	n.d.	n.d.
MgO	n.d.	n.d.	n.d.	0.049
SiO_2	<0.002	0.011	<0.002	0.009
Na_2O	0.040	0.004	0.004	0.008
BET (m^2/g)	17.8	17.3	13.7	7.1
Crist. (nm) size	25	27	28	550
Phases XRD (%)	10 m 90 t	10 m 90 t	100 m	95 α
Supplier	TOSOH			REYNOLDS

Table 1: Characteristics of starting materials

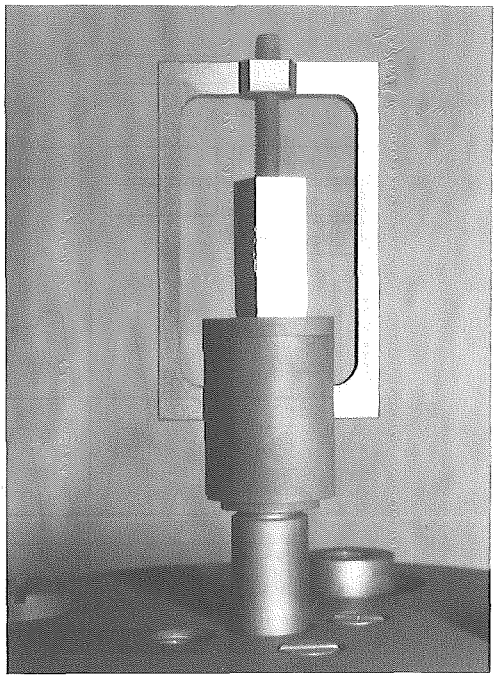

Fig. 2: Specimen holder of the HIP - dilatometer system

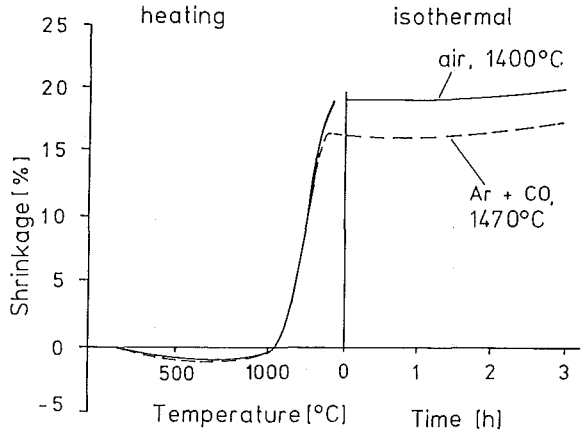

Fig. 3: Sintering behaviour of TZP - 3Y in CO-contaminated Ar atmospheres

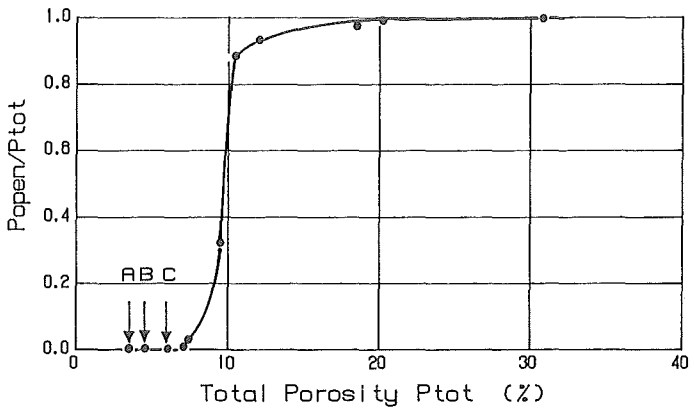

Fig. 4: Pore Closure in TZP - 3Y

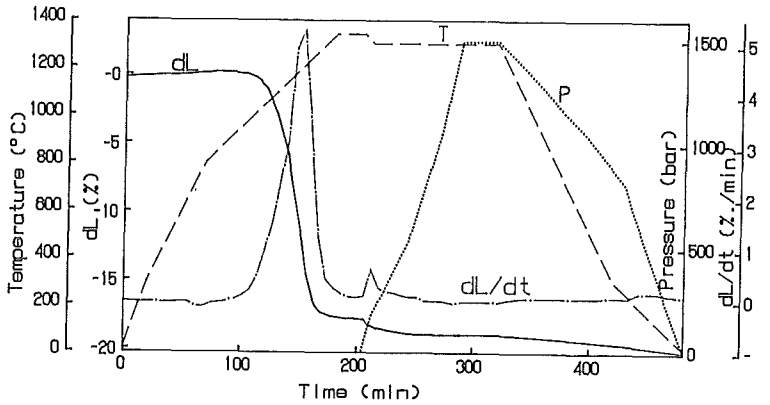

Fig. 5: Densification of TZP - 2Y during a Sinter-HIP cycle

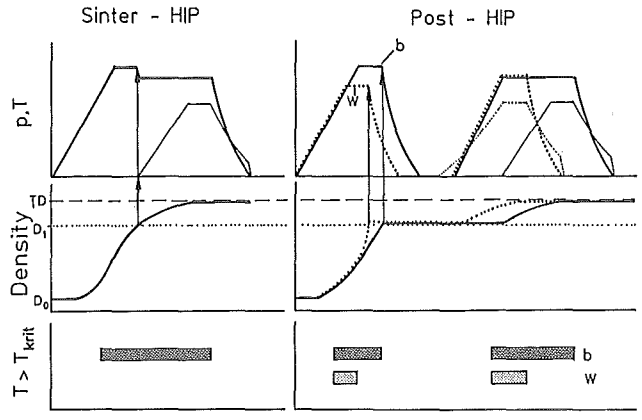

Fig. 6: Containerless HIP processing cycles used in the experiments

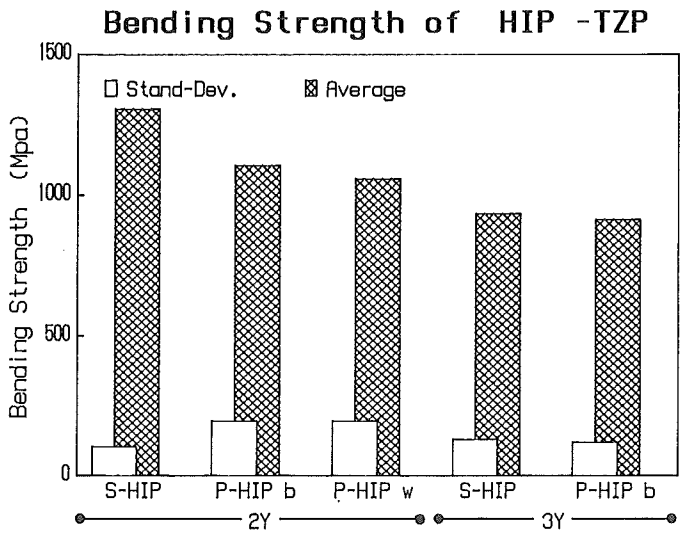

Fig. 7: Bending Strength of TZP produced by Post- and Sinter-HIP

	TZP - 2Y			TZP - 3Y	
	Sinter HIP	Post HIP b	Post HIP w	Sinter HIP	Post HIP b
Grain diam. $\bar{d}$ (μm)	0.25	0.26	0.20	0.24	0.28
Hardness HV 10	1025	1020	1180	1460	1475
K_{IC} (MI) Mpa$\sqrt{m}$	4.9	4.9	7.0	4.7	4.7
% monoclinic - as fired - ground - fr.- surf.	 -- 10	 <2 8 ≈50	 <2 7	 -- <2 ≈10	 -- <2
Bending Str.(MPa)	1304	1103	1057	934	914
Density (g/cm^3)	6.10	6.10	6.10	6.08	6.08

Table 2: Properties of TZP produced by different Post- and Sinter-HIP treatments (T= 1300°C, P= 150 MPa)

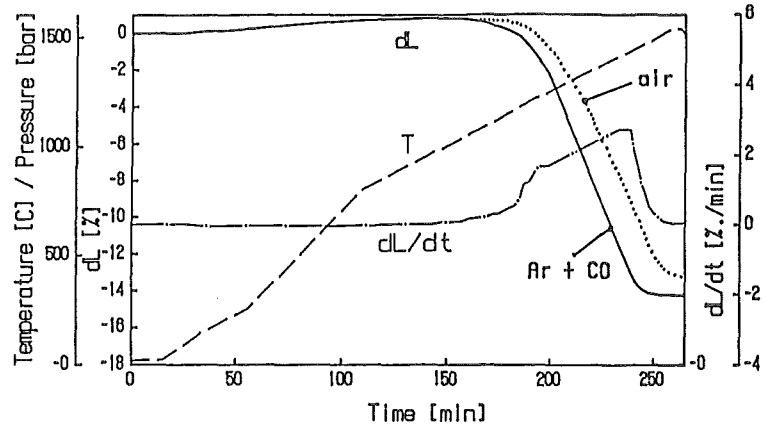

a)

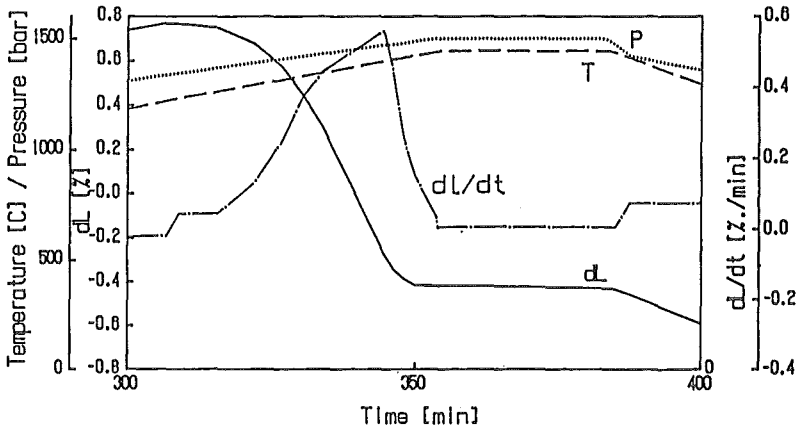

b)

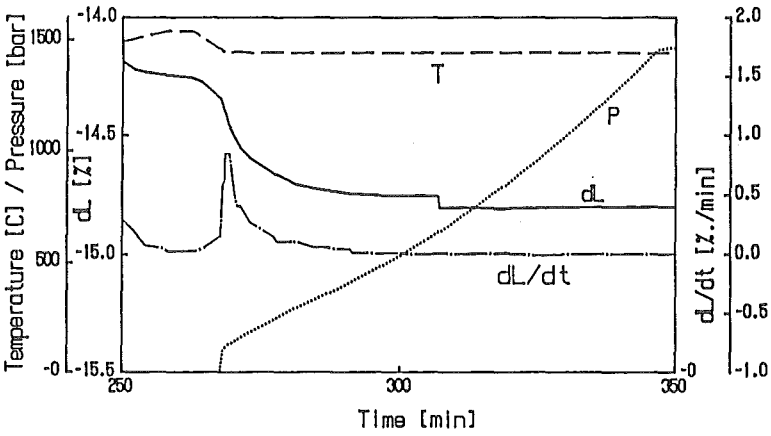

c)

Fig. 8: Densification of ZTA - 21 during Post- and Sinter-HIP treatment

a) Pressureless sintering

b) Pressure assisted densification during Post-HIP

c) Pressure assisted densification during Sinter-HIP

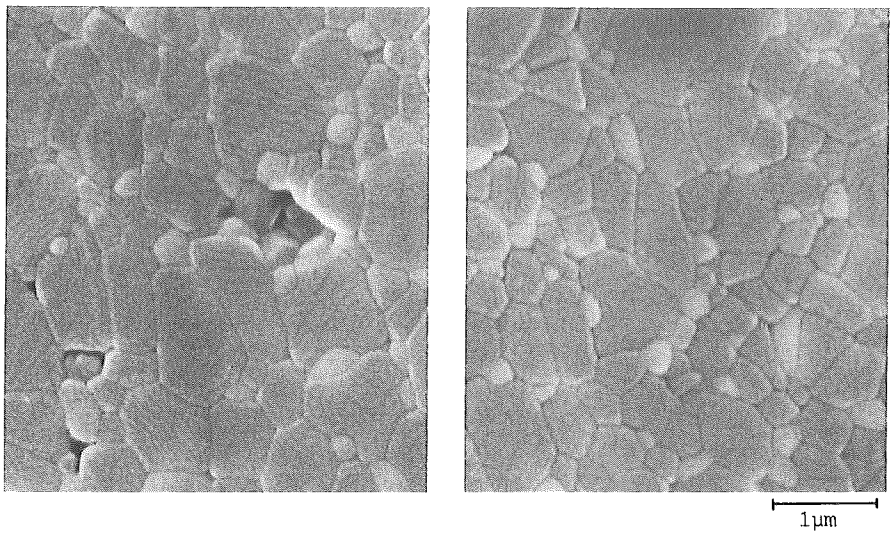

Fig. 9: Elimination of residual Porosity in ZTA-12 by Post - HIPing

	ZTA - 12			ZTA - 18		
	as sint.	Sinter HIP	Post HIP	as sint.	Sinter HIP	Post HIP
$\bar{d}$-Al_2O_3(µm)	0.67	0.80	0.72	0.58	0.78	0.58
HV 10	1715	1750	1810	1650	1625	1730
K_{IC} (NB)		4.8	5.7		4.1	5.7
% monoclinic -as fired -ground -fr.-surf.	9	5 37 39	5 35 25	66	68 64 80	65 62 75
σ_b (MPa)		560	550		463	520
ρ (g/cm^3)	4.18	4.22	4.22	4.29	4.32	4.32

Table 3: Properties of Post- and Sinter-HIPed ZTA

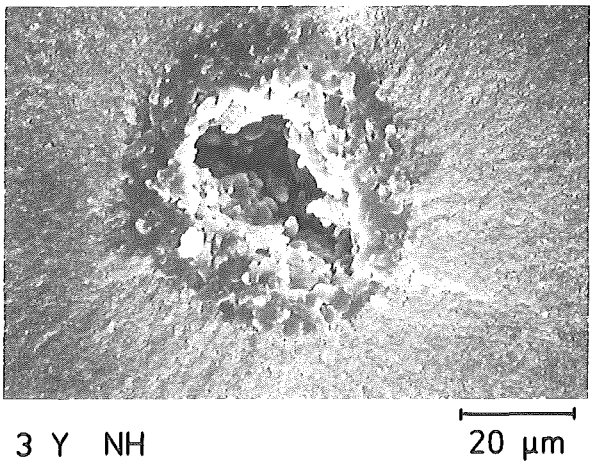

Fig. 10: Processing defect in Post-HIPed TZP-3Y

PROCESS DEVELOPMENT FOR SINTER-HIPING OF SIC

T. Fetahagic*, R. Oberacker, F. Thümmler

Institut für Werkstoffkunde II, Institut für Keramik im Maschinenbau,
Universität Karlsruhe

* Institut Jozef Stefan, Ljubljana

Abstract

Pressureless sintering of SiC to high density levels requires the presence of additives which often remain at the grain boundaries and deteriorate the mechanical high temperature properties. Encapsulated HIPing allows to avoid this problem but is very expensive due to the requirements for the capsule material at the high processing temperature which are necessary. Post-HIP treatments result only in a marginal increase of mechanical properties. Therefore Sinter-HIP processing of SiC is investigated. In the first part of the work a systematic investigation on sintering behavior of SiC is carried out with the goal, to reach the pore closure of the material with a minimal amount of additives at HIP-compatible temperatures. The microstructure present at this state of densification is characterised and will be correlated with the densification behaviour under high pressure investigated in the proceeding part of this work.

1. Introduction

Pressureless sintering is one of the most commonly used methods to produce high density silicon carbide ceramic. The manufacturing process is not yet fully optimized and presence of large pores, cracks, inclusions and inhomogenities are commom characteristics of this type of silicon carbide. The moderate mechanical strength (400 MPa) is a consequently result of this microstructural features. Also, the necessary sintering aids for obtaining high densitiy levels often remain at the grain boundaries and deteriorate the mechanical high temperature properties [1].

HIP process offers more advantages in ceramic processing [2]. The most important HIP advantages are: density increase, healing of major processing flaws, more reproducible properties and improved or even novel microstructure. There are different variants of HIP processing; and the basic HIP techniques (Fig 1) are: 1. Post-HIPing, 2. Encapsulated HIPing and 3. Sinter-HIP processing [3].

The application of these HIP-techniques for the fabrication of dense silicon carbide materials is "in principle" possible today, but for each HIP variant there exist some different problems or imperfections. So Post-HIP treatments result only in marginal increase of mechanical properties [4]. Encapsulated HIPing makes it possible to densify SiC without additives, but is very expensive due to the requirements for capsule material at the high

processing temperatures which are necessary [4]. Due to the low viscosity, use of silica glass as capsule material at a temperature of 2000°C is not possible as the glass flows from the SiC part (body). HIPing of SiC parts in glass foam or mixtures of SiC powder and glass at 2000°C were sucessful but are applicable only for simple forms of SiC parts from which it is easy to remove material of used support after HIPing [3].

There are not many references on Sinter-HIP. In fact there is only one publicated work [5] in which a cost analysis comparing sintering, Post-densification and Sinter-HIP has been carried out, indicating a cost factor reduction of about 35 % if Sinter-HIP was applied.Therefore, systematic research work related on uninvestigated problems of Sinter-HIP is necessary to realize. The present investigations are the first results of a research project on "Process Development for Sinter HIPing of SiC". In this first phase of the work a systematic investigation of sintering of SiC compositions was carried out with the goal to reach pore closure with minimal amounts of additives at Sinter-HIP compatible temperatures. Maximum processing temperature which can today be used in Sinter-HIP furnaces is about 2000°C at 1 bar pressure and in accordance with this fact, SiC compositions for Sinter-HIP have to be highly densified (to level pore closure) at temperatures below 2000°C. On the other hand decrease of processing (sintering) temperatures by increasing of the amount of additives or using additives which develop large quantities of a liquid phase have a negative influence on the mechanical characteristics of SiC materials. Since the promoting effect of simultaneous presence of aluminium, boron and carbon on sintering of ß-SiC was recently observed [6], same additives were used in this work, but the goal of the present investigation was to determine lower limits of additive amounts still effective to reach pore closure in α-SiC below 2000°C. For comparison the today already "classic" high temperature sintering SiC compositions with boron and carbon addition were also taken into account.

2. Experimental

The starting material was an experimental α-SiC powder with the usual characteristics of sinterable SiC-powders: a submicron medium particle size, the specific surface area 14-15m^2/g and low oxygen and metal impurities content. The main cristalline phases identified by X-ray analysis were 6H and 15R. Boron carbide, aluminium nitride and carbon were used as sintering aids. B_4C and AlN powders with a particle size of below 5 µm were directly introduced in the mixtures. Phenolformaldehyde resin solution in aceton served as a carbon source. The starting mixtures were prepared by mixing during minimum two hours in a polyamide jar with teflon balls under acetone. In addition, 2 wt-% oleic acid were added as pressing aid. After drying, the powder was granulated by passing through a 0.25 mm screen.

Green samples were prepared by two ways: 1. in a steel die by axial pressing with a variation of the pressure from 100-400 MPa (green density 63.0 - 69.5% TD) and 2. the samples were first formed in a steel die with a pressure of 10 MPa to about 50 % TD and then isostatically repressed (400 MPa) to final green density 65 - 70 % TD. The shape and the dimensions of these green samples were: round tablets Ø = 20mm, h = 6mm and prismatic tablets of 55x26x8mm. Pressureless sintering was performed in a high temperature

Astro furnace equiped with a high temperature dilatometer. The maximum sintering temperatures varied from 1900- 2150°C and the soaking time at these temperatures were 0-30 min. in flowing argon atmosphere under normal pressure.

Sintered SiC samples were characterised by dilatometric measurements (densification behaviour) and by determination of densities and porosity (Archimedean method). The SiC microstructures were analysed after grinding, polishing and etching with Murakami's agent by optical and scanning electron microscopy.

3. Results and discussion

3.1 Sintering in simultaneous presence of aluminium and boron

The effect of the additves B and Al on the sintering behaviour was investigated by using a high temperature dilatometer. In Figs. 2a, 2b and 2c linear shrinkage and sintering rate of three investigated SiC compositions with the addition: 1.0% Al, 0.1% B and 1.0% Al+0.1% B are shown. From these figures a difference in the sintering rate of Al or B additive containing SiC compositions may be observed, depending on temperature. The composition with Al addition (Fig 2a) has a maximum in sintering rate at about 1800°C, the maximum for B addition is at 1980°C (Fig 2b). By using Al and B simultaneousely (Fig 2c), the rate of sintering versus the temperature shows two maxima: the first from Al at 1850°C and the second from B at 1980°C. From this curve it may be also observed that this composition reached a high degree of densification already at 2000°C.

On the basis of these first experimental results, the composition with 1% Al and 0.1 %B was taken as the basic composition for extensive systematic investigations directed to get optimum SiC composition and sintering parameters for Sinter HIP-processing.

3.2 Pore closure and microstructures in investigated SiC compositions

Al+B doped and solely B doped SiC compositions with varied amounts of carbon were used for that examination:

Al+B doped SiC	B doped SiC
1. SiC+1.5%C+1.0%Al+0.1%B	4. SiC+1.5%C+0.4%B
2. SiC+3.0%C+1.0%Al+0.1%B	5. SiC+3.0%C+0.4%B
3. SiC+4.5%C+1.0%Al+0.1%B	6. SiC+4.5%C+0.4%B

Carbon is varied for its influence on the growth of SiC grains during sintering [7]. Sintering time in this set of experiments was always 0.5h and sintering temperature was varied from 1900 to 2150°C.

Figure 3 shows the effect of sintering temperature on density for Al+B doped and B doped SiC compositions with varied C additions. It can be obseved, that two Al+B doped compositions achieved densities greater than 95% TD already at 1950°C. At 2000°C all three compositions with the combined dopants have a density near 98% TD and further increasing of the temperature has not larger effect. On the other side curves of the compositions with B additive alone are shifted to higher sintering temperatures. At the temperature 2080°C high densities are achived (>95% TD), especially for compositions with 3.0 and 4.5% of carbon (ca 98.5% TD). It confirms our earlier investigations that an addition of 0.3-0.4 wt-% B will bring the maximum achievable densification of silicon carbide at temperatures of about 2100°C [8].

Closing of pores as the variation in the open and closed pore fraction versus the total porosity in the investigated SiC compositions is demonstrated by the curves in Figs. 4a and 4b. In the Al+B doped SiC compositions (Fig. 4a) closing of pores is intensive already at sintering temperatures above 1925°C. After 30 min. sintering at 1950°C total porosity of compositions with excess of carbon (3.0 and 4.5% C) is below 5% and fraction of open to closed pores is less than 0.2. Pore closure of third composition with 1.5% C is a little slower. Curves of B doped SiC compositions (Fig 4b) show a high degree of open porosity at a sintering temperature of 2000°C. The curve for 1.5 % carbon addition also slower decreases. From the curves related on 3% and 4.5% carbon addition it can be seen that the fraction of closed pores at 2040°C is large and after 30 min. sintering at 2080°C open porosity is nearly completely eliminated.

In Figures 5a and 5b the changes of the amount and the quality of the porosity in Al+B doped and B doped SiC with 3.0% carbon addition in both compositions is demonstrated again. From this figures it can be clearly seen, that the elimination of open porosity is depending on sintering temperature and it also can be concluded whether a Sinter-HIP process could be applied, this means, whether pore closure can be achieved below 2000°C. That was sucessfully realised with Al+B doped compositions (Fig 5a); residual porosity at 2000°C is only 2.5% and that is closed porosity. However, in B doped compositions (Fig 5b) closed porosity is predominant only at temperatures over 2040°C, but at a higher degree of total porosity. The different relations between open and closed porosity can be qualitatively correlated to the degree of exaggerated grain growth in the materials.

Figs 6 and 7 show the microstructure development of investigated SiC + 3% C compositions: (1.) with simultaneous presence of Al+B and (2.) only with B. From figures related on Al+B sintered SiC samples at various temperatures the anisotropic grain growth can be observed. This is already marked at lower temperatures (1950°C), and by increasing the sintering temperature the exaggerated grain growth is more significant. The longest grains at 1950°C are about 100 μm and at higher temperatures (2150°C) some grains reached 500 μm. This phenomenon of exaggerated grain growth can be released by the presence of aluminium in starting compositions [9]. In the Al-free SiC compositions (Fig 7) equiaxed grain growth is observed in samples sintered at 2080°C (equiaxed grains are under 10 μm) whereas in samples sintered at 2150°C anisotropic grain growth occurs remarkably and largest grains exceed 200 μm in length.

The positive effect of increasing the amount of the carbon additive on the inhibition of grain growth in SiC is demonstrated in Fig. 8. From these SiC microstructures it can be seen that the change in carbon content in starting compositions from 1.5% and 3.0% to

4.5% (samples sintered 30 min. at 2000°C) results in a smaller grain size of the sintered SiC. The exaggerated grain growth in low carbon content compositions (1.5% C) with largest grains of 200 µm in length (Fig. 8a) is in certain measure retarded by addition of 4.5% carbon. However, anisotropic grain growth remain further characteristic of this compositions with higher carbon content and some elongated grains to 100 µm in length are present in the microstructure (Fig. 8 c).

SEM micrographs of etched samples of the here developed low temperature sintering compositions (SiC + 3.0%C + 1.0%Al + 0.1%B) compared with high temperature sintering compositions (SiC + 3.0%C + 0.4%B) reveal better the difference in their microstructures (Fig. 9). Rapid grain growth in Al + B doped SiC compositions results in the appearence of anisotropic grains with entrapped porosity already after sintering at 1950°C (Fig. 9a). On the other side more uniform and equiaxed grains, only with some grain boundary porosity are a general characteristic of the microstructure of these boron doped SiC compositions sintered 30 min. at 2080°C (Fig. 9 b).

Generally, from the measurements of the porosity and microstructural examinations of the same SiC samples it is observed, that SiC compositions with more pronounced tendency toward to exaggerated grain growth (Al + B, low C) achieve pore closure at a lower degree of residual porosity than compositions with a higher resistance against grain growth (solely B, high C).

Although this comparison of microstructural features gives B doped SiC compositions a preference over Al + B doped SiC compositions; due to their high sintering temperatures (over 2000°C), B doped SiC compositions can not be used in Sinter-HIP-processing, but of course for Post-HIPing. However, the here developed SiC compositions with simultaneous presence of Al+B additives are attractive for Sinter-HIP processing, due to their high density and high rate of the pore closure at sintering temperatures as low as 1950 - 2000°C. Of course, further optimisation of this compositions and their microstructures seem to be necessary.

4. Conclusions

1. α-silicon carbide compositions with simultaneous presence aluminium and boron additives may achieve densities of ≥ 95 % TD by pressureless sintering at temperatures well below 2000°C.

2. Rate of pore closure in investigated SiC compositions is depending on sintering temperature and the amount of carbon additive. In Al+B doped SiC compositions, closed porosity is predominant at 1950°C, whereas in SiC compositions only with B-addition this state is achieved only at temperatures above 2040°C.

3. Exaggerated grain growth is a general characteristic of the microstructures of Al+B doped sintered SiC. Higher carbon contents have a positive effect on the inhibition of grain growth of investigated SiC compositions, but anisotropic grains with entrapped porosity are present already after sintering 30 min. at 1950°C.

4. As the maximum processing temperature which can today be used in Sinter HIP-furnaces is about 2000°C at 1 bar pressure, SiC compositions with simultaneous presence Al+B additives,which are achieving pore closure already at 1950°C are preferentially applicable for Sinter-HIP processing.

Literature:

1. R. Hamminger, G. Grathwohl, F.Thümmler; Microanalytical investigation of sintered SiC, J.Mat.Sci., 18 (1983), 3154-3160.

2. Davidge R. Sleurs J., Beukenhout L.: Hipping of Technical Ceramics: a Synopsis, Proceed. of Int. Conf.on Hot Isostatic Pressing of Materials, Antwerp. April 1988 Ed. Royal Flemisch Soc. of Engineers.

3. Oberacker, R., Kühne A., Thümmler F.; Einsatzmöglichkeiten für die Sinter-HIP-Technik bei der Herstellung keramischer Hochleistungswerkstoffe. In: Sinter/HIP Technologie. Pulvermetallurgie in Wissenschaft und Praxis 3, Verlag Schmidt (1987) 87-108.

4. Hunold K., Grellner W.; Möglichkeiten und Grenzen beim Heißpressen und Heißisotatpressen von Siliciumkarbid. In: Keramische Komponenten für Gasturbinen II. (Bunk W., Böhmer M.) Springer Verlag Berlin (1981) 499-516.

5. Hunold, K.; Sinterung und Heißisostatische Nachverdichtung von Siliciumkarbid; ibid lit. 3, 255-269.

6. Stutz, H., Prochaska, S.: Sintering and Microstructure Formation of α-Silicon Carbide; J. Amer. Ceramic. Soc. 68 (1985) 479-482.

7. Murata Y., Smoak R.H.; Densification of Silicon Carbide by the Addition of BN, BP, and B_4C, and Correlation to their Solid Solubilities, in Factors in Densification and Sintering of Oxide and Non-Oxide Ceramics (ed. S. Somiya, S. Saito), Assoc. Sci. Doc. Inform, Tokyo, (1978) 382-399.

8. Fetahagic, T., Kolar, D., J. Holc; In Contemporary Inorganic Materials: "Progress in Ceramics, Metals and Composites", Proc. 7^{th} German-Yugoslav Meeting on Engineering Materials Science and Technology, Bad Herrenalb, April 22-26, 1985., Ed. G. Ondracek, O. Vöhringer, KFA Jülich GmbH, 1985, 69-77.

9. Suzuki, H. and Hase, T.; Some Experimental Consideration of the Mechanism of Pressureless Sintering of Silicon Carbide, ibid.lit. 7, 345-365.

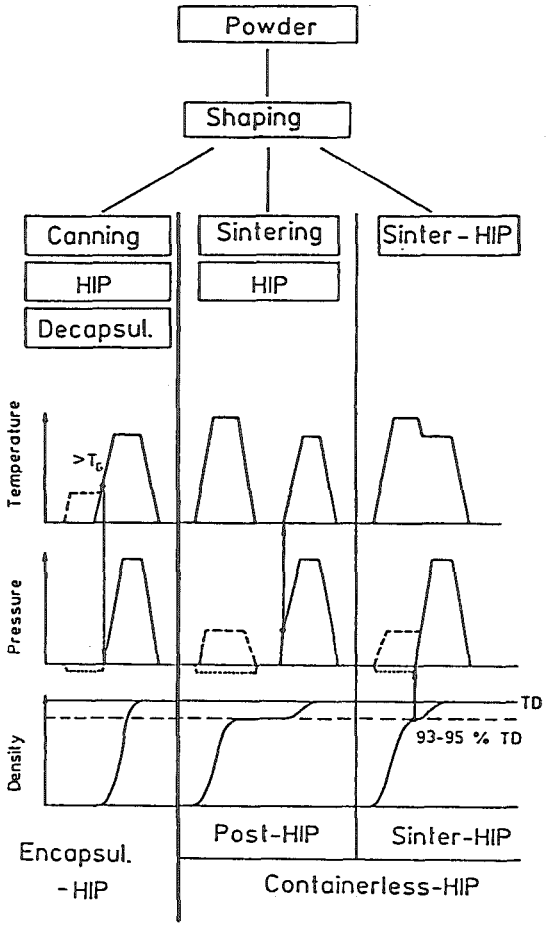

Fig. 1: HIP-Processing Routes

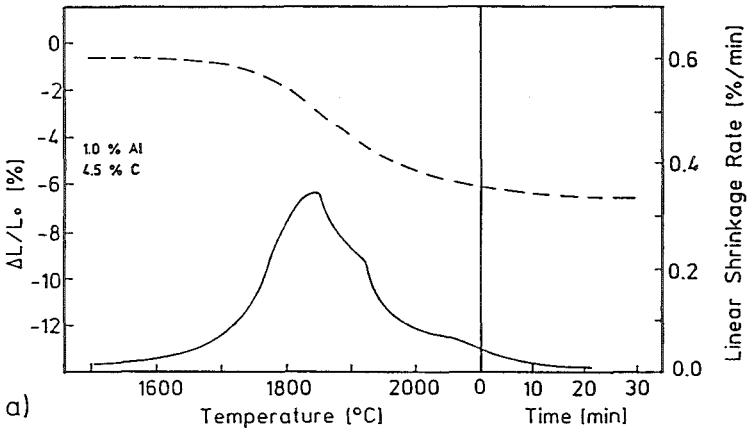

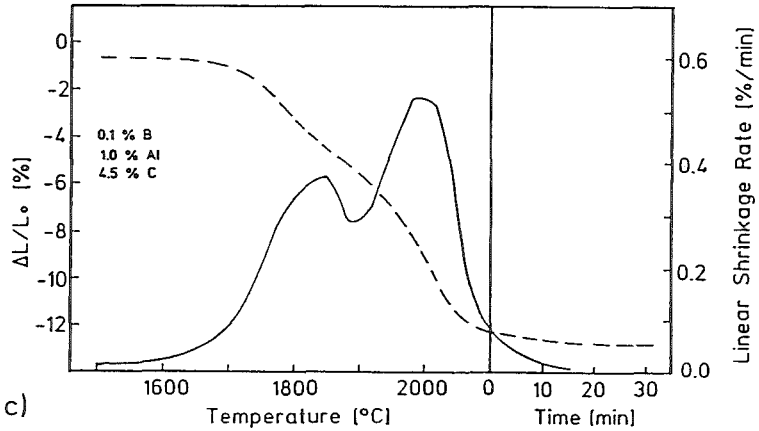

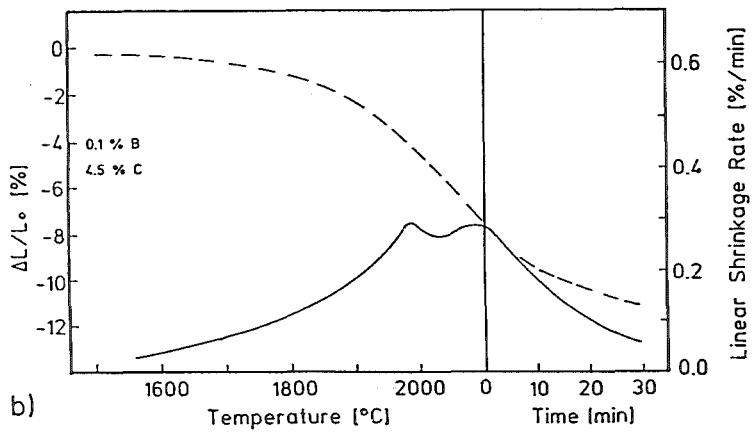

Fig. 2: Sintering behaviour of α-SiC with an addition
a) 1.0 wt% Al, b) 0.1 wt% B,
c) 1.0 wt% Al + 0.1 wt% B;
(carbon addition is const. 4.5 wt%).

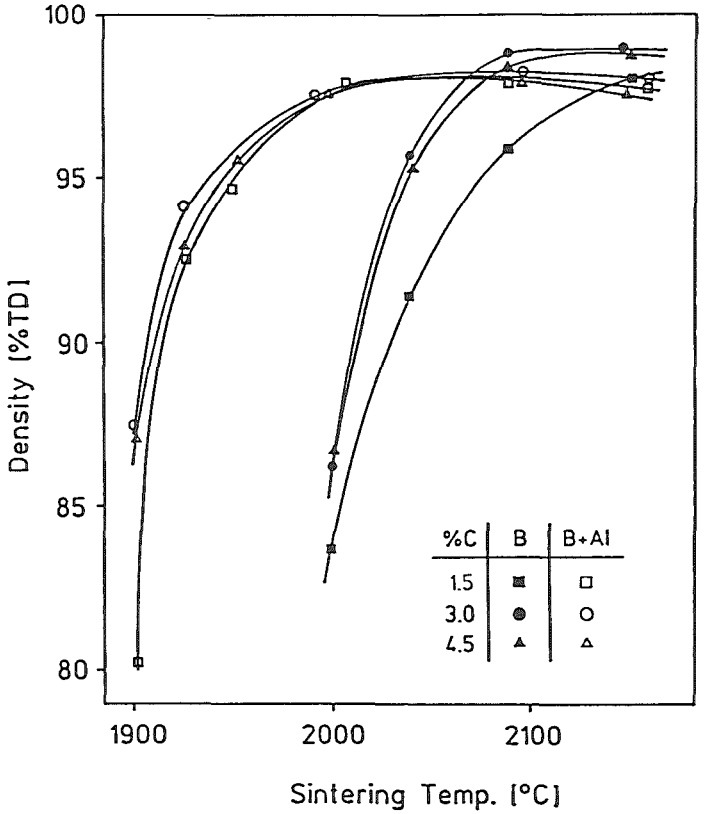

Fig. 3: Effect of sintering temperature on density Al + B doped and B doped SiC compositions with varied carbon additions (sintering time 30 min.)

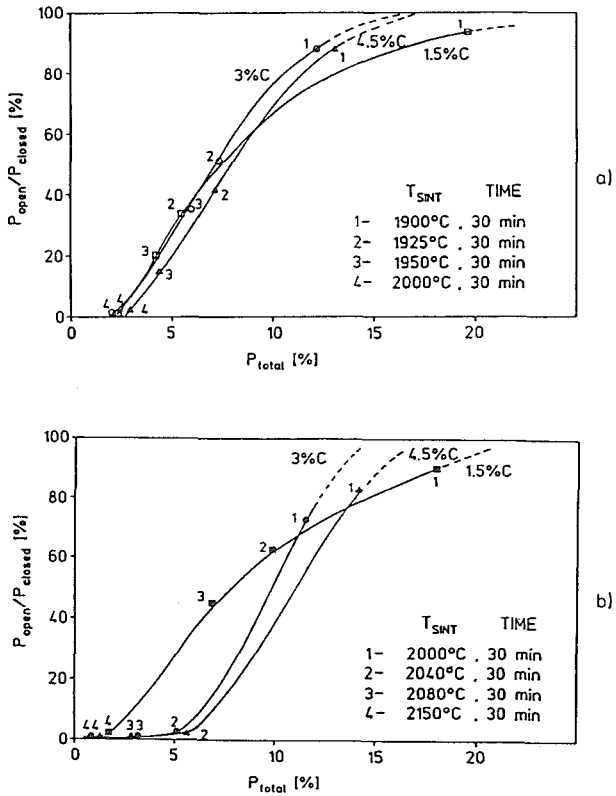

Fig. 4: Closing of pores in sintered SiC:
a) Al + B additives compositions and
b) B additiv compositions

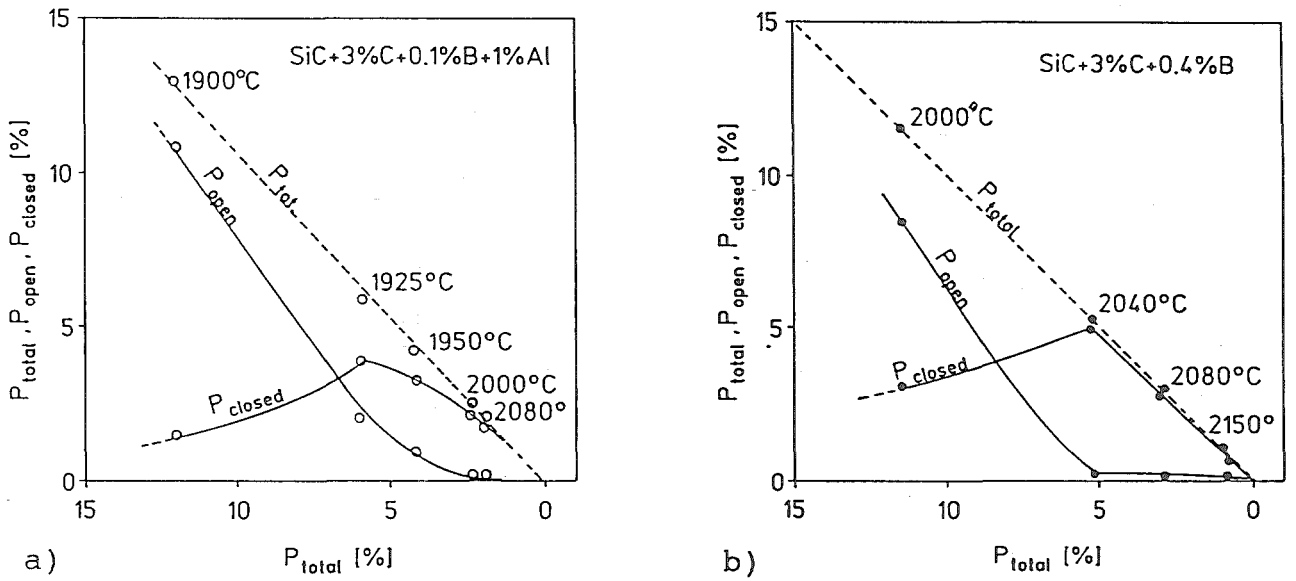

Fig. 5: Open and closed porosity in SiC samples sintered 30 min. at different temperatures:
a) composition SiC + 3,0 C + 1,0 Al + 0,1 B and
b) compsition SiC + 0,3 C + 0,4 B

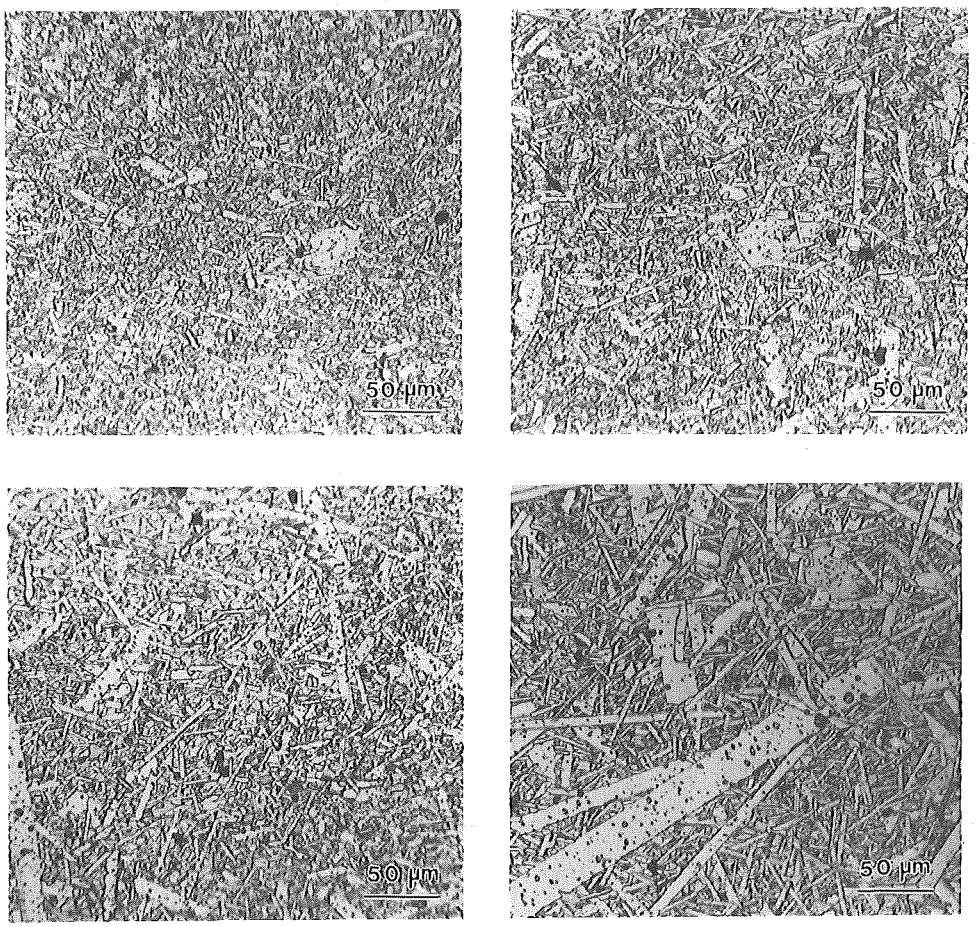

Fig. 6: Development of microstructure compositions
SiC + 3,0 C + 1,0 Al + 0,1 B sintered 30 min.:
a) at 1950 °C, b) at 2000 °C, c) at 2080 °C and
d) at 2150 °C.

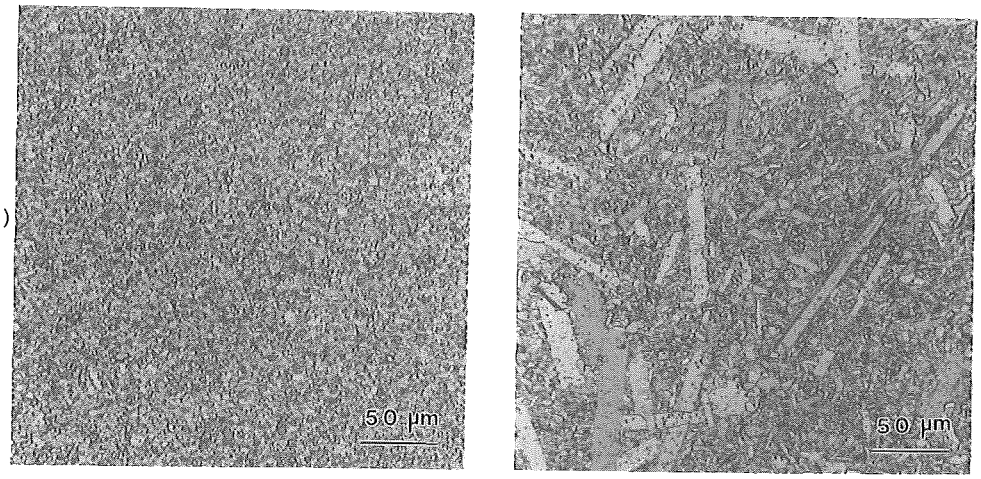

Fig. 7: Development of microstructure compositions SiC + 3,0 C + 0,4 B sintered 30 min.: a) at 2080 °C and b) at 2150 °C.

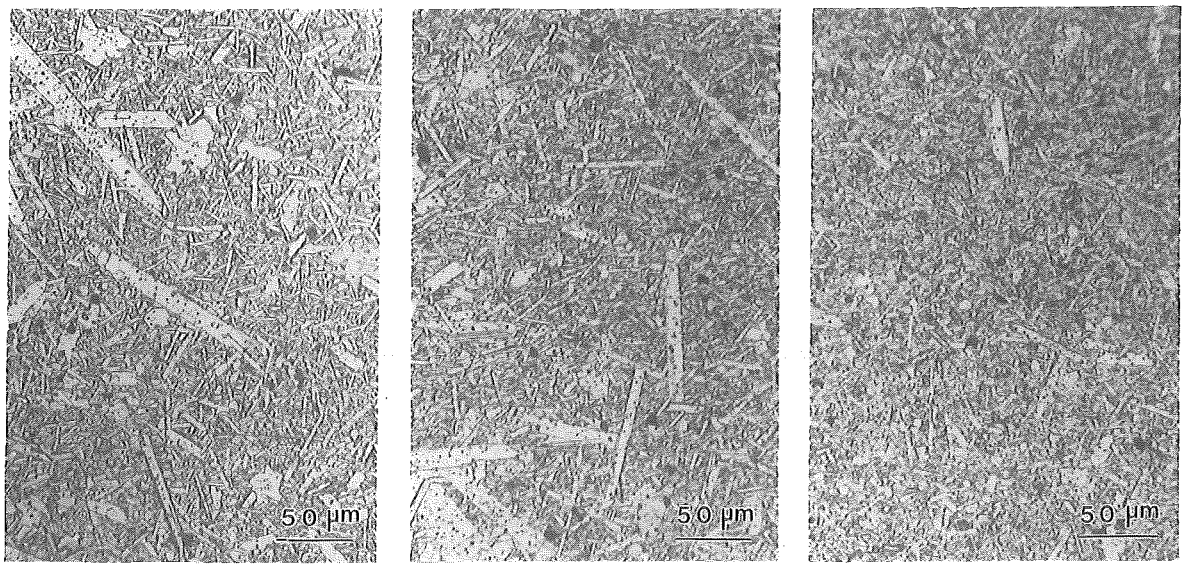

Fig. 8: Influence of carbon additions on the microstructure SiC + 1,0 Al + 0,1 B compositions sintered 30 min. at 2000 °C.
a) + 1,5 % C additive; density 97,8 % TD,
b) + 3,0 % C, density 97,9 % TD and
c) + 4,5 %, density 97,1 % TD.

a)

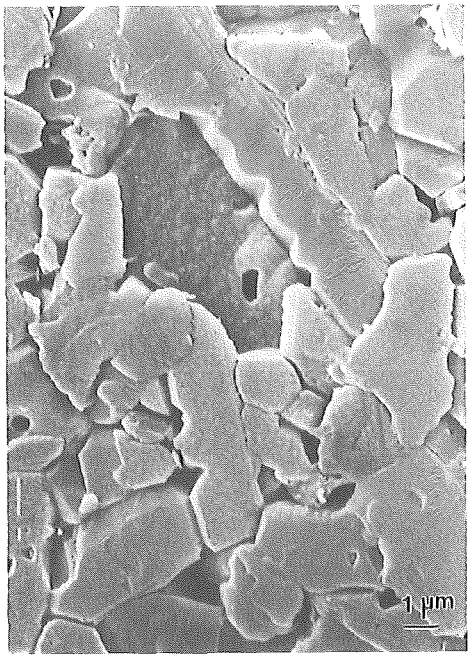

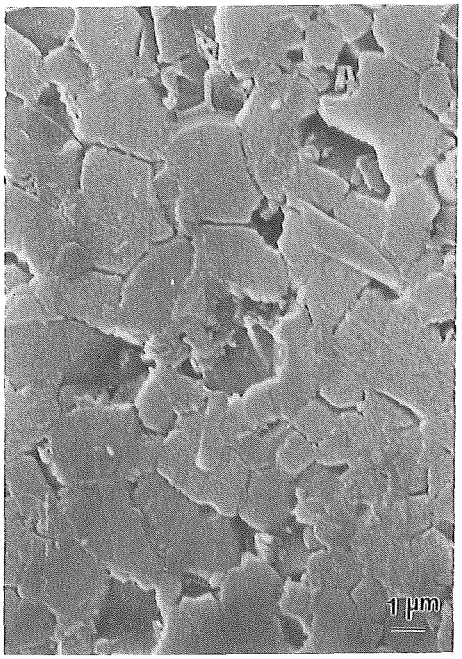

b)

Fig. 9: SEM-microstructure of etched SiC samples
a) SiC + 3 C + 1 Al + 0,1 B, T_s = 1950 °C, 30 min; density 95,8 % TD
b) SiC + 3 C + 0,4 B; T_s = 2080 °C, 30 min.; density 98,8 % TD.

PROPERTIES

PRECIPITATION MIXING OF SILICON NITRIDE WITH BIMETALLIC OXIDES

Wolfgang Oroschin, Michael Kulig and Peter Greil
Technische Universität Hamburg–Harburg
Arbeitsbereich Technische Keramik
Harburger Schlosstr. 20, D–2100 Hamburg 90, FRG

Sol–gel coating of submicron silicon nitride powder by hydroxide precipitation from bimetallic alkoxides in non–aqueous solution was examined. Mg–Al, Y–Al, and Nd–Al alkoxide mixtures were prepared with various intermetallic ratio. The precipitation of the bimetallic hydroxides in the silicon nitride powder resulted in an improved elemental distribution as compared to the mechanically mixed powder. Acoustophoretic measurements in aqueous solution indicate a surface coating of the silicon nitride with a hydroxide gel–layer which significantly changes the surface chemistry and the structure of the electric double layer. Depending on the dissolution and electrolyte adsorption behaviour of the metal hydroxides a surface activation may be observed in the precipitation mixed powder which may be used for optimizing the slip casting and pressing properties of sinterable silicon nitride powder mixtures.

1. Introduction

Sintering of silicon nitride powder is only possible in the presence of melt forming sintering aids, which promote a liquid phase sintering process by dissolution, diffusion and reprecipitation of silicon nitride upon heating /83 Wei/. Usually, multiphase oxide mixtures of alumina, magnesia, calcia, yttria or rare earth oxides are used as sintering aids. During cooling, part of the sintering liquid is retained in the grain boundary areas as a thin glassy layer. Crystallization of the liquid and glassy phases into refractory grain boundary phases by controlled heat treatment (devitrification) has been successfully utilized to improve the high temperature

mechanical properties of silicon nitride ceramics, in particular strength, creep and slow crack growth resistance /87 Gre/. The microstructure formation during sintering of the multicomponent powder mixtures and crystallization heat treatment, however, will be essentially influenced by the uniformity of chemical composition in the starting powder. Chemical inhomogeneities such as local concentration gradients and single phase agglomerates may generate pores and flaws upon sintering due to differential shrinkage /84 Raj/. Crystallization of ternary phases from the sintering liquid like $Y_3Al_5O_{12}$ (YAG) or higher component phases for example quaternary and quinary oxinitrides /87 Gre/ may be impeded by inhomogeneous elemental distribution and large chemical gradients (diffusion paths) resulting in the formation of a high amount of residual glassy phase at the grain boundaries.

Generally, the distribution of the various powder components is achieved by mechanical mixing techniques like ball or attrition milling. Decreasing grain size and increasing purity of newly developed silicon nitride powders, however, requires advanced powder processing techniques to avoid uncontrolled external as well as internal (particle–particle interaction) physical and chemical contamination. Colloidal processing techniques such as mixing of soluble compounds and precipitation in deflocculated and stabilized suspension may therefore provide an improved way for homogeneous distribution of sintering additives as compared to mechanical mixing of insoluble powders. Thus, a significant reduction of the necessary additive content and hence improved high temperature properties due to a reduced content of residual intergranular glassy phase can be expected by optimum additive distribution via wet chemical mixing techniques. Such powders seem to be of particular interest for slip casting and pressing techniques, which gain increasing interest for the formation of defect controlled and high dense green compacts from colloidal powder mixtures /89 Lan/.

Uniform mixtures of silicon nitride powders and additive precipitates were obtained by precipitation of Mg– and Y–hydroxide with tetraethylammonium–hydroxide from aqueous metal nitrate solutions. Samples from these mixtures showed a much greater green compact homogeneity and higher sintered densities than the mechanically mixed powder /86 Sha/. The hydrolytic or thermal decomposition of metal alkoxides was shown to be a convenient method for homogeneously dispersing very small quantities of oxides or mixed oxides in silicon nitride. Thus, high density silicon nitride with a minimum of Y_2O_3 or CeO_2 as the hot–pressing aid was

prepared by hydrolysis of Ce– or Y–isopropoxide from an isopropyl alcohol solution /79 Mah/. The chemistry of alkoxide synthesis is well known and a variety of synthetic routes is described in literature /86 Oka/. Monometallic alkoxides may be prepared under water free conditions by direct synthesis from metals, metal halides or indirectly via alcoholysis. Bimetallic alkoxy derivatives of a number of metals have been subject of investigations dealing with the structure chemistry aspects of more complex metal alkoxides /71 Meh/. Ultrapure $MgAl_2O_4$, for example, could be prepared from liquid (25 °C) double alkoxides of the type $MgAl_2(OR)_8$ where the secondary alkoxy group contained 4 to 7 carbon atoms /74 Tho/. Double alkoxides as homogeneous molecular compounds may provide the appropriate state of metal mixture on a molecular scale combined with potential surface active properties in non–aqueous solutions. The dispersability of silicon nitride powder in $n–C_6H_{14}$ was shown to be significantly improved by specific adsorption of $Al–(iOPr)_3$ on the Si_3N_4 particles surfaces /88 Kis/. A γ–alumina coating layer was formed via a surface ester reaction of silanol groups on the Si_3N_4 resulting in a shift of the isoelectric point (iep) from pH 5.2 to 8.2. Amorphous spinel layers were obtained by dip coating in an isopropanol solution of Mg–Al–isopropoxide where the precipitation of hydroxide was controlled by diethanolamine /87 Tak/.

It is the aim of this work to investigate the precipitation mixing of submicron silicon nitride powder with bimetallic Mg–Al, Y–Al and Nd–Al oxides. The preparation of the respective alkoxides in alcoholic solutions from which the hydroxides were precipitated into deflocculated silicon nitride suspensions will be described. The distribution of the precipitated hydroxides was examined by acoustophoretic measurements. Both the precipitation mixed and the mechanically mixed powder mixtures were sintered under equal conditions and the resulting strength values were statistically evaluated to describe the influence of processing technique on the microstructure–dependent property variations.

2. Experimental procedure

2.1. Double oxide preparation

Different aluminates were prepared via the alkoxide hydrolysis route starting from either homogeneous monomolecular bimetallic alkoxides (Mg–Al) or liquid mixtures

of separately prepared alkoxides (Y, Al) and (Nd, Al). For the starting compositions the metal ratios of Mg:Al = 1:2, Y:Al = 1:1, Nd:Al = 1:1 and 1:3 were chosen. All chemicals were analytical grade.

6.3 g of pure Mg–powder (0.26 mole) and 128 ml of liquid $Al(OC_4H_9)_3$ (0.5 mole) were reacted in nitrogen atmosphere with 38.5 g of C_4H_9OH (isobutylalcohol) (0.52 mole) in a molar mixture of 1.02 : 2 : 2.05 in water free toluene under reflux for 8h, according to the reaction

$$Mg + 2\ Al(OC_4H_9)_3 + 2\ C_4H_9OH \longrightarrow MgAl_2(OC_4H_9)_8 + H_2 \qquad [1]$$

until hydrogen release ceased. A small excess of Mg and isobutylalcohol is necessary to avoid residual Al–alkoxide. $MgAl_2(OC_4H_9)_8$ remained after evaporation of the toluene/isopropanol–mixture under reduced pressure as a highly viscous and clear liquid. Subsequently, the double–alkoxide was slowly hydrolyzed in air according to the reaction

$$MgAl_2(OC_4H_9)_8 + 8\ H_2O \longrightarrow MgAl_2(OH)_8 + 8\ C_4H_9OH \qquad [2]$$

with the hydroxide precipitating as a white powder. After removing the alcohol by destillation the hydroxide reaction product was subjected to calcination at 1000 °C for 1 h to form the spinel phase

$$MgAl_2(OH)_8 \longrightarrow MgAl_2O_4 + 4\ H_2O \qquad [3]$$

The preparation of the Y–Al–oxide mixture started from the appropriate mixture of $Y(OC_3H_7)_3$ and $Al(OC_4H_9)_3$, which where cohydrolyzed to form two separate, but intensively mixed hydroxides $Y(OH)_3$ and $Al(OH)_3$. The yttrium–alkoxide was synthesized from water free YCl_3 with an alkali–alkoxide according to the reaction

$$YCl_3 + 3\ K(OC_3H_7) \longrightarrow Y(OC_3H_7)_3 + 3\ KCL \qquad [4]$$

5.3 g of solid $Y(OC_3H_7)_3$ powder (0.05 mole) were dissolved in isobutyl–solution and mixed with 12.45 g of liquid $Al(OC_4H_9)_3$ (0.05 mole) in a molar ratio 1 : 1 and subsequently hydrolyzed by slowly adding 11 ml of a water/triethylenamine mixture (5:1). The oxide mixture was formed according to the same calcination

procedure as for $MgAl_2O_4$.

The preparation of the Nd–Al–oxide mixtures with two different Nd:Al ratios of 1:1 and 1:3 started from $Nd(OC_3H_7)_3$ which was prepared in a similar way as the yttrium–alkoxide. Appropriate amounts of $Nd(OC_3H_7)_3$ and $Al(OC_4H_9)_3$ were mixed in isopropanol and hydrolsed by adding the water/triethylenamine mixture. The precipitate was treated as described.

After hydrolysis of the alkoxides the hydroxide precipitation was subjected to thermogravimetric analysis (STA 409, Netzsch Gerätebau, Selb, FRG) up to 1200 ^{0}C. X–ray diffraction for phase analysis of the calcined products was carried out with monochromated $Cu_{K\alpha}$–radiation (PW 1820, Philips, Eindhoven/Neth).

2.2. Powder processing

Blending of the Si_3N_4 powder with 10 wt. % of the additives was achieved either by mechanical mixing (mm) of the presynthesized oxides or by in situ precipitation (pm) of the hydroxides in alcoholic Si_3N_4 suspensions. Fig. 1 shows the flow diagram of the applied powder processing routes. A high pure α–Si_3N_4 powder (LC 12, H.C. Starck, Berlin/FRG) with a specific surface area (BET) of 19.8 m^2/g and a mean grain size (FSSS) of 0.45 μm was used for the powder processing experiments. The major impurities in the starting silicon nitride powder were C and O with 0.19 and 1.98 wt.%, and a total metal content (Fe+Al+Ca) of 0.048 wt.%. Mechanical mixing was carried out in an attriton mill filled with Al_2O_3 balls for 4 h at 500 rpm in isopropanol. After milling, the powder mixture was dried in an rotary evaporator, sieved with 100 μm and cold isostatically pressed into cylindrical pellets (10 x 10 mm) or rectangular bars of 4 x 4 x 40 mm^3 with a pressure of 700 MPa. The green density was determined from the bar geometry.

Mixing by in situ precipitation of the hydroxides in isobutyl alcohol suspension required the presence of a well deflocculated system. To achieve deflocculation the pure silicon nitride powder was first ultrasonicated for 30 min. The appropriate amount of liquid alkoxide was added under intensive stirring. Subsequently, H_2O/triethylamine–solution was slowly dropped into the suspension which was stirred for 6 h to assure complete precipitation of the hydroxides. The solute was

removed under slight vacuum at rt in a rotary evaporator. The dried powder was calcined at 1000 °C for 1 h. Larger agglomerates that had been formed during calcination were destroyed by ball milling the powder in isopropanol for 4 h. Finally, the pm–powder was dried, sieved with 100 μm and pressed with similar conditions as the mm–powder.

2.3. Acoustophoretic measurements

Depending on the distribution and morphology of the additive phase in the Si_3N_4 powder mixtures, different surface charges will result which may severely influence the colloidal processing behavior, with respect to green compact formation by dry powder pressing or slurry casting techniques. The effective surface charge which dominates the rheological properties may be characterized by measurement of the particle mobilities from which zeta potentials may be derived /81 Hun/. An acoustophoretic measurement technique (PEN KEM 7000, PEN KEM Inc., Bedford Hills, NY) was used to determine relative acoustophoretic mobilities (RAM). For the acousto– phoretic measurements the powder was dispersed in aqueous solution at 25 °C and an ionic strength of 0.01 m/l KCl. During the measurement the charged particles are subjected to a compressional ultrasonic wave of 200 kHz which gives rise to a periodic polarization of the ionic atmosphere surrounding the particles. The resulting alternating potential (colloid vibration potential, CVP) can be measured from which the so–called relative acoustic mobility (RAM) is derived. For the case of small electric double layers ie. $\kappa a >> 1$ the RAM can be converted to an acoustic mobility, AM, under consideration of the particle volume fraction, ϕ, and the densities of the liquid, ρ_1, and solid phase, ρ_2, /88 Mar/

$$AM = \frac{RAM}{2\ \phi}\left[\frac{\rho_1}{\rho_2 - \rho_1}\right]. \qquad [5]$$

From the acoustic mobility the zeta potential, ζ, can be determined using similar relations as for electrophoretic mobility measurements. The zeta potential, ζ, was calculated from the acoustophoretic mobility and Helmholtz–Smoluchowski equation /86 Hie/ which is valid for large $\kappa a > 100$

$$\zeta = AM\,\frac{\eta}{\epsilon}. \qquad [6]$$

η and ϵ are the viscosity and dielectric constant for water at 25 °C (0.89 mPas and 6.95 x 10–10 C^2/Jm). The reciprocal Debye length κ in the KCl solution is $\approx$ 3.3 x 10^8 m^{-1} and the mean grain size of the silicon nitride powder a $\approx$ 4.5 x 10^{-7} m. The mobility measurements were completed in suspensions with solid concentrations of 1 vol.% (3.1 wt.%). A titration burette was used to contiously change the pH in the range 2 – 12 by adding 1n KOH or HCl, respectively. Prior to taking the measure–ments, the suspension was ultrasonicated and magnetically stirred under vacuum to ensure that only single particles were measured.

2.4. Sintering and strength evaluation

A gas pressure furnace equipped with carbon heating elements was used for sintering the Mg–Al–oxide doped specimens in nitrogen atmosphere at a maximum pressure of 2 MPa. The specimens were embedded in Si_3N_4 powder. Linear heating rates were applied up to the final temperature of 1900 °C i.e. no isothermal period was reached. The three major sections of the sintering schedule involved i) a rapid heating up to 1200 °C at vacuum within 60 min, ii) a heating period from 1200 up to 1800 °C with a linear heating rate of 10 K/min at 0.2 MPa with the maximum shrinkage and iii) a soaking period with a linear but slow heating rate of 1.7 K/min up to 1900 °C where the pore elimination can take place. During the temperature increase from 1800 to 1900 ° the nitrogen pressure was simultaneously increased from 0.2 to 2 MPa in order to prevent silicon nitride decomposition. After cooling weight change, total shrinkage, and density were measured.

The sintered microstructure was analyzed by XRD from polished surfaces. Rectan–gular bars of 4 x 4 x 40 mm^3 were cut with diamond and polished with diamond paste 1 μm. Strength was determined by four point and three point bending with 12/30 mm and 12 mm jigs, respectively, and a crosshead speed of 0.1 mm/min. From the strength data mean values and the Weibull parameter were derived from at least more than 12 (4–point) and 24 (3–point) specimens for each powder composition.

3. Results

3.1. Sol–Gel–oxide preparation

The thermal balance analyses show that the dehydration of the hydroxide precipitations was completed at 800 °C. X–ray analyses of the hydrolysed alkoxy products after calcination in air at 1000 °C for 1 h reveal the formation of metastable phase compositions, Table I, which may be attributed to the low temperature sol–gel route of oxide preparation.

In the oxide prepared from the Mg–Al–alkoxide $MgAl_2O_4$ and Al_2O_3 were found. The presence of Al_2O_3 indicates, that even at the low calcination temperatures of 1000 °C a loss of Mg by evaporation occurred. In the oxide specimen prepared from the Y–Al–alkoxide mixture, $Y_3Al_5O_{12}$ is the major phase with minor amounts of metastable $YAlO_3$. According to the Y_2O_3–Al_2O_3 phase diagram /67 Nog/ an Y:Al ratio of 1:1 is expected to result in a phase composition of $Y_3Al_5O_{12}$ + $Y_4Al_2O_9$ with a weight ratio of 51.7:48.3 (molar ratio 1:2). A significant amount of an Y_2O_3 –rich glass is assumed to account for the composition balance.

A similar formation of metastable phases was observed in the Nd–Al–alkoxide products. In contrast to the equilibrium diagram of the system Nd_2O_3–Al_2O_3 /77 Miz/ where only a hexagonal (< 1100 °C) an a cubic modification of $NdAlO_3$ exists as the stable ternary compound at all temperatures (a ß–alumina phase, $NdAl_{11}O_{18}$ also exists on the Nd–rich side) a metastable phase with a probable composition of $Nd_4Al_2O_9$ is observed as the major phase and the hexagonal $NdAlO_3$ as the minor phase in the specimen with a cation ratio of Nd:Al = 1:1.

3.2. Acoustophoretic measurements

Fig. 2 shows the zeta potentials of the as received silicon nitride and the Mg–Al–oxide containing powder mixtures in the pH range 2–12. While the as received silicon nitride reveals an isoelectric point, iep, (ζ = 0) at pH 7.4, the mm–powder exhibits the iep at pH 9.2 and the pm–powder at 10. At pH values above the iep a negative whereas at lower pH a positive surface charge is established on the silicon nitride particles by the adsorption of hydroxyls or protons on to an amphoteric silanole group /88 Gre/

$$\left[\text{Si–OH}_2\right]^+ \xleftarrow{H^+} \left[\text{Si–OH}\right] \xrightarrow{OH^-} \left[\text{Si–O}\right]^- + H_2O \quad . \qquad [7]$$

In the processed powder containing 10 wt.% of Mg–Al–oxide additives the surface charge is generated by the metal hydroxide surface sites of Mg and Al. Due to the basic character of $Mg(OH)_2$ as compared to the amphoteric behavior of $Al(OH)_3$ the formation of positive surface charge at intermediate and low pH will be dominated by the dissociation of basic Mg–OH sites on the partice surface

$$\left[\text{Mg–OH}\right] \longrightarrow \left[\text{Mg}(H_2O)_n\right]^+ + n\ OH^- \qquad [8]$$

which is essentially equivalent to the adsorption of protons. Thus, the iep is shifted to higher pH, which indicates an adsorption of cations on the charged surface /81 Hun/.

While the zeta potential of the Mg–Al– oxide containing powder is shifted to higher pH the corresponding curves of Y–Al and Nd–Al oxide containing pm–powders are shifted to significantly lower pH, fig. 3, with the iep found at pH 5.3 for the Y–Al and Nd–3Al and 4.3 for the Nd–Al powder mixtures, respectively. The shift to lower pH may now be attributed to an anion adsorption process, where negatively charged hydroxylated Y– and Nd– species are formed on the solid surface

$$\left[\text{Y(OH)}_n\right] + x\ OH^- \longrightarrow \left[\text{Y(OH)}_{n+x}\right]^{x-} \qquad [9]$$

$$\left[\text{Nd(OH)}_n\right] + x\ OH^- \longrightarrow \left[\text{Nd(OH)}_{n+x}\right]^{x-} \qquad [10]$$

or as hydroxylated metal species in solution which deposit on the surface.

The relatively small deviations of the mm–powder from the as received silicon nitride, fig. 2, indicates that the surface of the oxide particles as well as the free surface of the silicon nitride powder contribute to the experimentally measured zeta potential. The greater difference of the zeta potential curve of the pm–powder, however, as compared to the mm–powder may be attributed to a complete coating of the silicon nitride particles with the oxide layer, which dominates the surface

charge formation. Similar differences were observed in the Y–Al and Nd–Al oxide containing specimens with the zeta potential of the mm–powders lying always between that of the as received silicon nitride and the pm–powder. The pm–powder may then be addressed as a single phase powder as schematically shown in fig. 4, from which well deflocculated suspensions may be formed at significantly lower pH than the silicon nitride powder.

3.3. Sintering and strength measurements

The green densities of the cold isostatically pressed powder mixtures show slight differences between the mechanical and precipitation mixed powders, respectively. While the mm–powders attained densities of approximately 63 – 63.5 % th.d. the pm–powders reached only 61 – 61.5 % independent from the specific additive phase composition.

After sintering the Mg–Al–oxide containing specimens, significant differences where observed with respect to the density of the differently processed powders. The pm–powder attained a density of 3.20 g/cm^3 ($\cong$ 98.5 % of theoretical density , 3.25 g/cm^3) while the mm–powder reached only 3.12 g/cm^3 ($\cong$ 96 %). Thus, the pm–powder showed a 10 % higher volume shrinkage as compared to the mm–powder upon sintering. These differences are to be related to the characteristic distribution of the additives because amount and composition of the additives as well as the sintering programme where kept constant throughout all specimens.

Fracture strength of the Mg–Al–oxide containing specimens was determined by four (fpb) and three (tpb) point bending. The mm–powder attained less strength as compared to the pm–powder. From the four point measurements a mean fracture stress of 555 ± 31 (5.6 %) MPa was determined for the pm–powder and 438 ± 95 (21%) MPa for the mm–powder. Due to the reduced effective volume under stress the values of the three point bending experiments where higher with 658 ± 78 (11 %) MPa and 530 ± 128 (24%) MPa for the pm– and mm–powder, respecitvely. Fig. 5 shows the corresponding fracture probability versus fracture stress curves according to the Weibull statistics. From the slope of the Weibull curves the characteristic parameter m was determined. Again, the pm–powders show significantly higher values of 17 (fpb) and 9.7 (tpb) as compared to 5 (fpb) and 4.7 (tpb) for the mm–powders.

4. Discussion

Heterogeneous nucleation of a precipitating solid phase on a catalyst from liquid phase like hydroxide precipitation on dispersed silicon nitride particles, often results in a non–uniform coating due to growth of isolated nuclei. The major reasons for this inhomogeneous nucleation are : i) morphological inhomogeneities on the powder particle surface like asperities, necks, steps, ii) chemical inhomogeneities like hydrolysed and adsorbed impurities at defect sites and iii) crystallographic anisotropy of the surface energy of the catalyst, i.e. hexagonal α–Si_3N_4 crystal lattice. Thus, at equilibrium force balance the wetting angle θ at the contact point catalyst, precipitate, liquid /86 Hie/

$$\cos\theta = \frac{\gamma_{cl} - \gamma_{cp}}{\gamma_{sl}} \qquad [11]$$

will vary over the particle surface because the catalyst–precipitate interface energy γ_{cp} will be much more influenced by the above mentioned surface and crystallographic effects than the catalyst–liquid, γ_{cl}, and solid–liquid, γ_{sl}, interface energies.

A homogeneous, orientation independent coating of the powder particle with the precipitate phase, however, may be achieved by forming an amorphous intermediate layer which screens the surface energy variations on the particle surface. This layer may be generated by chemical adsorption of the metal alkoxide and subsequent growth of the surface layer by a gel polymerization process. A surface reaction involving a nuceophilic attack of the oxygen in the alkoxy group on the silicon atom is supposed to result in an ester formation reaction and simultaneous release of an alcohole

$$\equiv Si–OH + RO–Al(OR)_2 \longrightarrow \equiv Si–O–Al(OR)_2 + ROH \qquad [12]$$

The chemisorption of Al–alkoxides on silicon nitride has been reported to improve the dispersion stability in alcoholic suspensions by coating the powder surface with an alkoxide layer /88 Kis/. Hydrolysis reaction upon water addition links the

alkoxide molecules by a polymerization type of sol–gel–reaction. The thickness of the hydroxide layer may be controlled by the alkoxide concentration, the water/alkoxide ratio and the precipitation conditions /87 Tak/. The total amount of additive will then be mainly determined by the precipitate layer thickness and the silicon nitride grain size although an unknown amount of precipitate may be formed by homogeneous nucleation. Thus, agglomerates of pure hydroxide can be formed or silicon nitride particles can be bonded by hydroxide bridges which will form hard (high strength) agglomerates upon calcination as frequently observed in sol–gel prepared powders. During sintering these agglomerates may form large defects due to differential shrinkage between the matrix and the agglomerates /86 Hsu/. Thus, the relatively low level of the fracture strength measured at the Mg–Al–oxide containing specimens is attributed to the uncontrolled agglomeration during hydroxide precipitation and subsequent calcination.

To avoid the formation of hydroxide bonded agglomerates a surface coating by a chemisorption process may be more attractive. The alkoxide coated silicon nitride powder is directly calcined or transferred to a slip casting process without any hydrolysis reaction. Without linking the chemisorbed alkoxide groups a monomolecular layer should develop on the silicon nitride particles with a thickness determined by the effective size of the alkoxide molecule. The surface adsorbed alkoxide layer will transform to the corresponding oxide layer upon decomposition of the alkoxide

$$Me^{n+}(OR)_n \longrightarrow MeO_{n/2} + n/2\ OR_2 \qquad [13]$$

The total amount of alkoxide, m_a, which may be admixed assuming saturation of the surface of the powder of total mass, m_p, will then be determined by the effective surface area of the silicon nitride powder and the oxide layer thickness. Assuming monosized spherical particles the oxide/powder ratio, C_o, may simply be expressed as a function of the particle radius, r, and oxide layer thickness, dr, as

$$C_o = \frac{m_o}{m_p + m_o} = 1 - \left[\frac{\rho_o}{\rho_p} \frac{(r+dr)^3}{r^3} \right]^{-1}, \qquad [14]$$

where ρ_o and ρ_p are the densities of the oxide and silicon nitride phases. Fig. 6 shows a hypothetical particle size / oxide concentration relationship for a $MgAl_2O_4$

coating. A monomolecular spinel layer would correspond to a thickness of approximately 0.4 nm, i.e. half of the unit cell constant a_o of $MgAl_2O_4$. Hence, to obtain a powder with 10 wt.% of $MgAl_2O_4$ a silicon nitride powder with a particle radius of $r < 0.025$ μm would be required when only a monolayer adsorption occurs. Although, this estimation is based on hypothetical assumptions because the oxide layer structure is not really known, the simple picture clearly indicates that extremely fine grained colloidal powders with grain sizes below 100 nm are required.

Increasing the layer thickness by using multimetallic monomolecular or mixed alkoxides, however, may allow to significantly increase the amount of adsorbed sintering aids by linking the "first" alkoxide layer with further layers resulting in a multilayer adsorption process. Fig. 7 shows a schematic model for $MgAl_2(OBu)_8$ chemisorption (Bu = $C_4H_9^+$) which is based on the proposed molecular structures of Al–alkoxides /71 Meh/. Various types of di–, tri– and tetrameric clusters of the $Al(OR)_3$ with R = C_3H_7 or C_4H_9 are characterized by a bidentate ligand structure of the alkoxide group

It may be possible that a second metal atom like Mg, Y, or Nd may link these clusters to form thicker alkoxide layers on the silicon nitride surface in non–aqueous solution. Thus, powders with a mean grain size of $2r < 0.5$ μm could contain more than 5 wt.% of oxide when the layer thickness increases by a factor of ten. Bimetallic monomolecular or mixed alkoxides are therefore of particular interest for improving the homogenous distribution of complex oxide additives by a surface adsorption processing technique in non–aqueous solutions.

5. Conclusions

Generally, the precipitation mixing of sintering additives in silicon nitride powders results in a better elemental distribution as compared to mechanical mixing.The formation of hydroxide bonded agglomerates, however, has to be avoided by careful drying techniques. Alternatively, additive distribution by a pure chemisorption process using multimetallic alkoxide mixtures in non–aqueous solution may provide

an interesting tool especially for agglomeration controlled powder processing. The advanced processing of silicon nitride powders may therefore be divided into the following major steps :

i.) surface purification treatment to remove surface contaminants,
ii) dispersion of silicon nitride in non–aqueous solution,
iii) chemical adsorption of a (monomolecular) alkoxide layer (activating layer)
iv) hydrolysis to form a hydroxide surface coating by a sol–gel–growth process
or
linking the alkoxide monolayer with a second (and further) layer of an organo–metallic (multifunctional) compound
v) dehydration of the hydroxide
or
decomposition of the alkoxide to the oxide

The attractive advantages of precipitation or adsorption mixing seem to be :
- reduction of the amount of liquid forming sintering additives, which is necessary to obtain full densification upon pressureless sintering,
- reduction of the sintering temperatures due to reduced diffusion distances and intimate mixture of elements in the additive phase
- improved properties for colloidal filtration techniques because of single phase behavior dominated by the highly chargeable hydroxide/oxide layer
- control of oxygen contamination due to screening of the oxidation and hydrolysis sensitive silicon nitride surface

The processing properties for colloidal filtration techniques such as slip casting and colloidal pressing techniques may significantly be improved by using surface coated silicon nitride. As a result of the improved green compact microstructure the scattering of the properties of the sintered material will be reduced. Thus, the reliability of the material properties, which is considered as a key aspect for the applicability of high performance ceramics, may be improved.

References

/67 Nog/ T. Noguchi, M. Mizumo, Kogyo Kogaku Zashi 70 (1967) 839.
/71 Meh/ R.C. Mehrota, A. Mehrota, Inorg.Chim.Acta (1971) 127.
/74 Tho/ I.M. Thomas, US Patent No. 3786137, Jan 15 (1974)
/77 Miz/ M. Mizumo, T. Yamada, T. Noguchi, Yogyo Kyokai Shi 85 (1977) 90.
/81 Hun/ R.J. Hunter, Zeta Potentials in Colloid Science, Academic Press, London (1981)
/81 Raj/ R. Raj, F.F. Lange, Acta Met. 29 (1981) 1993.
/83 Wei/ J. Weiss, W.A. Kaysser, in F.L. Riley, Progress in Nitrogen Ceramics Nijhoff Publ., Boston/Ma (1983)
/84 Raj/ R.Raj, K. Bordia, Acta Met. 32 (1984) 1003.
/86 Hie/ P.C. Hiemenz, Principles of Colloid and Surface Chemistry, Marcel Dekker, NY (1986)
/86 Hsu/ C.H. Hsueh, A.G. Evans, R.M. Cannon, R.J. Brook, Acta Met. 34 (1986) 927.
/86 Oka/ H. Okamura, H.K. Bowen, Ceram.Int. 12 (1986) 161.
/87 Gre/ P. Greil, in Science of Ceramics 14 (1987) 645.
/87 Tak/ Y. Takahashi, H. Naganawa, Yogyo Kyokai Shi 95 (1987) 1107.
/88 Gre/ P. Greil, A. Nagel, H. Stadelmann, G. Petzow, in Proc. 3rd Int. Conf.Cer.Mat. and Comp.for Engines, Las Vegas/Nev (1988)
/88 Kis/ K. Kishi, S. Umebayashi, R. Pompe, M. Persson, J.Ceram.Soc.Jpn. 96 (1988) 698.
/88 Mar/ B.J. Marlow, D. Fairhurst, H.D. Pendse, Langmuir 4 (1988) 611.
/89 Lan/ F.F. Lange, J.Am.Ceram.Soc. 72 (1989) 3.

Table I Elemental and phase composition of the bimetalllic oxides prepared from alkoxide compounds

cation Me	molar ratio Me : Al	phase composition sol–gel–route (< 1000 °C)	phase diagramme
Mg	1 : 2	$MgAl_2O_4 + Al_2O_3$	$MgAl_2O_4$
Y	1 : 1	$Y_3Al_5O_{12} + \underline{YAlO_3}$	$Y_3Al_5O_{12} + 2\ Y_4Al_2O_9$
Nd	1 : 1	$\underline{Nd_4Al_2O_9} + NdAlO_3$ (hex)	$NaAlO_3$

$MgAl_2O_3$ spinel, (cub)
$YAlO_3$ perovskite (hex ?)
$Y_3Al_5O_{12}$ garnet (cub),YAG
$Y_4Al_2O_9$ melilithe (mcl),YAM
$NdAlO_3$ perovskite (hex<1100°C<cub)
$Nd_3Al_5O_{12}$ garnet (cub)
$Nd_4Al_2O_9$ melilithe (mcl)
_____ metastable phase at 1000 °C

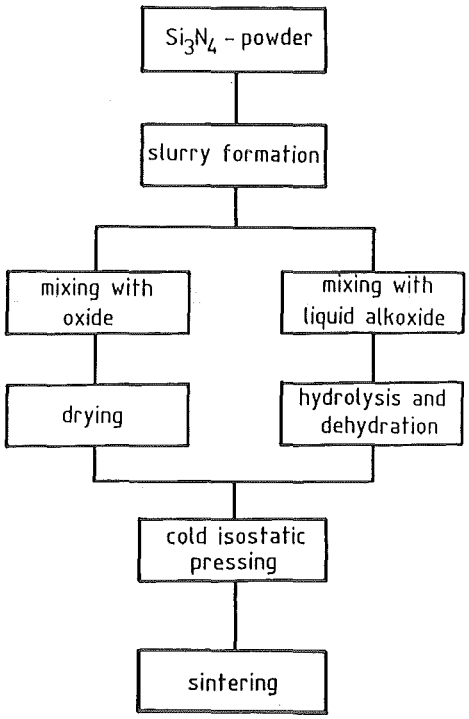

Fig. 1 Flow diagram of the powder processing routes.

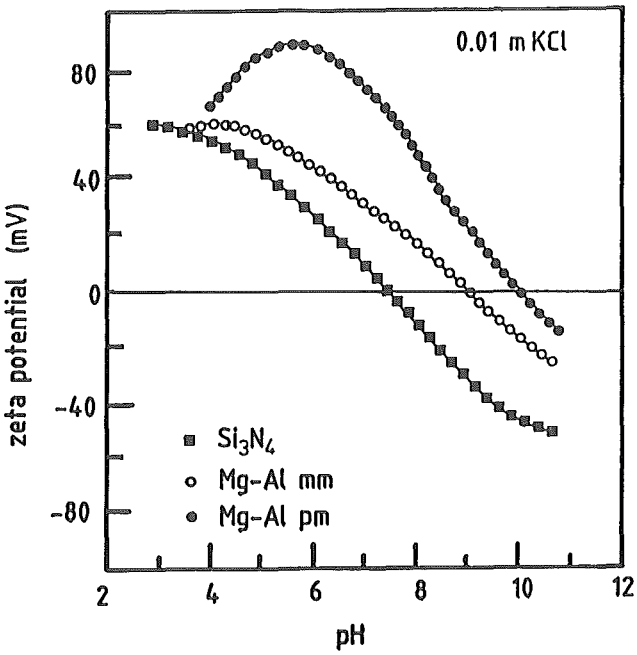

Fig. 2 Zeta potential, ζ, of the as received silicon nitride powder and the mechanical (mm) and precipitation (pm) mixed powders containing 10 wt.% of Mg–Al (1:2) oxide.

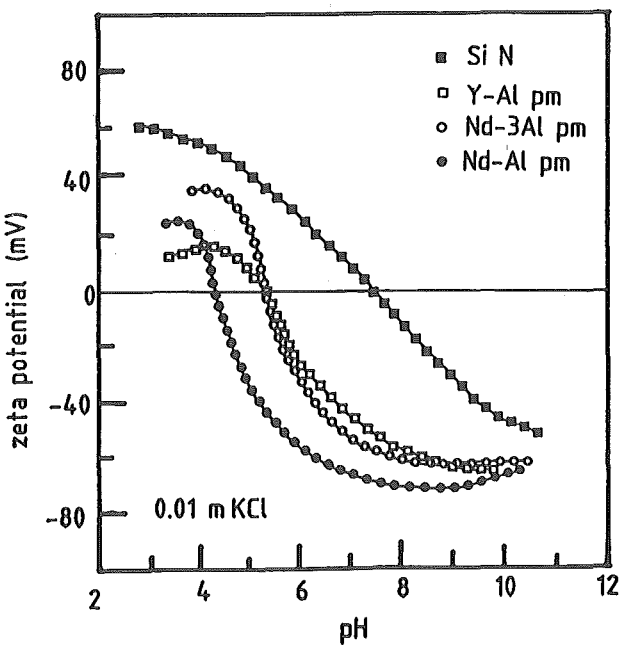

Fig. 3 Zeta potential, ζ, of the as received silicon nitride powder and the pm–powders containing Y–Al (1:1) and Nd–Al (1:1 and 1:3) oxides.

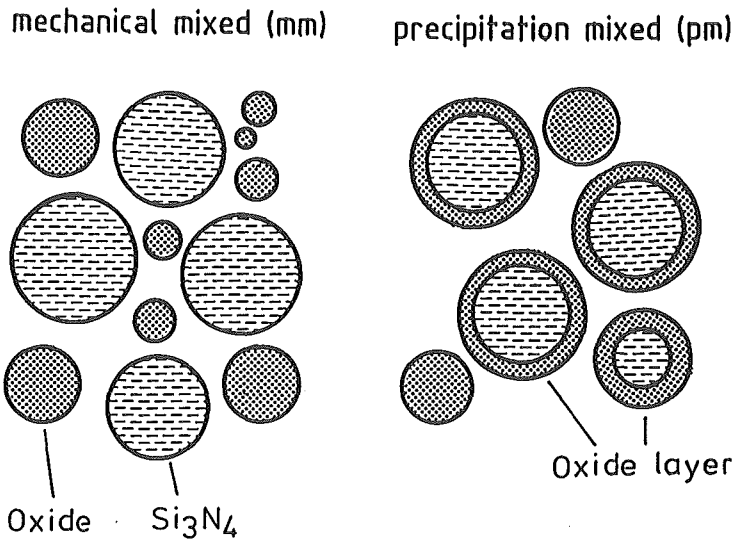

Fig. 4 Microstructure of the mechanical and precipitation mixed silicon nitride powders as concluded from the results of the acoustophoretic measurements (schematic).

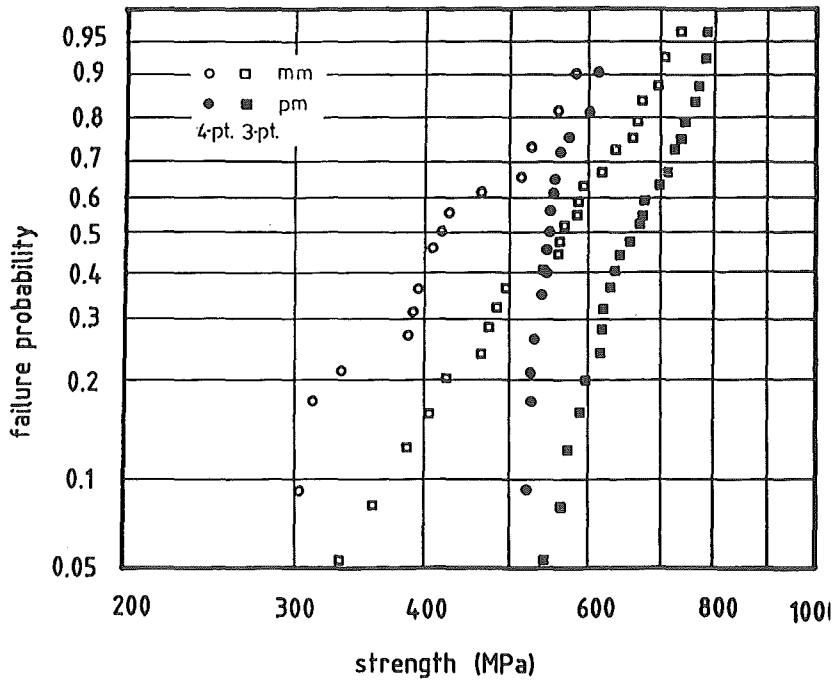

Fig. 5 Failure probability diagram (Weibull plot) of the sintered specimens containing 10 wt. % of Mg–Al oxide. Strength was measured by four (spheres) and three (squares) point bending.

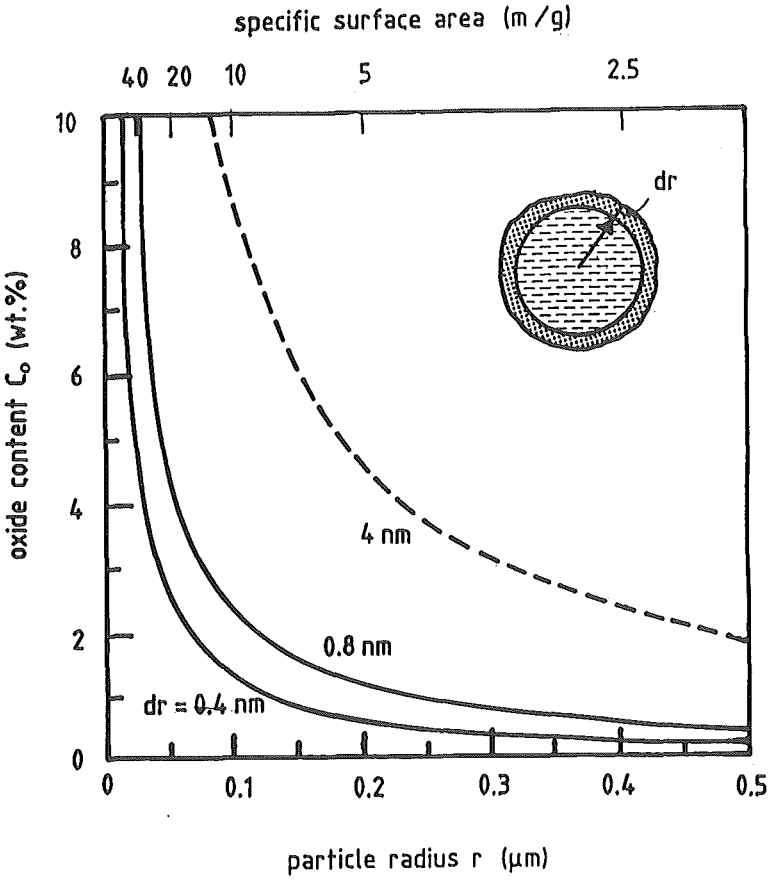

Fig. 6 Oxide concentration, C_o, in a powder of monosized spherical silicon nitride grains of radius r coated with a dense $MgAl_2O_4$–layer of thickness dr.

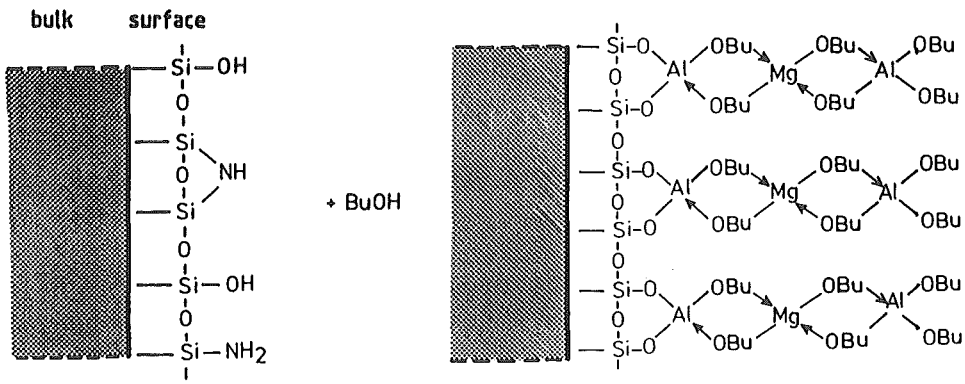

Fig. 7 Schematic model of $MgAl(OBu)_8$ chemisorption on a purified, silanol groups containing silicon nitride particle surface.

TEMPERATURE DEPENDENCE OF THE INTERFACIAL ENERGIES IN Al_2O_3-LIQUID METAL SYSTEMS

G. Angelopoulos, S. Agathopoulos, P. Nikolopoulos

Institute of Physical Metallurgy, Dept. of Chemical Engineering
University of Patras, GR-26110 Patras, Greece

INTRODUCTION

The interfacial energies in ceramic-metal systems determine the phase distribution, density and microstructure in cermet bodies and are important in considering the development of bond strength between metal and ceramic components.
The correlation between the wetting and bonding behaviour, at the interface in solid-liquid-vapour systems in Thermodynamic equilibrium, is given by the equation:

$$W_\alpha = \gamma_{SV} + \gamma_{LV} - \gamma_{SL} \qquad (1)$$

where γ_{SV}, γ_{LV} are the surface energies of the solid and liquid phases respectively, γ_{SL} is the interfacial energy of solid-liquid and W_α the work of adhesion, defined as the work needed to separate an interface.
An established method for studying the interfacial phenomena is that of sessile drop of liquid phase lying on a solid substrate (Fig. 1). In this case the following equation holds

$$\gamma_{SL} = \gamma_{SV} - \gamma_{LV} \cos\Theta \qquad (2)$$

where Θ is the contact angle.
Introducing equation (2) into equation (1) gives

$$W_\alpha = \gamma_{LV}(1+\cos\Theta) \qquad (3)$$

If the surface energies (γ_{SV}, γ_{LV}) of the solid and liquid phases

are known, the interfacial energy (γ_{SL}) and the work of adhesion (W_a) can be calculated from the experimental data of the contact angle (Θ).
The present work describes the methodology that has been applied in order to determine the temperature dependence of the interfacial energy and the work of adhesion in polycrystalline Al_2O_3-liquid metal systems.

EXPERIMENTAL RESULTS

The available literature data [1,2,3,4] of the temperature dependence of the surface energies for polycrystalline Al_2O_3 and for the pure liquid metals In, Sn, Bi, Pb, Ag, Cu, Ni, Co and Fe are summarized in Table I.
Owing to the fact that the wetting angle (Θ) in all the system examined was greater than 90°, the sessile drop has the form of ellipsoid of revolution. From the values of X_{90}, Z_{90}, X_0, Z_0 (Fig. 1) and by using the tables of Basfort and Adams [5], the wetting angle can be determined.
Fig. 2 shows the values of contact angles (Θ) deriven from the experimental measurements, under inert gas conditions (Ar).
The results indicate that

- The contact angle decreases with increasing temperature and melting points of the metals.
- The liquid metals, for the investigated temperature range, do not wet the ceramic.
- The wettability is not sufficient for high densification of composites during liquid phase sintering.

The results of the measurements of contact angle as well as the calculated values of the work of adhesion (eq. 3) and the interfacial energy (eq. 2) in the investigated systems Al_2O_3-In, Ag, Fe together with literature data for the systems Al_2O_3-Sn, Bi, Pb, Cu, Ni, Co [3,4] are given in Table II. The influence of metal vapours, existing in the furnace atmosphere, on the surface energy of Al_2O_3 was assumed to be negligible [3].

WORK OF ADHESION AND INTERFACIAL ENERGY

Fig. 3 exhibits both the magnitude of work of adhesion and its temperature dependence.
Linear extrapolation of W_α to the metal's melting point (Table III) indicates that, in general, metals with a high melting point exhibite a higher work of adhesion.
This result shows, that non-wetting systems can form a strong interface which influences positively the mechanical properties of sintered ceramic-metal composite material.
Fig. 4 depicts the temperature dependence of the magnitude of interfacial energy.
The linear extrapolation of the interfacial energies at the melting point of the metals (Table III) shows that their values vary in a restricted region (mean value about 2.5 J/m^2), with In and Sn having the greater deviation. The absolute values of the temperature coefficients of the interfacial energies increase with increasing melting point of the metals.
The interfacial energy values at T_m (metal) in the Al_2O_3-liquid metal systems are about 1.0 J/m^2 higher than in the UO_2-liquid metal [6] and ZrO_2-liquid metal [7] systems. This is often attributed to the domination of the ceramic surface by the oxygen anions.

REFERENCES

[1] G. Lang. Z. Metallkde 67 (1976) 549
[2] A.R. Miedema. R. Boom,Z. Metallkunde 69 (1978) 123
[3] P. Nikolopoulos, J. Mater. Sci. 20 (1985) 3993
[4] G. Angelopoulos. U. Jauch. P. Nikolopoulos. Mat.-wiss. u. Werkstofftech. 19 (1988) 168
[5] F. Basfort, S.C. Adams. "An attempt to test the theories of capillary action", University Press, Cambridge, 1983, p. 63.
[6] P. Nikolopoulos, G. Ondracek. J. Nucl. Mater. 98 (1981) 306-312-
[7] P. Nikolopoulos. G. Ondracek, D. Sotiropoulou. Ceramics International 15 (1989).

TABLE I

Linear temperature functions of the surface energies for solid Al_2O_3 and liquid metals.

Material	Surface energy ($J.m^{-2}$)	
Al_2O_3	$2.559-0.784\times10^{-3}$ T	$0\leq T\leq 2323$ K
In	$0.560-0.09\times10^{-3}(T-T_m)$	$T\geq T_m=429$ K
Sn	$0.544-0.07\times10^{-3}(T-T_m)$	$T\geq T_m=505$ K
Bi	$0.372-0.09\times10^{-3}(T-T_m)$	$T\geq T_m=544$ K
Pb	$0.468-0.13\times10^{-3}(T-T_m)$	$T\geq T_m=600$ K
Ag	$0.912-0.15\times10^{-3}(T-T_m)$	$T\geq T_m=1234$ K
Cu	$1.311-0.20\times10^{-3}(T-T_m)$	$T\geq T_m=1356$ K
Ni	$1.754-0.28\times10^{-3}(T-T_m)$	$T\geq T_m=1726$ K
Co	$1.610-0.29\times10^{-3}(T-T_m)$	$T\geq T_m=1768$ K
Fe	$1.825-0.27\times10^{-3}(T-T_m)$	$T\geq T_m=1809$ K

TABLE II

Wetting angle (Θ), work of adhesion (W_a) and interfacial energy in the Al_2O_3-liquid metal systems.

System	T (K)	Θ (deg)	Standard deviation	W_a ($J.m^{-2}$)	γ_{SL} ($J.m^{-2}$)
Al_2O_3-In	493	152.35	± 4.59	0.063	2.663
	798	145.63	± 5.01	0.092	2.368
	1128	124.29	± 4.98	0.217	1.954
-Sn	611	165.24	± 4.06	0.018	2.598
	726	161.74	± 2.68	0.027	2.491
	772	157.74	± 7.86	0.039	2.440
	975	148.26	± 4.37	0.076	2.229
	1183	141.96	± 1.71	0.106	2.022
	1280	138.95	± 2.67	0.120	1.924
-Bi	689	152.73	± 4.95	0.040	2,338
	890	137.38	± 2.99	0.090	2.112
	965	134.33	± 1.90	0.101	2.035
	1144	125.24	± 1.86	0.135	1.845
-Pb	667	165.30	± 3.05	0.015	2.480
	711	160.48	± 7.15	0.026	2.430
	860	149.00	± 5.18	0.062	2.257
	1073	139.82	± 10.05	0.096	2.029
-Ag	1273	146.22	± 3.62	0.153	2.314
	1473	127.19	± 1.01	0.347	1.933
	1673	119.67	± 2.58	0.427	1.666
-Cu	1370	143.87	± 2.82	0.252	2.541
	1450	131.86	± 2.66	0.430	2.284
	1575	123.97	± 2.30	0.559	2.032
	1695	118.42	± 1.42	0.651	1.822
	1720	116.10	± 1.19	0.693	1.756
-Ni	1843	129.28	± 2.98	0.631	2.204
	1908	121.20	± 1.34	0.821	1.945
	2003	111.30	± 0.66	1.067	1.598
-Co	1888	128.20	± 2.81	0.601	2.053
	1973	123.91	± 2.12	0.686	1.877
	2023	120.10	± 1.53	0.766	1.743
	2113	116.68	± 0.88	0.832	1.580
-Fe	1848	129.46	± 1.00	0.661	2.263
	1923	120.38	± 5.04	0.887	1.958

TABLE III

Linear temperature functions of the interfacial energies (γ_{SL}) and works of adhesion in the Al_2O_3-liquid metal systems.

Material	Interfacial energy (γ_{SL}) ($J.m^{-2}$)	Correlation Coefficient (R)
Al_2O_3-In	$2.750-1.118\times10^{-3}(T-429)$	0.9973
-Sn	$2.710-1.014\times10^{-3}(T-505$	0.9999
-Bi	$2.492-1.083\times10^{-3}(T-544)$	0.9998
-Pb	$2.552-1.112\times10^{-3}(T-600)$	0.9998
-Ag	$2.358-1.620\times10^{-3}(T-1234)$	0.9949
-Cu	$2.528-2.141\times10^{-3}(T-1356)$	0.9943
-Ni	$2.641-3.778\times10^{-3}(T-1726)$	0.9997
-Co	$2.305-2.128\times10^{-3}(T-1768)$	0.9978
-Fe	$2.423-4.067\times10^{-3}(T-1809)$	
	Work of adhesion (W_a)($J.m^{-2}$)	
Al_2O_3-In	$0.032+0.244\times10^{-3}(T-429)$	0.9484
-Sn	$0.0 +0.160\times10^{-3}(T-505)$	0.9967
-Bi	$0.013+0.208\times10^{-3}(T-544)$	0.9953
-Pb	$0.004+0.200\times10^{-3}(T-600)$	0.9940
-Ag	$0.145+0.685\times10^{-3}(T-1234)$	0.9723
-Cu	$0.278+1.158\times10^{-3}(T-1356)$	0.9811
-Ni	$0.318+2.715\times10^{-3}(T-1726)$	0.9994
-Co	$0.478+1.053\times10^{-3}(T-1768)$	0.9967
-Fe	$0.543+3.013\times10^{-3}(T-1809)$	

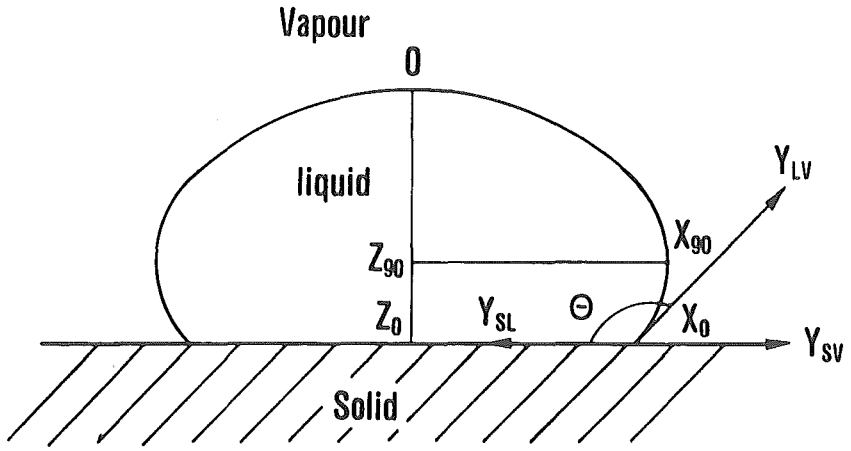

Fig. 1. Contact angle (Θ) in solid-liquid-vapour system in equilibrium.

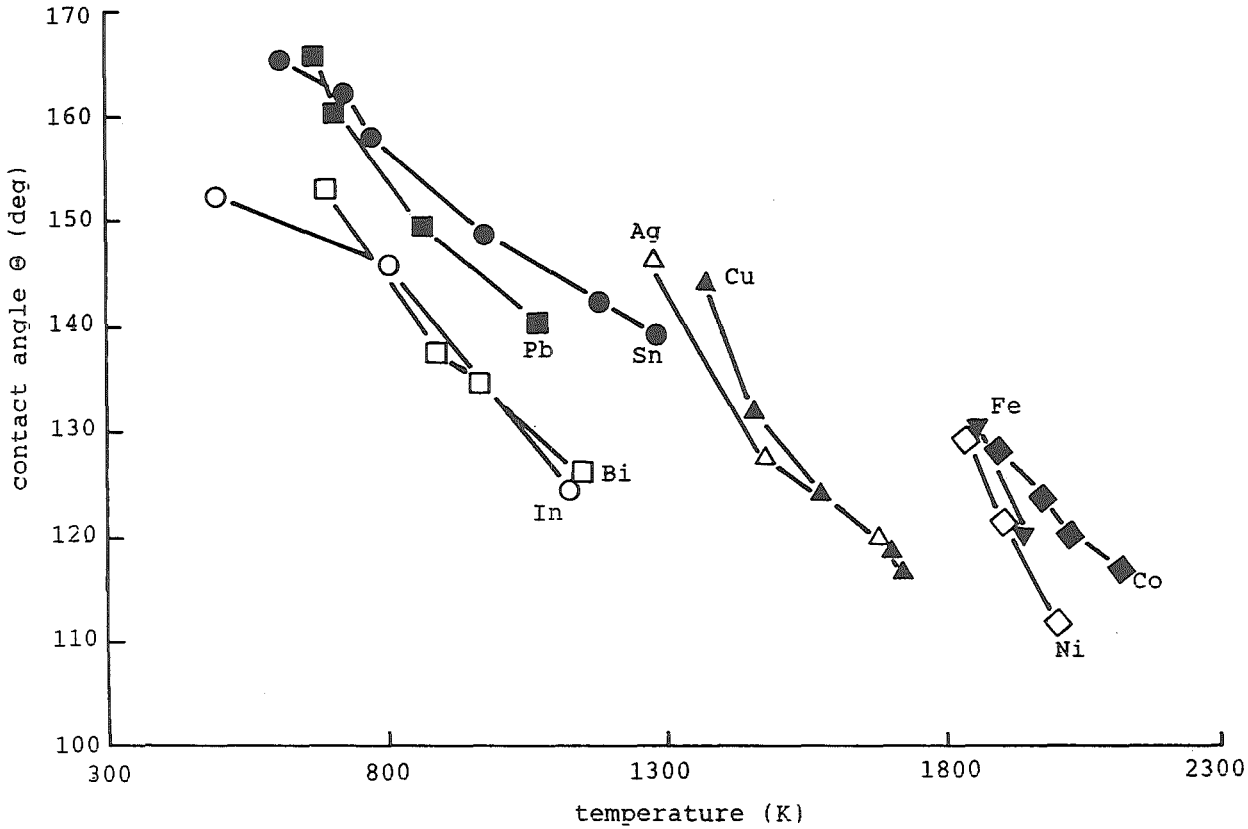

Fig. 2. Effect of temperature on contact angle formed by liquid metals on Al_2O_3.

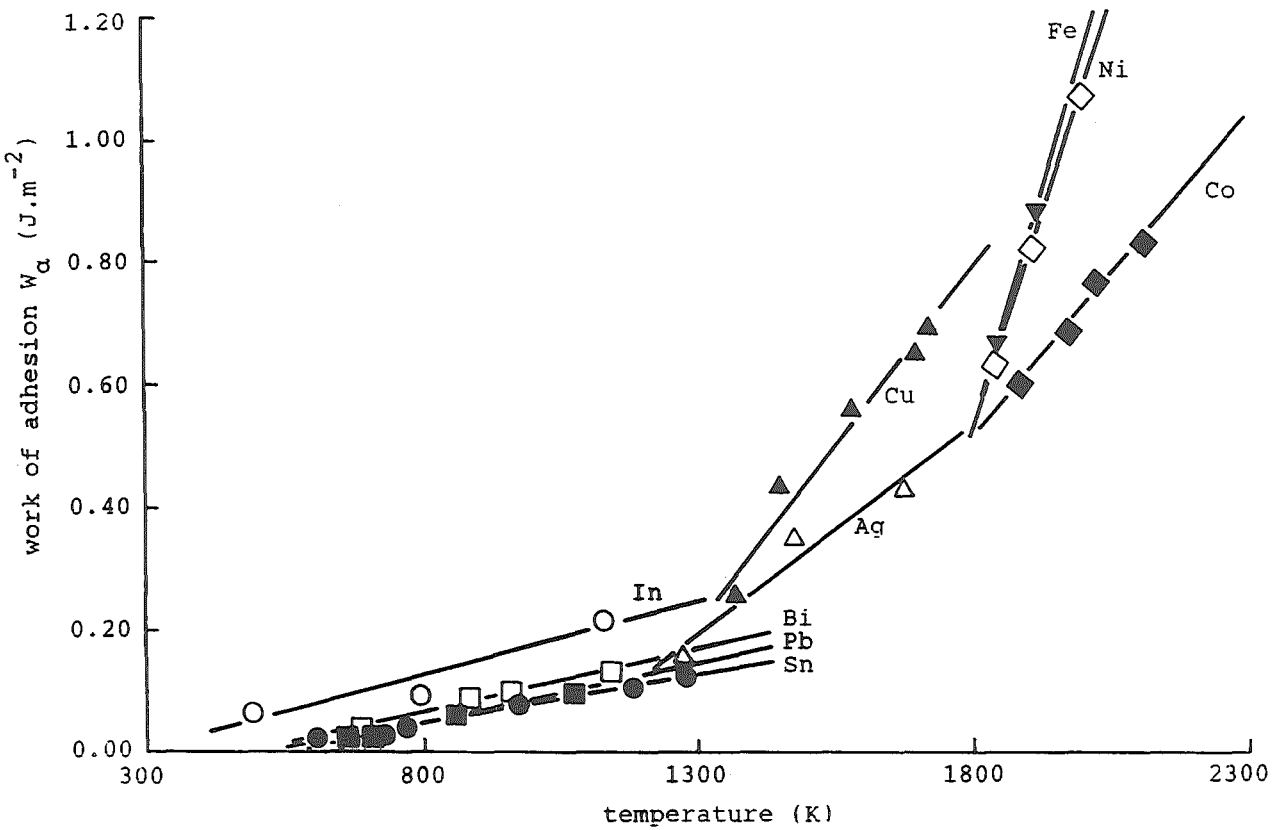

Fig. 3. Work of adhesion - temperature dependence in Al_2O_3-liquid metal systems.

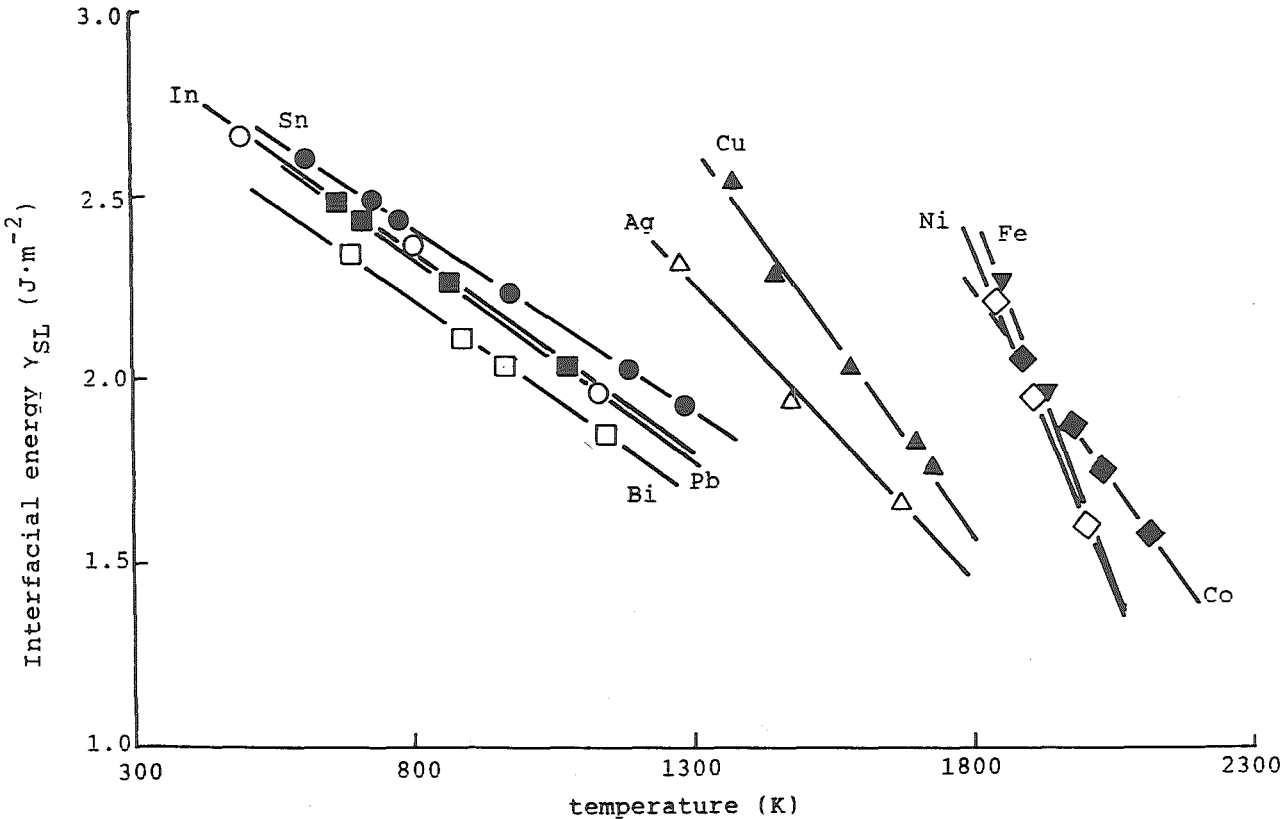

Fig. 4. Interfacial energy - temperature dependence in Al_2O_3-liquid metal systems.

SYNTHESIS AND MICROSTRUCTURAL EXAMINATION OF SYNROC B

M. Čeh, D. Kolar
"J. Stefan" Institute, "E. Kardelj" University,
Ljubljana, Yugoslavia

1. INTRODUCTION

SYNROC is an acronym (derived from SYNthetic ROCk), first used in 1978 by Ringwood et al[1] to describe concepts of very durable synthetic crystalline ceramic waste forms for immobilization of high level radioactive wastes. Synroc compositions are based on naturally occurring titanate and zirconate minerals which are known to accommodate a variety of naturally occurring radioactive elements within their crystal structure. In deep underground repositories these synthetic minerals could be stored for long periods of geological time (ranging upward to 600 million years). The most important phases identified in Synroc B material are hollandite ($BaAl_2Ti_6O_{16}$), perovskite ($CaTiO_3$) and zirconolite ($CaZrTi_2O_7$). Different Synroc formulations contain other phases as well, depending on the nature and the composition of the radioactive waste (i.e. Synroc C, Synroc D, Synroc E)[2]. Data on leach rates of radioactive elements from the Synroc material under different leachant conditions (composition of leachant, temperature and pressure) are of the upmost importance in determining Synroc stability and usefulness as a host material for HLW. Different leach tests are being developed[3,4] in order to imitate real conditions of leaching, and the results are usually compared with the leach rates for different widely used glasses[5,6]. The values of leach rates for Synroc materials are usually several orders of magnitude lower compared to values for borosilicate glasses. It is well known that self-radiation damage caused by alpha decay of fission products and actinides can induce certain structural changes within the Synroc matrix. Recent publications on self-radiation damage in $CaZrTi_2O_7$ [7,8,9], $CaTiO_3$ and $BaAl_2Ti_6O_{16}$[10,11] show that self-radiation damage of Synroc materials is not so substantial as to influence the potency of Synroc as an HLW host. Since powder preparation methods and sintering conditions for different Synroc materials are now well established so as to obtain dense, crack-free and mechanically durable samples, some fundamental work is being done on the structure, properties and phase relations in this multicomponent system. Recently, many investigators were interested in microstructural investigations of Synroc materials. High-resolution electron microscopy, analytical microscopy, and scanning electron microscopy were used in order to determine the phases in doped Synroc and to confirm the existence of thin intergranular films and "glassy" triple points between different phases[12,13,14].

The main objective of this work is microstructural examination of some phases in undoped and doped Synroc B. Our composition of Synroc B is mainly based on the formulation that was proposed by Palmour et al[15]. When 10 wt% of PW-4b simulated radioactive waste is added to the original Synroc B material, two new phases develop in the microstructure after sintering at 1280°C for 4 h in a flow of Ar/4%H_2. Qualitative and quantitative analysis of these new phases was made. The experimental techniques used were TEM, SEM and EPMA. In addition, the results of the MCC-1 static leach test on doped Synroc B are given.

2. EXPERIMENTAL METHODS

The starting powder composition for the synthesis of Synroc B is given in Table I. BaO and CaO were added as carbonates. The mixture of powders was wet milled in a zirconia mill with the addition of 3 wt% PVA binder. The resulting batch was removed from the mill after 6 hours of milling, screened and stored in a plastic jar. Pellets for sinterability and leaching tests were pressed at 140 MPa. The organic binder was slowly burnt out at 400°C in air. Firing of Synroc B was carried out in a controlled atmosphere tube furnace. Pellets were placed on zirconia grains in an alumina boat and fired in an Ar/4%H_2 flow at 900°C for 4 hours and at 1280°C for 4 hours. The heating rate was 10°C/min. The sintering procedure for doped Synroc B containing 10 wt% of PW-4b simulated radioactive waste is the same as for the undoped Synroc B. The composition of PW-4b is given in Table II.

X-ray diffraction patterns for both undoped and doped Synroc B specimens were recorded on a Philips PW-10 diffractometer using CuK_α radiation. Samples for TEM examination (Jeol JEM 2000-FX microscope with LINK EDS microanalyser) were prepared by ion-beam milling. Transmission electron microscopy (TEM), and selected area diffraction (SAD) were all carried out at 200 KeV. It was

TABLE I. Powder composition for the synthesis of Synroc B (wt %)

Al_2O_3	8.8
TiO_2	60.7
ZrO_2	6.7
BaO	13.2
CaO	10.6
	100.0

TABLE II. The composition of PW-4b (wt %)

CeO_2	14.8
Nd_2O_3	22.6
Fe_2O_3	9.9
MoO_3	16.9
ZrO_2	13.4
Cs_2O	7.5
SrO	5.7
NiO	2.9
UO_2	6.3
	100.0

essential that all crystallites should be identified by SAD prior to energy dispersive X-ray analysis (EDS), as many Synroc minerals have similar compositions. SEM analysis (Leitz AMR 1600 T microscope with PGT 4 EDS microanalyser) helped in qualitative analysis of different phases of doped Synroc. Although SEM was able to distinguish gross defects (e.g. pores and microcracks), the grain size distribution severely limited the interpretable data that could be obtained, as it was not generally possible to probe single-phase regions. However, the probe results helped in further more precise measurements by EPMA (Microscan 9, Cambridge Instruments).

Leach tests of undoped and doped Synroc B specimens were conducted according to the standard MCC-1[4] leach test. Polished pellets of Synroc B were leached in teflon containers of 40 ml capacity (Fig. 1). In each container, a single monolithic specimen was suspended from the lid by a nylon filament. The specimens were of cylindrical shape with a surface area of 130 mm^2. The volume of the leachants (mm^3) was equal to exactly 100 times the sample surface. The water used as a leachant and a solvent for preparation of the other two leachant media was produced by reverse osmosis, double deionization, filtration

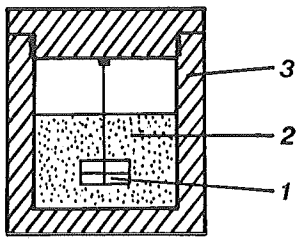

Figure 1. Leaching of doped Synroc samples with 10 wt% PW-4b. 1-sample, 2-leaching media, 3-teflon container

and organic filtration (Millipore Corporation, Milli-RO/Milli-Q System). Table III shows the composition of the other two leachants used in this test.

TABLE III. Leachant composition (mg/l)

Leachant	Potassium*	Magnesium*	Sodium*	Chlorine*	$HCO3^-$
Brine	24200	32300	32200	165800	--
Carbonate	--	--	54.8	--	145

* ions

In addition a single blank with distilled water was also run in this test. Leaching was carried out at 90°C for a period of 30 days. On completion of the test,

the specimens were removed from the containers, rinsed in water and then dried at 120°C. The concentration of Mo, Ni, Fe and Sr in all three leachants was determined by flame atomic absorption spectroscopy. The concentration of U was determined by neutron activation analysis. In some cases the concentration of a given element was below the limit of detection of the above mentioned methods.

3. RESULTS AND DISCUSSION

X-ray diffraction analysis of the undoped Synroc B matrix confirmed the existence of three major phases, as shown in Figure 2. These phases are perovskite ($CaTiO_3$), hollandite ($BaAl_2Ti_6O_{16}$) and zirconolite ($CaZrTi_2O_7$). According to the diffraction patterns, small amounts of as yet unidentified phases are still present. If 10 wt% of PW-4b simulated radioactive waste was added to the basic Synroc B composition, the diffraction pattern remains practically the same as for undoped Synroc B. Most of the peaks are slightly displaced, which in a way confirms that the mechanism of waste incorporation is formation of solid solutions. However some new peaks appear with very low intensity that probably belong to one or both new phases that develop in Synroc after addition of 10 wt% of PW-4b.

Undoped Synroc B fabricated by sintering at 1280°C for 4 hours in $Ar/4\%H_2$ flow was found to be fine grained, with crystal sizes in the range from 1 to 5 μm. TEM examination suggests that the different phases are randomly distributed with respect to each other. The principle Synroc B phases hollandite, perovskite and zirconolite possess structural peculiarities that make them relatively easy to identify[12]. In hollandite, the moire patterns are distinctive, probably due to sustained ion bombardment. Zirconolite has a mottled appearance and perovskite is inevitably twinned polysynthetically, which is recognizable as parallel bands of contrast. These structural peculiarities are shown in Figure 3. Each phase was identified by SAD and EDS analysis. In doped Synroc B with 10 wt% of PW-4b simulated radioactive waste, two additional phases can be observed in the microstructure after sintering. These are a magnetoplumbite-type phase (A), and an alloy (B) (Fig. 4).

The strongly reducing atmosphere during sintering ensures that several of the waste constituents are partially reduced to metal and thus alloys are formed (Fig. 5). These metal inclusions can be found in the grains or on the grain boundaries, and contain Mo, Ni and Fe. On the basis of quantitative EPMA analysis, it was determined that the intermetallic compound MoNi is formed with Fe in solid solution. The magnetoplumbite-type phase $(Ca,Sr,REE)(Al,Ti,Fe)_{12}O_{19}$ occurs as a minor phase in Synroc B (Fig. 6). It appears in the form of lamellae a few μm wide, up to 10 μm long and very thin. Figure 7 shows a TEM micrograph of the magnetoplumbite lamella with the corresponding diffraction pattern. The diffraction pattern can be indexed according to the ASTM diffraction standard for $CaAl_{12}O_{19}$, although the composition of the lamellae is not exactly $CaAl_{12}O_{19}$

because other elements are also present. From the X-ray spectrum (Fig. 8) of this magnetoplumbite phase, we can see that Al, Ca, Fe, Sr and Ti are also present. The peak of Ti is due to the X-ray signal from other phases around the magnetoplumbite-type lamella. The presence of Sr is understandable, since it is known that the magnetoplumbite phase incorporates elements such as Cs, Sr, Ba, La, Na, Si and K into its crystal structure. Considerable work on β-alumina and the magnetoplumbite crystal structure regarding their luminescence properties at the Philips Research Laboratories[16] showed that these structural types could contain many of these elements singly or in combination. It was also reported that the complete solid solution range from $XAl_{12}O_{19}$ to $XFe_{12}O_{19}$ is achievable. Also, single crystal refinement studies of the site occupancies of Al and Fe have been reported for $CaFe_6Al_6O_{19}$[17] and $SrFe_7Al_5O_{19}$[18]. Results of EDX analysis of this phase indicate the presence of a solid solution of $(Ca,Sr)(Fe,Al)_{12}O_{19}$. This phase can probably be completely eliminated by removing Al^{+3} ions from the precursor and relying on the presence of Ti^{+4} ions to faciliate the formation of the hollandite-type phase[19].

The results of the leaching tests on doped Synroc B with 10 wt% of PW-4b are given as normalized elemental mass loss per unit area (NL_i, g/mm^2) after 30 days leaching. These values, given in table IV, were calculated using the equation[4]

$$NL_i = \frac{m_i}{f_i.SA} \qquad (1)$$

where m_i is the mass of element i in the leachant (g), f_i is the mass fraction of element i in the unleached solid (unitless) and SA is the sample geometric surface area (m^2). The results are comparable with results reported by other authors[2]. The values are much lower than leach rates for some borosilicate glasses[5,6]. The leach rates are the highest for leaching in brine and lowest for leaching in carbonate (alkaline) water. We are still short of an explanation of the relatively high leach rate of U in distilled water. The leach rate for Sr was below the limit of detection in all three cases.

TABLE IV. NL_i values for elements of doped Synroc leached at 90°C for 30 days (g/m^2)

Element	Brine	Carbonate	distilled water
Mo	10.6	<8.9	8.9
Ni	27.3	<9.1	18.3
Fe	17.4	<2.9	5.8
Sr	<10.5	<10.5	<10.5
U	0.13	0.1	1.0

4. SUMMARY

Sintering of Synroc B was carried out at 900°C for 4 hours and at 1280°C for 4 hours in an Ar/4%H_2 flow. The densities obtained were 95 % of the theoretical density for undoped Synroc B and 93 % for doped Synroc B with 10 wt% of PW-4b simulated radioactive waste. When 10 wt % of simulated radioactive waste is added to the original Synroc B material, two new phases develop in the microstructure. One phase is the intermetallic compound MoNi with Fe in solid solution, and the other phase is $(Ca,Sr)(Al,Fe)_{12}O_{19}$, a compound isostructural with magnetoplumbite. Leach tests were performed on polished specimens according to the MCC-1 standard leach test. Normalized elemental loss per unit area was calculated for Fe, Ni, Mo, Sr and U. The values obtained can be compared to the values given in the literature.

5. LITERATURE

1. A.E. Ringwood et al, Nature, 278(1979), 219-223
2. K.D. Reeve, A.E. Ringwood, Proceedings of an International Conference on Radioactive Waste Management held in Seattle 1983, IAEA Vienna 1984, 307-324
3. D.G. Coles, F. Bazan, Nucl. Technol., 56(1982), 226-237
4. D.M. Strachan et al, Nucl. Techno., 56(1982), 306-311
5. C.R. Kennedy et al, Nucl. Technol., 56(1982), 278-288
6. A.E. Hughes et al, Nucl. Technol., 61(1983), 496-502
7. W.J. Weber, J.W. Wald, J. Nucl. Mater., 138(1986), 196-209
8. E.M. Foltyn et al, J. Nucl. Mater., 136(1985), 97-103
9. R.C. Ewig, T.J. Headley, J. Nucl. Mater., 119(1983), 102-109
10. W. Sinclair, A.E. Ringwood, Geochem. Journal, 15(1981), 229-243
11. W.J. Weber, F.P. Roberts, Nucl. Technol., 60(1983), 178-195
12. J.A. Cooper et al, J. Am. Ceram. Soc., 68(2), 64-70(1985)
13. J.A. Cooper et al, J. Am. Ceram. Soc., 69(4), 347-52(1986)
14. P.E.D. Morgan et al, J. AM. Ceram. Soc., 64(5), 249-257(1981)
15. H. Palmour III et al, Subsolidus Sintering of Synroc, Final Report, Contract DE-AC09-81SR 10957, NCSU 1980
16. J.M.P.J. Verstegen, A.L.W. Stevels, J. Lumin., 9(5), 406-414 (1974)
17. M. Harder, H. Mueller-Buschbaum, Z. Naturforsch. B: Anorg. Chem. Org. Chem., 31B(1976), 1148
18. M. Harder, H. Mueller-Buschbaum, Z. Naturforsch. B: Anorg. Chem. Org. Chem., 32B(1977), 833-834
19. S.E. Kesson, Radioact. Waste Manage., 4(1983), 53-72

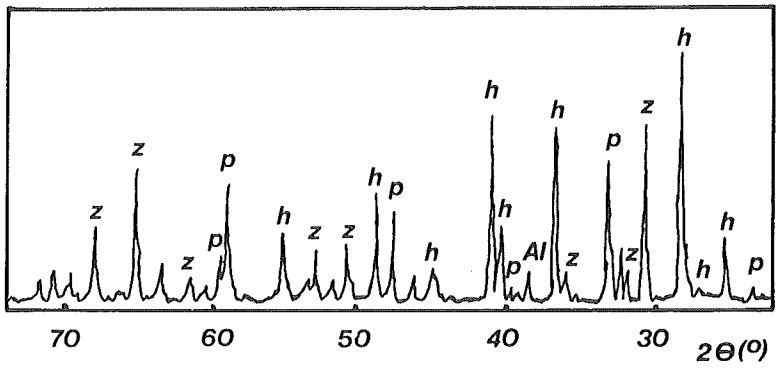

Figure 2. X-ray powder diffraction pattern of undoped Synroc B. h-hollandite, z-zirconolite, p-perovskite, Al-aluminium.

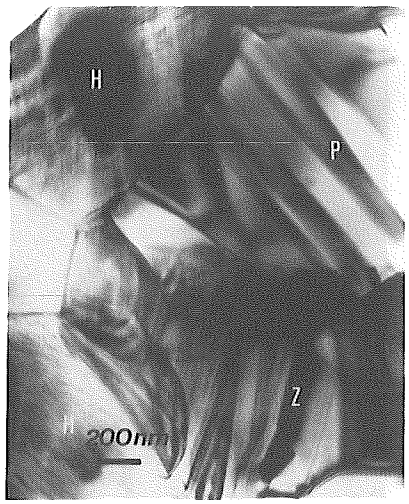

Figure 3. TEM micrograph of phases in undoped Synroc B. H-hollandite, Z-zirconolite, P-perovskite.

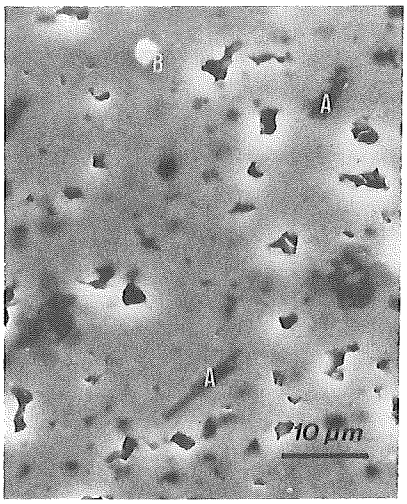

Figure 4. SEM micrograph of doped Synroc B with 10 wt% PW-4b. A-magnetoplumbite-type phase, B-alloy.

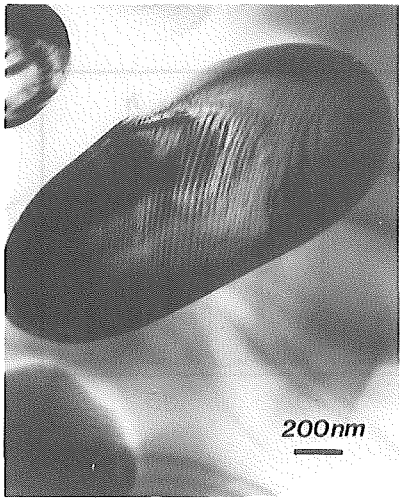

Figure 5. TEM micrograph of metallic phase containing Mo, Ni and Fe.

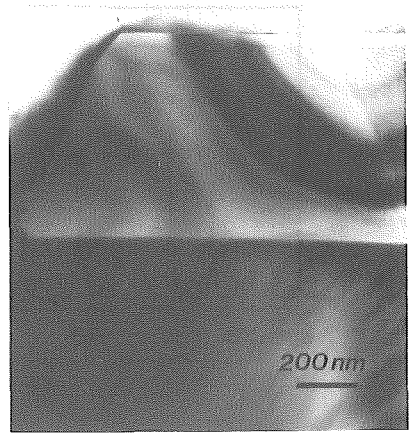

Figure 6. TEM micrograph of magnetoplumbite-type phase.

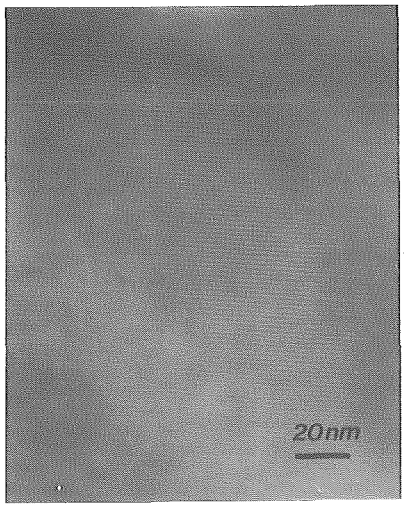

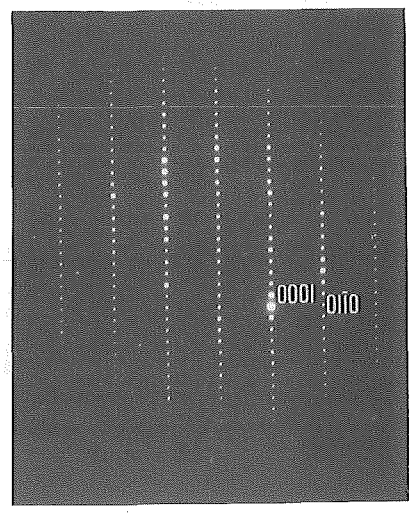

Figure 7. TEM micrograph of a lattice image of a basal plane in lamella with the corresponding diffraction pattern (zone $[2\bar{1}\bar{1}0]$).

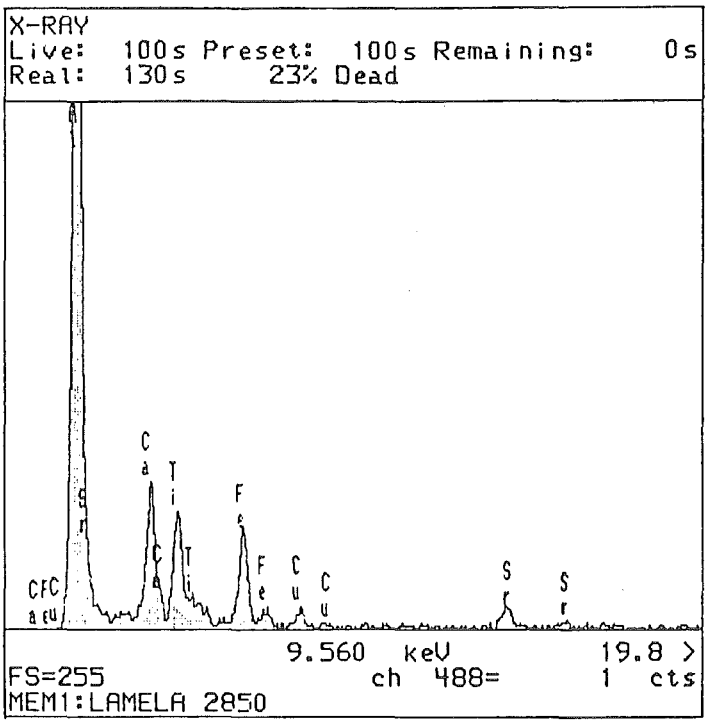

Figure 8. EDX spectrum of lamella in figure 7. The signal for Ti is from the surroundings and the signal for Cu is from Cu specimen holder.

Solid state investigation of ceramic-metal interface bonding

U. Jauch, G. Ondracek
Rheinisch-Westfälische Technische Hochschule
Institut für Gesteinshüttenkunde
- Glas, Keramik, Binde- und Verbundwerkstoffe -
Mauerstr. 5, D-5100 Aachen

ABSTRACT

Cermets are a potential class of composites, in which, however, the question of bonding at the ceramic-metal interface plays a key role: non bonding reduces the composite with respect to properties as Young's modulus, electrical conductivity or thermal expansion to those of the porous matrix phase material. This is why a new dilatometric technique is used to study the bonding between ceramic and metal phases selected to produce cermets.

The phases used as an example are aluminiumtitanate eutectic and nickel, the method is based on the effect,

- that before debonding the measured effective thermal expansion coefficient of the composite lies between the thermal expansion coefficients of its phases.
- that after debonding the effective thermal expansion coefficient drops to that of the matrix phase.

INTRODUCTION: BOUNDS AND PROPERTIES

As known by theory the properties of a multiphase material as a function of phase concentration may be determined by bounds of different order [6].

Supposing nothing more than that the material is two-phased, ultimate *I. order bounds* include all properties being

realized by the two-phase system, as shown in fig. 1 for cermets. There is no possibility to find properties outside first order bounds by theory. Knowing, however, that the material is two-phased and isotropic, closer *II. order bounds* follow according to *two* assumptions about the system: being two-phased and isotropic (fig. 1).

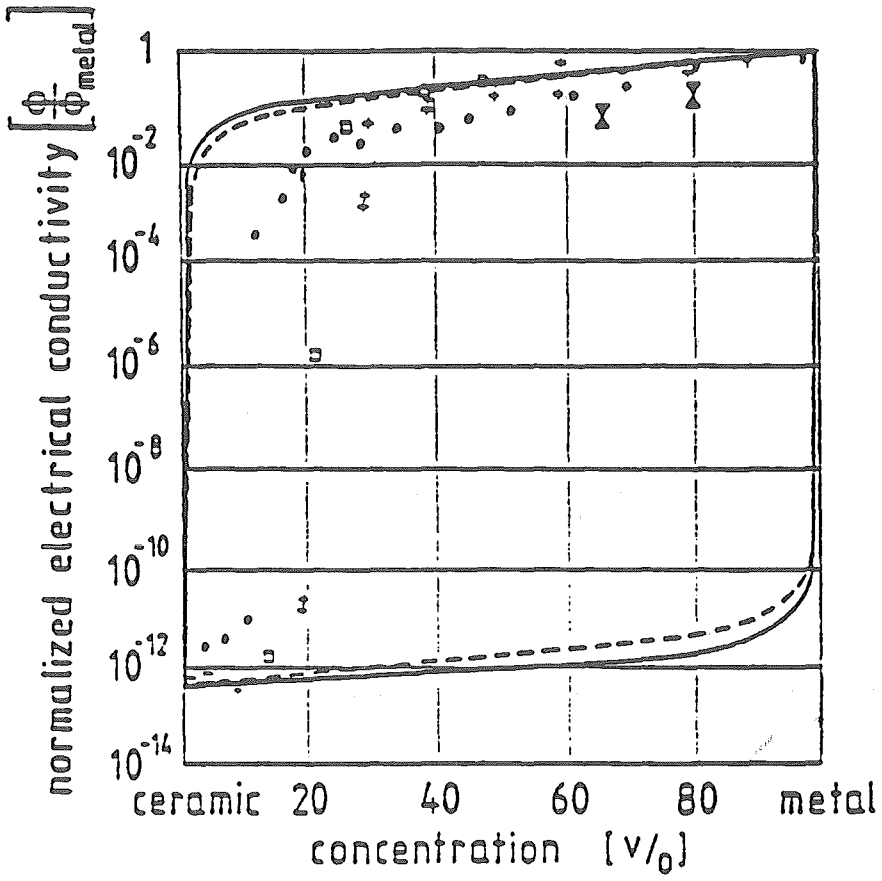

Figure 1. Electrical conductivity of cermets
(—— I. order bounds; --- II. order bounds;
experimental values) [6]

Continuing that way by increasing the number of presuppositions - or, in other words, becoming more and more definite about the materials microstructure - leads finally to total convergence of the bounds resulting in one single curve, which describes exactly the dependence of the properties on the microstructure of a two-phase material (fig. 2).

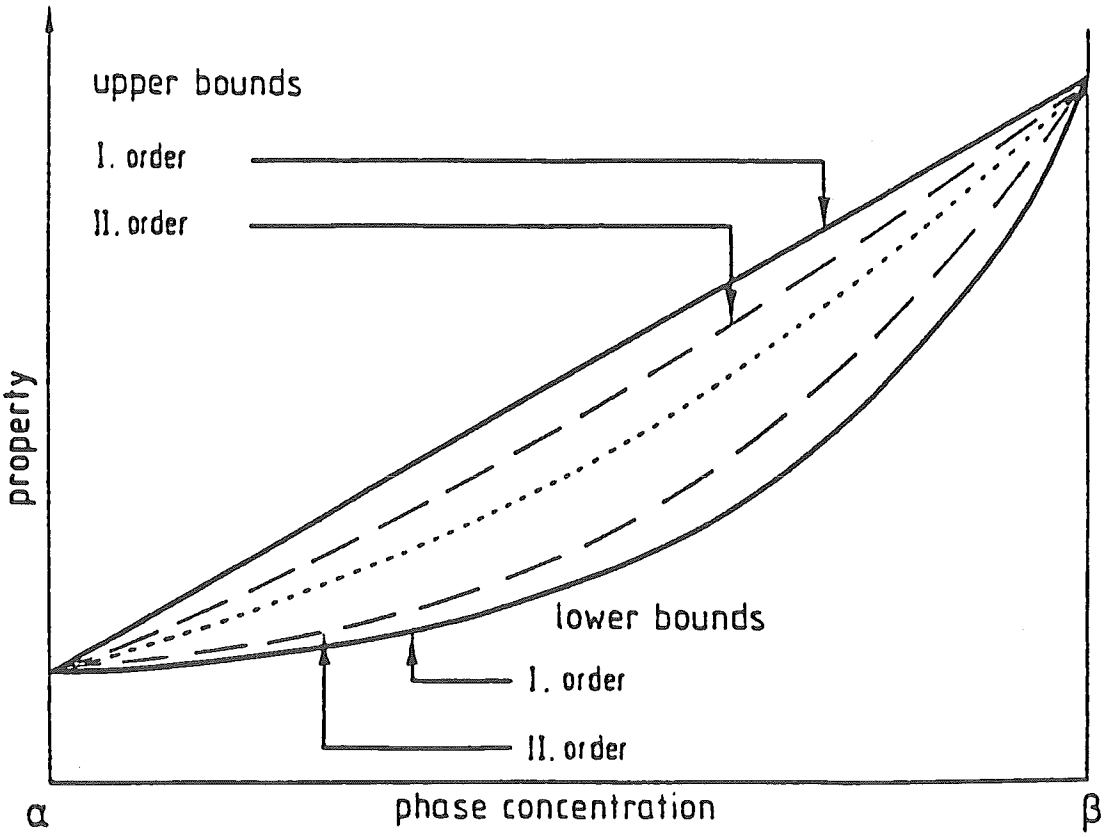

Figure 2. Bounds of different order

Again as theory points out, *5 parameters* control dominantly the microstructural effect on the properties of a multi-phase material (fig. 3) [6].

implicite parameters	1. number of phases	e.g. two-, three-, multiphased premise: thermochemical equilibrium
	2. type of microstructure matrix phase microstructure interconnecting phase microstructure	premise: continuum principle
explicite parameters	3. volume fraction of phase (concentration factor) volume x number of the phase particles 4. shape of phase particles (shape factor) 5. orientation of phase particles (orientation factor)	premise: spheroidal model mean values

Figure 3. Microstructural parameters and model concept premises

Others than these parameters may be neglected in the frame of an engineering approach to the problem.
For a two-phase material this statement means, that the five factors control definitely, where a *certain* property value inbetween the bounds has to be expected (fig. 4).

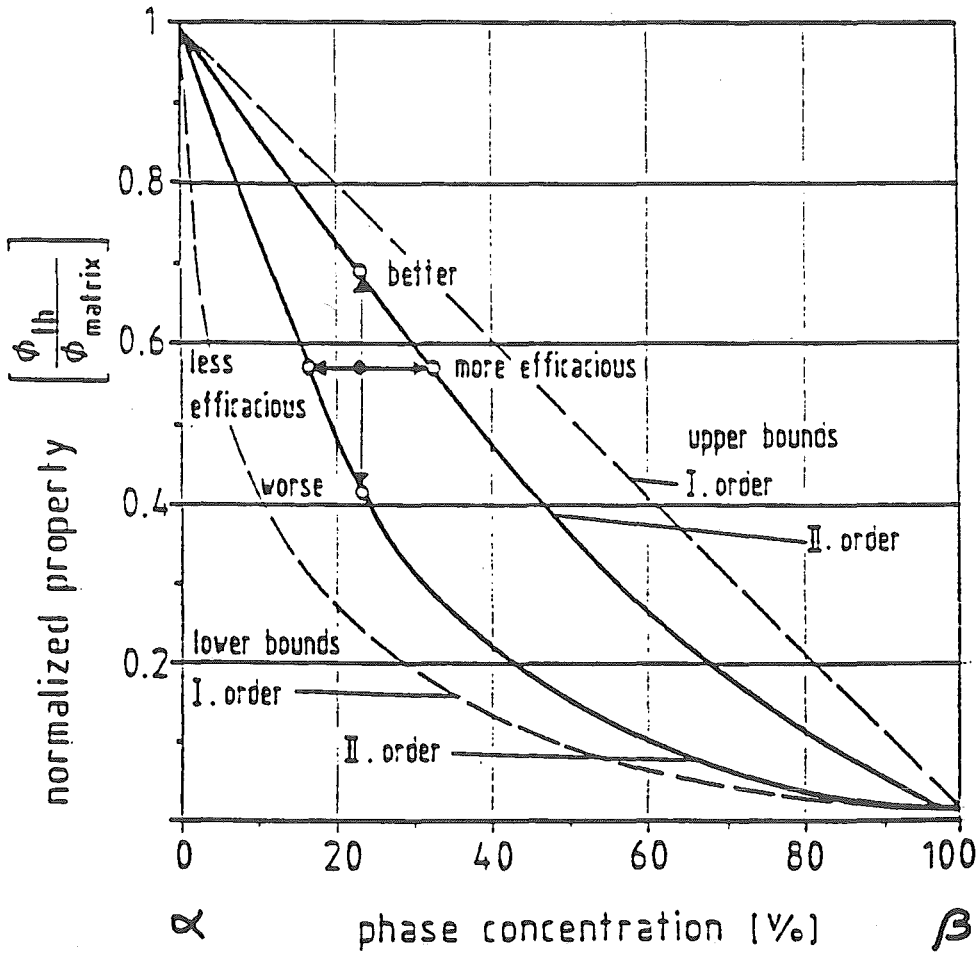

Figure 4. Bounds and tayloring multiphase materials

Based on the bound concept it may now be defined, how to change the in-situ microstructure of a two-phase material in order to construct taylor-made materials with desired properties.

If, for example, *the property of the in-situ material* lies at the spot inbetween the bounds as shown in fig. 4

- one may either save ß-phase assumed to be rare and expensive without changing the property

- or one may improve the property - as Youngs modulus or the thermal conductivity - at constant phase concentration

by precalculated changes in the microstructure.

Those precalculated changes - however - will only lead to the desired effective properties of the composite, if bonding exists between its phases. This is, why phase bonding plays a key role in tayloring multiphase materials. And this, exactly, is the major problem with composites as cermets, in which - preferentially - *incoherent phase boundaries* occur between the phases (fig. 5).

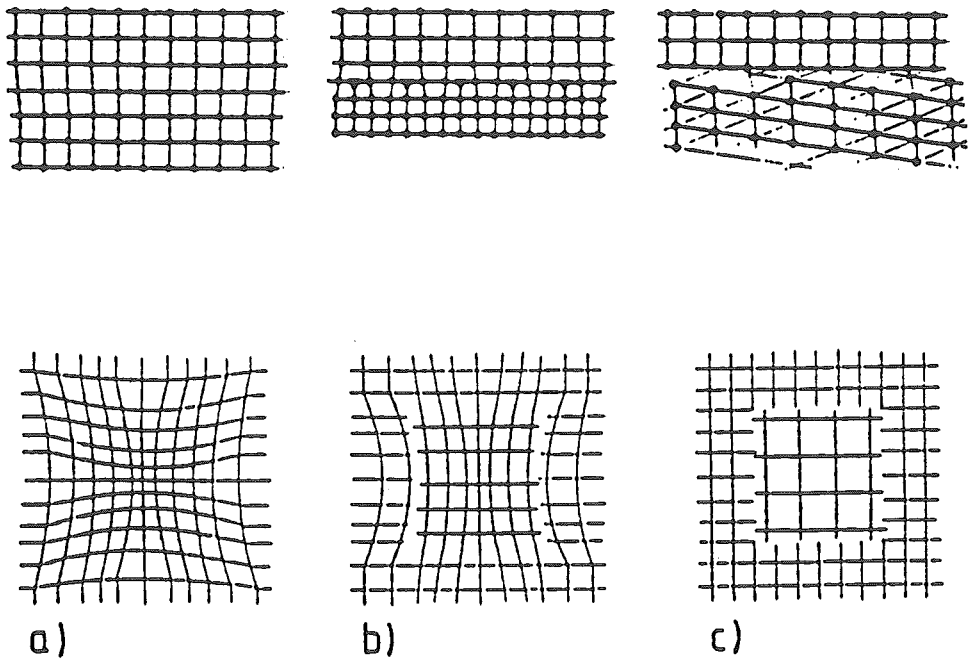

Figure 5. Coherence at phase boundaries schematically
a) coherent b) partly coherent c) incoherent

Additionally, these phases may have large differences in their thermal expansion coefficients, which complicates the bonding problem.

BOUNDS AND BONDING

Sintering, for instance, a cermet material consisting of a nonbonding ceramic matrix phase and a nonbonding included metal phase one obtains a porous ceramic material the pores of which are filled by loose metal particles. The same is true for concentrations, where the metal phase forms the matrix whilst ceramic particles fill the pores. That situation, for example, exists in the cermet system uranium dioxide-molybdenum (fig. 6).

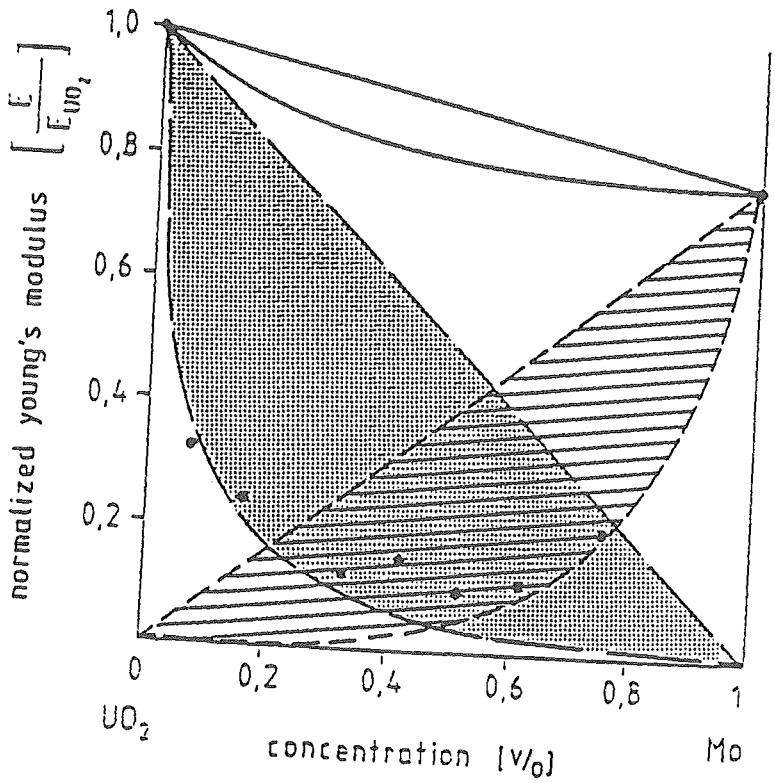

Figure 6. Phase bonding and bounds for Young's modulus of elasticity

As a consequence of the debonded phase boundary the Young's moduli of these cermets measured by tensile tests do not fit into the bounds for the UO_2-Mo-system but do fit inbetween the bounds for porous UO_2 or porous Molybdenum respectively.

Constructing taylor-made materials therefore needs to observe two conditions:

- the properties of the selected phases have to result in the desired effective properties of the composite

and

- phase bonding has to take place between the selected phases.

How to find out criteria about bonding is the content of the following chapter.

DILATOMETRIC BONDING TEST

As pointed out before the comparison between measured property values and calculated bounds provides a first, qualitative approach to the problem of bonding. In order to determine phase bonding quantitatively one once more starts from microstructure-property-correlations:

Considering the theoretical equation about the dependence of the thermal expansion coefficient of two-phase materials [1, 3]

$$\alpha_C = \alpha_M + (\alpha_D - \alpha_M) \frac{E_D[E_C(1 - 2\nu_M) - E_M(1 - 2\nu_C)]}{E_C[E_D(1 - 2\nu_M) - E_M(1-2\nu_D)]} \qquad (1)$$

(α = thermal expansion coefficient; E = Young's modulus of elasticity; ν = Poissons ratio of transversal contraction; C, D, M = Subscripts for Composite, Dispersed and Matrix phase)

and assuming the second phase to be pores one notices, that thermal expansion does not depend on porosity. In the equation subscript "D" denotes the included phase. If "E_D", the Youngs modulus for the included phase, becomes zero for pores, the second term of the equation disappears and the thermal expansion coefficient of the porous material is equal to the thermal expansion coefficient of the nonporous, compact material. This is an important result in so far,

- as any property as rupture strength, Young's modulus or conducitvity decreases with porosity except the thermal expansion coefficient (fig. 7) and
- as this result provides the basis to measure phase bonding by dilatometry.

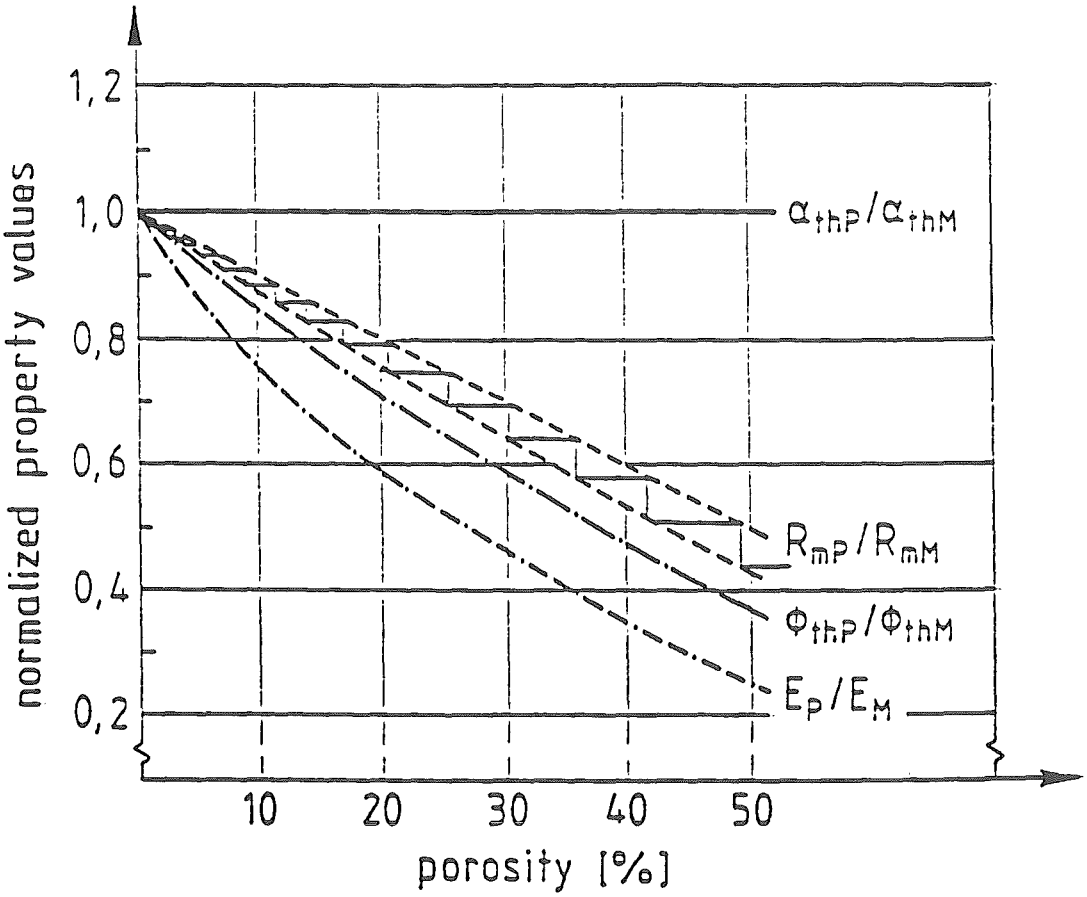

Figure 7. Normalized properties as a function of spherical porosity

α_{th} = thermal expansion coefficient
R_m = rupture strength
Φ_{th} = thermal conductivity
E = Young's modulus of elasticity
P,M = subscripts for porous (P) and compact material (M)

To demonstrate the method an aluminium titanate-titaniumoxide eutectic as ceramic matrix phase and nickel as the included metal phase of a cermet has been chosen. The thermal expansion coefficients of nickel and the ceramic phase have been measured separately in a Netzsch dilatometer (fig. 8).

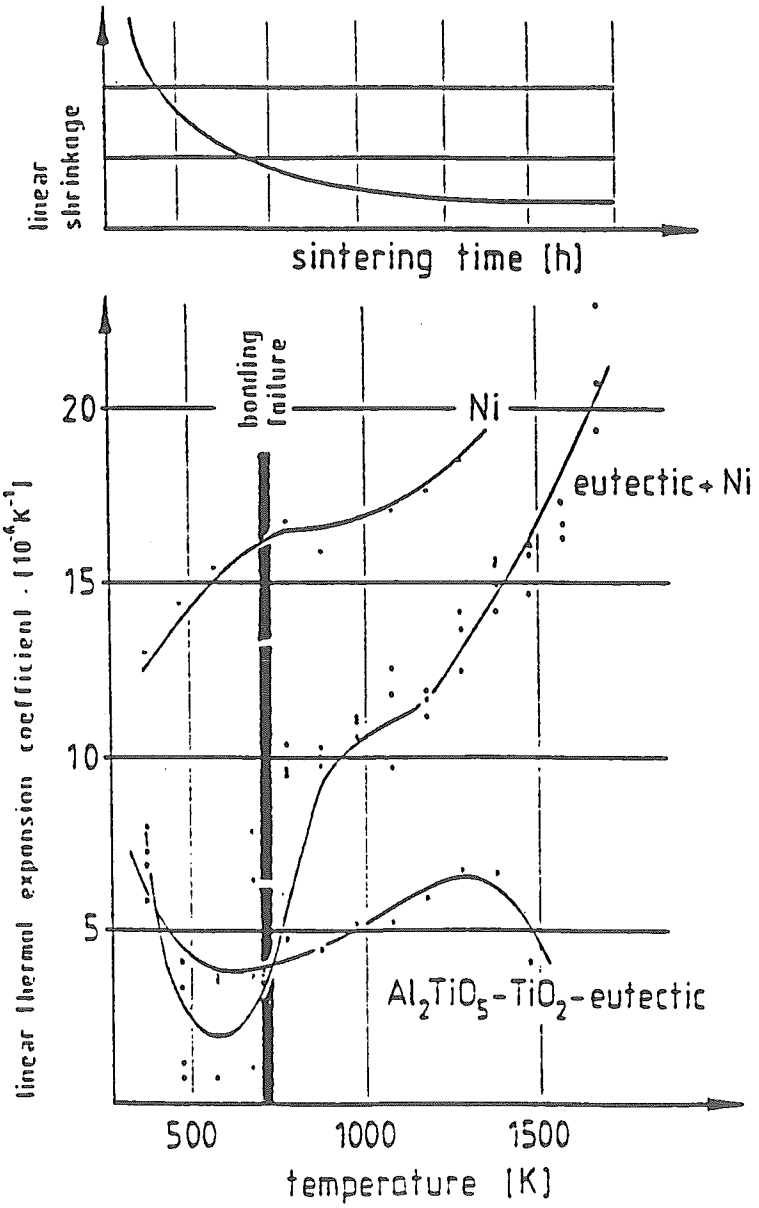

Figure 8. Shrinkage by sintering (above) and thermal expansion and phase bonding (below)

Afterwards a pressed pellet of Al_2TiO_5-TiO_2 eutectic and Nickel powders was sintered isothermally in the same dilatometer. Where the slope of the shrinkage curve pointed out, that the sintering process had been taken place, thermal contraction of the cermet - which means the thermal expansion coefficient during cooling - was measured dilatometrically (fig. 8). This thermal expansion coefficient of the cermet at elevated temperatures was found, as expected, between the thermal expansion coefficients of its two phases. By continued cooling however thermal stresses are induced at the phase boundaries, since the ceramic matrix phase contracts less than the metal inclusions do. If these stresses exceed the phase bonding strength debonding at the phase boundary takes place and the system changes from a cermet to a porous ceramic, where the pores contain loose metal particles. And since, as pointed out above, the thermal expansion coefficient of a porous ceramic will be identical with the one of the compact ceramic material, the thermal expansion coefficient of the chosen cermet system drops to the thermal expansion coefficient of the ceramic phase, when phase debonding occurs. In the present system the phase boundaries crack at about 700 degrees.

Knowing the temperature interval (ΔT) to cause debonding as well as the thermal expansion coefficients and bulk moduli of the phases we may now calculate the bonding strength by existing equations [3, 5]

$$\delta = 3\Delta T\,(\alpha_D - \alpha_M)\,\frac{K_m K_D}{K_D - K_M} \approx 3\Delta T\,(\alpha_D - \alpha_M)\,K_M \qquad (2)$$

which, of course, gives only a first engineering approach for two reasons:

1) In technical systems the phase boundaries are not smooth according to the rough surface and irregular shape of the inclusions. This may lead to additional mechanical bonding. For exact measurements the inclusions should therefore have smooth surfaces (or the surface roughness would have to be known quantitatively).

2) Whilst the brittle, ceramic phase will not suffer plastic deformation such plastic deformation will certainly take place in the metal inclusions above their yield strength and therefore partly compensate the thermal induced stresses. This is why for more accurate calculations of the bonding strength one needs to know the temperature function of the yield strength of the included metal phase.

Both sources of inaccuracy, however, can be eliminated by respective experimental measures.

Phase bonding strengthes achieved on this way are obviously correlated with the "WORK OF ADHESION" (σ)

$$\Delta G_{D/M}^{Gr} - \Delta G_D^{Gr} - \Delta G_M^{Gr} \approx \sigma \qquad (3)$$

Since this "WORK OF ADHESION" is a function of the surface energies of the phases (ΔG^{Gr}_{D}, ΔG^{Gr}_{M}) and the interface energy ($\Delta G^{Gr}_{D/M}$) and since this energy may be determined by wetting experiments and by interference microscopy (fig. 9) to measure the contact angles between the phases via the Young-Dupré-equation [4, 5, 7] an alternative way to investigate phase bonding in solid state, the region denoted still by question marks in fig. 10, is available, being started now supplementing the already existing results about wetting in ceramic-metal-composites (fig. 10).

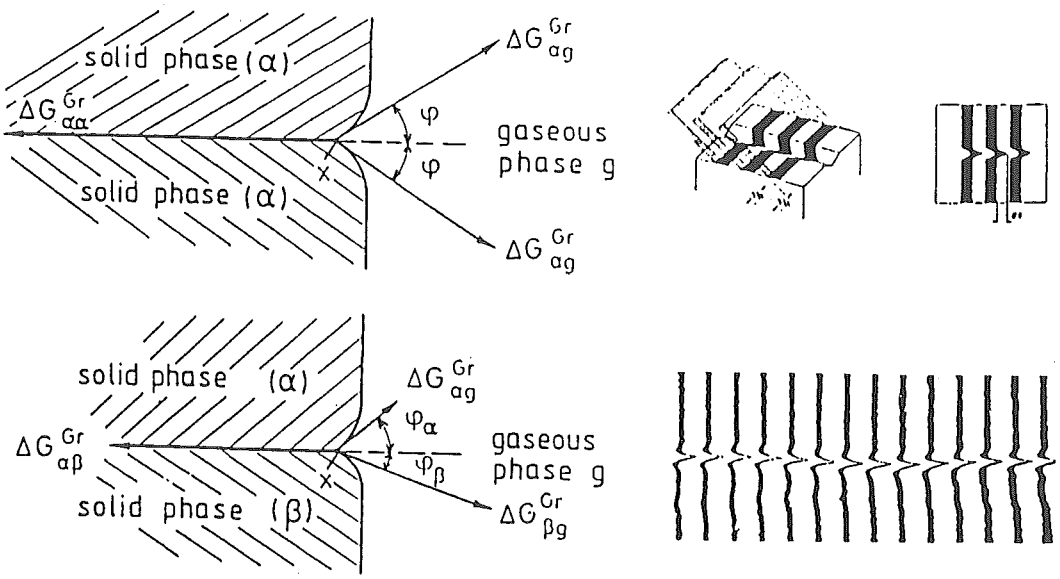

Figure 9. Phase boundary equilibrium and interference microscopy

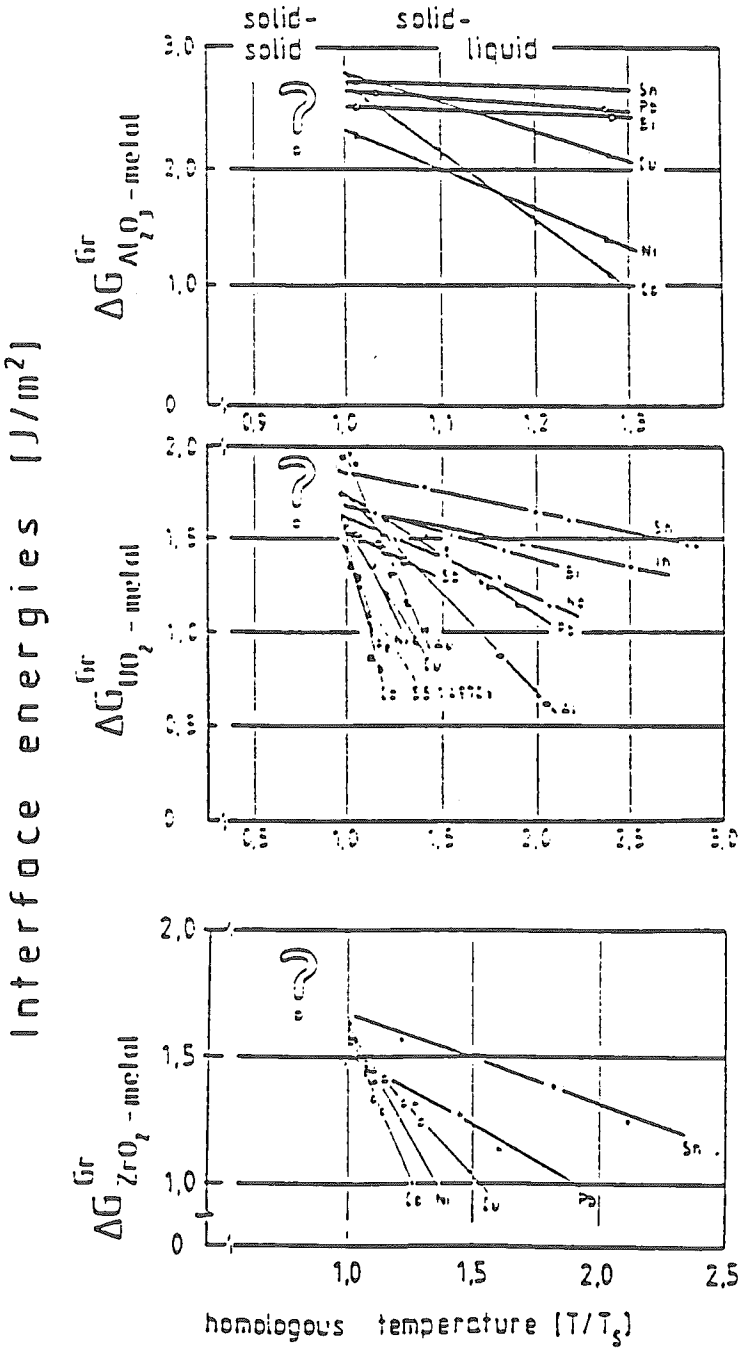

Figure 10. Interface energies between solid ceramics and liquid metals as function of homologous temperature (T = measuring temperature; T_s = metal melting point)

REFERENCES

1. Gribb, J.L., Nature 220, 1968, 576.

2. Ledbetter, H.M. and Austin, M.W., Proc. Conf. on Residual Stresses, Garmisch-Partenkirchen, ed. by E. Macherauch, V. Hauk, DGM-Oberursel, 1987.

3. Nazare, S. and Ondracek, G., Z. Werkstofftechnik, 1978, 9, 140.

4. Nikolopoulos, P. and Ondracek, G., Z. Werkstofftechnik, 1982, 13, 60 and J. Nucl. Mat., 1981, 98, 306.

5. Nikolopoulos, P., Sotiropoulou, D., Jauch, U. and Ondracek, G., Ceramics and Metals, Bilateral Seminars of the Int. Bureau, Kernforschungsanlage Jülich, 1987, 281.

6. Ondracek, G., Review on Powder Metallurgy and Physical Ceramics, 3-3/4, 1988, 1.

7. Ondracek, G., Werkstoffkunde, expert verlag Sindelfingen, 1986, 58 and 254.

ACKNOWLEDGEMENT

The present work was substantially supported by the Deutsche Forschungsgemeinschaft Bonn and partly performed at Kernforschungszentrum and Universität Karlsruhe. This support - as well as the assistance of Mrs. Peters, Mrs. Schmitz and Mr. Trechas - is gratefully acknowledged by the authors.

Thermophysical Properties of $MgAl_2O_4$

B. Schulz and G. Haase

Kernforschungszentrum Karlsruhe
Institut für Material-und Festkörperforschung I
Postfach 36 40, 7500 Karlsruhe 1
Federal Republic of Germany

The thermophysical properties of $MgAl_2O_4$ i. e. specific heat, thermal expansion and thermal conductivity were determined of samples of different origin and interpreted on the basis of knowledge of the binary system MgO - Al_2O_3 and mechanisms of heat transfer.

Introduction

$MgAl_2O_4$ is a candidate for window materials of additive heating of the fusion-plasma by microwaves in a potential fusion reactor. For this purpose the high optical transparency and low dielectric losses are the most important properties for this material. In second line a low thermal expansion coefficient and high thermal conductivity are required.
In the following, results on two kinds of samples are presented, where the most important information on the compound is the fact the spinel phase has a homogeneity range [1], which may influence especially the thermal conductivity.

Sample preparation and characterization

A commercial product (Raytheon, U.S.A) and samples hot pressed (1475 K, 300 bar, Ar) were used. The powder of the hot pressed materials was prepared by our Yugoslav coworkers, the process is described in detail in [2].
The samples were prepared by standard metallography, followed by SEM in the case of samples prepared in Yugoslavia from powder (1a, b). The most important difference is the high porosity of the hot pressed material. An electron micro-probe analysis

with SEM, to detect either MgO as second phase in the Raytheon material or a different Mg/Al - ratio in the hot pressed one was not successful.

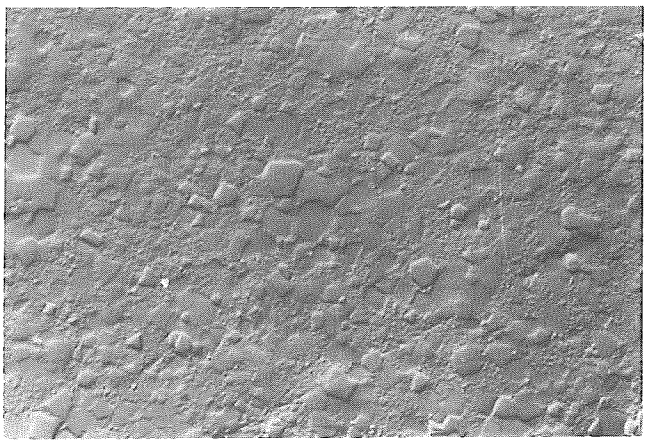

← 50 µm

a) Raytheon (high purity, high dense) optical microscopy, interference contrast

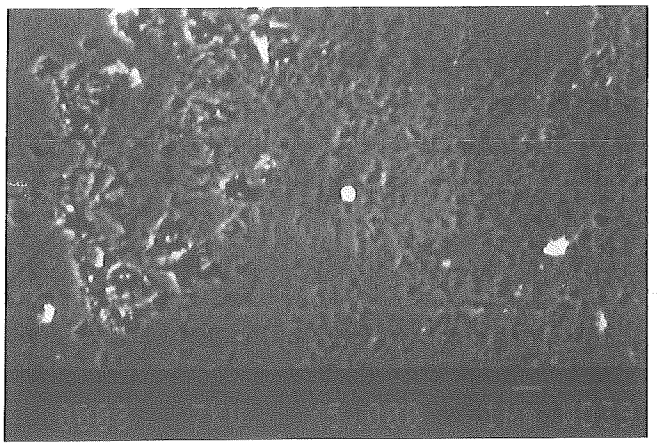

b) SEM, Yugoslavian powder

Abb. 1: Microstructure of $MgAl_2O_4$ samples

Characterization of $MgAl_2O_4$ - samples		
	Raytheon	Yugos.
Al [Gew %]	38.61 - 39.64 (37.93)	starting
Mg [Gew %]	15.91 - 16.13 (17.08)	substances
Fe [Gew %]	0.004	Merck, p. a.
Ca [Gew %]	0.005	
Ti [Gew %]	0.005	
C [Gew %]	0.012	
	solid product	solid product
	x-ray single	x-ray single
	phase	phase
Density	100 %	78 %

Table 1: Characterization of $MgAl_2O_4$-samples

Thermophysical properties

The methods used are described in detail in [3].

Specific heat

The specific heat c_p was measured in a Perkin-Elmer DSC 2 on thin platelets ($m \approx 50$ mg) in Ar-atmosphere. The mean values for c_p are shown in Fig. 2 and compared with the specific heat data of pure sapphire (NBS) and those of pure MgO [4]. The results are satisfactory, as expected the data are higher than those of MgO and lower than those of Al_2O_3, indicating that the Neumann-hopp-rule is fairly well satisfied. The standard deviation for c_p can be given with ± 1 %.

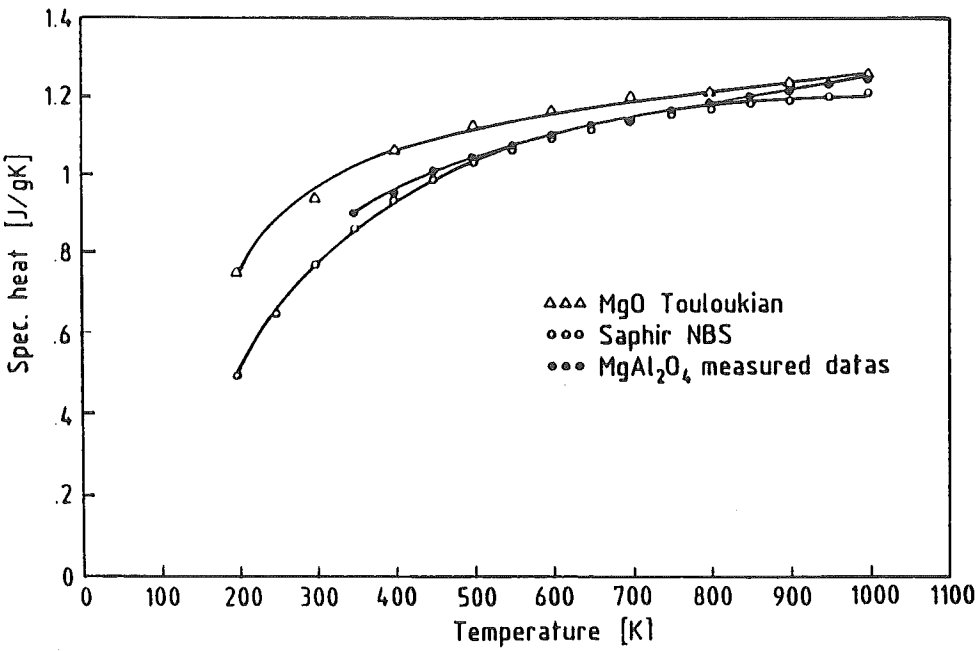

Abb. 2: Specific heat of Spinel, MgO and Al_2O_3

Thermal expansion

Cylindrical samples of ≈ 9-10 mm in length and 6 mm in diameter were employed in a differential-dilatometer with sapphire as reference material. Data were taken only under isothermal conditions, when they coincided with each other on heating and cooling, and no offset at room temperature exceeding the resolution of the instrument (1 µm) occurred. Fig. 3 gives the results compared to data of [5] in good agreement.

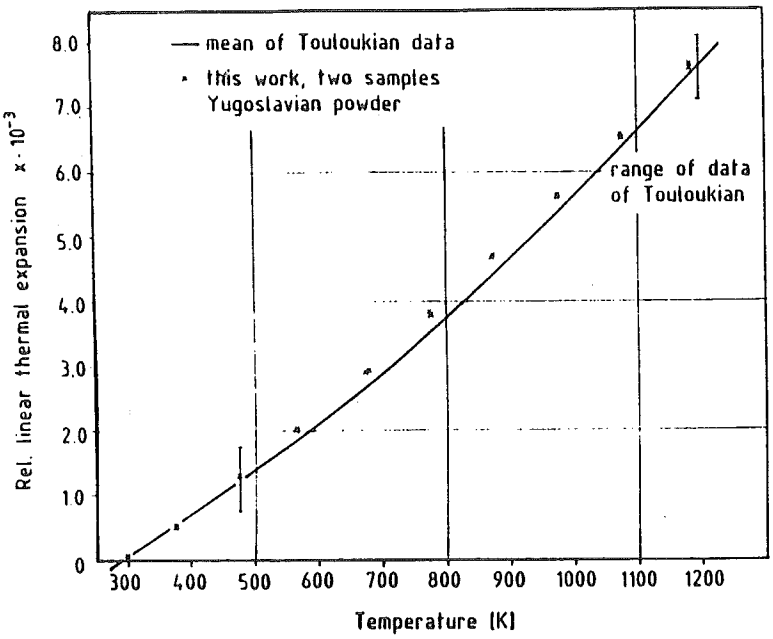

Abb. 3: Thermal expansion of $MgAl_2O_4$ samples

Thermal diffusivity

The thermal diffusivity α was measured using a laser flash equiment. The cylindrical samples (12.7 mm diameter, thickness varying from 1.5-4 mm) were sealed by a carbon coating against the optical transmission of the laser-flash light as described in detail [6]. The data of the hot pressed samples were corrected for porosity using the equation:

(1)

$$\alpha_p = \alpha_0 \left(\frac{4 - 9P}{10(1-P)} + \sqrt{\left(\frac{4 - 9P}{10(1-P)} \right)^2 + \frac{1}{5(1-P)}} \right) \qquad [3]$$

p, 0 - are indices for porous and dense samples, P-denotes Porosity. Fig. 4 shows the large difference in the temperature dependence of the thermal diffusivity.

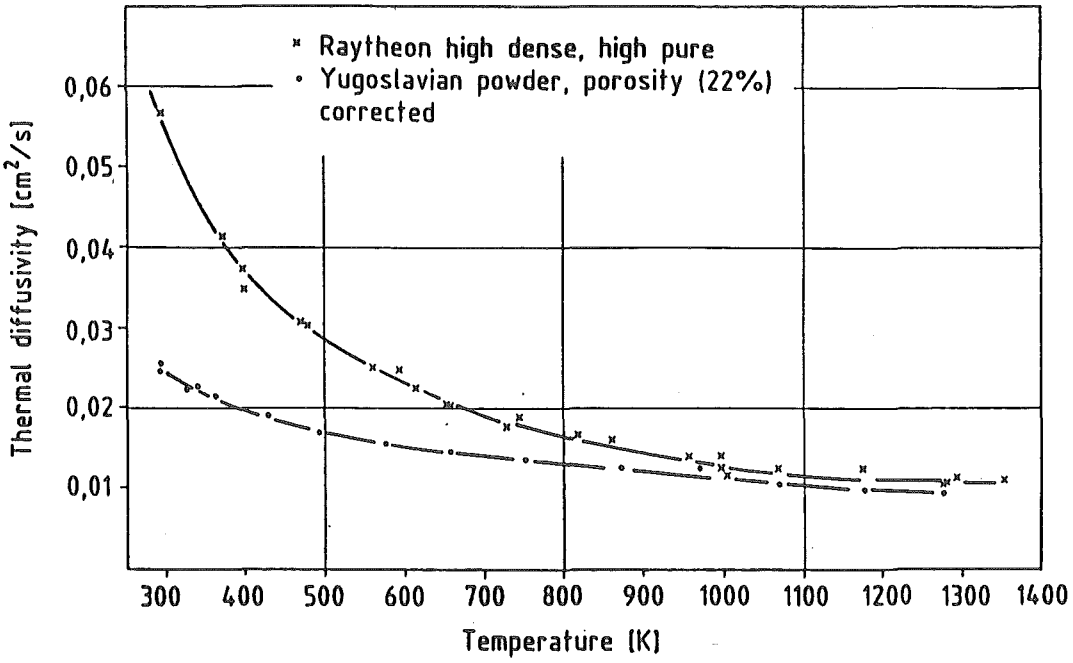

Abb. 4: Thermal diffusivity of $MgAl_2O_4$ 100 % T. D.

The thermal conductivity

From the density ρ, the specific heat c_p and the thermal diffusivity, the thermal conductivity was derived

$$\lambda = a \cdot c_p \cdot \rho \qquad (2)$$

$MgAl_2O_4$ is a typical isolating material with high electrical resistance and high optical transparency. Thus the temperature dependence of the thermal conductivity about and above the Debeye temperature should follow the equation

$$\lambda_{ph} = \frac{1}{a + b\,T} \qquad (3)$$

for a pure phonon conductor. The quantity a represents the influence of point defects and solved impurities, b represents the influence of phonon collisions on the thermal conductivity. The latter quantity b only presents the intrinsic parameter, giving the behaviour of the compound during heat transport. Thus b should be equal for all kinds of $MgAl_2O_4$, as was shown in a systematic analysis of our own and literature data of the thermal conductivity on the examples of α - Al_2O_3 (including sapphire) [6].

At higher temperatures an influence due to internal radiation may occur:

$$\lambda_{rad} \sim \frac{n^2}{k} \cdot T^3 \qquad (4)$$

n - refraction index
k - extinction coefficient

The resulting curve for a typical phonon conductor is shown in Fig. 5.

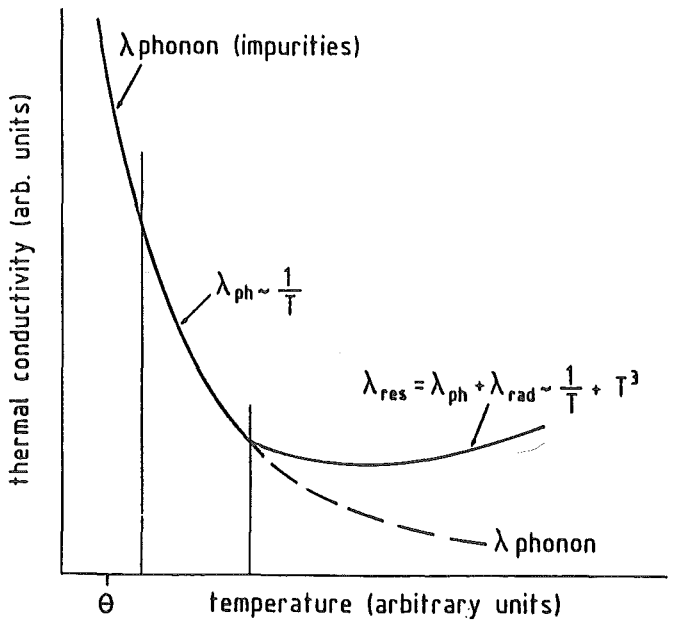

Abb. 5: Typical temperature dependance of thermal conductivity of an insulator

For the two $MgAl_2O_4$ materials the inverse of the thermal conductivity (resistivity) is shown in Fig. 6 by two very different curves.
The deviation of $1/\lambda$ from linearity above 1100 °C indicates the influence of internal radiation (increasing λ), the hot pressed samples contained ~ 0.01 % C (due to pressing in graphite dies), which suppresses internal radiation completely. The higher values of the resistivity of the hot pressed samples in general could be very well explained by a higher concentration of impurities solved in the lattice. It is the difference in the slope of the curves, which shows clearly that in fact two different materials were investigated. The data analysis of the thermal conductivity of α-Al_2O_3 give the result of $b = 1.17 \cdot 10^{-2}$ cm/W $\pm$ $0.16 \cdot 10^{-2}$ cm/W. From Fig. 6 the Raytheon material yields b equal to $1.5 \cdot 10^{-2}$ cm/W and for the hot pressed a value of $0.81 \cdot 10^{-2}$ cm/W, which is a factor of two.

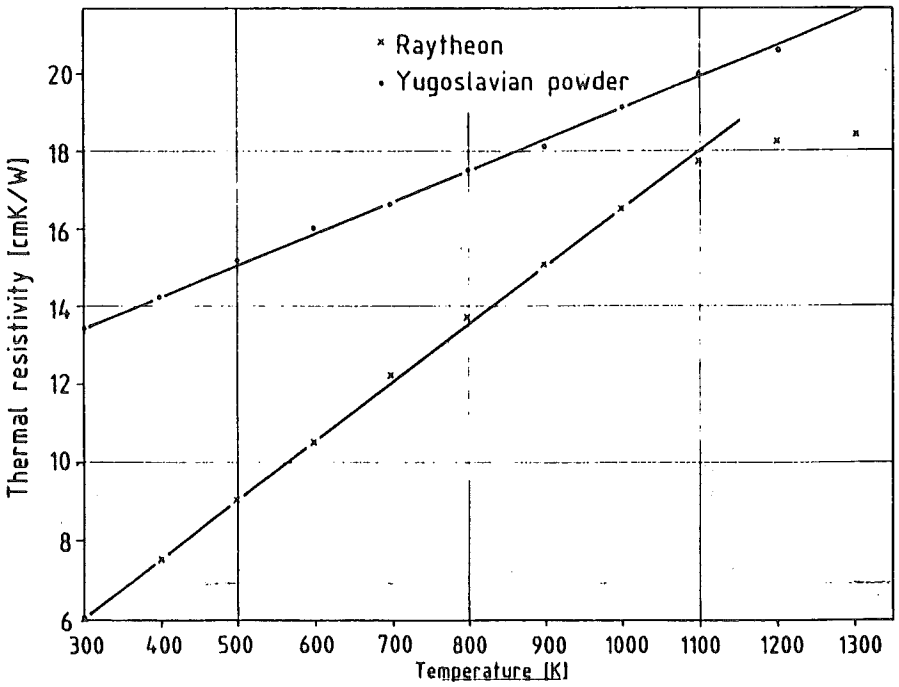

Abb. 6: Thermal resistivity of $MgAl_2O_4$

Thus it results that the knowledge of the true composition of both spinels (using electron microprobe analysis) is necessary for an interpretation of the results.

Literature

[1] M. K. Reser (Ed.): Phase diagrams for Ceramists, The American Ceramic Society, Columbus Ohio 1964, Fig. 259, 260

[2] M. Miloschewski, B. Bliznakowska: Paper presented in these Proceedings

[3] B. Schulz: in Proc. Int. Conf. für Technische Keramik 16.-18.11.87, Wiesbaden FRG Demat Exposition Managing Frankfurt/Main FRG

[4] Y. S. Touloukion (Ed.): Thermophysical Properties of Matter, IFI, Plenum New York Vol. Specific heat of Solids 1973

[5] Y. S. Touloukion (Ed.): Thermophysical Properties of Matter, IFI Plenum New York Vol. Thermal Expansion of Solids 1974

[6] B. Schulz: High Temp. High Press, 1989 in print

PREPARATION, SINTERING AND THERMAL EXPANSION OF $MgAl_2O_4$

M. Miloševski and B. Bliznakovska
Faculty of Technology and Metallurgy, Skopje, Yugoslavia

$MgAl_2O_4$ spinel was obtained by the method of coprecipitation. Sintering kinetics was studied during the initial and intermediate stage of the process. It was shown that the Mg^{2+} ions are the rate controlling species in the initial stage of $MgAl_2O_4$ sintering.

Coefficient of thermal expansion could be presented by the following relation:

$\alpha = 8{,}50 \cdot 10^{-6} + 4{,}90 \cdot 10^{-10} T + 1{,}11 \cdot 10^{-12} T^2$

Introduction and Literature Review

Optically transparent $MgAl_2O_4$, magnesium aluminate spinel has been recognized by virtue of its intristic infrared transmission characteristics as a very good optical material since long time ago. Moreover, it posseses the exellent mechanical and thermal schock resistence properties and chemical durability. These attractive properties make this material suitable for the application as infrared windows and missile domes. One of the potential application of the stoichiometric $MgAl_2O_4$ (single crystals) could be its use as an insulating substrate in metal-oxide semiconductors (MOS) devices(1). $MgAl_2O_4$ has found its use as a refractory material and as a support of catalysts (2).

The most direct method of spinel production is to start from a mixture of alumina and magnesia in an electric arc furnace, giving a dense refractory grog material, but it is expensive. Another method of grog production is firing suitable alumina-magnesia mixtures bearing raw materials at high temperatures (1650°C) (3). The chemistry of the sol-gel synthesis of $MgAl_2O_4$ spinel has been reported by Dislich (4).

Some of the important factors favouring the solid state reaction are the poor crystallinity, large surface area and intimate mixing of starting materials. All of these conditions would be satisfied if the magnesium and aluminium hydroxides could be coprecipitated in the appropiate proportion and used as a starting material in spinel production. Coprecipitation of Mg and Al-hydroxides by NH_4OH (liquid) from a solution of $Mg(NO_3)_2$ and $Al(NO_3)_3$ or $MgCl_2$ and $Al_2(SO_4)_3$ is described in the literature (5,6). It is known that aluminium and magnesium are completely precipitated as hydroxides at pH=6,5 - 7,5 and pH = 12, respectively (7). This difference in pH at which the two ions are precipitated from their salt solutions offered a problem in which it was anticipated that they would be either precipitated separately from a solution containing the mixture of salts at the corresponding pH-range or the precipitation of both of ions can take place at an intermadiate pH-range. The composition of the precipitate formed by the gradual addition of ammonia liquid to a mixture of aluminium and magnesium salts, as is given in Table I (6), showed that the stoichiometric ratio required for spinel production can be achieved at pH=9. The decrease in Al^{3+} content takes place at higher pH-values owing to the aluminate formation.

Table I. Precipitate composition at different pH(6)

pH	Molar ratio of MgO/Al_2O_3
6,5	0,11
7,5	0,36
8,5	0,88
9,0	1,00
9,5	1,08
10,0	1,11

Sintering investigation on spinel was carried out in some details by several authors recently(9-13), been concentrated on the sintering kinetics, grain growth, powder characterization and prefered conditions. The role of the stoichiometric deviations was not extensively examined in these investigations. Small deviation from the exact stoichiometric spinel composition leads to the formation of solid solutions at higher temperatures. Their defect structure can be described as follows (14):

$$2Al^{3+}_{Mg^{2+}} + 3MgO = 2Mg^{2+}_{Al^{3+}} + V_{O^{2-}} + MgAl_2O_4 \quad /1/$$

$$2Mg^{2+}_{Mg^{2+}} + 4Al_2O_3 = 2Al^{3+}_{Mg^{2+}} + V_{Mg^{2+}} + 3MgAl_2O_4 \quad /2/$$

Bratton (9,10) investigated the sintering mechanism and grain-growth kinetics of pure $MgAl_2O_4$ and found that volume diffusion was decisive mechanism of densification.

Analogously to these results, several authors (13,15) found a worse sintering in excess of Al_2O_3 within the solubility range. Parallel to this, a discontinous grain growth was also observed. Bakker and Lindsay (12) attribute this phenomenon to the inhibition of O^{2-} - diffusion. Bailey and Russel (15) note that high densities and small sizes are obtained as soon as Al_2O_3 appears as a second phase. An excess of MgO leads to an increase in sinter density with small final grains (11), even grains of periclase are observed as a second phase at the boundaries of the spinel (16).

Thermal expansion of $MgAl_2O_4$ has been investigated by many authors. Complete survey about this is given in (20).

Conduction of Experiments

To produce pure and reactive $MgAl_2O_4$ spinel, hydroxide coprecipitation method was used. The starting materials were aqueous solutions of Merck reagent grade, $MgCl_2 \cdot 6H_2O$ and $AlCl_3 \cdot 6H_2O$. pH at the coprecipitation was 9. During the coprecipitation we obtained highly dispersed precipitate which was practically unfilterable. The removal of the chloride ions from the precipitate was made by washing in the centrifuge. Drying of the coprecipitated magnesium and aluminium hydroxides was in air at 105°C.

Calcination temperatures were fixed after previous TG and x-ray examination of the mixtures and determination of the decomposition temperature. The production of the spinel started around 600°C.

In our experiment spinel was obtained at 1100°C in 4 hours, which was confirmed by x-ray analysis, Fig.1.
Sintering was carried out in a dilatometer Netzsch. The samples were rods (25x5x5 mm). To investigate sintering kinetics, shrinkage

was measured isothermally up to the total time of 360 min.Sintering temperatures were 1144°C,1187°C,1224°C and 1272°C.The sintering was also examined at stepwise heating over the temperature range of 1060 - 1400°C,with an isothermal part of 60 min.

The bulk linear thermal expansion was measured by dilatometer Netzsch using sapphire (NBS) as a standard.The samples were tested heating them from room temperature to 1300°C and cooling back to the room temperature,in air atmosphere.The measurements were performed in stepwise heating and cooling,using time of 3 hours at T = const. and heating rate of 2 K min^{-1} in the dynamic part of the thermal treatment.

Results and Discussion

Figure 1. shows the x-ray interferences of the product-spinel.

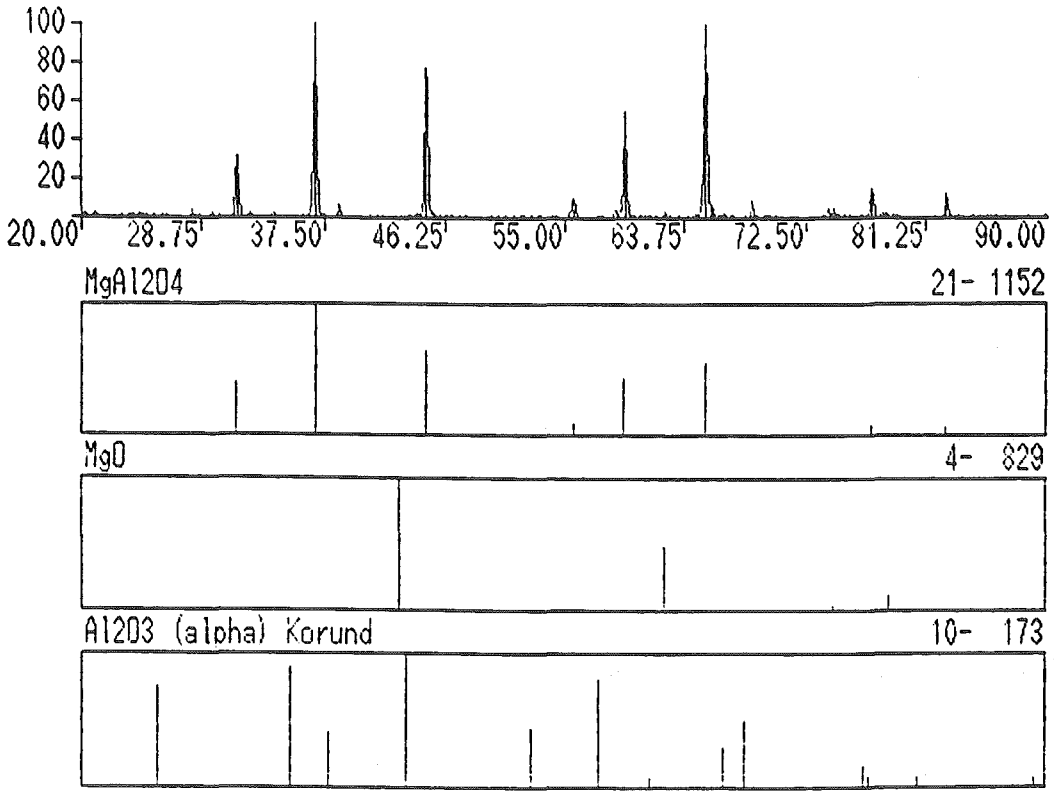

Fig.1. X-ray interferences of the product-spinel and ASTM data of $MgAl_2O_4$,MgO and Al_2O_3

Obtained spinel (more than 98% $MgAl_2O_4$) has an average particle size of 15 μm and specific surface area of 11 000 cm^2/g.

Sintering Kinetics

Shrinkage isotherms of $MgAl_2O_4$ compacts (grain density 50% TD) are shown in Figure 2.

The initial hot length (L_o) was the cold length corrected for the thermal expansion to the sintering temperature.It can be seen that the shrinkage rate increases with an increase in the sintering temperature.

Figure 3. shows the log-log plot of shrinkage Vs. time.The points lie on the straight line.Some deviations has been observed after the prolonged soaking at higher temperatures.

The log-log plot of shrinkage Vs. time indicates the slope of about $0,5 \pm 0,02$ at all sintering temperatures and therefore the volume diffusion is predominant diffusion mechanism in $MgAl_2O_4$ compacts sintering.

In general form,the diffusion shrinkage equation for the initial sintering of compacts composed of spherical particles at volume diffusion (17) is:

$$\frac{\Delta L}{L_o} = \left(\frac{2\gamma a^3 D_v}{K T r^3}\right)^{0,5} t^{0,5} \qquad /3/$$

where, t is the time; T is absolute temperature; K is Boltzman constant; γ is the surface energy; a^3 is the vacancy volume ; D_v is the diffusion coefficient.

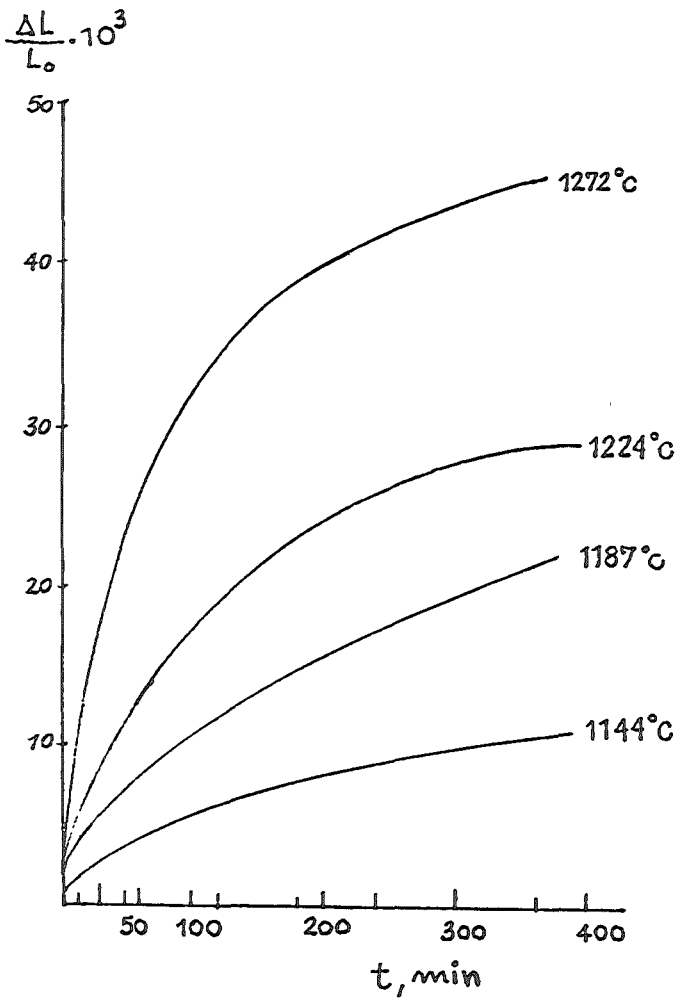

Fig.2. Shrinkage isotherms of $MgAl_2O_4$ compacts

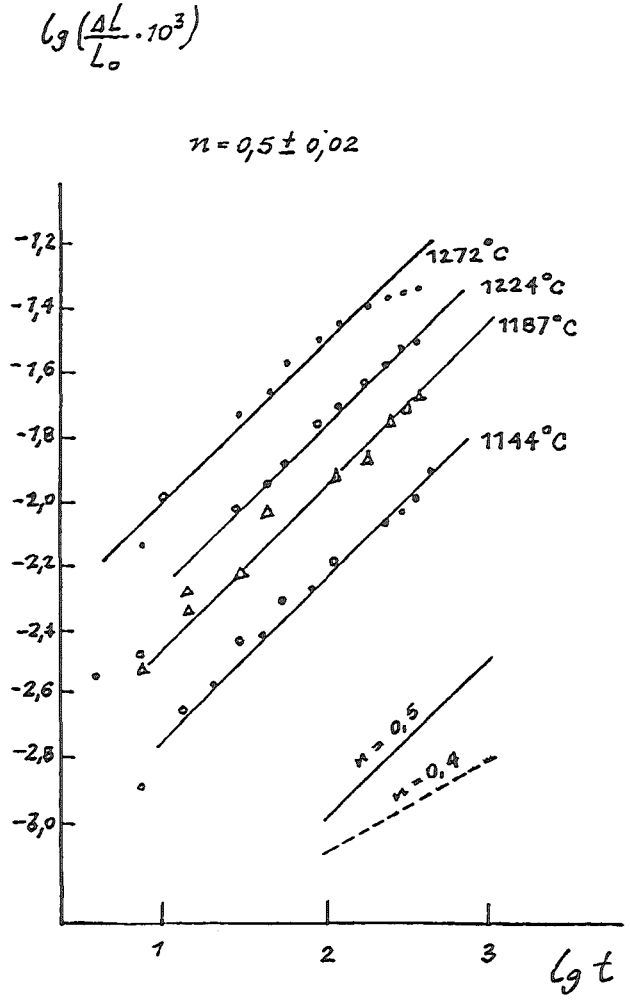

Fig.3.Log-log plot of shrinkage Vs. time

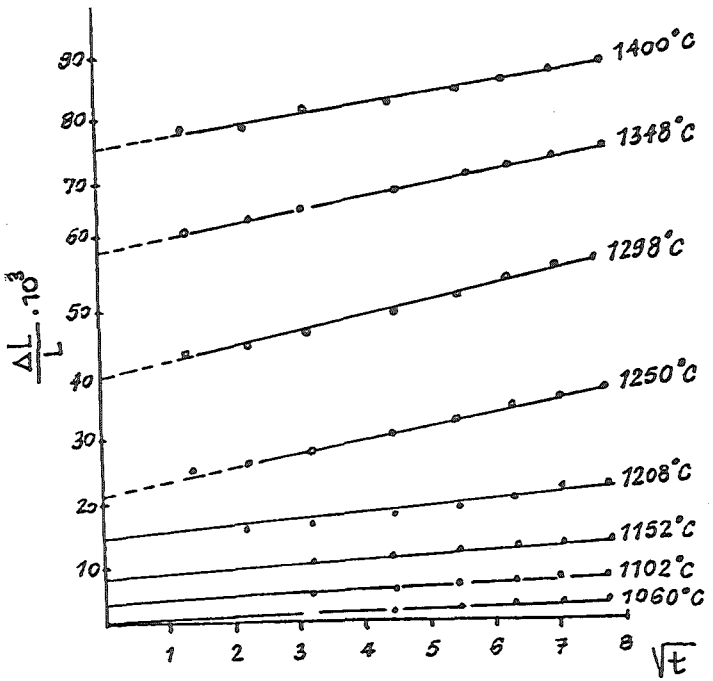

Fig.6. Linear shrinkage of $MgAl_2O_4$ in dependence of $\sqrt{t}$

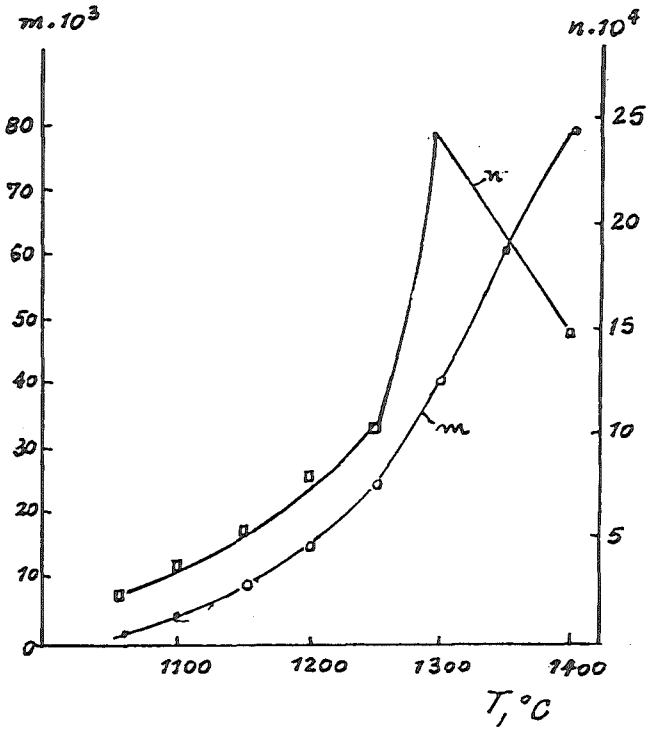

Fig.7. Change of parameters m and n in the temperature range 1060-1400°C

According to Pines and Geguzin (19) sintering kinetics at stepwise heating could be described by the following equation:

$$\Delta L/L_0 = m(T) + n(T)\sqrt{t} \qquad /4/$$

where,m is the constant of the process; n is the shrinkage rate of a single isotherm; t is the time.

In Figure 6. the linear shrinkage of $MgAl_2O_4$ in dependence of $\sqrt{t}$ is shown.

From Fig.6. the constant m and the value of n were estimated.The temperature variation in the constant m and n is shown in Fig.7.

The parameters m and n are functions of the temperature and the time of the isothermal heating.The parameter m (in fact,this is a shrinkage at the beginning of a particular isothermal step) shows a monotonous increase with a rise in the temperature,while the temperature dependence of the parameter n could be expressed by a function having a strongly pointed maximum which is in connection with the temperature range characterized by the biggest qualitative change in the material structure.The maximum on the curve could be a consecuitive effect of the change in the material structure as a result of the anihalation of the most part of deffects existing in the dispers system or,of the change in the number of pores.In order to find out whether the maximal shrinkage rate is a consequence of the material structure change since the powder activity changed, to experiment with samples of different porosity rises as a necessity. If completely the same temperature range in which the maximal change of shrinkage rate happens is registrated then,this is a proof that the maximal shrinkage rate is an effect of the change in the material structure.

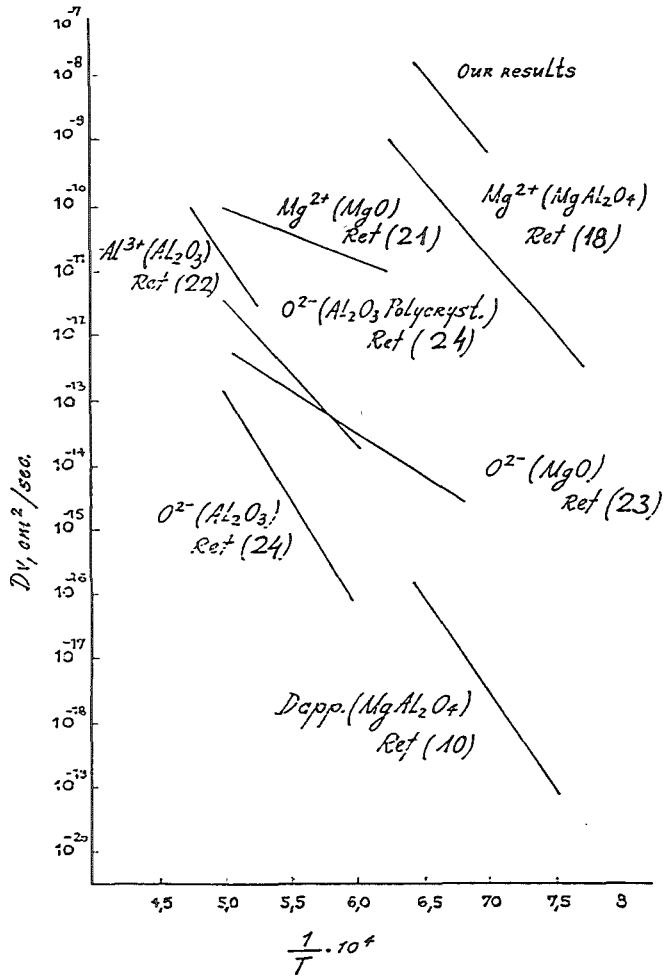

Fig.4. Temperature dependence of diffusion coefficients

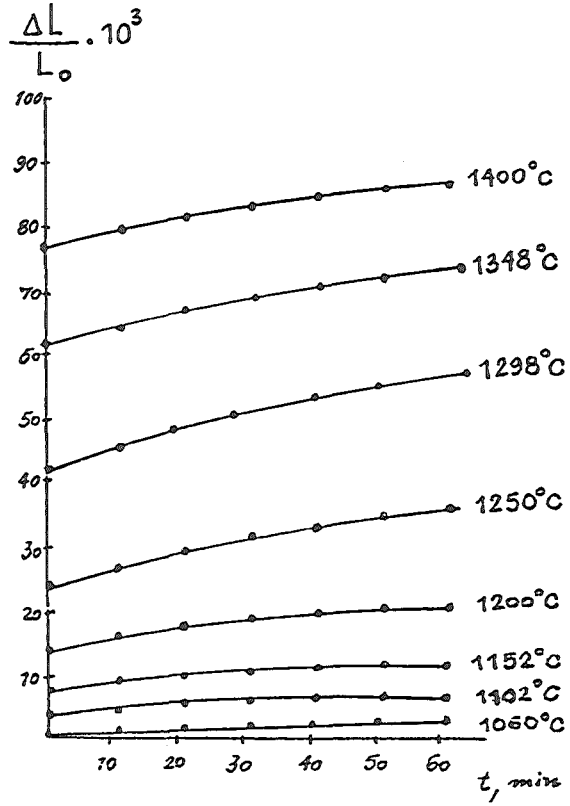

Fig.5. Linear shrinkage at stepwise heating

Apparent diffusion coefficient has been calculated from shrinkage equation. The value of surface energy has been taken to be 10^3 erg/cm^2 (10). Volume diffusion species (a^3) has been calculated from the formula:

$$a^3 = 1/3 \frac{(\text{molecular weight})}{(\text{density})} \cdot 1/N$$

where, value of $N = 2{,}93 \cdot 10^{-23}$ cm^3 .

The particle size is taken to be 15 μm.
The apparent diffusion coefficient has been calculated from the initial part of the curve where straight line realationship is followed. Calculated values are presented in Table II.

Table II. Diffusion coefficient at different temperatures

T, °C	diffusion coefficient, cm^2/s	activation energy, KJ/mol
1144	$8{,}17 \cdot 10^{-10}$	
1187	$3{,}07 \cdot 10^{-9}$	380
1224	$7{,}30 \cdot 10^{-9}$	
1272	$2{,}66 \cdot 10^{-8}$	

In Figure 4. the self-diffusion of ions in MgO, Al_2O_3 and $MgAl_2O_4$ are shown. The activation energy found in this study is 380 KJ/mol and energy of activation required for Mg^{2+} ion diffusion in $MgAl_2O_4$ is about 360 KJ/mol (18).

It seems that Mg^{2+} ions are the rate controlling species during the initial sintering of $MgAl_2O_4$.

The sintering kinetics of $MgAl_2O_4$ was also examined at stepwise heating in the temperature range of 1060 - 1400°C, with an isothermal part of 60 min. The shrinkage of the $MgAl_2O_4$ at stepwise heatup regime is shown in Figure 5.

Thermal Expansion of $MgAl_2O_4$

The conditions for the dilatometric determination of the thermal expansion of $MgAl_2O_4$ are as follows:

1. Calibration using the standard reference material-sapphire NBS
2. Stepwise heating and cooling
3. Data only at T=const.
4. Reproducibility within the true resolution of the instrument ($\pm$ 5 μm)
5. Baseline (expansion at room temperature) must be equal on heating and cooling with $\pm$ 5 μm.

The linear thermal expansion of $MgAl_2O_4$ in the temperature range of RT - 1300°C is shown in Figure 8.

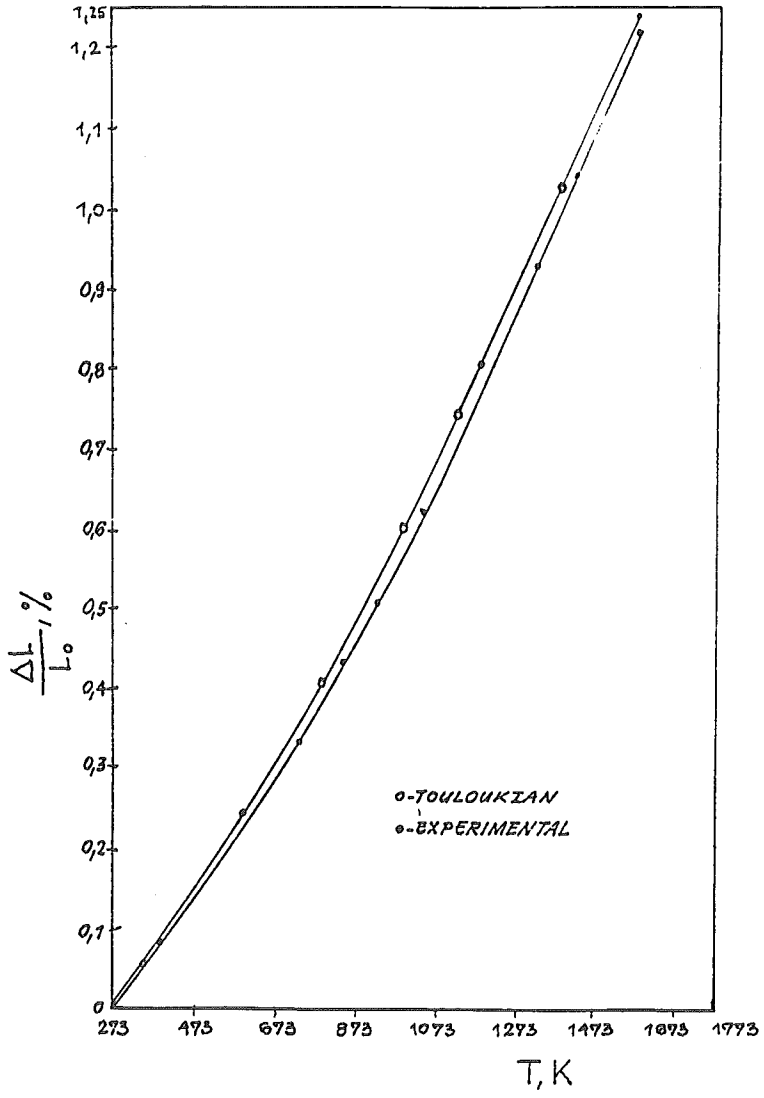

Fig.8. Linear thermal expansion of $MgAl_2O_4$

The third order polynomial, obtained using the method of the least squares, was fitted to the thermal expansion data:

$$\Delta L/L_o = -0,33 + 8,50 \cdot 10^{-4}\ T + 2,45 \cdot 10^{-8}\ T^2 + 3,39 \cdot 10^{-11} T^3 \quad /5/$$

where, $\Delta L/L_o$ (=) % ; T(=)K.

Coefficient of correlation is 0,998.

The coefficient of thermal expansion can be presented by the form obtained differentiating the equation /5/:

$$\alpha = 8,50 \cdot 10^{-6} + 4,90 \cdot 10^{-10} T + 1,11 \cdot 10^{-12} T^2 \quad /6/$$

On heating and cooling in the mentioned temperature region, the linear thermal expansion does not exibit any evidence of hysteresis.

Comparing our results with those recommended by Touloukian (20), accordance is very good.

REFERENCES

1. J.Debsikdar, Preparation of transparent non-crystalline stoichiometric magnesium aluminate gel-monolith by sol-gel process, J.Mat.Sci., 20, 4464 (1985)
2. G.G.Galimov, N.A.Berg, I.N.Zhitkova, I.A.Lenteva, N.F.Seliverstov, and L.M.Stepanova, Preparation of $MgAl_2O_4$ from sodium aluminate solutions and magnezium salts, Izvestiya Akademii Nauk SSSR, Neorganicheskie Materialy, 22(4)640 (1986)
3. D.O.Mc Creight and R.E.Birch, "Synthetic Spinel Refractory Products", U.S.Pat.No.2.805 167, September 1957
4. H.Dislich, Angew.Chem.(Int.End.Engl.) 10,363 (1971)
5. V.A.Dzisko, A.S.Ivanova, L.M.Plyasova and S.V.Ketchik, Chemical and phase composition and surface of an aluminium-magnesium system, Izvestiya Akademii Nauk SSSR, Ser.Khim.No.5,983 (1978)
6. S.G.Mukherjee and B.N.Samaddar, Spinel Formation from Co-precipitated hydroxides of aluminium and magnesium , Trans.Indian. Ceram.Soc. 25,33 (1968)
7. A.I.Vogel, A text book of qualitative inorganic analysis, the English Language book society and Longmans Green and Co, 3 rd edition, pp.440, 1962

8. V.A.Sokol,D.A.Bokolenko,L.I.Kononova and A.V.Bromberg,Izvestiya Akademii Nauk SSSR,Neorganicheskie Materialy,Vol.17,No.5,896 (1981)

9. J.R.Bratton,Characterization and Sintering of Reactive $MgAl_2O_4$ Spinel,Am.Ceram.Soc.Bull.,48,1069 (1969)

10. J.R.Bratton,Initial Sintering Kinetics of $MgAl_2O_4$,J.Am.Ceram. Soc.,54,141 (1971)

11. T.J.Bailey and R.Russel Jr.,Magnesia-Rich $MgAl_2O_4$ Spinel Ceramics, Am.Ceram.Soc.Bull.,50,493 (1971)

12. T.W.Bakker and G.J.Lindsay,Reactive Magnesia Spinel.Preparation and Properties, Am.Ceram.Soc.Bull.,46,1094 (1967)

13. T.J.Bailey and R.Russel Jr.,Sintered Spinel Ceramics,Am.Ceram. Soc.Bull. 47,1025 (1968)

14. D.W.Kingery,Introduction to Ceramics,Wiley and Son.

15. T.J.Bailey and R.Russel Jr., Preparation and Properties of Dense Spinel Ceramics in the $MgAl_2O_4$ - Al_2O_3 System, Trans.Brit. Ceram.Soc.Bull.,50,493 (1971)

16. K.Hamano,T.Ohtsuka,Z.Nakogava,Sintering of Spinel (Part 2), Bull.Tokio Inst.Techn.126,141 (1975)

17. D.W.Kingery and M.Berg,Study of Initial Stages of Sintering Solids by Viscous Flow,Evaporation-Condensation and Self-diffusion, J.Appl.Phys.26(10) 1205 (1955)

18. R.Lindner and A.Akerstrom, Diffusion of Ni^{63} in Nickel Spinel, Z.Physik.Chem.(Frankfurt),18 (5-6) 303 (1958)

19. Y.Geguzin,Fizika Spekaniya,M.1967

20. Y.Touloukian.R.Kirby,R.Teylor and T.Lee,Thermophysical Properties of Matter,Vol.13,IFI Plenum,New York,1973

21. R.Lindner and C.Parfitt,Diffusion of Radioactive Magnesium in Magnesium Oxide Crystals,J.Chem.Phys.,26 (1),182 (1957)

22. A.Paladino and W.Kingery,Aluminium Ion Diffusion in Al_2O_3, J.Chem.Phys.,37 (5) 957 (1962)

23. Y.Oishi and W.Kingery, Oxigen Diffusion in Periclase Crystals, J.Chem.Phys.,33(3) 905 (1960)

24. Y.Oishi and W.Kingery,Self-Diffusion of Oxigen in Single-Crystal and Polycrystalline Aluminium Oxide,J.Chem.Phys.,33(2)480 (1960)

MICROSTRUCTURAL STUDIES ON ALUMINA-ZIRCONIA AND METALLIZED ALUMINA CERAMICS

S. Bratovic, J. Derviskadic, B. Djuricic, M. Jamakosmanovic, M. Mulalic and M. Trubelja*

"Energoinvest" - CIRM, Sarajevo
*Now with the Max-Planck-Institut für Metallforschung, Stuttgart

ABSTRACT

Two separate topics are discussed in this paper. The microstructural aspects of high-tempereture metallizing of Al_2O_3 ceramics are described first. In this context, several observations on the ceramic-to-metal interfaces are presented. They lead to a broad conclusion about the bonding mechanism between alumina and the metallizing layer. In the second part, initial results on microstructural and phase analyses of Al_2O_3-ZrO_2 composites are presented. These results indicate that an "optimum" microstructure was achieved in the Al_2O_3-15 vol.% ZrO_2 composite. However, it was concluded that the processing route (particularly milling) needs modification in order to obtain the expected improvements in mechanical properties and/or thermal-shock resistance of the composites.

A. HIGH-TEMPERATURE METALLIZING

1. Experimental Procedure

Samples to be metallized were prepared from various grades of Al_2O_3 powder, either by uniaxial, or isostatic pressing. Sintering was performed in laboratory furnaces, or, alternatively, in tunnel kilns, at temperatures near 1600°C, in presence of SiO_2 and MgO as sintering aids. The metallizing was done by manually applying the Mo-Mn metallizing paint using a brush. The

organic part of the paint was baked-off and the metallic layer sintered at temperatures near 1400°C. In this case, wet protective atmosphere of cracked ammonia was used.

The characterization of the ceramic-to-metal interface was done on an SEM, with an EDS analyzer attached. The samples for electron microscopy were prepared by cutting the pieces of metallized ceramics using a diamond saw. Samples were subsequently polished to a 1 μm finish using the SiC grinding paper and diamond pastes. Finally, a discharging layer of gold and/or graphite (~300-400 Å thick) was applied to the samples prior to their viewing in the SEM.

The quantitative EDS analysis was performed with a main purpose of investigating the role of the glassy phase in the bonding mechanism between the metallic layer and the ceramic.

2. Results and Discussion

A typical microstructure of a metallized ceramic sample is shown in Fig. 1. Three layers can be distinguished in this microstructure. The dark gray phase in the upper portion of Fig. 1 is the Al_2O_3 ceramic substrate. The light-gray phase adhering to the ceramic is the Mo-Mn metallic layer. The 3-5 μm thick layer of Ni is also apparent in the lower portion of Fig. 1. This layer is essential if subsequent welding of the metallized ceramic to various metallic components is performed.

The most important result of this work is the development of a homogeneous, 10-15 μm thick metallizing layer. This layer consists of sintered metallic grains of the size 2-3 μm. Porosity between the grains is filled with the glassy phase. This microstructure is favorable since tight ceramic-to-metal seals are obtained only if the metallizing layer consists of a dense metal/glass composite.[1]

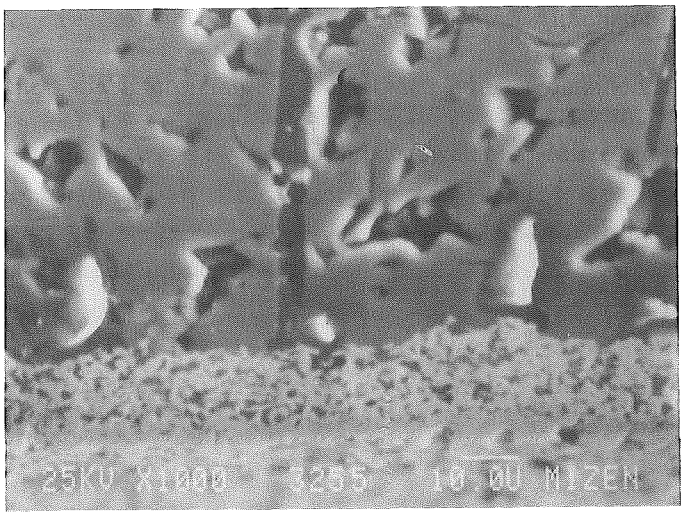

Fig. 1. The microstructure of a metallized Al_2O_3 ceramic

Qualitative EDS analysis showed that the metallic phase in the metallizing layer consisted only of molybdenum. On the other hand, manganese was found to segregate and dissolve in the glassy phase.

The role of manganese in the metallizing process had long been a subject of controversy. In fact, it was empirically found that a small amount of manganese in molybdenum paints improved the bond strength.[1-4] Thermodynamic data and experimental observations[2] indicate that under typical metallizing conditions MnO_2 and Mn transform to MnO, which can react with Al_2O_3 to form a manganese spinel ($MnAl_2O_4$). Certain authors[3] state that spinel ensures the adhesion between the metallizing layer and ceramic, but they neglect the glassy phase migration. However, subsequent studies[1,4] have shown that manganese is soluble in the glassy phase and also can penetrate deep into the ceramic. According to the EDS analysis of Si and Mn, the latter is true in our case. The manganese distribution was found to precisely follow the distribution of Si, thus suggesting the dissolution of manganese in the glassy phase.

3. Conclusions and Further Work

A homogeneous metallizing layer consisting of a metal/glass composite was developed on Al_2O_3 ceramics. This type of microstructure is favorable for the intended application of the metallized Al_2O_3 ceramics in vacuum technology, as it ensures optimum bond strengths of ceramic-to-metal seals. Bearing in mind the stringent conditions in which the metallized ceramics are to be used, vacuum tightness tests and quantitative bond evaluation are currently underway. However, at this point it is already possible to conclude that the mechanism of bonding between the ceramic and the metallizing layer is related to the capillary migration of the glassy phase, as indicated by the distribution of manganese found by EDS.

B. ALUMINA-ZIRCONIA COMPOSITES

1. Experimental Procedure

Mixtures of Al_2O_3 and t-ZrO_2 containing 5-25 vol.% ZrO_2 were ball-milled in alcohol for 4 h, dried, and pressed uniaxially at 340 MPa, using PVA as a binder. Samples were then calcined at 600°C for 2.5 h to remove the organics, and sintered in a resistance-heated Mo-laboratory furnace for 4 h at 1600°C.

The samples were characterized by SEM and x-ray diffraction. The SEM specimens were prepared in a manner similar to that described in part A. However, they were also thermally etched at 1400°C for 20 min to reveal the grain-boundary structure.

The qualitative x-ray analysis was performed on ϕ12x2 mm disc-shaped specimens. They were made thin for easier positioning into the focus of an x-ray beam. A diffractometer with Cu-K-alpha radiation was used for the analysis. The amount of m-ZrO_2 was approximated from the heights of the $(100)_t$, $(11\bar{1})_m$ and $(111)_m$ peaks.

2. Results

Theoretical densities of the samples were calculated on the basis of the starting materials densities given by the manufacturers, and the proportion of each individual powder in the mixtures. Sintered densities were measured by the Archimedes method and were found to be in the range 96-98% of the theoretical. However, these values have to be regarded as tentative, since m-ZrO_2 was present in all sintered samples.

Generally speaking, by comparison of microstructures developed in samples with varying concentrations of ZrO_2, it was observed that ZrO_2 inclusions inhibited grain growth of Al_2O_3. In terms of the homogeneity of the second-phase dispersion and the retention of t-ZrO_2 (> 90% as found by x-ray diffraction), the optimum microstructure was developed in the sample containing 15 vol.% ZrO_2 (Fig. 2). In this case a uniform grain size distribution of Al_2O_3 was observed, with a mean particle size of about

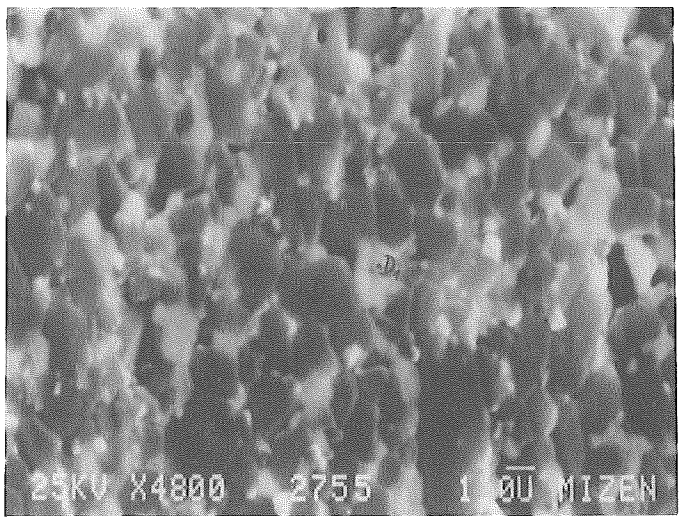

Fig. 2. The microstructure of an Al_2O_3-15 vol.% ZrO_2 composite.

4 μm. The ZrO_2 grains were predominantly of sub-micron sizes, with a mean of about 0.3 μm. However, there was still some ZrO_2

grain coalescence, leading to a significant presence of m-ZrO_2. In addition, some exaggarated grain growth of Al_2O_3 did occur in this case, preventing a more homogeneous dispersion of ZrO_2.

3. Conclusion

A comparatively favorable microstructure and phase composition were obtained in the Al_2O_3-15 vol.% ZrO_2 composite. However, an optimization of the processing route, particularly the milling and homogenization of the starting mixtures, requires further investigation. Only then the measurements of mechanical properties and/or thermal-shock resistance may be expected to yield significant results.

ACKNOWLEDGEMENTS

This work was financially supported by the Research Foundation of "Energoinvest" - Sarajevo. The authors are grateful to the co-workers at the Spark-Plug Factory in Tesanj for providing the use of processing facilities. They also wish to thank M. Trifunovic and F. Tabak for the assistance with the SEM. In addition, the help of M. Sljukic with x-ray diffraction is gratefully acknowledged.

REFERENCES

1. Twentyman, M. E.: J. Mat. Sci. 10, 765 (1975).
2. Cole, S. S. and G. Sommer: J. Am. Ceram. Soc. 44, 265 (1961).
3. Helgesson, C. I.: "Ceramics to Metal Bonding," Boston 1968.
4. Floyd, J. R.: Am. Ceram. Soc. Bull. 42, 65 (1963).

METALLIC LAYERS

ELECTRODEPOSITION OF METALS AND METAL OXIDES FROM MOLTEN SALTS

Branko Popov

Faculty of Technology and Metallurgy, University"Kiril and Metodij", Skopje, YU

INTRODUCTION

The use of molten salts as solvents provide media in which valuable information can be gained concerning high temperature chemical and electrochemical reactions. With increasing difficulty one can distinguish a number of general types of molten salts , according to the following classification:

- Simple ionic salt melts. These are , to a good approximation, completely ionic, with spherically symmetrical anions and cations(1).
- Oxyanionic melts. These have relatively low melting points, still remaining essentially ionic , but while responding reasonably well to modelling , require greater attention to polarization forces and other factors assosciated with deformable anion (2).
- Polymeric or network melts. These melts are stable viscous in which the extent of polymerization is determining their properties (3).
- Molecular melts. These are covalent liquides which exhibit limited self dissociation(4).
- Aqueous melts . These melt at very low temperatures, to form viscous, ionic liquids that need to be handled under controlled water vapor pressure(5).

Of special interest are the alkali halide melts because they offer to the experimentalist a medium for observing many phenomena which are inaccessible or unknown in other solvents. Some properties associated with this molten salt include : good electrochemical stability , good thermal stability , good heat transfer properties , high heat capacity , rapid chemical and electrochemical reaction rates and good solvent properties.These solvents are also excellent conductors of electricity since they consist essentially of highly dissociated ionic species.

From the electrochemical standpoint , the eutectic lithium chloride - potassium chloride is especially useful as a solvent due to its large range of stability towards oxidizing and reducing agents.

The large decomposition voltages and excellent conductivities of molten chlorides combined with the high temperature which cause many electrode reactions that are irreversible in other solvents to behave reversibly in these melts, encourages their widespread use in electrochemical studies.

PREPARATION AND PURIFICATION OF LiCl-KCl EUTECTIC MELT

The important disadvantages in using an LiCl-KCl eutectic melt is the difficulty in preparing a pure solvents. Because of the high sensitivity of electrochemical methods to low concentrations of reducible and oxidizable impurities, the standards of purity are quite high. The best commercial reagent grade salts are quite inadequate without further purification. A good purification method has been outlined by Laitinen , Tischer and Roe (6).

REFERENCE ELECTRODES

In chloride melts , the gas/gas ion electrode , Cl_2/Cl^- is the best primary reference electrode. Among the secondary reference half-cells wich have been employed in work on LiCl-KCl eutecti melt , the Pt/Pt(II) system has proved most popular, although the Ag/Ag(I) is also useful in higher-melting media(7). Pt/PtII) reference electrodes , are stable and reproducible in the eutectic melt above 725^{o}K.

ELECTROCHEMICAL METHODS USED IN MOLTEN SALTS

Electroanalytical techniques, similar to those employed in aqueous solutions can be adapted for use in molten salts to provide data on mechanistic analysis and product identification. Chronopotentiometry and linear sweep voltammetry are applied in molten salts in order to asses the general characteristics of the electrode process in melts. Using these methods one can determine : the slow step in the overall charge transfer process, the solution species which give rise to any well defined product follwing charge transfer, the predeposition of alkali metal or alkaline earth metal, the adsorption or chemical processes coupled with the main charge transfer step as well as to answer to preliminary question as - does the charge transfer occur in single or separately successive stages?

Polarography, cyclic potential step voltammetry and rotating disk methods have been also used in molten salt work. The experimental simplicity of chronopotentiometry still make it a first-choice electroanalytical technique for higher-temperature molten systems. Furthermore, in the current reversal mode , it is of only a few diagnostic techniques for assessing the classical reversibility of an electrode process.

KINETICS AND MECHANISMS OF ELECTRODE REACTIONS

Many electrode reactions in molten salts are purely diffusion controlled. In LiCl-KCl eutectic melt migration of solute ions is absent and mass transfer will generally proceed, according to linear diffusion. At very high temperature ,convective transport may become important.

Electrode reactions at solid metal electrodes may be divided into those processes which exhibit solution chemical reaction complications and those which do not exhibit such complications. Irreversibility in cathodic reactions can often arise from slow chemical process preceeding the slow charge transfer.

APPLICATIONS

Molten systems are of increasing importance as reaction media in a variety of technological applications, notably the manifacture of glasses and the electrowinning and electrorefining of metals.It is well known that only a few metals may be deposited in pure form at 100 % current efficiency from aqueous solution, partly because of the hydrogen evolution reaction. The disadvantages occuring in the deposition of metals from aqueous solutions are : hydride formation, oxide film formation , oxide deposition from stable oxidations as well as chemical reduction and oxidation reactions with the solvent water. These processes impede the primary electrodeposition of purely metal from aqueous media. Molten salts, on the other side are nonaqueous media for metal deposition which have distinct advantages such as : relatively small cathodic deposition overvoltages, good solvent properties , especially for oxide ores, high ionic conductivity as well as electrochemical stability.

An important disadvantage for using molten salts for electroplating is the the frequent mass-transfer controlled rate as well as the fact that many refractory container materials dissolve in the solvent media during the electrodeposition. Attempts to deposit refractory metals in a coherent , massive form do not give satisfactory results. Deposits may be dendritic if the electrodeposition proceeds under mass transfer controlled conditions or may be powdery if secondary reaction such as alkali metal deposition followed by back reaction with the eutectic melts occurs.

All the group IA and IIA metals may be extracted , either directly or indirectly by means of molten salt electrolysis. Many important refractory and other transition metals , the lantinides and some actinides extracted through molten salts are recovered as solids. Deposits have been obtained for most the group IVA, VA, and VIA metals in the Union Carbide electroforming process with fluoride melt.

DISCUSSION

Although there have been extensive electrochemical investigations of metal ions and metal ion complexes (8-14), the metal chlorides have not been the subject of complete thermodynamical and electrochemical investigations at elevated temperatures. There have also been only a few fundamental electrochemical studies of oxyanions in molten salts. From previous studies it is known that the electrochemical reduction of oxygeneted species in fused salts leads to the formation of an insoluble electrode deposit. The nature of this deposit is frequently assumed to be a particular compound as indicated by measuring fundamental electrochemical parameters.

Our research activities in this field are connected with the electrochemical deposition of molybdenum , indium and titanium as well as studies of complex systems involving chemical and electrochemical relatioships such as; electrochemical reduction of chromate in the presence of nickel chloride , study of the electrochemistry of molybdenum (VI) compounds in a lithium chloride-potassium chloride melt as well as studies of metal-oxychlorides in the eutecti melt.

Purpose of this research was to determine the deposition parameters of molybdenum indium and titanium in molten solutes , the slow step in the overall charge transfer process, the solution species which give rise to any defined product following charge transfer and to determine the kinetics of the charge transfer. Molybdenum (VI) and chromium(VI) compounds were studied in order to characterize the reduction product. It was also considered possible that some interesting aspects of molybdenum chemistry and interactions between molybdenum (VI), chromium (VI) compounds and chloride melt could be deduced.

The knowledge gained through such studies will contribute to the overall understanding of depostion of metals and metal oxides from molten salts and should aid the interpretation of thermal battery processes as well.

ELECTROCHEMICAL DEPOSITION OF MOLYBDENUM

One chronopotentiometric wave is observed for the electrochemical reduction of K_3MoCl_6 with quarter wave potential at -0.6 V vs. the Pt/Pt(II) reference electrode, Fig.(1). The elctrode process is diffusion controlled over the time interval investigated. The diffusion coefficient for the electroactive species in LiCl-KCl eutectic melt was estimated to be 1.45×10^{-5} cm^2 s^{-1}. Only one product was observed for the reduction of Mo(III) at -0.6 V. The product was analysed using standard procedures , and it was found to be a pure molybdenum. A small transition time is noted at potentials -0.45 V anodic to the main reduction wave Fig(2). Chronopotentriometric measurements indicated that the most positive redution step is not diffusion controlled. The monolayer charges (Q_m) are independent on both the current density and the concentration of the electroactive species, which precludes the possibility for the existence of an equilibrium between the species in the melt. The transition time in Fig.(2) was taken between the potential limits from -0.15 V to -0.45 V in order to exclude the oxidation of platinum working electrode and the deposition of molybdenum in bulk. The results were unexpected: a significant cathodic current was not expected till below -0.6 V vs the Pt(PT(II) resference electrode. Such transitions cannot arise from impurities. This is confirmed by the independence of the transition times upon the degree of melt purification. Also several chronopotentiograms of the melt were obtained before adding Mo(III) into a fritted compartment and no wave was observed at applied current densities. So it seems platinum electrode adsorb at undervoltage quantities of molybdenum. (Q_m) values were calculated without taking surface roughness effects into consideration and they compare reasonably with the (Q_m) value of 613 C/cm calculated on the assumption of a close packed layer.

Using the slope and intercept from Delahay-Berzins equation, the values of n_a and $k^o_{f,h}$ were calculated to be 0.6 abd 3.45×10^{-4} cm s^{-1}.

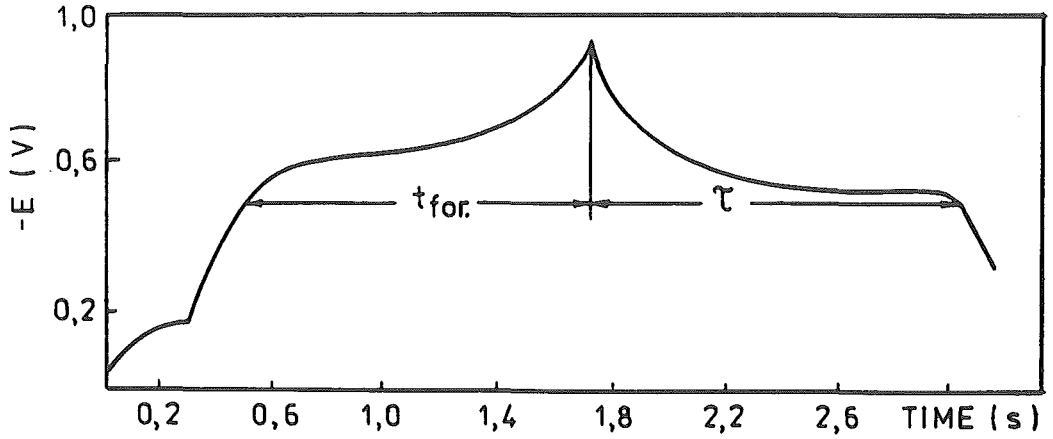

Fig. (1) Typical resverse current chronopotentiogram for the reduction step of molybdenum(III) $I_f=I_r$ = $7x10^{-3}$ A cm^{-2}. C(MoIII) = $1.45x10^{-2}$(M).

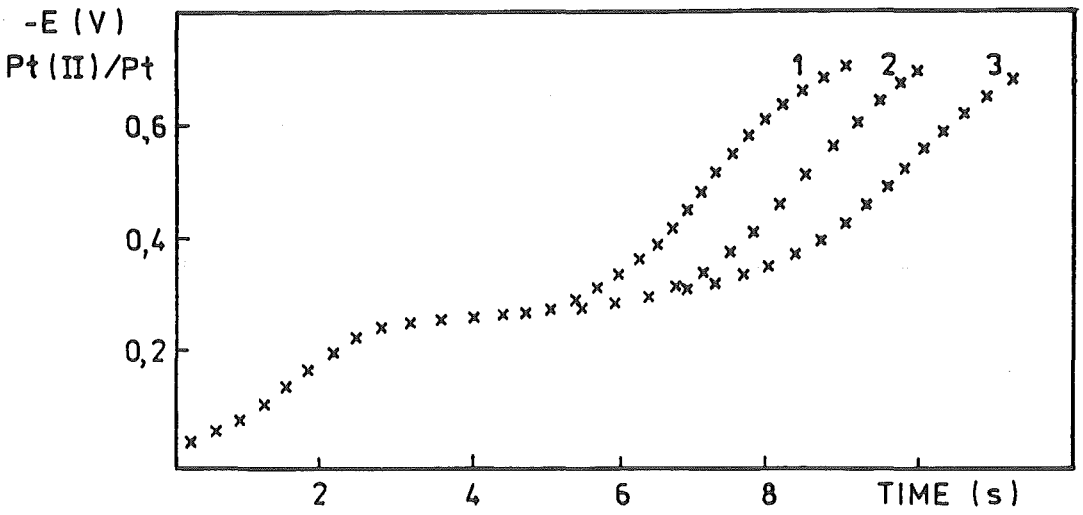

Fig. (2) Chronopotentiogram of Mo(III) predeposition step
Current density : 1). 0.180 mA/cm^2
2). 0.150
3). 0.110
Concentration of Mo(III) = 2.3 x 10^{-2}M.

In the presence of the oxygen in the melt, it has been obtained a brown-violet deposits with a layer of molybdenum crystals over it. In order to obtained a suitable samples for X-ray work , the product was boiled in distilled water and dried. The diffraction pattern of the deposit compares favorably to the ASTM patern of MoO_2 mixed with a metallic molybdenum.

ELECTROCHEMICAL REDUCTION OF INDIUM(III) IN MOLTEN LITHIUM CHLORIDE-POTASSIUM CHLORIDE EUTECTIC

The dependence of indium electrode potential vs. log. concentration of indium (III) is linear and the slopes determined are comparable with the slopes calculated from the Nernst equation, Fig(3), assuming n=3. The work is concerned with thermodynamic properties of indium (III) chloride as well as with reduction of indium (III) compounds in molten LiCl-KCl eutectic. This investigation was made with cells of the type $In/InCl_3$, LiCl-KCl//LiCl-KCl,$PtCl_2$/Pt. Partial thermodynamic values were determined from 693 K to 8000 K in the concentration range of 0.016 to 0.5 M. Indium (III) ions were therefore unimportant carrier of the current, and liquid junction potentials were consequently negligible.

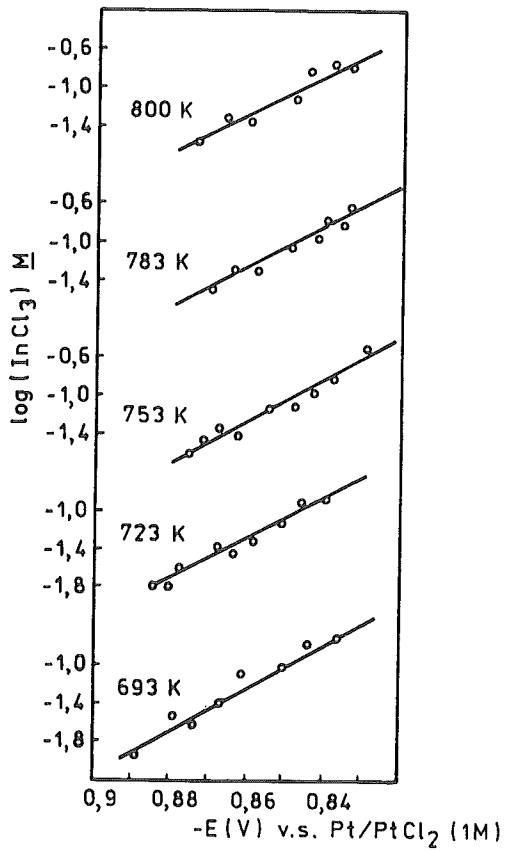

Fig.(3). Potentials of indium electrodes with respect to the platinum reference electrode as a function of the concentration of In(III)..

The potential of In/In(III) has been determined to be -0.85 ± 0.003 V with respect to the Pt(II)/Pt (1M). At 693 K the free energy of formation of the indium(III) chloride in a 1 m solution is-325,398 ± 500 J / mol.

A single chronopotentiometric wave is observed for the reduction of $InCl_3$ at -0.81 V vs the Pt(II)/Pt reference electrode. Based on analytical data n= 3, the diffusion coefficient was calculated to be 1.81 x 10^{-5} cm^2 s^{-1}. The value of αn_a and $k^o_{f,\,h}$ were calculated to be 0.6 and 3.25 x 10^{-3} cm s^{-1}.

Chronopotentiometry showed one step for the reduction of In_2O_3 The quarter wave potential was found to be -0.7 V vs the Pt(II)/Pt reference electrode. The reduction was found not to be diffusion controlled process over the time interval investigated. It was shown that In_2O_3 is not stable in the melt and enters in an acid-base reaction with the chloride melt.In order to interpret the electrochemistry of $InCl_3$, information is needed on the chemical composition of the electrode deposit when $InCl_3$ is reduced and the current efficiency with which it is produced. Samples of electrode deposit were prepared by constant current electrolysis using low current densities. The electrode was monitored during electrolysis and it was never more negative than -0.8 V. The electrode deposit was found dispersed into the melt , because indium is a liquid at temperatures at which the experiments were performed. The reduction product was analysed by standard procedures and was shown to be pure indium.

ELECTROCHEMICAL REDUCTION OF CHROMATE IN THE PRESENCE OF NICKEL CHLORIDE IN MOLTEN LITHIUM CHLORIDE -POTASSIUM CHLORIDE EUTECTIC

The reduction of K_2CrO_4 in the presence of $NiCl_2$ in fused lithium chloride - potassium chloride eutectic was found to involve 3 electrons and was diffusion controlled over concentration range and current densities studied.

In the presence of excess $NiCl_2$, chromate is reduced at -0.35 V , Fig.(4), vesus Pt(II)/Pt resulting in the formation of a green insoluble product which adheres strongly to the surface to the electrode. The stoichiometry of the reduction product was found to depend mainly upon the temperature at which the deposit is formed and slightly upon such parameters as the molar ratio of Ni to Cr and applied current density. At 500°C , the deposit approaches the composition $LiNi_2CrO_4$, Table (1).

T a b l e (1)

Composition of electrode deposit as function of temperature

$C_{K_2CrO_4}$ = 0.052 M					C_{NiCl_2} = 0.198 M
Temperature (°K)	Wt % Li_2O	Wt% NiO	Wt % Cr_2O_3	Total %	Formula
673	3.75	66.8	31.90	102.0	$Li_{0.60}Ni_{2.10}CrO_{3.91}$
723	4.09	64.5	30.60	99.2	$Li_{0.68}Ni_{2.12}CrO_{3.96}$
773	5.10	64.o	31.90	101.o	$Li_{0.83}Ni_{2.08}CrO_{3.96}$

Although Ni(II) is known to form a stable chlorocomplex $NiCl_4^=$ in chloride melts no chloride was found in the electrode deposit. The absence of chloride in the deposit requires that the nickel chloride complex dissociates before the Ni(II) is incorporated into the deposit. That such a dissociation occurs rapidly enough to prevent inclusion of chloride in the deposit is remarkable in view of the high stability of $NiCl_4^=$. In spite of the fact that the reduction potential of Ni(II) lies about 0.2 V below that of chromate in the absence of divalent metal ions , no evidence for the deposition of metallic nickel was obtained.

From X-ray data the deposit was found to be a single compound with a face cenetered cubic lattice. The length of the unit cell edge was determined to be 4.141 μm, Table (2).

When the deposit was heated to 1430°C , a weight loss was observed. X-ray diffraction studies showed the presence of two phases. These phases were identified as NiO and $NiCr_2O_4$(nickel chromite). The weight loss was attributed to volatization of Li_2O.

The face centered cubic phase corresponds reasonably well to NiO (a=4.176 μm) and the diamond cubic phase to $NiCr_2O_4$ (a = 8.32 μm). No lines were observed which could be assigned to the unheated nickel compound or to pure Li_2O.

ELECTROCHEMICAL REDUCTION OF MOLYBDENUM (VI) COMPOUNDS IN MOLTEN LITHIUM CHLORIDE-POTASSIUM CHLORIDE EUTECTIC

Molybdenum (VI)oxide reacts with molten LiCl-KCl eutectic at 450°C to form MoO_2Cl_2,(18) which probably is present as an anion $MoO_2Cl_4^=$, and pyromolybdate , Mo_2O_7(19). Both of these species are electrochemically reduced to MoO_2, which can be reoxidized to MoO_2Cl_2 by current reversal , Fig(5). A second reduction step , observed whether MoO_3 or $Mo_2O_7^=$ is added to the melt, can be attributed to the reduction of $MoO_4^=$, formed as a secondary reaction product in the first step. The reduction of molybdate proceeds in two steps, the first at -0.85 V and the second at -1.75 V vs the 1M Pt(II)/Pt reference electrode.

The first step shows an abnormally short transition time , attributable to a slow equilibrium. The second step corresponds to a diffusion-controlled reduction with n = 0.5, yielding a product of the empirical formula $Li_5Mo_2O_8$.

The electrode reaction of molybdate can be writen:

$$2\ MoO_4^= + e \rightarrow Mo_2O_8^{-5} \qquad (1)$$

The mechanism of this reaction is unclear. There is no evidence for dimerization of molybdate prior to reduction , and the diffusion coefficient is consistent with our expectation for a monomer. The simplest mechanism would be the formation of the anion MoO_4^{-3}, with the incorporation of equimolar amounts of MoO_4^{2-} with lithium ions to form the crystalline compound $Li_5Mo_2O_8$.

Samples of the first reduction product, prepared coulometrically from 0.35M MoO_3 solution using a platinum gauze cathode , in the form of a homogeneous, brown violet solid, were boiled in distilled water to remove chlorides and soluble molybdates and dried at 130°C. Analysis revealed only MoO_2, and the x-ray powder pattern agreed in d-spacings and approximate relative densities with the ASTM files for MoO_2.

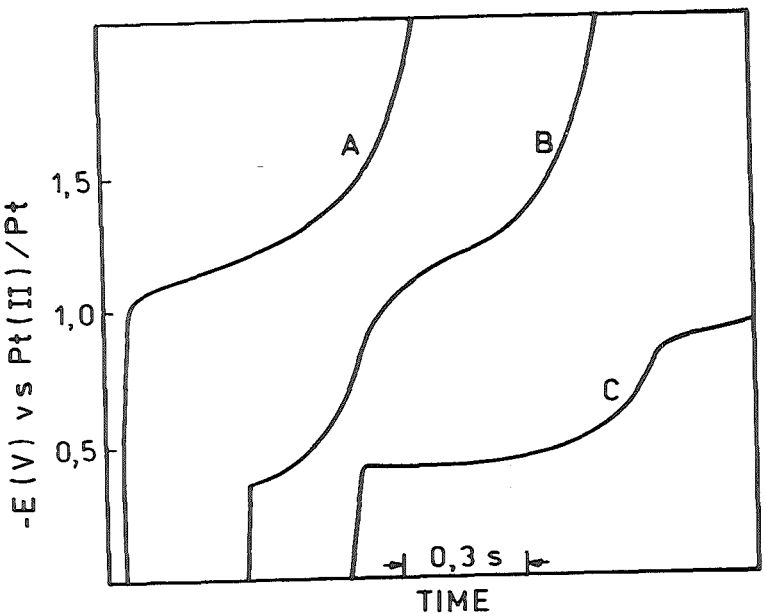

Fig.(4) Effect of nickel chloride concentration on reduction of chromate 1.56×10^{-2} M K_2CrO_4. A. No $NiCl_2$; B 7.29×10^{-3} $NiCl_2$; C. 3.28×10^{-2} M $NiCl_2$

T a b l e (2)
X-ray data for electrode deposit

d(m)	I/I_o	hkl	a(μm)
2.3840	60	111	4.129
2.0657	100	200	4.137
1.4622	60	220	4.136
1.2476	30	311	4.178
1.1957	20	222	4.1403
1.0352	10	400	4.1410

(Table (2) indicates that the deposit is a single compound with a face centered cubic latice.)

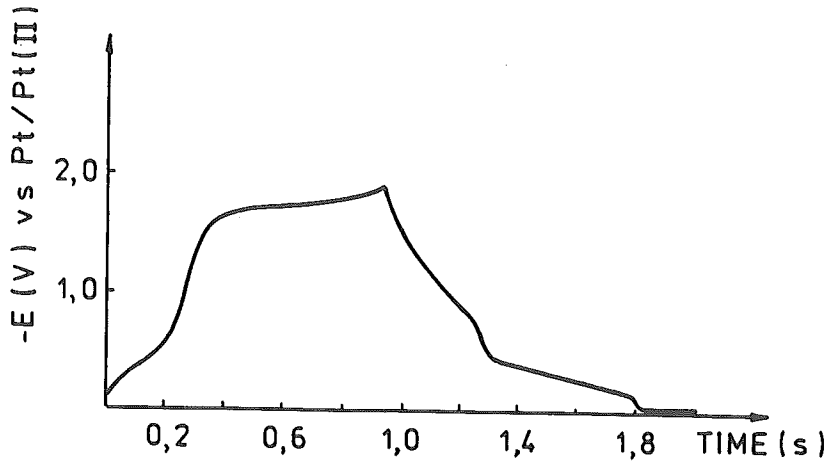

Fig.(5) Typical reverse current chronopotentiogram for the first and second reduction step of MoO_3. $I_f = Ir = 5$ mA/cm^2; $C_{MoO_3} = 3.25 \times 10^{-3}$.

Two chronopotentiometric waves were observed for the electrochemical reduction of molybdate in the presence of zinc chloride, with quarter wave potentials of -1.5 V and -1.75 V vs the Pt(II)/Pt reference electrode , respectively, Fig(6). It was observed that an increase in the molybdate concentration causes a decrease of the first transition time indicating a chemical reaction between $ZnCl_2$ (which is reduced at -1.5 V) and Li_2MoO_4 in the melt forming $ZnMoO_4$ which is sparingly dissociated in LiCl-KCl eutectic.

The equilibrium constant for the observed reaction:

$$Zn(II) + MoO_4^{2-} \rightleftharpoons ZnMoO_4 \qquad (2)$$

$$K = \frac{[ZnMoO_4]}{[Zn(II)][MoO_4^{2-}]} = \frac{X}{(C_{ZnCl_2} - X)(C_{Li_2MoO_4} - X)} \qquad (3)$$

was calculated to be k = 30. 1. X-ray powder diffraction patterns of the reduction product of $ZnMoO_4$ have been obtained. Samples of electrode deposit were prepared by constant current electrolysis. The cathode was immersed into $ZnMoO_4$ solution and attempts were made to prepare coulometrically the reduction product at -1.5 V. It was possible to monitor the electrode potential only at -1.65 V v Pt(II)/Pt reference electrode. The elctrode deposit was found to contain Li, Zn and Mo with empirical formula $Li_4Zn\,Mo_2O_8$.

From the preceding study of molybdate reduction in which the product $Li_5Mo_2O_8$ was identified (20), the simplest reduction mechanism for the formation of MoO_4^{2-} to MoO_4^{3-} , which is then incorporated into a crystal lattice with Li^+ and Zn(II), in the appropriate ratio. In the absence of Zn (II) , both MoO_4^{2-} and MoO_4^{3-} are involved in the final product.

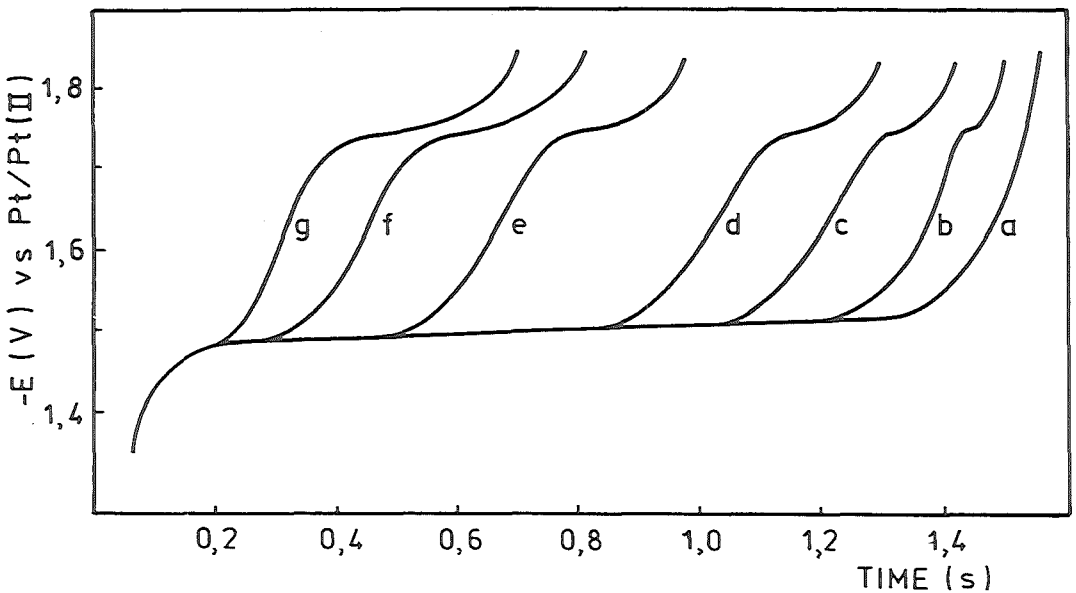

Fig. (6). Potential -time curves for chronopotentiometric reduction of mixture $ZnCl_2$-Li_2MoO_4. Current density = 50.4 mM / cm^2.

a.	74 mM $ZnCl_2$	0 mM Li_2MoO_4
b.	74	7.55
c.	74	19.30
d.	74	32.70
e	74	51.80
f.	74	87.80
g.	74	118.50

LITERATURE

1. L.W. Woodcock and K. Singer, Trans. Farad. Soc. , 67 (1971) 12.
2. L. Grantham and S. J. Yosim J. Phys. Chem. 67 (1963) 2506
3. D. G. Lovering, Trans. Faraday Soc. 67 , (1971) 2659.
4. D. Inman and D. G. Lovering, J. Electrochem. Soc. 121 (1974) 778.
5. D. Inman, Dj. Jovanović, and S. H. White, J. Electroanal. Chem. 43 (1973),37.
6. H. A. Laitinen, R.S. Tischer, D.K. Roe, J.Electrochem . Soc. 107(1960), 546.
7. H. A. Laitinen ,Pure Appl. Chem. 15 (1967), 227.
8. H. A. Laitinen and J. A. Plambeck , J. Am. Chem. Soc. 106 (1965) , 1202.
9. K. E. Johnson , and H. A. Laitinen , J. Electrochem. Soc. 110 , 314, (1963).
10. H. A. Laitinen and W. S. Ferguson , Anal. Chem. 29, 4 (1957).
11. B. Popov, H. A. Laitinen J. Electrochem. Soc. 117(1970), 645
12. B. Popov, H. A. Laitinen CHEM. SI APLICATA , Bukuresti 2 (1970), 188
13. B. Popov, H. A. Laitinen J. Electrochem. Soc. 120 (1973), 1346.
14. B. Popov , Thesis for the degree of Master of Science in Chemistry in the Graduate College of the University of Illinois (1970).
15. B. Popov, Ph. D. Thesis , Faculty of Technology , University of Zagreb (1972)
16. B. Popov, R. Cvetković , H. A. Laitinen, J. Electrochem. Soc.122 (1975), 1616
17. B. Popov Bull. Soc. Chim. Beograd 41 , 99 (1976).
18. B. Popov. Kem. Ind. 32 (1983) 65.
19. B. Popov , J. V. Ivshin , Croatica Chemica Acta 60 (2) (1987) , 315.
20. B. Popov, MANU CONTRIBUTIONS VI , 1 (1985) , 21
21. B. Popov Bull. Soc. Chim. , Skopje 4(1975), 3.

ELECTRODEPOSITION OF TITANIUM FROM MOLTEN SALTS

B. Popov, J. B. Wagner*, Jr., H. Wendt**, Z. Koneska

Faculty of Technology and Metallurgy, University"Kiril and Metodij",Skopje, YU
* Arizona State University, Tempe, Arizona , USA
** Institut für Chemische Technologie, Technische Hochschule, Darmstadt, FRG

INTRODUCTION

Titanium is electropositive as aluminium or beryllium and thus is doubtful that is possible to be electrodeposited from aqueous solutions, although reports in the literature indicate some degree of success(1-5). The electrochemistry of titanium subchlorides in molten salts and deposition of metallic titanium from titanium chlorides have been also a subject of many investigations.

Senderoff and Mellors (6) were able to plate titanium in ductile form by using molten fluorides, general the LiF-NaF-KF eutectic (FLINAK), as solvent and dissolving the metal as a fluoride , K_2TiF_6. A successful plating requires a temperature of 750 C with rigorous purification of the melt and dry inert atmosphere.

Rolland et al (7) studied the nature of the titanium deposit during prolonged electrolysis in LiCl-KCl eutectic melt, using $TiCl_2$ and a consumable titanium anode. In chloride melt , the crystal size and surface coverage improved with increasing temperature (450 - 830° C).

A. J. Horstik (8), D. M. Ferry et al (9) and G. M. Haarberg et al (10) determine the oxidation and reduction potential of titanium species in purified LiCl-KCl electrolyte using various electrochemical methods.

Ferry et al (11) also investigated the electrochemistry of titanium in the LiCl-KCl by means of pulse techniques and A.C. impedance measurements.

Besides the assumed advantages in economics and product quality as well as extensive investigations (12-16) , the electrolysis of titanium from chloride melts has not found commercial application mainly because titanium is present in the electrolyte in different valences which may favour reoxidation and disproportionation reactions resulting to a very low current density (17).

There is also a considerable disagreement in the literature even in the measured standard potential values of the three different titanium redox systems in molten LiCl-KCl eutectic melt, Ti(II)/Ti(0) , Ti(II)/Ti(III) and Ti(III)/Ti(IV) as well as their kinetic characteristics.

The present work is concerned with thermodynamic properties of titanium (II) and titanium (III) chloride as well as with reduction of titanium electroactive species in the melt. The work also covers: determination of the oxidation and reduction potential values of the various titanium species in LiCl-KCl eutectic melt, the equilibrium between the solution and metal (scrap Ti and TiC), as well as studies of oxidation/reduction processes taking place in the melt, when Ti scrap anode is used in the presence of Ti(II) and Ti(III) electroactive species.

The apparent valency of the metal ion in the melt immediately after the anodic dissolution was determined by Faraday's low while in the equilibrated melt it was determined by Faraday' s low and the slope of isothermal plots of the electrode potential vs. the log. of the concentration. It was also studied the rate of the corrosion reaction:

$$2Ti\ (III) + Ti \longrightarrow 3\ Ti\ (II)$$

and it has been determined its activation energy by extending rate determinations over a broader range of temperature.

EXPERIMENTAL

Solvent. - The eutectic mixture of potassium chloride (41 mole per cent(m/o) and lithium chloride (59 m/o) at 723°K was used as solvent system. The LiCl-KCl eutectic was obtained from Anderson Physics Labaratories, Incorporated , Champaign, Illinois. The method of purification has been described(18-19).

Electrolytic cell. - The cell used in this experiment has been previously described (20). Within this cell and under an atmosphere of dry, oxygen -free argon,the solvent was allowed to collect into the fritted compartments which were used as experimental cells. At the end of the experiment the volume of each compartment was determined by titrating its chloride content, and making calculations from the known density of the melt at 723°K.

Apparatus.- All electrochemical measurements were done using a PAR Model 273 potentiostat-galvanostat connected via a Model 273 interface, to an Apple IIe microcomputer. Experimental data were stored into 5 1/4 " flexible discs and plotted with a 7470 A Hewlett-Packard plotter.

Electrodes.- The reference electrode was a platinum foil in contact with platinum (II) solution.This reference electrode has been used instead of chlorine reference electrode because titanium has more than one stable valency under prevailing experimental conditions and chlorine gas can oxidize it from the lower to the higher state. Platinum reference electrode has been shown to be reproducible and nonpolarzable over a long period of time(21). Potentiodynamic and chronopotentiometric measurements were done using Ti(II)/Ti reference electrode(0.1 M). The Pt indicator electrode used in this study has been previously described(22-23). The electrode had a geometric area of 0.5 cm^2 and was constructed so that the glass-metal seal was always kept above the level of the melt. Titanium electrode potentials were measured against the platinum reference by a technique similar to that used by Laitinen and Liu (24). The carbon electrode which served as counter electrode in all electrochemical investigations in molten salts, was constructed as described by Propp (25). Titanium indicator electrode was prepared as follows: after addition of the anhydrous titanium chloride(III) it was allowed to equilibrate with titanium metal forming $TiCl_2$ and then pure titanium rod electrode was immediately immersed in the solution. Dilute solutions of titanium chlorides in LiCl-KCl eutectic melt were prepared by anodic dissolution of scrap metal and TiC. Carbon-bonding in TiC in the anode was achieved by forming a mixture of the carbide with pitch , molding to shape , and baking at 1000°-1200°C in inert atmosphere to drive off pitch volatiles. Anodes formed in this way had a good electrical conductivity and their use permited complete electrolytic extraction of Ti in the TiC. Anode composition (TiC) was Ti - 81 , C - 18% and Fe- 0.025 %.

Chemicals.- All chemicals used in this study were reagent grade . Those chemicals containing water of hydration were vaccuum dried at 383°K before being added to the melt. A blanket of argon was kept over the melt at all times to exclude oxygen and water vapor. The purification train used in purifying the argon has been described.

RESULTS AND DISCUSSION

The halides of titanium have been the subject of complete electrochemical and thermodynamical investigations in molten LiCl-KCl eutecti melt. Ti/Ti (II) equilibrium was studied with cell of the type Ti/Ti(II) ,LCl-KCl//LiCl, KCl,$PtCl_2$/Pt. The Pt electrode was used for convenience instead of measuring against the

chlorine electrode directly. The precise data of Laitinen and Pankey(26) are available for the cell: $Pt/PtCl_2$(1M) in LiCl-KCl//LiCl-KCl/Cl_2 in the form of the following equation:

$$E_{Pt/PtCl_2//Cl^-/Cl_2} = -0.3223 + 0.00034\ (t-450) \qquad (1)$$

Titanium electrode potentials with respect to the platinum reference electrode are normalized to the chlorine electrode , and the obtained values are numerically the same as the potential difference for the cell $Ti/TiCl_2$, LiCl-KCl// LiCl-KCl/Cl_2. The reaction corresponding to this cell is formation of titanium (II) chloride in the melt. In Fig(1) titanium electrode potentials are plotted vs. log of concentration of Ti(II) for five temperatures. The dependence is linear and the slopes determined are compared (Table II) with the slopes calculated from the Nernst equation , assuming n=2.

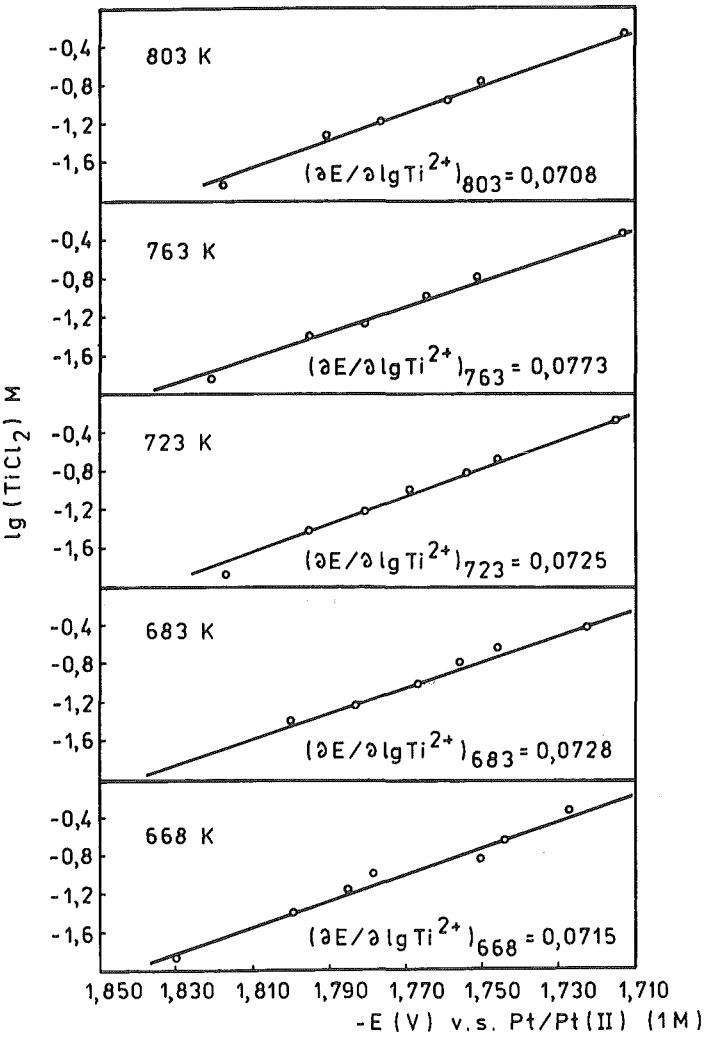

Fig(1)Titanium electrode potential as a function of Ti(II)

Standard potential measurement for the Ti/Ti(II) system are given in Table(1).

T a b l e (1)
Standard potential measurement for Ti/Ti(II) system

Molarity (M)	Log (M)	E (V) measured	E (V) vs 1 M Pt r. e.	E^o (V)
0.0125	-1.9020	-1.766	-1.816	-1.680
0.0354	-1.4508	-1.744	-1.794	-1.690
0.0564	-1.2476	-1.730	-1.780	-1.690
0.0835	-1.0779	-1.718	-1.768	-1.691
0.1010	-0.9956	-1.712	-1.762	-1.689
0.1350	-0.8696	-1.703	-1.753	-1.691
0.1687	-0.7728	-1.695	-1.745	-1.690
0.3512	-0.4544	-1.669	-1.719	-1.686

Using the relationships:

$$\Delta G = - nFE \quad (2)$$
$$\Delta S = nF \left(\partial E/\partial T\right)_p \quad (3)$$
$$\Delta H = \Delta G + T\Delta S \quad (4)$$

the partial thermodynamic quantities for the reaction were calculated from the data for these cells. Partial thermodynamic quatities for the formation of $TiCl_2$ in molten LiCl-KCl eutectic were calculated and are listed in Table(3).

T a b l e (2)
Nernst behaviour of the Ti / Ti (II) electrode

Temperature ^oK	$(\partial E/\partial \log(Ti(II)_T$ (V)	
	calculated	observed
668	0.0662	0.0715
683	0.0677	0.0728
723	0.0716	0.0725
763	0.0756	0.0773
803	0.0795	0.0808

Fig. (2) shows the variation of the Ti/Ti(II) electrode potential with temperature for different $TiCl_2$ concentrations in the melt. $(\partial E/\partial T)_p$ values obtained from this figure for each concentration were used to calculate the partial molar entropy values listed in Table (III).

The partial free energies of the formation of $TiCl_2$ at different temperatures and standard concentration are of considerable interest , and these values are listed in Table (4).

Chronopotentiometry of Ti(II) -LiCl-KCl system .

After obtaining several chronopotentiograms of the melt, titanium (III) chloride was introduced into the fritted compartment and it was allowed to equilibrate with titanium metal forming $TiCl_2$. Chronopotentiograms of $TiCl_2$ in molten LiCl-KCl were found to depend upon the concentration of $TiCl_2$. A typical cathodic chronopotentiogram is shown in Fig (3).

T a b l e (3)

Partial thermodynamic quantities for the formation $TiCl_2$ in molten LiCl-KCl eutectic melt

Concentration (M)	ΔG J/mol 723 K	ΔS J/K	ΔH J/mol 723 K
0.0125	-413,849 ±450	28.95± 1	434,779±3000
0.0354	-408,444	15.44	419,607
0.0654	-406,515	11,58	414,887
0.0835	-403,428	25.09	421,568
0.1350	-400,532	5.79	404,718
0.3512	-393,971	19.30	407,924

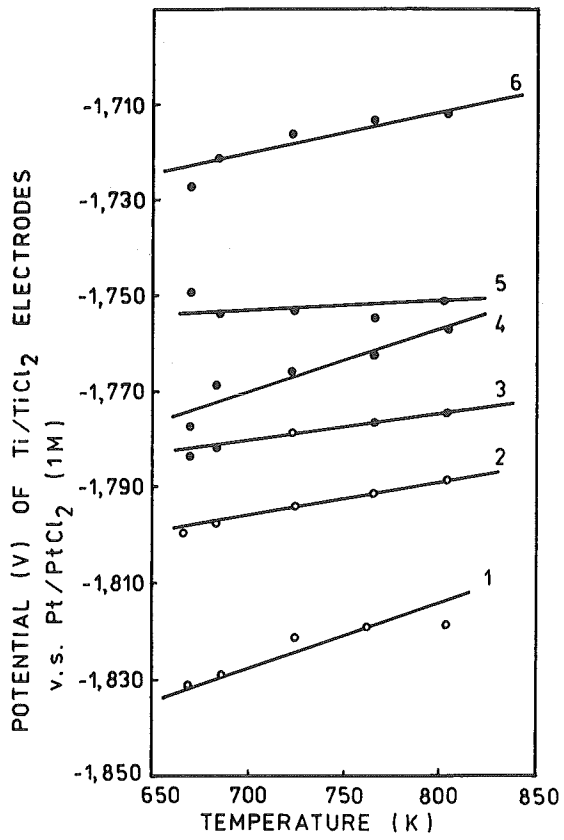

Fig(2). Temperature dependence of titanium electrode potential
C_{TiCl_2}(1) = 0.0125; (2)=0.0354 M; (3)= 0.0564 M; (4) 0.0835 M
(5)=0.1350 M; (6)= 0.3512 M.

T a b l e (4)
Partial molar free energies of $TiCl_2$ formation at standard concentration in LiCl-KCl eutectic melt

Temperature ^oK	ΔG J/ mol
668	388,374 $\pm$ 400
683	387,795
723	387,410
763	386,443
803	386,433

As it can be seen from Fig(3) , a single chronopotentiometric wave occurs at a quarter wave potential of - 1.91 V vs the Pt(II)/Pt reference electrode. The Sand equation was tested at five different Ti(II) concentrations. The area of the Pt electrode was measured to be 0.5 cm^2 in most cases. The transition time constant was found to be indipendent on I- current density, indicating that the electrode process is diffusion controlled over time interval investigated. These data are listed in Table (5). The average value of the transition time constant is 329.4 A s cm mol^{-1}.

Since the Sand's equation permits only the determination of the product $nD^{1/2}$, either n or D must be obtained by an independent method. Based on analytical data n=2 , the diffusion coefficient was calculated to be 1.25 $x10^{-5}$ cm^2 s^{-1}. Dahl et all (12) and Ferry et all (11) have estimated the diffusion coefficient of Ti(II) ion at 723 K in the range (1-3) x 10^{-5} cm^2 s^{-1}, and is very close to ours.

The potential -time curve for the reduction process at -1.91 V vs. the Pt(II)/Pt reference electrode was analyzed in an attempt to obtain information concerning the kinetics of the electrode process. If the electrode process is totally irreversible , the potential-time curve is described by Delahay -Berzins equation for the electrode process involving one rate determining step.

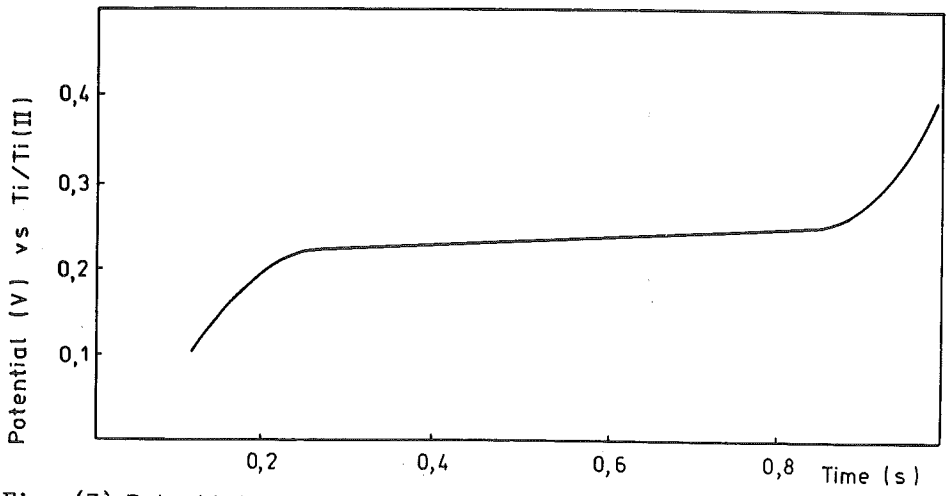

Fig. (3) Potential - time curve for the reduction of $TiCl_2$
Current density = 4 mA / cm^2, C_{TiCl_2} = 6.45 x 10^{-3} M.

The same form of the potential-time curve would be given by a reversible reaction leading to a solid reduction product of constant activity as it is obtained for the irreversible plot regardless of the solubility of the product. However , for a reversible reaction the slope would be different. Using the slope and intercept from the Delahay- Berzins equation:

$$E = 2.3\ RT/\alpha n_a F\ \log(\ nFCk^{o}_{f,h}/I^{o}\tau^{1/2}) + 2.3RT\ /\ \alpha n_a F\ \log(\tau^{1/2} - t^{1/2}) \qquad (5)$$

the values of αn_a and $k^{o}_{f,h}$ were calculated to be 0.46 and 2.08 x 10^{-6} cm s^{-1}. Haarberg et al. (10) , considered that titanium reduction is irreversible with $k^{o}_{f,h}$ = 1.5 x 10^{-6} cm s^{-1}, which is in the range with the value we have calculated in this study. Since the results indicate that the electrode reaction is irreversible , the potential of the indicator electrode is independent of the concentration of the reduced form.. It is impossible , therefore, to obtain information on the chemical properties of the reduced species from the analysis of the potential-time behaviour.

T a b l e (5)
Chronopotentiometric data for the reduction of $TiCl_2$ in LiCl-KCl eutectic melt

C_{TiCl_2} (M)	$I\tau^{1/2}$ (A $s^{1/2}$)x 10^3	$I_o\tau^{1/2}/C$ (A $s^{1/2} cm^3 mol^{-1}$)	
6.45 x 10^{-3}	1.95	302.3	
	2.08	322.4	
	2.12	328.6	av. 317.7
1.25 x 10^{-2}	4.01	321.4	
	4.35	348.0	
	4.17	333.6	av. 334.3
2.37 x 10^{-2}	7.71	325.3	
	7.65	322.8	
	7.89	332.9	av. 327.0
3.16 x 10^{-2}	10.25	324.3	
	10.78	341.1	
	10.10	319.6	av. 328.3
4.28	14.47	338.1	
	14.21	332.0	
	14.95	349.2	av. 339.7

It is well known that Ti(III) chloride ions react chemically with titanium surface by chemical redox reaction:

$$2Ti(III) + Ti = 3\ Ti\ (II) \qquad (6)$$

which is further reduced to metallic titanium. Anodic dissolution of titanium metal into this melts proceeds by formation , as will be shown later , of Ti(III) ions . This interference of chemical oxidation and anodic oxidation of titanium metal is certainly of high importance for the cathodic deposition of titanium metal from molten chlorides containing Ti (III) ions , since the subsequent

reduction Ti (III) + e = Ti(II) and Ti (II) + 2e = Ti(0) interferes with reaction (6). One should expect that the significant velocity of "chemical" redox reaction might hinder or slow electron exchange Ti (II) + 2e = Ti (0), compared to faster oxidation/reduction process of Ti(III) + 3e = Ti(0).

Dahl et al (11) and Rolland et al (7) have estimated the diffusion coefficient of Ti(II) ion in molten LiCl-KCl eutectic. In their work , $TiCl_3$ was added into eutectic melt and allowed to equilibrate with Ti metal according to the reaction (6) and the total titanium chloride content in the melt was calculated as $TiCl_2$ without to check for a preceding "chemical" redox reaction in order to determine if the reaction between Ti(III) species and Ti metal occured completely before electrolysis began. Thus in order to obtain a true value of the diffusion coefficient as well as the kinetic characteristics of Ti(II) reduction one should take into account the interference of chemical and anodic oxidation of titanium metal as well as the rate of the corrosion reaction (6).

For a slow chemical reaction preceding the electrode process $I_o x \tau^{1/2}/ C$ decreases with increasing I_o. For this case the transition time is given by the Delahay - Berzins equation (26):

$$I_o \tau_k^{1/2} = \pi^{1/2} nFC^o D^{1/2}/2 - \pi^{1/2} I_o/2K(k_f + k_b)^{1/2} erf \left[(k_f + k_b)^{1/2} \tau_k^{1/2}\right] \quad (7)$$

where k_f and k_b are the forward and backward rate constants of the preceding chemical equilibrium and $K = k_f/k_b$ is the equilibrium constant. The first term of the right-hand side of Equation (7) is recognized as the diffusion -controlled term. The second term has two limiting forms; 1) For values of $(k_f + k_b)\tau_k > 2$ the error function is approximately unity and the quantity $I_o\tau_k$ is linear function of I_o, with the intercept equal to the diffusion controlled value and the slope determined by the rate constants k_f and k_b. For a given set of values of k_f and k_b this condition is most closely obeyed at low current densities and correspodingly high values of "τ". For values of $(k_f + k_b)^{1/2} \tau^{1/2} < 0.1$ the error function is adequately represented by the first two terms of the expansion and the Equation (7) becomes:

$$(I_o \tau_k^{1/2})_{I_o \to \infty} = nFC^o \pi^{1/2} D^{1/2}/2(1 + 1/K) \quad (8)$$

In this case the quantity $I_o \tau_k^{1/2}/C_o$ is once more independent of the applied current density but its value is less that the diffusion-controlled value by the factor K/ (1 + K). Thus, for the case of a slow preceding chemical reaction a plot of $I_o \tau_k^{1/2}$ against I_o will show first a linearly decreasing region and at high value of I_o will show first a linearly decreasing region and at high value of I_o it may show a constant region if the values of k_f and K are sufficiently small.

Experimentally, it was necessary to restrict the range of current densities that can be used at a given concentration and to limit the transition time to a range of 0.2 to 2.0 s to minimize the double layer effects and convenction. The plot of $I_o \tau_k^{1/2}/C^o$ vs I_o is shown in Fig. (4) for the reduction of Ti(II). Chronopotentiometric measurement were performed using 0.102 M $TiCl_3$ and approximately the same concentration of pure titanium metal in the eutectic melt at 725 K. The transitiontimes were measured with quarter wave potentials of -1.9 V vs Pt(II)/Pt refernce electrode for different current densities, and for 2 miutes, 5 minutes,10minutes and 20 minutes after addition of $TiCl_3$ and pure Ti into eutectic melt. The transition time constant was calculated for each measured transition time supposing that the reaction between Ti(III) and Ti has been completed. The total titanium (II) chloride content was calculated from the amount of Ti(III) added into the melt.

The transition time constant in Fig. (4) increases with time , indicating that the product between transtion time and current density increases as a result of the increased concentration of Ti (II) species as time passes. The fact that there is a discernible downward slope un Fig. (4) may be used as evidence that the raction between Ti(III) and Ti species does not occur completely before the electrolysis begins. The transition time constant stabilizes after ten minutes , (curves 3 and 4 in Fig. 4) but still it is observed a downward slope. Our chronopotentiometric measurements were done after 20 minutes stabilization of the system.

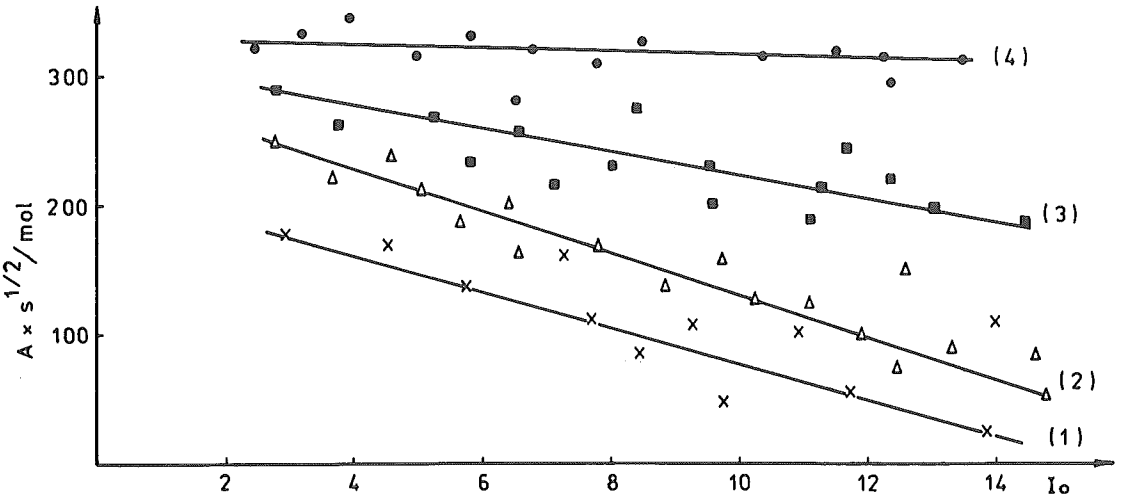

Fig. (4). Variation of $I_o \tau^{1/2} / C$ with I_o for the reduction of Ti(II) The transition time was measured after 2 minutes-curve (1), 5 minutes-curve (2) , 10 minutes-curve (3) and 20 minutes-curve (4) from the begining of the "chemical" redox reaction.

Fig.(5) shows the temperature dependence of the diffusion coefficient, from which the activation energy of the diffusion was calculated to be 48000 J/mol.

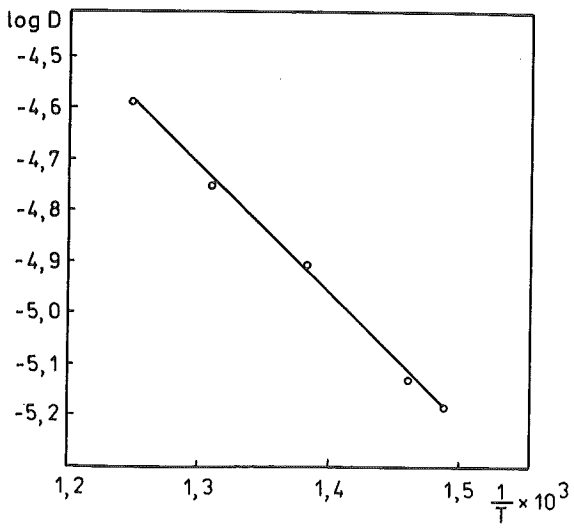

Fig.(5) Temperature dependence of the diffusion coefficient.

Cyclic voltammetry of Ti(II) - LiCl - KCl system

Fig (6) show the cyclic voltammetric curves obtained for $TiCl_2$ (6.35 X 10^{-2}M) in molten LiCl-KCl eutectic at 723 K for different sweep rates ranging from 0.005 V V/s to 0.5 V/s.

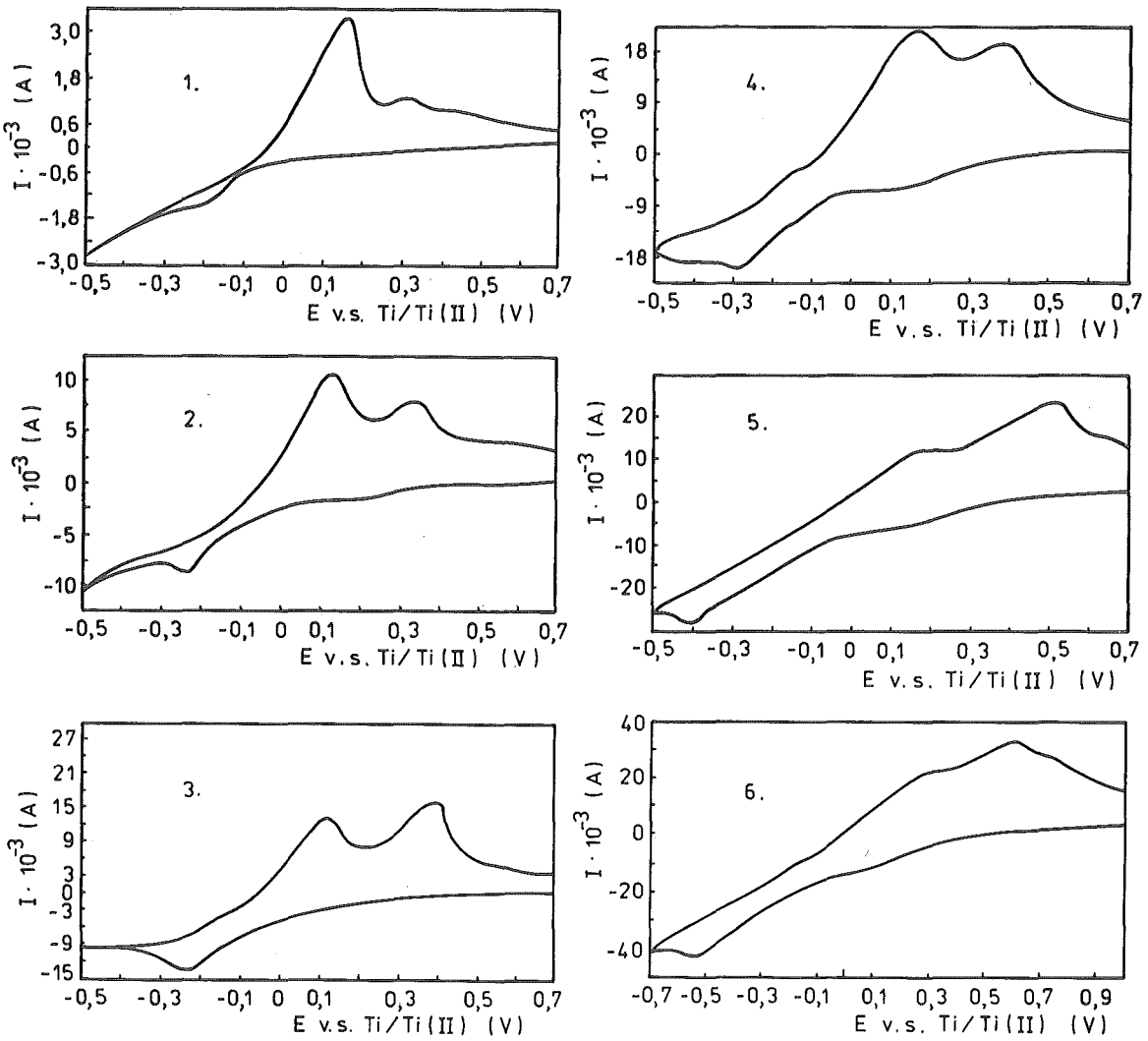

Fig. (6) Cyclic voltametric curves for Ti(II)
1. v = 0. 005 V/s , 2. v= 0.02 V/s , 3. v= 0.05 V/s
4. v = 0. 100 V/s , 5. v= 0.20 V/s , 6. v= 0.50 V/s

It can be seen that during negative - going potential a well distinguished peak appears at ca - 0.230 V vs. the Ti/Ti(II) electrode (i. e. -2.252 V vs the Cl^-/Cl_2 reference electrode). The peak potential (E_p) corresponding to the cathodic peak shifts to more cathodic values when increasing with time.

The size of this peak depends linearly upon the concentration of Ti(II) in the melt. Plots of the cathodic peak current vs the square root of the sweep rate are linear (Fig. 7), confirming the fact found by chronopotentiometry that the reduction of $TiCl_2$ is a diffusion controlled process.

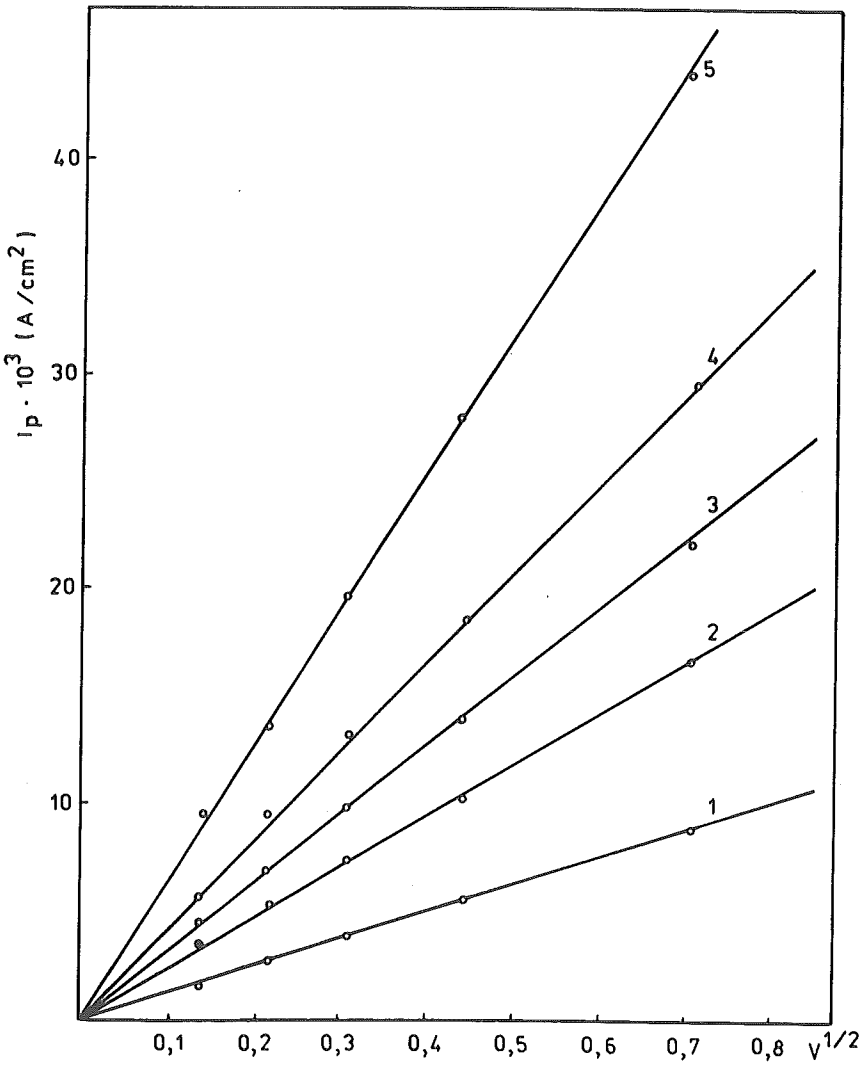

Fig. (7) Peak currents (i_p) vs square root of the sweep rate for the reduction of Ti(II) on Pt electrode in LiCl-KCl eutectic melt.

1. C_{TiCl_2} = 1.25 x 10^{-2} M
2. = 2.37 x 10^{-2} M
3. = 3.16 x 10^{-2} M
4. C_{TiCl_2} = 4.28 x 10^{-2} M
5. = 6.35 x 10^{-2} M

During positive going potential scan , two peaks at 0.120 V vs Ti/Ti(II) reference electrode (-1.902 V vs Cl^-/Cl_2 reference electrode) and at 0.390 V vs Ti/Ti(II) (-1.632 V vs Cl^-/Cl_2 reference electrode) are observed. The peak at 0.120 V is sharp stripping type peak and can be assigned to the dissolution reaction of Ti. The peak current at this potential increases with increasing the sweep rate (see Fig. 6) from 3.36×10^{-3} A for 0.005 V/s to 22.2×10^{-3} A for 0.1 V/s. Further increase of the sweep rate does not have any additional influence on the peak current value, which remains nearly constant at the value obtained for 0.1 V/s (for v = 0.5/s I_p = 21. 42 mA).

During successive cycles a small increase of the peak current from 10 mA to 15 mA is observed and the potentials move towards more positive potential value (from 0.120 V to 0.180 V vs Ti/Ti(II) reference electrode). The anodic shift also occurs in the experiments when potentiodynamic E/I profiles were recorded at different sweep rates.

The peak current at 0.390 V vs Ti(II)/Ti reference electrode (Fig.6) increases with increasing the sweep rate from 1.14 mA for 0.005 V/s to 32.85 mA for 0.5 V/s. The peak current is actually a linear function of the square root of the sweep rate.

The cyclic voltammetric measurements indicate that at -0.23 V vs Ti(II)/Ti reference electrode , Ti (II) ions are reduced to metallic titanium . Two consecutive anodic peaks appear at 0.120 V vs Ti(II)/Ti and at 0.390 V vs Ti(II)/Ti reference electrode and are atributed to the reaction:

$$Ti \longrightarrow Ti\ (II) + 2e \qquad (9)$$

$$Ti(II) \longrightarrow Ti(III) + e \qquad (10)$$

A parallel chemical reaction occurs at the anode, in which electrochemically formed Ti(III) reacts with metallic titanium to yield reduced titanium chloride at concentration set by the equilibrium (6).

For sweep rates higher than 0.005 V/s the peak current at 0.390 V vs Ti(II)/Ti r. e. increases , indicating that under such conditions a higher concentration of Ti (II) is formed at 0.120 V into the eutectic melt, which is further oxidized at 0.390 V to Ti(III).

As it has been pointed out earlier , the subsequent reduction of Ti(III) Ti(II) and Ti(II) → Ti(0) interferes with the corrosion reaction 2Ti(III) + Ti ⟶ 3 Ti (II), and it is of great importance to determine the rate of the "chemical " redox reaction , as well as to calculate its activation energy by extending this rate -determination over a broader range of temperature.

The rate of the corrosion reaction was studied using potentiodynamic method (in order to determine quantitatively the decrease of Ti(III) concentration when reacts with metallic titanium forming Ti(II).

The potentiodynamic measurements were performed using 0.102 M $TiCl_3$ and approximately the same concentration of pure titanium metal in the eutectic melt. I_p cathodic of Ti(II)reduction was measured after 0.2 minutes , 3 min. 5.5 minutes and 8 minutes from the beginning of the reaction. The concentration of Ti(III) species was then calculated from the concentration of titanium (II) and stoichiometry of the chemical redox reaction. Cyclic voltammograms obtained after 0. 2 minutes , 3 minutes , 5.5 minutes and after 8 minutes after addition of Ti(III) and Ti metal into the eutectic melt are shown in Fig. (8).Calculated rate constant of the corrosion reaction :

$$2Ti(III) + Ti \longrightarrow 3Ti(II)$$

is given in Table (6) . The average value of k = 1.052 min^{-1} mol^{-1} dm^3. The rate determination was extended from 668 K to 803 K and the activation energy was calculated from data and E_a = 88681,5 J/mol.

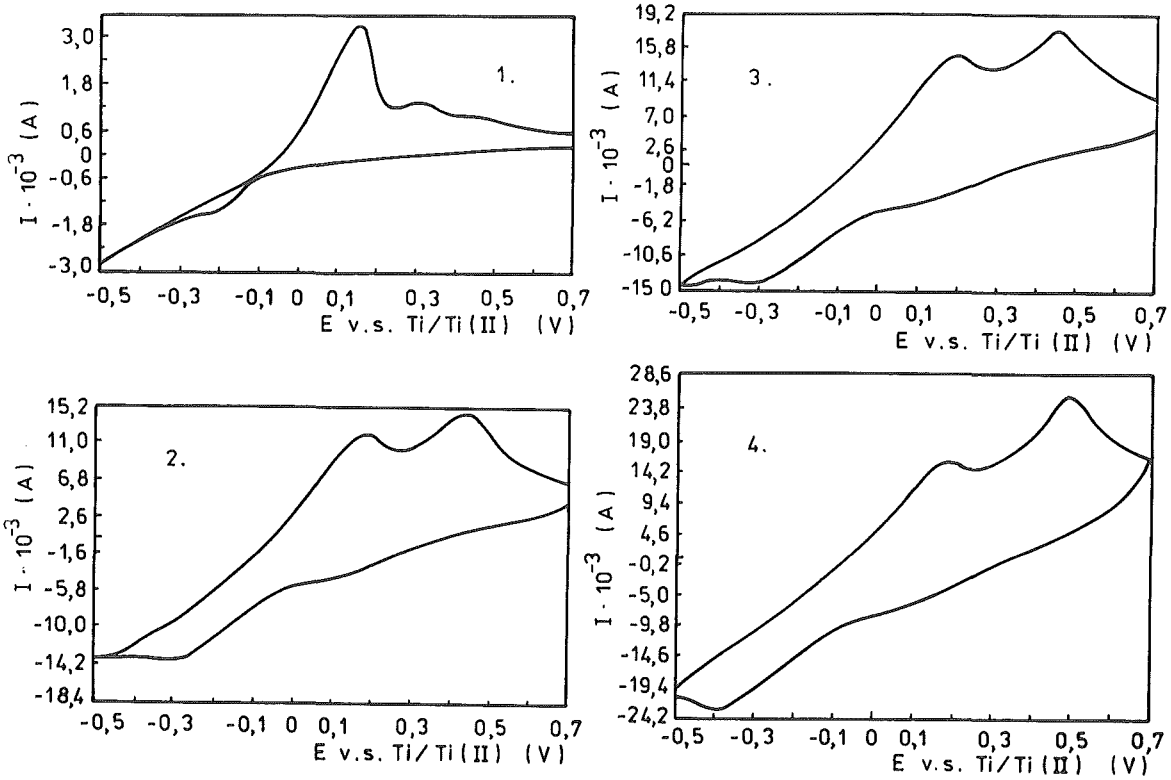

Fig. (8) Cyclic voltammograms obtained after 1) 0.2 minutes, 2) 3 minutes 3) 5.5 minutes , 4) 8 minutes . $C_{Ti(III)}$ = 0.102 M V=0.020 v/s

T a b l e (6)

The rate calculation of the corrosion reaction

$$2Ti(III) + Ti \longrightarrow 3\ Ti\ (II)$$

reaction time (minutes)	C_{TiCl_3} (M/dm^3)	k ($min^{-1}\ mol^{-1}dm^3$)
0	0.102	-
0.2	0.0976	1.1
3.0	0.0568	1.23
5.5	0.0520	0.85
8.0	0.0380	1.03
	k av.	1.0525

A very well defined increase of $I_{p,c}$ and $I_{p,a}$ and the anodic and cathodic charges are observed in Fig (8).

It was also found that the chemical redox reaction is of second order, Table (6).

The results obtained in this study indicate that the interference of chemical oxidation and anodic oxidation of titanium metal is of high importance for the cathodic deposition of titanium metal from molten electrolytes containing Ti(III) ions . The " chemical redox reaction which is preceding the electrode process is slower than the electron transfer. The rate of the corosion reaction between $TiCl_3$ and Ti controls the reduction of Ti(II).

Equilibrium between TiC and titanium chlorides in LiCl-KCl melt.

The cheapest ways to get metal from its oxide is to reduce the oxide with carbon. Reduction of titanium oxide with carbon does not yield metal but does yield metal like carbon from which metal can be produced electrolytically. Refining TiC may be accomplished by using a cell with TiC anode. It is of great importance to determine the apparent valency of the metal ions in the melt immediately after the anodic dissolution of TiC.The preparation and the composition of TiC anode is given in the experimental section of this paper.

The apparent valency of the metal ion in the melt immediately after the anodic dissolution of TiC was examined at various current densities and at various concentrations of the metal chloride (within 1.4×10^{-2} M to 0.263 M). The content of the metal chloride in the melt was obtained by the weight decrease of the TiC electrode. The apparent valency of the metal ion in the melt immediately after the anodic dissolution was determined from the charge passed during the electrolysis and the weight decrease of the TiC electrode , with Faraday's law.

The present work was made with cells of the type TiC/ Ti (X), LiCl-KCl// LiCl-KCl, $PtCl_2$/Pt. In Fig. (9) , TiC electrode potentials are plotted vs. log concentration of titanium ions for two temperatures. The dependence is linear and the slopes determined are compared in Table (7).

T a b l e (7)
Nernst Behaviour of TiC Electrodes in LiCl-KCl melt

Temperature/K	$\partial E / \partial \log$ Ti(III) $_T$/V	
	Calculated	Observed
723	0.0477	0.0487
873	0.0576	0.0540

The slopes were calculated from the Nernst equation , assuming n= 3. Standard potential measurements for the TiC/Ti(III) system are given in Table (8).

T a b l e (8)

Standard Potential Measurements for TiC (III) System

Molarity (M)	Log (M)	E(V) measured	E (V) vs. 1 M Pt r. e.	E^o(V)
0.0140	-1.853	-1.273	-1.323	-1.235
0.0450	-1.347	-1.254	-1.303	-1.240
0.0575	-1.240	-1.249	-1.299	-1.243
0.0705	-1.152	-1.240	-1.290	-1.246
0.0930	-1.031	-1.236	-1.286	-1.238
0.2630	-0.580	-1.214	-1.264	-1.244

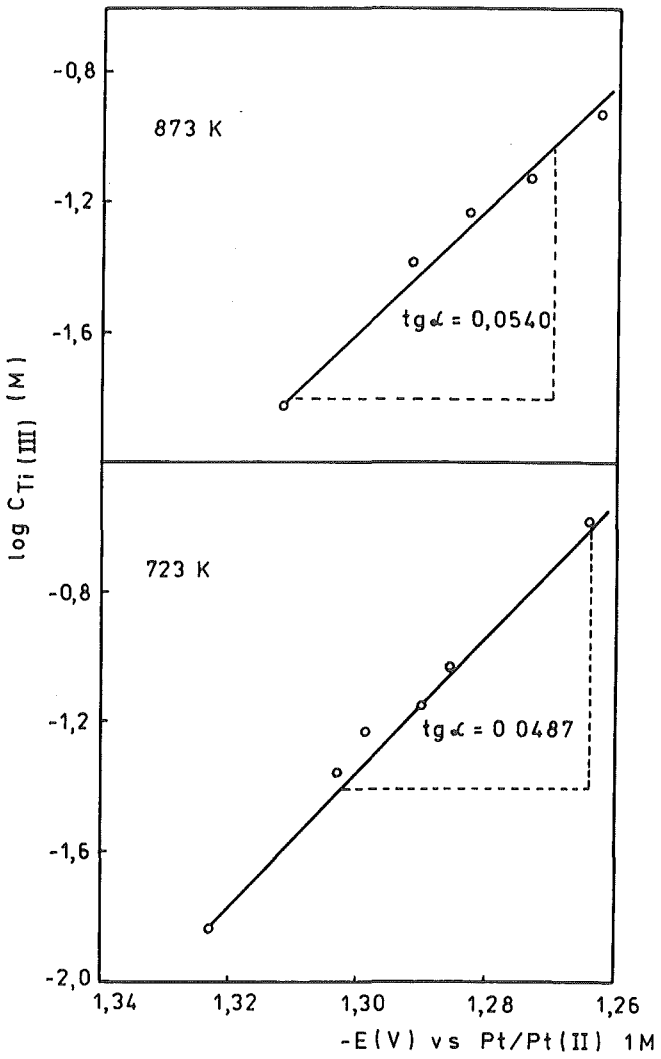

Fig. (9) Potentials of TiC electrode with respect to the Pt/Pt(II) reference electrode (1 M) as a function of Ti(III) concentration in molten LiCl-KCl eutectic melt.

From the results obtained one can conclude that the standard electrode potential for TiC/Ti(III) exceeds that for oxidation of Ti(II) to Ti(III) and one should expect that at this potential stable titanium species to be Ti(III) in the contrary to the behaviour of Ti metal anodes, where stable species are Ti (II) ions.

The observed slopes for TiC are close to the calculated for 3- electron process. The same results were also obtained at 723 K and 873 K.

The electrode potentials of TiC were also measured at the same temperature range and nearly the same concentration range with the cell of the type TiC/ Ti(III) , LiCl-KCl// LiCl-KCl , $PtCl_2$/Pt. A known amount of reagent grade $TiCl_3$ was inserted into the melt and the dilute solution was allowed to equilibrate before doing the measurements. The potential values obtained were the same as those for titanium chlorides prepared by anodic dissolution of TiC.

Cyclic Voltammetry of Ti(III)- LiCl-KCl system.

Fig. (10) shows a cyclic voltammogram obtained for 6.3×10^{-2}M $TiCl_3$ in molten LiCl-KCl eutectic at 723 K and sweep rate of 0.05 V/s.

Dilute solutions of titanium (III) species were prepared by anodic dissolutiom of the metal at high current densities. At low current density the anode dissolves to yield reduced titanium chlorides at concentrations set by the equilibrium :

$$2Ti\ (III) + Ti = 3\ Ti(II)$$

At higher current density one should expect an increasing amount of Ti(III) to be produced because of anodic polarization.

A complex cathodic contour is observed in this case , where one new peak , comparing with the cyclic voltammograms obtained for Ti(II) reduction, appears at -0.120 V vs Ti/Ti(II) reference electrode (-2.142 V vs Cl_2/Cl^- reference electrode). This cathodic peak is atributed to the reaction:

$$Ti(III) + e = Ti\ (II)$$

Ti(II) species are further reduced at ca - 0.230 V vs Ti(Ti(II) reference electrode (-2.252 V vs the Cl_2/Cl^- reference electrode) to metallic titanium.

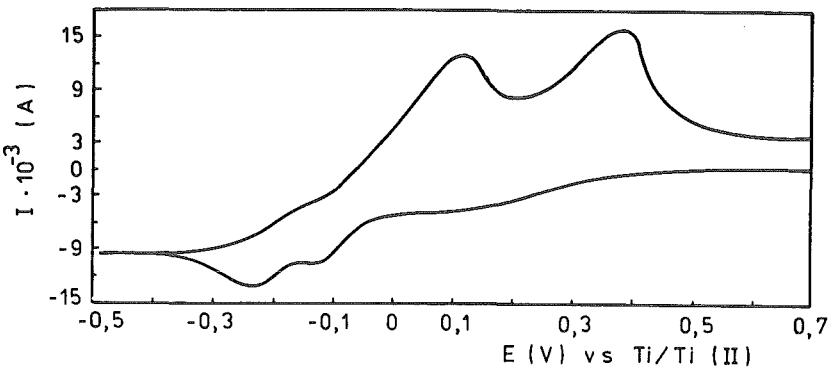

Fig. (10) Cyclic voltammogram of Ti(III) prepared by anodic dissolution of titanium metal , sweep rate 0.050 V/s , $C_{Ti(III)} = 6.35 \times 10^{-2}$M)

In a separate experiment , a known amount of reagent grade $TiCl_3$ was introduced in the eutectic melt, the solution was allowed to equilibrate and the cyclic voltammogram was obtained using carbon indicator electrode. The results obtained are given in Fig. (11) and Table (9).

A complex cathodic and anodic contour is observed which is identical with the cyclic voltammogram obtained for dilute solution of titanium species which were prepared by anodic dissolution of titanium metal at high current densities. It is obvious then that the anodic dissolution of titanium metal into this melts proceeds by formation of Ti(III) ions.

$TiCl_4$ is a covalent compound of high volatility and insoluble in fused alkali metal chlorides. Taking into account that the process of $TiCl_4$ formation, Fig(11) and electrolysis are carried out simmultanoeusly in the melt, it is possible to explain the anodic and cathodic peaks in Fig(11). The cathodic peaks are reduction of Ti(IV) to Ti(III) which is further reduced to Ti(II) and metallic titanium.

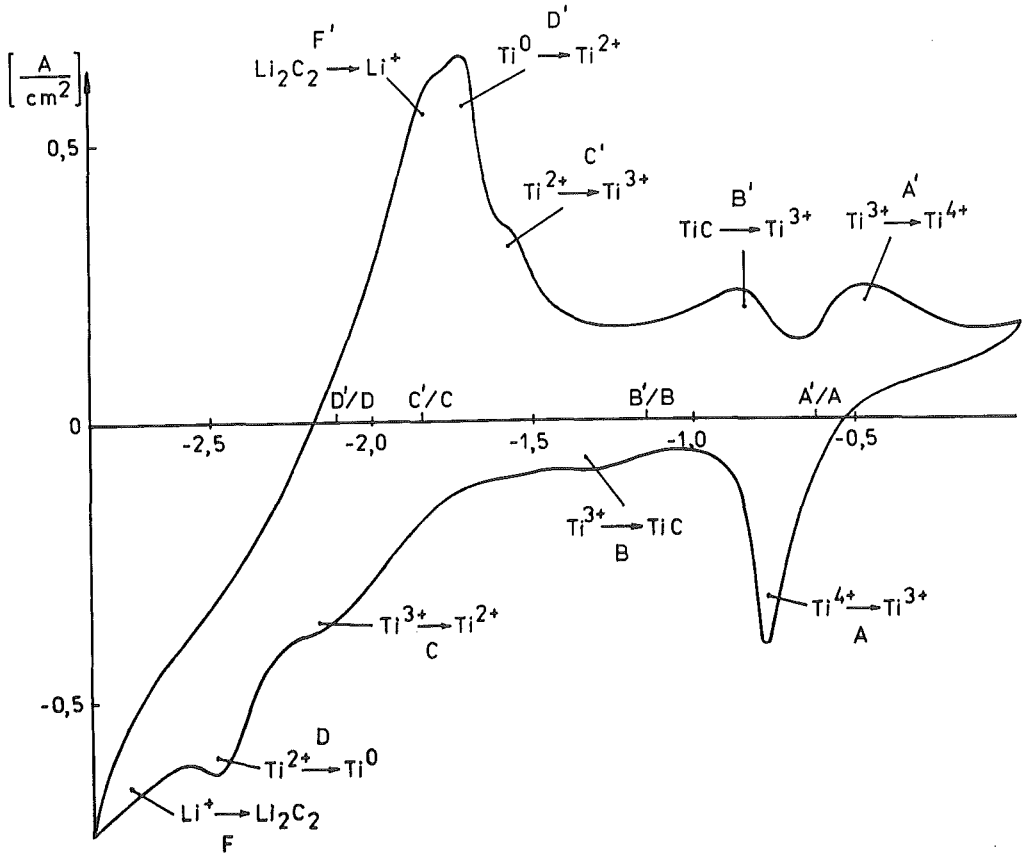

Fig. (11) Cyclic voltammogram of $TiCl_3$ obtained using carbon working electrode; the potentials were measured vs. Cl_2/Cl^- reference electrode, T = 723 K ; LiCl -KCl eutectic melt with 2 mol % $TiCl_3$

T a b l e (9)

Calculated standard redox potentials (E^o_o) and redox potentials (E^o) taken from cyclic voltammogram in Fig. (11) . The potentials are given vs. Cl_2/Cl^- r.e. in molten LiCl-KCl eutectic melt

	Equilibrium		E^o_o(calculated) (V)	E_o(V)
A:	$Ti(IV) + e^-$	$Ti(III)$	-0.923	-0.610
B:	$Ti(III) + C + 3e^-$	TiC	-1.420	-1.120
C:	$Ti(III) + e^-$	$Ti(II)$	-1.730	-1.820
D:	$Ti(II) + 2e^-$	$Ti(0)$	-2.080	-2.140
E:	$2\,Li(I) + 2C + 2e^-$	Li_2C_2	-3.390	-2.50

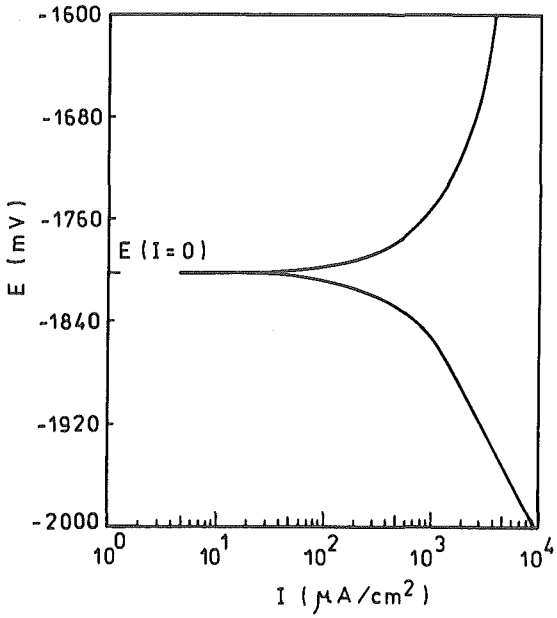

Fig. (12) Potentiodynamic curve obtained for Ti electrode in molten LiCl-KCl eutectic.

Fig. (12) shows a potentiodynamic curve run with titanium electrode. The anodic slope was found to be 0.070, which is close to the calculated value for three electron exchange process and $\beta = 0.5$.

ABSTRACT

ELECTRODEPOSITION OF TITANIUM FROM MOLTEN SALTS

B. Popov, J. B. Wagner,Jr., H. Wendt, Z. Koneska

Faculty of Technology and metallurgy, University"Kiril and Metoduj" Skopje, YU
Arizona State University , Tempe , Arizona, USA
Institut für Chemische Technologie , Technische Hochschule, Darmstadt, FRG.

The thermodynamic properties of titanium(II) and titanium (III) species as reduction of titanium (II) and titanium (III) in molten LiCl-KCl eutectic was studied. The work covers: determination of the oxidation and reduction potential values of the various titanium species in LiCl-KCl , the equilibrium between the solution and the metal (scrap Ti and TiC), as well as studies of oxidation/ reduction processes taking place in the melt, when Ti scrap anode is used in the presence of Ti(II) and Ti(III) electroactive species. The apparent valency of the metal ion in the melt immediately after the anodic dissolution was determined by Farady's low while in the equilibrated melt it was desternined by Faraday's low and the slope of isothermal plots of the elctrode potential vs. the log. of the concentration. It was also studied the rate of the corrosion reaction : $2\,Ti(III) + Ti \longrightarrow 3\,Ti(II)$ and it has been determined its activation energy .

LITERATURE

1. M. Kolthoff , F. Tomas, J. Electrochem. Soc. 9, (1964), 1065.
2. N. H. Sinha and D. Swarup, Indian Min. J. Spec. Issue , 1 (1975), 134.
3. A. W. Machu and W. Kamel , Werkst. Korros. 10, (1959) 14.
4. A. Levenskene , L. Siminavatchus, V. Akimov, Trudy Litvoskoj Akademii nauk Serija B , 51 (1977) , 37.
5. S. M. Kochergin and G. R. Pobedimski, Zh. Prikl. Kim. 33 (1960), 238.
6. S. Senderoff and G. W. Mellors, Science , 153 (1966) 1475.
7. W. K. Rolland, G. M. Haarberg, A. Sterten , J. Thonstad and S Øye, 38 th Meeting of the International Society of Electrochemistry, Extended Abstracts, Maastricht, The Netherlands , 3.17 (1987),267.
8. A. J. Horstik, G. J. M. van Eyden and A. Honders, 38 th Meeting of ISE , Extended Abstracts , Maastricht , The Netherlands , 8.88 (1987), 912.
9. D. M. Ferrry, G. S. Picard and B. L. Tremillon , The Electrochemical Society, (Etended Abstracts) San Diego, California , Vol. 86-2 (1986) 19.
10. G. M. Haarberg, W. K. Rolland, A. Sterten, J. Thonstad and S Øye, Communication presented at EUCHEM Conference on Molten Salts, Norway (1986).
11. D. M. Ferry, G. S. Picard and B. L. Tremillon, J. Electrochem. Soc. 135 (1988) 1443.
12. O. Dahl , A. Hjelset, W. K. Rolland, A. Sterten , J. Thonstad and R. Tunold, 34 th Meeting of ISE , Erlangen , Germany, Extended Abstracts, 1131(1983),18.
13. E. Chassaing, F. Basile , G. Lortoir, J. Appl. Electrochem. 11 (1981), 187.
14. B. Popov, Z. Koneska , S. Handjiski , 39 th Meeting of ISE , Glasgow , Abstracts 1 (1988), 558.
15. K. H. Stern, 38 th Meeting of ISE . Maastricht , The Netherlands , 13 (1987),478.
16. "Electrodeposition of Refractory Metals from fused Salt Electrolytes", Proc. Workshop, Imperial College , July (1985).
17. D. Ferry, E. Noyon and G. Picard, J. Less. Common Met. , 97 (1984),331.
18. B. Popov, Ph. D. Thesis , University of Zagreb, (1972).
19. B. Popov, H. A. Laitinen, J. Electrochem. Soc. 117,(1970),644.
20. B. Popov and H. A. Laitinen,J. Electrochem. Soc. 120, (1973) 1346.
21. B. Popov and H. A. Laitinen , J. Electrochem. Soc. 122, (1975), 1616.
22. B. Popov, J. W. Iwshin, Croatica Chemica Acta , 60 (2), (1987), 315.
23. B. Popov , Bull. Soc. Chim. Beograd, 41 , (1976), 99.
24. H.A. Laitinen and C. H. Liu , J. Am. Chem. Soc. 80, (1958), 1015.
25. J. H. Propp and H. A. Laitinen , Anal. Chem. , 41, (1969) 645.
26. H. A. Laitinen and J. W. Pankey, J. Am. Chem. Soc. 81,(1959) 1053.

ELECTROCHEMICAL DEPOSITION OF TITANIUM FROM NONAQUEOUS MEDIA

Z. Koneska , B. Popov , G.Jovanovski
Faculty of Technology and Metallurgy , University "Kiril and Metodij",Skopje , YU

INTRODUCTION

Numerous nonaqueous solutions of Ti were electrolyzed in an attempt to electrodeposit the metal. Ether solutions containing halids , hydrydes , boronhydrides and organo-metallic compounds of Ti were the most promising (1). A number of recent studies (2 -5) in nonaqueous solvents has yielded no positive results. It has been found (4) that in acetonitrile solutions the reduction to the metallic state has failed as a result of reaction between freshly deposited titanium with solvent molecules.

Later on (6) it has been suggested by Biallozor and Lisowska that processes of reduction/oxidation Ti(IV) - Ti(III) proceeds relatively easy in the study on electroreduction of titanium tetrachloride in acetonitrile solutions.It was also suggested that in A. N. solutions in the presence of supporting electrolyte $LiBF_4$, the process of chemical reduction : 3 Li (0) + Ti (III) $\longrightarrow$ Ti(0) + 3Li(I) can occur. Thus, the formation of Ti(0) takes place only at the lithium reduction potential.

Lisowska and Biallozor also studied the electroreduction of $TiCl_4$ in dimethylsulfoxide (DMSO) and in dimethylformamide (DMF) (7). It has been found that the first step of the cathodic reaction is reduction of Ti(IV) to Ti(III) with $\alpha = 0.38$ and $k_f = 6.52 \times 10^{-4}$ cm s^{-1} , and that a secondary chemical reaction follows the $TiCl_4$ reduction in DMSO.

Kazakov et al (8) also studied the electrochemical reduction of titanium in DMSO. It has been suggested that metallic titanium is formed either by the chemical electroreduction of the titanium ions or by the disproportionation reaction : 3 $TiCl_2 \rightarrow 2TiCl_3$ + Ti , which can take place according to Franklin et al (9) in DMSO solutions.

An attempt will be made in this study to electrodeposit titanium from organic solutions. Taking into account that a necessary prerequisite of a plating bath is that a high concentration of complexed ions be maintained in solution the electrochemical reduction of titanium will be studied in dimethylsulphoxide (DMSO) and in dimethylformamide in the presence of LiCl as a supporting electrolyte. Ti J_4 and $TiCl_3$ will be the subject of complete electrochemical investigations.

EXPERIMENTAL

The solutions were prepared by addition of the anhydrous titanium(III) chloride in DMSO. Dilute solutions of titanium species in DMSO were prepared by anodic dissolution of pure Ti metal. To obtain a solution of Ti(IV) , an anhydrous TiJ_4 was added to DMF. All operations on solutions were carried out in a dry box.

The reference electrode was calomel in DMSO or in DMF solution. All potentials were recalculated vs. (SCE). Working electrodes of Pt, Fe and Ni were mounted in a teflon holder with geometric area of 0.078 cm^2. The working electrodes were mechanically polished to a fine finish , activated in sulphuric acid, washed with ethanol and in doubly distilled water. The carbon or Pt electrodes served as counter electrodes in all electrochemical investigations.All chemicals used in this study were reagent grade. The solutions were deoxygenated with purified argon and the experiments were done at 23°C. Electrochemical measurements were done using PAR Model 273 potentostat- galvanostat connected via a Model 273 interface to an Apple II e microcomputer. Experimental data were stored into flexible discs and

plotted with a Hewlett - Packard plotter.

RESULTS AND DISCUSSION

Cyclic voltammetry of TiJ_4- DMF System

Fig. (1) show the cyclic voltammetric curve obtained for TiJ_4(0.016 M/dm^3) in DMF at 23° C , sweep rate v= 0.1 V/s. The solutions were prepared by addition of the anhydrous TiJ_4 in DMF.

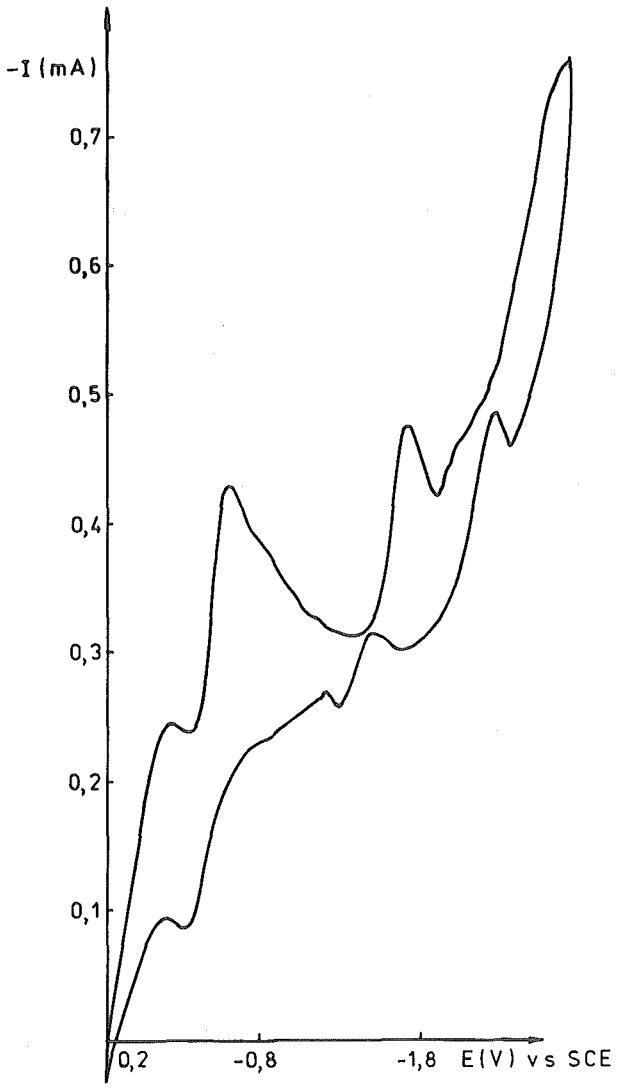

Fig.(1) Cyclic voltammetric curve for Ti(IV) in DMF
$C_{Ti(IV)}$= 0.016 M/dm^3)
v = 0.1 V/s , A_{Pt}= 0.078 cm^2

Characteristic data obtained for Ti(IV) reduction/oxidation processes at two different sweep rates are given in Table(1)

T a b l e (1)

Cyclic voltammetry data obtained in DMF of various concentrations of TiJ_4

Sweep rate v (V/s)	Concentration TiJ_4 (M dm^{-3})	E_I(pc)	E_{II}(pc)	E_{III}(pc)	E_I(pa)	E_{II}(pa)	E_{III}(pa)
			(V) vs $(SCE)_{aq}$				
0.5	0.0028		-0.703	-1.78	-0.23	-1.13	-1.18
	0.016	-0.191	-0.643	-1.72	-0.191	-1.17	-1.72
	0.024	-0.152	-0.585	-1.68	-0.152	-1.13	-
	0.027	-0.152	-0.565	-1.723	-0.152	-1.12	-1.75
	0.037	-0.354	-0.703	-1.970	-0.155	-1.14	-1.75
0.1	0.0028		-0.525	-1.703	-0.269	-1.15	-1.58
	0.016	-0.230	-0.565	-1.624	-0.230	-1.21	-1.88
	0.024	-0.231	-0.476	-1.605	-0.270	-1.17	-1.82
	0.027	-0.191	-0.447	-1.624	-0.240	-1.25	-1.80
	0.037	-0.152	-0.526	-1.703	-0.245	-1.20	-1.78

The potentiodynamic E/I profiles run with Pt in Ti(IV) iodide DMF solution in a potential range exceeding that of the thermodynamic stability of the supporting electrolyte involve a multiplicity of anodic and cathodic current peaks (Table 1.)

During the negative -going potential scan three sharp cathodic peaks, one at -0.23V vs (SCE) , at -0.55 V vs (SCE) and at -1.65 V are observed.

It was possible to obtain information regarding the values of kinetic parameters only for the first electroreduction process. The size of this peak depends linearly upon the concentration of TiJ_4 in DMF. , Fig (2) .

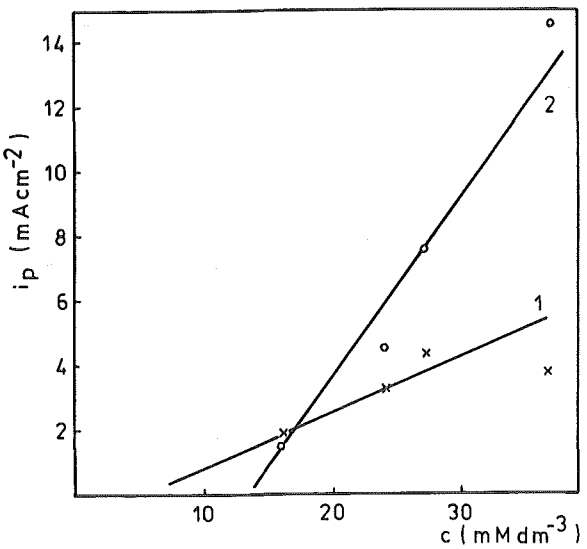

Fig. (2) Peak currents (I_p) vs. concentration of TiJ_4 , measured for 1. v= 0.5 V/s.
2. v= 0.1 V/s

Since the values of peak current is limited by linear diffusion of the electroactive species it is possible to calculate the diffusion coefficient using the relation:

$$I_p = 2.99 \times 10^5 \, A \, n^{3/2} \, D^{1/2} \, C^o v^{1/2} \qquad (1)$$

The value of $D_{TiJ_4(DMF)}$ calculated from the slope of the straight line in accordance with (1) is equal to 0.67×10^{-5} $cm^2 \, s^{-1}$. Lisowska and Biallozor (6) and Kolthoff and Thomas by applying c.v. method and polarographic method respectively , obtained similar results for D value of Ti(IV) in in acetonitrile solutions.

Value of k can be additionally calculated from the relation:

$$\log k = 1.1141 + 1/2 \log (\alpha n D v) + \frac{\alpha n}{0.058} (E_p - E_x) \qquad (2)$$

The transfer coefficient was calculated from Tafel'equation for $E_c - E_{p/2}$ to be 0.48 , whereas k value for the reduction process is calculated by assuming that the value of I_c for high polarization is mainly by the difussion process. Calculated k value is 1.58×10^{-4} cm s^{-1}.

The dependence of peak currents for the second and for the third cathodic peak is shown in Table (2).

T a b l e (2)
The dependence of peak currents (I_p) from the concentration of TiJ_4 in DMF solutions.

Sweep rate v (V/s)	Concentration TiJ_4(M dm^3)	E_{II}(cp) (V) (SCE)	I_{II}(pc) ($mA \, cm^{-2}$)	E_{III}(cp) (V)	I_{III}(pc) $mA \, cm^{-2}$
0.5	0.0028	-0.703	1.369	-1.781	4.52
	0.016	-0.643	7.13	-1.722	11.78
	0.027	-0.565	10.82	-1.723	14.65
	0.037	-0.703	23.88	-1.970	22.92

The cathodic peak (II) is apparently a consecutive peak of the first reduction.The size of this peak depends linearly upon the concentration of TiJ_4 in DMF.Cyclic voltammetry shows that the reduction of Ti(IV) effectively occurs in two sucessive steps , Fig(1) . The results obtained are in good agreement with an exchange of one lectron for the first reduction step and of one electron for the second one. The process could , therfore , proceed according to reactions:

I. Ti (IV) + e $\longrightarrow$ Ti(III)
II. Ti (III) + e $\longrightarrow$ Ti(II)

In other words at potential range of - .2 V - -0.55 V , the electroreduction reaction of Ti(IV) to Ti(II) occurs. It should be stressed that analogical process was observed by Thomas and Kolthoff (5) at reduction of $TiCl_4$ and AN solutions.

For DMF solutions containing only LiCl supporting electrolyte it has been obtained a cathodic peak at -1.7 V vs SCE, but no anodic peak appeared. After addition of TiJ_4 , the height of this peak increases from 4.52 mA cm^{-2} for 0.0028 M TiJ_4 DMF solution to 22.92 ma cm^{-2} for 0.037 M TiJ_4. These results are not in agreement with the findings of Biallozor et al (6). From their investigation on electroreduction of $TiCl_4$ in DMSO in the presence of Li(I)

salts, within the potential range of -1.7 V vs SCE, the height of the peak was practically independent of $TiCl_4$ concentration. Then , they have suggested a chemical reduction of titanium species by metallic lithium formed by the underpotential deposition at -1.7 V vs SCE.

From the results obtained in this study , within the potential range of the E_{pc}(III) , the following processes could take place:

I. Underpotential deposition of Li and chemical reduction of Ti(II)

$$Li(I) + e \longrightarrow Li(0)$$

$$2Li(0) + Ti(II) \longrightarrow 2Li(I) + Ti(0)_{ad.} \text{ , and}$$

II. A parallel electrochemical reduction of titanium species occurs at this potential:

$$Ti(II) + 2e \rightarrow Ti(0)$$

At higher potentials , above -3.0 V vs SCE one can observe , Fig.(1) decomposition of the supporting electrolyte.

The cyclic voltammetric measurements on the anodic portion of the cycle indicate that at -1.20 V vs SCE , the reaction could be attributed to:

$Ti(0) \longrightarrow Ti(II) + 2e$, which is further oxidized at -0.23 V according to the reaction:

$Ti(II) \longrightarrow Ti(III) + e$ and $Ti(III) \longrightarrow Ti(IV) + e$.

Visual observation of the electrode surface stored at -2.2 V shows the presence of a film with colours typical of metallic titanium , which is formed either by the chemical electroreduction of titanium or by the reduction of Ti(II). According to Franklin and Seklemian (10), the disproportionation reaction $3Ti(II) \longrightarrow 2\ Ti(III) + Ti(0)$ can also take place at the above potential.

Fig. (3B) shows a cyclic voltammogram obtained for titanium electroactive species in DMSO + 0.1 M LiCl solution and v= 0.5 V/s. Dilute solutions of titanium species were prepared by anodic dissolution of the metal at high current densities.

It was possible to obtain information regarding the values of kinetic parameters only for the first reduction process. The size of this peak depends linearly upon the concentration of Ti species in DMSO solutions, Fig(4). The value of D calculated from the straight line in accordance with (1) is equal 1.35×10^{-5} cm^2 s^{-1}.

In a separate experiment , a known amount of reagent grade $TiCl_3$ was introduced in the DMSO solution , the solution was allowed to equilibrate and the cyclic voltammogram was obtained using Pt indicator electrode. The results obtained are given in Fig. (3A). It was found that the size of the first peak depends linearly upon the concentration, Fig.(5) and upon the square root of the sweep rate , Fig. (6) indicated that this electroreduction process is diffusion controlled.The calculated D value is 0.8×10^{-5} cm^2 s^{-1}.

From Fig. (3) one can conclude that a complex cathodic and anodic contour is observed for Ti(III) reduction in DMSO which is identical with the cyclic voltammogram obtained for dilute solution of titanium species, which were prepared by anodic dissolution of titanium metal at high current densities and similar with c.v. curves obtained for Ti(IV) species in DMF solutions.

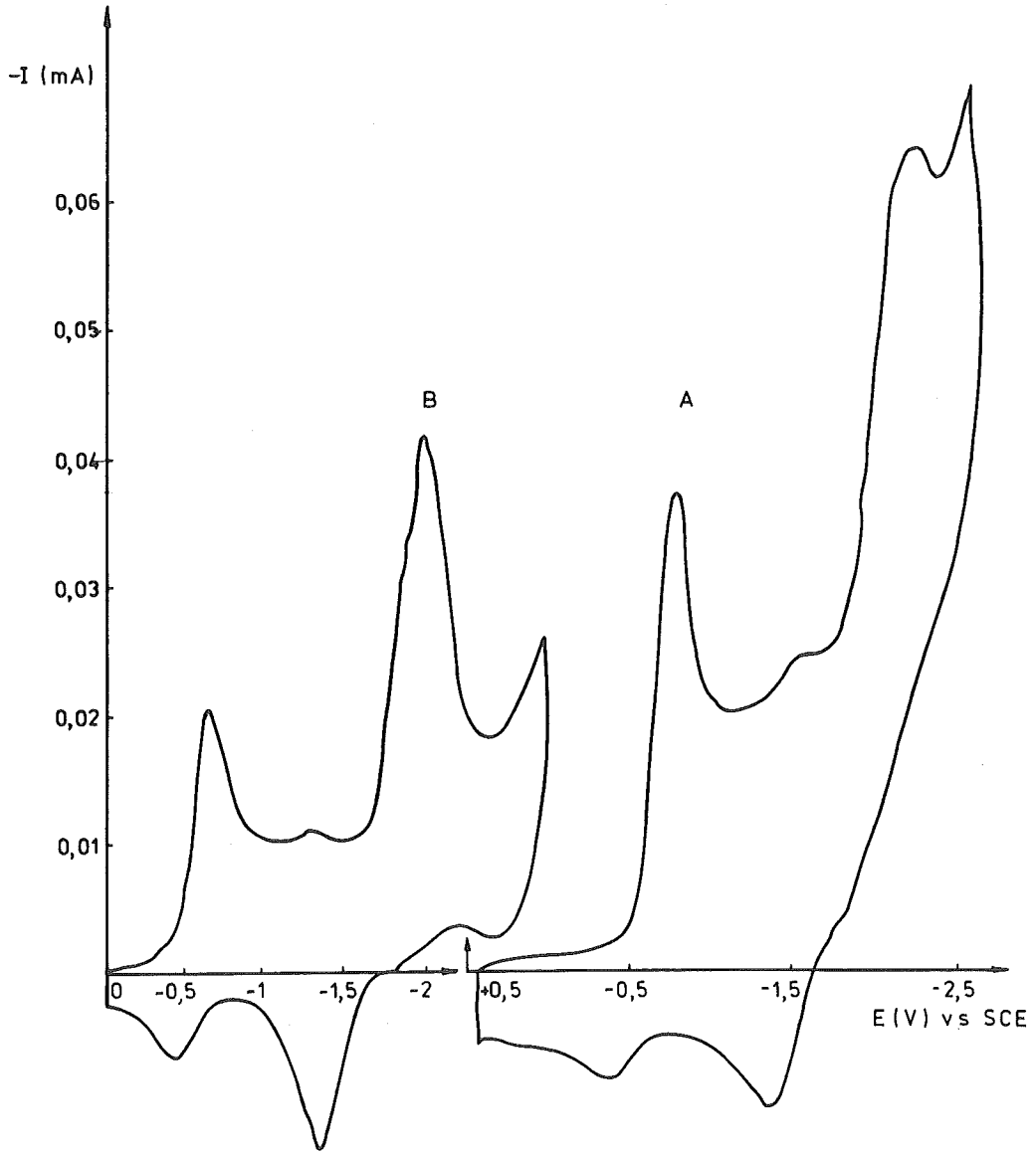

Fig.(3) A. Cyclic voltammogram of Ti(III) obtained using platinum working electrode; the potentials were measured vs SCE; T =23°C ; DMSO - 0.1 M LiCl with a $C_{Ti(III)}$= 0.023 M E_{pc}(I) = -0.612 V (SCE) ; E_{pc}(II)=-1.4 V(SCE) E_{pc}(III) -2.06 V (SCE). v = 0.5 V/s

B. Cyclic voltammogram of titanium electroative species prepared by anodic dissolution of titanium metal; DMSO -0.1 M LiCl with a sweep rate v = 0,5 V/s. E_{pc}(I) = -0.542 V ; E_{pc}(II)=-1.171 V ; E_{pc}(III) = -1.860

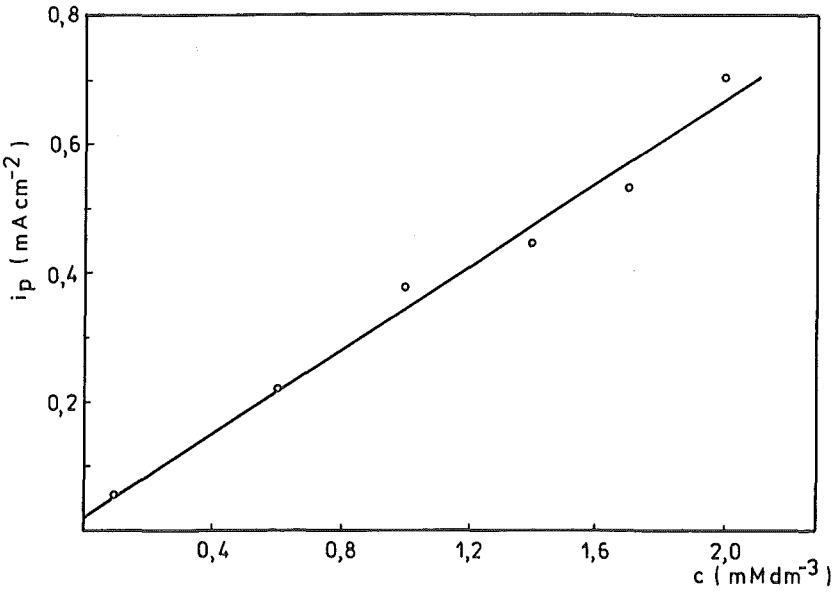

Fig. (4) Peak current (Ip) vs..concentration of titanium electroactive species in DMSO, measured for v = 0.5 V/s

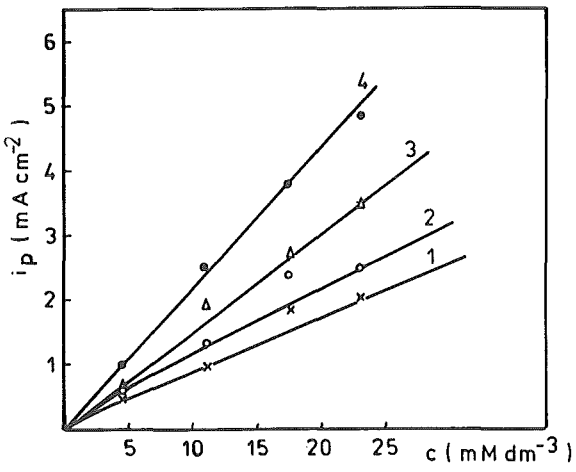

Fig. (5) Peak current (Ip) vs. concentration of $TiCl_3$
1. v = 0.05 V/s
2. v = 0.1 V/s
3. v = 0.2 V/s
4. v = 0.5 V/s

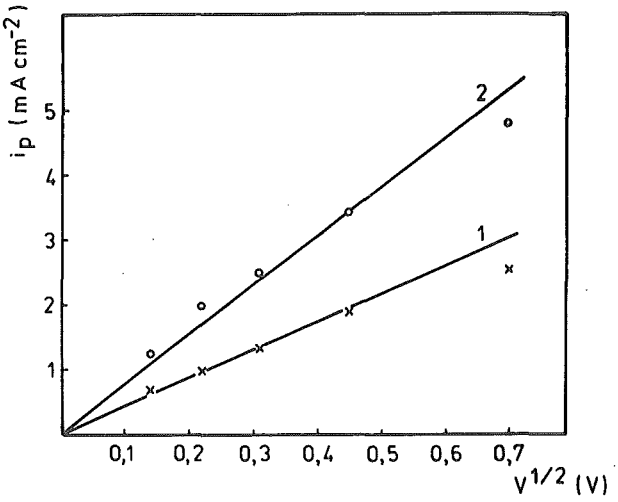

Fig. (6) Peak current vs. $v^{1/2}$
1. C_{TiCl_3} = 0.011 Mdm^{-3}
2. C_{TiCl_3} = 0.023 Mdm^{-3}

REFERENCES

1. N.H. Sinha and O. Swamp, Indian Min. Chem. Apstr. 54 (1980) 2053
2. A.J Parker, Proc. R. Austral. Chem Inst. 39, 163 (1972)
3. A. Brener, Advances in Electrochemistry and Electrochem. Engng Vol 5, p. 205. New York (1967)
4. W.E.Reid,JJ.M.Bish and A.Brenner, J. Electrochem. Soc 104,21 (1967)
5. I.M. Kolthoff and F.G. Thomas J. Electrochem. Soc 111,9 (1964)
6. S. Biallozor and A. Lisowska Electrochemica Acta Vol.25 p 1209-1214 (1980)
7. A. Lisowska and S. Biallozor Electrochemica Acta Vol 27 Noo1 (1982)
8. V.Kazakov, V. Titova and N. Petrova 33 Meeting of ISE IV A 36 (1982)
9. T. Franklin, H. Seklemian J. Inorganic Nuclear Chemistry Vol 12, (1959)

METALLIC LITHIUM AS ANODE MATERIAL IN POWER SOURCES

S. Pejovnik, M. Gaberšček, J. Jamnik, D. Metelko
Boris Kidrič Institute of Chemistry, Ljubljana, Yugoslavia

INTRODUCTION

Power sources using metallic lithium as anode material have in last ten years experienced a complete commercial recognition. The knowledge of chemical reactions and conducting mechanisms within the lithium batteries, however, is still limited and unsatisfactory. One of the important processes which still remains to be investigated is the chemical passivation of lithium. This paper reports on main results in this field obtained within last two years by the group at the Boris Kidrič Institute of Chemistry.

PASSIVE LAYER - SOLID ELECTROLYTE INTERFACE

Passivation of lithium (formation of a layer of reaction products on the surface of metallic lithium) in inorganic electrolytes is usually explained, by the solid electrolyte interface (SEI) model introduced by Peled (1). In the particular case of Li/$SOCl_2$ system the SEI consists of polycrystalline LiCl containing small amounts of impurities, such as aluminum ions, sulphur, etc. Such LiCl is relatively good ionic, and much poorer electronic conductor. There are two direct consequences of this fact: a) prevention of chemical corrosion of Li due to formation of SEI (also referred to a passive layer), and b) the so-called "voltage delay effect" which represents one of the major problems in application of lithium batteries. Voltage delay effect is a commonly used term for a sudden and unexpectedly large drop in a battery voltage which occurs immediately after connecting the battery to a load. After some seconds or even minutes the voltage increases (due to transformations of passive layer properties) to a normal operating value. Therefore many studies have been published on this phenomenon.

The following methods have up to now been used for investigation of LiCl passive layer properties: galvanostatic and potentiostatic method (1,2,3), x-ray diffractometry (4), micro-calorimetry (5), scanning electron microscopy (SEM) (3,6), pulse (transient) methods (7,8) and A.C. impedance spectroscopy (5,9,10). At Boris Kidrič Institute of Chemistry mainly experiments using last three methods have been carried out. Experimental details have

been published elsewhere (11, 12, 13, 14, 15). Here we report only on results and developed methods.

Generally, it is assumed that the observed extensive part of the impedance response of the passive layers is due to migration of charge carriers and electrical polarisation of the layer (11). In the case of polycrystalline ionic conductors, the extensive part of the impedance response consists of two semicircles. The lower frequency semicircle is usually ascribed to the conductivity of grain boundaries, whereas the higher frequency response pertains to the bulk conductivity (16). In (11) we showed that in the case of Li/$SOCl_2$ system the observed response of passive layer is due to intragranular (i.e.bulk) conductivity (Fig 1).

An approximate description of the impedance response corresponding to these physical processes can be obtained by using equations for a parallel plate capacitor with resistor in parallel (7,9). Such approximation, however, leads to inconsistencies with experimental data which can be summarised in three points (12):

a) The empirical equation (17) by means of which the extensive part of the impedance measurements of the passive layer can be satisfactorily described is:

$$H(\omega) = R/(1+(i\omega\tau_0)^{\alpha}) \qquad /1/$$

with $H(\omega)$ being transfer function, R resistance, τ_0 mean relaxation time, α dimensionless parameter and ω angular frequency. The empirical value of α is 0.8, while the above mentioned approximation requires a value of 1.

b) The mean relaxation time τ_0 increases considerably during film growth while according to the assumption of parallel plate capacitor τ_0 should be constant.

c) The thickness of the passive layer, calculated on the basis of the accepted assumptions, is up to 100-times smaller compared with the one observed by SEM (6).

In two recent papers (11,12) we suggested a possible explanation for the above mentioned discrepancies by taking the resistivity as a function of position while keeping the dielectric constant position independent. Our interpretation of impedance data is based on the formal representation of Eq. /1/ by the integral transformation of the transfer function:

$$1/(1+(i\omega\tau_0)^{\alpha}) = \int_{\infty}^{\infty} F(s)/(1+i\omega\tau)\, ds \qquad /2/$$

with s being a dimensionless parameter defined as $\ln(\tau/\tau_0)$ and F(s) a distribution function. In our model the distribution function in space x is regarded as normalised resistivity:

$$F(s)ds' = \rho(x)dx/SR \qquad /3/$$

with R being the layer resistance, S the layer's surface area and $\rho(x)$ position dependent resistivity. Of course, our choice expressed by equation /3/ is not uniquely determined by the transfer function $H(\omega)$ which determines only the "intensity" of different resistivities whereas their spatial arrangement depends on our model choice. The main result of our treatment is, as shown in (12), that the greater the accuracy and the frequency range of the impedance measurements, the greater is the "visible" part of the passive layer. That means that in using A.C. impedance spectroscopy of layers with position dependent resistivity it

is only correct to study those parts of the substances, which have relatively high resistivity (Fig 2).

In another set of experiments we used the A.C. impedance spectroscopy for investigation of processes accompanying the voltage delay effect. In (14) we reported that the voltage delay depended on conductive as well as on the mechanical properties of the passive layer. Actually, according to different authors, at least three processes are induced within the passive layer on its exposure to high electric fields:

a) injection of external mobile carriers (lithium ions) into the layer (8)

b) increase in layer conductivity due to excitation of carriers caused by the applied electric field (Young's equation) (1,8)

c) thermomechanical breakdown of the layer (1,5)

The fact that the above processes usually occur simultaneously causes serious difficulties in interpretations of galvanostatic and potentiostatic curves. In (15), however, we showed that by simultaneous impedance and open circuit voltage (OCV) measurements, taking place immediately after the exposure of the passive layer to electric fields of different magnitudes, it was possible to distinguish between processes a) and c).

In contrast to the processes a) and c), the relaxation time of the process b) is very short in comparison with the time needed to perform an impedance measurement. This means that the process b) cannot be studied by using the impedance method only.

From measurements of transfer functions of passive layers which underwent mechanical breakdown and injection of external mobile carriers we calculated the position dependence of resistivity of such passive layers. It was found that the higher the steady state value of resistivity, the greater was its decrease due to mechanical breakdown and injection of carriers. This phenomenon is in agreement with our model of position dependent resistivity. On the other hand, as we pointed out in (15), at highest values of resistivities either other processes prevail or the model of spatially distributed relaxation times is not valid in the corresponding frequency range.

PULSE MEASUREMENTS

A.C. impedance measurements require sophisticated and expensive equipment. Furthermore, performance of measurements and their analysis is usually slow and not very suitable for routine battery testing. Using pulse method, which is based on very simple electronics, quick and, as we found, "surprisingly accurate" acquisition of certain electrochemical parameters is possible. At least, this holds for the passive layer in the $Li/SOCl_2$ system. Here we discuss some theoretical and practical aspects of pulse method.

In following discussion we shall use a theory valid only for time invariable and linear systems (LTI systems). So, let us first define these two terms:

If $y_1(t)$ and $x_1(t)$ are any pair of functions that satisfy the constitutive relation of a system and if $y_2(t)$ and $x_2(t)$ are any other pair satisfying the same constitutive relation, then the system is said to obey the superposition principle (or equivalently to be linear) if the pair of functions $y(t) = ay_1(t) + by_2(t)$ and $x(t) = ax_1(t) + bx_2(t)$ also satisfy the constitutive relation for any choices of the constants a and b (22).

If y(t) and x(t) are any pair of functions that satisfy the constitutive relation of the system, then the element is time- invariant if y(t-T) and x(t-T) also satisfy the constitutive relation for any value of T (22).

If a system satisfies the above conditions we define it as linear and time invariable (LTI) system. On excitation of an LTI system in initial state by a delta function ($\delta(t)$), defined as:

$$\delta(t)=0 \quad t\neq 0$$
$$\int_{-\infty}^{\infty}\delta(t)dt=1 \qquad /4/$$

we obtain pulse response function h(t) of the system. By performing convolution between h(t) and an arbitrary excitation x(t) one obtains a system response y(t):

$$y(t)=\int_{0}^{\infty}h(t)\cdot x(t-\tau)d\tau \qquad /5/$$

Using Fourier transform on Eq.2, the system response is translated into frequency domain. In the frequency domain a convolution equation decays into a product of the Fourier transform of the response function $H(\omega)$ and excitation $X(\omega)$:

$$Y(\omega)=H(\omega)\cdot X(\omega) \qquad /6/$$

Eq. 6 resembles Ohm's law where the Fourier transform of the response function corresponds to resistance. $H(\omega)$ is usually referred to as a transfer function, i.e. a complex function of the real variable ω. A value $H(\omega)$ of a discrete frequency is denoted as impedance (or admittance) of the system.

In principle, transfer function of a system can be measured in two ways:

a) The system is excited by a monochromatic sine signal wherefrom the impedance of the system at discrete values is obtained. The array of such impedance values is defined as transfer function. At present, practically all commercially available measurement systems work on this principle.

b) A system is excited by frequency-reach signal, wherefrom deconvolution between the response y(t) and excitation x(t) is calculated. Thus, the pulse response function h(t) is obtained which, in frequency domain, corresponds to the transfer function $H(\omega)$:

$$H(\omega)=Y(\omega)/X(\omega) \qquad /7/$$

The excitation signal $X(\omega)$ can have an arbitrary shape.

Although used in certain important applications (e.g. NMR instruments), the latter principle has up to now not been applied in battery testing. The reason for this lies in a simple fact that for major part of batteries LTI criterion is not fulfilled, at least not in for practical use suitable amplitude and time ranges.

The Li/$SOCl_2$ system is, as seems, an exception. Namely, according to the length of measurements this system was found to be time invariable. Difficulties arise at the linearity

conditions. The principle of the measurement requires relatively high amplitudes in order to avoid noises superimposed on the response signal. However, higher amplitudes cause more nonlinearity. Beyond this, at determining the transfer function by using the deconvolution procedure a new problem arises. Frequency spectrum of a finite pulse of amplitude E and length T has a form:

$$X(\omega) = ETsin(\omega T/2) / (\omega T/2) \qquad /8/$$

It can be seen that in the vicinity of frequency values of $\omega T/2=2k\pi$, where k is an integer, the corresponding frequency components of the excitation signals take values around zero. This is a direct consequence of the system linearity condition; namely, on excitation by a zero signal one obtains zero response which means that Eq.4 is not determined at such values. In practice, this effect is also magnified by accompanying noise. Anyway, difficulties occurring by using this method are compensated for by the simplicity of the measurement equipment as well as by the promptness at acquiring results of measurements. The noise can be minimised by averaging successive results. In this case the noise decreases as square root of the number of measurements.

However, our procedure of determining the transfer function was different from the described one. Since it is difficult to obtain the correct transfer function from a transient response measurement without any idea how it should look like, we restricted ourselves to systems for which the type of transfer function is well known.

In this case the system can be described by a parametrical family of functions H_M. H_M is a model function uniquely defined by an array of parameters $g_1...g_n$. Our goal is to define parameters $g_1...g_n$ on the basis of the measured response y(t). If y(t) is determined from Eq. 6 using IFT one obtains:

$$y(t) = F^{-1}[H_M(g_1..g_n;\omega) \cdot X(\omega)] \qquad /9/$$

The parameters $g_1...g_n$ can be determined from the observed pulse response by fitting procedure. Using the model function, the problem of determining the transfer function changes from deconvolution into convolution procedure, the latter being much less sensitive to experimental noise. The method was used for characterisation of lithium passive layer in $Li/SOCl_2$ batteries. The empirical equation /1/ involving three parameters (α,τ and R) was used as the model function H_M.

The results were compared to the ones obtained by the impedance method, as well as to those obtained by fitting the response using a model function corresponding to the pure RC term (Fig. 3).

It is evident that deviations obtained by our method are essentially smaller. However, we believe that the results can still be improved by optimisation of pulse characteristics and improvement of the response measurements accuracy.

APPLICATIONS

We have already mentioned that in $Li/SOCl_2$ batteries the so - called voltage delay effect represents one of the greatest problems. In order to avoid it we synthesised two new types of electrolyte. The synthesis itself is described in (13).

According to literature (18), the corrosion rate of lithium in agressive media is determined by the ratio between the cationic and electronic conductivity. The larger the ratio the better the passivation properties and the smaller the delay effect. Conductive properties of the passive layer are directly influenced by composition of the electrolyte used (19,20,21).

When preparing an electrolyte, great care must be paid to avoid possible impurities, such as Fe and Na ions, the content of which must be as small as possible. It is well known that Fe^{2+}, if present in amounts greater than 10ppm, dopes a LiCl crystal which increases the crystal electronic conductivity(9). As the casing of our batteries consists of stainless steel, it is obvious that the battery electrolyte must be free of both HCl and water; the latter reacting with $SOCl_2$ yielding HCl and SO_2.

Properties of passive layers formed in the newly prepared electrolytes were examined using electrochemical (galvanostatic, A.C. impedance) as well as optical (scanning electron microscopy) methods.

The A.C.impedance method showed that resistances of passive layers formed in our electrolytes were several times smaller than the resistances of layers formed in the normally used $LiAlCl_4$ electrolyte (Fig. 4).

Galvanostatic measurements showed that the electrolyte A (i.e., the normal electrolyte with addition of PVC) decreased the voltage delay; by using the electrolyte B (addition of chlorosulphonic acid, which leads to formation of SO_2), however, we completely removed the voltage delay (Fig. 5).

SEM observations revealed that passive layers formed in electrolytes A and B are more compact, i.e. of less porous structure. Furthermore, in the case of electrolyte A (containing considerable amount of PVC) an additional layer, probably a sheet of PVC, was noticed. It seems that it is this layer which decisively determines conductive properties of layers formed in electrolyte A. On the other hand, the direct reason of reducing the voltage delay in the case of electrolyte B has not been established (Fig. 6).

CONCLUSIONS

An overview of contemporary research activities of the Power Sources Laboratory at Boris Kidrič Institute of Chemistry, Ljubljana is presented. At studying the lithium passive layer behavior a special emphasis was given on following topics:

1. Comparison between results obtained by using the A.C. impedance spectroscopy and those obtained by the pulse method.

2. On the basis of experimental results new models were given in order to explain migration and polarisation phenomena within the passive layer.

3. The influence of electrolyte composition on the passive layer properties was studied by using electrochemical as well as optical methods.

ACKNOWLEDGEMENT

The authors thank the Research Community of Slovenia and the ISKRA-Battery Industry "Zmaj" for financial support.

REFERENCES

1. E. Peled, in Lithium Batteries (Edited by J. P. Gabano), Academic Press, New York, p. 43 (1983).
2. J. Bressan, G. Feuillade and R. Wiart, J. Electrochem. Soc., 129, 2649(1982).
3. W. P. Hagan, N. A. Hampson and R. K. Packer, J. Power Sources,24, 95, (1988).
4. L. Friedmann, W. P. Wetter, J. Chem. Soc. (A), p. 36 (1967).
5. J. Phillips and J. Gibbard, in H. V. Venkatasetty (ed.), Proc. Symp. Lithium Batteries, Vol. 4, The Electrochemical Society, Pennington NJ, 1981, p. 54.
6. J. W. Boyd, J. Electrochem. Soc., 134, 18 (1987).
7. R. V. Moshtev, Y. Geronov and B. Puresheva, J. Electrochem. Soc., 128, 1851 (1981).
8. F. M. Delnick, in Proc. Symp. Lithium Batteries, Vol. 88-6, Pennington NJ, 1988, p. 212.
9. M. Mogensen, J. Power Sources, 14, 53 (1987).
10. J. Thevenin, J. Power Sources, 14, 45 (1985).
11. M. Gaberšček, J. Jamnik, S. Pejovnik, J. Power Sources, 25, 123 (1989).
12. J. Jamnik, M. Gaberšček, S. Pejovnik, Electrochim. Acta, in print.
13. M. Kovač, S. Pejovnik, Elektrotehniški Vestnik, 55, 275 (1988).
14. M. Gaberšček, J. Jamnik, S. Pejovnik, ibid., p. 271.
15. M. Gaberšček, J. Jamnik, S. Pejovnik, to be published in Proc. 1st International Symp. on EIS, Bombannes, May 22-26, 1989.
16. P. G. Bruce, R. W. West, J. Electrochem. Soc., 130, 662 (1983).
17. K. S. Cole and R. H. Cole, J. Chem. Phys., 9, 341 (1941).
18. A. M. Hermann, Proceedings of the Symposium on Lithium Batteries, (Ed.: H. V. Venkatasetty), The Electrochemical Soc. Inc., Pennington NJ, 1981, p. 83
19. N. A. Fleischer, S. M. Manske, in Lithium Batteries, Ed. A. N. Dey, Chap. 3, Electrochem. Soc. Inc. (1984).
20. S. D. James, ibid., Chap. 2
21. D. Vallin, P. Chenebault, Proceedings of 32nd Power Sources Symp., The Electrochemical Society Inc., Pennington NJ, 1986, p. 481.
22. W. McC. Siebert, Circuits, Signals, and Systems, McGraw-Hill, 1986, p. 4.
23. A. K. Jonscher, Dielectric Relaxation in Solids, Chelsea Dilectric Press, 1983, p. 192.
24. R. M. Fuoss, J. G. Kirkwood, J. Am. Chem. Soc., 63, 385 (1941).

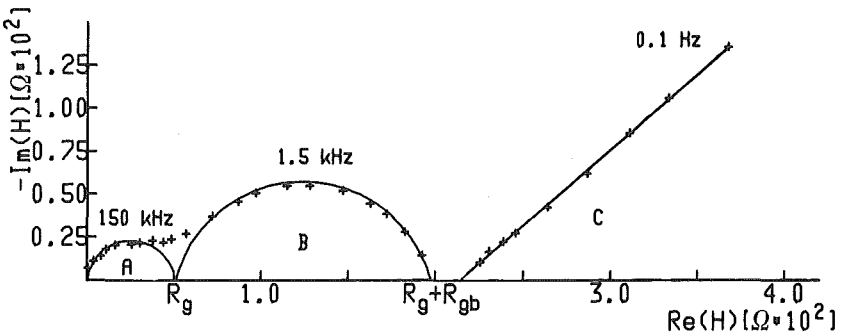

Fig.1. Transfer function of a superionic conductor at 59°C.
A-impedance response of grains (intragranular response)
B-impedance response of grain boundaries
C-impedance response due to diffusion of charge carriers

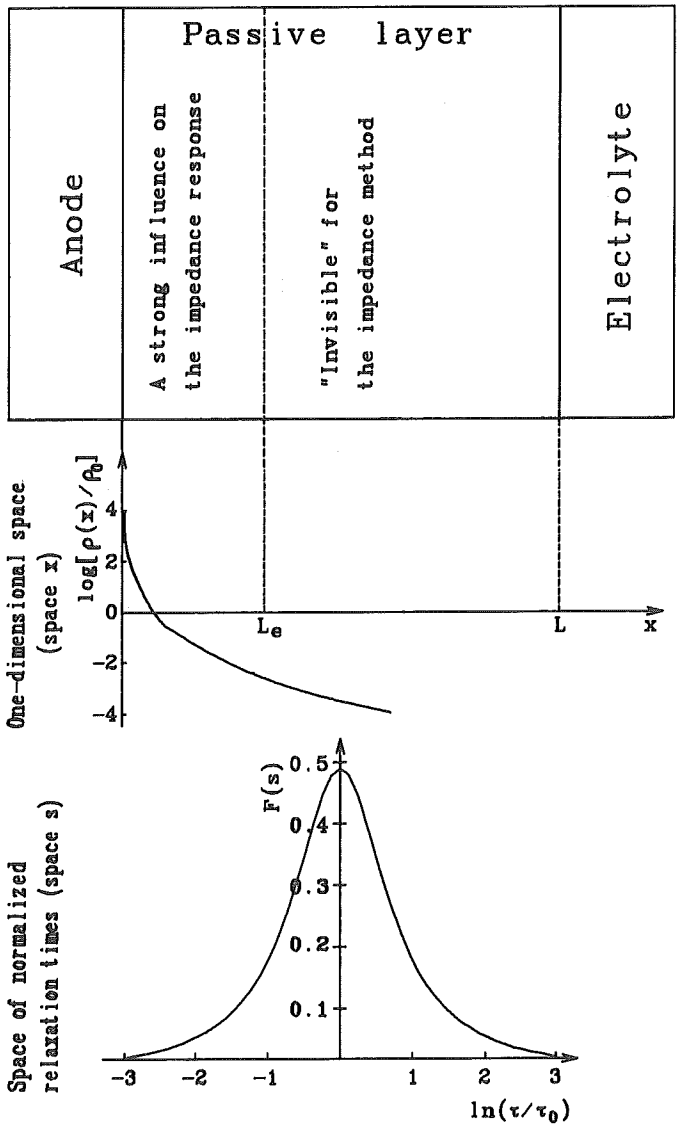

Fig. 2. A scheme of the passive layer which represents an interface between the anode and electrolyte. Although the layer was formally divided into two sheets, it should be noted that the corresponding A.C. response in the complex plane is only one semicircle. The influence of the part with low resistivity is noticeable only at high frequencies. We also show spaces s and x with corresponding representations of relaxation times (resistivities).

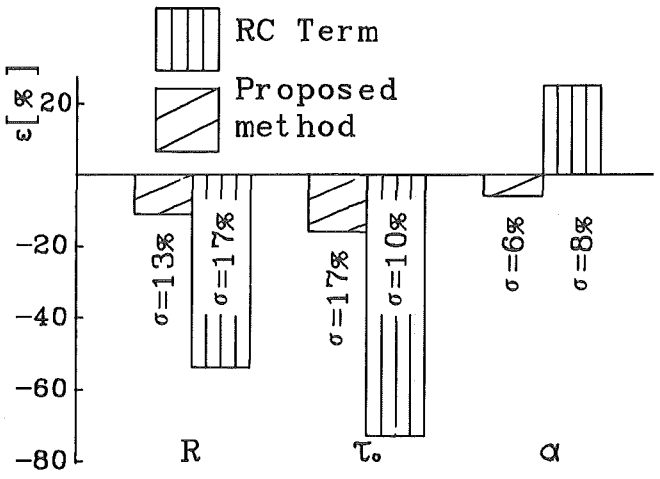

Fig. 3. Comparison between the results of different methods for determining parameters R, α and τ_o.

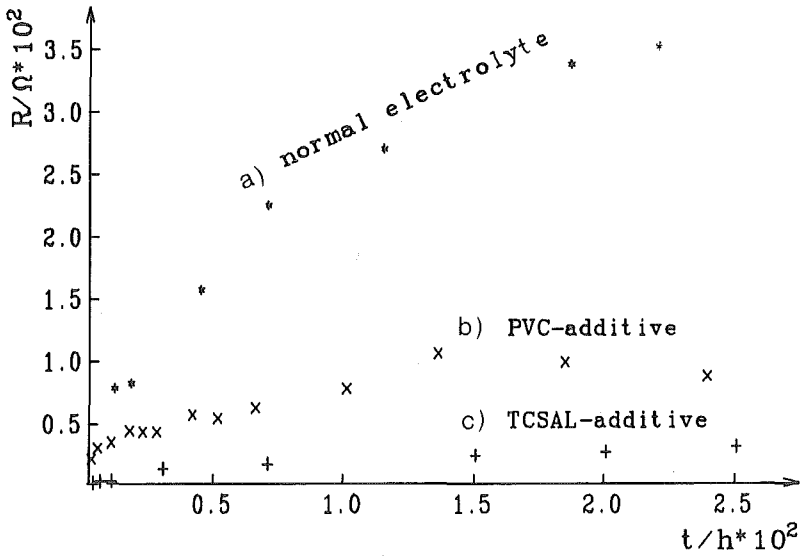

Fig. 4. Time dependence of the passive layer resistance
a) in electrolyte without additives
b) in electrolyte A (addition of PVC)
c) in electrolyte B (addition of TCSAL).

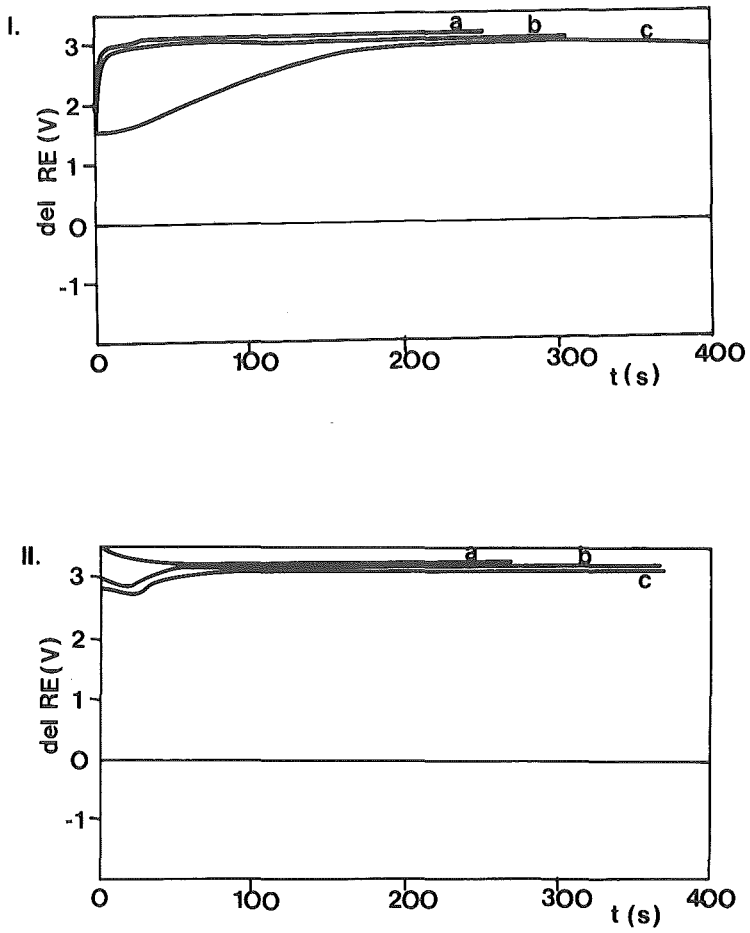

Fig. 5. I. Time dependence of battery voltage at constant discharge current (current density = 3mA/cm^2) for batteries containing electrolyte A:
a) layer resistivity R = 7469Ωcm^2; battery stored for 30 days at ambient temperature
b) R = 4672Ωcm^2; battery stored 14 days at ambient temperature and 20 days at -28°C
c) R = 8730Ωcm^2; battery stored 14 days at ambient temperature and 14 days at 72°C

II.Time dependence of battery voltage at constant discharge current (current density = 3mA/cm^2) for batteries containing electrolyte B:
a) layer resistivity R = 430Ωcm^2; battery stored for 30 days at ambient temperature
b) R = 998Ωcm^2; battery stored 14 days at ambient temperature and 20 days at -28°C
c) R = 5370Ωcm^2; battery stored 14 days at ambient temperature and 14 days at 72°C.

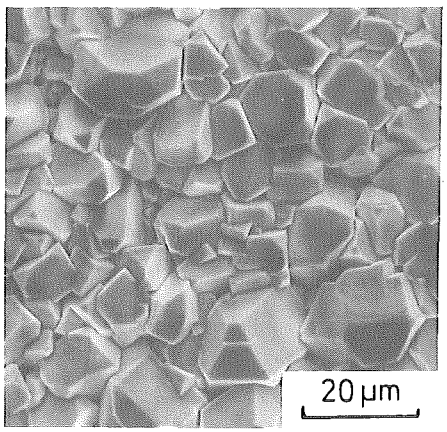

a)

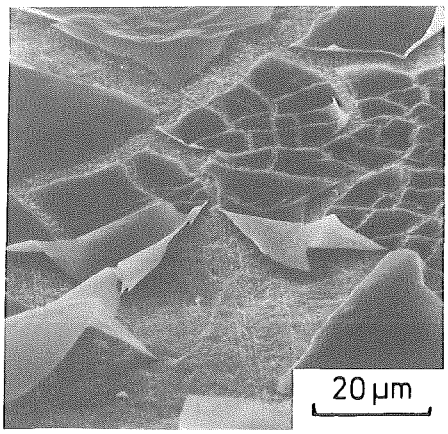

b)

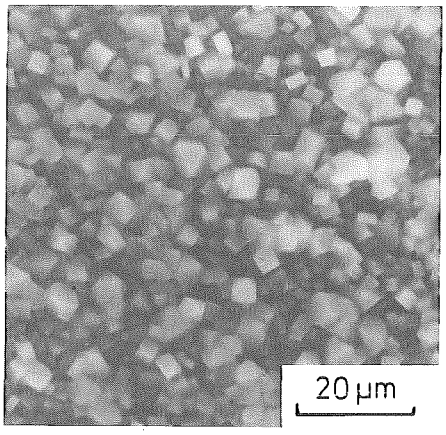

c)

Fig.6. a)Passive layer formed on lithium after 14 days of exposure in electrolyte without additives at ambient temperature. Magnification 1000X.

b) Passive layer formed on lithium after 20 days of exposure in electrolyte A at ambient temperature. Thin PVC sheets are clearly seen. Magnification: 1000X.

c) Passive layer formed on lithium after 14 days of exposure in electrolyte B at ambient temperature. Magnification: 1000X.

REDUCTION OF CHROMIUM (VI) WHEN SOLAR SELECTIVE BLACK CHROMIUM IS DEPOSITED

D. Slavkov, B. Popov and Z. Koneska
Faculty of Technology and Metallurgy, University "Kiril and Metodij", 91000 Skopje, Yugoslavia

Introduction

The cost of the collector often constitutes the major part of the total costs of a system for solar energy photothermal conversion. The development of an efficient and reliable solar collector is therefore one of the main problems in the field of the development of thermal applications of solar energy. At the same time, one should have in mind that the production of such collector must be at an economically acceptable cost.

An efficient collector should absorb almost all incident solar radiation and should have thermal losses by convection, conduction and radiation as small as possible. In this respect the radiation losses are most significant and they completely depend on the optical characteristics of the absorbing surface. The most attractive method of limiting the radiation losses from a collector is the use of a selective absorbing surface. Since 1956 when Tabor (1) originally recommended the application of a such surface as absorbing surface, a lot of work has been done in this field (2-6). An ideal selective surface is totally absorbing, or black to incident solar radiation and totally reflecting, or white to the infra-red radiation emitted by a black body at the temperature of operation of the collector. However, an ideal selective surface does not exist in practice, and therefore one can conceive real surface whose spectral reflection coefficient varies with wavelenght in a manner close to that of an ideal black body. Such surface can be characterized by its solar absorbtance $a_{(s)}$ and its thermal emittance $e_{(T)}$, which are respectively described by the following relations:

$$a_{(s)} = \frac{\int_0^\infty \alpha(\lambda,T)\, E^S(\lambda)\, d\lambda}{\int_0^\infty E^S(\lambda)\, d\lambda} \qquad (1),$$

$$e_{(T)} = \frac{\int_0^\infty \varepsilon(\lambda,T)\, M^0(\lambda,T)\, d\lambda}{\int_0^\infty M^0(\lambda,T)\, d\lambda} \qquad (2),$$

where $\alpha(\lambda,T)$ and $\varepsilon(\lambda,T)$ are, respectively, the hemispherical spectral absorptance and emittance, $E^S(\lambda)$ the spectral solar irradiance and $M^0(\lambda,T)$ the spectral emittance of the black body at temperature T.

In addition, a selective solar absorber should also be sufficiently mechanically, thermally and chemically stable so that it does not deteriorate under operating and stagnation conditions. These conditions depend on the design of the collector and on the working conditions, as first on the operating temperature range. In this respect it is clear that the physico-chemical properties of a selective surface of a flat plate absorber operating at low or medium temperature range will be different from those required for the absorber of a concentrating collector operating in the high temperature range. In the first case the solar absorption coefficient must be as close to unity as possible, while a low thermal emittance is of secondary importance. In the case of a high temperature range absorber keeping a low thermal emittance is also important as having a high solar absorption coefficient. And finally, it must be pointed out that the process for obtaining such selective surfaces must be suitable for serial production of large absorbers, and it must be economically acceptable, taking into acount the increase in conversion efficiency brought about by selectivity.

The process of electroplating of black chrome in our days is the most common process for preparing such selective surfaces, which are used for medium and high photothermal conversion temperature range.

Experimental

The classical process of chromium deposition begins simultaneously with formation of the oxide layer which rapidly deteriates permiting the access of Cr(VI) ions to the cathode and their reduction to metallic chromium. The sulphate ions present in conventional chroming bath favor the elimination of this preliminary oxide layer (7). According to Saiddington and Hoey (8), reduction of pure chromic acid in the absence of sulphate ions results in formation of an amorphous oxide film which grows on the cathode. This film prevents the metal reduction processes from taking place on the cathode surface, while allowing the reduction of hydrogen only. The existence of such films has been proved by double layer capacity measurements (9) and optical microscope studies (10).

The deposition of black chromium is generally done with conventional chroming bath free from sulphates, to which catalyst such as acetic acid, sodium nitrate, amonium methavanadate or fluorine compounds are added (4, 5, 11). The exact mechanism by which the catalyst ions enable chromium reduction which leads to formation of black chrome deposits is still open to conjecture.

One of the most common comercial solution for black chrome deposition is ChromOnyx plating solution from the Harshaw Chemical Co. (12), which contains acetic acid as catalyst. But, as reported in literature (3), this solution may lead to production of black chrome surfaces with different optical properties as a result of degradation processes of the catalyst. Because of this, we have tried another formulation of plating bath containing fluorine compounds as catalyst.

In order to establish the influence of the constituents as well as that of the catalyst on the process of reduction of chromic acid, measurements of rest potential at open circuit and cyclic voltammetry measurements were made. All C.V. experiments were performed in a special tephlon cell because of the presence of fluorine ions. Working electrodes of Pt mounted into a tephlon holder with a geometric area of $6.2 \cdot 10^{-3}$ cm^2 were used. The working electrodes were mechanically polished, ultrasonically cleaned in in alcohol and rinced with destilled water prior each measurement. SCE was used as a reference electrode. Black

chrome was electrodeposited from a solution containing 4 M CrO_3 and 0,05 M $BaCO_3$ in presence of fluorine ions. The fluorine compounds were added in the cathode compartment during the course of the run.

Results and Discussion

Rest potential observed on Pt cathodes in chromic acid solutions with fluorine ions additions are listed in Table I. The rest potentials are probably mixed potential of the reduction of dichromate ion and oxidation of Pt. PtO formed in a such way is further reduced when the cathode is polarized at negative potentials.

Table I

Rest potential values obtained on Pt electrode in chromate solutions catalyzed by F^- ion

Solution	F^- Conc. M	E/V vs SCE
	0.024	1.043
	0.048	1.020
	0.078	1.025
$H_2Cr_3O_{10}$ 4M	0.115	1.015
	0.166	1.010
	0.261	1.010
	0.357	1.015

Fig. (1) shows typical C.V. curves for electrodeposition of black chrome from pure chromic acid solution (4M) in which only 0.05 M $BaCO_3$ was added in order to precipitate $SO_4^=$ ions. The scans were initiated at -0.2 V vs SCE with different sweep rates. As it can be seen from Fig. (1), C.V. curve shows a cathodic maximum at -0.9 V which is formed during cathodic course of the run, which can be attributed to the process of reduction of Cr(VI) ions. There is no evidence of corresponding anodic peak during anodic course of the run, which means that the product formed on the cathode can not be dissolved during anodic course of the run. Repetitive cycles (curve 2 on the same figure) shows no more cathodic peak at -0.9 V, and evidence only

for hydrogen evolution exists, which indicates that the electrode became completely passive during anodic course of previous cycle.

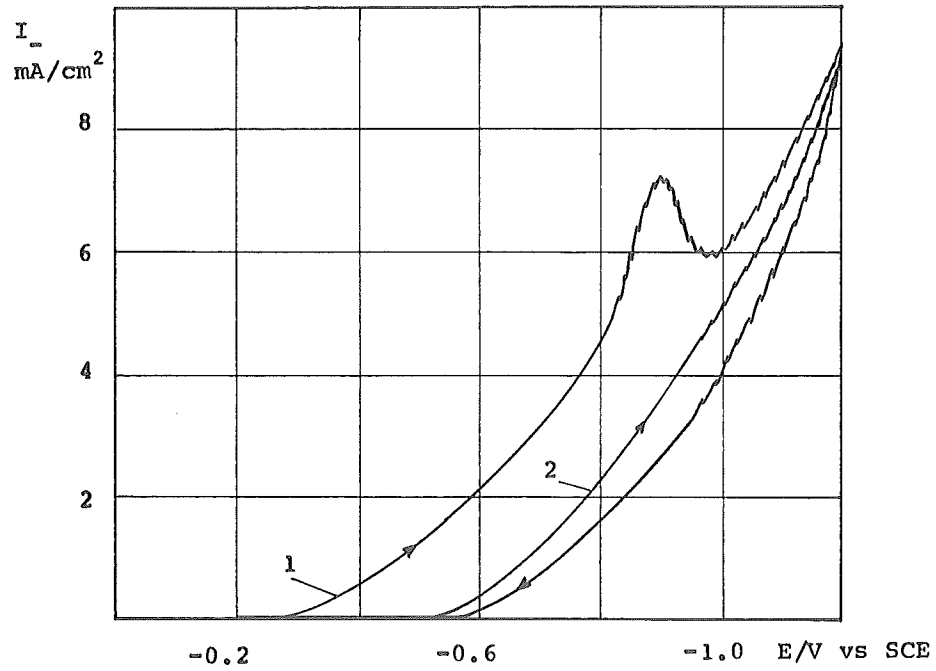

Fig. (1) Typical C.V. curve for electroreduction of pure chromic acid; v=50 mV/s, 1. first cycle, 2. second cycle

Fig. (2) shows cyclic voltammograms taken at 0.02 V/s for electrochemical reduction of chromic acid at different concentrations of fluorine ions (from 0.074 to 0.357 M). In the presence of catalyst ions two more cathodic peaks appear at -0.35 V and at -0.50 V vs SCE. It has been found that the first one is not depended on the concentration of fluorine, but, it appears only at concentrations higher than 0.35 M. On the other hand the peak height at -0.50 V depends on the concentration of fluorine ions, but this dependence does not suggest that the process is diffusion controlled.

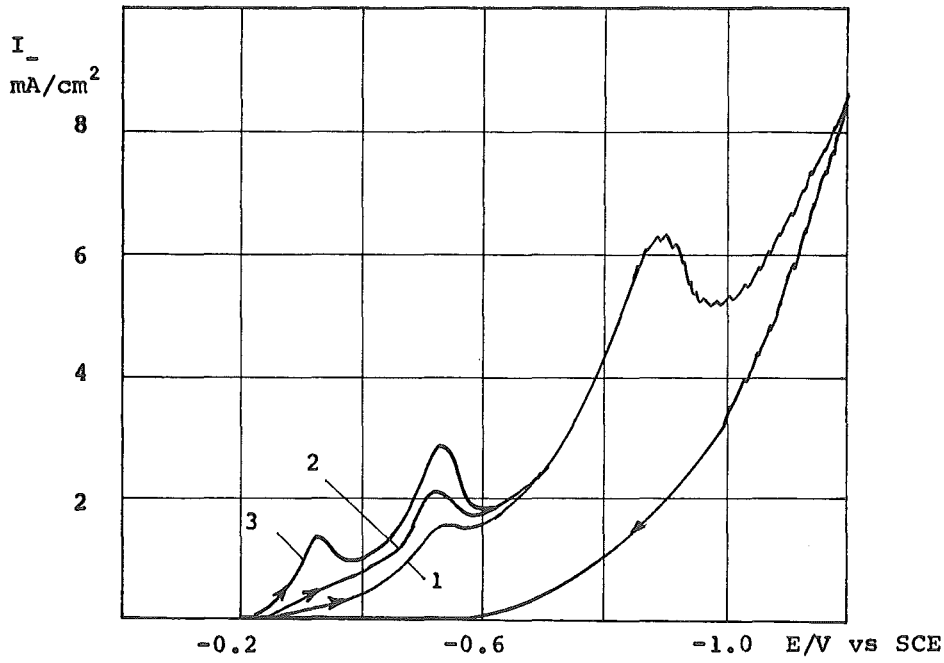

Fig. (2) Cyclic voltammograms taken at different concentrations of fluorine ions; 1. 0.074M, 2. 0.256M, 3. 0.357 M

In order to see what is going on at the electrode surface when these processes take place, optical microscope investigations were made on the electrodes held at a potential of -0.35 V, -0.50 V and -0.9 V respectively. In each case no evidence was found that some type of deposit is formed on the Pt surface under these conditions. Evidence of "black chrome" deposit on the Pt surface was found only in the case when electrode was polarized at potentials more negative than -1.1 V vs SCE. But, in the case when no cathodic maximum at -0.35 V was observed, dark greyish deposits were obtained, while when concentration of fluorine was 0.35 M or higher, completely black deposits were obtained. This means that each of the processes plays a specific role in the whole process which leads to a formation of black chrome deposits. Detailed investigations of these three processes is still going on.

On the basis of these preliminary C.V. measurements we have formulated our own composition of chromate bath, which was used for electrodeposition of black chrome, in order to use such deposits as a selective surface material for covering collector tube (3.5 m long and 3 cm in diameter) of a concentrating trough collector which is developed at Metalski Zavod TITO in Skopje.

In order to determine the optimal operating conditions of electrolysis under which selective black chrome surface appears, spectral reflectance of black chrome deposits on nickel plated copper was measured as a function of deposition parameters.

Normal reflection spectra of the samples were measured on the Perkin-Elmer Model 180 spectrophotometer equipped with reflection cells. A gold mirror was used as reference for reflection for measuring the reflectivity of the samples. The measured spectral range was from 2.5 μm to 50 μm. The reflection spectra of the samples in the range between 0.4 μm and 2.5 μm has been measured with Opton II instrument equiped with an integrating sphere for measurement of the hemispherical reflectivity.

A computer program for PDP-11 computer was used for calculation of the normal thermal emittance (e_T) and the hemispherical absorptance ($\hat{a}_s$) from specular normal and hemispherical reflectivities according to the formulas:

$$e_T = \frac{\int_{0.3\,\mu m}^{\lambda_c} P(\lambda,T)\cdot(1 - r_\lambda)\,d\lambda}{\int_{0.3\,\mu m}^{\lambda_c} P(\lambda,T)\,d\lambda} \qquad (3)$$

$$\hat{a}_S = \frac{\int_{\lambda_c}^{50\,\mu m} P(\lambda,T)\cdot(1 - \hat{r}_\lambda)\,d\lambda}{\int_{\lambda_c}^{50\,\mu m} P(\lambda,T)\,d\lambda} \qquad (4)$$

For opaque materials (transmittance $\tau=0$) to which black chrome deposits belong spectral absorptance for directional incidence and the directional emittance can be calculated from the spectral.

reflectance for directional irradiation as:

$$a_S = \varepsilon = 1 - r \qquad (5).$$

Fig. (3) shows reflection spectra of two black chrome deposits prepared onto nickel plated copper at 0.5 A/cm^2 for 1 min (curve 1) and 2 min (curve 2). in "as prepared" state. It is obvious that specimen 1 has better optical characteristics, which can be explained with thickness of obtained black chrome deposits.

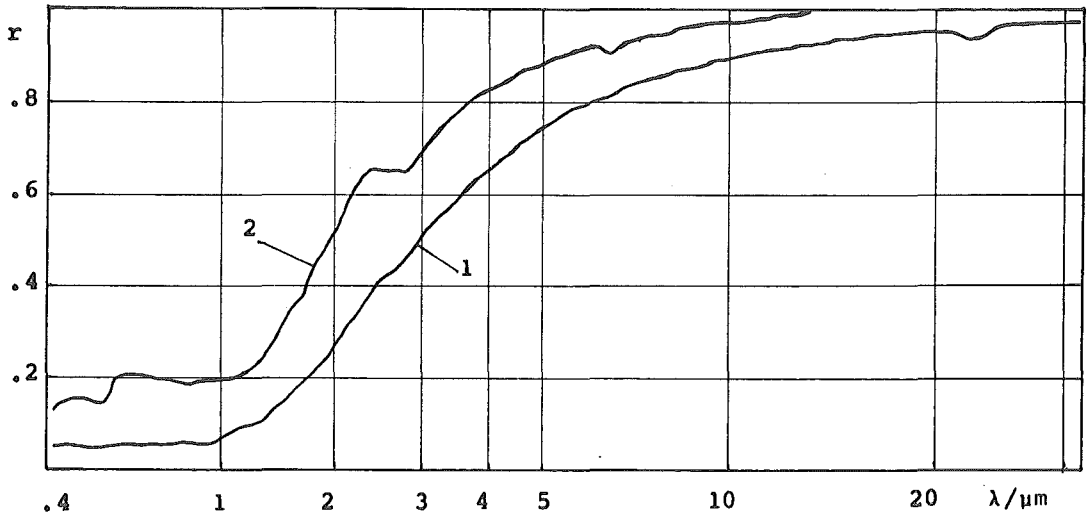

Fig. 3 Spectral reflectance of black chrome coatings

Variation of optical properties of these two black chrome specimens is given in Table II.

Table II

Optical properties of black chromium deposits (1. 1 min, 2. 2 min)

Optical properties	1	2
a_S	0.916	0.928
e_T (40 °C)	0.039	0.100
a_S/e_T (40 °C)	23.490	9.280
e_T (200 °C)	0.100	0.167
a_S/e_T (200 °C)	9.160	5.650

AES measurements have revealed Cr and O and some F to be the main constituents of obtained black chrome deposits, while some S, C and Ca was found only as impurities and after some ion bombardement the peaks of these elements have disappeared from the spectra. This is in agreement with literature data (2, 3, 11) that black chrome deposits consist of metallic chromium particles dispersed in a matrix of chromium oxides.

In order to check the thermal stability of black chrome coatings two different types of thermal treatment have been used. In the first one black chrome specimens were heated up to 450 ^{o}C for 10 hours in electrical furnace at an air atmosphere. In the second serie heating was done in a medium vacuum (better than 10^{-2} torr). From the AES spectra of thermally treated specimens, as well as from SEM investigations we have concluded that our black chrome is stable up to 350 ^{o}C. Prolonged heating over this temperature especially in an air atmosphere will result in oxidation of small metallic chromium particles, so that after 5 hours heating at 500 ^{o}C no metallic chromium in black chrome deposit was found. This will result also in degradation of selective optical responce.

Fig. (4) gives the surface morphologies of black chrome deposit as defined by SEM. Dendritic growth of the chromium particles is obvious. This is rather different structure from the structure of black chromium coatings deposited from acetic acid baths reported in literature (2, 6). Fig. 4a and b represent surface structure of "as-plated" specimens, and 4c and d structure of thermally treated specimens. As it can be seen from Fig. 4c and d thermal treatment at lower temperatures (400 ^{o}C) leads to formation of microcracks . Higher temperature thermal treatment results in complete structure degradation of black chrome deposits.

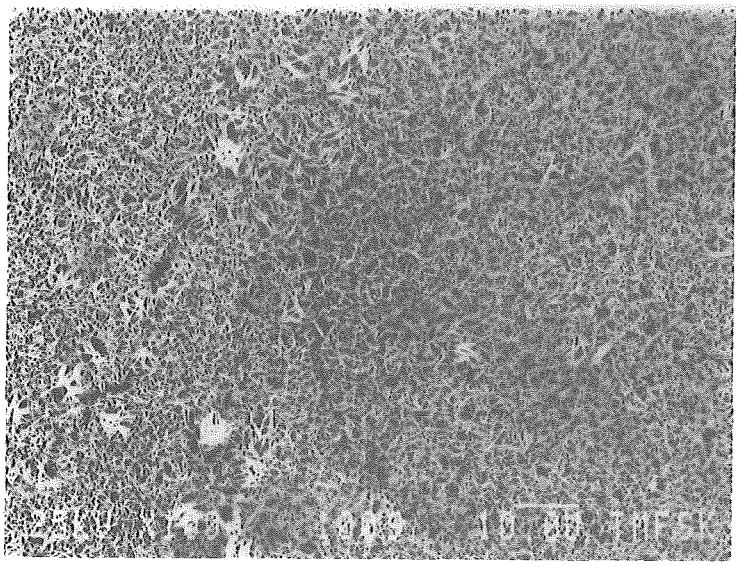

A

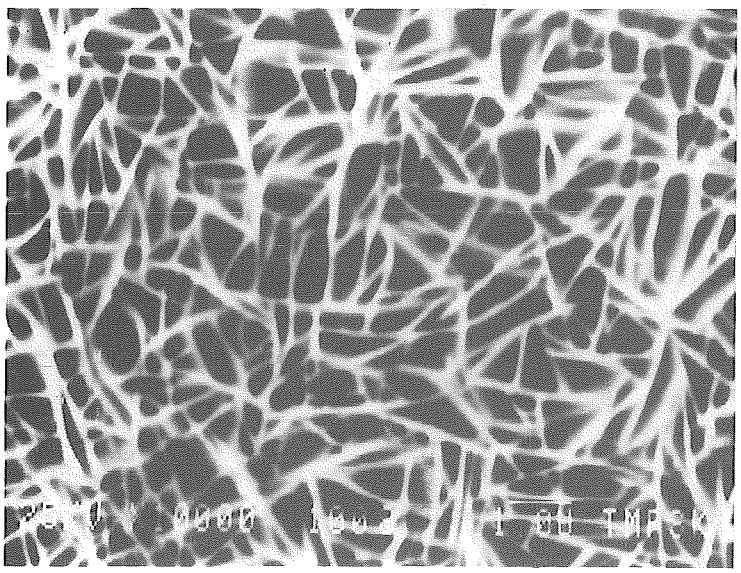

B

Fig. 4
SEM micrographs of black chrome deposits in "as-plated" state

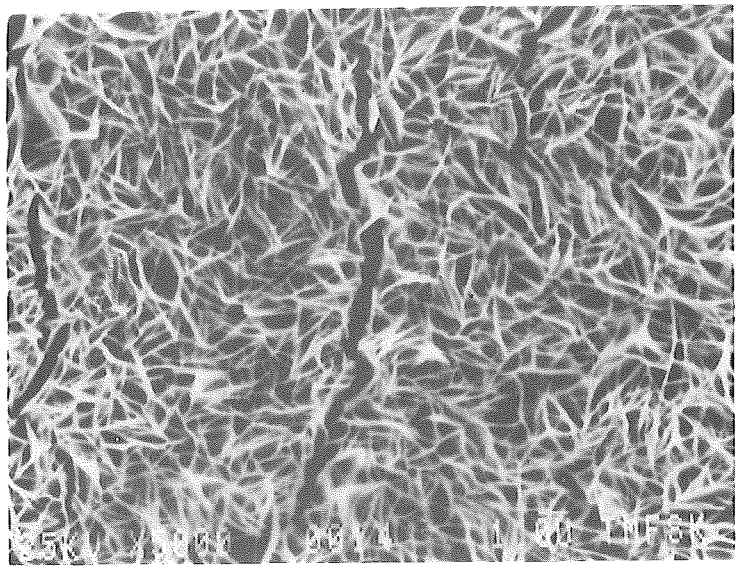

C

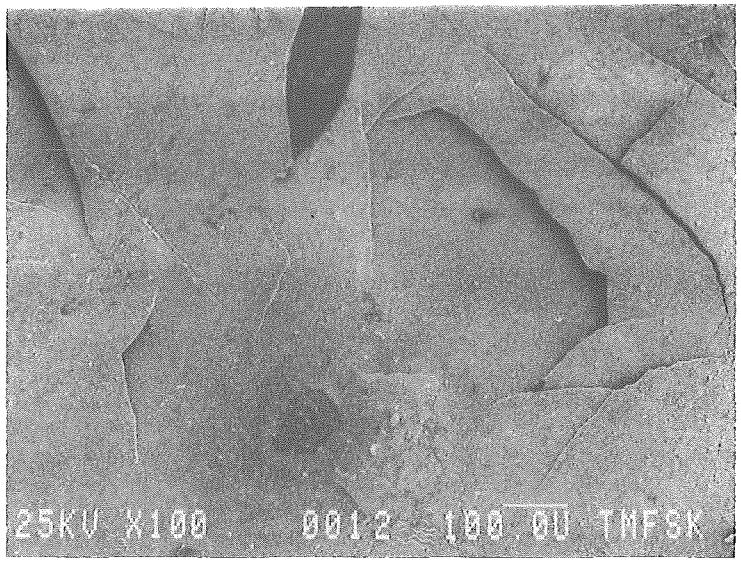

D

Fig. 4
SEM micrographs of black chrome deposits after thermal treatment

References

1. H. Tabor, Trans.Conf. on the Use of Solar Energy, 1955, Vol.2 University of Arizona Press (Arizona, 1958)
2. Lampert C.M. and Washburn J., Solar Energy Materials, 1-1, 82 (1979)
3. G.B. Smith and A. Ignatiev, Solar Energy Materials, 2 (1980) 461-467
4. Carl M. Lampert, Thin Solid Films, 7 (1980) 75-83
5. G.B. Smith, G. Zajac and A. Ignatiev, Solar Energy, Vol.29, No 4 (1982) 279-289
6. D. Bacon and A. Ignatiev, Solar Energy Materials, 9 (1983) 3-19
7. G. Dubpernell, Plating, 47 (1960) 35
8. J.C. Saiddington and G.R. Hoey, J.Electrochem.Soc., 117 (1970) 1001
9. J.A. Soloveva and A.T. Vagramyan, Zh.Fiz.Khim., 36(1962) 711
10. J.C. Saiddington and G.R. Hoey, J.Electrochem.Soc., 120 (1973) 1475
11. J. Spitz, Tran Van Danh and A. Aubert, Solar Energy Materials, 1 (1979) 189-200
12. The Harshaw Chemical Co., 1945 E. 97th St., Cleveland OH 44106

PHASE DIAGRAMS

Thermodynamic Optimization of Phase Diagrams

Hans Leo Lukas and **Rada Novaković***

Max-Planck-Institut f. Metallforschung, Inst. f. Werkstoffwissenschaft, PML, Heisenbergstr. 5, D–7000 Stuttgart 80

* Serbian Academy of Science and Art, Institute of Technical Science, Knez Mihajlova 35/IV, YU–11000 Beograd

Abstract

For the computer calculation of phase diagrams first the thermodynamic functions must be expressed by analytical descriptions. These descriptions contain specific heat C_p, enthalpy H, entropy S, and Gibbs energy G as well as integral and partial functions. As these functions are correlated, the analytical descriptions must satisfy these correlations.

The descriptions may either be based on physical models, or are only curve fitting formula. Usually the main part of the description should be based on a model, but for deviations from the pure models or for additional minor effects curve fitting expressions may be used.

The analytical expressions of higher order solution phases are mainly based on the binary descriptions. Deviations from these extrapolated binary descriptions may be calculated by adding higher order correction terms.

The adjustable coefficients of these analytical descriptions are fitted to experimental values. Thermodynamic values like calorimetrically measured enthalpies or chemical potentials measured by e.m.f. or vapor pressure as well as phase diagram values are used. A least squares program for this purpose was written at Stuttgart.

Some problems of this least squares calculation are discussed, like the weighting of the different measurements and the decision, which coefficients can be adjusted by a given set of measurements. Some measurements are related to such combinations of thermodynamic functions, which are difficult to be analysed by conventional methods, but they can be used for the least squares optimization.

If all the adjustable coefficients are determined, single equilibria can be calculated, which may be combined to a whole phase diagram.

For the practical importance of the thermodynamic calculation of phase diagrams three topics are discussed.

1) Thermodynamically optimized phase diagrams are consistent as far as possible with all measured values and therefore are the most reliable ones.
2) Starting from the binaries approximately higher order phase diagrams can be calculated, which may be optimized by relatively few experimental data.
3) The analytical descriptions and the optimized coefficients easily can be stored in a computer data bank and retrieved from there.

An example of the usage of this method is given in the next lecture, the optimization of the Na–Tl system.

Analytical Descriptions

The computer calculation of phase diagrams is based on thermodynamics. With the usual side conditions of constant temperature, pressure and amounts of the components the equilibrium is determined by a minimum of the Gibbs energy.

To do such a calculation by computer, first the Gibbs energy must be expressed in a suitable form, that is an analytical description. The total Gibbs energy is expressed by summing up the molar Gibbs energies times the amounts of the individual phases present in the equilibrium. The molar Gibbs energies of the single phases are functions of temperature and composition, the pressure dependence usually is neglected in condensed metallic systems.

Models and Curve Fitting Expressions.

The analytical descriptions can be either based on physical models or may be pure mathematical curve fitting formulas. The formulas based on models are preferable for two reasons:

1) They usually need less adjustable coefficients than approximation formulas.

2) If the description has to be extropolated outside the range, where it is adjusted to experimental values, formulas based on models are much safer in use, than pure approximation formulas.

In reality not all features of the G vs. T or G vs. x curves can be described by models. Then at least the general shape of this function should be given by a model. Deviations due to secondary or minor effects may be added using curve fitting formulas.

Temperature Dependence

For the temperature dependence of the thermodynamic functions of a pure element the relevant model is the Dulong-Petit rule. It assumes a constant molar heat capacity C_p. It is approximately valid above the Debye temperature. As nearly no phase diagram data are relevant below the Debye temperatures of the components, this is a suitable basic model. Deviations are described by a power series of the temperature T, most often restricted to the powers -2, 0, 1 and 2 [67Kub]:

$$C_p \approx C + D \cdot T + E \cdot T^{-2} + F \cdot T^2 \qquad (1)$$

The coefficients C, D, E and F are adjustable constants. Only in the case of ferromagnetism, antiferromagnetism or chemical ordering this description is not sufficient above the Debye temperature.

The functions enthalpy H, entropy S and Gibbs energy G are derived from this description by the formulas:

$$H = \int_{T_0}^{T} C_p \, dT + H_0, \qquad S = \int_{T_0}^{T} \frac{C_p}{T} \, dT + S_0, \qquad G = H - T \cdot S \qquad (2)$$

giving with the same adjustable constants and two additional ones A and B:

$$\begin{array}{lllllll} H & = A & & + C \cdot T & + \frac{D}{2} \cdot T^2 & - E \cdot T^{-1} & + \frac{F}{3} \cdot T^3 \\ S & = & B & + C \cdot \ln T & + D \cdot T & - \frac{E}{2} \cdot T^{-2} & + \frac{F}{2} \cdot T^2 \\ G & = A & + B & + C \cdot T \cdot (1 - \ln T) & - \frac{D}{2} \cdot T & - \frac{E}{2} \cdot T^{-1} & - \frac{F}{6} \cdot T^3 \end{array} \qquad (3)$$

Concentration Dependence

To describe the concentration dependence of G of a binary system the simplest model is the ideal solution:

$$^{id}G \quad = \quad \sum_{i=1}^{n} {}^{\circ}G_i \cdot x_i \; + \; R \cdot T \cdot x_i \cdot \ln(x_i) \qquad (4)$$

But, except for the gas phase at high temperatures and low pressures (at or below 1 bar), it is not sufficient. Therefore an excess Gibbs energy is added, which may be expressed by a polynomial of the concentration x, in the meaning of a curve fitting formula.

The simplest polynomial defines the so called regular solution. But this regular solution may be considered also as a model and not only a curve fitting formula. Here random mixing is assumed and to each pair of neighbour atoms a "bonding energy" is attached. If that bonding energy is constant for each type of neighbour pairs, we get the regular solution:

$$^{reg}G \quad = \quad ^{id}G \; + \; x \cdot (1 - x) \cdot K \qquad (5)$$

The regular solution coefficient K is just the difference of the bonding energy of a A-B pair to the mixture of A-A and B-B pairs, multiplied by the number of bonds in one mole of atoms.

We may drop the assumption of constant bonding energy, which means the bond energy depends on the surrounding of the bond. That may be described by replacing the constant regular solution parameter K by a function of the concentration, for example a polynomial. The polynomial preferably should be symmetric in x and $1-x$. Such a polynomial is the Redlich Kister description [48Red]:

$$G \quad = \quad ^{id}G \; + \; x \cdot (1 - x) \cdot \sum_{\nu=0}^{m} K_\nu \cdot (1 - 2x)^\nu \qquad (6)$$

All the parameters, ${}^{\circ}G_i$ of eq. (4), K of eq. (5) and K_ν of eq. (6) are expressed as functions of temperature after eq. (3). For K and K_ν usually linear functions of T (terms A and B of eq. (3) only) are used.

Other models, which shall not all be described in detail here, are the associate model for liquids or the Wagner Schottky model for strongly ordered solid phases. G vs x curves derived from these models cannot well be described by taking the Redlich Kister equation as a curve fitting formula.

Because of its use in the following contribution, the Wagner Schottky model [30Wag] will be shortly described here. In an ideal binary compound the two elements strictly occupy different lattice sites. Now so called "defects" are assumed, which are either vacancies, interstitial atoms or "antistructure atoms", which means atoms on the sites of the other element. Each defect has an enthalpy and entropy and therefore also a Gibbs energy of formation, which are assumed to be concentration independent. The defects are distributed randomly on their sublattices and contribute to the configurational entropy. Only those two defects with the smallest Gibbs energy of formation are assumed to be significant, one for deviation from stoichiometry to A (A interstitials, B vacancies or A antistructure atoms) and one for deviation from stoichiometry to B (B interstitials, A vacancies or B antistructure atoms). In the case of A and B antistructure atoms the Gibbs energy is:

$$\begin{aligned} G \quad = \quad & \\ & {}^{\circ}G_1 \cdot (1-x) \; + \; {}^{\circ}G_2 \cdot x \; + \\ & + \; G^* \; + \; G_{12} \cdot n_{12} \; + \; G_{21} \cdot n_{21} \; + \\ & + \; R \cdot T \cdot (n_{11} \cdot \ln y_{11} \; + \; n_{12} \cdot \ln y_{12} \; + \; n_{21} \cdot \ln y_{21} \; + \; n_{22} \cdot \ln y_{22}) \end{aligned} \tag{7}$$

where G^*, G_{12} and G_{21} are the molar Gibbs energies of formation of the ideal compound and of the defects respectively, n_{ij} the moles of element i on sublattice j per one mole of atoms and the y_{ij} the site fractions $y_{ij} \; = \; n_{ij} / \sum_j n_{ij}$.

The first line describes the reference state to which G^* and the G_{ij} are referred to, the second line describes the formation of all species present and the third line describes the configurational entropy.

By the relations:

$$n_{11} \; = \; 1 - \xi - y \quad n_{21} \; = \; \xi - x + y \quad n_{12} \; = \; y \quad n_{22} \; = \; x - y \tag{8}$$

all the n_{ij} and therefore also the y_{ij} are related to the ideal composition of the compound ξ, the real composition of the sample x, and one additional parameter y.

By the condition $\partial G / \partial y = 0$ y implicitely is defined as a function of x, of the temperature T and of the parameters G^* and G_{ij}. The value of y can be calculated by Newton's method.

Concentration Dependence in Higher Order Systems.

Describing the Gibbs energy G of a ternary phase, the three descriptions of the binary subsystems are combined. Different formulas are proposed for that (Kohler [60Koh], Toop [65Too], Bonnier [60Bon], Muggianu [75Mug], ...), which give slightly different results. Two principles are used to construct these formulas, which are contradictory except for the regular solution: (i) the three binary subsystems shall be treated equally and, (ii) if the two elements B and C become equal, the description shall reproduce the binary A–B = A–C system in the whole "ternary" range.

Deviations between experimentally derived G values and those calculated by one of these formulas may be expressed by a curve fitting polynomial with the common factor $x_1 \cdot x_2 \cdot x_3$. This polynomial vanishes in any of the binary boundary systems.

Binary descriptions based on other models may have their own extrapolation formulas into the ternary, based on the model itself.

In quaternary and higher systems generalizations of the formulas of Kohler, Muggianu, Toop or Bonnier are used. Also correction polynomials can be used. By a common factor containing all the concentrations, this polynomial vanishes in all the subsystems.

Adjustable Parameters

All analytical descriptions contain some parameters, which must be adjusted to the phases in question. Theoretically that can be done by a first principle calculation using quantum mechanics. But today that is possible with the necessary accuracy only in exceptional cases.

The most common way is, to derive these parameters from experimental values. Since the Gibbs energies are connected with all other thermodynamic functions of state, we can use all kinds of experimental thermodynamic values for that purpose. These are all kinds of calorimetric measurements as enthalpies of mixing, of melting or of transformation as well as heat contents or specific heats; special equilibrium measurements, like vapor pressure or electromotive forces of reversible galvanic cells, which yield partial Gibbs energies; and finally all quantitative phase diagram measurements like liquidus temperatures, solubility limits, eutectic or peritectic temperatures or even the amounts of two phases in equilibrium at a known composition and temperature.

To calculate the adjustable parameters from the experimental values we can use the least squares method, provided that there are enough values and that there are no systematic errors in the values [77Luk].

If there are only few parameters to be adjusted, the trial and error method may be used. Also this method may be very effective, if the influence of each parameter on the shapes of the curves describing thermodynamic functions is considered individually.

The least squares method compares each measured value with a value calculated using the chosen analytical descriptions with an initial set of the adjustable parameters. The difference is called "*Error*".

$$Error \quad = \quad measured\ value \ - \ calculated\ value \tag{9}$$

As condition of optimum the sum of the squares of these errors should have a minimum. To make errors of different types of measurements comparable, they must be multiplied by a weight factor. As weight factor the division by the estimated accuracy of the measurement is chosen [77Luk]. By this method we get dimensionless errors (fraction of error related to standard deviation or related to the 99% confidence range), which can be compared between all the different types of measured values.

$$error_i \quad = \quad Error_i / accuracy_i$$

$$\sum_i (error_i)^2 \ = \ Minimum \quad (i = \text{all measured values}) \tag{10}$$

To find the set of adjustable parameters ("coefficients"), which satisfies eq. (10), Gauss expanded the dependence of the errors on the coefficients into a Taylor series and truncated after the linear terms.

$$error = error_0 + \sum_j \frac{\partial error}{\partial coeff_j} \cdot \Delta coeff_j \quad (j = \text{all coefficients}) \qquad (11)$$

The conditions for the minimum, eq. (10) are:

$$\frac{\partial \sum_i (error_i)^2}{\partial coeff_j} = 2 \cdot \sum_i (error_i \cdot \frac{\partial error_i}{\partial coeff_j}) = 0 \qquad (12)$$

Eq. (11) inserted into eq. (12) yields a set of linear equations (Gaussian normal equations), which can be solved for the corrections $\Delta coeff_i$ of the coefficients. After severeal repetitions the coefficients usually converge to a final set.

The Gauss method is able to diverge, if the initial set of coefficients is chosen too far from the final set and if the linearization of eq. (10) is problematic. In this case the Marquardt method [65Mar], which combines the Gauss method with the steepest descent method, may help for convergence.

If some coefficients are not defined by the experimental values, the Gauss method may give strange results for them. As an example let us assume the enthalpy and entropy of formation of a phase are taken as unknown coefficients, but there are only measurements of the Gibbs energy of formation of this phase at one temperature or in a small range of temperatures only. The Gauss method tries to approximate the measured values by a straight line $G = H - T \cdot S$, where H and S are two adjustable parameters. As Fig. 1 shows, the G values measured at one temperature by their scatter define a vertical straight line, giving H and S infinite values. If G is measured in a small range of temperatures, the straight line tends to be more steep than the true function $H - T \cdot S$. Only, if either H is independently measured or if G is measured in a large range of temperatures, H and S both can be adjusted correctly. Otherwise only one of the parameters H and S can be adjusted. The other one must be estimated. Here a rule, given as Fig. 22 in the book of Kubaschewski and Alcock [67Kub] is helpful: $H = S \cdot T^*$, where T^* is a factor between 2000 and 4000 K.

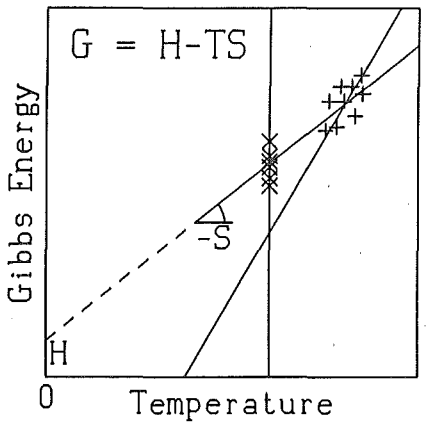

FIG. 1

Gibbs energy measured at one temperature only (×). or in a narrow range of temperatures (+)

Similar situations may occur with other coefficients, but they may be much less easily recognized than the above example. A help to detect them is the so called correlation matrix, which is derived from the inverse of the Gaussian normal equations (see eq. (3)) by normalizing the diagonal elements to unity.

Equilibrium Calculation.

After the analytical descriptions are chosen for each phase and the numerical values of the parameters are adjusted, equilibria can be calculated by the computer. One calculation gives a single equilibrium, for example a single tie line. Combining systematically many single equilibria results in a phase diagram.

The calculation uses the condition of minimal Gibbs energy, if temperature, pressure and amounts of components are kept constant. The conditions after Gibbs, that the chemical potentials of each component are equal in each phase, are equivalent and can also be used. Inserting the analytical descriptions into these conditions yields a set of nonlinear equations, which may be solved for the unknowns, e. g. the concentrations of the phases, by iteration methods, for example the Newton Raphson method.

For a two phase tie line for example first the temperature must be fixed. That means, we select a single tie line out of the whole two phase field. Then the Gibbs conditions give two equations for the two unknowns, the concentrations of the two phases. For a binary three phase equilibrium, which is nonvariant, the temperature is treated as an unknown. There are four independent equations in the Gibbs equilibrium conditions corresponding to the four unknowns, the concentrations of the three phases and the temperature.

To combine single equilibria to a whole phase diagram, two different strategies are used. Either the area of the phase diagram is mapped by a pattern of points, in each of which all possible equilibria are calculated. The stable one is that with the lowest Gibbs energy. The points now indicate the differnt fields of the phase diagram. If

necessary, the calculation may be continued with a more dense pattern of points in doubtful areas.

Another strategy first calculates the univariant equilibria (Two phase equilibria in a binary system) in steps of the temperature. These univariant equilibria start at the unary systems (pure components) at melting or transformation temperatures. Where they meet, nonvariant equilibria are expected and now can be calculated. From these nonvariant equilibria there start other univariant equilibria. Finally all the non- and univariant equilibria are found; metastable parts of them are recognized, where other equilibria are more stable (for example shown by a smaller solubility) [82Luk].

Also combinations of both strategies are used. The Thermo-Calc [85Sun] program in calculating a univariant equilibrium in steps of T, at each step asks, if another phase became more stable than the present equilibrium. There a nonvariant equilibrium is calculated. Now all the other univariant equilibria starting from there are calculated until all of them end at the boundaries or at $T = 0$ K.

Applications.

After these examples I want to mention some aspects, why such calculations are useful.

Reliability of Optimized Systems.

The first point of view is the reliability of a thermodynamically optimized system. The description is cross checked with all available experimental values from thermodynamics and from phase equilibria and therefore more reliable than a diagram derived from equilibrium measurements only. Thermodynamically impossible parts of the phase diagram can be avoided, for example initial slopes of liquidus and solidus, which are in contradiction to Raoult's law. On the other hand one has to be careful in selecting the analytical descriptions of the Gibbs energies, otherwise it may not be sufficient to describe the real Gibbs energies adequately.

Extropolation into Higher Order Systems

Another point of view is the approximate calculation of higher order systems from their boundary systems, if these are already optimized. The extrapolation of thermodynamic functions from the binary subsystems into a ternary system is much better defined than a pure geometrical extrapolation of the binary phase diagrams into a ternary diagram.

The same considerations are valid in going from ternary to quaternary systems, or to even higher order systems. The significance of the additional analytical terms is assumed to decrease with the order of the system.

If the systems already optimized are stored in a computer data bank, these extrapolations can be done quickly.

Graphical Representation of Higher Order Systems

For a complete graphical representation of a quaternary system as a $T-x$ diagram four dimensions are necessary. Usually it is not possible to represent this by projection into two dimensions without loosing clearness. The problem becomes still more important in higher systems. The phase diagrams are not constructed for themselves, but to answer specific questions, for example the path (number and concentrations of phases), which a selected sample follows on cooling.

As a computer has no difficulty to store information represented in four or more dimensions, it is possible to calculate answers on such questions and plot them directly in clear two dimensional diagrams. For the future it is just necessary to formulate such typical problems to be calculated from higher order systems and to construct typical plots for the answers.

Literature.

30Wag C. Wagner and W. Schottky, *Z. Phys. Chem.* **11** (1930) 163.

48Red O. Redlich and A. T. Kister, *Ind. Engng. Chem.* **40** (1948) 345.

60Bon E. Bonnier and R. Caboz, *C. R. Acad. Sci.* **250** (1960) 527.

60Koh F. Kohler, *Monatsh. Chemie* **91** (1960) 738.

63Mar D. W. Marquardt, *J. Soc. Indust. Appl. Math.* **11** (1963) 431.

65Too G. W. Toop, *Trans. AIME* **233** (1965) 850.

67Kub. O. Kubaschewski, E. Ll. Evans and C. B. Alcock, "Metallurgical Thermochemistry", Pergamon Press, Oxford, 1967.

75Mug Y.-M. Muggianu, M. Gambino and J.-P. Bros, *J. Chimie Physique* **72** (1975) 83.

77Luk H. L. Lukas, E.-Th. Henig and B. Zimmermann, *Calphad* **1** (1977) 225.

82Luk H. L. Lukas, J. Weiss and E.-Th. Henig, *Calphad* **6** (1982) 229.

85Sun B. Sundman, B. Jansson and J.-O. Andersson *Calphad* **9** (1985) 153.

Optimization of the Na–Tl System

R. Novaković, G. Ghosh*, H. L. Lukas, and M. M. Ristić**

Serbian Academy of Science and Art, Institute of Technical Science,
Knez Mihajlova 35/IV, YU–11000 Beograd

* Dept. of Materials Science and Engineering,
The Technological Institute, Northwestern University,
2145 Sheridan Road, Evanston, Il 60208, USA

** Max-Planck-Institut f. Metallforschung, Inst. f. Werkstoffwissenschaft, PML,
Heisenbergstr. 5, D–7000 Stuttgart 80

Abstract

The Na-Tl system was thermodynamically optimized, using the methods described in the previous lecture.

The liquid phase, the hcp and the bcc solid solution of Tl are described by Redlich Kister polynomials with three terms for enthalpy and entropy each. For the phase NaTl the Wagner Schottky model is chosen with antistructure atoms on the Na as well as on the Tl sublattice. The remaining phases, Na_6Tl, Na_2Tl and $NaTl_2$, are treated as stoichiometric phases.

To adjust the parameters of these thermodynamic descriptions experimental values from the literature (see references below) were used: Phase diagram values (liquidus temperatures, three phase equilibrium temperatures, and solubility limits of the phase NaTl), enthalpies of mixing of the liquid and partial Gibbs energies of Na in the liquid.

The calculation had to be done in several steps. The selection of these steps is described in detail. The resulting description is compared with the input experimental values, the agreement is good.

Introduction

A modern method in assessing phase diagrams is the thermodynamic optimization by computer. It was described in the previous lecture. Here the application on the Na–Tl binary system is described.

Experimental Values from the Literature.

Phase Diagram Data.

The first investigation 1902 by Kurnakov and Pushin [02Kur] shows only the liquidus line. In 1936 Grube and Schmidt [36Gru] established the whole phase diagram

by thermal analysis and electric resistivity. They found the phases Na_6Tl, Na_2Tl, NaTl, and $NaTl_2$. NaTl shows a large range of homogeneity and melts congruently at 305°C. The other phases are formed peritectically or peritectoidally and are strictly stoichiometric. The two modifications of Tl show large solubility for Na, wheras solid Na dissolves only ca. 1 mole% of Tl.

Thermodynamic Data.

The enthalpy of mixing of the liquid phase was measured calorimetrically by Kleinstuber [61Kle]. Some older calorimetric measurements of this quantity by us, not yet published, agree fairly well with these values. The enthalpy of formation of NaTl was determined by [41Kub]. The partial Gibbs energy of Na in the liquid phase was measured by several authors [49Hau, 60Mor, 66Mor, 70Bar, 76Mai, 84Iwa] using reversible galvanic cells, their results agree well.

Analytical Description of the Phases.

The descriptions of the pure elements after eq. (3) of the previous lecture were taken from the SGTE data file [88SGT]. They are listed in Table 1. The difference of the Gibbs energy G between stable bcc Na and the not stable hcp Na were taken from [88Sau].

TABLE 1.

Phase Stabilities of the Elements [88SGT]. (eq. (3) of previous contribution).

A	B	C	D	E	F
Na (bcc), 273 to 371 K					
24465.1	592.4073	−116.33780	0.537088	2705006.	$-5.18209\cdot10^{-4}$
Na (liquid), above 371 K					
−8007.6	−150.3931	37.46964	−0.019140	0.	$1.06119\cdot10^{-5}$
Tl (hcp), 273 to 507 K					
−7956.8	−93.4987	28.38960	−0.020360	0.	$4.49767\cdot10^{-5}$
Tl (bcc), 507 to 577 K					
−8848.2	−94.4609	27.15420	0.009581	0.	0.
Tl (liquid), above 577 K					
−4583.7	−97.9802	29.70640	0.000000	0.	0.

Phase stability of metastable Na (hcp), relative to Na (bcc) [88Sau].

Species	H	S
Na(hcp)	−104.0	−2.000

The concentration dependence of G of the liquid phase and of the solid solutions based on Na(bcc), Tl(bcc) and Tl(hcp) were described by Redlich Kister polynomials (eq. (6) of the previous lecture). The NaTl phase was described after the Wagner Schottky model, assuming antistructure atoms on both sublattices as the only relevant defects (eq. (7) of the previous lecture). The three strictly stoichiometric phases Na_6Tl, Na_2Tl and $NaTl_2$ were described each by an enthalpy and entropy of formation assuming C_p to obey Kopp Neumann's rule, that is to be equal to that of the mechanical mixture of the stable pure elements.

Optimization

A first attempt to use all the data simultaneously in the optimization program after [77Luk] failed. As the reason there was recognised: the coefficients describing the "defects" in the Wagner Schottky model for the phase NaTl and the coefficients describing the excess quantitities of the two solid solutions based on the solid Tl modifications are too sensitive to be easily defined by the measurements.

Therefore the least squares calculation was done excluding the two solid solutions based on Tl and the phase $NaTl_2$ and treating NaTl as a stoichiometric phase. Thus the coefficients describing the liquid (Redlich Kister formula with three terms ($m = 2$ in eq. (6) of the previous contribution)), the Na solid solution, the phases Na_6Tl and Na_2Tl and for the Wagner Schottky description of NaTl H^* and S^* only were defined. After that, H_{12}, H_{21}, S_{12} and S_{21} of the phase NaTl were adjusted by trial and error to the few experimental points showing the solubility limits of NaTl. The shapes of the two phase fields liquid + Tl(bcc) and Tl(bcc) + Tl(hcp) show, that there are very small differences between the excess terms of liquid and Tl(bcc) as well as between Tl(bcc) and Tl(hcp). These differences are much better defined than the excess terms themselves. Therefore in the next step the excess terms of Tl(bcc) were set equal to those of the liquid, then only the first Redlich Kister term was allowed to change in a following least squares calculation, where all the other coefficients were kept constant. This procedure resulted in a description, which reproduces the liquid + Tl(bcc) two phase field fairly well. Then the excess terms of Tl(hcp) were set equal to those of Tl(bcc), but here the three H terms of the Redlich Kister expression of Tl(hcp) could be adjusted, keeping the S terms constant. Finally the phase $NaTl_2$ was adjusted. Here only the G of formation at the temperature of its peritectoid formation is defined by measurements. Therefore the S of formation was given an estimated value of -5 J·K^{-1}·mol^{-1} and H of formation given the value, which makes G at the peritectoid temperature equal to the G value of the two phase equilibrium mixture of NaTl and Tl(hcp) at the same temperature and overall composition.

The resulting coefficients are listed in Table 2. In Figs. 1 to 3 the phase diagram, the enthalpy of mixing of the liquid and the chemical potential of Na in the liquid,

described by this optimized set of coefficients, are compared with the experimental points from the literature. The agreement is good.

TABLE 2.
The Optimized Excess Terms.

Phase	Type of model or polynom.	ν or parameter	A_ν or H	B_ν or S	Reference states
liquid	Redlich-Kister	0	−41669.8	−12.49337	liquid Na and Tl
		1	−300.0	−6.85134	
		2	6125.3	−1.63076	
Na(bcc)	Redlich-Kister	0	−19500.0	0.00000	Na(bcc) and Tl(bcc)
Tl(bcc)	Redlich-Kister	0	−41840.0	−12.49337	Na(bcc) and Tl(bcc)
		1	−300.0	−6.85134	
		2	6125.3	−1.63076	
Tl(hcp)	Redlich-Kister	0	−43430.0	−12.49337	Na(hcp) and Tl(hcp)
		1	−1170.0	−6.85134	
		2	6065.3	−1.63076	
Na_6Tl	Stoichiometric	$\Delta^f G$	−4786.0	0.00000	Na(bcc) and Tl(hcp)
Na_2Tl	Stoichiometric	$\Delta^f G$	−12800.0	−6.59750	Na(bcc) and Tl(hcp)
NaTl	Wagner Schottky	G^*	−14000.0	−2.19583	Na(bcc) and Tl(hcp)
		G_{21}	34000.0	18.78074	
		G_{12}	25300.0	1.93520	
$NaTl_2$	Stoichiometric	$\Delta^f G$	−12581.8	−5.00000	Na(bcc) and Tl(hcp)

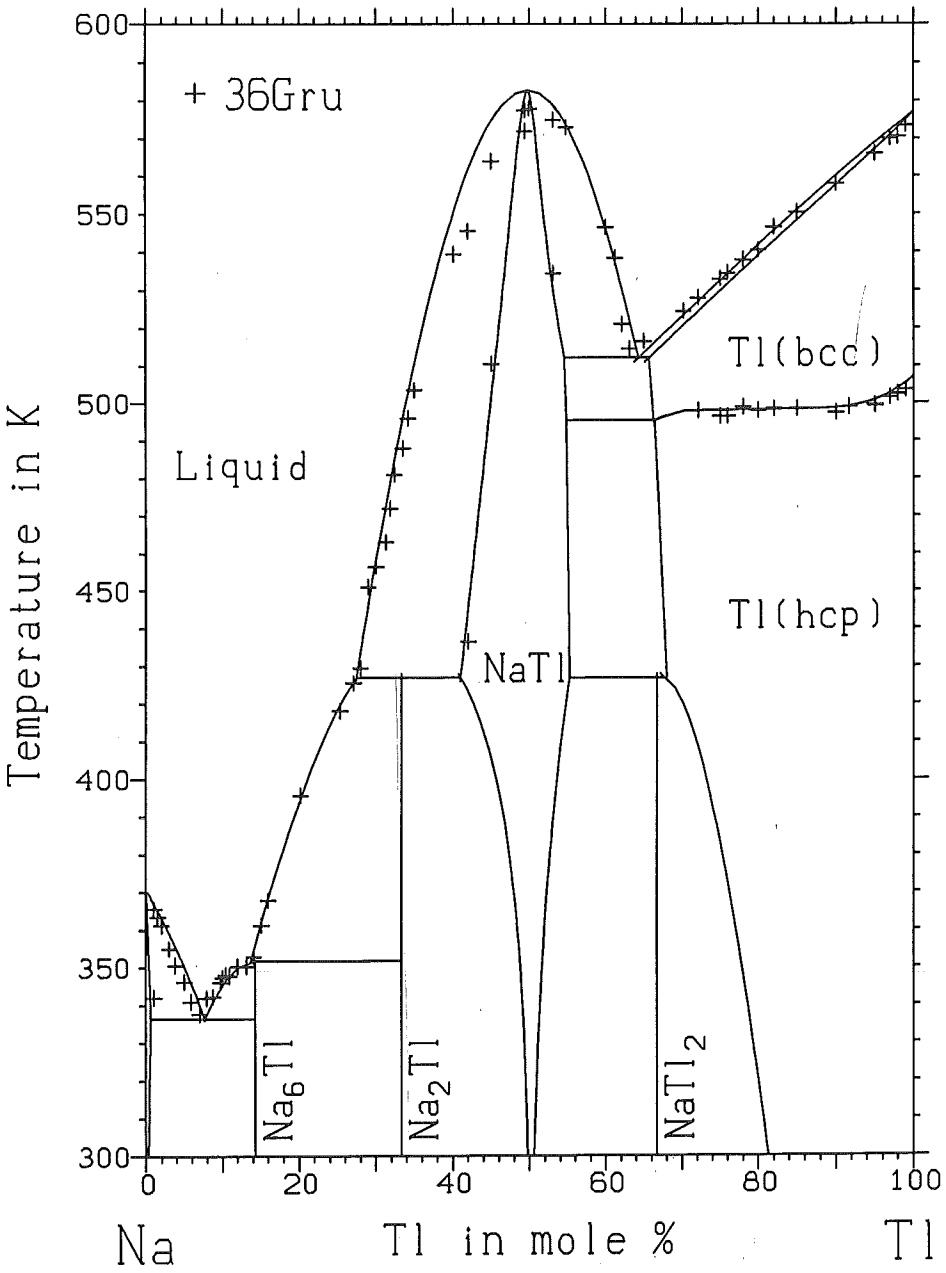

Fig. 1. The Na-Tl phase diagram

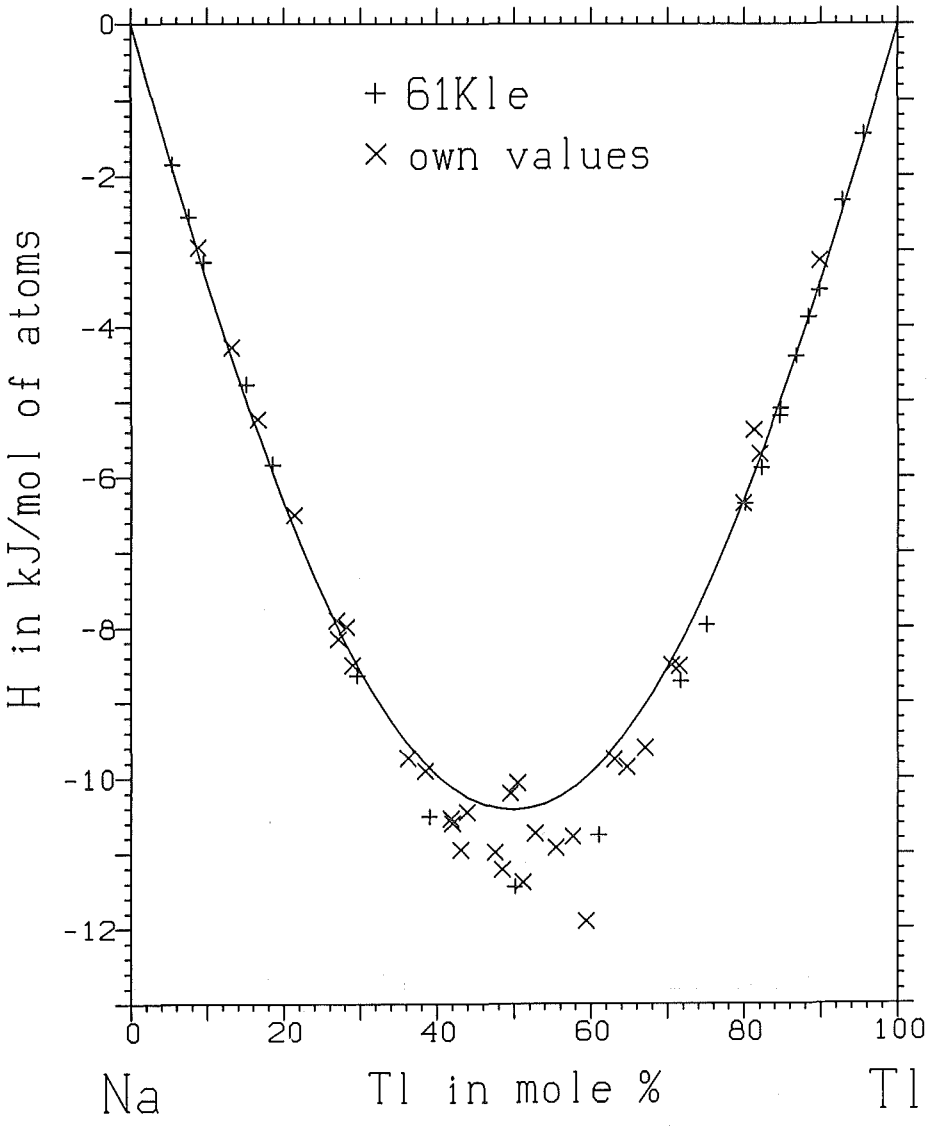

Fig. 2
Enthalpy of Mixing of
molten Na-Tl alloys

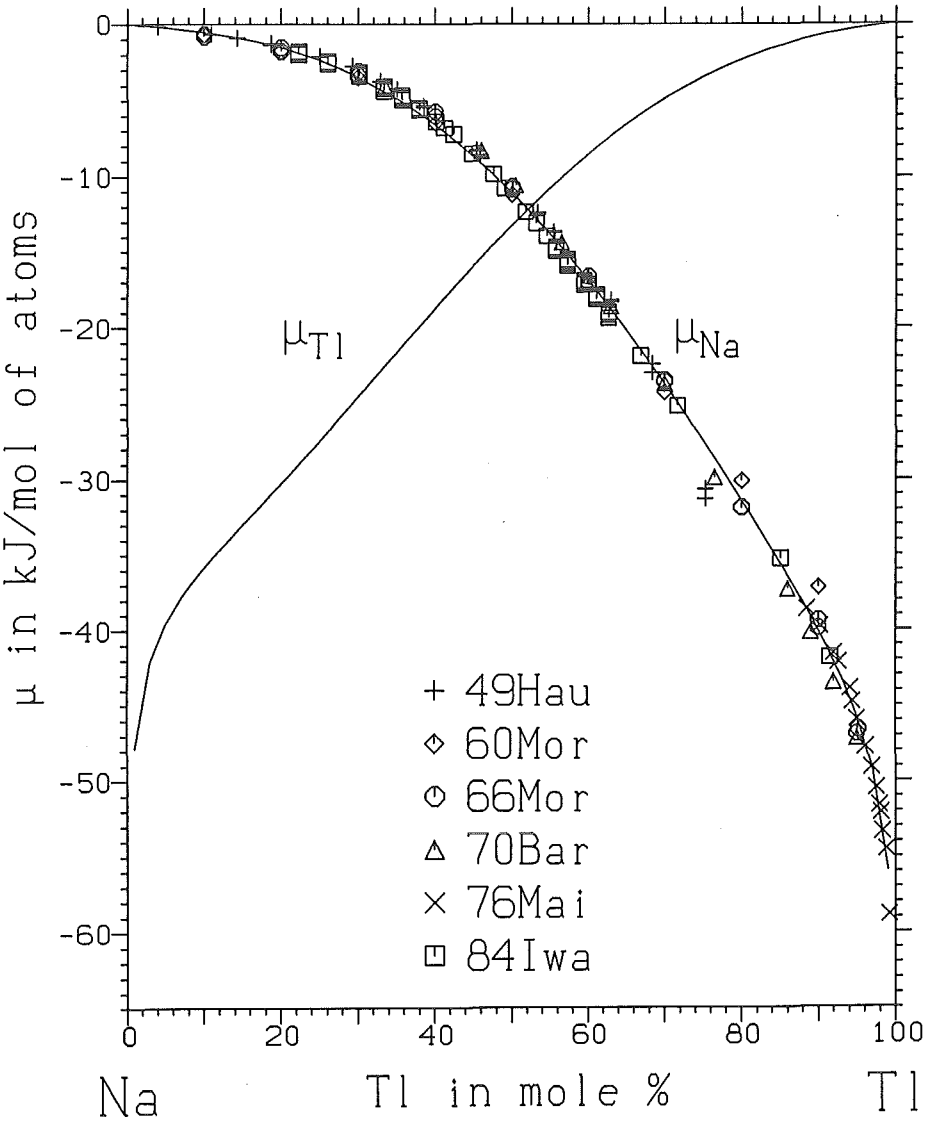

Fig. 3
Partial Gibbs Energies
of molten Na-Tl alloys

Literature

02Kur N. S. Kurnakov and N. A. Pushin, *Z. anorg. allg. Chem.* **30** (1902) 86., referenced by [36Gru].

36Gru G. Grube and A. Schmidt, *Z. Elektrochem.* **42** (1936) 201-209.

41Kub O. Kubaschewski, *Z. Elektrochem.* **47** (1941) 623-630.

49Hau K. Hauffe und A. L. Vierk, *Z. Elektrochem.* **53** (1949) 151-161.

60Mor A. G. Morachevskii and A. F. Alabyshev, *Izv. Vyssh. Uchebn. Zaved., Tsvetn. Metall.*, **1960** pp. 105-107

61Kle T. Kleinstuber, Ph. D. Thesis, Univ. München, 1961.

66Mor A .G. Morachevskii, S. I. Statsenko and V. B. Busse-Machukas, *Russ. J. Phys. Chem.* **40** (1966) 1395-1397.

70Bar H. E. Bartlett, A. J. Neethling and P. Crowther, *J. Chem. Thermodyn* **2** (1970) 583-590.

76Mai E. A. Maiorova and A. G. Morachevskii, *Izv. Vyssh. Uchebn. Zaved., Tsvetn. Metall.*, **1976** pp. 58-60.

77Luk H. L. Lukas, E.-Th. Henig and B. Zimmermann, *Calphad* **1** (1977) 225-236.

84Iwa M. Iwase, S. Sugino, E. Ichise and Y. Waseda, *High Temperature Materials and Processes*, **6** (1984) 143-153.

88Sau N. Saunders, A. P. Miodownik and A. T. Dinsdale, *Calphad* **12** (1988) 351-374.

88SGT The SGTE substance data file, version April 1988.

Phase relations in the Y-Si-Al-O-N system : Controlled manufacturing of α/ß-SiAlON composites

S. Bošković[1], K.G. Nickel[2] & G. Petzow[2]

[1]Boris Kidrič Institut, Vinča, Belgrade

[2]Max- Planck- Institut für Metallforschung
Institut für Werkstoffwissenschaft
Pulvermetallurgisches Laboratorium
Heisenbergstr. 5
D- 7000 Stuttgart 80

Abstract

A systematic study of phase relations in the Si_3N_4- rich corner of the Si_3N_4- $SiAl_2O_2N_2$- YAl_3N_4 plane of the Y- Si- Al- O- N system showed the existance of a compositional window in which composites of α- + ß- SiAlON coexisting with minor amounts of a glass phase may be obtained. Within this window the relative amount of either type of SiAlON is controlled by the Y- content and is nearly temperature independent in the range between 1600° to 1800° C.

Equilibrium is approached closely at 1600° C after 4hrs, at T ≥ 1700° C 2 hrs are sufficient.

Both α- and ß- SiAlON lattice parameters vary with composition. The data indicate a solubilty of Y in both types of SiAlON.

Introduction

Hardness and oxidation resistance of α- SiAlONs[1-3] give them a good potential for cutting tools and other applications. The development of composite α- ß- SiAlON ceramics is a feasible way to improve properties further, especially strength and fracture toughness.

Phase relations in the Y- Si- Al- O- N system were therefore the subject of a number of studies[4-6] but remain difficult and controversial e.g. whether there is a strong temperature dependence on the α- SiAlON formation[6] or just a compositional dependence[3].

α- SiAlON solid solutions may be described as $M_xSi_{16-(y+z)}Al_{(y+z)}O_zN_{16-z}$, where M is any modifying cation such as Ca or a rare earth element. α- SiAlON without modifying cations has only been synthesized at very low partial pressures of nitrogen[7].

In this study we focus on Y- bearing SiAlONs, in particular on those of the Si_3N_4- rich corner of the compositional plane between the endmembers Si_3N_4, α- and ß- SiAlON.

The formulas for stoichiometric ß- and α- SiAlONs are $Si_{6-x}Al_xO_xN_{8-x}$ and $Y_xSi_{12-(3x+y)}Al_{3x+y}O_yN_{16-y}$ respectively. From the formulation of α- SiAlONs it is clear that the cation/anion ratio differs from those of the ß- SiAlONs (3:4). The phase diagram description of the SiAlON solid solutions may either

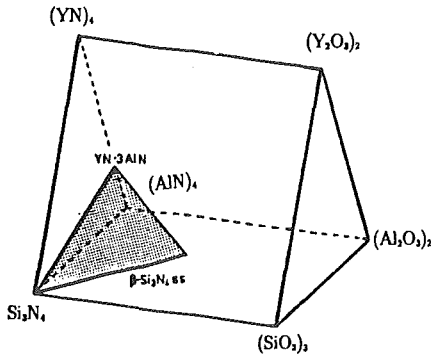

Fig. 1: Jänicke prism of the system Si_3N_4- SiO_2- Al_2O_3- AlN- - YN- Y_2O_3. The solid line indicates the extend of the ß- SiAlON solid solution series, the stippled area the theoretical range of α- SiAlONs.

be done on the basis of 3 cations or 4 anions (or multiples thereof). Accordingly phase diagrams will show different hypothetical end-members of α- and ß- SiAlONs. At a constant number of anions we have Si_3N_4 (pure silicon nitride), Al_3O_3N (ß- SiAlON) and YAl_3N_4 (YN·3AlN, α- SiAlON). We use a set with a constant number of cations, $Si_{12}N_{16}$, $Si_4Al_8N_8O_8$ and $Y_3Al_9N_{12}$, because the determined solid solution range of ß- SiAlON ends close to the composition $Si_4Al_8O_8N_8$[8]. The appropriate compositional plane in the Si_3N_4- SiO_2- - Al_2O_3- AlN- YN- Y_2O_3 concentration prism is shown in Fig. 1.

In the following we concentrate on the phase relationships and their consequences, i.e. how to manufacture the desired composite. The corresponding mechanical properties will be presented elsewhere[9].

Experiments and analytical procedures

Compositions in the $Si_{12}N_{16}$- $Si_4Al_8O_8N_8$- $Y_3Al_9N_{12}$ plane of the Y- Si- Al- - O- N system were prepared by attritor milling powders of Si_3N_4 (LC 12, Starck), Al_2O_3 (Alcoa), Y_2O_3 (Ventron) and AlN (Q:C, Starck) in isopropanol.

To avoid contamination and to obtain the desired composition Si_3N_4 milling balls were used and the oxygen content of AlN as analysed was taken into account during the process of preparing the mixtures.

The composition of the mixtures are listed in table 1 and shown in Fig. 2. The compositions have been chosen to allow for differing α/ß- ratios at equilibrium. The mixtures were hot- pressed at temperatures between 1600° C and 1800° C in a nitrogen atmosphere.

Table 1: Composition of starting mixtures

label	wt-% Si_3N_4	Y_2O_3	Al_2O_3	AlN	mole-% $Y_3Al_9N_9$	$Si_4Al_8O_8N_8$
A	82.96	2.5	5.8	8.6	4.29	14.80
B	90.62	3.5	0.0	5.9	5.88	3.31
C	85.80	3.5	3.5	7.2	5.90	10.64
D	82.40	3.5	5.5	8.8	5.92	14.92
E	78.90	5.7	4.3	11.1	9.65	14.50
F	79.90	7.1	1.6	11.3	11.97	10.09
G	73.53	7.1	5.2	14.2	12.10	17.85
H	75.70	7.4	3.4	13.5	12.61	14.31
I	75.56	9.2	0.8	14.4	15.61	10.47

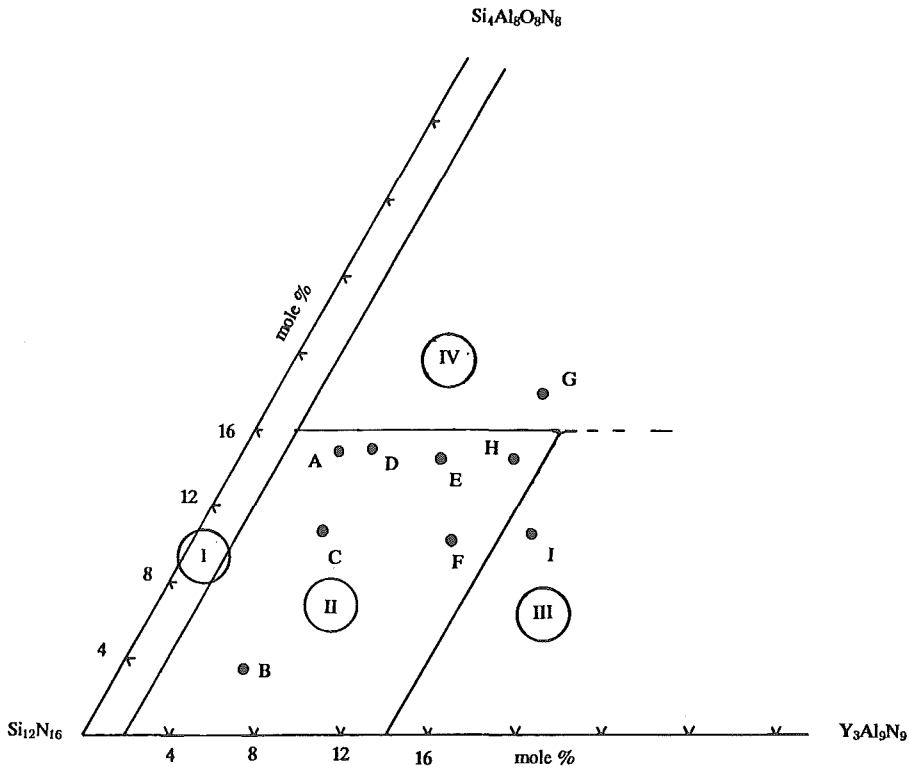

Fig. 2: Si_3N_4 rich corner of the compositional plane $Si_{12}N_{16}$-$Y_3Al_9N_{12}$ - $Si_4Al_8O_8N_8$ (stippled area in Fig. 1). Letters mark the positions of the compositions chosen in the experiments. Lines separate phase fields at 1600- 1800° C: I: ß- SiAlON, II: α- + ß- SiAlON, III: α- SiAlON, IV: α- + ß- SiAlON + phase x

To identify phases and to determine the relative contents of α- and ß- Si_3N_4 in the runs we have used XRD- measurements. From mixtures of α- and ß- Si_3N_4 of known composition we calibrated the relative intensities of the (210)- peaks $[I_\alpha/(I_\alpha+I_\beta)]$ as a function of the α:ß- ratio of the mixtures, which gives a linear relationship.

From the measured d- values we used the 110, 200, 210 reflexions to calculate the a parameter of the lattice according to

$$\frac{1}{d^2_{hkl}} = \frac{4}{3a^2}\,(h^2 - hk - k^2) + \frac{l^2}{c^2} \qquad \{ 1 \}$$

and the c parameter from pairs of reflection (α- Si_3N_4: 201/200 and 102/101; ß- Si_3N_4: 111/110 and 201/200) according to

$$\sin^2\Theta_{hkl} = \frac{\lambda}{3a^2}\,(l^2 - hk - k^2) + \frac{\lambda}{4c^2}\,l^2 \qquad \{ 2 \}.$$

Results

We have used mixtures A and E to determine the time necessary to obtain equilibrium by hotpressing at 1600° C and 1800° C. We have varied run times between ½ to 8 hrs and determined the relative amounts of α- and ß- Si_3N_4 subsequently.

The results of the time study are shown in Fig. 3. The run products coexist in each case with a remaining glass phase (1- 5Vol%). The determination of α/ß- ratios is estimated to be accurate to ± 5 Vol%.

In view of the low percentage of remaining glass phase it is assumed that after 4 hrs at 1600° C and 2 hrs at 1800° C equilibrium is approached close enough to allow an evaluation of the system.

Fig. 3 demonstrates that equilibrium is approached quickly at high temperatures (1- 2 hrs at 1700- 1800° C) and can only be compared with longer run durations (≥ 4 hrs) at 1600° C. Studies at still lower temperatures will therefore produce results with kinetic significance only.

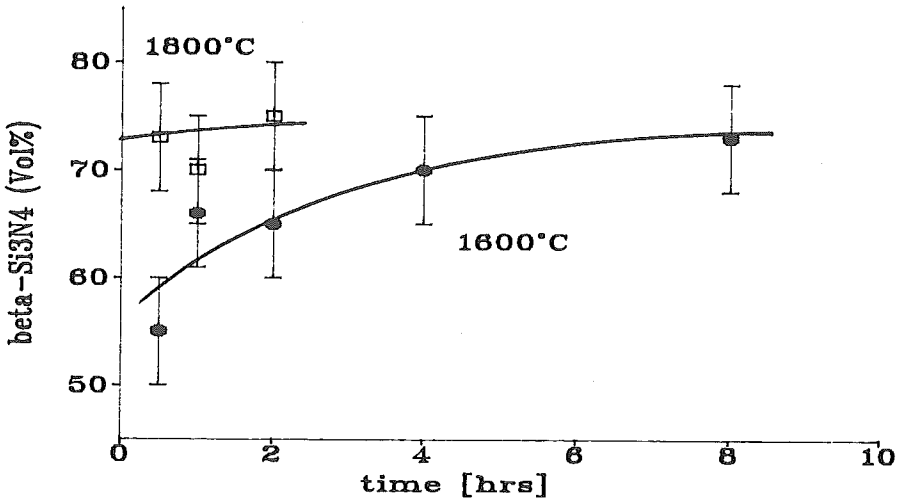

Fig. 3: Time vs. ß/α- SiAlON ratio (Vol.%) for hot- pressed starting material A at 1600° C (dots) and 1800° C (squares).

Experimental data are presented in table 2. In addition to the results on the relative amounts of SiAlONs lattice parameters for α- and ß- SiAlONs are given for the runs accepted as close to equilibrium. It was not possible in all cases to determine the lattice parameters, because a large fraction of the phase is needed to determine the d- values of the peaks accurately enough to allow such an analysis.

All runs with composition G showed the presence of another phase (x). Because it was only a minor phase it could not be identified positively. The phase regions in Fig. 2 are drawn accordingly.

Table 2: Experimental Results

Compos.	T °C	time hrs	ß-SiAlON Vol%	lattice parameter of SiAlONs (Å) a (ß)	c (ß)	a (α)	c (α)
A	1600	0.5	55				
		1.0	66				
		2.0	65				
		4.0	70	7.619	2.916		
		8.0	73				
	1700	2.0	70	7.644	2.925		
	1800	0.5	73				
		1.0	70				
		2.0	75	7.646	2.928		
B	1700	2.0	65	7.630	2.926	7.764	5.682
	1800	2.0	65	7.635	2.923	7.808	5.644
C	1600	4.0	68	7.594	2.921		
	1700	2.0	70	7.576	2.915		
	1800	2.0	73	7.613	2.919		
D	1700	2.0	71	7.645	2.928		
E	1600	0.5	37				
		1.0	33				
		2.0	34				
		4.0	44	7.621	2.944	7.792	5.658
		8.0	43				
	1700	2.0	44				
	1800	0.5	43				
		1.0	41				
		2.0	49	7.629	2.929	7.811	5.683
F	1700	2.0	24				
	1800	2.0	19	7.628	2.919	7.809	5.694
G┐	1700	2.0	30				
	1800	2.0	25	7.627	2.933	7.803	5.682
H	1700	2.0	25				
	1800	2.0	19	7.625	2.934	7.807	5.675
I	1600	2.0	0				
	1700	2.0	0				
	1800	2.0	0			7.799	5.681

┐ additional phase (x) present;

Discussion

α- SiAlONs are stabilized by Y, the big Y^{3+}- ion may be accustomed in interstitial sites of its lattice. Y in α- SiAlON has, despite its size, a decreasing effect on the unit cell, because the interstitial positions have short bond length. The substitution of Al for Si causes an increase of the cell volume because of differing ionic radii.

ß- SiAlON has the formula $Si_{6-x}Al_xO_xN_{8-x}$, the solution of Al_3O_3N in it increases its unit cell[10]. For crystallographic reasons Y is difficult to accomodate in ß- SiAlON. In order to evaluate the possibility of Y- substitution in ß- SiAlON we plotted the lattice parameter data of the compositions A, D, E, and H in Fig. 4, because they do change little in their Al/O content (14.3 - 15 mole% $Si_4Al_8O_8N_8$), but spread in Y.

There is a strong correlation of the a parameter of ß- SiAlON with the Y- content of the bulk composition (Fig. 4), indicating a solubility of Y in ß- SiAlON. Some data[3] obtained with an analytical transmission electron microscope showed an apparent solubility of app. 0.5 wt% Y.

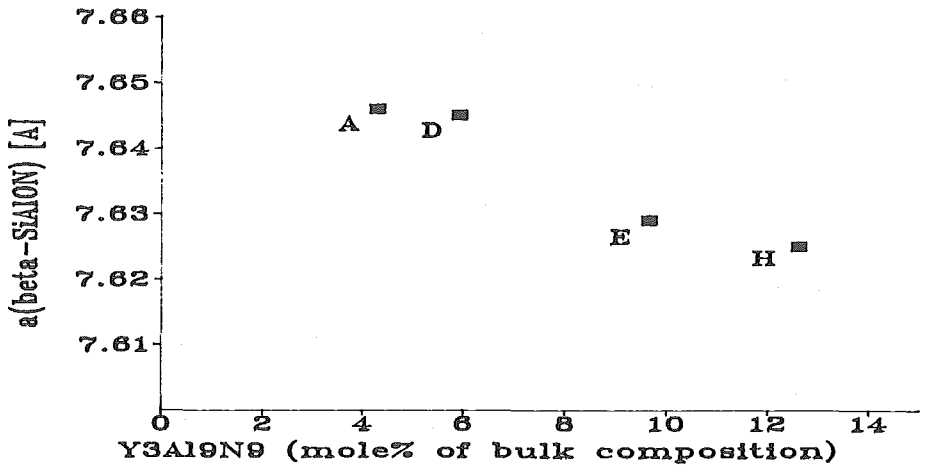

Fig. 4: Variation of lattice parameter a of ß- SiAlON with changing bulk composition at 1700- 1800° C. Letters correspond to the compositions listed in table 1.

Comparing the α/ß- ratios of a given composition (table 2) at equilibrium it is obvious that the ratio is not strongly temperature dependent. Using all data of this work Fig. 5 shows that the ratio is mainly controlled by the Y- content of the bulk composition.

The regression of the data plotted in Fig. 5 for individual temperatures are listed in table 3. These regressions indicate a slight temperature dependency. The intercepts of the regression lines with the x- coordinate ($Y_3Al_9N_9$ in mole%) moves towards higher values with increasing temperature. Hence there is an increasing Y- content of the bulk composition, at which no α- SiAlON is formed. This is a further proof for the solubility of Y in ß- SiAlON and an indication that this solubility increases with increasing temperature.

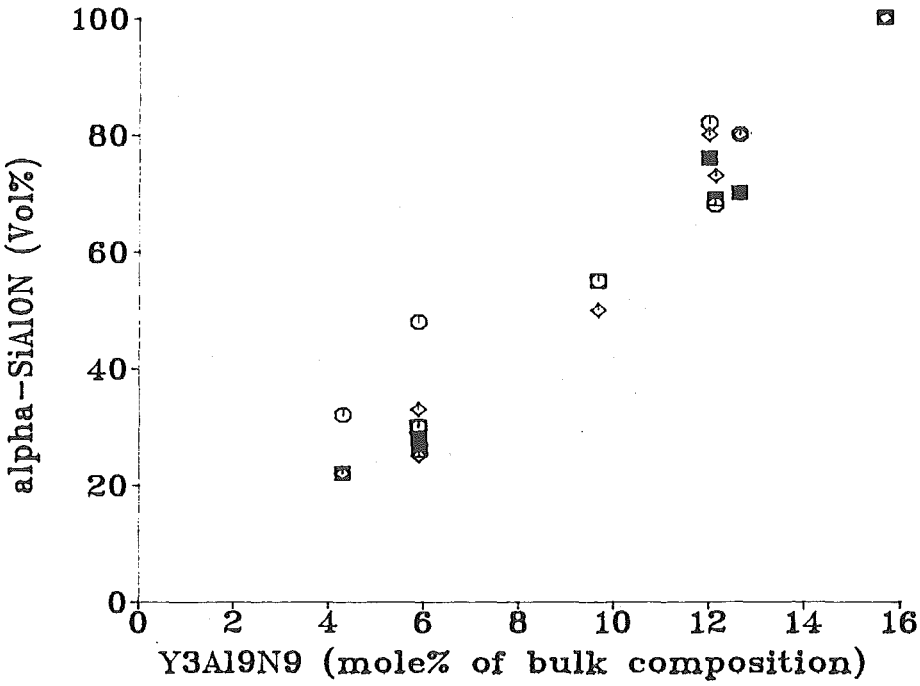

Fig. 5: Volume- % α- SiAlON in the composite for different Y- contents of the bulk composition at 1600° C (circles), 1700° C (diamonds) and 1800° C (squares).

For the practical purpose of manufacturing a particular composite it is of no consequence, whether the α/ß- ratio is obtained as a metastable or equilibrium value. However, as has been shown above, at temperatures ≥ 1700° C equilibrium in this part of the Si- Al- O- N- Y system is approached rather quickly. It is therefore advisable to use the straightforward relations shown in Fig. 5 and table 3 to manufacture the desired composite.

Table 3: Covariance of α/ß- SiAlON (Vol%) with Y- content calculated as
α- SiAlON(Vol%) = a · $Y_3Al_9N_{12}$(mole%) + b

T(°C)	a	b	r
1600	6.42	-2.33	.992
1700	6.58	-5.24	.989
1800	7.03	-9.23	.987

r: corr.coeff.

Acknowledgements

We greatfully acknowlege support and funding from a bilateral project ("composites") between our institutes, organized by the International Bureau of the KFA Jülich within the framework of German- Yugoslav agreements (YUZAMS).

References:

[1]K.H. Jack and W.I. Wilson, "Ceramics Based on the Si- Al- O- N and Related Systems.", *Nature Phys.Sci.* 238, 28- 29 (1972)

[2]M. Mimoto, H. Tanaka and K. Muramatsu, "The strength of α- SiAlON Ceramics", *J.Mater.Sci.* 15: 2661- 2662 (1980)

[3]D. Peuckert, "Herstellung und Untersuchung von mehrphasigen Si_3N_4- Mischkristallkeramiken", PhD thesis, University of Stuttgart, 159 pp, (1987)

[4]Z.- K. Huang, P. Greil and G. Petzow, "Formation of α- Si_3N_4 Solid Solutions in the System Si_3N_4- AlN- Y_2O_3", *J.Am.Ceram.Soc.* 66: C 96- 97 (1983)

[5]W.Y. Sun, Z.- K. Huang, G.Z. Cao and D.S. Yan, "Phase relationships involving mixed O'- ß'- SiAlONs in the Y- Si- Al- O- N system", *Int.J.High Techn.Ceramics*, 3: 277- 284 (1987)

[6]W.Y. Sun, F.Y. Wu and D.S. Yan, "Studies of the Formation of α' and α'- ß' SiAlON", *Mat.Lett.* 6, 11- 15 (1987)

[7]M. Fukuhara, "Effect of Nitrogen on the α/ß phase conversion in silicon nitride", *J.Am.Ceram.Soc.*, 68, C- 226- 228 (1985)

[8] L.J. Gauckler, H.L. Lukas and G. Petzow, "Contribution to the Phase Diagram Si_3N_4- AlN- Al_2O_3- SiO_2", *J.Am.Ceram.Soc.* 58, 346- 347 (1975)

[9]S. Bošković and K.G. Nickel, "Microstructure and properties of α/ß SiAlON composites", 1st European Ceramic Conference, Maastricht, *Abst.Vol* (1989)

[10]S. Wild, H. Elliott and D.P. Thomson, "Combined Infra- Red and X- ray studies of ß- Silicon Nitride and ß'- SiAlONs", *J.Mater.Sci*, 13

PARTICIPANTS' ADDRESSES

Angelopoulos, Dr. George

University of Patras
Institute of Physical Metallurgy
GR - 26110 Patras
GREECE
Tel.: 0030/61/991832

Bossert, Dipl.-Ing. Jörg

Rhein.-Westf. Technische Hochschule
Aachen
Institut für Gesteinshüttenkunde
Mauerstr. 5
D - 5100 Aachen
Tel.: 0241/80-4967
Fax: 0241/26085

Brook, Prof. Dr. Richard J.

Max-Planck-Institut
für Metallforschung
Institut für Werkstoffwissenschaft
Pulvermetallurgisches Laboratorium
Heisenbergstr. 5
D - 7000 Stuttgart 80
Tel.: 0711/6861-202
Fax: 0711/6861-131

Čeh, Dipl.-Ing. Miran

Jožef Stefan Institute
Edvard Kardelj University, Ljubljana
P.O.B. 100
Jamova 39
YU - 61000 Ljubljana
YUGOSLAVIA
Tel.: 0038/61/214-399, -341
Telex: 31296 JOSTIN YU

Claaßen, Dipl.-Ing. Thomas

Technische Universität
Hamburg-Harburg
AB Technische Keramik
Postfach 90 14 03
Harburger Schloßstr. 20
D - 2100 Hamburg 90
Tel.: 040/7718-2363
FAX: 040/7718-2288

Djurić, Dr. Branko

Boris Kidrič Institute
of Nuclear Sciences, Vinča
Institute of Materials
P.O.B. 522
YU - 11001 Beograd
YUGOSLAVIA
Tel.: 0038/11/439454
FAX: 0038/11/4440175

Dužević, Dr. D.

Rade Končar -
Electrotechn. Institute
Baštijanova bb
YU - 41000 Zagreb, Croatia
YUGOSLAVIA

Fetahagić, MSc., Arifa

Kernforschungszentrum Karlsruhe
IMF
Postfach 36 40
D - 7500 Karlsruhe 1
Tel.: 07247/82-2918, -2916
Telex: 17724716

Fetahagić, MSc., Tarik

Universität Karlsruhe
Institut für Keramik im Maschinenbau
Haid- und Neu-Straße 7
D - 7500 Karlsruhe 1
Tel.: 0721/608-4246
Telex: 17721170

Gašić, Dr. Miroslav

Boris Kidrič Institute
of Nuclear Sciences, Vinča
Mat. Dept.
P.O.B. 522
YU - 11001 Beograd
YUGOSLAVIA
Tel.: 0038/11/458-222, -780
FAX: 0038/11/4440175

Greil, Prof. Dr.-Ing. Peter

Technische Universität
Hamburg-Harburg
Arbeitsbereich Keramik
Forschungsschwerpunkt 2
Postfach 90 14 03
Harburger Schloßstr. 20
D - 2100 Hamburg 90
Tel.: 040/7718-2383
FAX: 040/7718-2288

Gutsfeld, Dipl.-Ing. Christoph

Kernforschungszentrum Karlsruhe
IMF I
Postfach 36 40
D - 7500 Karlsruhe
Tel.: 07247/82-2876
Telex: 17724716

Janssen, Dipl.-Ing. Rolf

Technische Universität
Hamburg-Harburg
AB Technische Keramik
Postfach 90 14 03
Harburger Schloßstr. 20
D - 2100 Hamburg 90
Tel.: 040/7718-2802
FAX: 040/7718-2288

Kaysser, Dr. Wolfgang

Max-Planck-Institut
für Metallforschung
Institut für Werkstoffwissenschaft
Pulvermetallurgisches Laboratorium
Heisenbergstr. 5
D - 7000 Stuttgart 80
Tel.: 0711/6861-105
Fax: 0711/6861-131

Kevorkijan, MSc., Varužan

Jožef Stefan Institute
Edvard Kardelj University, Ljubljana
P.O.B. 100
Jamova 39
YU - 61000 Ljubljana
YUGOSLAVIA
Tel.: 0038/61/214-399
Telex: 31296 JOSTIN YU

Kolar, Prof. Dr. Drago

Jožef Stefan Institute
Edvard Kardelj University, Ljubljana
P.O.B. 100
Jamova 39
YU - 61000 Ljubljana
YUGOSLAVIA
Tel.: 0038/61/214-399
Telex: 31296 JOSTIN YU
Fax: 0038/61/219-385

Komac, Dr. Miloš

Jožef Stefan Institute
Edvard Kardelj University, Ljubljana
P.O.B. 100
Jamova 39
YU - 61000 Ljubljana
YUGOSLAVIA
Tel.: 0038/61/214-399
Telex: 31296 JOSTIN YU
Fax: 0038/61/219-385

Koneska, Dr. Zagorka

University Kiril i Metodij
Faculty of Technology and Metallurgy
Rudjer Bošković 16
YU - 91000 Skopje
YUGOSLAVIA
Tel.: 0038/91/259725

Kosmač, Dr. Tomaž

Jožef Stefan Institute
Edvard Kardelj University, Ljubljana
P.O.B. 100
Jamova 39
YU - 61000 Ljubljana
YUGOSLAVIA
Tel.: 0038/61/214-399
FAX: 0038/61/219-385

Kostić, Dr. P.

SASA
Serbian Academy of Sciences and Arts
Institute of Technical Sciences
Knez Mihajlova 35
YU - 11000 Beograd
YUGOSLAVIA
Tel.: 0038/11/637-239

Krawczynski, Dr. Johanna

Kernforschungsanlage Jülich GmbH
Internationales Büro
Postfach 19 13
D - 5170 Jülich
Tel.: 02461/61-3422, -3388
Telex: 83355630 kf d
Fax: 02461/61-3635

Lukas, Dr. H.L.

Max-Planck-Institut
für Metallforschung
Institut für Werkstoffwissenschaft
Pulvermetallurgisches Laboratorium
Heisenbergstr. 5
D - 7000 Stuttgart 80
Tel.: 0711/6861-106
Fax: 0711/6861-131

Miloševski, Prof. Dr. Miloslav

University Kiril i Metodij
Faculty of Technology and Metallurgy
Rudjer Bošković 16
YU - 91000 Skopje
YUGOSLAVIA
Tel.: 0038/91/259725-84

Mitkov, Dr. Mirjana

Boris Kidrič Institute
of Nuclear Sciences, Vinča
Institute for Materials
P.O.B. 522
YU - 11001 Beograd
YUGOSLAVIA
Tel.: 0038/11/4440871-779
FAX: 0038/11/4440175

Naoumidis, Dr. Aristides

Kernforschungsanlage Jülich
Institut für Reaktorwerkstoffe
P.O.B. 19 13
D - 5170 Jülich
Tel.: 02461/61-3059
Telex: 8335560 kf d

Nickel, Dr. Klaus

Max-Planck-Institut
für Metallforschung
Institut für Werkstoffwissenschaft
Pulvermetallurgisches Laboratorium
Heisenbergstr. 5
D - 7000 Stuttgart 80
Tel.: 0711/6861-208
Fax: 0711/6861-131

Nikolopoulos, Prof. Dr. Panajotis

University of Patras
Institute of Physical Metallurgy
Dept. of Chemical Engineering
GR - 26110 Patras
GREECE
Tel.: 0030/61/991832

Novaković, MSc., Rada

SASA
Serbian Academy of Sciences and Arts
Committee for Physical Chemistry
Knez Mihajlova 35/IV
YU - 11000 Beograd
YUGOSLAVIA
Tel.: 0038/11/187-144, -151

Oberacker, Dr. Rainer

Universität Karlsruhe
Institut für Keramik im Maschinenbau
Haid- und Neu-Straße 7
D - 7500 Karlsruhe 1
Tel.: 0721/608-4246
Telex: 17721170

Ondracek, Prof. Dr. Gerhard

Rhein.-Westf. Technische Hochschule
Aachen
Institut für Gesteinshüttenkunde
Mauerstr. 5
D - 5100 Aachen
Tel.: 0241/80-4966
Telex: 832704 thac d

Pejovnik, Prof. Dr. Stanko

Boris Kidrič Institute
of Chemistry
Hajdrihova 19
YU - 61000 Ljubljana
YUGOSLAVIA
Tel.: 0038/61/263-380
Fax: 0038/61/263-285

Petzow, Prof. Dr. Günter

Max-Planck-Institut
für Metallforschung
Institut für Werkstoffwissenschaft
Pulvermetallurgisches Laboratorium
Heisenbergstr. 5
D - 7000 Stuttgart 80
Tel.: 0711/6861-200
Fax: 0711/6861-131

Popov, Prof. Dr. B.N.

University Kiril i Metodij
Faculty of Technology and Metallurgy
Rudjer Bošković 16
YU - 91000 Skopje
YUGOSLAVIA
Tel.: 0038/91/259-725, -726

Rottmann, Dr. J.

Kernforschungsanlage Jülich GmbH
Institut für Reaktorwerkstoffe
P.O.B. 19 13
D - 5170 Jülich
Tel.: 02461/61-5704

Schulz, Dr. Brigitte

Kernforschungszentrum Karlsruhe
Institut für Material- und
Festkörperforschung
P.O.B. 36 40
D - 7500 Karlsruhe 1
Tel.: 07247/82-3884, - 3885
FAX: 07247/82-5070

Seide, Dipl.-Min. Otmar

Rhein.-Westf. Technische Hochschule
Aachen
Institut für Gesteinshüttenkunde
Mauerstr. 5
D - 5100 Aachen
Tel.: 0241/80-4993

Sindel, Dipl.-Ing. Manfred

Technische Universität
Hamburg-Harburg
AB Technische Keramik
Postfach 90 14 03
Harburger Schloßstr. 20
D - 2100 Hamburg 90
Tel.: 040/7718-2364
FAX: 040/7718-2288

Slavkov, Dr. Dragan

University Kiril i Metodij
Faculty of Technology and Metallurgy
Rudjer Bošković 16
YU - 91000 Skopje
YUGOSLAVIA
Tel.: 0038/91/259-725

Spaseska, Dr. Dijana

University Kiril i Metodij
Faculty of Technology and Metallurgy
Rudjer Bošković 16
YU - 91000 Skopje
YUGOSLAVIA
Tel.: 0038/91/259-725

Stamenković, Dr. Ivan

Rhein.-Westf. Technische Hochschule
Aachen
Institut für Gesteinshüttenkunde
Mauerstr. 5
D - 5100 Aachen
Tel.: 0241/80-4967

Thümmler, Prof. Dr.-Ing. Fritz

Kernforschungszentrum Karlsruhe
Universität Karlsruhe
P.O.B. 36 40
D - 7500 Karlsruhe 1
Tel.: 07247/82-2918
Telex: 17724716

Trubelja, Dr. Mladen

"Energoinvest" - CIRM
Stup, Tvornička 3
YU - 71000 Sarajewo
YUGOSLAVIA

Uskoković, Prof. Dr. Dragan

SASA
Serbian Academy of Sciences and Arts
Institute of Technical Sciences
Knez Mihajlova 35
YU - 11000 Beograd
YUGOSLAVIA
Tel.: 0038/11/637-239

**Joint German-Indonesian Seminar on
R & D Activities using the MPR-30**

Jakarta August 19-21, 1985

GERMAN-INDONESIAN COOPERATION

ISBN 3-89336-011-5

**Joint German-Indonesian seminar on
Public Acceptance, Waste-Management, and Nuclear Safety**

Jakarta, October 7-9, 1986

GERMAN-INDONESIAN COOPERATION

ISBN 3-89336-012-3

**VIIIth German-Yugoslav Meeting on Materials Science and Development
Ceramics and Metals**

edited by Drago Kolar, Marija Kosec and Johanna Krawczynski

Brdo pri Kranju, May 18-21, 1987

GERMAN-YUGOSLAV COOPERATION

ISBN 3-89336-001-8

**Proceedings of the Fourth Workshop
on Two-Phase Flow Predictions**

edited by M. Sommerfeld and H. Zeisel

Erlangen, October 21-23, 1987

GERMAN-YUGOSLAV COOPERATION

ISBN 3-89336-002-6

IInd Workshop on Process Automation

Darmstadt, November 2-6, 1987

GERMAN-YUGOSLAV COOPERATION

ISBN 3-89336-003-4

**Ist German-Yugoslav Meeting in the
Framework of the Bilateral Project
Development of Innovation Structures in Yugoslavia**

edited by G. Bräunling and V. Matejić

Innovation Consultancy Centers Plitvice September 5-7, 1988

GERMAN-YUGOSLAV COOPERATION

ISBN 3-89336-024-7

**Proceedings of the 8th Winter Scool on
Proteinases and their Inhibitors: Recent Developments**

edited by E. Auerswald, H. Fritz and V. Turk

Tiers, March 8-12, 1989

GERMAN-YUGOSLAV COOPERATION

ISBN 3-89336-020-4

**Second German-Greek Workshop on
Materials Research for Information Technology**

edited by G. Kaiser and H. Wenzel

Jülich, May 22-23, 1989

GERMAN-GREEK COOPERATION

ISBN 3-89336-018-2

Seminar Fertigungsplanung und -steuerung

zusammengestellt von
Burghild Wieneke-Toutaoui, Rolf Albrecht

Split, 7. und 8. Juni 1989

GERMAN-YUGOSLAV COOPERATION

ISBN 3-89336-025-5

Vertrieb: KFA Jülich GmbH, Zentralbibliothek
Postfach 1913 D-5170 Jülich
Telefon: 02461/61-5367 Telex: 833556-70 kfa d

ISSN 0944-2952